CHARACTERIZATION OF MOLECULAR EXCITED STATES FOR NONLINEAR OPTICS

By

ROBERT J. KRUHLAK

A dissertation submitted in partial fulfillment of
the requirements for the degree of

DOCTOR OF PHILOSOPHY

WASHINGTON STATE UNIVERSITY
Department of Physics

May 2000

To the Faculty of Washington State University:

The members of the Committee appointed to examine the dissertation of ROBERT J. KRUHLAK find it satisfactory and recommend that it be accepted.

_____

Chair

_____

_____

_____

ACKNOWLEDGEMENTS

I would like to thank my advisor, Mark Kuzyk, for all his help, patience, and enthusiasm. I would also like to thank my family and friends for all their wonderful support. We acknowledge the Air Force Office of Scientific Research and the Alberta Heritage Scholarship Fund for generously supporting this work, professor Kaino for supplying the deuterated MMA, professor Dirk for supplying the squaraine dyes, and Dr. Sounik for supplying the SiPc dye.

CHARACTERIZATION OF MOLECULAR EXCITED STATES
FOR NONLINEAR OPTICS

Abstract

by Robert J. Kruhlak, Ph.D.

Department of Physics

Washington State University

May 2000

Chair: Mark G. Kuzyk

Organic nonlinear optics is a fast growing sub-field of nonlinear optics where the organic dye molecules control the nonlinear properties of the system and the polymer host controls the bulk properties of the system. This dissertation reports on the fabrication and characterization of dye-doped thin films and multimode fibers. We use several traditional and one novel technique to probe molecular excited states. The novel spectroscopic technique is applicable to optical fibers and is called side-illumination fluorescence spectroscopy. We characterize both linear and nonlinear optical responses using both the standard Lorentzian model and a novel inhomogeneous-broadening model for electronic transitions.

Contents

Acknowledgements **iii**

List of Figures **xxvi**

List of Tables **xxviii**

1 Introduction **1**

1.1 Conventions and Units . . . 3

1.2 Dye Molecules . . . 6

1.2.1 Squaraines . . . 7

1.2.2 Phthalocyanines . . . 10

1.3 Nonlinear Transverse Loss . . . 13

1.4 Laser-induced Color Changes . . . 16

1.5 Transverse Fluorescence . . . 20

1.6 Side-illumination Fluorescence . . . 21

1.7 Laser induced color changes via SIF . . . 24

1.8 Quadratic Electroabsorption . . . 25

1.9 Reading this dissertation . . . 26

2 Theory **32**

2.1 Nonlinear Polarization . . . 33

2.2 Molecular vs. Bulk . . . 35

2.3 Time-dependent perturbation theory . . . 39

2.4 Energy denominators . . . 40

2.4.1 Homogeneous-Broadening . . . 41
2.4.1.1 First-order . . . 42
2.4.1.2 Third-order . . . 43
2.4.2 Inhomogeneous-Broadening . . . 44
2.4.2.1 First-order . . . 46
2.4.2.2 Third-order . . . 50
2.4.2.2.1 Third harmonic generation (THG) . . . 56
2.4.2.2.2 Quadratic electrooptic effect . . . 73
2.4.2.2.3 Optical Kerr effect . . . 91
2.5 Molecular Reorientation . . . 115
2.6 Guest-Host systems . . . 115
2.6.1 Core Fibers and Preforms . . . 116
2.6.2 Electrooptic Thin Films . . . 118
2.7 Fluorescence Generation . . . 120
2.7.1 Side-illumination . . . 121
2.7.1.1 Plane wave source . . . 122
2.7.1.2 Point source . . . 123
2.7.2 Correlation length . . . 124
2.8 Photosensitivity . . . 127

3 Sample Preparation 134

3.1 Thin Film Fabrication . . . 134
3.1.1 Electrooptic ITO slides . . . 134
3.1.2 Thin film solution . . . 136
3.1.3 Electrooptic thin film . . . 137
3.2 Fiber Fabrication . . . 139
3.2.1 Preparation of monomer . . . 139
3.2.2 Dye-doped polymer fabrication . . . 141
3.2.3 Core preform fabrication . . . 143
3.2.4 Preform slice preparation . . . 145

3.2.5 Core fiber fabrication 146

4 Experiments **151**

4.1 Transmission Spectroscopy 152

4.2 Emission Spectroscopy 153

4.3 Side-Illumination Fluorescence Spectroscopy 155

4.4 Quadratic Electrooptic Absorption Spectroscopy 162

4.5 Photosensitivity 166

5 Results and Discussion **169**

5.1 Absorption Spectra 169

5.1.1 Bulk Preform Slices 169

5.1.1.1 HSQ, PSQ, TSQ 170

5.1.1.2 ISQ 171

5.1.1.3 SiPc 173

5.1.2 Thin films 174

5.1.2.1 ISQ 175

5.1.2.2 SiPc 176

5.2 SIF spectra 176

5.2.1 Propagation distance dependence 177

5.2.1.1 BSQ 178

5.2.1.2 HSQ 180

5.2.1.3 PSQ 181

5.2.1.4 TSQ 182

5.2.1.5 ISQ 184

5.2.1.6 SiPc 186

5.2.1.7 DR1 188

5.2.1.8 SP1822 189

5.2.2 Fiber diameter dependence 191

5.2.3 Concentration dependence 192

5.2.3.1 BSQ 192

5.2.3.2 PSQ . . . 193
5.2.3.3 TSQ . . . 193
5.2.3.4 ISQ . . . 195
5.2.3.5 SiPc . . . 197
5.2.4 Polymer dependence . . . 198
5.2.4.1 HSQ and PSQ . . . 199
5.2.4.2 ISQ . . . 201
5.2.5 Incident wavelength dependence . . . 203
5.2.5.1 BSQ . . . 204
5.2.5.2 HSQ and PSQ . . . 204
5.2.5.3 TSQ . . . 205
5.2.5.4 ISQ . . . 207
5.2.5.5 SiPc . . . 209
5.3 Fluorescence Quantum Yield . . . 212
5.3.1 Core fibers . . . 213
5.4 Bulk Emission Spectra . . . 217
5.4.1 Squaraines . . . 217
5.4.2 SiPc . . . 220
5.4.2.1 Incident Wavelength Dependence . . . 223
5.5 Photosensitivity . . . 225
5.5.1 Preform Slices . . . 225
5.5.2 Core Fibers . . . 235
5.6 Linear absorption in core fibers . . . 238
5.6.0.1 BSQ . . . 240
5.6.0.2 HSQ and PSQ . . . 242
5.6.0.3 TSQ . . . 244
5.6.0.4 ISQ . . . 247
5.6.0.5 SiPc . . . 249
5.6.0.6 DR1 . . . 252
5.6.0.7 SP1822 . . . 253

5.7 Linear Spectroscopy . . . 254
5.7.1 Preform Slices . . . 255
5.7.1.1 HSQ, PSQ, TSQ . . . 256
5.7.1.2 ISQ . . . 259
5.7.1.3 SiPc . . . 260
5.7.2 Thin Films . . . 262
5.7.2.1 ISQ . . . 262
5.7.2.2 SiPc . . . 266
5.7.3 Core Fibers . . . 268
5.7.3.1 HSQ, PSQ, and TSQ . . . 269
5.7.3.2 ISQ . . . 272
5.7.3.2.1 Two-Level Model . . . 274
5.7.3.2.2 Three-Level Model . . . 274
5.7.3.3 SiPc . . . 277
5.8 QEA Spectroscopy . . . 280
5.8.1 ISQ . . . 281
5.8.2 SiPc . . . 291

6 Conclusions 299

A Third-Order Inhomogeneous-Broadening Energy Denominators 305
A.1 Intensity Dependent Refractive Index . . . 305
A.2 Pump-Probe . . . 306

B Beam Diameter 309

C Matlab Code 312
C.1 Quadratic Electrooptic Effect . . . 312
C.1.1 $D_{ll}(-\omega;\omega,0,0)$ . . . 312
C.1.2 $D_{ln}(-\omega;\omega,0,0)$ . . . 314
C.1.3 $D_{lml}(-\omega;\omega,0,0)$ . . . 315
C.1.4 $D_{lmn}(-\omega;\omega,0,0)$ . . . 317

D Two-photon Absorption **319**

D.1 Theory 319

D.2 Transverse two-photon absorption 322

List of Figures

1.1 Flow chart of the progression of knowledge about light-interaction with dye-doped polymers. 3

1.2 Figure 1.1 continued. 4

1.3 An example of a σ and π bond. 7

1.4 An example of a typical squaraine chromophore (TSQ -tertbutyl squaraine) . 8

1.5 Silicon phthalocyanine chromophore (SiPc). 11

1.6 Observation transverse to the fiber axis (propagation direction). 14

1.7 Illumination pattern on a bulk preform slice of dye doped-polymer. 17

1.8 A step-index dye-doped polymer optical fiber. 18

1.9 Schematic of the DDM method. 19

1.10 Observation of the fluorescence transverse to the fiber axis. 20

1.11 Observation of side-illumination fluorescence at the end of the fiber. 21

1.12 Observation of side-illumination fluorescence as a function of exposure time. . 24

2.1 (a) Real and imaginary parts of $D_1(-\omega;\omega)$ for a single excited state centered about 653 nm, (b) Imaginary part of $D_1(-\omega;\omega)$ for the correct (negative) and incorrect (positive) sign for the imaginary part of the transition frequency (energy) 43

2.2 (a) Real and imaginary parts of $D_1(-\omega;\omega)$ for a single excited state centered about 653 nm. The solid curves represent the inhomogeneous-broadening theory of the electronic transition with three different Γ_{g1}, and the dashed curve represents the homogeneous-broadening theory of the electronic transition. . . 50

2.3 Resonance enhancements of $D_{ll}(-3\omega;\omega,\omega,\omega)$ for third-harmonic generation. Each arrow represents a one-photon transition in the specified direction, the solid horizontal lines represent real energy levels, and the dashed horizontal lines represent virtual energy levels. 58

2.4 Real part of $-D_{11}(-3\omega;\omega,\omega,\omega)$ for a single excited state centered about 653 nm. The solid lines represent the inhomogeneously broadened electronic transitions for three different values of Γ_{g1} and the dashed line represents the homogeneously-broadened transitions when $n = l = 1$. 61

2.5 Resonant enhancements of $D_{ln}(-3\omega;\omega,\omega,\omega)$ for third-harmonic generation. . 64

2.6 Real part of $\xi^{(3)}(-3\omega;\omega,\omega,\omega)$ for two one-photon excited states centered about 653 nm and 365 nm. The solid lines represent the inhomogeneously-broadened electronic transitions for three different values of Γ_{g1} and the dashed lines represent the homogeneously-broadened transitions when n and $l \in \{1,3\}$. The homogeneous-broadened curve is specifically broken in the visible because the next value in the function is a large negative number. 65

2.7 Resonance enhancement of $D_{lml}(-3\omega;\omega,\omega,\omega)$ for third-harmonic generation. 67

2.8 Real part of $\xi^{(3)}(-3\omega;\omega,\omega,\omega)$ for one-photon excited state centered about 653 nm and one two-photon excited state centered about 365 nm. The solid lines represent the inhomogeneously-broadened electronic transitions for three different values of Γ_{gk}, where $k \in \{1,3\}$, and the dashed lines represent the homogeneously-broadened transitions when $l = 1$ and $m = 2$. 69

2.9 Real part of $\xi^{(3)}(-3\omega;\omega,\omega,\omega)$ for two one-photon excited states centered about 653 nm and 365 nm, and one two-photon state centered about 600 nm. The solid lines represent the inhomogeneously-broadened electronic transitions for three different values of Γ_{g1} and the dashed lines represent the homogeneously-broadened transitions when n and $l \in \{1,3\}$, and $m = 2$. The dashed curve is broken in the visible because the next value in the function is a large negative number. 71

2.10 Resonant enhancements due to $D_{ll}(-\omega;\omega,0,0)$ and $D_{ln}(-\omega;\omega,0,0)$, respectively. Each arrow represents a one-photon transition in the specified direction, solid horizontal lines represent real excited states, and dashed lines represent virtual excited states. 74

2.11 Real and imaginary parts of $D_{11}(-\omega;\omega,0,0)$ for a single excited state centered about 653 nm. The solid lines represent the inhomogeneously broadened electronic transitions for three different values of Γ_{g1} and the dashed line represents the homogeneously-broadened transitions when $n = l = 1$. 77

2.12 Real and imaginary parts of $D_{13}(-\omega;\omega,0,0)$ for two one-photon excited states centered about 653 nm and 614 nm. The solid lines represent the inhomogeneously broadened electronic transitions for three different values of Γ_{gk} where $k \in \{1,3\}$ and the dashed line represents the homogeneously-broadened transitions. 80

2.13 Real and imaginary parts of $\xi^{(3)}(-\omega;\omega,0,0)$ for two one-photon excited states centered about 653 nm and 614 nm. The solid lines represent the inhomogeneously broadened electronic transitions for three different values of Γ_{gk} where $k = \{1,3\}$ and the dashed line represents the homogeneously-broadened transitions. 82

2.14 Resonant enhancements for D_{lml} and D_{lmn}, respectively. Each arrow represents a one-photon transition in the specified direction. Solid horizontal lines represent real energy levels and dashed horizontal lines represent virtual energy levels. 83

2.15 Real and imaginary parts of $D_{121}(-\omega;\omega,0,0)$ for one one-photon excited state and one two-photon state centered about 653 nm and 600 nm, respectively. The solid lines represent the inhomogeneously broadened electronic transitions for three different values of Γ_{gk} where $k \in \{1,2\}$ and the dashed line represents the homogeneously-broadened transitions. 85

2.16 Real and imaginary parts of $\xi^{(3)}(-\omega;\omega,0,0)$ for one one-photon excited state and one two-photon state centered about 653 nm and 600 nm, respectively. The solid lines represent the inhomogeneously broadened electronic transitions for three different values of Γ_{gk} where $k \in \{1,2\}$ and the dashed lines represent the homogeneously-broadened transitions. 86

2.17 Real and imaginary parts of $D_{123}(-\omega;\omega,0,0)$ for two one-photon excited states centered about 653 nm and 614 nm, and one two-photon state centered about 600 nm. The solid lines represent the inhomogeneously-broadened electronic transitions for three different values of Γ_{gk}, where $k \in \{1,2,3\}$ and the dashed lines represent the homogeneously-broadened transitions when $l = 1, m = 2, n = 3$. 88

2.18 Real and imaginary parts of $\xi^{(3)}(-\omega;\omega,0,0)$ for two one-photon excited states centered about 653 nm and 614 nm, and one two-photon state centered about 600 nm. The solid lines represent the inhomogeneously-broadened electronic transitions for three different values of Γ_{gk}, where $k \in \{1,2,3\}$, and the dashed lines represent the homogeneously-broadened transitions when n and $l \in \{1,3\}$, and $m = 2$. 89

2.19 Resonant enhancements due to $D_{ll}(-\omega;\omega,\omega,-\omega)$ and $D_{ln}(-\omega;\omega,\omega,-\omega)$, respectively. Each arrow represents a one-photon transition in the specified direction, solid horizontal lines represent real excited states, and dashed lines represent virtual excited states. 92

2.20 Real and imaginary parts of $\xi^{(3)}(-\omega;\omega,\omega,-\omega)$ for a single excited state centered about 653 nm. The solid lines represent the inhomogeneously broadened electronic transitions for three different values of Γ_{g1} and the dashed line represents the homogeneously-broadened transitions when $n = l = 1$. 94

2.21 Real and imaginary parts of $\xi^{(3)}(-\omega;\omega,\omega,-\omega)$ for a single excited state centered about 653 nm. The solid lines represent the inhomogeneously broadened electronic transitions for three different values of Γ_{g1} and the dashed line represents the homogeneously-broadened transitions when $n = l = 1$. 95

2.22 Real and imaginary parts of $\xi^{(3)}(-\omega;\omega,\omega,-\omega)$ for two one-photon excited states centered about 653 nm and 614 nm. The solid lines represent the inhomogeneously broadened electronic transitions for three different values of Γ_{gk} where $k = \{1, 3\}$ and the dashed line represents the homogeneously-broadened transitions. 97

2.23 Energy level diagrams for $D_{lml}(-\omega;\omega,\omega,-\omega)$ and $D_{lmn}(-\omega;\omega,\omega,-\omega)$, respectively. Each arrow represents a one-photon transition in the specified direction. 98

2.24 Real and imaginary parts of $\xi^{(3)}(-\omega;\omega,\omega,-\omega)$ for one one-photon excited state and one two-photon state centered about 653 nm and 600 nm, respectively. The solid lines represent the inhomogeneously broadened electronic transitions for three different values of Γ_{gk} where $k \in \{1, 2\}$ and the dashed line represents the homogeneously-broadened transitions. 100

2.25 Real and imaginary parts of $\xi^{(3)}(-\omega;\omega,\omega,-\omega)$ for two one-photon excited states centered about 653 nm and 614 nm, and one two-photon state centered about 600 nm. The solid lines represent the inhomogeneously-broadened electronic transitions for three different values of Γ_{gk}, where $k \in \{1, 2, 3\}$, and the dashed lines represent the homogeneously-broadened transitions when n and $l \in \{1, 3\}$, and $m = 2$. 102

2.26 Resonant enhancements due to $D_{ll}(-\omega_1;\omega_1,\omega_2,-\omega_2)$ and $D_{ln}(-\omega_1;\omega_1,\omega_2,-\omega_2)$, respectively. Each arrow represents a one-photon transition in the specified direction, solid horizontal lines represent real excited states, and dashed lines represent virtual excited states. 104

2.27 Real and imaginary parts of $\xi^{(3)}(-\omega_1;\omega,\omega_2,-\omega_2)$ for a single excited state centered about 653 nm. The solid lines represent the inhomogeneously broadened electronic transitions for three different values of Γ_{g1} and the dashed line represents the homogeneously-broadened transitions when $n = l = 1$. 106

2.28 Real and imaginary parts of $\xi^{(3)}(-\omega_1;\omega_1,\omega_2,-\omega_2)$ for two one-photon excited states centered about 653 nm and 614 nm. The solid lines represent the inhomogeneously broadened electronic transitions for three different values of Γ_{gk} where $k=\{1,3\}$ and the dashed line represents the homogeneously-broadened transitions. 109

2.29 Energy level diagrams for $D_{lml}(-\omega_1;\omega_1,\omega_2,-\omega_2)$ and $D_{lmn}(-\omega_1;\omega_1,\omega_2,-\omega_2)$, respectively. Each arrow represents a one-photon transition in the specified direction. 110

2.30 Real and imaginary parts of $\xi^{(3)}(-\omega_1;\omega_1,\omega_2,-\omega_2)$ for one one-photon excited state and one two-photon state centered about 653 nm and 600 nm, respectively. The solid lines represent the inhomogeneously broadened electronic transitions for three different values of Γ_{gk} where $k\in\{1,2\}$ and the dashed line represents the homogeneously-broadened transitions. 112

2.31 Fluorescence generated in a core fiber with a monochromatic laser source. . . 122

2.32 Broadband fluorescence plane wave source model. 122

2.33 Broadband fluorescence point source model where the distance traveled by a ray at angle θ is $z/\cos\theta$. 123

2.34 Side-illumination fluorescence (SIF) for point source model (PSM) and plane wave model (PWM) for three values of α. 124

2.35 Side-illumination of an inhomogeneous dye-doped fiber. 125

2.36 Dye-doped polymer slab divided into 50 slices of thickness, δ. The first slab has a uniform number density, the second slab has 3 slices photobleached, and the third slab has 20 slices photobleached. 128

3.1 ITO electrode pattern on glass slide. 135

3.2 Electrooptic thin film. 137

3.3 Oven used to squeeze electrooptic sample. 138

3.4 Vacuum distillation apparatus for purifying liquid monomer. 139

3.5 Structures of squaraine dye molecules used as dopants in core material. 141

3.6 Structures of other dye molecules used as dopants in core material. 142

3.7 Rail-squeezer used to compress preform. 144
3.8 Preform slice used for transmission spectroscopy experiments. 145
3.9 Fiber drawing tower with a core fiber. 146
3.10 Temperature profile and oven cross section. 148

4.1 Fiber preform slice and thin film transmission experiment. 152
4.2 Resonant linear absorption spectra of HSQ, and ISQ (wt.% $\approx 10^{-4}$ for both dyes) 152
4.3 Reflection geometry for measuring the fluorescence spectrum. 153
4.4 (a)Reflected fluorescence from an HSQ/PMMA thin film for incident wavelengths of 633 nm and 693 nm, (b) Reflected fluorescence from a PSQ/PMMA preform slice for an incident wavelength of 633 nm 154
4.5 Side-illumination fluorescence experiment with the light source on a translation stage. 156
4.6 Side-illumination fluorescence experiment with the fiber on a translation stage. 157
4.7 SIF intensity from a multimode ISQ/P(MMA-d8) fiber for three wavelengths as a function of the incident power ($\lambda_{inc} = 693$ nm). The illumination position is 1.23 cm from the front face of the fiber. 159
4.8 Normalized SIF intensity at 706 nm from a TSQ-doped PMMA fiber. The blue and purple curves are due to an incident power of 0.2 mW at 633 nm. The red curve is due to an incident power of 8 mW, and the green curve is due to an incident power of 0.2 mW after the 8 mW experiment. 160
4.9 SIF spectra for HSQ- and ISQ-doped PMMA fibers for an excitation position of $z = 1.0$ cm. 161
4.10 The quadratic electroabsorption experiment. 163
4.11 Experimental apparatus for measuring the transmission through a preform slice as a function of position. 166

5.1 Resonant linear absorption of PSQ/PMMA core preform slices for four concentrations (N= 1.5×10^{15} cm^{-3}). 170
5.2 Resonant linear absorption of ISQ/PMMA core preform slices for three concentrations (N= 3.1×10^{15} cm^{-3}). 171

5.3 Resonant linear absorption of ISQ/PMMA core preform slices at various stages of degradation (N= 2.4×10^{16} cm^{-3}). 172
5.4 Resonant linear absorption for a 225 μm thick SiPc/PMMA core preform slice (N= 1.28×10^{17} cm^{-3}). 174
5.5 Resonant linear absorption for an ISQ/PMMA thin film (N= 1.9×10^{19} cm^{-3}). 175
5.6 Resonant linear absorption for a SiPc/PMMA thin film (N= 5.7×10^{18} cm^{-3}). 176
5.7 SIF spectra for propagation distances, 1.1 cm $\leq z \leq$ 2.0 cm, in a multimode BSQ/P(MMA-d8) fiber (λ_{inc} = 633 nm). Each subsequent curve is measured for an excitation position 0.3 cm further into the fiber. 178
5.8 SIF spectra for propagation distances, 2.9 cm $\leq z \leq$ 3.8 cm, in a multimode BSQ/P(MMA-d8) fiber (λ_{inc} = 633 nm). Each subsequent curve is measured for an excitation position 0.3 cm further into the fiber. 179
5.9 SIF spectra for propagation distances, 1.1 cm $\leq z \leq$ 2.48 cm, in a multimode HSQ/P(MMA-d8) fiber (λ_{inc} = 633 nm). Each subsequent curve is measured for an excitation position 0.46 cm further into the fiber. 181
5.10 SIF spectra for propagation distances, 4.2 cm $\leq z \leq$ 5.58 cm, in a multimode HSQ/P(MMA-d8) fiber (λ_{inc} = 633 nm). Each subsequent curve is measured for an excitation position 0.46 cm further into the fiber. 182
5.11 SIF spectra for maximum room temperature concentration HSQ/PMMA and PSQ/PMMA multimode core fibers at z = 2.0 cm (λ_{inc} = 693 nm). 183
5.12 SIF spectra for propagation distances, 1.85 cm $\leq z \leq$ 3.8 cm, in a multimode TSQ/PMMA fiber (λ_{inc} = 633 nm). Each subsequent curve is measured for an excitation position 0.65 cm further into the fiber. 184
5.13 SIF spectra for propagation distances, 1.2 cm $\leq z \leq$ 2.58 cm, in a multimode 30 % deuterated ISQ/P(MMA-d8) fiber (λ_{inc} = 633 nm). Each subsequent curve is measured for an excitation position 0.46 cm further from the front of the fiber. 185
5.14 SIF spectra for propagation distances, 3.3 cm $\leq z \leq$ 4.68 cm, in a multimode 30 % deuterated ISQ/P(MMA-d8) fiber (λ_{inc} = 633 nm). Each subsequent curve is measured for an excitation position 0.46 cm further from the front of the fiber. 186

5.15 SIF spectra for propagation distances, 1.1 cm $\leq z \leq$ 1.7 cm, in a multimode SiPc/PMMA fiber (λ_{inc} = 693 nm). Each subsequent curve is measured for an excitation position 0.2 cm further into the fiber. 187

5.16 SIF spectra for propagation distances, 1.1 cm $\leq z \leq$ 1.7 cm, in a multimode SiPc/PMMA fiber (λ_{inc} = 633 nm). Each subsequent curve is measured for an excitation position 0.2 cm further into the fiber. 188

5.17 SIF spectra for propagation distances, 1.2 cm $\leq z \leq$ 3.0 cm, in a multimode SP1822/PMMA fiber (λ_{inc} = 633 nm). Each subsequent curve is measured for an excitation position 0.6 cm further into the fiber. 190

5.18 SIF spectra for PSQ/P(MMA-d8) core fibers with diameters of 680 μm and 375 μm. Each subsequent curve is measured for an excitation position 1.0 cm further into the fiber. 191

5.19 SIF spectra for two excitation positions (i.e. propagation distances) for two different concentrations of BSQ-doped multimode core fibers (λ_{inc} = 633 nm). The BSQ/PMMA fiber has a number density, N = 4 $\times 10^{18}$ cm^{-3}, and the BSQ/P(MMA-d8) has a number density, N = 5.8 $\times 10^{18}$ cm^{-3}. 193

5.20 SIF spectra for two excitation positions (i.e. propagation distances) and concentrations in multimode PSQ/PMMA fibers (λ_{inc} = 693 nm). N_H = 4 $\times 10^{18}$ cm^{-3} (saturation concentration for samples polymerized at 60 °C), and N_L = 1.1 $\times 10^{18}$ cm^{-3} (Saturation concentration for samples polymerized at 25 °C.). 194

5.21 SIF spectra from z=1.5 cm (a) and z=3.0 cm (b) for three low concentrations of multimode TSQ/PMMA fibers ($N_k \in \{N, 4N, 8N\}$ for λ_{inc} = 633 nm. The lowest concentration TSQ/PMMA fiber studied has a number density, N = 1.6 $\times 10^{16}$ cm^{-3}. Note the y-axis for (a) and (b) are measured in the same units which are arbitrary. 194

5.22 SIF spectra from z=1.3 cm (a) and z=2.8 cm (b) for four concentrations of multimode ISQ/PMMA fibers ($N_k \in \{N, 3N, 27N, 45N\}$) for λ_{inc} = 633 nm (N = 1.4 $\times$ 10^{17} cm^{-3}). Note the y-axis for (a) and (b) are measured in the same units which are arbitrary. 196

5.23 SIF spectra for two illumination positions (1.1 cm and 1.5 cm) and two concentrations of multimode SiPc/PMMA fibers for $\lambda_{inc} = 693$ nm. $N_H = 1.2 \times 10^{18}$ cm^{-3} , and $N_L = 1.3 \times 10^{17}$ cm^{-3}. 197

5.24 SIF spectra for HSQ/PMMA (2.0 cm) and HSQ/P(MMA-d8) (1.8 cm) fibers. 200

5.25 Normalized SIF spectrum for a HSQ/PMMA (2.0 cm) fiber subtracted from the normalized SIF spectrum for a HSQ/P(MMA-d8) (1.8 cm) fiber. 200

5.26 SIF spectra for various propagation distances in multimode ISQ/PMMA and 30 % deuterated ISQ/P(MMA-d8) fibers ($\lambda_{inc} = 693$ nm). The inset shows the difference in fluorescence for the two spectra that propagated 3.0 cm. 202

5.27 SIF spectrum for a ISQ/P(MMA-d8) (3.0 cm) fiber subtracted from the SIF spectrum for a HSQ/PMMA (3.0 cm) fiber. 203

5.28 Normalized SIF spectrum for a BSQ/PMMA core fiber for two illumination positions (1.1 cm and 2.5 cm) and two incident wavelengths (633 nm and 693 nm). 204

5.29 Side-illumination fluorescence (SIF) spectra for incident wavelengths of 633 nm and 693 nm in multimode HSQ/PMMA and PSQ/PMMA fibers. The spectra for PSQ is recorded for illumination 1.0 cm into the fiber and the spectrum for HSQ is from illumination 2.0 cm into the fiber. 205

5.30 Normalized SIF spectrum for a high concentration TSQ/PMMA core fiber for two illumination positions (1.1 cm and 2.1 cm) and two incident wavelengths (633 nm and 693 nm). 206

5.31 SIF spectra (at $z = 2.0$ cm) for incident wavelengths of 633 nm and 693 nm in ISQ-doped PMMA and partially deuterated PMMA fibers. The spectra for the partially deuterated fibers are denoted $dISQ_3$ and $dISQ_9$, and the spectra for the PMMA fibers are denoted ISQ_3 and ISQ_9, where 3 and 9 refer to 633 nm and 693 nm incident illumination respectively. 207

5.32 SIF spectra for incident wavelengths of 693 nm and 723 nm in high concentration SiPc/PMMA copolymer fiber ($N_H = 1.2 \times 10^{18}$ cm^{-3}) . The solid lines represent $z = 1.1$ cm, and the dashed lines represent $z = 1.4$ cm. 209

5.33 SIF spectra from $z = 1.0$ cm and $z = 1.5$ cm for incident wavelengths of 633 nm, 693 nm, 703 nm, and 713 nm of low concentration SiPc/PMMA copolymer fiber ($N_L = 1.3 \times 10^{17}$ cm^{-3}). 211

5.34 Relative fluorescence yield for the low concentration SiPc/PMMA copolymer core fiber. Each spectrum is relative to the fluorescence generated by 633 nm (N= 1.3×10^{17} cm^{-3}). 215

5.35 Relative fluorescence yield for the low concentration SiPc/PMMA copolymer core fiber. Each point is relative to the fluorescence generated by 633 nm (N= 1.3×10^{17} cm^{-3}). 216

5.36 Reflection geometry emission spectra from PSQ/PMMA ($N_H = 3.8 \times 10^{17}$ cm^{-3} and $N_L = 9.6 \times 10^{16}$ cm^{-3}) and TSQ/PMMA ($N_H = 4.4 \times 10^{17}$ cm^{-3} and $N_L = 6.8 \times 10^{15}$ cm^{-3}) preform slices. The spectra are normalized to unity at 750 nm. 218

5.37 Emission spectra from HSQ/MMA and ISQ/PMMA preform slices in the transmission geometry. 219

5.38 Reflection geometry emission spectra from a Blue ISQ/PMMA preform slice and a Green ISQ/PMMA preform slice. The spectra are normalized to unity at 740 nm. 220

5.39 Reflection geometry emission spectra from three concentrations of SiPc/PMMA copolymer preform slices when excited with 633 nm light ($N_H = 2.4 \times 10^{18}$ cm^{-3}, $N_M = 1.2 \times 10^{18}$ cm^{-3}, and $N_L = 1.3 \times 10^{17}$ cm^{-3}). The spectra are normalized to unity at 747 nm. 221

5.40 Reflection geometry emission spectra from two concentrations of SiPc/PMMA copolymer preform slices when excited with 693 nm light ($N_M = 1.2 \times 10^{18}$ cm^{-3}, and $N_L = 1.3 \times 10^{17}$ cm^{-3}). The spectra are normalized to unity at 747 nm. 223

5.41 Reflection geometry emission spectra from the N_M SiPc/PMMA copolymer preform slice when it is excited with 633 nm or 693 nm light ($N_M = 1.2 \times 10^{18}$ cm^{-3}). The spectra are normalized to unity at 747 nm. 224

5.42 Reflection geometry emission spectra from the N_L SiPc/PMMA copolymer preform slice when it is excited with 633 nm, 643 nm, or 693 nm light (N_L = 1.3 $\times 10^{17}$ cm^{-3}). The spectra are normalized to unity at 747 nm. 225
5.43 Progress of UV exposure in a ISQ/PMMA preform slice: (a) Initial exposure at 355 nm, (b) 2 days time delay and rotation of 57°, (c) Final exposure at 355 nm. 226
5.44 Change in absorption of the ISQ sample 2 days after initial 26 minute exposure to 355 nm laser light. Probed at 693 nm. 227
5.45 Change in transmission contours for the ISQ sample 2 days after the initial bleaching with 355 nm laser light. Viewed at the incident wavelength, 693 nm. 228
5.46 Change in transmission contours for the ISQ sample immediately after the final bleaching with 355 nm laser light. Viewed at the incident wavelength, 633 nm. 230
5.47 Change in transmission contours for the ISQ sample immediately after the final bleaching with 355 nm laser light. Viewed at a fluorescence wavelength, 724 nm ($\lambda_{inc} = 633$ nm). 231
5.48 Resonant absorption of a line through an ISQ/PMMA preform slice that was previously exposed to 633 nm light for 3 hours at 0.5 mW. The beam was centered at zero mm, and the diameter was 400 μm. 232
5.49 Natural log of the photon flux as a function of exposure time for an ISQ/PMMA preform slice. The solid line represents a least-squares for to the data for two decay speeds ($\beta_1' = 2.4 \times 10^1$ cm/hour, and $\beta_2' = 2.4 \times 10^1 \mu$m/hour. 234
5.50 SIF intensity for a BSQ/PMMA core fiber: before, immediately after, 1 hour after, and 14 hours after a 40 minute exposure at 3.0 mm with 633 nm light (P_{inc} =0.4 mW, $\lambda_f = 758$ nm). 236
5.51 SIF intensity for a BSQ/PMMA core fiber: before, immediately after, and 15 hours after a 40 minute exposure at 3.0 mm with 633 nm light (P_{inc} =1 mW, $\lambda_f = 721$ nm). 237
5.52 SIF as a function of z for PSQ/P(d-PMMA) at 744 nm , and the two theories for the absorption: plane wave model (PWM) and point source model (PSM). The plane wave and point source curves are coincident on this scale. 239

5.53 Linear absorption spectrum, $\alpha(\lambda)$, of PSQ/P(MMA-d8) determined from SIF data using plane wave (PWM) and point source (PSM) models in the range, 720 nm $< \lambda <$ 840 nm. 240

5.54 Linear absorption coefficient measured using the point source model for BSQ/PMMA (N= 4.1 $\times 10^{18}$ cm^{-3}) and BSQ/P(MMA-d8) (N= 5.8 $\times 10^{18}$ cm^{-3})core fibers. 241

5.55 Linear absorption coefficient calculated using the point source model for the HSQ-doped and PSQ-doped core fibers studied discussed in Section 5.2. The error associated with each curve is denoted by the error bar except for the HSQ/P(MMA-d8) curve since there was only one fiber measured. All fibers are room temperature maximum concentration except the fiber denoted N_{60} = 4.0 $\times 10^{18}$ cm $^{-3}$. 242

5.56 Absorption cross-section for 3 concentrations of PSQ/PMMA core fiber. ($N_k \in$ { N , 2.7N, 3.6N}). 244

5.57 Linear absorption coefficient measured using the point source model for 4 concentrations of TSQ/PMMA core fiber. ($N_k \in$ { N , 4N 8N, 200N}, where N= 0.16 $\times 10^{17}$). 245

5.58 Absorption cross-section for 4 concentrations of TSQ/PMMA core fiber. ($N_k \in$ { N, 4N, 8N, 200N}). 246

5.59 Linear absorption coefficient measured using the point source model for 4 concentrations of ISQ/PMMA core fiber. ($N_k \in$ { N , 9N, 27N, 45N}, where N= 1.4 $\times 10^{17}$). 248

5.60 Absorption cross-section for 4 concentrations of ISQ/PMMA core fiber. ($N_k \in$ { N, 9N, 27N, 45N}, where N= 1.4 $\times 10^{17}$). 248

5.61 Linear absorption coefficient determined from the SIF spectra shown in Figure 5.32 using the point source model for the high concentration, N_H = 1.2 $\times 10^{18}$ cm^{-3}, SiPc/PMMA core fiber. ($\lambda_{inc} \in$ {693 nm, 723 nm }). 250

5.62 Linear absorption coefficient calculated using the point source model for the low concentration, N_L = 1.3 $\times 10^{17}$ cm^{-3}, SiPc core fiber. ($\lambda_{inc} \in$ { 633 nm, 693 nm, 703 nm, 713 nm }). 251

5.63 Linear absorption coefficient using the point source model for DR1- (blue) and SP1822-doped (green) core fibers. (λ_{inc} = 633 nm). 253
5.64 Bulk PSQ/PMMA resonant absorption modeled as a Lorentzian (L) transition and an inhomogeneously-broadened (IB) transition (N = 1.5 × 10^{15} cm^{-3}). . . 256
5.65 Bulk ISQ/PMMA resonant absorption modeled as a Lorentzian (L) transition and an inhomogeneously-broadened (IB) transition (N= 1.4 ×10^{17} cm^{-3}). . . 259
5.66 Bulk SiPc/PMMA resonant absorption modeled as a Lorentzian (L) transition and an inhomogeneously-broadened (IB) transition (N= 1.3 ×10^{17} cm^{-3}). . . 261
5.67 Thin film ISQ/PMMA resonant absorption compared with Lorentzian (L) transitions up to a 4-Level model (N = 19.4 ×10^{18} cm^{-3}). 263
5.68 Thin film ISQ/PMMA resonant absorption compared with inhomogeneously-broadened (IB) transitions up to a 4-Level model (N = 19.4 ×10^{18} cm^{-3}). . . 264
5.69 Thin film SiPc/PMMA resonant absorption modeled as Lorentzian (L) transitions and inhomogeneously-broadened (IB) transitions (N = 5.7 ×10^{18} cm^{-3}). 267
5.70 SIF measurement as a function of propagation distance (—) and theory for inhomogeneous broadening (- -). 270
5.71 SIF spectra for a PSQ/PMMA core fiber (—) and theory for inhomogeneous broadening (- -). 271
5.72 Side-illumination fluorescence for an ISQ/PMMA fiber (N = 1.4 ×10^{17} cm^{-3}) for z_0 = 1.3 cm and z_1 = 2.8 cm and a comparison with the two-level IB model for the self-absorption where the z_0 = 1.3 cm SIF data is used as the initial condition. 273
5.73 Side-illumination fluorescence at two propagation distances (z_o = 1.4 cm and z_1 = 2.4 cm) for ISQ/PMMA (N = 6.3 ×10^{18} cm^{-3}) and two- and three- level models for self-absorption of the SIF intensity, which use the z_o SIF data as the initial condition. 275
5.74 Strength of the resonant excited and aggregate states as a function of the relative number density (N_b is the number density of the bulk sample). The red line denotes the theoretical value for no aggregation. 277

5.75 Side-illumination fluorescence at two propagation distances (z_o = 1.2 cm and z_1 = 2.0 cm) for SiPc/PMMA (N = 0.13 $\times 10^{18}$ cm^{-3}) and two-, three-, and four-level models for self-absorption of the SIF intensity, which use the z_o SIF data as the initial condition. 278

5.76 $\chi_I^{(3)}(-\omega;\omega,0,0)$ for an ISQ/PMMA thin film in comparison to Lorentzian (L) (dashed-red) and inhomogeneously-broadened (IB) (solid-red) two-level models (N = 19.4 $\times 10^{18}$ cm^{-3}). 281

5.77 $\chi_I^{(3)}(-\omega;\omega,0,0)$ for an ISQ/PMMA thin film in comparison to Lorentzian (L) (dashed-red) and inhomogeneously-broadened (IB) (solid-red) four-level models (N = 19.4 $\times 10^{18}$ cm^{-3}). 282

5.78 $\chi_I^{(3)}(-\omega;\omega,0,0)$ for an ISQ/PMMA thin film in comparison to three variations on a 5-Level Lorentzian (L) model (N = 19.4 $\times 10^{18}$ cm^{-3}). 5-level (a) model allows all three one-photon states to couple to the additional two-photon state, 5-level (b) only allows transitions to the two-photon state through the resonant one-photon state at 657 nm, and 5-level (c) only allows transitions to the two-photon state through the resonant one-photon state at 657 nm and considers the two high-lying states to be conformational isomers of the resonant excited state. 284

5.79 $\chi_I^{(3)}(-\omega;\omega,0,0)$ for an ISQ/PMMA thin film in comparison to various inhomogeneously broadened (IB) models (N = 19.4 $\times 10^{18}$ cm^{-3}). 5-level (a) model allows all three one-photon states to couple to the additional two-photon state, 5-level (b) only allows transitions to the two-photon state through the resonant one-photon state at 657 nm, and 5-level (c) only allows transitions to the two-photon state through the resonant one-photon state at 657 nm and considers the two high-lying states to be conformational isomers of the resonant excited state, and 5-level (d) is 5-level (b) plus 0.1% reorientational effect. 286

5.80 $\chi_I^{(3)}(-\omega;\omega,0,0)$ for an ISQ/PMMA thin film in comparison to 3-level (blue-dashed), 4-level (green-dotted), and 5-level (solid-red) Lorentzian (L) models (N = 8.8 $\times 10^{18}$ cm^{-3}). 287

5.81 $\chi_I^{(3)}(-\omega;\omega,0,0)$ for an ISQ/PMMA thin film in comparison to 3-level (blue-dashed), 4-level (green-dotted), and 5-level (solid-red) inhomogeneously-broadened (IB) models (N = 8.8 $\times 10^{18}$ cm^{-3}). 289

5.82 $\chi_I^{(3)}(-\omega;\omega,0,0)$ for an SiPc/PMMA thin film in comparison Lorentzian (L) (dashed-red) and inhomogeneously-broadened (IB) (solid-red) models (N = 5.7 $\times 10^{18}$ cm^{-3}). The blue theory curves are the red electronic effects plus a 0.1% reorientational effect. 292

5.83 $\chi_I^{(3)}(-\omega;\omega,0,0)$ for an SiPc/PMMA thin film in comparison to a 5-level inhomogeneously broadened (IB) model (N = 5.7 $\times 10^{18}$ cm^{-3}). The four theoretical curves correspond to $\mu_{12} = \{5.5, 6.0, 6.5, 7.0\}$ D. 293

6.1 Energy level diagram for ISQ/PMMA. The dashed-green states were determined using SIF spectroscopy, the blue states were determined using linear absorption spectroscopy, and the red states were determined using QEA spectroscopy. Each number on the right-hand-side of the energy level diagram corresponds to the state as tabulated in Chapter 5, and g refers to the ground state. 302

6.2 Energy level diagram for SiPc/PMMA. The dashed-green states were determined using SIF spectroscopy, the blue states were determined using linear absorption spectroscopy, and the red states were determined using QEA spectroscopy. Each number on the right-hand-side of the energy level diagram corresponds to the state as tabulated in Chapter 5, and g refers to the ground state. 303

B.1 Knife-edge experiment to determine the beam diameter of a laser. 309

B.2 Knife-edge experimental data fit to an error function to determine the beam diameter of a laser. 311

D.1 The transverse two-photon absorption experiment. 323

D.2 Transmitted intensity as a function of fiber length and incident intensity. The solid lines indicate the linear regime and the dashed lines indicate the nonlinear regime. 324

List of Tables

2.1 Denominator contributions to the linear molecular susceptibility for homogeneously-broadened and inhomogeneously-broadened electronic transitions. 48

2.2 Fundamental denominator contributions to homogeneously broadened and inhomogeneously broadened electronic transitions. 56

3.1 Maximum dye solubilities in PMMA. 143

5.1 Excited state fit parameters for HSQ/PMMA, PSQ/PMMA, and TSQ/PMMA preform slices with comparison to thin film measurements. IB – inhomogeneous broadening, L – Lorentzian, G – Gaussian, and M – Mathis. 258

5.2 Excited state fit parameters for ISQ/PMMA preform slices with comparison to thin film (TF) and liquid ($CHCl_3$) measurements. IB – inhomogeneous broadening, L – Lorentzian, G – Gaussian, and M – Mathis. 260

5.3 Excited state fit parameters for ISQ/PMMA thin films (TF) with comparison to ISQ/PMMA preform slice measurements (BULK). IB – inhomogeneous broadening, L – Lorentzian, and M – Mathis. 265

5.4 Excited state fit parameters for a 1 wt. % SiPc/PMMA thin film (TF) with comparison to SiPc/PMMA copolymer preform (BULK). IB – inhomogeneous broadening, and L – Lorentzian. 268

5.5 Excited state fit parameters for HSQ-, PSQ-, and TSQ-doped core fibers measured in the SIF experiment and analyzed using the inhomogeneous-broadening (IB) model. 272

5.6 Excited state fit parameters for ISQ/PMMA fibers with comparison to bulk ISQ/PMMA sample. S^b_{gn}= strength of the resonant state for the bulk preform slice, and N_b is the number density of the bulk preform slice. 276
5.7 Excited state fit parameters for SiPc/PMMA copolymer core fibers from the inhomogeneous-broadening (IB) model. 279
5.8 Excited state fit parameters for the two-photon state in ISQ/PMMA thin films from QEA spectroscopy (TF) using the Lorentzian (L) model. 283
5.9 Excited state fit parameters for the two-photon state in ISQ/PMMA thin films from QEA spectroscopy (TF) using the inhomogeneous-broadening (IB) model. 285
5.10 Excited state fit parameters for ISQ/PMMA thin films from QEA and transmission spectroscopy (TF) after the number density has been corrected (L – Lorentzian). 288
5.11 Excited state fit parameters for ISQ/PMMA thin films from QEA and transmission spectroscopy (TF) after the number density has been corrected (IB – inhomogeneous broadening). 290
5.12 Excited state fit parameters for a 1 wt. % SiPc/PMMA thin film for QEA and transmission spectroscopy (TF). IB – inhomogeneous broadening, L – Lorentzian. 294

Chapter 1

Introduction

For the last decade, the Nonlinear Optics Laboratory (NLOL) at Washington State University (WSU) has been investigating the linear and nonlinear optical properties of dye-doped polymers. Research on dye-doped polymers dates back over 20 years. Polymers are of interest because of their promise as materials for optical information processing.

Optical circuits can carry more information than their electrical counterparts due to larger bandwidths, and lower loss and cross talk. When optical interconnects and nonlinear components are realized, optical computing and all-optical telecommunication networks will follow. To this end, fundamental research must address material characterization for optical logic devices like switches, modulators, and amplifiers, which are the building blocks for optical circuits.

The NLOL has its foundation in basic research towards these optical logic devices. Most recently, Dennis Garvey characterized single-mode squaraine-doped polymer fibers for their potential as optical switches using a Sagnac interferometer [1]; Karen Mathis [2] and Constantina Poga [3] studied basic nonlinear optical mechanisms of dye-doped thin films in terms of their potential for electrooptic modulators (A hybrid bridging the gap between purely electronic and purely optical devices.); and David Welker has demonstrated the first dye-doped polymer electrooptic fiber, where the electrodes are embedded in the cladding of a single-mode dye-doped polymer optical fiber [4]. This work builds on the knowledge base defined by these former students at the NLOL and other researchers in the field of nonlinear optics.

While the original intent of this thesis was to study two-photon absorption, my work evolved into inventing and applying a new technique to study the optical properties of a material in a fiber. Studies include:

- Side-illumination fluorescence (SIF) spectroscopy: A novel method for measuring the linear absorption in a dye-doped polymer optical fiber.
- Determination of relative quantum fluorescence yields through the use of SIF.
- Identification of vibronic states in phthalocyanine side-chain polymer fibers through the use of SIF.
- A model for inhomogeneously-broadened electronic transitions in third-order optical processes.
- Characterization of silicon-phthalocyanine/PMMA electrooptic thin films.
- Material stability studies, which show a better polymer host and more stable dyes are necessary for the realization of optical logic devices.

Obviously, these six contributions did not follow from a single experiment, but come from variations on five measurements: linear transmission spectroscopy, linear emission spectroscopy, side-illumination fluorescence spectroscopy, time-dependent laser illumination spectroscopy, and quadratic electrooptic absorption (QEA) spectroscopy. Before these experiments can be discussed, the basic language of nonlinear optics must be presented. This description occurs in the Section 1.1. A history of the research on two classes of dye molecules, squaraines and phthalocyanines, pertaining to experiments relevant to this work, will be presented in Sections 1.2.1 and 1.2.2. We also describe, historically (chronologically), the motivations linking the five experiments together in this dissertation. To help the reader with the "big" picture, a flow chart of the chronological progression of my experiments is shown below as Figures 1.1 and 1.2. The final section in the introduction suggests a non-sequential way to read the remainder of this work since there are so many interconnections between the various experiments and results.

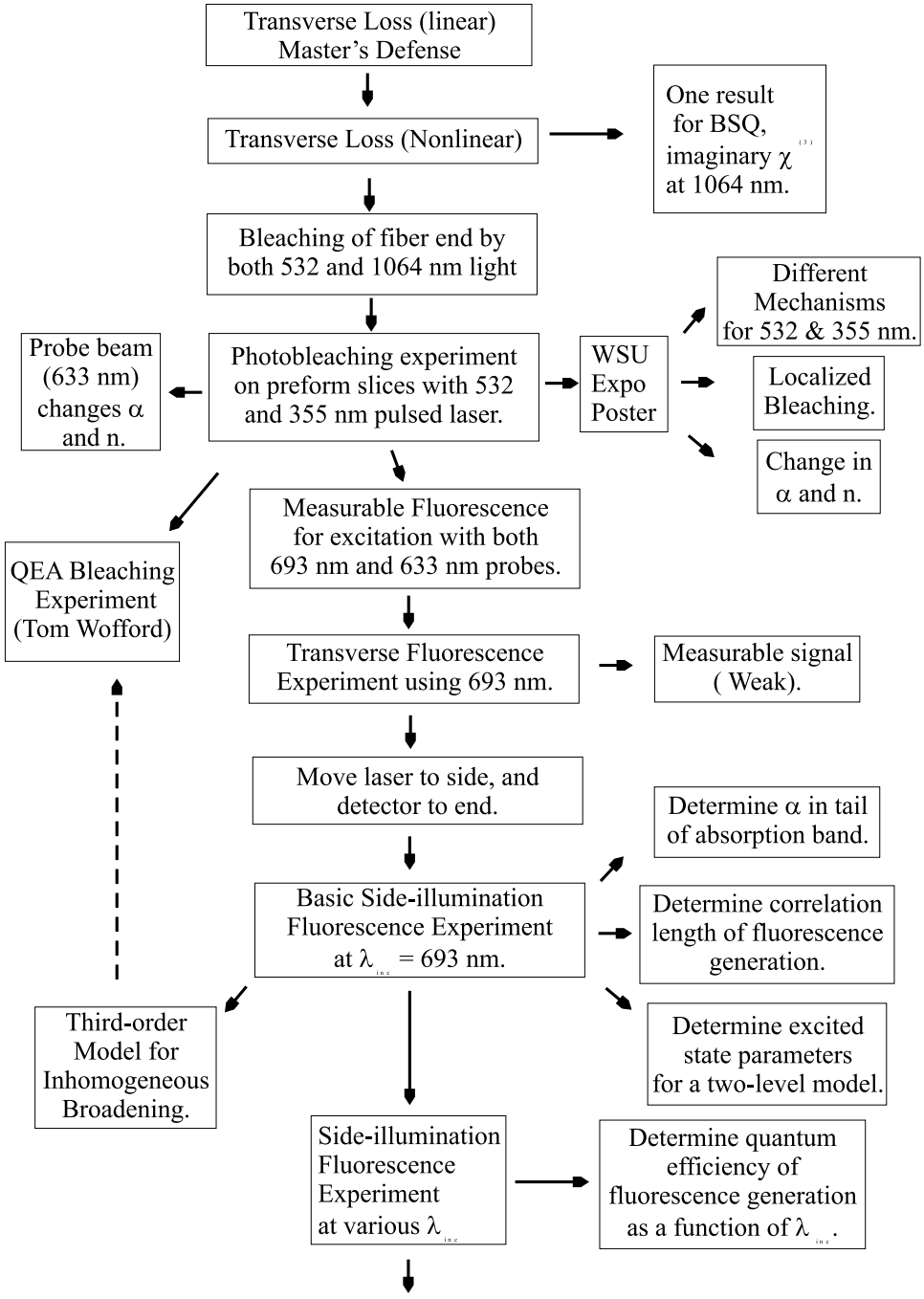

Fig. 1.1: Flow chart of the progression of knowledge about light-interaction with dye-doped polymers.

1.1 Conventions and Units

Currently, there are numerous ways to define the polarization and optical susceptibilities, which describe how a material interacts with light [5, 6]. Thus, it is important that we

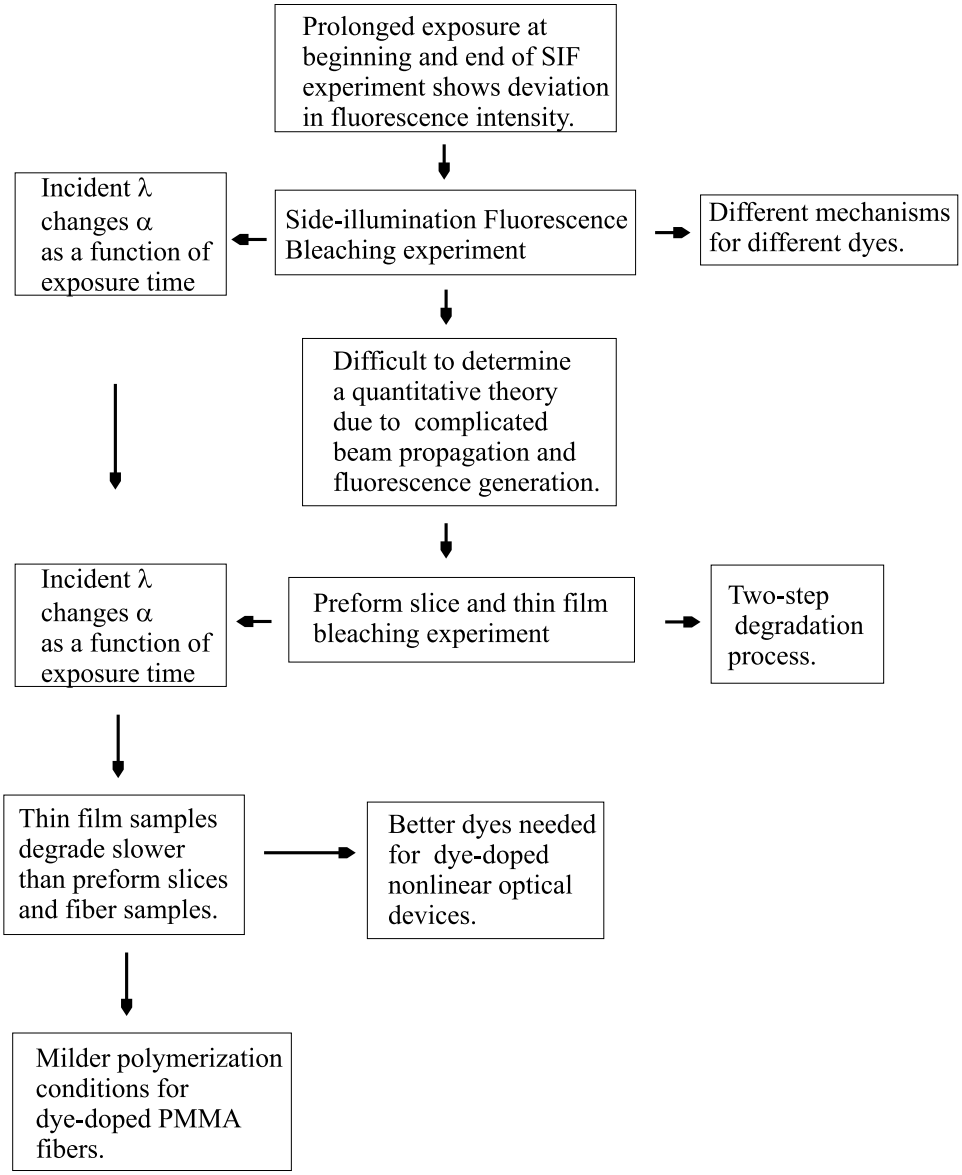

Fig. 1.2: Figure 1.1 continued.

clearly define the polarization and optical susceptibilities so our results can be compared with others in the field. We begin by defining the electric displacement vector, in SI units, as,

$$\mathbf{D} = \epsilon_{\mathbf{o}}\mathbf{E} + \mathbf{P}, \tag{1.1}$$

where ϵ_o is the permittivity of free-space, $\mathbf{E}$, is the electric field which oscillates in

time, and $\mathbf{P}$, is the polarization vector, which characterizes how the electric dipoles of the specific media radiate when illuminated by the oscillating electric field.

In linear optics the dipoles oscillate at the same frequency as the applied electric field. However, this is a low intensity approximation that is valid when the electric field does not cause a large oscillation in the electric dipoles. If the intensity of light is increased (i.e. coherent excitation by a laser) the dipoles will not necessarily radiate at the applied electric field frequency, ω. To account for this possibility, we can expand the scalar polarization as a power series in the applied electric field:

$$P = \epsilon_o(\chi^{(1)}E + \chi^{(2)}E^2 + \chi^{(3)}E^3 + \cdots), \tag{1.2}$$

where $\chi^{(1)}$ is the linear optical susceptibility, and $\chi^{(2)}$, $\chi^{(3)}$, $\cdots$, are called the nonlinear optical susceptibilities and are the basic bulk quantities that we are interested in determining for each material of interest. This definition will be expanded upon in Chapter 2 to account for the tensor nature of the optical susceptibilities. It is important to note that the permittivity of free-space multiplies each term in the power series. Our definition is consistent with Butcher and Cotter [5]. The optical susceptibilities are in units of $(\mathrm{V}^{-1}\ \mathrm{m})^{n-1}$, which is the inverse of the electric field to the n-1 power, and the total polarization has units of C m^{-2}.

We also define two quantities, the intensity dependent refractive index and the two-photon absorption (TPA) coefficient, that will be helpful when reading the remainder of the introduction. To define the intensity dependent refractive index, we expand the index of refraction, n, in a power series with respect to the intensity, I, as follows,

$$n = n_0 + n_2\, I, \tag{1.3}$$

where n_0 is the linear refractive index, and n_2 is the intensity dependent refractive index, which is related to the real part of the third-order susceptibility, $\chi_R^{(3)}$ (Note that all refractive indices in Equation (1.3) are assumed to be real quantities.).

Similarly, we can expand the absorption coefficient,

$$\alpha = \alpha_0 + \alpha_2\, I, \tag{1.4}$$

where α_0 is the one-photon (linear) absorption coefficient, and α_2 is the two-photon absorption coefficient, which is related to $\chi^{(3)}$. The details of the relationships between n_2, α_2, and $\chi^{(3)}$ will be explained in Chapter 2.

Before moving on to a description of the dye molecules, we need to define the oscillating electric field and the time-averaged intensity in terms of the electric field. Again, we follow Butcher and Cotter by defining the applied electric field as,

$$E = E_o \cos(\omega t) = \frac{E_o}{2}(\exp(-i\omega t) + \exp(i\omega t)), \tag{1.5}$$

so that the electric field is real, and the intensity as,

$$I = \frac{1}{2}\epsilon_o n_{o_R} |E|^2, \tag{1.6}$$

where n_{o_R} is the real part of the linear refractive index. The definition of the applied electric field is similar to Kuzyk [6] except that our amplitude, E_o is in SI units instead of Gaussian units (statvolt/cm), which were favored in the early days of nonlinear optics [5], but differs from Boyd [7] by a factor of 1/2, which is also in Gaussian units.

Unfortunately, this factor is the beginning of many of the headaches in nonlinear optics because nth order nonlinear processes have n of these factors (Degeneracy factors are the climax of the headaches and will be discussed in Chapter 2.). Since many researchers are inconsistent in their definitions of both the electric field and the susceptibilities, it makes comparing values of nonlinear optical susceptibilities nearly impossible. Hopefully by providing the definitions early on we will eliminate some of the confusion.

1.2 Dye Molecules

Highly conjugated, $\pi-$ electron, organic molecules that absorb light in the visible region are often referred to as dyes or chromophores, which is in contrast to typical organic molecules that absorb in the ultraviolet and hence appear white or slightly yellowish. Chromophores exhibit unusually large non-resonant second- and third-order optical susceptibilities (See for example [6]). These large nonlinear susceptibilities can be attributed to the delocalized π-electrons, which are typically correlated in 1- or 2-D, and exhibit lower transition energies and large transition moments than σ-electrons [8].

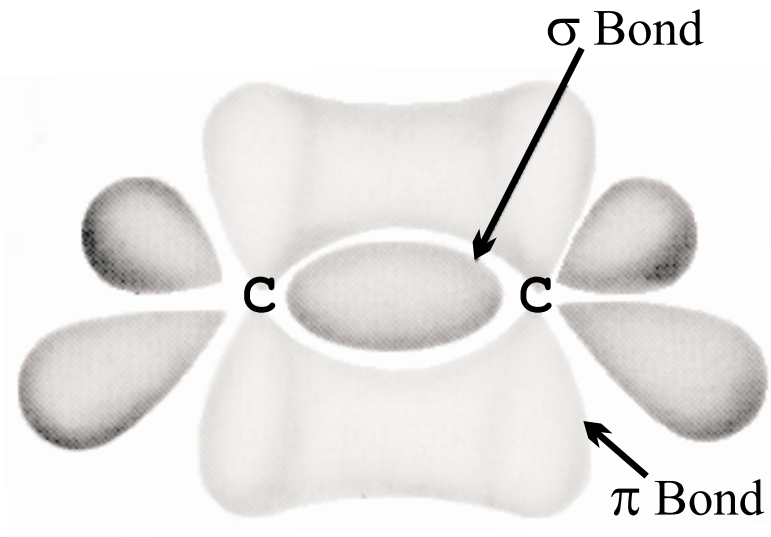

Fig. 1.3: An example of a σ and π bond.

In our research we have focused on two main classes of dye molecules. Squaraine dyes, which are representative of 1-D conjugated systems and make up the bulk of this research, and the phthalocyanine dyes, which represent 2-D conjugated systems. Unfortunately, we did not have any fullerenes (3-D conjugated structures) for doping into guest/host fibers, but may be an interesting future project. The following sections describe brief relevant histories of linear and nonlinear optical measurements on squaraine and phthalocyanine dye molecules.

1.2.1 Squaraines

Figure 1.4 shows a squaraine dye molecule that is based on the central carbon square and is synthesized from squaric acid. Notice that the $\pi-$ electrons are conjugated along the entire backbone of the molecule. Therefore it can be considered one dimensional in terms of its electronic properties, which are dominated by the $\pi-$ electrons for optical frequencies.

The molecule is excited when electric fields oscillate parallel to its length because the $\pi-$ electrons can only oscillate along the backbone. Since the molecule is has a long length over which the $\pi-$ electrons can oscillate the frequencies that will cause it to resonate are

in the visible region of the spectrum – specifically in the red. The molecules described below will all be variations on the TSQ dye which is based on the central carbon square, and approximately 1-D in terms of the π – electrons oscillating along the length of the molecule.

Using semi-empirical molecular orbital calculations, Bigelow and coworkers [9] determined that a symmetric configuration about the central carbon square should lead to considerable intramolecular charge transfer. They determined that the squaraine model has single-double bond length alternation (i.e. single bonds are longer than the double bonds). Since bond lengths expand or contract during excitation, the bond length alternation plays a significant role in the nonlinear optical susceptibility [10].

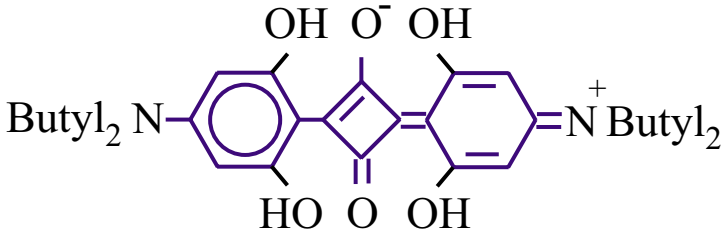

Fig. 1.4: An example of a typical squaraine chromophore (TSQ - tertbutyl squaraine)

Luong and coworkers [11] outlined a method for observing the change in index of refraction in a dye-doped polymer when a voltage is applied across the sample. They called the resultant change in the index of refraction the electrooptic coefficient, which is similar to n_2 (Section1.1) and is related to $\chi^{(3)}$.

Using quadratic electrooptic (QEO) experiments and other methods, Dirk and coworkers [12] determined that complex damping corrections, which broaden the electronic transitions, are necessary to describe the dispersion of $\chi^{(3)}$ for dye-doped polymer films. These studies concluded squaraines should be good nonlinear optical molecules because of their large solubilities, linear dependence of $\chi^{(3)}$ on number density, relatively narrow resonance absorption, and predominantly electronic response.

The narrow resonance absorption and predominantly electronic response to light were important because it was predicted by Kuzyk and coworkers that a maximum (negative) third-order response would occur for two-level centrosymmetric molecules [13].

The two-level model which only includes the ground state and a one-photon excited state, forces the third-order susceptibility to depend only on the transition moment between the ground and first-excited state. Dispersion measurements using QEO confirmed that the ISQ (indole squaraine) molecule roughly corresponds to a two-level system [14]. Many-electron quantum chemistry calculations which explicitly consider electron - electron correlations verified [15] that general squaraines possess an inherently large and negative third-order susceptibility.

In electric-field-induced second harmonic (EFISH) measurements, it was found that the two-level model is too restrictive and an additional two-photon state was necessary to effectively model the dispersion of $\chi^{(3)}$ for the ISQ molecule [16]. However, the one-photon contribution was still dominant.

Both third-harmonic generation (liquid) [17, 18] and QEA experiments [3, 2] (thin-films) re-confirmed the existence of a higher energy two-photon state which contributes to the dispersion of the third-order susceptibility of squaraine dye molecules. The results of the QEA experiments by Poga [19] also showed that the nonlinear response was predominantly electronic throughout the visible region. Thus there is a fairly good description of the squaraine molecules in liquids and dye-doped thin films using a three-level model for the third-order susceptibility. However, there was no work done on squaraine dyes doped into polymer fibers.

Garvey [20] was the first to report on squaraine doped single-mode step index polymer fibers. It was shown that the loss at 1.3 μm was largely due to the polymer host. Most recently Garvey [1] reported that several single-mode squaraine doped polymer fibers showed about a third of the necessary π phase shift for all-optical switching. It was suggested that a polymer host with a larger damage threshold would bring the phase shift even closer to the required 180 °. Obviously, more research on dye-doped fibers is required.

Ashwell and coworkers [21, 22] reported the unusual result that they had generated second-harmonic light from Langmuir-Blodgett thin films of various squaraine dyes. This was unexpected since some of the squaraines involved were centrosymmetric and should not generate second-harmonic light, which is second-order process. The results were

discussed in terms of squaraine aggregates. Specifically they proposed that the squaraine dye forms non-centrosymmetric "T"-shaped dimers, called J-aggregates, under certain processing conditions.

1.2.2 Phthalocyanines

Figure 1.5 shows the chemical structure for silicon phthalocyanine monoacrylate (SiPc) – there is a very similar molecule called silicon phthalocyanine diacrylate that has the $(C_6H_{13})_3$ replaced by a second acrylate group which we did not study. The chromophores mentioned in this introduction have similar ring structures (or π-electron systems) to SiPc. The differences occur when the Si molecule is replaced in the interior of the ring with a metal or hydrogen and the outer benzenoid rings have some of their hydrogens replaced with various organic groups. These substitutions typically shift the linear absorption maxima and the corresponding vibronics but the general features of the linear absorption are due to the π electrons within the conjugated ring. Thus we should be able to attribute some of the general characteristics of the following phthalocyanine molecules to the SiPc molecules that we are studying.

The phthalocyanine class of molecules are of interest to the nonlinear optics community due to there high thermal stability (400 °C) [23, 24], flexibility of guest/host or copolymer systems [25, 26, 27], fast response times [23, 25, 28] , and there large third-order optical susceptibilities [29, 8, 30, 26, 27]. The large third-order susceptibilities are typically due to large Q and Soret (B) absorption bands which occur in the visible between 600-800 nm and the near ultra-violet (UV) between 300-400 respectively. The exact locations depend on the various substitutions to the phthalocyanine ring.

Ho and coworkers [29] conducted third-harmonic generation experiments at 1064 nm in a reflection geometry on polycrystalline thin films of chloro-aluminum and fluoro-aluminum phthalocyanines, where they determined a lower limits of $\chi^{(3)}(-3\omega;\omega,\omega,\omega) = 2.5 \times 10^{-11}$ esu and $\chi^{(3)}(-3\omega;\omega,\omega,\omega) = 5 \times 10^{-11}$ esu, respectively. These large values are about 1/5 that of Si and GaAs. They also reported that the linear absorption spectrum was inhomogeneously broadened in comparison to solutions of the two dye molecules.

In a second study, Ho and coworkers [23], determined that the nonlinear optical response of the previously studied fluoro-aluminum phthalocyanine molecules was much faster than electron-hole recombination in inorganic semiconductors. They determined that the ground state was repopulated via exciton-exciton annilation (550 fs) and exciton-phonon coupling (4 ps), thus the phthalocyanines should be suitable candidates for high speed optical switching.

Shirk and coworkers [30] determined $\chi^{(3)}$ using degenerate four wave mixing at 1.064 nm, in solutions of a metal free phthalocyanine (Pc), a platinum phthalocyanine (PtPc), and a Lead phthalocyanine (PbPc) in $CHCl_3$. They reported almost an order of magnitude increase in the nonresonant third-order susceptibility from Pc (4×10^{-12} esu) to PbPc (2×10^{-11} esu), and another order of magnitude increase from PbPc to PtPc (2×10^{-10} esu), which was due to low lying metal-to-ligand and ligand-to-metal charge transfer states. For the PtPc they also saw two decay rates, where between 80-90 % of the signal decayed within 35 ps, and the remainder stayed visible for longer than 500 ps.

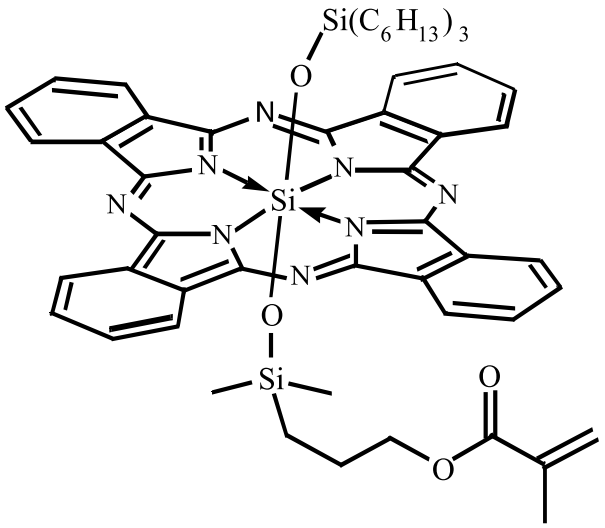

Fig. 1.5: Silicon phthalocyanine chromophore (SiPc).

Kaltbeitzel and coworkers [25] reported that thin film preparation is very important in terms of both linear absorption characteristics and $\chi^{(3)}$ relaxation times. They showed that the linear absorption spectrum was very inhomogeneously broadened for Langmuir-Blodgett (LB) thin films of polymerized SiPc in comparison to dilute monomer solutions – the dilute solutions can be modeled as individual molecules. The inhomogeneous broadening was not as great for monomer SiPc LB thin films, was reduced even further for SiPc doped polystyrene thin films, and very similar to dilute monomer solutions for

SiPc/styrene copolymer films (Note: a copolymer is where the SiPc monomer and the styrene monomer are polymerized together forming a polymer that has both monomer units interspersed in its chain.). The inhomogeneous broadening is reduced in the styrene systems because they have a lower concentration of SiPc and thus there is a reduction in dipole-dipole interactions between adjacent SiPc rings. Copolymerization reduces the inhomogeneity in comparison to the guest/host system because the SiPc molecules are fixed in the polymer chain in the copolymer while they can take any number of configurations in a guest host solid solution. In degenerate four wave mixing (DFWM) experiments, an inverse trend, compared to the inhomogeneous broadening, was seen for the decay of the nonlinearity. The relaxation times of the excited state was seen to increase from about 7 ps for the monomer films to over 50 ps for the SiPc/styrene copolymers. Which suggests that electronic coupling between rings increases the decay of the nonlinearity. Unfortunately, they were only able to measure order of magnitude values for $\chi^{(3)}$ which were between 10^{-9} to 10^{-10} esu for all systems measured, and only stated that the wavelength used was between 560 nm and 760 nm.

Sauer and coworkers [24] reported that the introduction of non-conjugated spacers in between the rings of similar silicon phthalocyanines reduces the inhomogeneous broadening to monomer levels. The side-bands in the Q band are due to vibronics of the $\pi^* \leftarrow \pi$ electronic transition within the phthalocyanine ring, and the fluorescence intensity decreases with aggregation due to a radiationless decay to a forbidden exciton state. This radiationless decay is most likely the source of the shorter decay times for the inhomogeneously broadened systems reported in the aforementioned research. They also noted a phthalocyanine/polysilane copolymer showed an electronic coupling between the phthalocyanine ring and the polymer chain, which red-shifted the UV-absorption band of polysilane to the near UV and reduces the strength of the Q-band.

Casstevens and coworkers [31] reported an effective $\chi^{(3)}_{eff} = 2 \times 10^{-9}$ esu from subpicosecond time-resolved four wave mixing experiments at 602 nm in SiPc diacrylate in Langmuir-Blodgett thin films. They also concluded that there are fast (< 1 ps) exciton-exciton and slow (picoseconds) decay mechanisms for repopulation of the ground state.

Norwood and coworkers [27] reported that the third-order nonlinearity is primarily electronic because the ratio of $\chi^{(3)}_{xxxx}/\chi^{(3)}_{xyyx}$ was 3 in degenerate four wave mixing experiments at 598 nm. The relaxation time for the copolymer was reported as $\approx$ 15 ps which is significantly faster than the greater than 50 ps relaxation time for the SiPc/stryene copolymer. Norwood and coworkers [28] used much of the previously obtained knowledge to demonstrate a nonlinear Bragg mirror in a diacrylate SiPc/PMMA copolymer, where the reflectivity decreases as the incident intensity increases at 690 nm.

Sounik and coworkers [32] demonstrated a slab-waveguide directional coupler using SiPc/PMMA copolymer and determined with Norwood that the ratio of $\chi^{(3)}/\alpha_o$ decreases when the loading of SiPc is above 2%.

It is interesting to note that all the aforementioned studies on the various phthalocyanine systems measured or referred to the linear absorption spectra in there research. However, there were no systematic characterizations of the linear absorption spectra other than assigning names to the regions. The inhomogeneous broadening of polymer spectra in comparison to monomer spectra were qualitatively characterized. In this work we quantitatively model the inhomogeneous broadening of the linear absorption and quadratic electroabsorption spectra for SiPc/PMMA.

1.3 Nonlinear Transverse Loss

The nonlinear transverse loss measurement grew out of my Master's research on transverse loss (linear regime) [33]. The basic idea behind the transverse loss measurement is that the light scattered out of the fiber will be proportional to the light inside the fiber. Thus if we observe the fiber transverse to the propagation direction we will see a signal proportional to the light inside the fiber. In the linear transverse loss measurement, we vary the transverse observation point along the propagation direction in order to determine the absorption coefficient, α for low intensity 1064 nm laser light. By observing the transversely scattered light, the fiber can be left intact for future measurements or applications, unlike the cut-and-measure technique [20].

In the nonlinear regime we are interested in how the light gets absorbed as a function of intensity, because at large intensities we may observe nonlinear (multiphoton) absorption in addition to linear (one-photon) absorption. Typical nonlinear absorption measurements observe the light exiting the end of the fiber [34]. If the fiber is reduced to its $1/e$ absorption length (where the nonlinear absorption will be the largest), the high intensity exiting the fiber end will overload the photodetector, thus optical density filters are needed between the detector and end of the fiber. These filters must then be characterized in terms of their linear and nonlinear absorption in order to get an accurate description of the dye-doped polymer. If the fiber length is longer than the $1/e$ absorption length, the magnitude of the nonlinear absorption is reduced because the light intensity is diminished by linear absorption. However, by observing the transversely scattered light, which is much smaller in magnitude than the intensity exiting the end of the fiber, we can observe at the $1/e$ absorption distance without optical density filters. Thus we were motivated to extend the transverse loss measurement to the nonlinear regime.

By fixing the observation point to at the $1/e$ absorption distance, which is determined in the linear regime using the transverse loss measurement, we observe the scattered intensity as a function of intensity illuminating the front of the fiber. When there is significant nonlinear absorption at high intensities, the intensity of light in the fiber, and hence the transversely scattered light, will not vary linearly with the incident intensity. This implies that α is no longer a constant but a function of intensity.

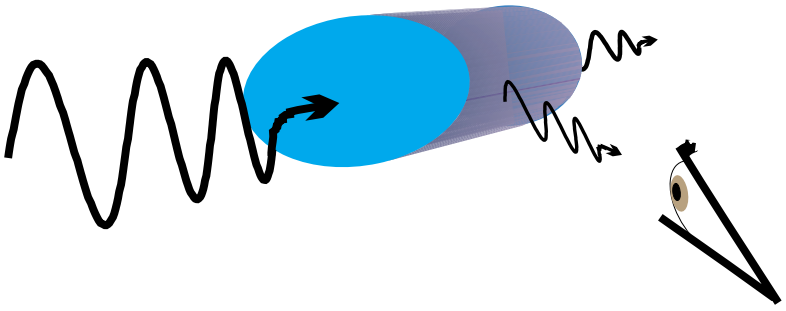

Fig. 1.6: Observation transverse to the fiber axis (propagation direction).

In the nonlinear regime the absorption coefficient is written as a power series in intensity as shown in Section 1.1. The process where two photons are absorbed simultaneously is called two-photon absorption (TPA) and the strength of the absorption is described

by α_2. Thus the goal of the nonlinear transverse loss measurement is to observe how the transversely scattered light varies as a function of intensity and determine the deviation from linearity.

The two-photon absorption (TPA) coefficient for dye-doped polymer optical fibers needs to be determined for several reasons. It is a fundamental property of the dye-doped fiber based on the excited state structure of the dye. Large TPA adversely effects the realization of optical switches and amplifiers because it lowers the two-photon figure of merit [34] which is a gauge of the maximum switching or gain capacity of a device, or the minimum effectiveness of optical limiting devices. For dye-doped polymers to move past the experimental stage to the application stage, novel dye-doped polymers must be characterized in terms of their one- and two-photon absorption coefficients.

While performing the nonlinear transverse loss experiments to determine TPA coefficients for several squaraine-doped polymer fibers, we noticed that the results differed for experiments that started at low intensities and went to high intensities in comparison to experiments that started at high intensities and went to low intensities. Because of these results, we studied the ends of the fiber, where the intensities were the highest, after the TPA experiments were performed. In some instances the fiber ends had black burn spots, which meant we had exceeded the damage threshold of the polymer. However, in other instances there was a general increase in the transparency of the fiber end. This increase in transparency is most likely caused by the dye breaking down at the higher intensities, resulting in smaller molecules whose peak absorption is in the ultra-violet (UV). Thus they appear yellowish-white instead of the typical blue found for squaraine-dye molecules. This degradation appeared to be localized in the first centimeter of fiber where the intensity is the largest but made measuring an accurate TPA coefficient in squaraine-doped PMMA fibers at 1064 nm impractical. Chapter 2 discusses theoretical predictions for TPA in squaraine-doped fibers that show there is minimal TPA near 1064 nm, and Appendix D presents the transverse two-photon absorption experimental details.

1.4 Laser-induced Color Changes

Because of this localized color change in the dye-doped fiber ends during the nonlinear transverse loss experiments, we became interested in the laser-induced characteristics of dye-doped polymers. There are bleaching studies for other dye-doped polymers [35, 36, 37, 38, 39], but none, to our knowledge, on squaraine dyes. Being able to precisely modify the optical properties of a dye-doped polymer fiber opens the door to many optical devices. For example, by inducing a color change in the core of a dye-doped optical fiber, we can create graded-index dye-doped POFs instead of step-index fibers. The advantages of the graded-index fiber are larger core areas so light couples into the fiber more easily and lower signal dispersion, meaning the fiber can carry higher bandwidth signals.

A second example of precisely modifying the index of refraction in dye-doped fibers is bleaching a periodic index of refraction grating into the length of the fiber. The grating is created by interfering two slightly non-parallel laser beams on the fiber transverse to the propagation direction. The wavelengths are chosen so that the dye breaks down or the polymer cross-links in the high intensity regions. Both of these phenomena slightly change the index of refraction in the high intensity regions, where dye breakdown lowers the index of refraction and cross-linking increases the index of refraction. This type of fiber is called a fiber Bragg grating, and the reflectivity/transmissivity is controlled by the grating characteristics.

However, we are initially interested in working with the dye-doped polymer in its bulk form – roughly the same size as a test tube – because we want to determine if the laser light will modify the optical properties of these dye-doped polymers. Two shorter wavelengths (355 nm and 532 nm) are used in these experiments because ultra-violet is the typical region of the electromagnetic spectrum used in laser-induced color change experiments.

The experiments were conducted to determine how precisely we could control color change region. Therefore a mask was used to block specific regions of the circular cross section of the incident illumination which created a very distinct pattern on the illuminated portion of the sample. For example, Figure 1.7 shows a mask that allows a “WSU”

pattern of green (532 nm) light to illuminate the bulk preform sample (Note: A preform is the initial solid form of the dye-doped polymer, roughly test-tube sized, and portions of its end can be parted into slices of desired width before the remainder is drawn into a fiber).

In reality a more mundane double slit mask is used so that the width of each bleached area, and the separation distance between the bleached regions can be compared to the physical dimensions of the mask. If the dimensions are similar, the dye-doped polymer is a good candidate for use as a specialty fiber like a fiber Bragg grating.

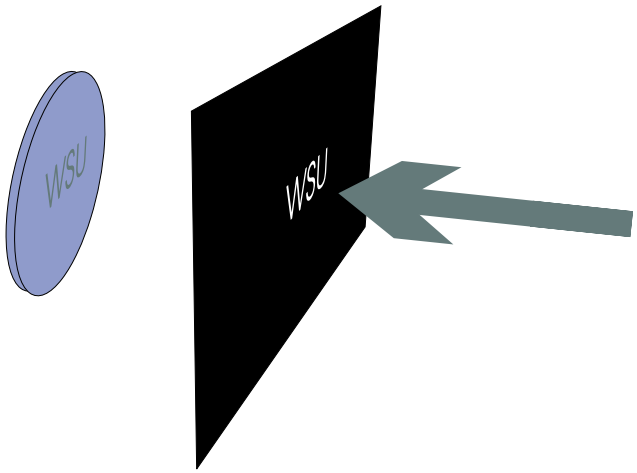

Fig. 1.7: Illumination pattern on a bulk preform slice of dye doped-polymer.

This experiment allowed us to induce color changes in the bulk dye-doped polymer samples which were visible to the naked eye. However, the naked eye is not the best way to quantitatively determine what happened in the exposed region. Thus two experiments, to be described below, were used to quantitatively determine how the index of refraction and the absorption coefficient changed in the affected region.

The first experiment measures the gradient of relative index of refraction as a function of position in a bulk sample of dye-doped polymer. The change in index of refraction is measured using the direct deflection method (DDM) which was developed by Brian Canfield [40] at Washington State University in the Nonlinear Optics Laboratory (NLOL) for measuring the index of refraction change between the core and cladding of step-index dye-doped polymer preforms, and graded-index polymer preforms. The experimental details of DDM can be found in the work done by Canfield [40], but the main observable in the measurement is the deflection of a laser beam as it passes through a sample of dye-

doped polymer. This deflection is proportional to the gradient in the index of refraction in the sample. Thus as the beam position is moved throughout the sample the magnitude of the deflection, captured on a 2-D CCD array, maps the magnitude of the gradient in the index of refraction. Thus by scanning a tightly collimated laser beam in an X-Y raster pattern across the sample the difference in index of refraction can be determined relative to the starting position.

Using a very similar experimental set-up we can also measure the change in absorption coefficient as a function of position in the bulk sample. The main modification in the experiment is that the CCD array is replaced by an ocean optics 2000 spectrometer which is placed closer to the sample so as not to be affected by the small deflection of the laser beam. Thus a white light source or a laser source can be raster scanned across the sample and the absolute absorption spectrum will be recorded at each position.

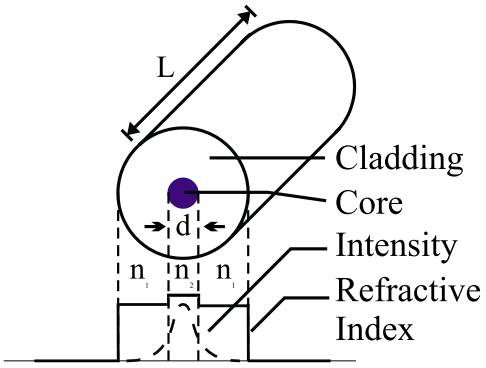

Fig. 1.8: A step-index dye-doped polymer optical fiber.

Thus to totally describe the laser-induced color change in a dye-doped polymer preform slice a three stage cycle is performed. Initially, the preform's index of refraction and absorption coefficient are measured over the entire "fresh" preform to determine if there are any inhomogeneities introduced in the polymerization process. Then the preform is illuminated with 355 nm or 532 nm laser light in a specific pattern determined by the mask placed in the laser beam. Finally, the index of refraction and absorption coefficient are again determined over the entire face of the preform. By comparing the before and after experimental data, we quantitatively determine the changes in both the index of refraction and absorption coefficient due to the laser exposure.

During the course of these experiments several new experiments were designed. We observed that not only could we measure the absorption as a function of position (expo-

sure) in the dye-doped preform slices but for specific combinations of dye-concentration and path length, we could also observe the fluorescence as a function of position (exposure) in the preform slice. Thus without changing the experimental apparatus we gained information about how the fluorescence changed as a function of the laser exposure by choosing an appropriate sample width because we were fortunate enough to be testing out a new Ocean Optics 2000 spectrometer. The details of the laser-induced color change experiments are discussed in Chapter 4.

Two more experiments evolved from the original laser-induced color change experiment. The first involves the Quadratic Electroabsorption (QEA) spectroscopy experiment [3, 2]. Briefly, the change in absorbance due to an applied voltage and mediated by the third-order susceptibility is determined as a function of wavelength in the QEA experiment by applying a voltage across a thin film sample of dye-doped polymer. A new three cycle process (QEA experiment, laser-induced color change, QEA experiment) determines how the third-order susceptibility is affected by 355 nm or 532 nm laser light. Presently, Tow Wofford is working on this project. The second experiment came from the realization that it may be possible to induce a measurable fluorescence in dye-doped fibers using the transverse loss experimental apparatus of Section 1.3.

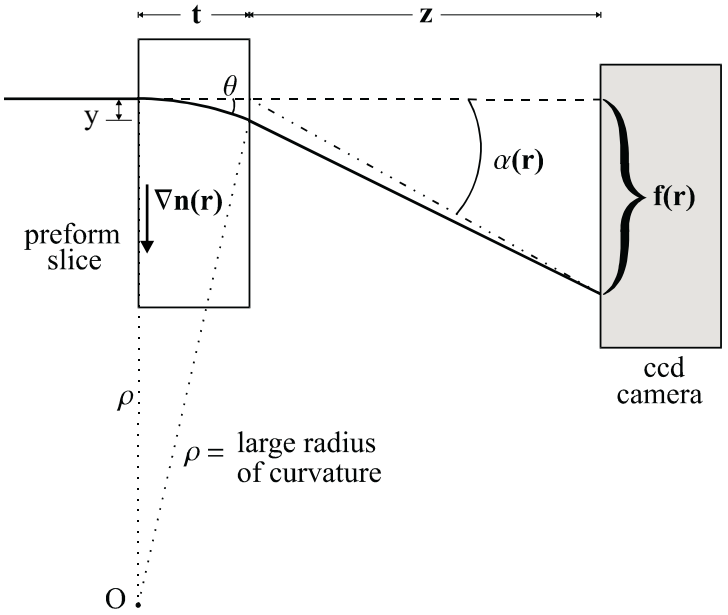

Fig. 1.9: Schematic of the DDM method.

1.5 Transverse Fluorescence

In the absorption experiment described in Section 1.4, the fluorescence signal was the same order of magnitude as the incident signal for ~ 400 μm thick preform slices that were prepared by polymerizing a monomer solution at half the room temperature saturation concentration. With this foreknowledge we realized that the 1.8 m linear translation stage used for the transverse loss measurement was overkill, so moved the new experiment to a different area.

At this point, we only had a vertical translation stage which could house our 693 nm laser diode. The vertical stage allows a precise alignment for exciting the fiber by end-fire coupling. We also machined a fiber chuck, to less than a centimeter in length (typical fiber chucks are about 6 cm in length), so that it could still be mounted in a standard fiber holder and allow measurement near the front fiber face. This was done to maximize the transversely scattered fluorescence. Unfortunately, this fiber chuck was not short enough and the signal measured by the Ocean Optics spectrometer was quite small for an incident illumination at 693 nm.

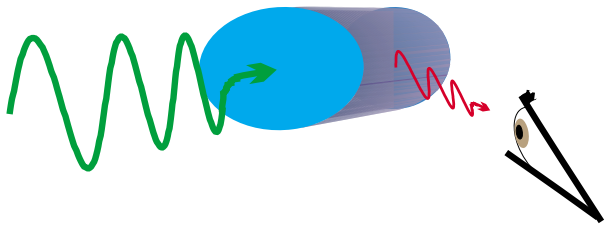

Fig. 1.10: Observation of the fluorescence transverse to the fiber axis.

We also tried moving the light source to the side of the fiber and the detector to the front of the fiber because the fiber geometry is excellent at trapping light due to total internal reflection and should be able to capture the fluorescence more efficiently . When the fluorescence is measured transverse to the fiber axis, we only observed a small fraction of the light that was generated within the possible 360 degrees. The following section describes the evolution of the side-illumination fluorescence measurement which has the light source transverse to the fiber axis and the detector at one end of the fiber.

1.6 Side-illumination Fluorescence

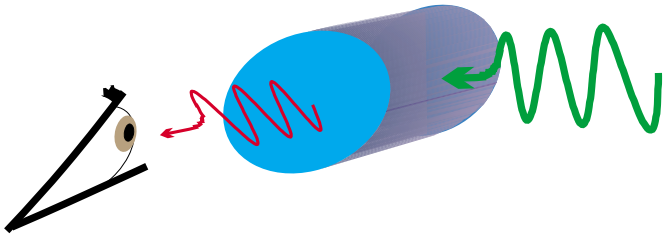

Fig. 1.11: Observation of side-illumination fluorescence at the end of the fiber.

After determining that there was plenty of signal when the fiber was illuminated from the side, we started by observing how the fluorescence signal changes as a function of vertical displacement from the diameter of the excitation. We determined the maximum fluorescence is generated, as expected, when the fiber is illuminated along its diameter. We did experiments as a function of incident intensity, which told us that the transmitted fluorescence is linear in intensity – again as expected, since we were using a continuous wave mW laser diode. Measuring the fluorescence as a function of the incident angle with which the laser illuminates the diameter of the fiber revealed only a small influence on the amount of fluorescence observed at the end of the fiber. The details of these experiments will be explained in Chapter 4.

At this point, we were about to move on to bleaching experiments of QEA samples, as described in Section 1.4, because we did not think there was much more to learn from the side-illumination fluorescence measurement. Fortunately, before the transition could occur, a late afternoon discussion with Steve Vigil lead to the reconstruction of the translation stage for the laser diode so that it could translate in both the vertical and horizontal directions. This recaptured the ability to observe the transmitted signal as a function of propagation distance or illumination position, similar to the transverse loss measurement.

The majority of this work focuses on the side-illumination fluorescence measurement as a function of propagation distance, which we call SIF for short. We probed the majority of the dye-doped fibers that were available at the Nonlinear Optics Laboratory using the SIF technique as our looking glass. Over the course of several months an additional apparatus was constructed that allows the entire fiber system to translate in the vertical

and horizontal directions. This was a large improvement in that we could now use lasers that are fixed to the optical table and could not be mounted in the original stage like the 693 nm laser diode.

During this time we also purchased laser diodes at 645 nm and 670 nm. In addition, we also have a He/Ne 10 mW laser, a continuous wave (cw), argon ion pumped, Ti:Sapphire laser (700 nm - 900 nm), a nanosecond Surlite laser ND:YAG at 1064 nm, and a continuously tuneable optical parametric generator/amplifier (450 nm - 2000 nm) that is pumped with a picosecond tripled ND:YAG laser at our disposal. There is potential of a cw Krypton ion laser for future measurements. This gave us a broad range of incident wavelengths, with various pulse widths, to excite the side-illumination fluorescence in the dye-doped polymer fiber. Thus it was a logical extension of the basic side-illumination experiment at 693 nm, to include SIF measurements as a function of propagation distance for other incident wavelengths that generated sufficient transmitted signal. The experimental details of the SIF measurements will be expanded upon in Chapter 4.

At this stage, we had developed a set of side-illumination measurements that could potentially tell us how the fluorescence is attenuated as it propagates inside the fiber, and how the fluorescence changes as a function of incident wavelength. To quantitatively model the fluorescence attenuation as function of propagation distance we developed two methods: The first method observes monochromatic rays at a wavelength within the fluorescence band as they propagate from the excitation position to the front of the fiber and hence the detector, and the second method compares the entire fluorescence band at two specific positions in the fiber to determine the attenuation spectrum. To determine how a monochromatic rays propagate through multimode fibers we had to familiarize ourselves with geometrical optics. The details are discussed in Chapter 2.

The second method requires the general theory of electronic transitions. The details can be found in Chapter 2. When studying how to model electronic transitions, we learned that there were two general methods for modeling the broadening of the transitions. They are called homogeneous and inhomogeneous broadening and are modeled using a Lorentzian lineshape and a Gaussian envelope of Lorentzian lineshapes, respec-

tively. Because of the two different models we determined that it would be beneficial to test the theories on a simpler system.

Thus we performed some white light transmission experiments on preform slices of available guest-host systems (Chapter 4). These experiments supplied data of the linear absorption near resonance which could be easily fitted using a least-squares analysis for each excited state model (Chapter 2). Using the excited state parameters that we determined from fits to the transmission spectroscopy data, we were then able to propagate the entire fluorescence spectrum from one point in the fiber to another and compare it to the SIF data. The results for both the ray method and the excited state method will be discussed in great detail in Chapter 5.

Models of electronic transitions that were used to analyze the SIF data, were also applied to nonlinear systems. In particular, we were interested in inhomogeneously broadened transitions in the nonlinear regime because they describe the linear absorption more accurately than homogeneously broadened transitions. At the time there was a quantitative theory for second-order nonlinear processes [41], but nothing had been developed for third-order processes. Thus, we established a theory of inhomogeneously broadened electronic transitions for third-order processes based on the framework established by Toussaere [41]. The details are discussed in Chapter 2.

At this point we had determined how the fluorescence was propagating, but we had not explored how the fluorescence changes as a function of incident wavelength and the potential quantities that could be determined from the results of these experiments. We considered factors which effect the generation of fluorescence in dye-doped fibers. From this, we established that we could determine the relative quantum yield of the fluorescence as a function of incident wavelength for each wavelength in the fluorescence band. This is a step beyond the typical quantum efficiency measurement that looks at the integrated fluorescence as a function of incident wavelength by using a photodiode (Note that we can also determine the integrated fluorescence intensity by integrating the total fluorescence measured by the spectrometer over the wavelengths that make a significant contribution.). The details of the theory for determining the relative quantum efficiency of fluorescence generation as a function of incident wavelength at each wavelength within

the fluorescence band are described in Chapter 2.

Over the several months of data taking and data analysis we observed that there was a noticeable change in side-illumination fluorescence signal when the incident intensity was high and the exposure time was long. The extended exposure typically occurred at the beginning and end of the data set. The starting and ending positions experience extended exposure because we illuminate the fiber at these positions to fine adjust the horizontal alignment before the experiment begins. Additional exposure occurs at the end position because there is no shutter to block the laser beam after an experiment finishes. Thus when an absent minded researcher forgets about the experiment, the final position is exposed until something reminds him to turn off the laser, or repeat the run to make sure that data is reproducible.

1.7 Laser induced color changes via SIF

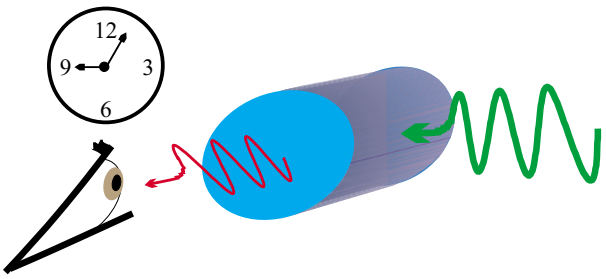

Fig. 1.12: Observation of side-illumination fluorescence as a function of exposure time.

To quantify the dependence of the side-illumination fluorescence signal on exposure time, we devised a new set of experiments which were similar to the laser induced color change experiments, described in Section 1.4, on dye-doped preform slices. The main difference in these sets of experiments is that we were able to monitor the color changes as a function of time for the majority of the fibers studied. In the experiments described in Section 1.4, we only had the "fresh" sample and the exposed sample for comparison because the transmission was too large to monitor as a function of time.

Thus we developed a three step experiment where the side-illumination experiment as a function of propagation distance was performed on a new fiber with low incident intensity, then a specific position was exposed for a finite amount of time at a higher

incident intensity, and finally the side-illumination experiment as a function of propagation distance was repeated at a low incident intensity. We stress that for all but a few fibers we were able to monitor the side-illumination fluorescence signal as a function of exposure time for these larger intensities. This capability is due to the long propagation distances in the side-illumination geometry. The experimental details will be discussed in more detail in Chapter 4.

With the ability to monitor the SIF signal as a function of exposure time, we became interested in modeling the mechanism(s) responsible for the change in fluorescence. This led us to photodegradation in dye-doped polymers. The details of our exposure to this literature are discussed in Chapter 2.

1.8 Quadratic Electroabsorption

We introduced bleaching experiments in conjunction with quadratic electroabsorption in Section 1.4 and a new model for inhomogeneously broadened (IB) electronic transitions in third-order processes in Section 1.6. In this section we discuss the motivation for connecting the QEA experiment to the IB model.

For most dye-doped systems there is inhomogeneous broadening of the electronic transitions due to the dyes interaction with the polymer matrix. In 1969, Stoneham [42] thoroughly discussed inhomogeneously broadened electronic transitions for linear optical processes, and, in 1993, Toussaere discussed inhomogeneously broadened electronic transitions for second-order optical processes. However, the dye molecules used as guests in our polymer fibers are centrosymmetric and only exhibit odd-order nonlinear optical phenomena (3rd,5th, ..-order). Thus to describe inhomogeneously broadened electronic transitions involved in the nonlinear processes for our dye-doped polymers, we must have a theory that is valid for at least third-order processes.

With this goal in mind we searched for a test case to determine if our model actually described third-order optical phenomena. Mathis [2] extended the QEA work of Poga [3] by characterizing five different squaraine dye molecules in PMMA thin films, and Wofford is currently experimenting on laser induced color changes in QEA samples. Because of

this large data base of QEA experimental results, we decided that QEA should be the test case for our IB model of third-order processes.

We also performed some QEA experiments to reproduce the data and develop better intuition for the intricacies of the experiment. Thus the ISQ molecule (see Section 1.2.1), which had been thoroughly studied, and the SiPc molecule (see Section 1.2.2), which had not been studied in a QEA experiment, were chosen for these experiments. The details of the QEA experiment are discussed in Chapter 4, and results of the QEA experiments are found in Chapter 5.

1.9 Reading this dissertation

It is apparent from the chronological description of the experiments performed that there are many intricate connections that weave these experiments into a tapestry that describes how dye-doped polymers behave when illuminated with light. In organizing the remainder of this work we break from the chronological order and describe the theories, experiments, and results in a manner that hopes to be as concise as possible. Thus we develop models (Chapter 2) in terms of both linear and nonlinear optical phenomena, when applicable, and refer back to the specific cases during the discussion of the results. Chapter 3 discusses how to fabricate dye-doped thin films, core preforms, and core fibers. In Chapter 4, the experimental details are discussed in terms of a general molecule. The results and discussion (Chapter 5) are separated first by experiment and when applicable by dye molecule. For example Section 5.2 discusses side-illumination fluorescence spectra from the SIF experiment with subsections for each of the molecules studied. Thus it may be beneficial for the reader not to read the remainder of this work in sequential order, but instead to read the experiment, theory, and results sections for one experiment at a time. We hope to provide sufficient cross referencing as to make this a reasonable endeavor. The final Chapter ties together the results from all the experiments discussed in this introduction and makes recommendations for new directions of research.

Bibliography

[1] D. W. Garvey, "Nonlinear optics in polymer fibers," Ph. D. dissertation (Washington State University, Pullman, WA, 1999).

[2] K. S. Mathis, M. G. Kuzyk, C. W. Dirk, A. Tan, S. Martinez, and G. Gampos, "Mechanisms of the nonlinear optical properties of squarainne dyes in poly(methyl methacrylate) polymer," J. Opt. Soc. Am. B **15**, 871–883 (1998).

[3] C. Poga, "Characterization of the excited states of a squaraine molecule with quadratic electroabsorption spectroscopy," Ph. D. dissertation (Washington State University, Pullman, WA, 1994).

[4] D. J. Welker, J. Tostenrude, D. W. Garvey, B. K. Canfield, and M. G. Kuzyk, "Fabrication and characterization of single mode electrooptic polymer optical fibers," Opt. Lett. **23**, 1826–1828 (1998).

[5] P. N. Butcher and D. Cotter, *The elements of nonlinear optics*, 1st ed. (Cambridge University Press, Cambridge, 1990).

[6] M. G. Kuzyk and C. W. Dirk, eds., *Characterization techniques and tabulations for organic nonlinear optical materials*, 1st ed. (Marcel Dekker, New York, 1998).

[7] Robert W. Boyd, *Nonlinear Optics* (Academic Press, San Deigo, 1992).

[8] J. W. Wu, J. R. Heflin, R. A. Norwood, K. Y. Wong, O. Zamani-Khamiri, A. F. Garito, P. Kalyanaraman, and J. Sounik, "Nonlinear-Optical Processes in Lower-Dimensional Conjugated Structures," J. Opt. Soc. Am. B **6**, 707–20 (1989).

[9] R. W. Bigelow and H.-J. Freund, "An MNDO and CNDO/S(S+DES CI) study on the structural and electronic properties of a model squaraine dye and related cyanine," Chem. Phys. **107**, 159–174 (1986).

[10] S. Marder, J. W. Perry, G. Bourhill, C. B. Gorman, B. G. Tiemann, and K. Mansour, "Relation between bond-length alternation and second electronic hyperpolarizability of conjugated organic molecules," Science **261**, 186 (1993).

[11] J. C. Luong, N. F. Borrelli, and A. R. Olszewski, "Quadratic electro-optical characterization of molecular nonlinear optical materials," Mat. Res. Soc. Symp. Proc. **109**, 251 (1988).

[12] C. W. Dirk and M. G. Kuzyk, "Damping corrections and the calculation of optical nonlinearities in organic molecules," Phys. Rev. B **41**, 1636–39 (1990).

[13] M.G. Kuzyk and C.W. Dirk, "Effects of centrosymmetry on the nonresonant electronic third-order nonlinear optical susceptibility," Phys. Rev. A **41**, 5098 (1990).

[14] M. G. Kuzyk, J. E. Sohn, and C. W. Dirk, "Mechanisms of quadratic electro-optic modulation of dye-doped polymer systems," J. Opt. Soc. Am. B **7**, 842–58 (1990).

[15] Q. L. Zhou, R. F. Shi, O. Zamani-Kamari, and A. F. Garito, "Negative third-order optical responses in squaraines," Nonlinear Opt. **6**, 145–154 (1993).

[16] R. D. Dureiko, D. E. Schuele, and K. D. Singer, "Modeling relaxation processes in poled electro-optic polymer films," J. Opt. Soc. Am. B **15**, 338–50 (1998).

[17] J. H. Andrews, J. D. V. Khaydarov, and K. D. Singer, "Contribution of the 2^1Ag state to the third-order optical nonlinearity in a squaraine dye," Opt. Lett. **19**, 984–986 (1994).

[18] J. H. Andrews, J. D. V. Karydarov, K. D. Singer, D. L. Hull, and K. C. Chuang, "Characterization of excited states of centrosymmetric and noncentrosymmetric squaraines by third-harmonic spectral dispersion," J. Opt. Soc. B **12**, 2360–2371 (1995).

[19] C. Poga, T. M. Brown, M. G. Kuyzk, and Carl W. Dirk, "Characterization of the excited states of a squaraine molecule with quadratic electrosorption spectroscopy," J. Opt. Soc. Am. B **12**, 531–43 (1995).

[20] D. W. Garvey, K. Zimmerman, P. Young, J. Tostenrude, J. S. Townsend, Z. Zhou, M. Lobel, M. Dayton, R. Wittorf, and M. G. Kuzyk, "Single-mode nonlinear-optical polymer fibers," J. Opt. Soc. Am. B **13**, 2017–23 (1996).

[21] G. J. Ashwell, P. C. Williamson, A. Green, G. S. Bahra, and C. R. Brown, "Aggregation-induced linear and non-linear optical properties of four hydroxy-substituted analogues of 2,4-Bis[4-(dibutylamino)phenyl]squaraine," Aust. J. Chem. **51**, 599–604 (1998).

[22] G. J. Ashwell, P. Leeson, G. S. Bahra, and C. R. Brown, "Aggregation-induced second-harmonic generation," J. Opt. Soc. Am. B **15**, 484–8 (1998).

[23] Z. Z. Ho and N. Peyghambarian, "Femtosecond dynamics in organic thin films of fluoro-aluminium phthalocyanine," Chem. Phys. Lett. **148**, 107–111 (1988).

[24] T. Sauer, W. Caseri, and G. Wegner, "Novel phthalocyanine polymers for applications in optical devices," Mol. Cryst. Liq. Cryst. **183**, 387–402 (1990).

[25] A. Kaltbeitzel, D. Neher, C. Bubeck, T. Sauer, G. Wegner, and W. Caseri. "Influence of the Film Preparation on the Nonlinear Optical properties of Phthalocyanine Films,". in H. Kuzmany, M. Mehring, and S. Roth, eds., *Electronic properties of conjugated polymers III*, Vol. 91 of *Springer Series in Solid-State Sciences*, pages 220–24. Springer-Verlag, Berlin, (1989).

[26] J. R. Sounik, "Side-chain copolymers for third-order nonlinear optical applications," Polym. Prepr. Am. Chem. Soc. **32**, 158–159 (1991).

[27] R. A. Norwood and J. R. Sounik, "Third-order nonlinear optical response in polymer thin films incorporating porphyrin derivatives," Appl. Phys. Lett. **60**, 295–297 (1992).

[28] R. A. Norwood, J. R. Sounik, D. Holcomb, J. Popolo, D. Swanson, R. Spitzer, and G. Hansen, "Nonlinear Bragg mirror made from a silicon phthalocyanine/methyl methacrylate copolymer," Opt. Lett. **17**, 577–579 (1992).

[29] Z. Z. Ho, C. Y. Ju, and W. M. Hetherington III, "Third harmonic generation in phthalocyanines," J. Appl. Phys. **62**, 716–718 (1987).

[30] J. S. Shirk, J. R. Lindle, F. J. Bartoli, C. A. Hoffman, Z. H. Kafafi, and A. W. Snow, "Off-resonant third-order optical nonlinearities of metal-substituted phthalocyanines," Appl. Phys. Lett. **55**, 1287–8 (1989).

[31] M. K. Casstevens, M. Samoc, J. Pfleger, and P. N. Prasad, "Dynamics of third-order nonlinear optical processes in Langmuir-Blodgett and evaportated films of phthalocyanines," J. Chem. Phys. **92**, 2019–2024 (1990).

[32] J. R. Sounik, "Silicon phthalocyanine/methyl methacrylate copolymer slab directional couplers for all-optical switching," J. Appl. Polymer Sci. **53**, 677–685 (1994).

[33] R. J. Kruhlak, J. Young, and M. G. Kuzyk, "Loss and correlation measurements in squaraine-doped nonlinear polymer optical fibers," SPIE Proc. **3147**, 118–28 (1997).

[34] V. Mizrahi, K. W. DeLong, G. I. Stegeman, M. A. Saifi, and M. J. Andrejco, "Two-photon absorption as a limitation to all-optical switching," Opt. Lett. **14**, 1140–2 (1989).

[35] R. S. Moshrefzadeh, D. K. Misemer, M. D. Radcliffe, C. V. Francis, and S. K. Mohapatra, "Nonuniform photobleaching of dyed polymers for optical waveguides," Appl. Phys. Lett. **61**, 16–18 (1993).

[36] K. Kinoshita, K. Horie, S. Morino, and T. Nishikubo, "Large photoinduced refractive index changes of a polymer containing photochromic norbornadiene groups," Appl. Phys. Lett. **70**, 2940–42 (1997).

[37] X-y Zhang, Q. Li, J-z Liu, and S. Sottini, "Chemical mechanism of photobleaching of poly-3BCMU film," J. Photochemistry and Photobiology A **95**, 239–44 (1996).

[38] H. Hayashi, T. Kurando, K. Oka, T. Dohmaru, and Y. Nakayama, "Photobleaching Process in Polysilane Films," Jpn. J. Appl. Phys. **35**, 4096–100 (1996).

[39] O. Watanabe, M. Tsuchimori, and A. Okada, "Two-step refractive index changes by photoisomerization and photobleaching processes in the films of non-linear optical polyurethanes and a uretane-urea copolymer," J. Mater. Chem **6**, 1487–92 (1996).

[40] B. Canfield, J. Clearman, M. G. Kuzyk, and C.S. Kwiatkowski, "Refractive index profiles of polymer optical fiber preforms," SPIE Proc. – Nonlinear optical properties of organic materials X **3147**, 128–37 (1997).

[41] E. Toussaere, "Polymer electrooptiques pour l'optique non lineare characterisation optique et modeles statisques," Ph. D. dissertation (University of Paris, Paris, Paris, 1993).

[42] A. M. Stoneham, "Shapes of inhomogeneously broadened resonance lines in solids," Rev. Mod. Phys. **41**, 82–108 (1969).

Chapter 2

Theory

To model wave propagation in nonlinear dielectric media we begin with the two pertinent Maxwell's equations,

$$\nabla \times \mathbf{E}(t) = -\frac{\partial \mathbf{B}(t)}{\partial t}, \tag{2.1}$$

and

$$\nabla \times \mathbf{H}(t) = \frac{\partial \mathbf{D}(t)}{\partial t}. \tag{2.2}$$

We assume there are no free charges or currents, and the medium is non-magnetic because we are modeling pure dielectrics. These assumptions lead us to the following relations,

$$\mathbf{B}(t) = \mu_0 \mathbf{H}(t), \tag{2.3}$$

and

$$\mathbf{D}(t) = \epsilon_0 \mathbf{E}(t) + \mathbf{P}(t), \tag{2.4}$$

where all quantities are defined in SI units. To couple Equations (2.1) and (2.2) and eliminate $\mathbf{H}(t)$, we operate on Equation (2.2) with $\nabla\times$, operate on Equation (2.1) with $\mu_0 \frac{\partial}{\partial t}$ and subtract the results. A driven vector wave equation in the electric field is the final result,

$$\nabla \times \nabla \times \mathbf{E}(t) = -\frac{1}{c^2}\frac{\partial^2 \mathbf{E}(t)}{\partial t^2} - \mu_0 \frac{\partial^2 \mathbf{P}(t)}{\partial t^2}. \tag{2.5}$$

Since we typically deal with monochromatic illumination we may prefer the transform of Equation (2.5) in the frequency domain,

$$\nabla \times \nabla \times \mathbf{E}_\omega = \frac{\omega^2}{c^2}\,\mathbf{E}_\omega + \mu_0 \omega^2 \mathbf{P}_\omega. \tag{2.6}$$

2.1 Nonlinear Polarization

In this section the relationships between the bulk polarization and the bulk susceptibilities are defined under the assumption that the polarization can be expressed as a power series in the applied electric field. The bulk susceptibilities typically represented to characterize the relationships between the polarization amplitudes and the electric field amplitudes in the frequency domain for specific processes and systems; however, we need to briefly return to the time domain to expand the total bulk polarization in a power series with respect to the electric field,

$$\mathbf{P}(t) = \mathbf{P}^{(0)}(t) + \mathbf{P}^{(1)}(t) + \mathbf{P}^{(2)}(t) + \cdots + \mathbf{P}^{(n)}(t) + \cdots, \tag{2.7}$$

where $\mathbf{P}^{(1)}(t)$ is linear in the electric field, $\mathbf{P}^{(2)}(t)$ is quadratic in the electric field, $\mathbf{P}^{(n)}(t)$ is proportional to the n^{th} power of the electric field, and so on. Note that $\mathbf{P}^{(0)}(t)$ represents a static polarization and is independent of the electric field; however, it will be considered zero for the remainder of this work because we study only centrosymmetric materials.

We define the electric field vector, as in Section 1.1, and the n^{th} order polarization vector in the time domain as:

$$\begin{aligned}
\mathbf{E}(t) &= \frac{1}{2}\sum_{\omega' \geq 0} \left[\mathbf{E}_{\omega'} \exp(-i\,\omega' t) + \mathbf{E}_{-\omega'} \exp(i\,\omega' t)\right] \\
&= \sum_{\omega' \geq 0} \Re\left[\mathbf{E}_{\omega'} \exp(-i\,\omega' t)\right], \text{ and} \qquad (2.8) \\
\mathbf{P}^{(n)}(t) &= \frac{1}{2}\sum_{\omega \geq 0} \left[\mathbf{P}^{(n)}_{\omega} \exp(-i\,\omega t) + \mathbf{P}^{(n)}_{-\omega} \exp(i\,\omega t)\right] \\
&= \sum_{\omega \geq 0} \Re\left[\mathbf{P}^{(n)}_{\omega} \exp(-i\,\omega t)\right], \qquad (2.9)
\end{aligned}$$

where $\Re[\,]$ represents the real part, and the frequency argument, ω', of the electric field is not necessarily the same as the polarization frequency, ω. This will be discussed in

detail when we consider specific nonlinear processes. Note that the applied electric field amplitude $(\mathbf{E}_{\omega'})^* = \mathbf{E}_{-\omega'}$ and the polarization amplitude $(\mathbf{P}^{(n)}_{\omega})^* = \mathbf{P}^{(n)}_{-\omega}$ since both $\mathbf{E}(t)$, and $\mathbf{P}(t)$ are real quantities.

Using the procedure found in Butcher and Cotter [1], we write the ν^{th} cartesian component of the n^{th} order Fourier amplitude of the polarization at frequency ω_σ, in SI units, as:

$$\left(P^{(n)}_{\omega_\sigma}\right)_\nu = \epsilon_0 K(-\omega_\sigma;\omega_1,\cdots,\omega_n)\chi^{(n)}_{\nu a....n}(-\omega_\sigma;\omega_1,\cdots,\omega_n)(E_{\omega_1})_a\cdots(E_{\omega_n})_n, \tag{2.10}$$

where $(E_{\omega_n})_n$ is the electric field amplitude at ω_n along the n^{th} cartesian coordinate, $\chi^{(n)}_{\nu a....n}$ is an (n+1) order tensor representing the n^{th} order susceptibility, and K is a degeneracy factor given by the relation:

$$\begin{aligned} K(-\omega_\sigma;\omega_1,\cdots,\omega_n) &= 2^{(l+m-n)}\,\wp \\ \text{where } \wp &= \#\text{ of distinct permutations of } \omega_1,\cdots,\omega_n \\ n &= \text{ order of nonlinearity} \\ m &= \#\text{ of d.c. fields in } \{\omega_1,\cdots,\omega_n\} \\ l &= \begin{cases} 1 & \text{if } \omega_\sigma \neq 0 \\ 0 & \text{otherwise.} \end{cases} \end{aligned} \tag{2.11}$$

Note that the Einstein summation notation is used for repeated indices, and for conservation of energy we require that $\omega_\sigma = \omega_1 + \omega_2 + \cdots + \omega_n$. The polarization amplitude is written with the degeneracy factor multiplying the susceptibility so that the susceptibility will not exhibit a discontinuous jump when any of the frequency arguments tend to zero (i.e. the electrooptic effect) and can be easily compared between different nonlinear processes. This is consistent with Butcher and Cotter [1] but differs from Kuzyk and Dirk [2], Andrews and coworkers [3], Poga [4], and Mathis [5] who define the susceptibility, in Gaussian units, as:

$$\left[\chi^{(n)}_{\nu a....n}(-\omega_\sigma;\omega_1,\cdots,\omega_n)\right]_{eff} = K(-\omega_\sigma;\omega_1,\cdots,\omega_n)\chi^{(n)}_{\nu a....n}(-\omega_\sigma;\omega_1,\cdots,\omega_n) \tag{2.12}$$

For the remainder of this work, we use the Butcher and Cotter convention where the degeneracy factor, $K(-\omega_\sigma;\omega_1,\cdots,\omega_n)$, multiplies the susceptibility and all quantities are defined in SI units.

2.2 Molecular vs. Bulk

Before looking at some concrete examples of higher order susceptibilities, we need to develop a relationship between the bulk polarization and the molecular polarizabilities. To establish a link between the bulk and molecular frames an intermediate reference frame is often defined. This intermediary frame is called the dressed frame and describes how the molecular polarizabilities are related to applied electric fields; the bulk frame describes the relationship between the bulk polarization and applied electric fields and the molecular frame describes the relationship between the molecular polarization and the local (molecular) electric fields.

In the previous section we defined how the bulk polarization is related to the applied electric field. We now consider how the external field $\mathbf{E}$ relates to the electric field at an individual molecule, $\mathbf{F}$ (the local electric field), in order to relate the bulk polarization to the dressed molecular polarization. In general the relation between the applied field and the local field can be written as, $\mathbf{F} = \mathbf{f}(\omega)\cdot\mathbf{E}$, where $\mathbf{f}(\omega)$ is called the tensor local field factor [1].

With this relationship in mind, we define the bulk polarization in terms of the dressed molecular polarization (denoted by $^\bigstar$) as,

$$\mathbf{P}(t) = N\left\langle \mathbf{p}(t)^\bigstar \right\rangle, \tag{2.13}$$

where <> denotes an orientational average, and the dressed frame is used because it is more closely related to what the experimentalist measures [6] than the molecular frame. The molecular dipole moment in the dressed frame can be expanded in a power series in the local electric field (similar to Equation (2.9) [1]):

$$\mathbf{p}(t)^{\bigstar} = (\mathbf{p}^{(0)}(t))^{\bigstar} + (\mathbf{p}^{(1)}(t))^{\bigstar} + (\mathbf{p}^{(2)}(t))^{\bigstar} + \cdots + (\mathbf{p}^{(n)}(t))^{\bigstar}, \tag{2.14}$$

where $(\mathbf{p}^{(n)}(t))^{\bigstar}$ is proportional to the n^{th} power of the applied electric field. We set the zeroth order term in Equation (2.14) to zero, as we did with the zeroth order bulk polarization in Section 2.1, since it represents a static dipole moment.

From Equation (2.14), the first-order dressed molecular polarization amplitude is written as [1],

$$(\mathbf{p}_{\omega}^{(1)})^{\bigstar} = f(\omega)\boldsymbol{\varsigma}^{(1)}(-\omega;\omega)\cdot\mathbf{E}_{\omega} \tag{2.15}$$

where the $\boldsymbol{\varsigma}^{(1)}$ is the molecular polarizability tensor, and $f(\omega)$ is the scalar local field factor at the frequency ω – a good approximation for an isotropic medium. Since there are several models for the molecular polarizability, and the local field factor, they will be discussed in general until it becomes necessary to define the specific models.

For $n \geq 2$, the n^{th} order dressed molecular polarization amplitude is written as,

$$\begin{aligned}(\mathbf{p}_{\omega_\sigma}^{(n)})^{\bigstar} &= (n!)^{-1}Kf(\omega_\sigma)\boldsymbol{\varsigma}^{(n)}(-\omega_\sigma;\omega_1,\cdots,\omega_n)\,|\,f(\omega_1)\cdot\mathbf{E}_{\omega_1}\cdots f(\omega_n)\cdot\mathbf{E}_{\omega_n} \\ &= (n!)^{-1}Kf(\omega_\sigma)f(\omega_1)...f(\omega_n)\boldsymbol{\varsigma}^{(n)}(-\omega_\sigma;\omega_1,\cdots,\omega_n)\,|\,\mathbf{E}_{\omega_1}\cdots\mathbf{E}_{\omega_n},\end{aligned} \tag{2.16}$$

where $K = K(-\omega_\sigma;\omega_1,\cdots,\omega_n)$, the vertical bar, $|$, replaces n vertical dots, and $\boldsymbol{\varsigma}^{(n)}(-\omega_\sigma;\omega_1,\cdots,\omega_n)$ represent the molecular hyperpolarizability tensors. At first glance it seems as though we have an extra local field factor in comparison to the linear molecular polarizability. However, this is correct and is a direct consequence of using the

molecular polarizability, $\boldsymbol{\varsigma}^{(1)}(-\omega;\omega)$, as an approximation in the calculation of the local field [7, 1, 8].

The molecular polarizability is often represented by α or $\gamma^{(1)}$, the molecular hyperpolarizability is often represented by β or $\gamma^{(2)}$, and the second molecular hyperpolarizability is often represented by γ or $\gamma^{(3)}$. The use of α as the molecular polarizability is quite confusing since the bulk absorption coefficient is also denoted by α. We have chosen to leave the linear absorption coefficient in standard notation as α. In Section 2.7.2 we use β to represent a distribution parameter, and in Section 2.4.2 we use γ to represent the inhomogeneous linewidth. For these reasons we have adopted a novel symbol to represent the molecular polarizability and the molecular hyperpolarizabilities.

In our notation, $\boldsymbol{\varsigma}^{(2)}(-\omega_\sigma;\omega_1,\omega_2)$ can be referred to as the molecular hyperpolarizability or the second molecular polarizability, and $\boldsymbol{\varsigma}^{(3)}(-\omega_\sigma;\omega_1,\omega_2,\omega_3)$ can be referred to as the second (quadratic) molecular hyperpolarizability or the third molecular polarizability, which often leads to confusion. We eliminate some of the confusing nomenclature by introducing molecular susceptibilities after defining how the bulk susceptibilities are related to the molecular polarizability and hyperpolarizabilities.

Assuming that the orientation variables, defined in the operation $\langle\ \rangle$, are separable from the polarizability variables[1], we get the following relation between the orientationally averaged dressed molecular polarization and the dressed molecular polarization,

$$\left\langle \mathbf{p}(t)^{\bigstar} \right\rangle = \hat{\phi}\, \mathbf{p}(t)^{\bigstar}, \tag{2.17}$$

where $\hat{\phi}$ is the integral orientational operator. $\hat{\phi}$, in general, depends on the system being studied and the order of the nonlinearity. It will be specified at the same time as the

local field model. Combining Equations (2.2), (2.10), (2.13), (2.15), and (2.17) results in the following relations between the bulk susceptibilities, and the molecular polarizability and hyperpolarizabilities:

$$\boldsymbol{\chi}^{(1)}(-\omega;\omega) = \frac{Nf(\omega)}{\epsilon_o 1!}\left[\hat{\phi}\,\boldsymbol{\varsigma}^{(1)}(-\omega;\omega)\right], \tag{2.18}$$

and

$$\boldsymbol{\chi}^{(n)}(-\omega_\sigma;\omega_1,\cdots,\omega_n) = \frac{N}{\epsilon_o n!} f(\omega_\sigma)f(\omega_1)\cdots f(\omega_n)\left[\hat{\phi}\,\boldsymbol{\varsigma}^{(n)}(-\omega_\sigma;\omega_1,\cdots,\omega_n)\right], \tag{2.19}$$

when $n \geq 2$.

Following the conventions outlined by Butcher and Cotter [1], we define the molecular susceptibilities as,

$$\boldsymbol{\xi}^{(n)} = \frac{\boldsymbol{\varsigma}^{(n)}}{\epsilon_0 n!} \tag{2.20}$$

The use of $\boldsymbol{\xi}^{(n)}$ to represent the molecular susceptibilities is similar to Kuzyk [8], with the exception of the choice in units systems. Thus $\boldsymbol{\xi}^{(1)}$ is the first-order molecular susceptibility and $\boldsymbol{\xi}^{(n)}$ the n^{th}-order molecular susceptibility in contrast to the more clumsy notation where $\boldsymbol{\varsigma}^{(n)}$ is the "$(n-1)^{st}$-order hyperpolarizability". For the remainder of the this work we will use the molecular susceptibility terminology when referring to molecular quantities. As a result of Equation (2.20), the bulk susceptibilities are related to the molecular susceptibilities as follows,

$$\boldsymbol{\chi}^{(1)}(-\omega;\omega) = Nf(\omega)\left[\hat{\phi}\,\boldsymbol{\xi}^{(1)}(-\omega;\omega)\right], \tag{2.21}$$

and

$$\boldsymbol{\chi}^{(n)}(-\omega_\sigma;\omega_1,\cdots,\omega_n) = Nf(\omega_\sigma)f(\omega_1)\cdots f(\omega_n)\left[\hat{\phi}\,\boldsymbol{\xi}^{(n)}(-\omega_\sigma;\omega_1,\cdots,\omega_n)\right], \tag{2.22}$$

when $n \geq 2$.

2.3 Time-dependent perturbation theory

With a general relation between the macroscopic and molecular susceptibilities defined, we focus on defining the frequency dependence of molecular susceptibilities. Because we are interested in centrosymmetric media (no even order contributions to the polarization) to lowest order in the nonlinearity, the following discussion is limited to the first- and third-order molecular susceptibilities. The time-dependent quantum mechanical perturbation theory result of Orr and Ward [9] for the frequency dependence of nonlinear optical transitions is the standard method because it accounts for non-physical secular singularities that appear in a simple application of time-dependent perturbation theory. Orr and Ward use a method of averages in which all zero-denominator contributions cancel. So instead of reproducing their result we update it using a slightly more modern notation for the frequency dependence of the third-order molecular susceptibility [10, 3, 4, 5].

The first-order molecular susceptibility is defined as,

$$\xi^{(1)}_{\nu\alpha}(-\omega;\omega) = \frac{1}{\epsilon_0 1!}\frac{1}{\hbar}\sum_n \left\{ \frac{\mu^{\nu}_{gn}\mu^{\alpha}_{ng}}{\Omega_{gn}-\omega} + \frac{\mu^{\alpha}_{gn}\mu^{\nu}_{ng}}{\Omega^{*}_{gn}+\omega} \right\}, \tag{2.23}$$

where μ^{ν}_{gn} is the ν^{th} component of the transition moment from the ground, g, to n^{th} one-photon excited state, Ω_{gn} is the transition frequency (energy), and ω is the incident and transmitted photon frequency (energy). Note the * on the transition frequency denotes complex conjugation (not to be confused with the dressed frame used for the molecular polarization [Equation (2.14)]).

For a one-dimensional centrosymmetric system the third-order molecular susceptibil-

ity is,

$$\xi^{(3)}(-\omega_\sigma;\omega_1,\omega_2,\omega_3) = \frac{1}{\epsilon_0 3!}\frac{1}{\hbar^3}\left\{\sum_{l,m,n}{}' D_{lmn}(-\omega_\sigma;\omega_1,\omega_2,\omega_3)\mu_{gl}\mu_{lm}\mu_{mn}\mu_{ng} - \sum_{l,n}{}' D_{ln}(-\omega_\sigma;\omega_1,\omega_2,\omega_3)\mu_{gl}\mu_{lg}\mu_{gn}\mu_{ng}\right\}, \quad (2.24)$$

where the $'$ represents the neglect of the ground state in the summation [2], l and n represent one-photon excited states, and m represents two-photon excited states of the system. By convention $D_{lmn}(-\omega_\sigma;\omega_1,\omega_2,\omega_3)$ and $D_{ln}(-\omega_\sigma;\omega_1,\omega_2,\omega_3)$ represent energy denominators (frequency contributions) for two-photon and one-photon contributions to the third-order molecular susceptibility respectively. The discussion the third-order energy denominators will be detailed in Section 2.4.1, where we discuss specific nonlinear experiments.

2.4 Energy denominators

Below we define the energy denominators for homogeneous systems, that is, we assume that the local electric field at each molecule in the dielectric is the same, hence the local field factors can be written as scalars. However, guest-host polymers are typically inhomogeneous due to the dye molecule's interaction with the polymer matrix [11]. In addition to discussing the energy denominators for homogeneous systems (Section 2.4.1), we will develop a method to quantify inhomogeneous systems (Section 2.4.2) such as dye-doped polymer systems. This technique is an extension of Toussaere's [12] method for second-order optical systems, which is based on the method by Stoneham [13] for linear optical systems.

2.4.1 Homogeneous-Broadening

Time-dependent perturbation theory demands that the transition energy is real if the Hamiltonian is to be Hermitian. However, experiments tell us that electronic transitions have a finite lifetime or "energy width". To model the finite lifetime or homogeneous-broadening of electronic transitions we define

$$\Omega_{gn} = \omega_{gn} - i\Gamma_{gn} \tag{2.25}$$

as the complex transition frequency. The real transition frequency, which is a direct result of perturbation theory, is denoted by ω_{gn} and can be used to good approximation for Ω_{gn} when measurements are done far from resonance. However, near an electronic transition it becomes necessary to add an imaginary phenomenological parameter, $i\Gamma_{gn}$, to the transition frequency (energy) [9] since the system typically spends a finite amount of time in an excited state. This phenomenological parameter accounts for various homogeneous broadening mechanisms and characterizes the linewidth (transition width) of the specific electronic transition. The linewidth, Γ_{gn}, is commonly called the Lorentzian, natural, or homogeneous linewidth, and is defined for a transition between the ground and n^{th} excited state. This approximation is typically valid for homogeneous systems like dilute liquids and gases.

A note on the sign choice in Equation (2.25): We have chosen to make the damping term negative which seems counter-intuitive because a complex quantity is usually defined as $z = x + iy$. This break from tradition has it roots in the integral transforms from the time domain to the frequency domain. When the negative sign is used the integrals converge to the familiar form of a Lorentzian denominator; however, when a positive sign

is used the integrals diverge and are unphysical. Since the majority of researchers do not evaluate the time integrals but start in the frequency domain, this subtlety can be overlooked [10, 12, 4]. The most apparent consequence of using a positive sign, when starting in the frequency domain, is that the imaginary part of the susceptibility will have the opposite sign to the actual imaginary part of susceptibility. However, additional consequences are beyond the scope of this work.

2.4.1.1 First-order

Referring to Equation (2.23), the 1-D linear molecular susceptibility can be written as,

$$\begin{aligned} \xi^{(1)}(-\omega;\omega) &= \frac{1}{\epsilon_0 \hbar} \sum_n \left\{ \frac{\mu_{gn}\mu_{ng}}{\Omega_{gn} - \omega} + \frac{\mu_{gn}\mu_{ng}}{\Omega^*_{gn} + \omega} \right\} \\ &= \frac{1}{\epsilon_0 \hbar} \sum_n D_n(-\omega,\omega)\mu_{gn}\mu_{ng}, \end{aligned} \tag{2.26}$$

where we have taken the liberty of reassigning the dummy index, n, from the order of the nonlinearity to the number of excited states and,

$$D_n(-\omega,\omega) = \left\{ \frac{1}{\Omega_{gn} - \omega} + \frac{1}{\Omega^*_{gn} + \omega} \right\}. \tag{2.27}$$

The purpose of defining $D_n(-\omega,\omega)$ will become apparent when higher-order inhomogeneously-broadened electronic transitions are considered.

Figure 2.1a shows the real and imaginary parts of $D_1(-\omega;\omega)$ (i.e. when $n = 1$), which is proportional to the linear molecular susceptibility. Clearly, the real part of $D_1(-\omega;\omega)$ is related to the index of refraction of the material and the imaginary part is related to the absorption. However, if we were to use the opposite sign for the complex part of the transition energy we would get the result shown in Figure 2.1b. Thus in the linear

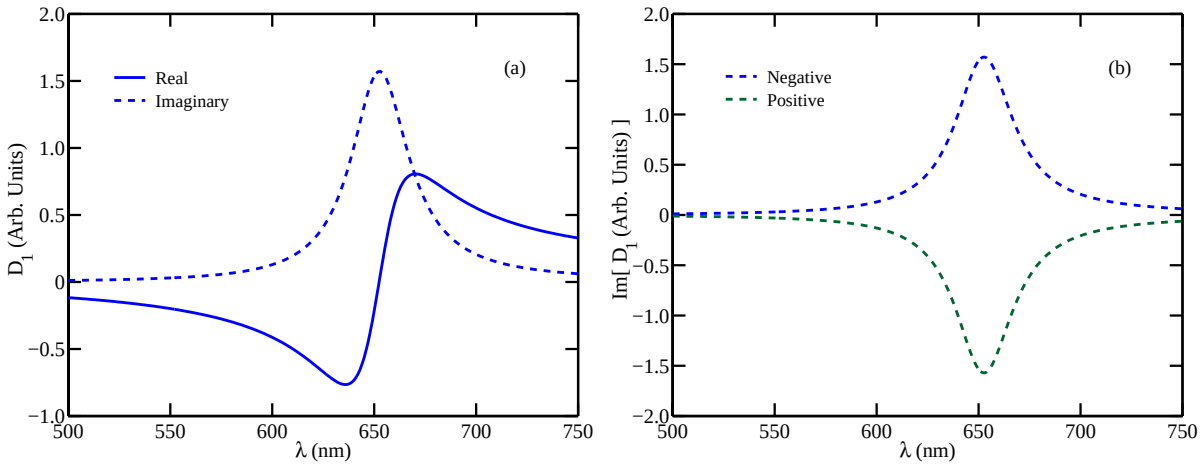

Fig. 2.1: (a) Real and imaginary parts of $D_1(-\omega;\omega)$ for a single excited state centered about 653 nm, (b) Imaginary part of $D_1(-\omega;\omega)$ for the correct (negative) and incorrect (positive) sign for the imaginary part of the transition frequency (energy) .

case an incorrect sign for the imaginary part of the transition frequency results in gain instead of absorption.

2.4.1.2 Third-order

Now that the linear energy denominator is familiar, we introduce the complete definitions for the one-photon and two-photon energy denominator contributions to the third-order molecular susceptibility,

$$\begin{aligned} D_{ln}(-\omega_\sigma;\omega_1,\omega_2,\omega_3) \quad = \mathbf{S}_{1,2,3} \Big\{ & \big[(\Omega_{lg}-\omega_\sigma)(\Omega_{lg}-\omega_3)(\Omega_{ng}-\omega_1)\big]^{-1} + \\ & \big[(\Omega_{lg}-\omega_3)(\Omega^*_{ng}+\omega_2)(\Omega_{ng}-\omega_1)\big]^{-1} + \\ & \big[(\Omega^*_{lg}+\omega_\sigma)(\Omega^*_{lg}+\omega_3)(\Omega^*_{ng}+\omega_1)\big]^{-1} + \\ & \big[(\Omega^*_{lg}+\omega_3)(\Omega_{ng}-\omega_2)(\Omega^*_{ng}+\omega_1)\big]^{-1} \Big\}, \end{aligned} \tag{2.28}$$

and

$$
\begin{aligned}
D_{lmn}(-\omega_\sigma;\omega_1,\omega_2,\omega_3) \;= \mathbf{S}_{1,2,3}\,\Big\{&\left[(\Omega_{lg}-\omega_\sigma)(\Omega_{mg}-\omega_1-\omega_2)(\Omega_{ng}-\omega_1)\right]^{-1}+\\
&\left[(\Omega^*_{lg}+\omega_3)(\Omega_{mg}-\omega_1-\omega_2)(\Omega_{ng}-\omega_1)\right]^{-1}+\\
&\left[(\Omega^*_{lg}+\omega_1)(\Omega^*_{mg}+\omega_1+\omega_2)(\Omega_{ng}-\omega_3)\right]^{-1}+\\
&\left[(\Omega^*_{lg}+\omega_1)(\Omega^*_{mg}+\omega_1+\omega_2)(\Omega^*_{ng}+\omega_\sigma)\right]^{-1}\Big\}, \qquad (2.29)
\end{aligned}
$$

respectively.

The symbol $\mathbf{S}_{1,2,3}$ represents the intrinsic permutation operator, which is a concise way of telling us to sum all distinct permutations of ω_1, ω_2, and ω_3 for each term in the curly braces. For example, if $\omega_2 = \omega_3 = 0$ (electrooptic effect), there are three distinct permutations (ω, 0, 0), (0, ω, 0), and (0, 0, ω). This implies that D_{lmn} and D_{ln} each contain 12 terms, some of which may be duplicates, as shown for the electrooptic effect. The semi-colon is used to separate the input frequencies from the output frequency. In other words the three frequencies the right of the semi-colon are input frequencies and the remaining frequency is the output frequency.

2.4.2 Inhomogeneous-Broadening

Unfortunately, most guest-host materials exhibit inhomogeneous broadening due to coupling between the guest and host, aggregation of the guest, thermal fluctuations, etc. This suggests that the homogeneous-broadening theory may not be adequate to accurately model well resolved spectroscopic experiments. Thus, our goal is to develop a new model which can account for homogeneous- and inhomogeneous-broadening mechanisms of the nonlinear optical response in a guest-host system.

Before this method can be developed, we need to introduce the Gaussian probability distribution,

$$g_{mn}(z) = \frac{1}{\gamma_{mn}\sqrt{\pi}} \exp(-\frac{z^2}{\gamma_{mn}^2}), \tag{2.30}$$

and the complex error function [14],

$$W(z) = \frac{i}{\pi} \int_{-\infty}^{\infty} \frac{\exp(-t^2)}{z-t} dt = \exp(-z^2)\mathrm{erfc}(-iz), \tag{2.31}$$

respectively.

The Gaussian function is used to model the distribution of molecular properties of an ensemble of dye molecules in a polymer matrix. The electronic response of this system of molecules behaves as the sum of individual molecules whose electronic resonances differ due to slightly different configurations, positions, and local fields within the polymer matrix. Thus we use a Gaussian envelope to model this distribution of sites where γ_{mn} describes the breadth of the distribution between the m^{th} and n^{th} state and is often called the inhomogeneous linewidth.

The argument, z, to the Gaussian function and the complex error function is an arbitrary complex number. Because we are modeling an ensemble of dye molecules, the scalar local field factor, $f(\omega)$, becomes the average local field factor of the ensemble. Equation (2.30) is written so the integral of $g_{mn}(z)$ is normalized to unity:

$$\int_{-\infty}^{\infty} g_{mn}(z) dz = 1. \tag{2.32}$$

By introducing the complex error function, $W(z)$, which is used to model distributions of Lorentzian's, we remain compatible with the theory of inhomogeneous-broadening for second-order processes [12]. $W(z)$ also has standard numerical approximations [14]

for all values of z which makes numerical computations straight forward. With the aforementioned definitions, we are ready to discuss the transformation from the standard Lorentzian model for homogeneous-broadening to a model which accounts for inhomogeneous-broadening.

2.4.2.1 First-order

We begin with the linear transform, which was worked out as far back as 1969[13], and then we tackle the more complicated nonlinear transform in the following section. To account for the inhomogeneous-broadening of a molecular system, in which the individual molecules are each homogeneously-broadened, the energy denominator is modeled as the integral of the product of Equation (2.27) and (2.30) as follows [13, 12, 15, 16],

$$\begin{aligned} D_n^{IB}(-\omega;\omega) &= \int_{-\omega_{gn}}^{\infty} D_n^{L}(-\omega;\omega) g_{gn}(\delta\omega_{gn}) d(\delta\omega_{gn}), \\ &= \int_{-\omega_{gn}}^{\infty} \left[\frac{1}{\omega_{gn}^{'} - i\Gamma_{gn} - \omega} + \frac{1}{\omega_{gn}^{'} + i\Gamma_{gn} + \omega} \right] g_{gn}(\delta\omega_{gn}) d(\delta\omega_{gn}), \end{aligned} \quad (2.33)$$

where $\delta\omega_{gn} = \omega_{gn}^{'} - \omega_{gn}$, and the superscripts stand for the following: IB = inhomogeneous-broadening, and L = Lorentzian(homogeneous)-broadening. To be completely rigorous the lower limit of integration is $-\omega_{gn}$ instead of $-\infty$ because of the positive valued restriction on $\omega_{gn}^{'}$ (i.e. $0 \leq \omega_{gn}^{'} \leq \infty$). In the optical regime the lower limit can be set to $-\infty$ with out affecting the value of the integral because the negative argument in the exponential centers the function about $\delta\omega_{gn} = 0$; however, we work through the derivation rigorously in case this approximation is not valid in special cases probed by certain experiments. In this linear regime, Equation (2.33) is often referred to as a Voigt profile, and there are several different methods that have been used to evaluate

the integrals (Direct numerical integration, Fourier Transforms, complex error functions, etc).

We choose to manipulate the integrals in Equation (2.33) into complex error functions [12, 15, 16]. Focusing on the first term in Equation (2.33), we substitute Equation (2.30) for the Gaussian function, change the integration variable to $t = (\omega'_{gn} - \omega_{gn})/\gamma_{gn}$, and rearrange the denominator so that $z = (-\omega_{gn} + i\Gamma_{gn} + \omega)/\gamma_{gn}$ to get the following

$$\begin{aligned}
&\int_{-\omega_{gn}}^{\infty} \frac{1}{\omega'_{ng} - i\Gamma_{ng} - \omega} g_{ng}(\omega'_{ng} - \omega_{ng}) d(\omega'_{ng} - \omega_{ng}) \\
&= \frac{1}{\gamma_{ng}\sqrt{\pi}} \int_{-\omega_{gn}}^{\infty} \frac{\exp(-(\frac{\omega'_{ng}-\omega_{ng}}{\gamma_{ng}})^2)}{\omega'_{ng} - i\Gamma_{ng} - \omega} d(\omega'_{ng} - \omega_{ng}), \\
&= \frac{1}{\gamma_{gn}\sqrt{\pi}} \int_{-\frac{\omega_{gn}}{\gamma_{ng}}}^{\infty} \frac{\exp(-t^2)}{t + (\frac{\omega_{ng} - i\Gamma_{ng} - \omega}{\gamma_{ng}})} dt, \\
&\simeq -\frac{1}{\gamma_{gn}\sqrt{\pi}} \int_{-\infty}^{\infty} \frac{\exp(-t^2)}{z - t} dt, \\
&= \frac{i\sqrt{\pi}}{\gamma_{gn}} W(z). \qquad (2.34)
\end{aligned}$$

Thus we have the first term in Equation (2.33) in terms of $W(z)$, which can be evaluated for all values of z using the results in Abramowitz and Stegun [14].

This procedure can be generalized for any complex denominator when there is a linear dependence on the transition frequency, ω'_{gn}. Table 2.1 shows the results of the transforms for the two terms in Equation (2.33), and the general transform for a complex denominator which is linear in the transition frequency.

In the final entry in Table 2.1, C_1 represents an arbitrary constant or function that does not involve ω_{mn} and the variable z_{mn} is an arbitrary complex number which has a linearly dependence on the transition frequency, ω_{mn}. Thus the final form of the linear

Table 2.1: Denominator contributions to the linear molecular susceptibility for homogeneously-broadened and inhomogeneously-broadened electronic transitions.

Homogeneous-Broadening	Inhomogeneous-Broadening
$\frac{1}{\Omega_{gn}-\omega}$	$\frac{i\sqrt{\pi}}{\gamma_{gn}} W\left(\frac{-(\Omega_{gn}-\omega)}{\gamma_{gn}}\right)$
$\frac{1}{\Omega^*_{gn}+\omega}$	$\frac{i\sqrt{\pi}}{\gamma_{gn}} W\left(\frac{-(\Omega^*_{gn}+\omega)}{\gamma_{gn}}\right)$
$\frac{C_1}{z_{mn}}$	$\frac{i\sqrt{\pi}C_1}{\gamma_{mn}} W\left(\frac{-(z_{mn})}{\gamma_{mn}}\right)$

energy denominator, which accounts for inhomogeneous-broadening, can be written as,

$$D_n^{IB}(-\omega;\omega) = \frac{i\sqrt{\pi}}{\gamma_{gn}}\left[W\left(\frac{-(\Omega_{gn}-\omega)}{\gamma_{gn}}\right) + W\left(\frac{-(\Omega^*_{gn}+\omega)}{\gamma_{gn}}\right)\right]. \tag{2.35}$$

Equation (2.35) has two terms, similar to Equation (2.27). The first term is the resonant term because it becomes large when the photon frequency is close to the real part of the transition frequency, and the second term is the non-resonant term.

Usually, the homogeneous linewidth, Γ, is fixed for a specific molecule and the inhomogeneous linewidth, γ varies based on the characteristics of the host material. However, the majority of results in the literature are based on the standard Lorentzian theory, so the measured linewidth has been called the homogeneous linewidth independent of the host material. This suggests that we do not know the homogeneous linewidth. Thus, we fix the inhomogeneous linewidth and vary the homogeneous linewidth for comparisons of the inhomogeneous-broadening and Lorentzian theories in this chapter.

Figure 2.2 shows the real and imaginary parts of $D_1^L(-\omega;\omega)$, Equation (2.27), and

$D_1^{IB}(-\omega;\omega)$, Equation (2.35) for a one-photon excited state ($n = 1$) centered about 653 nm. The dashed curves represent the homogeneously-broadened electronic transition and the solid curves represent inhomogeneously-broadened electronic transitions. Figure 2.2 shows three cases of inhomogeneous-broadening: The first case depicts the homogeneous linewidth, Γ_{g1}, equal to the inhomogeneous linewidth, γ_{g1}; the second depicts Γ_{g1} equal to 2/5's of γ_{g1}, and the third depicts Γ_{g1} equal to 1/5 of γ_{g1}. These three values of Γ_{g1} were chosen to show that the maximum value of both the real and imaginary parts of the energy denominator increase with decreasing homogeneous linewidth when the inhomogeneous linewidth is fixed. 50 meV was chosen for the inhomogeneous linewidth because it is a good starting point for modeling electronic transitions in squaraine-doped PMMA systems [4, 17, 5] and meV is a common unit used to represent transition widths (i.e. $\hbar\Gamma$, when $\hbar$ is given in eV·s). The dependence of the inhomogeneous-broadening theory on the homogeneous linewidth will be discussed in greater detail in Section 2.4.2.2.1.

Notice that there is a significant difference in both the real and imaginary parts of the energy denominator when inhomogeneous-broadening is taken into account. However, the differences between the two theories is most recognizable in the plot of the imaginary part of $D_1(-\omega;\omega)$ which is proportional to the linear absorption coefficient, α. When $\Gamma_{g1} = \gamma_{g1}$ the Lorentzian characteristics (i.e. large (broad) wings) dominate the shape of the resonance absorption. As Γ_{g1} decreases in magnitude the absorption resonance tends towards Gaussian features (i.e. small wings) until it is completely Gaussian when $\Gamma_{g1} = 0$. Thus linear absorption data can be fit to both homogeneous and inhomogeneous theories to determine which theory better describes the system. Once the appropriate

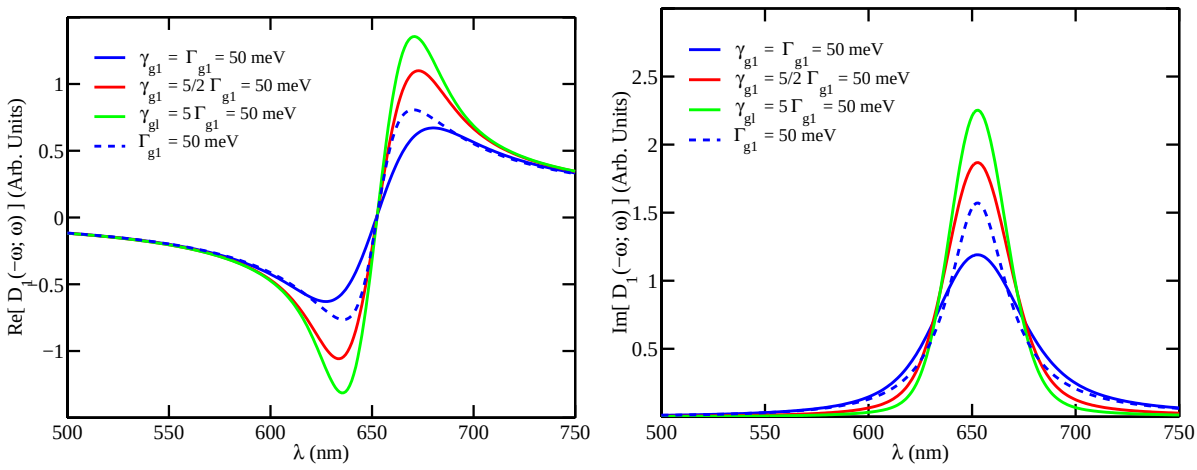

Fig. 2.2: (a) Real and imaginary parts of $D_1(-\omega;\omega)$ for a single excited state centered about 653 nm. The solid curves represent the inhomogeneous-broadening theory of the electronic transition with three different Γ_{g1}, and the dashed curve represents the homogeneous-broadening theory of the electronic transition.

model has been determined for the linear phenomena, it can be used to describe nonlinear (third-order) phenomena which is the topic of the next section.

2.4.2.2 Third-order

The conversion from a Lorentzian description of electronic transitions to an inhomogeneously broadened description is not as straight forward for nonlinear optical processes. Toussaere [12] made a large stride forward when he described how to model two second-order processes in terms of inhomogeneously-broadened electronic transitions (Second Harmonic Generation (SHG) and the Pockels effect). However, the molecules and/or systems that we are interested in are centrosymmetric, so the third-order susceptibility is the first non-zero nonlinear susceptibility we can expect to observe. To model

inhomogeneous-broadening in third-order systems, the second-order inhomogeneous-broadening theory **must** be extended to a third-order theory. This section describes how to transform the Lorentzian third-order energy denominators (Equations (2.28) and (2.29)) to third-order energy denominators that account for inhomogeneous-broadening.

Unfortunately the transformation from homogeneously-broadened electronic transitions to inhomogeneously-broadened electronic transitions is process-specific in the nonlinear regime. This means that for each different experiment the transformation must be worked out from the beginning – by beginning, we mean substituting the three specific input frequencies into Equations (2.28) and (2.29)– and is most likely why Toussaere [12] only worked out the details for two second-order processes.

The procedure for nonlinear processes, although more complicated because of the products of unique functions of the transition frequency in the denominators, can be reduced to linear transforms discussed in Section 2.4.2.1, for most cases, using partial fraction expansions. For the few terms that cannot be coerced into complex denominators that are linear in the transition frequency, we can use integration by parts to reduce the nonlinear dependence on the transition frequency to a linear dependence. Since the partial fraction expansions of the energy denominators are process specific, we will discuss them in the following three sections 2.4.2.2.1, 2.4.2.2.2, and 2.4.2.2.3 which describe in detail the transformations from homogeneously-broadened electronic transitions to inhomogeneously-broadened electronic transitions for third harmonic generation, the quadratic electrooptic effect, and the optical Kerr effect (intensity dependent refractive

index and pump-probe experiments), respectively.

However, we initially derive the fundamental transforms from the homogeneous formulation to the inhomogeneous formulation for both quadratic and cubic dependencies on the transition frequency, ω_{gn}. Beginning with a quadratically dependent term like the following,

$$\frac{C_2}{(\omega'_{gn} - i\Gamma_{gn} - \omega)^2} \tag{2.36}$$

we integrate its product with the Gaussian function (Equation (2.30)),

$$\int_{-\omega_{gn}}^{\infty} \frac{C_2}{(\omega'_{gn} - i\Gamma_{gn} - \omega)^2} g_{gn}(\omega'_{gn} - \omega_{gn})\, d(\omega'_{gn} - \omega_{gn}), \tag{2.37}$$

as the initial step in the transform. Substituting Equation (2.30) for $g_{gn}(\omega'_{gn} - \omega_{gn})$, and changing the integration variable to $t = (\omega'_{gn} - \omega_{gn})/\gamma_{gn}$, results in the following:

$$\begin{aligned}
&\int_{-\omega_{gn}}^{\infty} \frac{C_2}{(\omega'_{gn} - i\Gamma_{gn} - \omega)^2} g_{gn}(\omega'_{gn} - \omega_{gn}) d(\omega'_{gn} - \omega_{gn}) \\
&= \frac{C_2}{\gamma_{gn}\sqrt{\pi}} \int_{-\omega_{gn}}^{\infty} \frac{\exp(-(\frac{\omega'_{gn} - \omega_{gn}}{\gamma_{gn}})^2)}{(\omega'_{gn} - i\Gamma_{gn} - \omega)^2} d(\omega'_{gn} - \omega_{gn}), \\
&= \frac{C_2}{\gamma_{gn}\sqrt{\pi}} \int_{-\frac{\omega_{gn}}{\gamma_{gn}}}^{\infty} \frac{\gamma_{gn} \exp(-t^2)}{(\omega'_{gn} - i\Gamma_{gn} - \omega)^2} dt, \\
&= \frac{C_2}{\gamma_{gn}\sqrt{\pi}} \int_{-\frac{\omega_{gn}}{\gamma_{gn}}}^{\infty} \frac{\gamma_{gn} \exp(-t^2)}{(\omega_{gn} + \gamma_{gn} t - i\Gamma_{gn} - \omega)^2} dt, \\
&= \frac{C_2}{\gamma_{gn}\sqrt{\pi}} \int_{-\frac{\omega_{gn}}{\gamma_{gn}}}^{\infty} \frac{\gamma_{gn} \exp(-t^2)}{\gamma_{gn}^2 (t + \frac{\omega_{gn} - i\Gamma_{gn} - \omega}{\gamma_{gn}})^2} dt, \\
&= \frac{C_2}{\gamma_{gn}^2\sqrt{\pi}} \int_{-\frac{\omega_{gn}}{\gamma_{gn}}}^{\infty} \frac{\exp(-t^2)}{(z - t)^2} dt,
\end{aligned} \tag{2.38}$$

where $z = (-\omega_{gn} + i\Gamma_{gn} + \omega)/\gamma_{gn}$. Equation (2.38) looks very similar to Equation (2.34) just before substituting for $W(z)$ except that the denominator in the integral is second-order in $(z - t)$. To reduce the denominator to first-order in $(z - t)$ so that the integral

can be replaced with $W(z)$, we perform integration by parts twice:

$$\begin{aligned}\int_{-\frac{\omega_{gn}}{\gamma_{gn}}}^{\infty} \frac{\exp(-t^2)}{(z-t)^2}dt &= \int_{-\frac{\omega_{gn}}{\gamma_{gn}}}^{\infty} \frac{2t\exp(-t^2)}{(z-t)}dt, \\ &= 2z\int_{-\frac{\omega_{gn}}{\gamma_{gn}}}^{\infty} \frac{\exp(-t^2)}{(z-t)}dt - 2\int_{-\frac{\omega_{gn}}{\gamma_{gn}}}^{\infty} \exp(-t^2)dt, \\ &\simeq -2i\pi z W(z) - 2\sqrt{\pi}, \end{aligned} \tag{2.39}$$

where the two terms that are not integrals from the integration by parts are zero because the argument of the exponential is $\approx -10^3$ at the lower limit because $\omega \gg \gamma$ in the visible. Note Equation (2.39) is equal to the result that would have been obtained if the integral was over all space from the very beginning. However, we keep the lower limit of integration in case future experiments explore frequency ranges where the approximation does not hold (i.e in the far infrared). Therefore we can write Equation (2.37) as the following,

$$\begin{aligned}&\int_{-\omega_{gn}}^{\infty} \frac{C_2}{(\omega'_{gn} - i\Gamma_{gn} - \omega)^2} g_{gn}(\omega'_{gn} - \omega_{gn})d(\omega'_{gn} - \omega_{gn}) \\ &= \frac{C_2}{\gamma_{gn}^2\sqrt{\pi}}\left\{-2i\pi z W(z) - 2\sqrt{\pi}\right\} \\ &= \frac{C_2 i\sqrt{\pi}}{\gamma_{gn}}\left\{\frac{-2z}{\gamma_{gn}}W(z) + \frac{2i}{\sqrt{\pi}\gamma_{gn}}\right\}. \end{aligned} \tag{2.40}$$

Thus we have derived a transformation for a second-order denominator term which can be generalized to any complex term that has a second-order dependence on $(z-t)$. However, we need to derive a transformation for third-order denominator terms in order to model all the third-order experiments. As an example function for the third-order case we use,

$$\frac{C_3}{(\omega'_{gn} - i\Gamma_{gn} - \omega)^3} \tag{2.41}$$

The third-order procedure initially follows the linear and second-order derivations. Equation (2.41) multiplied by the Gaussian function is integrated with respect to $\delta\omega_{gn}$, the integration variable is changed to $t = (\omega'_{gn} - \omega_{gn})/\gamma_{gn}$, and z replaces $(-\omega_{gn} + i\Gamma_{gn} + \omega)/\gamma_{gn}$, to get the following:

$$\begin{aligned}
&\int_{-\omega_{gn}}^{\infty} \frac{C_3}{(\omega'_{gn} - i\Gamma_{gn} - \omega)^3} g_{gn}(\omega'_{gn} - \omega_{gn}) d(\omega'_{gn} - \omega_{gn}) \\
&= \frac{C_3}{\gamma_{gn}\sqrt{\pi}} \int_{-\omega_{gn}}^{\infty} \frac{\exp(-(\frac{\omega'_{gn} - \omega_{gn}}{\gamma_{gn}})^2)}{(\omega'_{gn} - i\Gamma_{gn} - \omega)^3} d(\omega'_{gn} - \omega_{gn}), \\
&= \frac{C_3}{\gamma_{gn}\sqrt{\pi}} \int_{-\frac{\omega_{gn}}{\gamma_{gn}}}^{\infty} \frac{\gamma_{gn} \exp(-t^2)}{(\omega'_{gn} - i\Gamma_{gn} - \omega)^3} dt, \\
&= \frac{C_3}{\gamma_{gn}^3\sqrt{\pi}} \int_{-\frac{\omega_{gn}}{\gamma_{gn}}}^{\infty} \frac{\exp(-t^2)}{(t + \frac{\omega_{gn} - i\Gamma_{gn} - \omega}{\gamma_{gn}})^3} dt, \\
&= \frac{-C_3}{\gamma_{gn}^3\sqrt{\pi}} \int_{-\frac{\omega_{gn}}{\gamma_{gn}}}^{\infty} \frac{\exp(-t^2)}{(z - t)^3} dt. \qquad (2.42)
\end{aligned}$$

Again we have reached a point where the integral looks very similar to $W(z)$ except that the denominator is third-order in $(z - t)$ instead of first-order. To reduce the denominator to first-order in $(z-t)$ we use integration by parts. The first two integration by parts result in the following:

$$\begin{aligned}
\int_{-\frac{\omega_{gn}}{\gamma_{gn}}}^{\infty} \frac{\exp(-t^2)}{(z - t)^3} dt &= \int_{-\frac{\omega_{gn}}{\gamma_{gn}}}^{\infty} \frac{t \exp(-t^2)}{(z - t)^2} dt, \\
&= 2\int_{-\frac{\omega_{gn}}{\gamma_{gn}}}^{\infty} \frac{t^2 \exp(-t^2)}{(z - t)} dt - \int_{-\frac{\omega_{gn}}{\gamma_{gn}}}^{\infty} \frac{\exp(-t^2)}{(z - t)} dt, \qquad (2.43)
\end{aligned}$$

where the two terms that are not integrals from the integration by parts are zero because the argument of the exponential is $\approx -10^3$ at the lower limit because $\omega \gg \gamma$ in the visible.

The second term in Equation (2.43) is now related to $W(z)$, but it is necessary to manipulate the first term using $(z + t) = (z^2 - t^2)/(z - t)$. The $t/(z - t)$ integrates to

zero, so we get following:

$$\begin{aligned}
\int_{-\frac{\omega_{gn}}{\gamma_{gn}}}^{\infty} \frac{\exp(-t^2)}{(z-t)^3}dt &= 2z^2\int_{-\frac{\omega_{gn}}{\gamma_{gn}}}^{\infty} \frac{\exp(-t^2)}{(z-t)}dt - 2z\int_{-\frac{\omega_{gn}}{\gamma_{gn}}}^{\infty} \exp(-t^2)dt - \int_{-\frac{\omega_{gn}}{\gamma_{gn}}}^{\infty} \frac{\exp(-t^2)}{(z-t)}dt, \\
&= (2z^2-1)\int_{-\infty}^{\infty} \frac{\exp(-t^2)}{(z-t)}dt - 2z\int_{-\frac{\omega_{gn}}{\gamma_{gn}}}^{\infty} \exp(-t^2)dt, \\
&\simeq (1-2z^2)i\pi W(z) - 2z\sqrt{\pi}. \qquad (2.44)
\end{aligned}$$

Therefore the final form of the transform from a homogeneously-broadened to inhomogeneously-broadened electronic transitions for a denominator contribution that has a cubic dependence on the transition frequency is,

$$\begin{aligned}
&\int_{-\infty}^{\infty} \frac{C_3}{(\omega'_{gn} - i\Gamma_{gn} - \omega)^3} g_{gn}(\omega'_{gn} - \omega_{gn})d(\omega'_{gn} - \omega_{gn}) \\
&= \frac{-C_3}{\gamma_{gn}^3\sqrt{\pi}}\left\{(1-2z^2)i\pi W(z) - 2z\sqrt{\pi}\right\}, \\
&= \frac{i\sqrt{\pi}C_3}{\gamma_{gn}}\left\{\frac{2z^2-1}{\gamma_{gn}^2}W(z) - \frac{2iz}{\sqrt{\pi}\gamma_{gn}^2}\right\}, \qquad (2.45)
\end{aligned}$$

where $z = (-\omega_{gn} + i\Gamma_{gn} + \omega)/\gamma_{gn}$.

Since the transformations from the standard Lorentzian description (homogeneous-broadening) to one that accounts for inhomogeneous-broadening are general, we summarize the fundamental transformations in Table 2.2 for first-, second-, and third-order denominators. It should be noted that $\omega \geq 0$ for the transforms listed in Table 2.2, and the transition frequency is written as its real and imaginary parts to show that the following combinations of transition widths and frequencies, -$i\Gamma_{gn}$ - ω, -$i\Gamma_{gn}$+ω, +$i\Gamma_{gn}$ - ω, +$i\Gamma_{gn}$+ω can occur in the nonlinear regime.

Table 2.2: Fundamental denominator contributions to homogeneously broadened and inhomogeneously broadened electronic transitions.

Homogeneous-Broadening	Inhomogeneous-Broadening
$\frac{C_1}{\omega_{gn}\mp i\Gamma_{gn}\mp\omega}$	$\frac{i\sqrt{\pi}C_1}{\gamma_{gn}}W\left(\frac{-\omega_{gn}\pm i\Gamma_{gn}\pm\omega}{\gamma_{gn}}\right)$
$\frac{C_2}{(\omega_{gn}\mp i\Gamma_{gn}\mp\omega)^2}$	$\frac{i\sqrt{\pi}C_2}{\gamma_{gn}}\left\{\frac{2(\omega_{gn}\mp i\Gamma_{gn}\mp\omega)}{\gamma_{gn}^2}W\left(\frac{-\omega_{gn}\pm i\Gamma_{gn}\pm\omega}{\gamma_{gn}}\right)+\frac{2i}{\sqrt{\pi}\gamma_{gn}}\right\}$
$\frac{C_3}{(\omega_{gn}\mp i\Gamma_{gn}\mp\omega)^3}$	$\frac{i\sqrt{\pi}C_3}{\gamma_{gn}}\left\{\left(\frac{2(\omega_{gn}\mp i\Gamma_{gn}\mp\omega)^2-\gamma_{gn}^2}{\gamma_{gn}^4}\right)W\left(\frac{-\omega_{gn}\pm i\Gamma_{gn}\pm\omega}{\gamma_{gn}}\right)+\frac{2i(\omega_{gn}\mp i\Gamma_{gn}\mp\omega)}{\sqrt{\pi}\gamma_{gn}^3}\right\}$

2.4.2.2.1 Third harmonic generation (THG) As was previously mentioned, the transformation from a homogeneous system to an inhomogeneous system must be performed for each specific process. In this section the transformation from homogeneous-broadening to inhomogeneous-broadening is discussed in terms of third harmonic generation (THG). Third harmonic generation occurs when three input photons are converted to one output photon at triple the frequency. Thus the frequency arguments of the third-order molecular susceptibility are $\omega_1 = \omega_2 = \omega_3 = \omega$, and $\omega_\sigma = \omega_1 + \omega_2 + \omega_3 = 3\omega$. For the homogeneously-broadened case, Equation 2.24 is specified as the following:

$$\xi^{(3)}(-3\omega;\omega,\omega,\omega) = \frac{1}{\epsilon_0 3!}\frac{1}{\hbar^3}\left\{\sum_{l,m,n}{}' D_{lmn}(-3\omega;\omega,\omega,\omega)\mu_{gl}\mu_{lm}\mu_{mn}\mu_{ng} - \sum_{l,n}{}' D_{ln}(-3\omega;\omega,\omega,\omega)|\mu_{gl}|^2|\mu_{gn}|^2\right\}. \quad (2.46)$$

Although we have not done any third harmonic generation experiments in this work, we have chosen third harmonic generation as a model process because the Lorentzian theory which describes it is the easiest third-order process to transform to the inhomogeneous-broadening theory. There are also very nice experimental results in the literature [3, 17] for THG in squaraine-doped liquids which have not been compared to this formalism. The THG process is much simpler to model than other third-order experiments because there is only one input frequency, ω, which occurs three times. This means that $\mathbf{S}_{1,2,3}$ does not create any extra terms in Equations (2.28) and (2.29) so there are only four terms in the expressions for each energy denominator compared to 12 or 24 terms for the quadratic electrooptic and pump-probe experiments, respectively. By beginning the discussion with the simplest third-order case, we hope to present the general procedure for converting the energy denominators from the Lorentzian theory to the inhomogeneous-broadening theory in a manor which does not obscure the method in the fine details.

One-photon contributions Remembering that the sum over D_{lmn} models the two-photon contributions, and the sum over D_{ln} models the one-photon contributions to the third-order susceptibility, we initially focus on the one-photon contributions by expanding D_{ln} for two specific cases: when $n = l$ there is only one excited state that individually contributes to the third-order electronic response, and when $n \neq l$ there are two excited states that together contribute multiplicatively to the third-order electronic response.

In the Lorentzian theory both cases can be written from the general case, Equation (2.28), but this is not the case for the inhomogeneous-broadening (IB) theory because of the convolution integral(s). Thus there are two specific expressions for the energy denominator that characterizes the one-photon contributions to the third-order susceptibility. This will become apparent as the transformation procedure is developed. Since the response due to one excited state is simpler (i.e. more closely related to the linear case) than the response due to two excited states we begin the discussion of the procedure for converting a third-order Lorentzian energy denominator to a third-order inhomogeneous-broadening energy denominator with $D_{ll}(-3\omega;\omega,\omega,\omega)$.

Figure 2.3 shows the two combinations of a one-photon excited state and three incident photons which give rise to a resonance enhancement of the third-order molecular susceptibility and hence the third harmonic output. The solid horizontal lines denoted by g and l represent the ground and l^{th} one-photon excited state respectively, and the dashed horizontal lines represent virtual energy levels. A virtual energy level is permitted under the Heisenberg uncertainty principle and are observable under high photon flux.

The first resonant enhancement to the third harmonic susceptibility occurs when the input photon energy is approximately equal to the energy difference between the ground and l^{th} excited state, while the second resonant enhancement occurs when the output photon energy (third harmonic photon energy) is approximately equal to the energy difference between the ground and l^{th} excited state. Figure 2.3 shows these resonant enhancements which are clearly represented in Lorentzian theory of the $D_{ll}(-3\omega;\omega,\omega,\omega)$ energy denominator as follows:

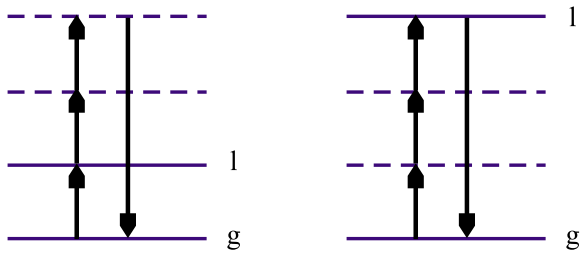

Fig. 2.3: Resonance enhancements of $D_{ll}(-3\omega;\omega,\omega,\omega)$ for third-harmonic generation. Each arrow represents a one-photon transition in the specified direction, the solid horizontal lines represent real energy levels, and the dashed horizontal lines represent virtual energy levels.

$$
\begin{aligned}
&D^{L}_{ll}(-3\omega;\omega,\omega,\omega) \\
&= \left\{ \frac{1}{(\Omega_{gl}-3\omega)(\Omega_{gl}-\omega)^2} + \frac{1}{(\Omega_{gl}-\omega)^2(\Omega^*_{gl}+\omega)} + \right. \\
&\qquad \left. \frac{1}{(\Omega^*_{gl}+3\omega)(\Omega^*_{gl}+\omega)^2} + \frac{1}{(\Omega^*_{gl}+\omega)^2(\Omega_{gl}-\omega)} \right\}, \qquad (2.47) \\
&= \left\{ \frac{1}{(\omega_{gl}-i\Gamma_{gl}-3\omega)(\omega_{gl}-i\Gamma_{gl}-\omega)^2} + \frac{1}{(\omega_{gl}-i\Gamma_{gl}-\omega)^2(\omega_{gl}+i\Gamma_{gl}+\omega)} + \right. \\
&\qquad \left. \frac{1}{(\omega_{gl}+i\Gamma_{gl}+3\omega)(\omega_{gl}+i\Gamma_{gl}+\omega)^2} + \frac{1}{(\omega_{gl}+i\Gamma_{gl}+\omega)^2(\omega_{gl}-i\Gamma_{gl}-\omega)} \right\}. \qquad (2.48)
\end{aligned}
$$

Unfortunately, Equation (2.47) is not in a convenient form for the transformation

to the inhomogeneous-broadening theory because we cannot integrate terms that have products of two or more functions of ω_{gl}. For example the first term is the reciprocal of the product of $(\Omega_{gl}-3\omega)$ and $(\Omega_{gl}-\omega)^2$ which we cannot integrate, but we could integrate each term individually. Thus partial fraction expansions are necessary to isolate the six unique functions of ω_{gl}, where $(\Omega_{gl}-\omega)^2$ and $(\Omega^*_{gl}+\omega)^2$ are considered to be unique in comparison to $(\Omega_{gl}-\omega)$ and $(\Omega^*_{gl}+\omega)$, so that we can perform the convolution integral described in Section 2.4.2.1.

The result of using partial fractions on each of the four terms in Equation (2.48) and grouping all terms with one of the six specific ω_{gl} dependencies together is the following:

$$\begin{aligned} D^L_{ll}(-3\omega;\omega,\omega,\omega) = \frac{1}{4\omega^2}\Bigg[&\frac{1}{(\omega_{gl}-i\Gamma_{gl}-3\omega)}+\frac{1}{(\omega_{gl}+i\Gamma_{gl}+3\omega)} \\ &-\frac{1}{\omega_{gl}-i\Gamma_{gl}-\omega}-\frac{1}{\omega_{gl}+i\Gamma_{gl}+\omega}\Bigg] \\ &+\frac{i\Gamma_{gl}}{2\omega(\omega+i\Gamma_{gl})}\left[\frac{1}{(\omega_{gl}+i\Gamma_{gl}+\omega)^2}-\frac{1}{(\omega_{gl}-i\Gamma_{gl}-\omega)^2}\right], \quad (2.49) \\ = \frac{1}{4\omega^2}\Bigg[&\frac{1}{(\Omega_{gl}-3\omega)}+\frac{1}{(\Omega^*_{gl}+3\omega)}-\frac{1}{\Omega_{gl}-\omega}-\frac{1}{\Omega^*_{gl}+\omega}\Bigg] \\ &+\frac{i\Gamma_{gl}}{2\omega(\omega+i\Gamma_{gl})}\left[\frac{1}{(\Omega^*_{gl}+\omega)^2}-\frac{1}{(\Omega_{gl}-\omega)^2}\right]. \quad (2.50) \end{aligned}$$

Equations (2.48) and (2.49) are shown explicitly to remind us that it is necessary to expand Ω_{gl} and Ω^*_{gl} in terms of their real and imaginary parts for the partial fraction expansion procedure, but will be neglected in future descriptions for brevity.

Now that Equation (2.50) has been determined, the transformation procedure for converting $D^L_{ll}(-3\omega;\omega,\omega,\omega)$ to the inhomogeneous-broadening energy denominator $D^{IB}_{ll}(-3\omega;\omega,\omega,\omega)$ becomes very similar to that of the linear transform. As in the linear case there is one possible real electronic transition – ground to the l^{th} excited state or vice versa (see Figure 2.3). Thus it is only necessary to perform one convolution integral over the entire expression with respect to the transition frequency, $\delta\omega_{gl}$. The integral expression for the inhomogeneously-broadened energy denominator is,

$$D_{ll}^{IB}(-3\omega;\omega,\omega,\omega) = \int_{-\omega_{gl}}^{\infty} D_{ll}^{L}(-3\omega;\omega,\omega,\omega) g_{gl}(\delta\omega_{gl}) d(\delta\omega_{gl})$$
$$= \int_{-\omega_{gl}}^{\infty} \left\{ \frac{1}{4\omega^2} \left[\frac{1}{(\Omega_{gl}^{'} - 3\omega)} + \frac{1}{(\Omega_{gl}^{'^*} + 3\omega)} - \frac{1}{\Omega_{gl}^{'} - \omega} - \frac{1}{\Omega_{gl}^{'^*} + \omega} \right] \right.$$
$$\left. + \frac{i\Gamma_{gl}}{2\omega(\omega + i\Gamma_{gl})} \left[\frac{1}{(\Omega_{gl}^{'^*} + \omega)^2} - \frac{1}{(\Omega_{gl}^{'} - \omega)^2} \right] \right\} g_{gl}(\delta\omega_{gl}) d(\delta\omega_{gl}), \quad (2.51)$$

where $\delta\omega_{gl} = \omega_{gl}^{'} - \omega_{gl} = \Omega_{gl}^{'} - \Omega_{gl}$, $\Omega_{gl}^{'} = \omega_{gl}^{'} - i\Gamma_{gl}$, and the star denotes complex conjugation. The most general formulation would allow for a convolution over the homogeneous linewidth, Γ_{gl}, as well. However, the natural linewidth is an phenomenological construct to begin with, so we restrict our description to a single convolution. Thus the convolution integral can be regarded as a Gaussian probability distribution of Lorentzian transitions which all have the same natural (Lorentzian) linewidth, Γ_{gl}.

Since the integral of each term in Equation (2.51) is known from the discussion in Section 2.4.2 it is simply a matter of replacing each term in Equation (2.51) with the appropriate result from Table 2.2 to complete the conversion from the Lorentzian theory to the inhomogeneous-broadening theory. The relevant results in Table 2.2 are the linear and quadratic transforms. After making the appropriate substitutions, the inhomogeneous-broadening energy denominator becomes,

$$D_{ll}^{IB}(-3\omega;\omega,\omega,\omega) = \frac{\sqrt{\pi}}{\omega\gamma_{gl}} \left\{ \frac{i}{4\omega} \left[W\left(\frac{-(\Omega_{gl} - 3\omega)}{\gamma_{gl}} \right) + W\left(\frac{-(\Omega_{gl}^{*} + 3\omega)}{\gamma_{gl}} \right) \right.\right.$$
$$\left. - W\left(\frac{-(\Omega_{gl} - \omega)}{\gamma_{gl}} \right) - W\left(\frac{-(\Omega_{gl}^{*} + \omega)}{\gamma_{gl}} \right) \right]$$
$$+ \frac{\Gamma_{gl}}{(\omega + i\Gamma_{gl})} \left[\frac{(\Omega_{gl} - \omega)}{\gamma_{gl}^2} W\left(\frac{-(\Omega_{gl} - \omega)}{\gamma_{gl}} \right) \right.$$
$$\left.\left. - \frac{(\Omega_{gl}^{*} + \omega)}{\gamma_{gl}^2} W\left(\frac{-(\Omega_{gl}^{*} + \omega)}{\gamma_{gl}} \right) \right] \right\}, \quad (2.52)$$

Figure 2.4 shows the negative of the real part of $D_{11}(-3\omega;\omega,\omega,\omega)$, which is proportional to the third-order molecular susceptibility, as a function of incident wavelength for a one-photon excited state centered about 653 nm (Note that the transmitted wavelength is 1/3 of the corresponding incident wavelength.). When the incident wavelength is near 653 nm there is a resonant enhancement in the energy denominator due to the

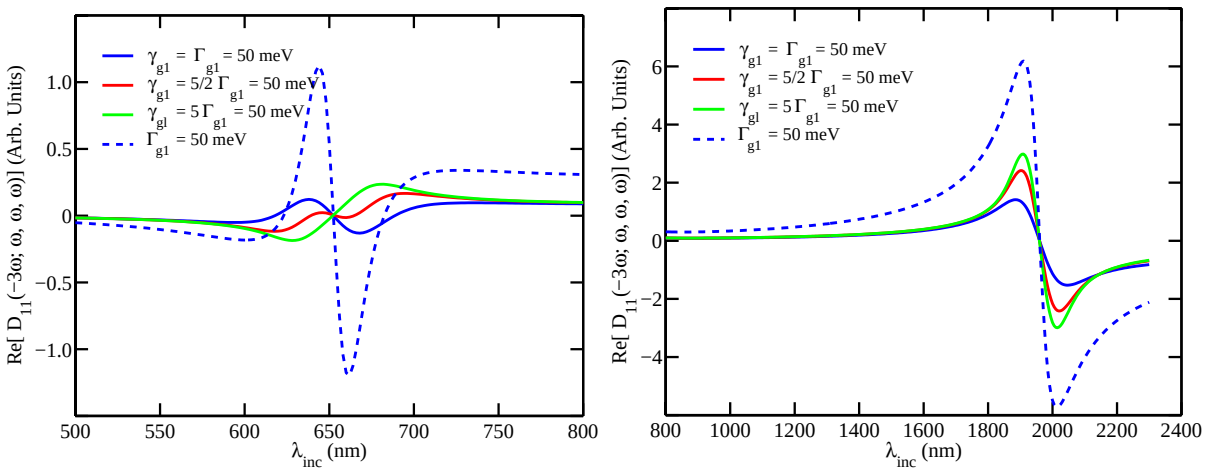

Fig. 2.4: Real part of $-D_{11}(-3\omega;\omega,\omega,\omega)$ for a single excited state centered about 653 nm. The solid lines represent the inhomogeneously broadened electronic transitions for three different values of Γ_{g1} and the dashed line represents the homogeneously-broadened transitions when $n = l = 1$.

incident photon energy being approximately equal to the transition energy, $\hbar\omega_{g1}$, and when the incident wavelength is near 1950 nm there is a resonant enhancement in the energy denominator due to the transmitted photon energy being approximately equal to the transition energy.

The inhomogeneous-broadening prediction of third-order electronic response for one excited state is shown for three values of the homogeneous linewidth for comparison to the linear response shown in Figure 2.2. An interesting difference between the linear and third-order responses occurs for the maximum of the resonance in the energy denominators. In the linear response the maximum of the real part is larger when inhomogeneous-broadening is modeled for both $\Gamma_{gl} = 20$ meV, and $\Gamma_{gl} = 10$ meV. However, in the third-order response of the same excited state the purely homogeneously-broadened response has the largest maximum.

Clearly there is a significant change in the real part of electronic response in the two resonant enhanced regions when the inhomogeneous-broadening of the electronic transitions is modeled. Like the linear response, the purely Lorentzian third-order response is

sharper in the peak and broader in the wings (off-resonance) than the inhomogeneously-broadened response. The off-resonance difference is most evident in the incident wavelength range of 700-1500 nm where the homogeneous response is much larger than the inhomogeneous response. In fact the resonant response at 1950 nm is so broad for the homogeneous case that it contributes to the resonant response at 653 nm.

When the homogeneous linewidth is reduced from 50 meV to 10 meV, the electronic response at about 660 nm in Figure 2.4 goes from negative to positive. Other wavelength within the 600 nm to 700 nm range experience similar sign inversions. This behavior is a consequence of the second term in square brackets in Equation (2.52) being proportional to Γ_{lg}. Thus a reduction in the Lorentzian linewidth causes the first term in square brackets to dominate the resonant responses. In the first square bracket quantity, the three-photon resonant term, $W\left(\frac{-(\Omega_{gl}-3\omega)}{\gamma_{gl}}\right)$, is of the opposite sign to the one-photon resonant term, $W\left(\frac{-(\Omega_{gl}-\omega)}{\gamma_{gl}}\right)$, confirming that the two resonant responses should have opposite sign in the limit of a small homogeneous linewidth.

To briefly recap, Figures 2.2 and 2.4 show that there can be very important differences between the electronic response for homogeneous and inhomogeneous media. Therefore it seems necessary to model inhomogeneous media using inhomogeneously-broadened electronic transitions for both first-order (linear) and third harmonic generation in order to accurately model the electronic response of the system.

However, the transform of $D_{ll}^{IB}(-3\omega;\omega,\omega,\omega)$ is not the golden egg, because it only allows a single one-photon excited state to be modeled for the nonlinear response (two-level model). To extend the inhomogeneous-broadening theory to multiple one-photon excited states, we proceed to transform $D_{ln}^{L}(-3\omega;\omega,\omega,\omega)$ to $D_{ln}^{IB}(-3\omega;\omega,\omega,\omega)$. This transformation is slightly more complicated because there are two one-photon states, n^{th} and l^{th}, involved in the response. Since the excited states are independent of one another, they will in general have different broadening properties. Therefore two convolution integrals are necessary to transform $D_{ln}^{L}(-3\omega;\omega,\omega,\omega)$ to $D_{ln}^{IB}(-3\omega;\omega,\omega,\omega)$ as

follows:

$$D_{ln}^{IB}(-3\omega;\omega,\omega,\omega) = \int_{-\omega_{gl}}^{\infty}\int_{-\omega_{gn}}^{\infty} D_{ln}^{L}(-3\omega;\omega,\omega,\omega)g_{gn}(\delta\omega_{gn})g_{gl}(\delta\omega_{gl})d(\delta\omega_{gn})d(\delta\omega_{gl}), \tag{2.53}$$

where the Lorentzian energy denominator is given by,

$$\begin{aligned} &D_{ln}^{L}(-3\omega;\omega,\omega,\omega) = \\ &\left\{\frac{1}{(\Omega_{gl}-3\omega)(\Omega_{gl}-\omega)(\Omega_{gn}-\omega)} + \frac{1}{(\Omega_{gl}-\omega)(\Omega_{gn}^{*}+\omega)(\Omega_{gn}-\omega)} + \right. \\ &\left.\frac{1}{(\Omega_{gl}^{*}+3\omega)(\Omega_{gl}^{*}+\omega)(\Omega_{gn}^{*}+\omega)} + \frac{1}{(\Omega_{gl}^{*}+\omega)(\Omega_{gn}-\omega)(\Omega_{gn}^{*}+\omega)}\right\}. \end{aligned} \tag{2.54}$$

Additional resonant enhancements can occur when there is more than one one-photon excited state. $D_{ln}^{L}(-3\omega;\omega,\omega,\omega)$ characterizes the electronic response when two one photon states are involved. One resonant enhancement occurs when the incident photon energy is approximately equal to the transition energies of both one-photon excited states (shown in Figure 2.5) and a second occurs when transmitted photon energy is approximately equal to the transition energies of both the one-photon excited states (not shown). However, these enhancements occur because the energies levels are roughly degenerate. A more interesting enhancement occurs when the incident photon energy is approximately equal to the transition energy of the lower energy excited state and the transmitted photon energy is approximately equal to the transition energy of the higher energy excited state.

In Figure 2.5, each arrow represents a one-photon transition in the specified direction. The solid horizontal lines represent real energy levels, and the dashed horizontal lines represent virtual energy levels which were previously discussed in Section 2.4.2.2.1.

As in the previous case the Lorentzian denominator is not in a practical form as written because there are products of unique functions of ω_{gl}. Thus we need to complete a partial fraction expansion for each term in Equation (2.54) that involves a product of two or more unique functions of ω_{gl}. Because the two convolution integrals are independent, terms which have a product of one function of ω_{gl} and one function of ω_{gn} do not need to be expanded using partial fractions. Thus the partial fraction expansion of $D_{ln}^{L}(-3\omega;\omega,\omega,\omega)$ is simpler than the partial fraction expansion of $D_{ll}^{L}(-3\omega;\omega,\omega,\omega)$. The use of partial

fractions to expand each term in Equation (2.54) results in the following,

$$
\begin{aligned}
&D^{L}_{ln}(-3\omega;\omega,\omega,\omega) = \\
&\quad \frac{1}{2}\left\{\frac{1}{\omega}\left[\frac{1}{(\Omega_{gn}-\omega)}\left\{\frac{1}{(\Omega_{gl}-3\omega)}-\frac{1}{(\Omega_{gl}-\omega)}\right\}+\right.\right. \\
&\qquad \left.\left.\frac{1}{(\Omega^{*}_{gn}+\omega)}\left\{\frac{1}{(\Omega^{*}_{gl}+\omega)}-\frac{1}{(\Omega_{gl}+3\omega)}\right\}\right]+\right. \\
&\qquad \left.\frac{1}{(\omega+i\Gamma_{gn})}\left[\left\{\frac{1}{(\Omega_{gl}-\omega)}+\frac{1}{(\Omega^{*}_{gl}+\omega)}\right\}\left\{\frac{1}{(\Omega_{gn}-\omega)}-\frac{1}{(\Omega^{*}_{gn}+\omega)}\right\}\right]\right\}. \qquad (2.55)
\end{aligned}
$$

Equation (2.55) looks much more complicated than Equation (2.54) but the four unique functions of ω_{gl} have been isolated so the convolution integrals shown in Equation (2.53) can be evaluated. Since all the integrals in (2.53) are over linear functions of ω_{gl} or ω_{gn} the results shown in Table 2.1 are used to replace each Lorentzian term with the appropriate inhomogeneous-broadening term to produce the following:

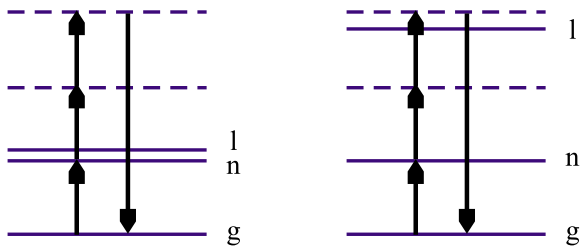

Fig. 2.5: Resonant enhancements of $D_{ln}(-3\omega;\omega,\omega,\omega)$ for third-harmonic generation.

$$
\begin{aligned}
&D^{IB}_{ln}(-3\omega;\omega,\omega,\omega) = \frac{-\pi}{2\gamma_{gl}\gamma_{gn}}\times \\
&\quad \left\{\frac{1}{\omega}\left[W\left(\frac{-(\Omega_{gn}-\omega)}{\gamma_{gn}}\right)\left\{W\left(\frac{-(\Omega_{gl}-3\omega)}{\gamma_{gl}}\right)-W\left(\frac{-(\Omega_{gl}-\omega)}{\gamma_{gl}}\right)\right\}+\right.\right. \\
&\qquad \left.\left.W\left(\frac{-(\Omega^{*}_{gn}+\omega)}{\gamma_{gn}}\right)\left\{W\left(\frac{-(\Omega^{*}_{gl}+\omega)}{\gamma_{gl}}\right)-W\left(\frac{-(\Omega^{*}_{gl}+3\omega)}{\gamma_{gl}}\right)\right\}\right]+\right. \\
&\quad \left.\frac{1}{(\omega+i\Gamma_{gn})}\left[\left\{W\left(\frac{-(\Omega_{gl}-\omega)}{\gamma_{gl}}\right)+W\left(\frac{-(\Omega^{*}_{gl}+\omega)}{\gamma_{gl}}\right)\right\}\right.\right. \\
&\qquad \left.\left.\left\{W\left(\frac{-(\Omega_{gn}-\omega)}{\gamma_{gn}}\right)-W\left(\frac{-(\Omega^{*}_{gn}+\omega)}{\gamma_{gn}}\right)\right\}\right]\right\}. \qquad (2.56)
\end{aligned}
$$

Figure 2.6 shows the real part of the third-order molecular susceptibility, $\xi^{(3)}(-3\omega;\omega,\omega,\omega)$, for a three level model as a function of incident wavelength. Since we are focusing on one-photon contributions, the second sum in Equation 2.66 is the

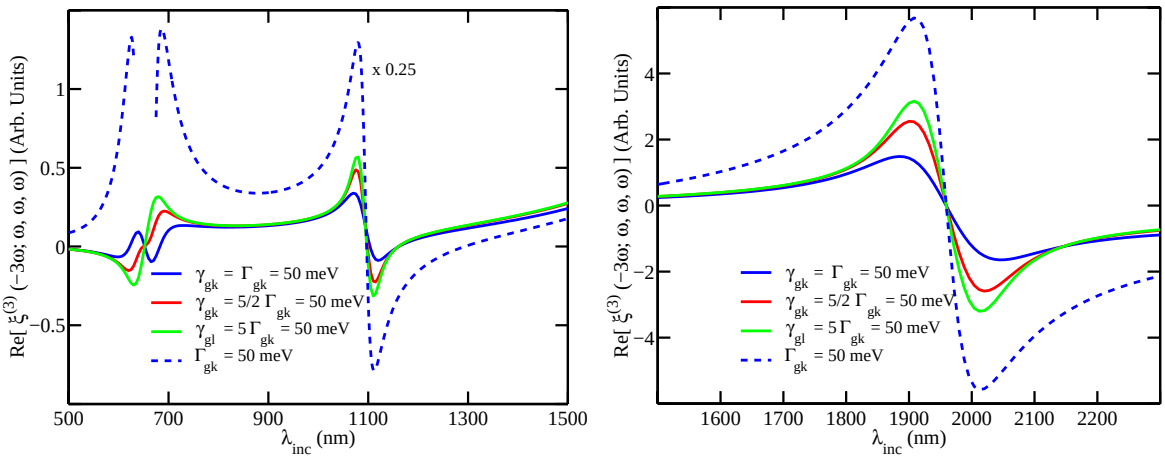

Fig. 2.6: Real part of $\xi^{(3)}(-3\omega;\omega,\omega,\omega)$ for two one-photon excited states centered about 653 nm and 365 nm. The solid lines represent the inhomogeneously-broadened electronic transitions for three different values of Γ_{g1} and the dashed lines represent the homogeneously-broadened transitions when n and $l \in \{1,3\}$. The homogeneous-broadened curve is specifically broken in the visible because the next value in the function is a large negative number.

only contribution to the electronic response in the third-order molecular susceptibility:

$$\xi^{(3)}(-3\omega;\omega,\omega,\omega) = \frac{-1}{\epsilon_0 3!}\frac{1}{\hbar^3} \times \Big\{|\mu_{g1}|^4 D_{11}(-3\omega;\omega,\omega,\omega) + |\mu_{g3}|^4 D_{33}(-3\omega;\omega,\omega,\omega) + |\mu_{g1}|^2|\mu_{g3}|^2\left[D_{13}(-3\omega;\omega,\omega,\omega) + D_{31}(-3\omega;\omega,\omega,\omega)\right]\Big\} \quad (2.57)$$

The two one-photon excited states are centered about 653 nm and 365 nm. The excited state centered about 365 nm was chosen to show that there can be a noticeable enhancement in the electronic response for incident light near 1 μm. It should be noted that $|\mu_{g3}| = 1/2|\mu_{g1}|$, so the majority of the enhancement near 1 μm is due to the mixing term, $D_{ln}(-3\omega;\omega,\omega,\omega)$.

We have used the same three homogeneous linewidths for the inhomogeneous-broadening theory that were used in Figure 2.4. Figure 2.6 shows is an appreciable difference between the responses predicted for each theory, and that the Lorentzian theory predicts much larger third-order electronic responses than the inhomogeneous-broadening theory for constant transition strengths. This is similar to the THG response in the two-level

limit (see Figure 2.4), but opposite to the linear response.

In this section the one-photon contributions to the third-order molecular susceptibility for both homogeneously- and -broadened electronic transitions in the THG experiment were discussed with an emphasis on the development of the inhomogeneous-broadening model. We showed that there is a significant difference predicted in the real part of the third-order electronic response over a very broad wavelength range for a system that is inhomogeneous in comparison to one that is homogeneous. It was also shown that the third-order response for the THG experiment should have the largest magnitude for a homogeneous system, when the transition moments are fixed, which is the opposite of the prediction for the linear response. The next section develops the two possible two-photon contributions to the electronic response in a THG experiment for a system that is inhomogeneously-broadened and compares the inhomogeneously-broadened response to the homogeneously-broadened response.

Two-photon contributions We begin the discussion of transforming energy denominators which involve two-photon states with $D_{lml}(-3\omega;\omega,\omega,\omega)$, which characterizes the electronic response caused by one one-photon excited state and one two-photon excited state. For third harmonic generation Equation (2.29) yields,

$$D^L_{lml}(-3\omega;\omega,\omega,\omega) = \frac{1}{\Omega_{gm}-2\omega}\left\{\frac{1}{(\Omega_{gl}-3\omega)(\Omega_{gl}-\omega)}+\frac{1}{(\Omega^*_{gl}+\omega)(\Omega_{gl}-\omega)}\right\}+ \frac{1}{\Omega^*_{gm}+2\omega}\left\{\frac{1}{(\Omega^*_{gl}+\omega)(\Omega_{gl}-\omega)}+\frac{1}{(\Omega^*_{gl}+\omega)(\Omega^*_{gl}+3\omega)}\right\}. \quad (2.58)$$

The resonant enhancements for the $D_{lml}(-3\omega;\omega,\omega,\omega)$ energy denominator are shown in Figure 2.7. Additional enhancements occur when the incident photon energy is coincident with the one-photon excited state and twice the incident photon energy is coincident with the two-photon excited state, or when twice the incident photon energy is coincident with the two-photon excited state, and the third harmonic output photon energy is coincident with the one-photon excited state.

The transformation from the Lorentzian theory to the inhomogeneous-broadening theory for $D^L_{lml}(-3\omega;\omega,\omega,\omega)$ is nearly identical to the transformation for $D^L_{ln}(-3\omega;\omega,\omega,\omega)$

because there are two excited states involved. Since these two excited states, n^{th} and m^{th}, will, in general, have different broadening properties, it is necessary that two convolution integrals be used to transform $D^{L}_{ln}(-3\omega;\omega,\omega,\omega)$ to $D^{IB}_{ln}(-3\omega;\omega,\omega,\omega)$ as follows:

$$D^{IB}_{lml}(-3\omega;\omega,\omega,\omega) = \int_{-\omega_{gl}}^{\infty}\int_{-\omega_{gm}}^{\infty} D^{L}_{lml}(-3\omega;\omega,\omega,\omega)g_{gm}(\delta\omega_{gm})g_{gl}(\delta\omega_{gl})d(\delta\omega_{gm})d(\delta\omega_{gl}), \tag{2.59}$$

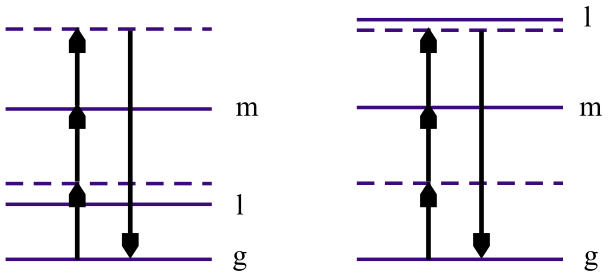

Fig. 2.7: Resonance enhancement of $D_{lml}(-3\omega;\omega,\omega,\omega)$ for third-harmonic generation.

As in the two previous one-photon cases the Lorentzian denominator is not in a practical form in Equation (2.58) to complete the integrals because there are products of unique functions of ω_{gl}. Thus we need to complete a partial fraction expansion for each term in Equation (2.58) that involves a product of two or more unique functions of ω_{gl}. Because the two convolution integrals are independent, terms that have a product of one function of ω_{gl} and one function of ω_{gm} do not need to be expanded.

After completing the partial fraction expansions on all four terms in curly braces in Equation (2.58) the Lorentzian energy denominator takes the following form,

$$\begin{aligned} &D^{L}_{lml}(-3\omega;\omega,\omega,\omega) = \\ &\quad\frac{1}{2}\left\{\frac{1}{\omega}\left[\frac{1}{(\Omega_{gm}-2\omega)}\left\{\frac{1}{(\Omega_{gl}-3\omega)}-\frac{1}{(\Omega_{gl}-\omega)}\right\}\right.\right. \\ &\qquad\left.\left.+\frac{1}{(\Omega^{*}_{gm}+2\omega)}\left\{\frac{1}{(\Omega^{*}_{gl}+\omega)}-\frac{1}{(\Omega^{*}_{gl}+3\omega)}\right\}\right]\right. \\ &\qquad\left.+\frac{1}{(\omega+i\Gamma_{gl})}\left\{\frac{1}{(\Omega_{gm}-2\omega)}+\frac{1}{(\Omega^{*}_{gm}+2\omega)}\right\}\left\{\frac{1}{(\Omega_{gl}-\omega)}-\frac{1}{(\Omega^{*}_{gl}+\omega)}\right\}\right\}. \end{aligned} \tag{2.60}$$

Equation (2.60) has the exact form of Equation (2.54) but the subscripts and the frequency arguments are different. This result shows that the partial fraction expansions are identical for $D^{L}_{ln}(-3\omega;\omega,\omega,\omega)$ and $D^{L}_{lml}(-3\omega;\omega,\omega,\omega)$ cases which means that only one partial fraction expansion is necessary for each third-order electronic response involving

two excited states – independent of the nature of the excited states. This result will be exploited to its fullest when the more complicated third-order processes are discussed.

Since the four unique functions of ω_{gl} have been isolated in Equation (2.60), the convolution integrals shown in Equation (2.59) can be performed. Each integral in Equation (2.59) involves linear functions of ω_{gl} or ω_{gm}, so the results shown in Table 2.1 can be used to replace each Lorentzian term with the appropriate inhomogeneous-broadening term as follows:

$$\begin{aligned} D^{IB}_{lml}(-3\omega;\omega,\omega,\omega) = & \frac{-\pi}{2\gamma_{gl}\gamma_{gm}}\times \\ & \left\{\frac{1}{\omega}\left[W\left(\frac{-(\Omega_{gm}-2\omega)}{\gamma_{gm}}\right)\left\{W\left(\frac{-(\Omega_{gl}-3\omega)}{\gamma_{gl}}\right)-W\left(\frac{-(\Omega_{gl}-\omega)}{\gamma_{gl}}\right)\right\}+\right.\right. \\ & \left.\left. W\left(\frac{-(\Omega^{*}_{gm}+2\omega)}{\gamma_{gm}}\right)\left\{W\left(\frac{-(\Omega^{*}_{gl}+\omega)}{\gamma_{gl}}\right)-W\left(\frac{-(\Omega^{*}_{gl}+3\omega)}{\gamma_{gl}}\right)\right\}\right]+ \\ & \frac{1}{(\omega+i\Gamma_{gl})}\left[\left\{W\left(\frac{-(\Omega_{gm}-2\omega)}{\gamma_{gm}}\right)+W\left(\frac{-(\Omega^{*}_{gm}+2\omega)}{\gamma_{gm}}\right)\right\}\right. \\ & \left.\left.\left\{W\left(\frac{-(\Omega_{gl}-\omega)}{\gamma_{gl}}\right)-W\left(\frac{-(\Omega^{*}_{gl}+\omega)}{\gamma_{gl}}\right)\right\}\right]\right\}. \end{aligned} \tag{2.61}$$

Equation (2.61) contributes to a three-level model (one one-photon excited state, and one two-photon excited state) of the third-order electronic response in the following manor,

$$\begin{aligned} \xi^{(3)}(-3\omega;\omega,\omega,\omega) &= \frac{1}{\epsilon_0 3!}\frac{1}{\hbar^3}\left\{|\mu_{g1}|^2|\mu_{12}|^2 D_{121}(-3\omega;\omega,\omega,\omega)-\right. \\ &\qquad \left.|\mu_{g1}|^4 D_{11}(-3\omega;\omega,\omega,\omega)\right\}. \end{aligned} \tag{2.62}$$

Figure 2.8 shows the real part of the third-order molecular susceptibility (Equation (2.62)) when there is one one-photon excited state and one two-photon excited state for both the homogeneous-broadening and inhomogeneous-broadening theories. The same three homogeneous linewidths are used in the inhomogeneously-broadened susceptibilities.

Again, the Lorentzian theory predicts a much larger response in the visible and near IR than the inhomogeneous-broadening theory, but is not nearly as large as the three level model when two one-photon excited states are modeled. The resonance enhancement near 1950 nm is slightly decreased due to the two-photon state; however, the resonance near 653 nm is much different for the Lorentzian theory than the three-level model for

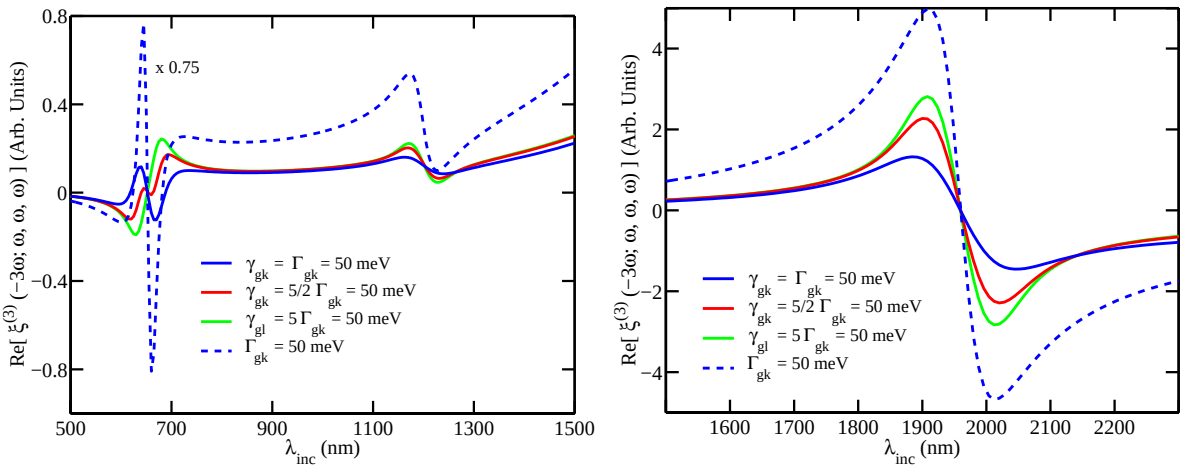

Fig. 2.8: Real part of $\xi^{(3)}(-3\omega;\omega,\omega,\omega)$ for one-photon excited state centered about 653 nm and one two-photon excited state centered about 365 nm. The solid lines represent the inhomogeneously-broadened electronic transitions for three different values of Γ_{gk}, where $k \in \{1,3\}$, and the dashed lines represent the homogeneously-broadened transitions when $l = 1$ and $m = 2$.

two one-photon states. The enhancement is qualitatively similar to the resonance near 653 nm in the two-level model shown in Figure 2.4.

An additional resonant enhancement occurs near 1200 nm, in comparison to the two-level model (see Figure 2.4), which has similar features to the resonant enhancement near 1100 nm in Figure 2.6. Thus is seems as though the experimentalist must be careful in deciding whether a resonant enhancement in the 1-1.2 μm range is due to a second one-photon state or a two-photon state.

One last transformation must be completed before we can construct a general n-level model for the third-order electronic response for a THG experiment. The two-photon state will also contribute to the third-order molecular susceptibility with a mixed term of the form:

$$D^{L}_{lmn}(-3\omega;\omega,\omega,\omega) = \frac{1}{(\Omega_{gn}-\omega)(\Omega_{gm}-2\omega)}\left\{\frac{1}{\Omega_{gl}-3\omega}+\frac{1}{\Omega^{*}_{gl}+\omega}\right\}+ \frac{1}{(\Omega^{*}_{gl}+\omega)(\Omega^{*}_{gm}+2\omega)}\left\{\frac{1}{(\Omega_{gn}-\omega)}+\frac{1}{(\Omega^{*}_{gn}+3\omega)}\right\}. \quad (2.63)$$

This energy denominator characterizes the electronic response when two one-photon states and one two-photon state are involved in the process. Thus it only becomes applicable in a model that has at least three excited states, one of which must be a two-photon state. Since there are three states involved in the electronic response there are no products of unique functions of the same transition frequency, ω_k.

Because there are no terms in Equation (2.63) that need to be isolated, a partial fraction expansion is unnecessary for $D^L_{lmn}(-3\omega;\omega,\omega,\omega)$. It should be noted that all the terms are linear in the their respective transition frequencies, so we can substitute directly from Table 2.1 to produce the inhomogeneous-broadening energy denominator:

$$\begin{aligned} D^{IB}_{lmn}(-3\omega;\omega,\omega,\omega) = & \frac{-i\pi^{3/2}}{\gamma_{gl}\gamma_{gm}\gamma_{gn}} \\ & \left\{ W\left(\frac{-(\Omega_{gn}-\omega)}{\gamma_{gn}}\right) W\left(\frac{-(\Omega_{gm}-2\omega)}{\gamma_{gm}}\right) \times \right. \\ & \left[W\left(\frac{-(\Omega_{gl}-3\omega)}{\gamma_{gl}}\right) + W\left(\frac{-(\Omega^*_{gl}+\omega)}{\gamma_{gl}}\right) \right] + \\ & W\left(\frac{-(\Omega^*_{gl}+\omega)}{\gamma_{gl}}\right) W\left(\frac{-(\Omega^*_{gm}+2\omega)}{\gamma_{gm}}\right) \times \\ & \left. \left[W\left(\frac{-(\Omega_{gn}-\omega)}{\gamma_{gn}}\right) + W\left(\frac{-(\Omega^*_{gn}+3\omega)}{\gamma_{gn}}\right) \right] \right\}. \end{aligned} \tag{2.64}$$

Equation (2.64) occurs twice in a four-level model for the third-order molecular susceptibility when there is a two-photon state:

$$\begin{aligned} \xi^{(3)}(-3\omega;\omega,\omega,\omega) = & \frac{1}{\epsilon_0 3!}\frac{1}{\hbar^3}\times \\ & \left\{ |\mu_{g1}|^2|\mu_{12}|^2 D_{121}(-3\omega;\omega,\omega,\omega) + |\mu_{g3}|^2|\mu_{32}|^2 D_{323}(-3\omega;\omega,\omega,\omega) \right. \\ & +\mu_{g1}\mu_{12}\mu_{32}\mu_{g3}\left[D_{123}(-3\omega;\omega,\omega,\omega) + D_{321}(-3\omega;\omega,\omega,\omega)\right] \\ & -|\mu_{g1}|^4 D_{11}(-3\omega;\omega,\omega,\omega) - |\mu_{g3}|^4 D_{33}(-3\omega;\omega,\omega,\omega) \\ & \left. -|\mu_{g1}|^2|\mu_{g3}|^2\left[D_{13}(-3\omega;\omega,\omega,\omega) + D_{31}(-3\omega;\omega,\omega,\omega)\right] \right\}. \end{aligned} \tag{2.65}$$

This occurs because the expression is not symmetric with respect to the exchange of l and n.

Figure 2.9 shows the real part of the third-order molecular susceptibility when there are two one-photon excited states and one two-photon excited state, Equation (2.62), for

both the homogeneous-broadening and inhomogeneous-broadening theories. The same three homogeneous linewidths are used in the inhomogeneously-broadened susceptibilities.

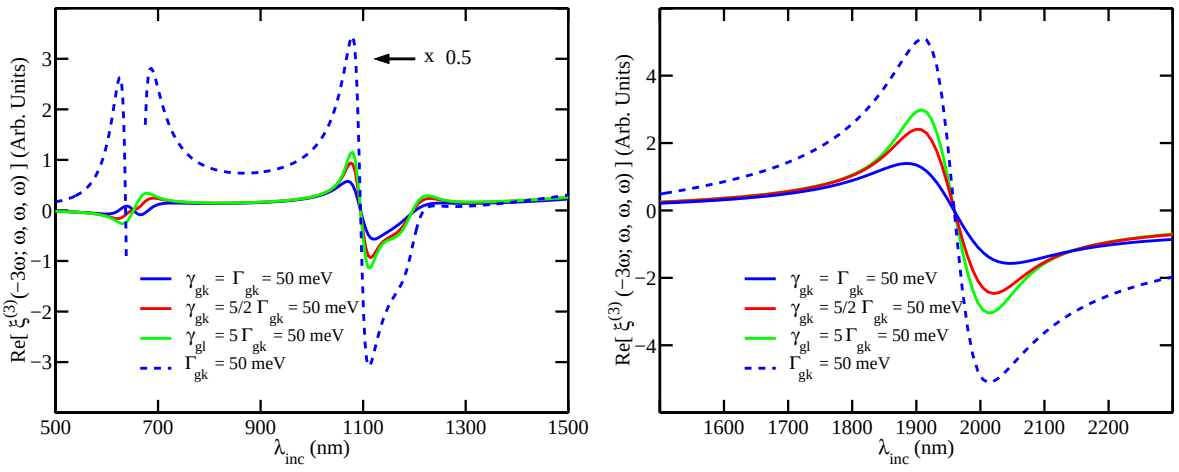

Fig. 2.9: Real part of $\xi^{(3)}(-3\omega;\omega,\omega,\omega)$ for two one-photon excited states centered about 653 nm and 365 nm, and one two-photon state centered about 600 nm. The solid lines represent the inhomogeneously-broadened electronic transitions for three different values of Γ_{g1} and the dashed lines represent the homogeneously-broadened transitions when n and $l \in \{1,3\}$, and $m = 2$. The dashed curve is broken in the visible because the next value in the function is a large negative number.

At this point we have shown four transformations from the standard Lorentzian theory to the inhomogeneous broadening theory, $D^{IB}_{ll}(-3\omega;\omega,\omega,\omega)$, $D^{IB}_{ln}(-3\omega;\omega,\omega,\omega)$, $D^{IB}_{lml}(-3\omega;\omega,\omega,\omega)$, and $D^{IB}_{lmn}(-3\omega;\omega,\omega,\omega)$. It was necessary to complete these four transformations so that a general n-level, inhomogeneous-broadening theory for the third-order molecular susceptibility of the THG experiment could be constructed. Two energies denominators are not sufficient because the convolution integrals are different for the degenerate cases (ll and lml) due to additional quadratic dependencies on the transition frequency, ω_{gl}.

For the first three energy denominators it was necessary to perform many partial fraction expansions of the standard Lorentzian equations so that the convolution integrals could be evaluated. The final energy denominator did not have any products of two or

more unique functions of the same transition frequency, so the partial fraction expansions were not necessary. This is a general result for third-order energy denominators and can be used for the transformations of the energy denominators for the quadratic electrooptic and the optical Kerr effects. Once the standard Lorentzian energy denominators have been written in a form that isolates the unique functions of each transition frequency, a convolution integral is performed for each excited state involved in the energy denominator. Since the three fundamental convolution integrals were evaluated in Section 2.4.2, it is simply a matter of replacing the convolution integral of each fundamental Lorentzian term with its corresponding inhomogeneous-broadening result in Table 2.1 or 2.2 to complete the transformation to the inhomogeneous-broadening theory.

This brings the discussion of third-harmonic generation to a close. The next two sections discuss the development of n-level inhomogeneous-broadening models for the quadratic electrooptic and optical Kerr effects. Since the general procedure has been developed here, the following sections will be brief with regards to the actual transformation procedure. The reader will be frequently referred back to this section.

2.4.2.2.2 Quadratic electrooptic effect In the previous section, the standard Lorentzian (homogeneous) theory for third-order electronic responses was converted to an inhomogeneous-broadening theory for third harmonic generation. This section discusses the transformation from homogeneous-broadening to inhomogeneous-broadening for the quadratic electrooptic effect. The quadratic electrooptic effect occurs when a pseudo-d.c. field is applied across a sample, while it is illuminated with an optical field. The d.c. field is referred to as "pseudo" because it is actually an a.c. field but the frequency ($\approx 10^3$ Hz) is negligible in comparison to the frequency of the optical field ($\approx 10^{15}$ Hz). Thus the frequency arguments of the third-order molecular susceptibility are $\omega_1 = \omega$ (the optical field), $\omega_2 = \omega_3 = 0$, and $\omega_\sigma = \omega$.

In the quadratic electrooptic experiment it is possible to measure both the real and imaginary parts of the bulk third-order susceptibility by observing the change in index of refraction and/or the change in absorption when the electric field is applied. When the quadratic electrooptic experiment is set up to measure the change in index of refraction it is often referred to as the QEO experiment, and when it is set-up to measure the change in absorption it is often referred to as the quadratic electroabsorption (QEA) experiment. To show how the real and imaginary parts of the third-order response behave for the homogeneous-broadening and inhomogeneous-broadening theories, both the real and imaginary parts of the third-order susceptibility will be represented in figures similar to Section 2.4.2.2.1.

For the quadratic electrooptic effect the third-order molecular susceptibility, Equation 2.24, is written as follows:

$$\begin{aligned}\xi^{(3)}(-\omega;\omega,0,0) &= \frac{1}{\epsilon_0 3!}\frac{1}{\hbar^3}\left\{\sum_{l,m,n}{}' D_{lmn}(-\omega;\omega,0,0)\mu_{gl}\mu_{lm}\mu_{mn}\mu_{ng} - \right. \\ &\qquad \left. \sum_{l,n}{}' D_{ln}(-\omega;\omega,0,0)|\mu_{gl}|^2|\mu_{gn}|^2\right\}. \qquad (2.66)\end{aligned}$$

One-photon contributions As previously stated the sum over D_{lmn} models the two-photon contributions, and the sum over D_{ln} models the one-photon contributions to

the third-order susceptibility, so we follow the procedure in Section 2.4.2.2.1 by beginning with the simplest one photon contribution. The Lorentzian theory for $D_{ln}(-\omega;\omega,0,0)$ can be expanded as follows:

$$D_{ll}^{L}(-\omega;\omega,0,0) = \left\{ \frac{2}{\Omega_{gl}(\Omega_{gl}-\omega)^2} + \frac{2}{\Omega_{gl}^{*}(\Omega_{gl}^{*}+\omega)^2} + \frac{2}{\Omega_{gl}\Omega_{gl}^{*}(\Omega_{gl}-\omega)} + \frac{2}{\Omega_{gl}\Omega_{gl}^{*}(\Omega_{gl}^{*}+\omega)} + \frac{1}{(\Omega_{gl})^2(\Omega_{gl}-\omega)} + \frac{1}{(\Omega_{gl})^2(\Omega_{gl}^{*}+\omega)} + \frac{1}{(\Omega_{gl}^{*})^2(\Omega_{gl}-\omega)} + \frac{1}{(\Omega_{gl}^{*})^2(\Omega_{gl}^{*}+\omega)} \right\} \quad (2.67)$$

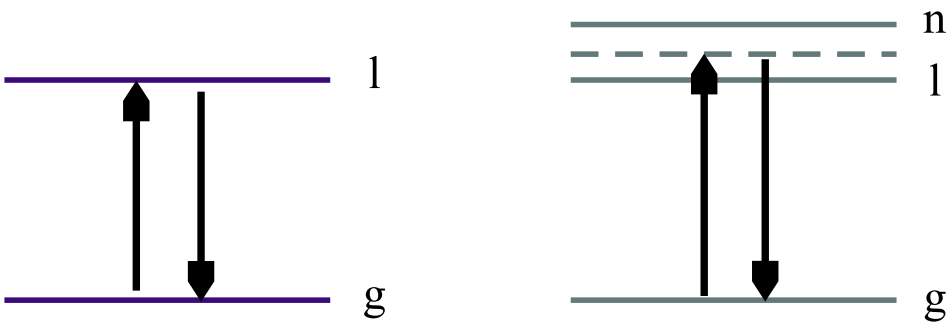

Fig. 2.10: Resonant enhancements due to $D_{ll}(-\omega;\omega,0,0)$ and $D_{ln}(-\omega;\omega,0,0)$, respectively. Each arrow represents a one-photon transition in the specified direction, solid horizontal lines represent real excited states, and dashed lines represent virtual excited states.

Figure 2.10 shows a pictorial version the resonant enhancements for the energy denominators, $D_{ll}(-\omega;\omega,0,0)$ and $D_{ln}(-\omega;\omega,0,0)$, respectively. When only one excited state is involved in the third-order response there is a resonant enhancement if the incident optical photon energy close to the transition energy. An additional resonant enhancement can occur when there is a second one-photon excited state involved. It occurs when the incident photon energy is close to the transitions energies of both the excited states so that both excited states contribute resonantly to the response.

Following the procedure developed in Section 2.4.2.2.1, the Lorentzian denominator is converted to the following using partial fractions:

$$
\begin{aligned}
D_{ll}^{L}(-\omega;\omega,0,0) = 2\Bigg\{ & \frac{1}{\omega(\omega_{gl}-i\Gamma_{gl}-\omega)^2} - \frac{1}{\omega(\omega_{gl}+i\Gamma_{gl}+\omega)^2} \\
& + \frac{(1+2\frac{\Gamma_{gl}^2}{\omega^2})}{(\omega+2i\Gamma_{gl})^2}\left[\frac{1}{(\omega_{gl}-i\Gamma_{gl}-\omega)} + \frac{1}{(\omega_{gl}+i\Gamma_{gl}+\omega)}\right] \\
& - \frac{(1+2\frac{\Gamma_{gl}^2}{\omega^2})}{(\omega+2i\Gamma_{gl})^2}\left[\frac{1}{(\omega_{gl}-i\Gamma_{gl})} + \frac{1}{(\omega_{gl}+i\Gamma_{gl})}\right] \\
& + \frac{i\Gamma_{gl}}{\omega(\omega+2i\Gamma_{gl})}\left[\frac{1}{(\omega_{gl}+i\Gamma_{gl})^2} - \frac{1}{(\omega_{gl}-i\Gamma_{gl})^2}\right]\Bigg\} \qquad (2.68) \\
= 2\Bigg\{ & \frac{1}{\omega(\Omega_{gl}-\omega)^2} - \frac{1}{\omega(\Omega_{gl}^{*}+\omega)^2} \\
& + \frac{(1+2\frac{\Gamma_{gl}^2}{\omega^2})}{(\omega+2i\Gamma_{gl})^2}\left[\frac{1}{(\Omega_{gl}-\omega)} + \frac{1}{(\Omega_{gl}^{*}+\omega)} - \frac{1}{\Omega_{gl}} - \frac{1}{\Omega_{gl}^{*}}\right] \\
& + \frac{i\Gamma_{gl}}{\omega(\omega+2i\Gamma_{gl})}\left[\frac{1}{(\Omega_{gl}^{*})^2} - \frac{1}{(\Omega_{gl})^2}\right]\Bigg\}. \qquad (2.69)
\end{aligned}
$$

The expanded form of the transition frequency is shown in Equation (2.68) to remind us that Equation (2.69) had to be in this form when the partial fraction analysis was performed.

Since Equation (2.69) is the result of expanding each term in Equation (2.67) using partial fractions, then re-grouping all terms with similar dependencies on ω_{gl} together, it is not reasonable to compare the individual terms in Equation (2.67) to the individual terms in Equation (2.69). However, it should be noted that the eight distinct functions of ω_{gl} have been isolated.

$D_{ll}^{L}(-\omega;\omega,0,0)$ can now be integrated because the unique functions of the transition frequency, ω_{gl} have been isolated. One convolution integral is performed on Equation (2.69) with respect to the transition frequency, ω_{gl} because there is only one excited state involved in the electronic response. The integral expression for the inhomogeneously-broadened energy denominator is,

$$
D_{ll}^{IB}(-\omega;\omega,0,0) \;=\; \int_{-\omega_{gl}}^{\infty} D_{ll}^{L}(-\omega;\omega,0,0)\, g_{gl}(\delta\omega_{gl})\, d(\delta\omega_{gl}) \qquad (2.70)
$$

where $\delta\omega_{gl} = \omega_{gl}^{'} - \omega_{gl} = \Omega_{gl}^{'} - \Omega_{gl}$, $\Omega_{gl}^{'} = \omega_{gl}^{'} - i\Gamma_{gl}$, and $D_{ll}^{L}(-\omega;\omega,0,0)$ is given by Equation (2.69). Equation (2.70) can be regarded as a Gaussian probability distribution

of Lorentzian transitions which all have the same natural (Lorentzian) linewidth, Γ_{gl}.

Because the integral of each term in Equation (2.70) is known from the results of Section 2.4.2, we follow the procedure developed in Section 2.4.2.2.1 and replace each Lorentzian term with the appropriate inhomogeneous-broadening transform in Table 2.2. In the electrooptic experiment, there are no cubic dependencies so only the first and second transforms in Table 2.2 are applicable. After making these substitutions, the final result for the energy denominator that accounts for inhomogeneous-broadening is

$$\begin{aligned} D_{ll}^{IB}(-\omega;\omega,0,0) = \frac{2i\sqrt{\pi}}{\gamma_{gl}} \Bigg\{ & \frac{2}{\omega\gamma_{gl}^2}\left[(\omega_{gl}-i\Gamma_{gl}-\omega)W\left(\frac{-\omega_{gl}+i\Gamma_{gl}+\omega}{\gamma_{gl}}\right)\right. \\ & \left. -(\omega_{gl}+i\Gamma_{gl}+\omega)W\left(\frac{-\omega_{gl}-i\Gamma_{gl}-\omega}{\gamma_{gl}}\right)\right] \\ & +\frac{(1+2\frac{\Gamma_{gl}^2}{\omega^2})}{(\omega+2i\Gamma_{gl})^2}\left[W\left(\frac{-\omega_{gl}+i\Gamma_{gl}+\omega}{\gamma_{gl}}\right)+W\left(\frac{-\omega_{gl}-i\Gamma_{gl}-\omega}{\gamma_{gl}}\right)\right] \\ & -\frac{(1+2\frac{\Gamma_{gl}^2}{\omega^2})}{(\omega+2i\Gamma_{gl})^2}\left[W\left(\frac{-\omega_{gl}-i\Gamma_{gl}}{\gamma_{gl}}\right)+W\left(\frac{-\omega_{gl}+i\Gamma_{gl}}{\gamma_{gl}}\right)\right] \\ & +\frac{2i\Gamma_{gl}}{\omega(\omega+2i\Gamma_{gl})\gamma_{gl}^2}\left[(\omega_{gl}+i\Gamma_{gl})W\left(\frac{-\omega_{gl}-i\Gamma_{gl}}{\gamma_{gl}}\right)\right. \\ & \left. -(\omega_{gl}-i\Gamma_{gl})W\left(\frac{-\omega_{gl}+i\Gamma_{gl}}{\gamma_{gl}}\right)\right] \Bigg\}, \end{aligned} \tag{2.71}$$

$$\begin{aligned} = \frac{2i\sqrt{\pi}}{\gamma_{gl}} \Bigg\{ & \frac{2}{\omega\gamma_{gl}^2}\left[(\Omega_{gl}-\omega)W\left(\frac{-(\Omega_{gl}-\omega)}{\gamma_{gl}}\right)\right. \\ & \left. -(\Omega_{gl}^*+\omega)W\left(\frac{-(\Omega_{gl}^*+\omega)}{\gamma_{gl}}\right)\right] \\ & +\frac{(1+2\frac{\Gamma_{gl}^2}{\omega^2})}{(\omega+2i\Gamma_{gl})^2}\left[W\left(\frac{-(\Omega_{gl}-\omega)}{\gamma_{gl}}\right)+W\left(\frac{-(\Omega_{gl}^*+\omega)}{\gamma_{gl}}\right)\right] \\ & -\frac{(1+2\frac{\Gamma_{gl}^2}{\omega^2})}{(\omega+2i\Gamma_{gl})^2}\left[W\left(\frac{-\Omega_{gl}^*}{\gamma_{gl}}\right)+W\left(\frac{-\Omega_{gl}}{\gamma_{gl}}\right)\right] \\ & +\frac{2i\Gamma_{gl}}{\omega(\omega+2i\Gamma_{gl})\gamma_{gl}^2}\left[\Omega_{gl}^*W\left(\frac{-\Omega_{gl}^*}{\gamma_{gl}}\right)-\Omega_{gl}W\left(\frac{-\Omega_{gl}}{\gamma_{gl}}\right)\right] \Bigg\}. \end{aligned} \tag{2.72}$$

We have written the result with the transition frequency expanded into its real and imaginary parts to help the reader see how each term compares to Equation (2.68).

Figure 2.11 shows the (negative) real and imaginary parts of the energy denominators

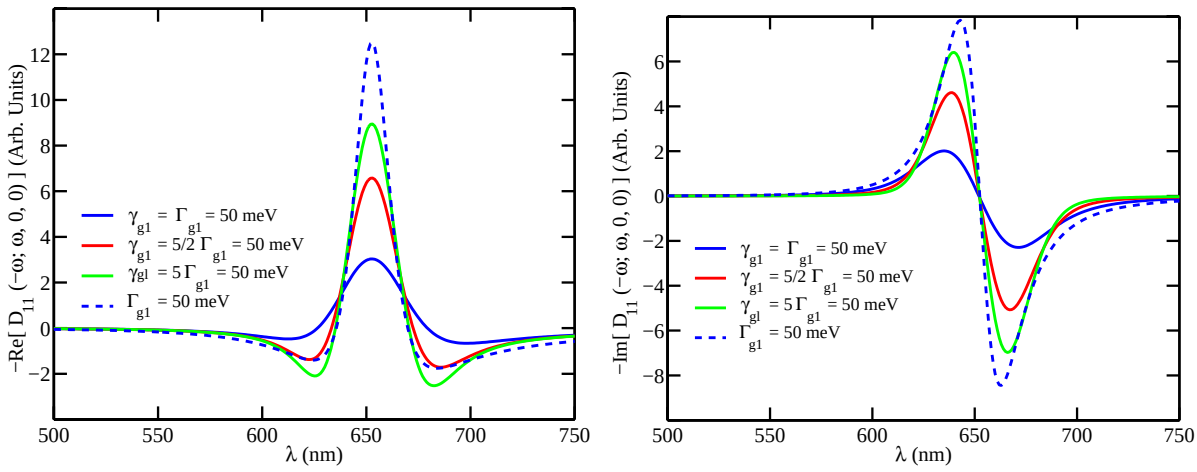

Fig. 2.11: Real and imaginary parts of $D_{11}(-\omega;\omega,0,0)$ for a single excited state centered about 653 nm. The solid lines represent the inhomogeneously broadened electronic transitions for three different values of Γ_{g1} and the dashed line represents the homogeneously-broadened transitions when $n = l = 1$.

$D^{L}_{11}(-\omega;\omega,0,0)$, Equation (2.73), and $D^{IB}_{11}(-\omega;\omega,0,0)$, Equation (2.72), when $n = l = 1$ for a transition that is centered about 653 nm. The negative of $D_{11}(-\omega;\omega,0,0)$ is used because it appears this way in the third-order molecular susceptibility (see Equation (2.24)). It is interesting to note that the real part of $D_{11}(-\omega;\omega,0,0)$ is similar to the imaginary part of $D_1(-\omega;\omega)$, while the imaginary part of $D_{11}(-\omega;\omega,0,0)$ is similar to the real part of $D_1(-\omega;\omega)$.

Clearly there is a significant change in both the real and imaginary parts of the electronic response when inhomogeneous-broadening is included in the model. The values of Γ_{gl} for the inhomogeneously-broadened responses are the same as the values of Γ_{gl} used in Figure 2.2 so that a direct comparison can be made. Like the linear response, we see that a purely Lorentzian response is sharper in the peak and broader in the wings (off-resonance) than the inhomogeneously-broadened response. Therefore it seems necessary to model inhomogeneous media using -broadened electronic transitions for both THG and quadratic electrooptic experiments to accurately model the third-order electronic response of the system.

Again an interesting difference between the linear and QEO responses occurs for the maximum value of the energy denominator. In the linear response, the magnitudes of both the real and imaginary parts are larger for both $\Gamma_{gl} = 20$ meV, and $\Gamma_{gl} = 10$ meV. However, in the QEO (real) and QEA (imaginary) responses for the same excited state, the purely homogeneously-broadened response has the largest magnitude like that of the two-level response for third harmonic generation.

With the transform of $D_{ll}^{IB}(-\omega;\omega,0,0)$ complete, we proceed to transform $D_{ln}^{L}(-\omega;\omega,0,0)$ to $D_{ln}^{IB}(-\omega;\omega,0,0)$ by writing Equation (2.28) for the quadratic electrooptic experiment as follows,

$$\begin{aligned} D_{ln}^{L}(-\omega;\omega,0,0) = \Bigg\{ & \frac{1}{(\Omega_{gl}-\omega)\Omega_{gl}(\Omega_{gn}-\omega)} + \frac{1}{\Omega_{gn}(\Omega_{gl}-\omega)^2} + \frac{1}{\Omega_{gl}^{*}\Omega_{gn}^{*}(\Omega_{gl}^{*}+\omega)} \\ & + \frac{1}{(\Omega_{gl}-\omega)(\Omega_{gl})(\Omega_{gn})} + \frac{1}{(\Omega_{gl}-\omega)(\Omega_{gn}^{*})(\Omega_{gn})} + \frac{1}{(\Omega_{gl})(\Omega_{gn}^{*})(\Omega_{gn}-\omega)} \\ & + \frac{1}{(\Omega_{gl})(\Omega_{gn}^{*}+\omega)(\Omega_{gn})} + \frac{1}{(\Omega_{gl}^{*}+\omega)(\Omega_{gl}^{*})(\Omega_{gn}^{*}+\omega)} + \frac{1}{(\Omega_{gl}^{*}+\omega)^2(\Omega_{gn}^{*})} \\ & + \frac{1}{(\Omega_{gl}^{*}+\omega)(\Omega_{gn})(\Omega_{gn}^{*})} + \frac{1}{(\Omega_{gl}^{*})(\Omega_{gn})(\Omega_{gn}^{*}+\omega)} + \frac{1}{(\Omega_{gl}^{*})(\Omega_{gn}-\omega)(\Omega_{gn}^{*})} \Bigg\}, \end{aligned} \tag{2.73}$$

Equation (2.73) has products of two unique functions of the transition frequency, ω_k, for $k = l$ and $k = n$. Thus partial fraction expansions must be performed on Equation (2.73) with respect to both transition frequencies to produce the following,

$$\begin{aligned} D_{ln}^{L}(-\omega;\omega,0,0) = \Bigg\{ & \frac{1}{\Omega_{gn}(\Omega_{gl}-\omega)^2} + \frac{1}{\Omega_{gn}^{*}(\Omega_{gl}^{*}+\omega)^2} \\ & + \frac{1}{\omega}\left[\frac{1}{\Omega_{gl}-\omega} - \frac{1}{\Omega_{gl}}\right] \times \left[\frac{1}{\Omega_{gn}-\omega} + \frac{1}{\Omega_{gn}}\right] \\ & + \frac{1}{\omega}\left[\frac{1}{\Omega_{gl}^{*}} - \frac{1}{\Omega_{gl}^{*}+\omega}\right] \times \left[\frac{1}{\Omega_{gn}^{*}+\omega} + \frac{1}{\Omega_{gn}^{*}}\right] \\ & + \frac{1}{2i\Gamma_{gn}}\left[\frac{1}{\Omega_{gl}-\omega} + \frac{1}{\Omega_{gl}^{*}+\omega}\right] \times \left[\frac{1}{\Omega_{gn}} - \frac{1}{\Omega_{gn}^{*}}\right] \\ & + \frac{1}{\omega+2i\Gamma_{gn}}\left[\frac{1}{\Omega_{gl}} + \frac{1}{\Omega_{gl}^{*}}\right] \times \left[\frac{1}{\Omega_{gn}} - \frac{1}{\Omega_{gn}^{*}}\right] \\ & + \frac{1}{\omega+2i\Gamma_{gn}}\left[\frac{1}{\Omega_{gl}} + \frac{1}{\Omega_{gl}^{*}}\right] \times \left[\frac{1}{\Omega_{gn}-\omega} - \frac{1}{\Omega_{gn}^{*}+\omega}\right] \Bigg\}. \end{aligned} \tag{2.74}$$

Equation (2.74) produces the same result as Equation (2.73) for the Lorentzian theory. All the unique functions of each transition frequency have been isolated so that convolutions integrals can be performed on each term for the inhomogeneous-broadening theory.

Since two one-photon states, n^{th} and l^{th}, which will in general have different broadening properties, are involved in the response due to Equation (2.74), two convolution integrals are necessary to transform $D_{ln}^{L}(-\omega;\omega,0,0)$ (Equation (2.73)) to $D_{ln}^{IB}(-\omega;\omega,0,0)$ as follows:

$$D_{ln}^{IB}(-\omega;\omega,0,0)=\int_{-\omega_{gl}}^{\infty}\int_{-\omega_{gn}}^{\infty}D_{ln}^{L}(-\omega;\omega,0,0)g_{gn}(\delta\omega_{gn})g_{gl}(\delta\omega_{gl})d(\delta\omega_{gn})d(\delta\omega_{gl}), \quad (2.75)$$

where $D_{ln}^{L}(-\omega;\omega,0,0)$ is given by Equation (2.74). This follows the procedure for transforming $D_{ln}^{L}(-3\omega;\omega,\omega,\omega)$ in Section 2.4.2.2.1 but is much more time consuming because it has a greater number of terms.

However, the results of the convolution integrals for each term in Equation (2.75) can be found in Table 2.2. Therefore we can model inhomogeneously-broadened electronic transitions for more than one one-photon state in an electrooptic experiment by replacing each Lorentzian term with the appropriate result from Table 2.2 as follows:

$$\begin{aligned}
D_{ln}^{IB}(-\omega;\omega,0,0)=&\frac{-\pi}{\gamma_{gl}\gamma_{gn}}\times\\
&\left\{W\left(\frac{-\Omega_{gn}}{\gamma_{gn}}\right)\left[\frac{2(\Omega_{gl}-\omega)}{\gamma_{gl}^{2}}W\left(\frac{-(\Omega_{gl}-\omega)}{\gamma_{gl}}\right)+\frac{2i}{\sqrt{\pi}\gamma_{gl}}\right]\right.\\
&+W\left(\frac{-\Omega_{gn}^{*}}{\gamma_{gn}}\right)\left[\frac{2(\Omega_{gl}^{*}+\omega)}{\gamma_{gl}^{2}}W\left(\frac{-(\Omega_{gl}^{*}+\omega)}{\gamma_{gl}}\right)+\frac{2i}{\sqrt{\pi}\gamma_{gl}}\right]\\
&+\frac{1}{\omega}\left[\left\{W\left(\frac{-\Omega_{gl}^{*}}{\gamma_{gl}}\right)-W\left(\frac{-(\Omega_{gl}^{*}+\omega)}{\gamma_{gl}}\right)\right\}\left\{W\left(\frac{-(\Omega_{gn}^{*}+\omega)}{\gamma_{gn}}\right)+W\left(\frac{-\Omega_{gn}^{*}}{\gamma_{gn}}\right)\right\}+\right.\\
&\left.\left\{W\left(\frac{-(\Omega_{gl}-\omega)}{\gamma_{gl}}\right)-W\left(\frac{-\Omega_{gl}}{\gamma_{gl}}\right)\right\}\left\{W\left(\frac{-(\Omega_{gn}-\omega)}{\gamma_{gn}}\right)+W\left(\frac{-\Omega_{gn}}{\gamma_{gn}}\right)\right\}\right]\\
&+\frac{1}{2i\Gamma_{gn}}\left[\left\{W\left(\frac{-(\Omega_{gl}-\omega)}{\gamma_{gl}}\right)+W\left(\frac{-(\Omega_{gl}^{*}+\omega)}{\gamma_{gl}}\right)\right\}\left\{W\left(\frac{-\Omega_{gn}}{\gamma_{gn}}\right)-W\left(\frac{-\Omega_{gn}^{*}}{\gamma_{gn}}\right)\right\}\right]\\
&+\frac{1}{(\omega+2i\Gamma_{gn})}\left[\left\{W\left(\frac{-\Omega_{gn}}{\gamma_{gn}}\right)-W\left(\frac{-\Omega_{gn}^{*}}{\gamma_{gn}}\right)+W\left(\frac{-(\Omega_{gn}-\omega)}{\gamma_{gn}}\right)-W\left(\frac{-(\Omega_{gn}^{*}+\omega)}{\gamma_{gn}}\right)\right\}\right.\\
&\left.\left.\times\left\{W\left(\frac{-\Omega_{gl}}{\gamma_{gl}}\right)+W\left(\frac{-\Omega_{gl}^{*}}{\gamma_{gl}}\right)\right\}\right]\right\}. \quad (2.76)
\end{aligned}$$

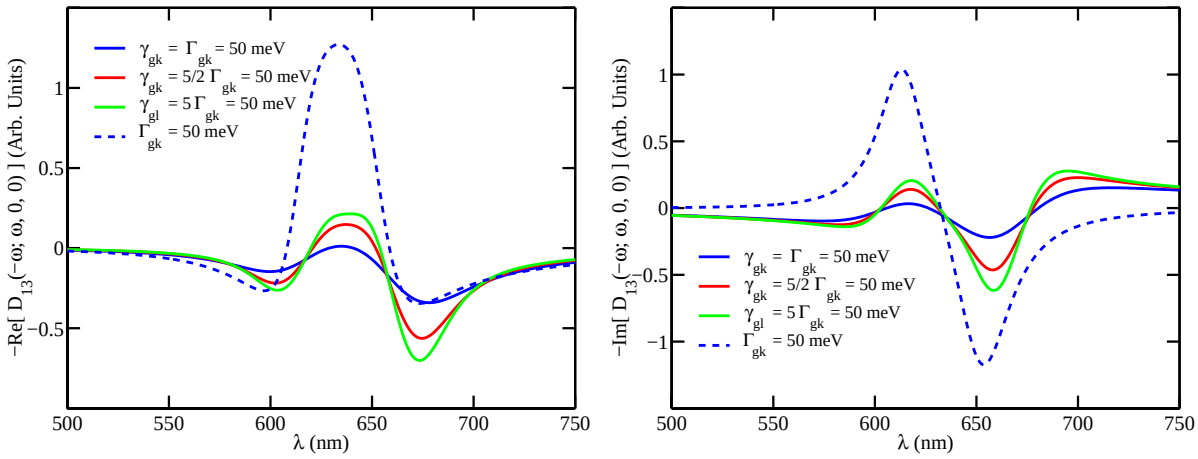

Fig. 2.12: Real and imaginary parts of $D_{13}(-\omega;\omega,0,0)$ for two one-photon excited states centered about 653 nm and 614 nm. The solid lines represent the inhomogeneously broadened electronic transitions for three different values of Γ_{gk} where $k \in \{1,3\}$ and the dashed line represents the homogeneously-broadened transitions.

Figure 2.12 shows the real and imaginary parts of the energy denominators $D_{13}^{L}(-\omega;\omega,0,0)$ and $D_{13}^{IB}(-\omega;\omega,0,0)$, where $l = 1$ and $n = 3$ (Note: 3 is used to denote a second one-photon excited state because 2 is usually reserved for the first two-photon state.). Similar to Figure 2.11, the maximum of the response is largest for the homogeneous-broadening theory independent of the three values of Γ in the inhomogeneous-broadening theory. The difference between the two theories is much more exaggerated for the $D_{13}(-\omega;\omega,0,0)$ response in comparison to the $D_{11}(-\omega;\omega,0,0)$ response. This large difference is most likely due to $D_{13}(-\omega;\omega,0,0)$ being highly dependent on the overlap between the responses of the two one-photon excited states centered at 614 nm and 650 nm. Thus the Lorentzian theory which has the broader response in the tail of the resonance has a larger contribution from $D_{13}(-\omega;\omega,0,0)$. Even though there is a large difference in the magnitudes predicted by the two theories, the maximum of the real part of the response is centered in between the two individual excited states for both theories.

It is not possible to experimentally isolate $D_{13}(-\omega;\omega,0,0)$, but the total third-order response of two one-photon excited states can be measured. This leads us to a three-level

model for the third-order molecular susceptibility, $\xi^{(3)}(-\omega;\omega,0,0)$ (Equation (2.66)), as follows:

$$\xi^{(3)}(-\omega;\omega,0,0) = -\frac{1}{\epsilon_0 3!}\frac{1}{\hbar^3}\left\{|\mu_{g1}|^4 D_{11}(-\omega;\omega,0,0) + |\mu_{g3}|^4 D_{33}(-\omega;\omega,0,0) \right. \\ \left. +|\mu_{g1}|^2|\mu_{g3}|^2\left[D_{13}(-\omega;\omega,0,0) + D_{31}(-\omega;\omega,0,0)\right]\right\}. \quad (2.77)$$

The energy denominators for the Lorentzian theory are calculated using Equations (2.67) and (2.73) or just Equation (2.73) and the energy denominators for the inhomogeneous-broadening theory are calculated using Equations (2.72) and (2.76).

Figure 2.13 shows the results of these calculations in terms of the real and imaginary parts of the third-order molecular susceptibility. The two one-photon excited states are centered about 653 nm and 614 nm, and the strength, μ, of the $g \rightarrow 1$ transition is twice that of the $g \rightarrow 3$ transition. The difference in the strengths of the transitions is apparent when considering the peaks at 614 nm and 653 nm in the real part of the susceptibility for the homogeneous-broadening theory. If there were no mixing terms (energy denominators which include both excited states) the ratio of the magnitude of the peak at 653 nm to the magnitude of the peak at 614 nm would be about $2^4 = 16$; however, it is only about 14. This tells us that there is a contribution from the mixing terms, $D_{13}(-\omega;\omega,0,0)$ and $D_{31}(-\omega;\omega,0,0)$, but the majority of the response is controlled by $D_{11}(-\omega;\omega,0,0)$ and $D_{33}(-\omega;\omega,0,0)$.

In Figure 2.13 the maximum of the third-order susceptibility for the Lorentzian theory is larger than the maximum for all three cases of the inhomogeneous-broadening theory with constant transition moments. This follows directly from the individual energy denominator contributions being larger for the third-order homogeneous-broadening theory (see Figures 2.11 and 2.12).

The one-photon contributions to the third-order molecular susceptibility for both homogeneously- and -broadened electronic transitions in the QEO experiment where discussed in this section. We showed that there is a significant difference predicted for both the real and imaginary parts of the total electronic response and its individual parts for a system that is inhomogeneously-broadened in comparison to one that can be regarded as homogeneous. It was also shown that the third-order response for the

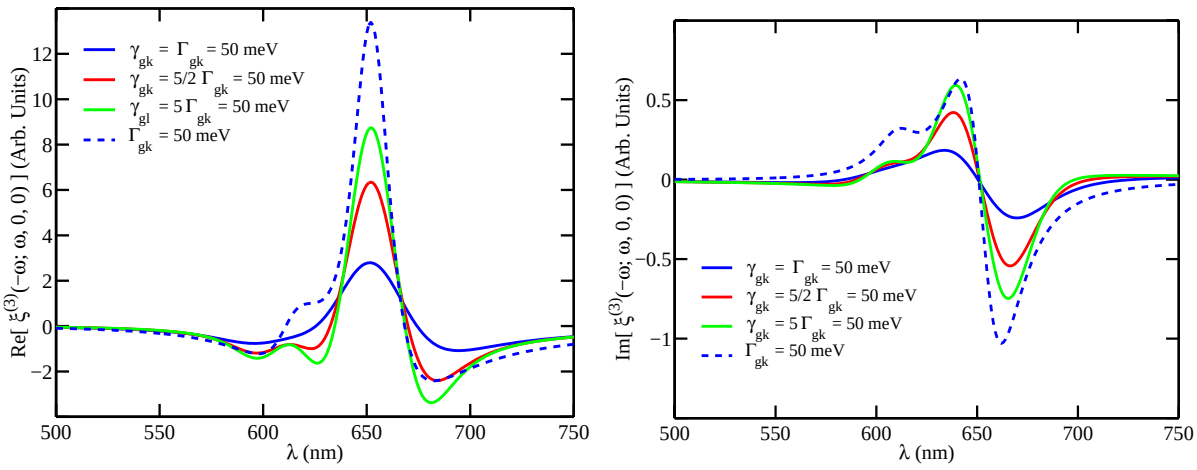

Fig. 2.13: Real and imaginary parts of $\xi^{(3)}(-\omega;\omega,0,0)$ for two one-photon excited states centered about 653 nm and 614 nm. The solid lines represent the inhomogeneously broadened electronic transitions for three different values of Γ_{gk} where $k = \{1,3\}$ and the dashed line represents the homogeneously-broadened transitions.

quadratic electrooptic experiment has a larger magnitude for the Lorentzian theory which is opposite to the linear response prediction.

At this stage a n-level inhomogeneous-broadening model of the quadratic electrooptic experiment which only allows one-photon states can be constructed. The following section develops the two possible two-photon contributions to the electronic response in the QEO experiment for a system that is inhomogeneously-broadened and compares the inhomogeneously-broadened response to the homogeneously-broadened response. This will allow us to construct an n-level inhomogeneous-broadening model that can include any number of one- and two-photons states for the quadratic electrooptic experiment.

Two-photon contributions Like the one-photon contributions to the electronic response, there are two different cases for the two-photon contributions. Figure 2.14 shows the two-photon enhancements to the third-order molecular response when there is one one-photon state, and one two-photon state, and a two-photon enhancement when there are two one-photon states and one two-photon state. The solid horizontal lines represent real states and the dashed horizontal lines represent virtual states as discussed

in Section 2.4.2.2.1.

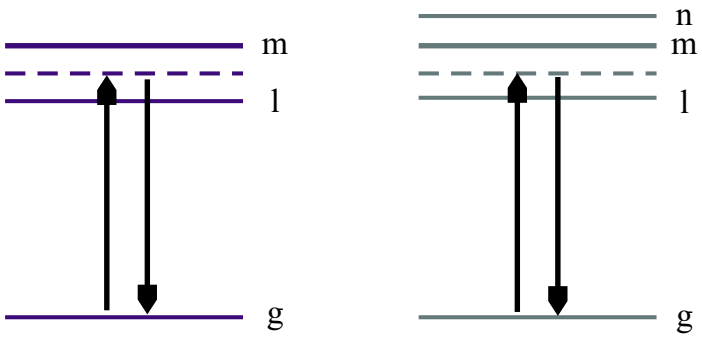

Fig. 2.14: Resonant enhancements for D_{lml} and D_{lmn}, respectively. Each arrow represents a one-photon transition in the specified direction. Solid horizontal lines represent real energy levels and dashed horizontal lines represent virtual energy levels.

Following the established procedure, we separate the two-photon contributions (Equation (2.29)) for the different processes in the quadratic electrooptic effect:

$$\begin{aligned} D^L_{lml}(-\omega;\omega,0,0) &= \frac{1}{(\Omega_{gl}-\omega)^2(\Omega_{gm}-\omega)} + \frac{1}{(\Omega_{gl}-\omega)(\Omega_{gm}-\omega)\Omega_{gl}} \\ &+ \frac{1}{(\Omega_{gl}-\omega)\Omega_{gm}\Omega_{gl}} + \frac{1}{\Omega^*_{gl}(\Omega_{gm}-\omega)(\Omega_{gl}-\omega)} \\ &+ \frac{1}{\Omega^*_{gl}\Omega_{gl}(\Omega_{gm}-\omega)} + \frac{1}{(\Omega^*_{gl}+\omega)\Omega_{gm}\Omega_{gl}} \\ &+ \frac{1}{\Omega_{gl}(\Omega^*_{gl}+\omega)(\Omega^*_{gm}+\omega)} + \frac{1}{\Omega^*_{gl}\Omega_{gl}(\Omega^*_{gm}+\omega)} \\ &+ \frac{1}{\Omega^*_{gl}(\Omega^*_{gl}+\omega)(\Omega^*_{gm}+\omega)} + \frac{1}{\Omega^*_{gl}\Omega^*_{gm}(\Omega^*_{gl}+\omega)} \\ &+ \frac{1}{\Omega^*_{gl}\Omega^*_{gm}(\Omega_{gl}-\omega)} + \frac{1}{(\Omega^*_{gl}+\omega)^2(\Omega^*_{gm}+\omega)}, \end{aligned} \tag{2.78}$$

and

$$\begin{aligned} D^L_{lmn}(-\omega;\omega,0,0) = &\frac{1}{\Omega_{gl}-\omega}\left[\frac{1}{(\Omega_{gm}-\omega)(\Omega_{gn}-\omega)} + \frac{1}{(\Omega_{gm}-\omega)\Omega_{gn}} + \frac{1}{\Omega_{gm}\Omega_{gn}}\right] \\ &+\frac{1}{\Omega^*_{gl}}\left[\frac{1}{(\Omega_{gm}-\omega)(\Omega_{gn}-\omega)} + \frac{1}{(\Omega_{gm}-\omega)\Omega_{gn}} + \frac{1}{(\Omega^*_{gm}+\omega)\Omega_{gn}}\right. \\ &\left.+\frac{1}{(\Omega^*_{gm}+\omega)(\Omega^*_{gn}+\omega)} + \frac{1}{\Omega^*_{gm}(\Omega_{gn}-\omega)} + \frac{1}{\Omega^*_{gm}(\Omega^*_{gn}+\omega)}\right] \\ &+\frac{1}{\Omega^*_{gl}+\omega}\left[\frac{1}{\Omega_{gm}\Omega_{gn}} + \frac{1}{(\Omega^*_{gm}+\omega)\Omega_{gn}} + \frac{1}{(\Omega^*_{gm}+\omega)(\Omega^*_{gn}+\omega)}\right]. \end{aligned} \tag{2.79}$$

Since there are two excited states involved in the electronic response for $D^{L}_{lml}(-\omega;\omega,0,0)$, the procedure for transforming $D^{L}_{ln}(-\omega;\omega,0,0)$ to $D^{IB}_{ln}(-\omega;\omega,0,0)$ can be recycled to generate $D^{IB}_{lml}(-\omega;\omega,0,0)$. Equation (2.78) is expanded using the same partial fraction results as $D^{L}_{ln}(-\omega;\omega,0,0)$ to isolate the unique functions of ω_{gl} and ω_{gm}, and then two convolution integrals are performed – one with respect to ω_{gl} and the other with respect to ω_{gm}. Because the convolution integrals are known, the appropriate results from Table2.2 are substituted to give the following,

$$
\begin{aligned}
D^{IB}_{lml}(-\omega;\omega,0,0) = \frac{-\pi}{\gamma_{gl}\gamma_{gm}}\times
&\left\{ W\left(\frac{-(\Omega_{gm}-\omega)}{\gamma_{gm}}\right)\left[\frac{2(\Omega_{gl}-\omega)}{\gamma_{gl}^{2}}W\left(\frac{-(\Omega_{gl}-\omega)}{\gamma_{gl}}\right)+\frac{2i}{\sqrt{\pi}\gamma_{gl}}\right]\right.\\
&+W\left(\frac{-(\Omega^{*}_{gm}+\omega)}{\gamma_{gm}}\right)\left[\frac{2(\Omega^{*}_{gl}+\omega)}{\gamma_{gl}^{2}}W\left(\frac{-(\Omega^{*}_{gl}+\omega)}{\gamma_{gl}}\right)+\frac{2i}{\sqrt{\pi}\gamma_{gl}}\right]\\
&+\frac{2(1+i\frac{\Gamma_{gl}}{\omega})}{(\omega+2i\Gamma_{gl})}\left[W\left(\frac{-(\Omega_{gm}-\omega)}{\gamma_{gm}}\right)W\left(\frac{-(\Omega_{gl}-\omega)}{\gamma_{gl}}\right)\right.\\
&\qquad\left.-W\left(\frac{-(\Omega^{*}_{gm}+\omega)}{\gamma_{gm}}\right)W\left(\frac{-(\Omega^{*}_{gl}+\omega)}{\gamma_{gl}}\right)\right]\\
&+\frac{(1+i\frac{\omega}{2\Gamma_{gl}})}{\omega}\left[W\left(\frac{-(\Omega^{*}_{gm}+\omega)}{\gamma_{gm}}\right)W\left(\frac{-\Omega^{*}_{gl}}{\gamma_{gl}}\right)\right.\\
&\qquad\left.-W\left(\frac{-(\Omega_{gm}-\omega)}{\gamma_{gm}}\right)W\left(\frac{-\Omega_{gl}}{\gamma_{gl}}\right)\right]\\
&+\frac{2(1-i\frac{\omega}{4\Gamma_{gl}})}{(\omega+2i\Gamma_{gl})}\left[W\left(\frac{-(\Omega^{*}_{gm}+\omega)}{\gamma_{gm}}\right)W\left(\frac{-\Omega_{gl}}{\gamma_{gl}}\right)\right.\\
&\qquad\left.-W\left(\frac{-(\Omega_{gm}-\omega)}{\gamma_{gm}}\right)W\left(\frac{-\Omega^{*}_{gl}}{\gamma_{gl}}\right)\right]\\
&+\frac{2i\frac{\Gamma_{gl}}{\omega}}{(\omega+2i\Gamma_{gl})}\left[W\left(\frac{-\Omega^{*}_{gm}}{\gamma_{gm}}\right)W\left(\frac{-\Omega^{*}_{gl}}{\gamma_{gl}}\right)-W\left(\frac{-\Omega_{gm}}{\gamma_{gm}}\right)W\left(\frac{-\Omega_{gl}}{\gamma_{gl}}\right)\right]\\
&+\frac{1}{\omega}\left[W\left(\frac{-\Omega_{gm}}{\gamma_{gm}}\right)W\left(\frac{-(\Omega_{gl}-\omega)}{\gamma_{gl}}\right)-W\left(\frac{-\Omega^{*}_{gm}}{\gamma_{gm}}\right)W\left(\frac{-(\Omega^{*}_{gl}+\omega)}{\gamma_{gl}}\right)\right]\\
&+\frac{1}{(\omega+2i\Gamma_{gl})}\left[W\left(\frac{-\Omega^{*}_{gm}}{\gamma_{gm}}\right)W\left(\frac{-(\Omega_{gl}-\omega)}{\gamma_{gl}}\right)\right.\\
&\qquad\left.\left.-W\left(\frac{-\Omega_{gm}}{\gamma_{gm}}\right)W\left(\frac{-(\Omega^{*}_{gl}+\omega)}{\gamma_{gl}}\right)\right]\right\},
\end{aligned}
\tag{2.80}
$$

$D^{IB}_{lml}(-\omega;\omega,0,0)$ allows us to model two-photon transitions in the third-order response for the quadratic electrooptic experiment.

Similar to Figure 2.12, the electronic response of the inhomogeneous-broadening model is compared to the homogeneous-broadening model. Figure 2.15 shows the real and imaginary parts of $D_{121}(-\omega;\omega,0,0)$, respectively, for both inhomogeneous-broadening and homogeneous-broadening, where 1 stands for the one-photon state and the 2 stands for the two-photon state. The same three values of Γ_{gk}, where $k \in \{1,2\}$, are used for the inhomogeneous-broadening model for comparison to the linear response and one-photon quadratic electrooptic responses.

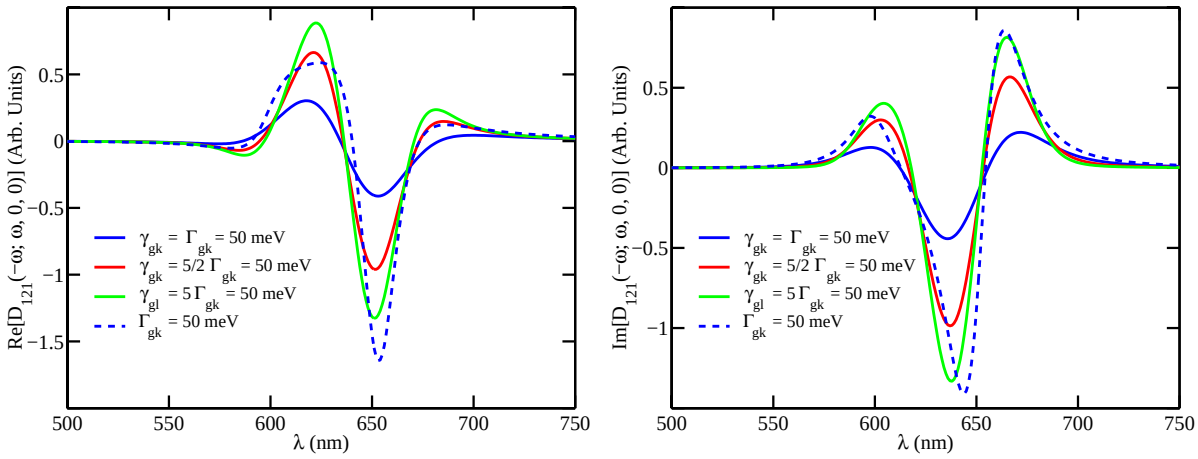

Fig. 2.15: Real and imaginary parts of $D_{121}(-\omega;\omega,0,0)$ for one one-photon excited state and one two-photon state centered about 653 nm and 600 nm, respectively. The solid lines represent the inhomogeneously broadened electronic transitions for three different values of Γ_{gk} where $k \in \{1,2\}$ and the dashed line represents the homogeneously-broadened transitions.

In general there is a noticeable difference in the features of the response for both the real and imaginary parts of $D_{lml}(-\omega;\omega,0,0)$ predicted by the inhomogeneous-broadening theory. It should also be noted that the magnitude of the two-photon contribution for the Lorentzian theory is much closer to the magnitude of the inhomogeneous-theory than in the one-photon contributions to the third-order electronic response (see Figure 2.12). The response is much more complicated when a two-photon state is involved making it difficult to compare to the linear response.

However, it is naive to isolate the two-photon contribution from the total response because the total response usually will not have the two-photon contribution without a

corresponding one-photon contribution to the third-order molecular susceptibility. Thus we need to discuss the total third-order molecular response in the three-level limit when there is one one-photon excited state and one two-photon excited state. Equation (2.66) can be reduced to the following when considering the aforementioned model,

$$\begin{aligned}\xi^{(3)}(-\omega;\omega,0,0) &= \frac{1}{\epsilon_0 3!}\frac{1}{\hbar^3}\left\{|\mu_{g1}|^2|\mu_{12}|^2 D_{121}(-\omega;\omega,0,0) - \right. \\ &\qquad \left. |\mu_{g1}|^4 D_{11}(-\omega;\omega,0,0)\right\}. \end{aligned} \tag{2.81}$$

The energy denominators are given by Equations (2.67) and (2.78) for the Lorentzian theory and by Equations (2.72) and (2.80) for the inhomogeneous-broadening theory.

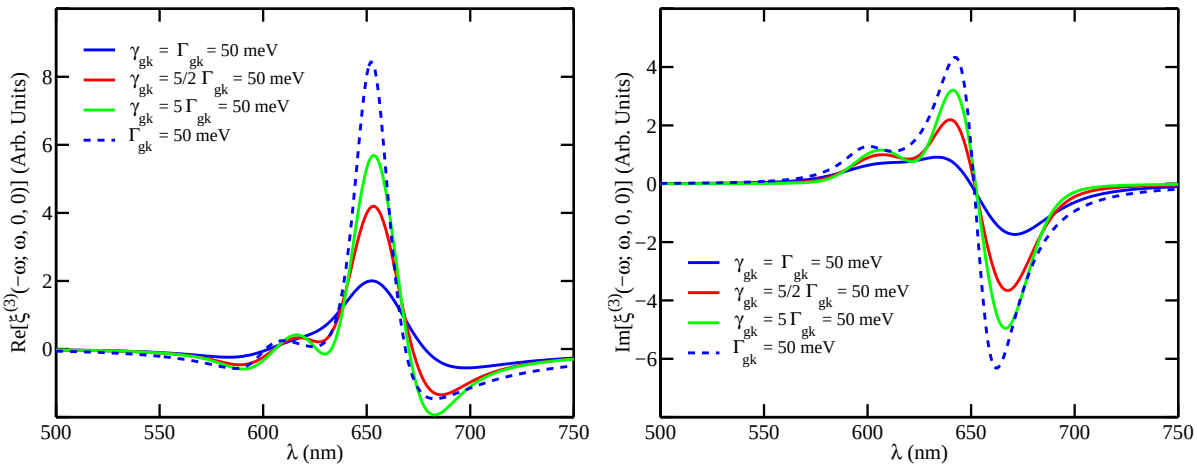

Fig. 2.16: Real and imaginary parts of $\xi^{(3)}(-\omega;\omega,0,0)$ for one one-photon excited state and one two-photon state centered about 653 nm and 600 nm, respectively. The solid lines represent the inhomogeneously broadened electronic transitions for three different values of Γ_{gk} where $k \in \{1,2\}$ and the dashed lines represent the homogeneously-broadened transitions.

Figure 2.16 shows the real and imaginary parts of the third-order electronic response from Equation (2.81), where the strength of the $g \rightarrow 1$ is 4 times stronger than the $1 \rightarrow 2$ transition. As with the previous three-level model (see Figure 2.13) the magnitude of the response for the Lorentzian theory is larger than all three variations of the inhomogeneous-broadening theory, which tells us that the one-photon transition is dominating the response in this instance. The $1 \rightarrow 2$ transition moment was chosen to be 4

times smaller than the $g \rightarrow 1$ transition moment to show that the molecular third-order susceptibility can be very similar when there are either two one-photon excited states, Figure 2.13, or one one-photon excited state and one two-photon excited state, Figure 2.16. Thus it may be difficult to distinguish between a two-photon and a second one-photon contribution to the third-order electronic response in the quadratic electrooptic effect, and other experiments may be needed to verify which type of state is responsible for the response.

The procedure used for transforming $D^{L}_{lmn}(-\omega;\omega,0,0)$ to $D^{IB}_{lmn}(-\omega;\omega,0,0)$ follows the procedure used to transform $D^{L}_{lmn}(-3\omega;\omega,\omega,\omega)$ which was previously discussed in Section 2.4.2.2.1. Because there are three excited states involved in the electronic response, a partial fraction expansion is unnecessary. Therefore three convolution integrals – one with respect to ω_{gl}, a second with respect to ω_{gm}, and a third with respect to ω_{gn} are performed on Equation (2.79). These integrals are all known and can be found in Table 2.1 since there is no quadratic or cubic functions of the transition frequencies. After performing the appropriate substitutions from Table 2.1 the final result for the energy denominator that characterizes the electronic response for two one-photon (l and n) excited states and one two-photon (m) excited state in the -broadened regime is:

$$
\begin{aligned}
D^{IB}_{lmn}(-\omega;\omega,0,0) = \frac{-i\pi^{3/2}}{\gamma_{gl}\gamma_{gm}\gamma_{gn}}\times \\
\left\{W\left(\frac{-(\Omega_{gl}-\omega)}{\gamma_{gl}}\right)\left[W\left(\frac{-(\Omega_{gm}-\omega)}{\gamma_{gm}}\right)\left\{W\left(\frac{-(\Omega_{gn}-\omega)}{\gamma_{gn}}\right)+W\left(\frac{-\Omega_{gn}}{\gamma_{gn}}\right)\right\}\right. \\
\left. +W\left(\frac{-\Omega_{gm}}{\gamma_{gm}}\right)W\left(\frac{-\Omega_{gn}}{\gamma_{gn}}\right)\right] \\
+W\left(\frac{-\Omega^{*}_{gl}}{\gamma_{gl}}\right)\left[W\left(\frac{-(\Omega_{gm}-\omega)}{\gamma_{gm}}\right)\left\{W\left(\frac{-(\Omega_{gn}-\omega)}{\gamma_{gn}}\right)+W\left(\frac{-\Omega_{gn}}{\gamma_{gn}}\right)\right\}+\right. \\
W\left(\frac{-(\Omega^{*}_{gm}+\omega)}{\gamma_{gm}}\right)\left\{W\left(\frac{-\Omega_{gn}}{\gamma_{gn}}\right)+W\left(\frac{-(\Omega^{*}_{gn}+\omega)}{\gamma_{gn}}\right)\right\}+ \\
\left. W\left(\frac{-\Omega^{*}_{gm}}{\gamma_{gm}}\right)\left\{W\left(\frac{-(\Omega_{gn}-\omega)}{\gamma_{gn}}\right)+W\left(\frac{-(\Omega^{*}_{gn}+\omega)}{\gamma_{gn}}\right)\right\}\right] \\
+W\left(\frac{-(\Omega^{*}_{gl}+\omega)}{\gamma_{gl}}\right)\left[W\left(\frac{-(\Omega^{*}_{gm}+\omega)}{\gamma_{gm}}\right)\left\{W\left(\frac{-\Omega_{gn}}{\gamma_{gn}}\right)+W\left(\frac{-(\Omega^{*}_{gn}+\omega)}{\gamma_{gn}}\right)\right\}+\right. \\
\left. W\left(\frac{-\Omega_{gm}}{\gamma_{gm}}\right)W\left(\frac{-\Omega_{gn}}{\gamma_{gn}}\right)\right]\right\}. \qquad (2.82)
\end{aligned}
$$

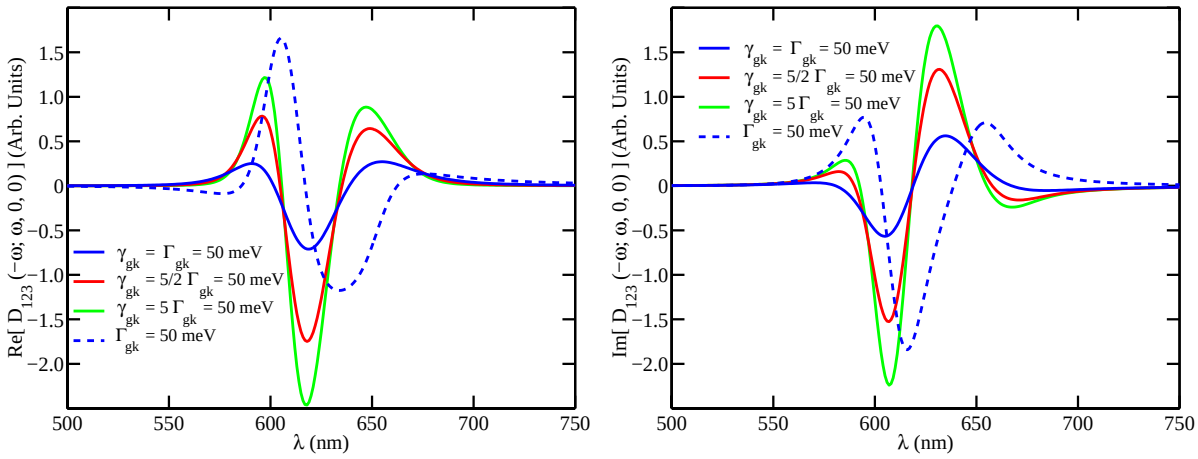

Fig. 2.17: Real and imaginary parts of $D_{123}(-\omega;\omega,0,0)$ for two one-photon excited states centered about 653 nm and 614 nm, and one two-photon state centered about 600 nm. The solid lines represent the inhomogeneously-broadened electronic transitions for three different values of Γ_{gk}, where $k \in \{1,2,3\}$ and the dashed lines represent the homogeneously-broadened transitions when $l = 1, m = 2, n = 3$.

Figure 2.17 shows the real and imaginary parts of the Equation (2.82) for both the homogeneous-broadening and inhomogeneous-broadening theories. The same three homogeneous linewidths, which were used in previous calculations, are used in the calculation of the three inhomogeneously-broadened curves. It is interesting to note that the inhomogeneous-broadening theory predicts a larger negative value for the response than the homogeneous broadening theory which is similar to the linear response (See Figure 2.2) but opposite to the other three electrooptic derivations. Again it is not very realistic to isolate the individual energy denominator so a four-level model for the third-order molecular susceptibility is written as follows,

$$\begin{aligned}\xi^{(3)}(-\omega;\omega,0,0) = \frac{1}{\epsilon_0 3!}\frac{1}{\hbar^3}\Big\{&|\mu_{g1}|^2|\mu_{12}|^2 D_{121}(-\omega;\omega,0,0) + |\mu_{g3}|^2|\mu_{32}|^2 D_{323}(-\omega;\omega,0,0)\\ &+\mu_{g1}\mu_{12}\mu_{32}\mu_{g3}\left[D_{123}(-\omega;\omega,0,0) + D_{321}(-\omega;\omega,0,0)\right]\\ &-|\mu_{g1}|^4 D_{11}(-\omega;\omega,0,0) - |\mu_{g3}|^4 D_{33}(-\omega;\omega,0,0)\\ &-|\mu_{g1}|^2|\mu_{g3}|^2\left[D_{13}(-\omega;\omega,0,0) + D_{31}(-\omega;\omega,0,0)\right]\Big\}. \quad (2.83)\end{aligned}$$

The four-level model for the third-order molecular susceptibility, Equation (2.83), involves

two one-photon excited states and one two-photon excited state even though there are eight energy denominator contributions.

Figure 2.18 shows the real and imaginary parts of Equation (2.83), for both the homogeneous-broadening and inhomogeneous-broadening theories. The same three homogeneous linewidths, which were used in previous calculations, are used in the calculation of the three inhomogeneously-broadened susceptibilities. The transition moments between the first one-photon state and the two-photon state, and the second one-photon state and the two-photon state are 1/4 of the transition moment for the transition between the ground and first excited state. The transition moment for the ground to second one-photon state is 1/2 the transition moment for the ground to first one-photon excited state.

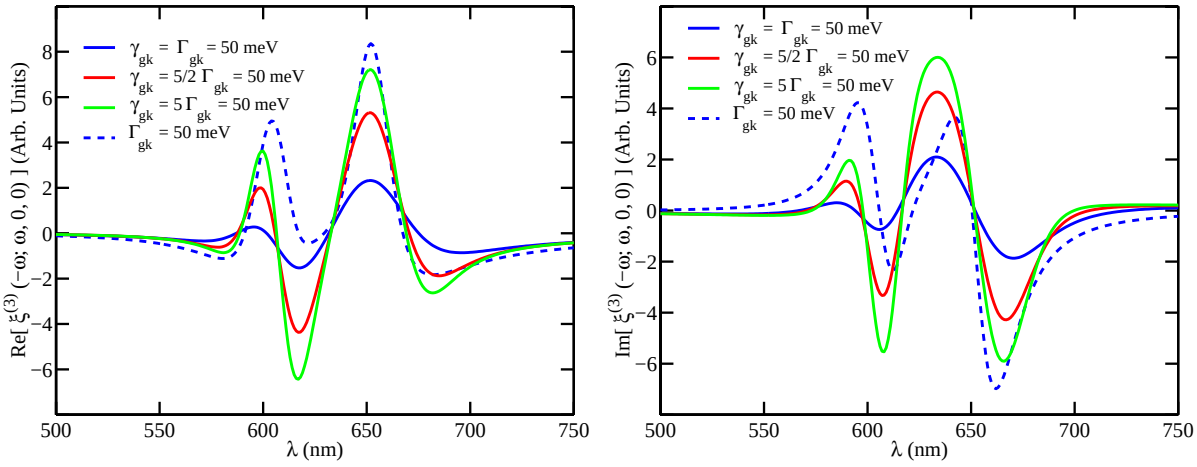

Fig. 2.18: Real and imaginary parts of $\xi^{(3)}(-\omega;\omega,0,0)$ for two one-photon excited states centered about 653 nm and 614 nm, and one two-photon state centered about 600 nm. The solid lines represent the inhomogeneously-broadened electronic transitions for three different values of Γ_{gk}, where $k \in \{1,2,3\}$, and the dashed lines represent the homogeneously-broadened transitions when n and $l \in \{1,3\}$, and $m = 2$.

When there are four excited states contributing to the total electronic response it becomes very difficult to pick out features that are due to the individual states. However, Figure 2.18 suggests that the two-photon and the second one-photon states at 600 nm and

614 nm are making a large contribution to the response in the 610 nm range even though the strengths of these transitions are individually weaker than the transition strength between the ground and first excited state. Further analysis of the four level model will be deferred until Section 5.8.

In this section we have developed a general n-level inhomogeneous-broadening model of the third-order molecular susceptibility for the quadratic electrooptic effect. The predicted response due to 2-, 3-, and 4-level models for the homogeneous-broadening and inhomogeneous-broadening theories are much closer in magnitude than the predictions for THG. This should be compared to experimental results in the future. The following section discusses the development of a general n-level inhomogeneous-broadening model for the optical Kerr effect.

2.4.2.2.3 Optical Kerr effect Two specific cases of the optical Kerr effect will be discussed in this section. The first will be the degenerate four wave mixing experiment or the intensity dependent refractive index experiment, and the second will be the pump-probe experiment. The frequency contributions to the third-order susceptibility in an intensity dependent refractive index measurement are $(-\omega;\omega,-\omega,\omega)$. In a pump-probe measurement the frequency contributions to the third-order susceptibility are $(-\omega_1;\omega_1,-\omega_2,\omega_2)$, where ω_2 is the frequency of the high intensity pump beam and ω_1 is the intensity of the low intensity probe beam. We, initially, discuss the intensity dependent refractive index process in terms of the transformation from the homogeneous-broadening theory to the inhomogeneous-broadening theory because there are fewer permutations in the energy denominators making it the simpler of the two processes. Then we complete the discussion on the optical Kerr effect with the transformation from the homogeneous-broadening theory to the inhomogeneous-broadening theory for the pump-probe experiment.

Intensity dependent refractive index In this section we develop the transformation from a homogeneous-broadened system to an inhomogeneous-broadened system in terms of degenerate four wave mixing. This leads to two phenomena that are of particular interest at the nonlinear optics laboratory: an intensity dependent refractive index which is related to the real part of the third-order susceptibility and two-photon absorption which is related to the imaginary part of the third-order susceptibility. By substituting the frequency arguments into the third-order molecular susceptibility, Equation (2.24), we get the following for the homogeneously-broadened case,

$$\begin{aligned}\xi^{(3)}(-\omega;\omega,\omega,-\omega) &= \frac{1}{\epsilon_0 3!}\frac{1}{\hbar^3}\left\{\sum_{l,m,n}{}' D_{lmn}(-\omega;\omega,-\omega,\omega)\mu_{gl}\mu_{lm}\mu_{mn}\mu_{ng} - \right. \\ &\left. \sum_{l,n}{}' D_{ln}(-\omega;\omega,-\omega,\omega)|\mu_{gl}|^2|\mu_{gn}|^2\right\}, \qquad (2.84)\end{aligned}$$

where we have assumed that μ_{gl}=μ_{lg}, and μ_{gn}=μ_{ng}.

At this stage of the discussion on inhomogeneous-broadening we hope that the pro-

cedure for transforming Lorentzian energy denominators to inhomogeneous-broadening denominators is well understood by the reader so we limit the following discussion to the contracted Lorentzian energy denominators and the full blown versions of the inhomogeneous-broadening denominators. We refer the reader back to Section 2.4.2.2.1 for a review of the transformation procedure.

One-photon contributions As was previously mentioned, the frequency arguments for the intensity dependent refractive index experiment are $\omega_1 = \omega_3 = -\omega_2 = \omega$ and $\omega_\sigma = \omega$ so the contracted form of the Lorentzian energy denominator for one-photon contributions to the third-order susceptibility is

$$\begin{aligned} D^L_{ln}(-\omega;\omega,-\omega,\omega) \quad &= \mathbf{S}_{1,2,3}\ \Big\{\left[(\Omega_{lg}-\omega)(\Omega_{lg}-\omega)(\Omega_{ng}-\omega)\right]^{-1} + \\ &\quad \left[(\Omega_{lg}-\omega)(\Omega^*_{ng}-\omega)(\Omega_{ng}-\omega)\right]^{-1} + \\ &\quad \left[(\Omega^*_{lg}+\omega)(\Omega^*_{lg}+\omega)(\Omega^*_{ng}+\omega)\right]^{-1} + \\ &\quad \left[(\Omega^*_{lg}+\omega)(\Omega_{ng}+\omega)(\Omega^*_{ng}+\omega)\right]^{-1}\Big\}, \end{aligned} \tag{2.85}$$

where the operator $\mathbf{S}_{1,2,3}$ tells us to sum the 3 distinct permutations of the input frequencies. Thus there would be twelve terms in Equation (2.85) if we were to completely expand $D^L_{ln}(-\omega;\omega,-\omega,\omega)$. Figure 2.19 represents resonant enhancements for the energy

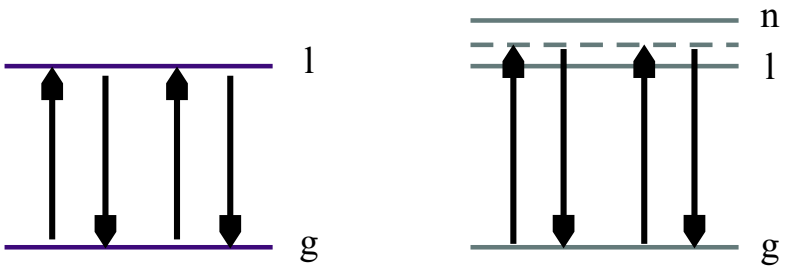

Fig. 2.19: Resonant enhancements due to $D_{ll}(-\omega;\omega,\omega,-\omega)$ and $D_{ln}(-\omega;\omega,\omega,-\omega)$, respectively. Each arrow represents a one-photon transition in the specified direction, solid horizontal lines represent real excited states, and dashed lines represent virtual excited states.

denominators, $D_{ll}(-\omega;\omega,\omega,-\omega)$ and $D_{ln}(-\omega;\omega,\omega,-\omega)$, respectively. When only one excited state is involved in the third-order response there is a resonant enhancement if

the photon energy is near the transition energy. An additional resonant enhancement can occur when there is a second one-photon excited state involved in electronic response. It occurs when the photon energy is similar to the transitions energies of both the excited states so that both excited states contribute to the response. Notice that there are four optical photons, of equal energy, involved in the third-order enhancement unlike the quadratic electrooptic experiment where there are two optical photons and two zero-frequency photons.

As in previous derivations $D_{ln}^{L}(-\omega;\omega,\omega,-\omega)$ must be expanded using partial fractions. However, this expansion would not add to the discussion so we relegate the expanded version of Equation (2.85) to Appendix A. Once the partial fraction expansion is complete, the results from Table 2.2 can be substituted for each Lorentzian term to produce the following inhomogeneous-broadening energy denominator (when $l=n$),

$$\begin{aligned} D_{ll}^{IB}(-\omega;\omega,-\omega,\omega) = \frac{i\sqrt{\pi}}{\gamma_{gl}}\times \\ \left\{ \frac{2(\Omega_{gl}-\omega)^2-\gamma_{gl}^2}{\gamma_{gl}^4} W\left(\frac{-(\Omega_{gl}-\omega)}{\gamma_{gl}}\right) + \frac{2(\Omega_{gl}^*+\omega)^2-\gamma_{gl}^2}{\gamma_{gl}^4} W\left(\frac{-(\Omega_{gl}^*+\omega)}{\gamma_{gl}}\right) + \right. \\ \frac{2\Gamma_{gl}^2-\omega^2+2i\Gamma_{gl}\omega}{4\Gamma_{gl}^2\omega^2}\left[W\left(\frac{-(\Omega_{gl}+\omega)}{\gamma_{gl}}\right) + W\left(\frac{-(\Omega_{gl}^*-\omega}{\gamma_{gl}}\right) - \right. \\ \left. W\left(\frac{-(\Omega_{gl}^*+\omega)}{\gamma_{gl}}\right) - W\left(\frac{-(\Omega_{gl}-\omega)}{\gamma_{gl}}\right)\right] + \frac{4i\omega_{gl}}{\sqrt{\pi}\gamma_{gl}^3} + \\ \left. \frac{\omega+2i\Gamma_{gl}}{2i\omega\Gamma_{gl}}\left[\frac{2(\Omega_{gl}-\omega)}{\gamma_{gl}^2} W\left(\frac{-(\Omega_{gl}-\omega)}{\gamma_{gl}}\right) - \frac{2(\Omega_{gl}^*+\omega)}{\gamma_{gl}^2} W\left(\frac{-(\Omega_{gl}^*+\omega)}{\gamma_{gl}}\right)\right]\right\} \end{aligned} \quad (2.86)$$

More details on the transformation procedure can be found in Section 2.4.2.2.1 since Equation (2.86) was developed using the procedure that was used to determine $D_{ll}^{IB}(-3\omega;\omega,\omega,\omega)$. Unfortunately, there is no simple way to use the intrinsic permutation operator with the inhomogeneous-broadening denominators. Hence as the frequency arguments become more complex so do the results.

Using Equation (2.86) for the inhomogeneous-broadening theory or Equation (2.85) for the Lorentzian theory, we can construct a three-level model of the third-order molecular susceptibility for the intensity dependent refractive index experiment as follows:

$$\xi^{(3)}(-\omega;\omega,\omega,-\omega) = -\frac{1}{\epsilon_0 3!}\frac{1}{\hbar^3}\left\{|\mu_{g1}|^4 D_{11}(-\omega;\omega,\omega,-\omega)\right\}. \quad (2.87)$$

Note that the susceptibility is proportional to the energy denominator, $D_{11}(-\omega;\omega,\omega,-\omega)$, so we expect $\xi^{(3)}(-\omega;\omega,\omega,-\omega)$ to be enhanced when the transition frequency is close to the incident photon energy (see Figure 2.19).

Figure 2.20 represents the real and imaginary parts of Equation (2.87) for both homogeneously-broadened and inhomogeneously-broadened third-order electronic responses of an electronic state centered about 653 nm in the visible region. The predicted two-

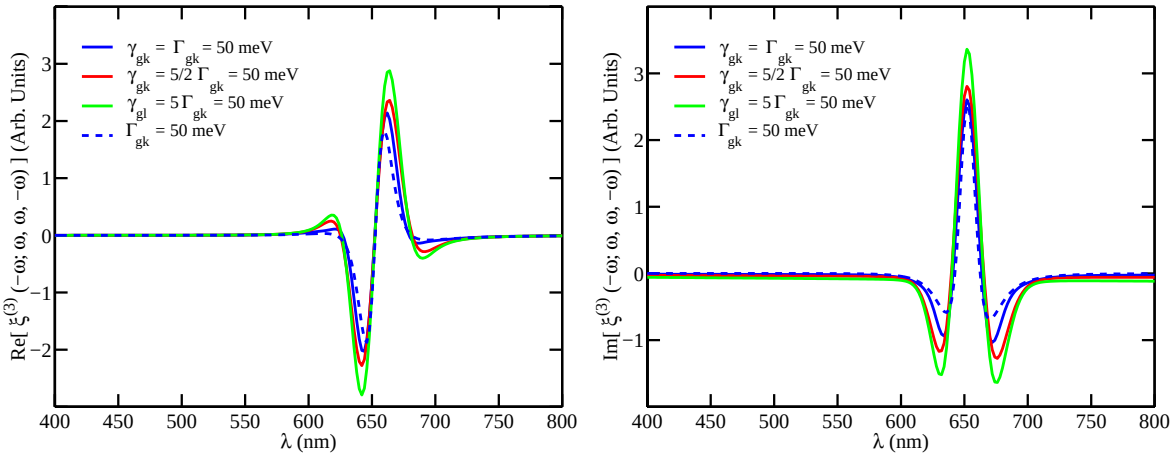

Fig. 2.20: Real and imaginary parts of $\xi^{(3)}(-\omega;\omega,\omega,-\omega)$ for a single excited state centered about 653 nm. The solid lines represent the inhomogeneously broadened electronic transitions for three different values of Γ_{g1} and the dashed line represents the homogeneously-broadened transitions when $n = l = 1$.

level response for the intensity dependent refractive index experiment is quite intriguing because the imaginary part of the response is very similar to the real part of the two-level response for the quadratic electrooptic experiment. The real part of the two-level response for the intensity dependent refractive index experiment is also predicted to be similar to the negative of the imaginary part of the two-level response for the quadratic electrooptic experiment.

We should also note that the predicted resonant response for the Lorentzian theory is smaller than the inhomogeneous-broadening response. This result is similar to the prediction for the linear response but opposite to the predicted resonant response for the THG and quadratic electrooptic experiments.

Since intensity dependent refractive index experiments are typically performed in the near IR, we are also interested in the off-resonant response. Figure 2.21 shows the real and imaginary parts of the two-level response from Equation (2.87) for both the Lorentzian and inhomogeneous-broadening theories in the near IR.

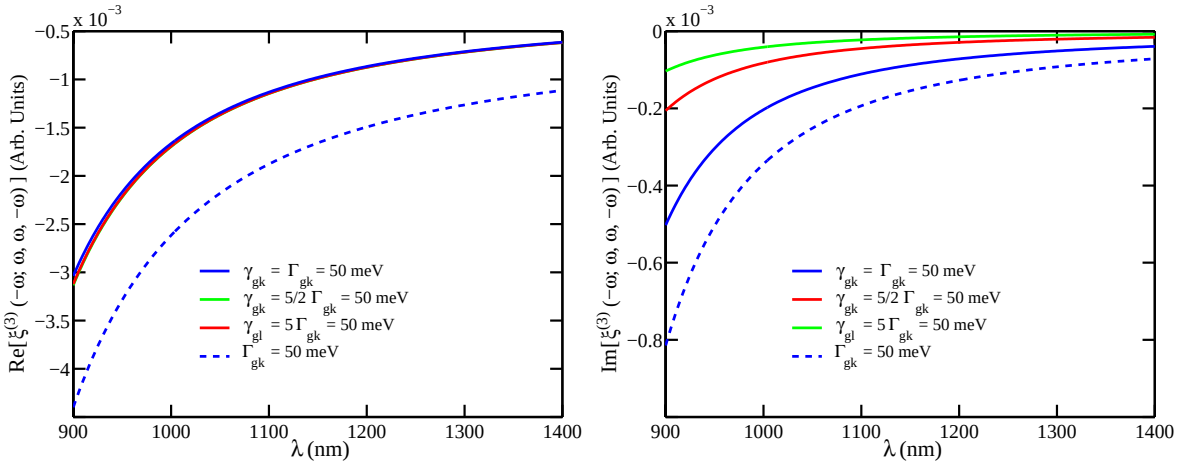

Fig. 2.21: Real and imaginary parts of $\xi^{(3)}(-\omega;\omega,\omega,-\omega)$ for a single excited state centered about 653 nm. The solid lines represent the inhomogeneously broadened electronic transitions for three different values of Γ_{g1} and the dashed line represents the homogeneously-broadened transitions when $n = l = 1$.

Although the units on the y-axis are arbitrary, they are consistent between Figures 2.20 and 2.21, and will be consistent from the visible region to the IR region of the spectrum for the remainder of this section. In other words, the near IR third-order response is roughly three orders of magnitude smaller than the response in the visible. Although the third-order response is much smaller in the near IR so is the linear response which can be beneficial for nonlinear optical device fabrication.

The off-resonant response, although not very intriguing in comparison to the resonant response, does show that the homogeneous-broadening theory predicts a larger negative response than the inhomogeneous-broadening theory. As more states are allowed to contribute to the third-order molecular susceptibility the near IR region becomes more interesting.

Before additional states can be added to the IB-model of $\xi^{(3)}(-\omega;\omega,\omega,-\omega)$, we must

transform $D_{ln}^{L}(-\omega;\omega,\omega,-\omega)$ to $D_{ln}^{IB}(-\omega;\omega,\omega,-\omega)$. The result of transforming Equation (2.85), when $l \neq n$, to the inhomogeneous-broadening theory is the following:

$$
\begin{aligned}
D_{ln}^{IB}(-\omega;\omega,\omega,-\omega) = {} & \frac{-\pi}{\gamma_{gl}\gamma_{gn}} \times \\
& \left\{ \left[W\left(\frac{-(\Omega_{gn}-\omega)}{\gamma_{gn}}\right) + W\left(\frac{-(\Omega_{gn}+\omega)}{\gamma_{gn}}\right) \right] \times \right. \\
& \qquad \left[\frac{2(\Omega_{gl}-\omega)}{\gamma_{gl}^{2}} W\left(\frac{-(\Omega_{gl}-\omega)}{\gamma_{gl}}\right) + \frac{2i}{\sqrt{\pi}\gamma_{gl}} \right] + \\
& \left[W\left(\frac{-(\Omega_{gn}^{*}+\omega)}{\gamma_{gn}}\right) + W\left(\frac{-(\Omega_{gn}^{*}-\omega)}{\gamma_{gn}}\right) \right] \times \\
& \qquad \left[\frac{2(\Omega_{gl}^{*}+\omega)}{\gamma_{gl}^{2}} W\left(\frac{-(\Omega_{gl}^{*}+\omega)}{\gamma_{gl}}\right) + \frac{2i}{\sqrt{\pi}\gamma_{gl}} \right] + \\
& \frac{1}{2i\Gamma_{gn}} \left[W\left(\frac{-(\Omega_{gn}-\omega)}{\gamma_{gn}}\right) + W\left(\frac{-(\Omega_{gn}+\omega)}{\gamma_{gn}}\right) \right. \\
& \qquad \left. -W\left(\frac{-(\Omega_{gn}^{*}-\omega)}{\gamma_{gn}}\right) - W\left(\frac{-(\Omega_{gn}^{*}+\omega)}{\gamma_{gn}}\right) \right] \times \\
& \qquad \left[W\left(\frac{-(\Omega_{gl}-\omega)}{\gamma_{gl}}\right) + W\left(\frac{-(\Omega_{gl}^{*}+\omega)}{\gamma_{gl}}\right) \right] + \\
& \frac{1}{2(\omega+i\Gamma_{gn})} \left[W\left(\frac{-(\Omega_{gn}-\omega)}{\gamma_{gn}}\right) - W\left(\frac{-(\Omega_{gn}^{*}+\omega)}{\gamma_{gn}}\right) \right] \times \\
& \qquad \left[W\left(\frac{-(\Omega_{gl}+\omega)}{\gamma_{gl}}\right) + W\left(\frac{-(\Omega_{gl}^{*}-\omega)}{\gamma_{gl}}\right) \right] + \\
& \frac{1}{2\omega} \left[W\left(\frac{-(\Omega_{gn}-\omega)}{\gamma_{gn}}\right) \left\{ W\left(\frac{-(\Omega_{gl}-\omega)}{\gamma_{gl}}\right) - W\left(\frac{-(\Omega_{gl}+\omega)}{\gamma_{gl}}\right) \right\} + \right. \\
& \qquad \left. \left. W\left(\frac{-(\Omega_{gn}^{*}+\omega)}{\gamma_{gn}}\right) \left\{ W\left(\frac{-(\Omega_{gl}^{*}-\omega)}{\gamma_{gl}}\right) - W\left(\frac{-(\Omega_{gl}^{*}+\omega)}{\gamma_{gl}}\right) \right\} \right] \right\}. \qquad (2.88)
\end{aligned}
$$

The procedure used to determine Equation (2.88) is identical to the procedure used to determine Equation (2.56) in Section 2.4.2.2.1.

Now that both $D_{ll}^{IB}(-\omega;\omega,\omega,-\omega)$ and $D_{ln}^{IB}(-\omega;\omega,\omega,-\omega)$ have been derived, a limited n-level model can be constructed for $\xi^{(3)}(-\omega;\omega,\omega,-\omega)$ because we can only model one-photon interactions. To understand the contribution from $D_{ln}(-\omega;\omega,\omega,-\omega)$, we limit ourselves to two one-photon states for the intensity dependent refractive index experiment as follows,

$$\xi^{(3)}(-\omega;\omega,\omega,-\omega) = -\frac{1}{\epsilon_0 3!}\frac{1}{\hbar^3}\left\{|\mu_{g1}|^4 D_{11}(-\omega;\omega,\omega,-\omega) + |\mu_{g3}|^4 D_{33}(-\omega;\omega,\omega,-\omega) \right. \\ \left. +|\mu_{g1}|^2|\mu_{g3}|^2\left[D_{13}(-\omega;\omega,\omega,-\omega) + D_{31}(-\omega;\omega,\omega,-\omega)\right]\right\}. \quad (2.89)$$

The energy denominators for the Lorentzian theory are calculated using Equation (2.85) and the energy denominators for the inhomogeneous-broadening theory are calculated using Equations (2.86) and (2.88).

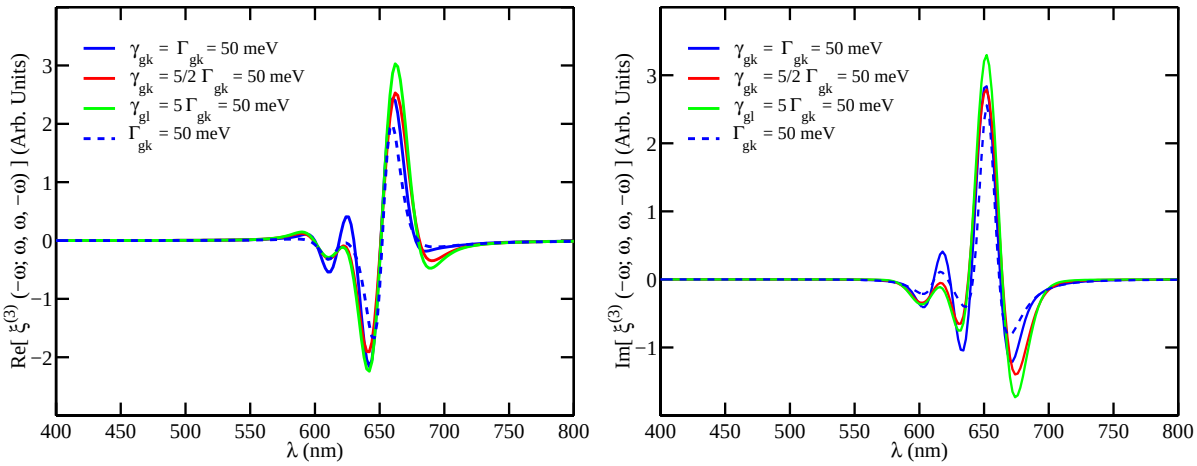

Fig. 2.22: Real and imaginary parts of $\xi^{(3)}(-\omega;\omega,\omega,-\omega)$ for two one-photon excited states centered about 653 nm and 614 nm. The solid lines represent the inhomogeneously broadened electronic transitions for three different values of Γ_{gk} where $k = \{1,3\}$ and the dashed line represents the homogeneously-broadened transitions.

Figure 2.22 shows the real and imaginary parts of Equation (2.89) when the two one-photon excited states are centered about 653 nm and 614 nm, and $|\mu_{g1}| = 2|\mu_{g3}|$. The dashed curves represent the Lorentzian response and the solid curves represent the inhomogeneously-broadened response for the three standard homogeneous linewidths ($\Gamma_{g1} = \Gamma_{g3} \in \{$ 10 meV, 20 meV, 50 meV $\}$).

When the second one-photon state is included in the third-order response there is a very localized change in the electronic response. The change occurs about 614 nm, where the new state is located, and does not effect the near IR response significantly. Therefore

we do not show the real and imaginary parts of the third-order susceptibility in the near IR but refer the reader back to the two-level response in Figure 2.21.

Two-photon Contributions At this point, we have developed an inhomogeneous-broadening theory for the intensity dependent refractive index experiment that can account for any number of one-photon excited states in an inhomogeneous system. To model two-photon interactions for the intensity dependent refractive index experiment, we need to transform the following Lorentzian energy denominator,

$$\begin{aligned} D_{lmn}(-\omega_\sigma;\omega,\omega,-\omega) \quad &= \mathbf{S}_{1,2,3}\,\Big\{\big[(\Omega_{lg}-\omega)(\Omega_{mg}-\omega-\omega)(\Omega_{ng}-\omega)\big]^{-1} + \\ &\quad \big[(\Omega^*_{lg}-\omega)(\Omega_{mg}-\omega-\omega)(\Omega_{ng}-\omega)\big]^{-1} + \\ &\quad \big[(\Omega^*_{lg}+\omega)(\Omega^*_{mg}+\omega+\omega)(\Omega_{ng}+\omega)\big]^{-1} + \\ &\quad \big[(\Omega^*_{lg}+\omega)(\Omega^*_{mg}+\omega+\omega)(\Omega^*_{ng}+\omega)\big]^{-1}\Big\}, \end{aligned} \tag{2.90}$$

where $\mathbf{S}_{1,2,3}$ represents the intrinsic permutation operator. Like the electrooptic experiment, there are three distinct permutations of the input frequencies, which implies that Equation (2.90) has twelve terms after the intrinsic permutation operation is performed.

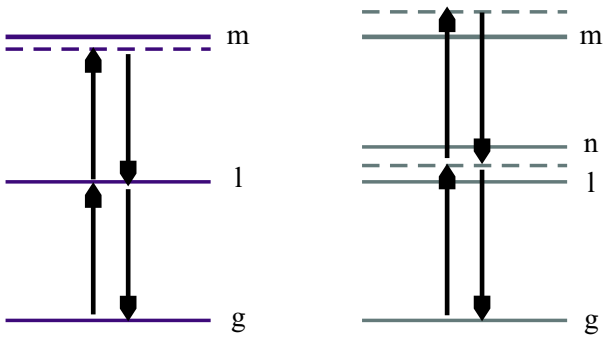

Fig. 2.23: Energy level diagrams for $D_{lml}(-\omega;\omega,\omega,-\omega)$ and $D_{lmn}(-\omega;\omega,\omega,-\omega)$, respectively. Each arrow represents a one-photon transition in the specified direction.

As we have seen in previous third-order experiments, there are two specific cases ($n = l$ and $n \neq l$) of Equation (2.90) that need to be transformed to the inhomogeneous-broadening theory so that a general n-level model can be constructed for $\xi^{(3)}(-\omega;\omega,\omega,-\omega)$. Figure 2.23 shows the resonant enhancements for a system that has one one-photon and one two-photon excited state ($l = n$), and a system that has two one-photon excited states and one two-photon excited state ($l \neq n$). A two-photon state is determined by symmetry considerations. For an electronic transition to occur the

two states involved must have opposite parity. Thus a one-photon transition occurs between states that are odd-even or even-odd in terms of parity. However, for a two-photon transition to occur there must be a real or virtual transition in between the ground and two-photon state because they both have the same parity. Thus it takes two photons to reach a two-photon excited state.

In Figure 2.23, the solid horizontal lines represent real states and the dashed horizontal lines represent virtual states as discussed in Section 2.4.2.2.1. Because the two-photon state can only be reached through a two-photon process a large resonant enhancement occurs when the two-photon transition energy is double the incident photon energy. This is clearly represented in the energy denominators by the arguments $(\Omega_{gm} - 2\omega)$.

After performing the partial fraction expansions on Equation (2.90), when $n = l$, the result of the inhomogeneous-broadening transform of $D^{L}_{lml}(-\omega;\omega,\omega,-\omega)$ is:

$$
\begin{aligned}
D^{IB}_{lml}(-\omega;\omega,\omega,-\omega) = {} & \frac{-\pi}{\gamma_{gl}\gamma_{gm}} \\
& \left\{ \left[W\left(\frac{-(\Omega_{gm}-2\omega)}{\gamma_{gm}}\right) + W\left(\frac{-\Omega_{gm}}{\gamma_{gm}}\right) \right] \left[\frac{2(\Omega_{gl}-\omega)}{\gamma_{gl}^2} W\left(\frac{-(\Omega_{gl}-\omega)}{\gamma_{gl}}\right) + \frac{2i}{\sqrt{\pi}\gamma_{gl}} \right] + \right. \\
& \left[W\left(\frac{-(\Omega^*_{gm}+2\omega)}{\gamma_{gm}}\right) + W\left(\frac{-\Omega^*_{gm}}{\gamma_{gm}}\right) \right] \left[\frac{2(\Omega^*_{gl}+\omega)}{\gamma_{gl}^2} W\left(\frac{-(\Omega^*_{gl}+\omega)}{\gamma_{gl}}\right) + \frac{2i}{\sqrt{\pi}\gamma_{gl}} \right] + \\
& \frac{1}{2i\Gamma_{gl}} \left[\left\{ W\left(\frac{-(\Omega_{gm}-2\omega)}{\gamma_{gm}}\right) + W\left(\frac{-\Omega^*_{gm}}{\gamma_{gm}}\right) \right\} \times \right. \\
& \qquad \left\{ W\left(\frac{-(\Omega_{gl}-\omega)}{\gamma_{gl}}\right) - W\left(\frac{-(\Omega^*_{gl}-\omega)}{\gamma_{gl}}\right) \right\} + \\
& \qquad \left\{ W\left(\frac{-(\Omega^*_{gm}+2\omega)}{\gamma_{gm}}\right) + W\left(\frac{-\Omega_{gm}}{\gamma_{gm}}\right) \right\} \times \\
& \qquad\qquad \left. \left\{ W\left(\frac{-(\Omega_{gl}+\omega)}{\gamma_{gl}}\right) - W\left(\frac{-(\Omega^*_{gl}+\omega)}{\gamma_{gl}}\right) \right\} \right] + \\
& \frac{1}{2(\omega+i\Gamma_{gl})} \left[W\left(\frac{-\Omega_{gm}}{\gamma_{gm}}\right) + W\left(\frac{-\Omega^*_{gm}}{\gamma_{gm}}\right) \right] \times \\
& \qquad \left[W\left(\frac{-(\Omega_{gl}-\omega)}{\gamma_{gl}}\right) - W\left(\frac{-(\Omega^*_{gl}+\omega)}{\gamma_{gl}}\right) \right] + \\
& \frac{1}{2\omega} \left[W\left(\frac{-\Omega_{gm}}{\gamma_{gm}}\right) \left\{ W\left(\frac{-(\Omega_{gl}-\omega)}{\gamma_{gl}}\right) - W\left(\frac{-(\Omega_{gl}+\omega)}{\gamma_{gl}}\right) \right\} + \right. \\
& \qquad \left. \left. W\left(\frac{-\Omega^*_{gm}}{\gamma_{gm}}\right) \left\{ W\left(\frac{-(\Omega^*_{gl}-\omega)}{\gamma_{gl}}\right) - W\left(\frac{-(\Omega^*_{gl}+\omega)}{\gamma_{gl}}\right) \right\} \right] \right\}. \qquad (2.91)
\end{aligned}
$$

A third-order molecular response in the three-level limit, when there is one one-photon excited state and one two-photon excited state, can now be written for the inhomogeneous-broadening theory of the intensity dependent refractive index experiment. Equation (2.84) can be reduced to the following, for the aforementioned model,

$$\xi^{(3)}(-\omega;\omega,\omega,-\omega) = \frac{1}{\epsilon_0 3!}\frac{1}{\hbar^3}\left\{|\mu_{g1}|^2|\mu_{12}|^2 D_{121}(-\omega;\omega,\omega,-\omega) - |\mu_{g1}|^4 D_{11}(-\omega;\omega,\omega,-\omega)\right\}. \quad (2.92)$$

The energy denominators are given by Equations (2.85) and (2.90) for the Lorentzian theory and by Equations (2.86) and (2.91) for the inhomogeneous-broadening theory.

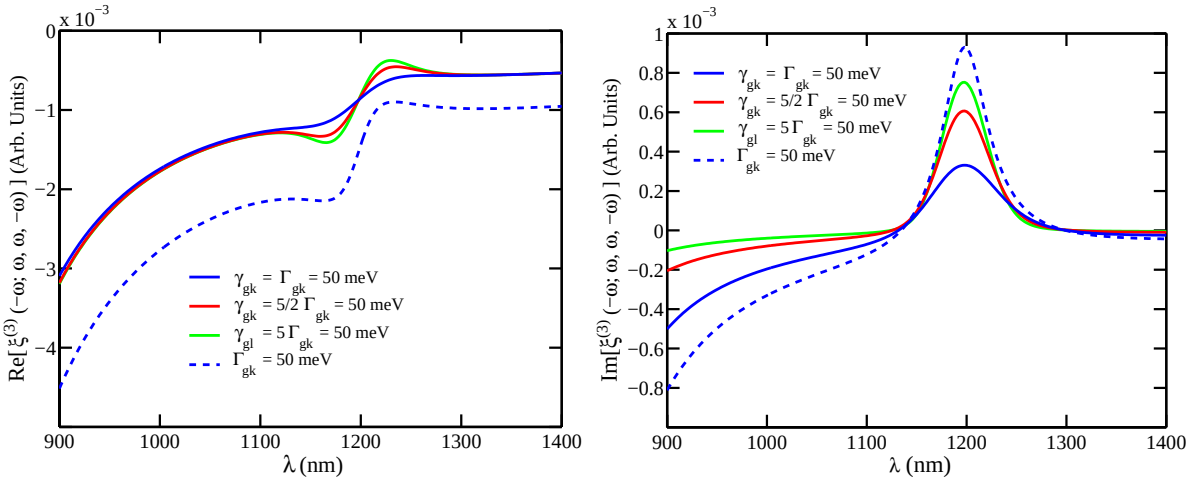

Fig. 2.24: Real and imaginary parts of $\xi^{(3)}(-\omega;\omega,\omega,-\omega)$ for one one-photon excited state and one two-photon state centered about 653 nm and 600 nm, respectively. The solid lines represent the inhomogeneously broadened electronic transitions for three different values of Γ_{gk} where $k \in \{1,2\}$ and the dashed line represents the homogeneously-broadened transitions.

Figure 2.24 represents the real and imaginary parts of Equation (2.92), in the near IR, when the one-photon state is centered about 653 nm, and the two-photon state is centered about 600 nm ($|\mu_{g1}| = 4|\mu_{12}|$). We see that there is a significant change in the off-resonant response, in comparison to the two-level model, centered about half the transition energy of the two-photon state. There is not a significant change in the visible region so we refer the reader back to Figure 2.20.

As in Figure 2.21, the Lorentzian theory predicts a larger response in the near IR than all three cases of the inhomogeneous-broadening theory, which is opposite to the visible region. Because each theory predicts very distinct responses for all regions of the electromagnetic spectrum, it should be straight forward to determine, from well resolved spectroscopic data, which theory models the system of interest more accurately.

Equation (2.90) , when $n \neq l$, must be transformed to the inhomogeneous-broadening theory so a general n-level model can be constructed for the intensity dependent refractive index experiment. Since there are three independent excited states involved in the response, a partial fraction expansion is unnecessary. However, Equation (2.90) must be expanded using the intrinsic permutation operator before the inhomogeneous-broadening terms from Table 2.1 can replace the Lorentzian. The expanded version of Equation (2.90) will not add to this discussion so the expansion has been left to the reader, and the final result of the inhomogeneous-broadening transform of Equation (2.90), when $n \neq l$, is the following,

$$
\begin{aligned}
D^{IB}_{lmn}(-\omega;\omega,\omega,-\omega) = \frac{-i\pi^{3/2}}{\gamma_{gl}\gamma_{gm}\gamma_{gn}}\Bigg\{ & \\
& W\left(\frac{-\Omega_{gm}}{\gamma_{gm}}\right)\left[W\left(\frac{-(\Omega_{gn}-\omega)}{\gamma_{gn}}\right)+W\left(\frac{-(\Omega_{gn}+\omega)}{\gamma_{gn}}\right)\right]\times \\
& \quad \left[W\left(\frac{-(\Omega_{gl}-\omega)}{\gamma_{gl}}\right)+W\left(\frac{-(\Omega^*_{gl}+\omega)}{\gamma_{gl}}\right)\right]+ \\
& W\left(\frac{-\Omega^*_{gm}}{\gamma_{gm}}\right)\left[W\left(\frac{-(\Omega_{gn}-\omega)}{\gamma_{gn}}\right)+W\left(\frac{-(\Omega^*_{gn}+\omega)}{\gamma_{gn}}\right)\right]\times \\
& \quad \left[W\left(\frac{-(\Omega^*_{gl}+\omega)}{\gamma_{gl}}\right)+W\left(\frac{-(\Omega^*_{gl}-\omega)}{\gamma_{gl}}\right)\right]+ \\
& W\left(\frac{-(\Omega_{gm}-2\omega)}{\gamma_{gm}}\right)W\left(\frac{-(\Omega_{gn}-\omega)}{\gamma_{gn}}\right)\times \\
& \quad \left[W\left(\frac{-(\Omega_{gl}-\omega)}{\gamma_{gl}}\right)+W\left(\frac{-(\Omega^*_{gl}-\omega)}{\gamma_{gl}}\right)\right]+ \\
& W\left(\frac{-(\Omega^*_{gm}+2\omega)}{\gamma_{gm}}\right)W\left(\frac{-(\Omega^*_{gl}+\omega)}{\gamma_{gl}}\right)\times \\
& \quad \left[W\left(\frac{-(\Omega_{gn}+\omega)}{\gamma_{gn}}\right)+W\left(\frac{-(\Omega^*_{gn}+\omega)}{\gamma_{gn}}\right)\right]\Bigg\}. \qquad (2.93)
\end{aligned}
$$

A four-level model for the third-order molecular susceptibility, that uses all the energy denominators derived in this section, can be written as follows,

$$\begin{aligned}\xi^{(3)}(-\omega;\omega,\omega,-\omega) = \frac{1}{\epsilon_0 3!}\frac{1}{\hbar^3}\times \\ \Big\{|\mu_{g1}|^2|\mu_{12}|^2 D_{121}(-\omega;\omega,\omega,-\omega) + |\mu_{g3}|^2|\mu_{32}|^2 D_{323}(-\omega;\omega,\omega,-\omega) \\ +\mu_{g1}\mu_{12}\mu_{32}\mu_{g3}\left[D_{123}(-\omega;\omega,\omega,-\omega) + D_{321}(-\omega;\omega,\omega,-\omega)\right] \\ -|\mu_{g1}|^4 D_{11}(-\omega;\omega,\omega,-\omega) - |\mu_{g3}|^4 D_{33}(-\omega;\omega,\omega,-\omega) \\ -|\mu_{g1}|^2|\mu_{g3}|^2\left[D_{13}(-\omega;\omega,\omega,-\omega) + D_{31}(-\omega;\omega,\omega,-\omega)\right] \Big\}. \end{aligned} \quad (2.94)$$

The four-level model for the third-order molecular susceptibility, Equation (2.94), involves two one-photon excited states (653 nm and 614 nm) and one two-photon excited state (600 nm) even though there are eight energy denominator contributions. The transition moments are related as follows,

$$|\mu_{g1}| = 2|\mu_{g3}| = 4|\mu_{12}| = 4|\mu_{23}|. \quad (2.95)$$

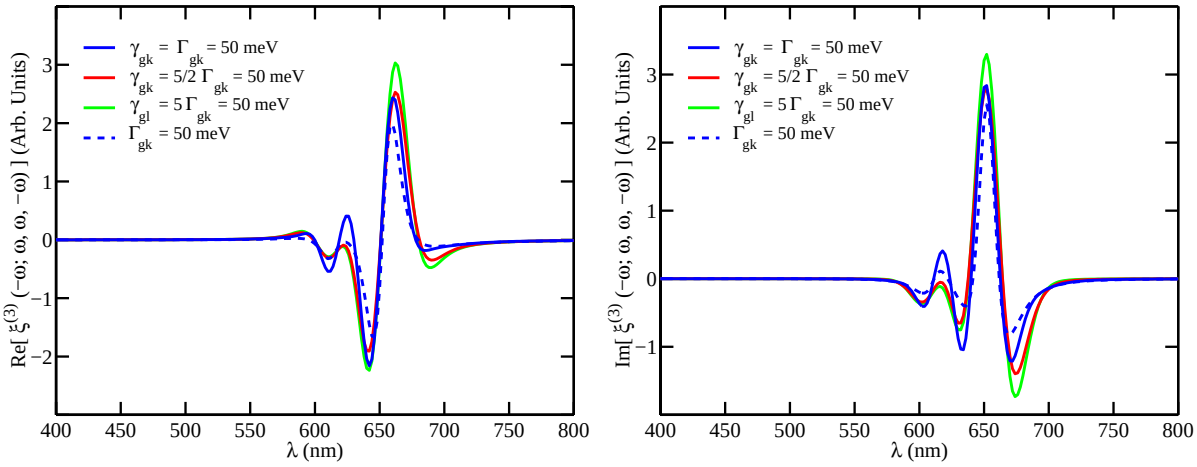

Fig. 2.25: Real and imaginary parts of $\xi^{(3)}(-\omega;\omega,\omega,-\omega)$ for two one-photon excited states centered about 653 nm and 614 nm, and one two-photon state centered about 600 nm. The solid lines represent the inhomogeneously-broadened electronic transitions for three different values of Γ_{gk}, where $k \in \{1,2,3\}$, and the dashed lines represent the homogeneously-broadened transitions when n and $l \in \{1,3\}$, and $m = 2$.

With the transition moments in the ratio specified in Equation (2.95), Figure 2.25 represents the real and imaginary parts of Equation (2.94). The four-level response is very similar to the addition of the two three-level models. In other words, the mixing terms do not contribute significantly to the overall response. This is very different from four-level model of the third-order response for the quadratic electrooptic experiment, where there was a large contribution from the mixing terms.

The four derivations performed in this section enable us to construct a general n-level inhomogeneous-broadening model of the third-order molecular susceptibility for the intensity dependent index of refraction experiment. In the following section we complete the discussion of the optical Kerr effect by deriving the four inhomogeneous-broadening denominators which contribute to the general n-level model of the third-order molecular susceptibility for the pump-probe experiment.

Pump-Probe The pump-probe experiment has numerous applications from intensity dependent optical switching to probing ultra-fast chemical reactions. For the homogeneous-broadening theory, the n-level model of the third-order molecular susceptibility, is the following,

$$\xi^{(3)}(-\omega_1;\omega_1,\omega_2,-\omega_2) = \frac{1}{\epsilon_0 3!}\frac{1}{\hbar^3}\left\{\sum_{l,m,n}{}' D^L_{lmn}(-\omega_1;\omega_1,\omega_2,-\omega_2)\mu_{gl}\mu_{lm}\mu_{mn}\mu_{ng} - \sum_{l,n}{}' D^L_{ln}(-\omega_1;\omega_1,\omega_2,-\omega_2)|\mu_{gl}|^2|\mu_{gn}|^2\right\}, \quad (2.96)$$

where ω_2 is the frequency of the high intensity pump, ω_1 is the frequency of the low intensity probe, and we have assumed that μ_{gl}=μ_{lg}, and μ_{gn}=μ_{ng}. The Lorentzian energy denominators can be specified from Equations (2.28) and (2.29):

$$\begin{aligned} D_{ln}(-\omega_1;\omega_1,\omega_2,-\omega_2) \;= \mathbf{S}_{1,2,3}\; \{&[(\Omega_{lg}-\omega_1)(\Omega_{lg}+\omega_2)(\Omega_{ng}-\omega_1)]^{-1} + \\ &\left[(\Omega_{lg}+\omega_2)(\Omega^*_{ng}+\omega_2)(\Omega_{ng}-\omega_1)\right]^{-1} + \\ &\left[(\Omega^*_{lg}+\omega_1)(\Omega^*_{lg}-\omega_2)(\Omega^*_{ng}+\omega_1)\right]^{-1} + \\ &\left[(\Omega^*_{lg}-\omega_2)(\Omega_{ng}-\omega_2)(\Omega^*_{ng}+\omega_1)\right]^{-1}\Big\}, \end{aligned} \quad (2.97)$$

and,

$$D_{lmn}(-\omega_1;\omega_1,\omega_2,-\omega_2) = \mathbf{S}_{1,2,3}\left\{[(\Omega_{lg}-\omega_1)(\Omega_{mg}-\omega_1-\omega_2)(\Omega_{ng}-\omega_1)]^{-1}\right.$$
$$+\left[(\Omega_{lg}^*-\omega_2)(\Omega_{mg}-\omega_1-\omega_2)(\Omega_{ng}-\omega_1)\right]^{-1}$$
$$+\left[(\Omega_{lg}^*+\omega_1)(\Omega_{mg}^*+\omega_1+\omega_2)(\Omega_{ng}+\omega_2)\right]^{-1}$$
$$\left.+\left[(\Omega_{lg}^*+\omega_1)(\Omega_{mg}^*+\omega_1+\omega_2)(\Omega_{ng}^*+\omega_1)\right]^{-1}\right\}, \quad (2.98)$$

respectively.

One-photon contributions As in the previous third-order derivations we begin by transforming the simplest, one-photon energy denominator (when $n = l$). The Lorentzian denominator, $D_{ll}^L(-\omega_1;\omega_1,\omega_2,-\omega_2)$ can be expanded using $\mathbf{S}$ to get:

$$D_{ll}^L(-\omega_1;\omega_1,\omega_2,-\omega_2) = 2\left\{\left[\frac{1}{\Omega_{gl}-\omega_1}+\frac{1}{\Omega_{gl}^*+\omega_1}\right]\times\left[\frac{1}{\Omega_{gl}-\omega_2}+\frac{1}{\Omega_{gl}^*+\omega_2}\right]\right.$$
$$\times\left[\frac{1}{\Omega_{gl}+\omega_2}+\frac{1}{\Omega_{gl}^*-\omega_2}\right]$$
$$+\frac{1}{(\Omega_{gl}-\omega_1)^2}\left[\frac{1}{\Omega_{gl}+\omega_2}+\frac{1}{\Omega_{gl}-\omega_2}\right]$$
$$\left.+\frac{1}{(\Omega_{gl}^*+\omega_1)^2}\left[\frac{1}{\Omega_{gl}^*-\omega_2}+\frac{1}{\Omega_{gl}^*+\omega_2}\right]\right\}, \quad (2.99)$$

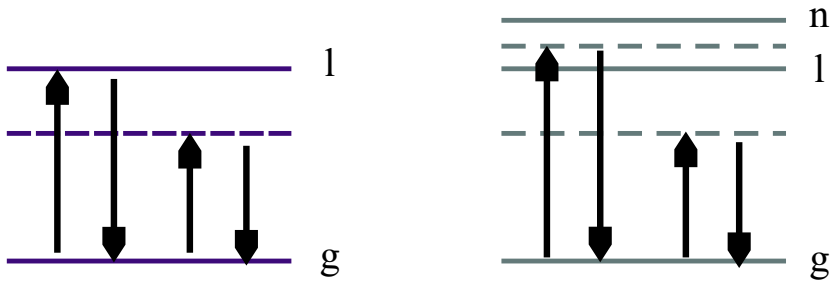

Fig. 2.26: Resonant enhancements due to $D_{ll}(-\omega_1;\omega_1,\omega_2,-\omega_2)$ and $D_{ln}(-\omega_1;\omega_1,\omega_2,-\omega_2)$, respectively. Each arrow represents a one-photon transition in the specified direction, solid horizontal lines represent real excited states, and dashed lines represent virtual excited states.

Figure 2.26 shows a pictorial version the resonant enhancements for the energy denominators, $D_{ll}(-\omega_1;\omega_1,\omega_2,-\omega_2)$ and $D_{ln}(-\omega_1;\omega_1,\omega_2,-\omega_2)$, respectively. The solid horizontal lines represent real excited states, and dashed lines represent virtual excited states.

When only one excited state is involved in the third-order response there is a resonant enhancement if the probe photon frequency, ω_1 is similar to the transition frequency.

An additional resonant enhancement can occur when there is a second one-photon excited state involved in electronic response. It occurs when the probe photon frequency is similar to the transitions frequencies of both the excited states so that both excited states contribute to the response. Notice that there are there two probe photons, ω_1, and two pump photons, ω_2, involved in the third-order enhancement which is similar to the quadratic electrooptic experiment except the pump photons are now at optical frequencies.

The partial fraction expansion of Equation (2.99) is very ugly so we relegate it to Appendix A. Once the partial fraction expansion of Equation (2.99) has been completed, each Lorentzian term can be replaced with the appropriate inhomogeneous-broadening terms from Table 2.2. We neglect the details and show the final version of the inhomogeneous-broadening transform, when $n = l$, as:

$$
\begin{aligned}
D_{ll}^{IB}(-\omega_1;\omega_1,\omega_2,-\omega_2) = \frac{2i\sqrt{\pi}}{\gamma_{gl}}\times \\
\Bigg\{ & \frac{2\,\omega_1}{(\omega_1+\omega_2)(\omega_1-\omega_2)} \\
& \qquad \times \left[\frac{2(\Omega_{gl}-\omega_1)}{\gamma_{gl}^2} W\left(\frac{-(\Omega_{gl}-\omega_1)}{\gamma_{gl}}\right) - \frac{2(\Omega_{gl}^*+\omega_1)}{\gamma_{gl}^2} W\left(\frac{-(\Omega_{gl}^*+\omega_1)}{\gamma_{gl}}\right) \right] \\
& + \frac{2(\omega_1^4 - 2\,\omega_1^2\,\omega_2^2 + \omega_2^4 + 2i\Gamma_{gl}^2\omega_1^2 + 6\Gamma_{gl}^2\omega_2^2 - 8i\Gamma_{gl}\omega_1\omega_2^2)}{(\omega_1+\omega_2)^2(\omega_1-\omega_2)^2(\omega_1+\omega_2+2i\Gamma_{gl})(\omega_1-\omega_2+2i\Gamma_{gl})} \\
& \qquad \times \left[W\left(\frac{-(\Omega_{gl}-\omega_1)}{\gamma_{gl}}\right) + W\left(\frac{-(\Omega_{gl}^*+\omega_1)}{\gamma_{gl}}\right) \right] \\
& + \frac{(\omega_2^3 - \omega_1\omega_2^2 + 3i\Gamma_{gl}\omega_2^2 - i\Gamma_{gl}\omega_1\omega_2 - 3\Gamma_{gl}^2\omega_2 + \Gamma_{gl}^2\omega_1)}{i\Gamma_{gl}\omega_2(\omega_1-\omega_2)^2(\omega_1+\omega_2+2i\Gamma_{gl})} \\
& \qquad \times \left[W\left(\frac{-(\Omega_{gl}-\omega_2)}{\gamma_{gl}}\right) + W\left(\frac{-(\Omega_{gl}^*+\omega_2)}{\gamma_{gl}}\right) \right] \\
& + \frac{(\omega_2^3 + \omega_1\omega_2^2 - 3i\Gamma_{gl}\omega_2^2 - i\Gamma_{gl}\omega_1\omega_2 - 3\Gamma_{gl}^2\omega_2 - \Gamma_{gl}^2\omega_1)}{i\Gamma_{gl}\omega_2(\omega_1+\omega_2)^2(\omega_1-\omega_2+2i\Gamma_{gl})} \\
& \qquad \times \left[W\left(\frac{-(\Omega_{gl}+\omega_2)}{\gamma_{gl}}\right) + W\left(\frac{-(\Omega_{gl}^*-\omega_2)}{\gamma_{gl}}\right) \right] \Bigg\}. \qquad (2.100)
\end{aligned}
$$

An extreme amount of effort was needed to reduce Equation (2.100) to four terms, which is same number as the original contracted version Lorentzian denominator. How-

ever, the coefficients describing each term are so complicated that it is difficult to discern possible trends. Therefore we will not expend the effort to compress the IB results for the three remaining terms.

The development of $D_{ll}^{IB}(-\omega_1;\omega_1,\omega_2,-\omega_2)$ allows us to construct a two-level model for $\xi^{(3)}(-\omega_1;\omega_1,\omega_2,-\omega_2)$ using both the inhomogeneous-broadening and homogeneous-broadening theories. Equation (2.96) reduces to the following for a two-level model of the pump-probe experiment,

$$\xi^{(3)}(-\omega_1;\omega_1,\omega_2,-\omega_2) \;=\; -\frac{1}{\epsilon_0 3!}\frac{1}{\hbar^3}\left\{|\mu_{g1}|^4 D_{11}(-\omega_1;\omega_1,\omega_2,-\omega_2)\right\}. \qquad (2.101)$$

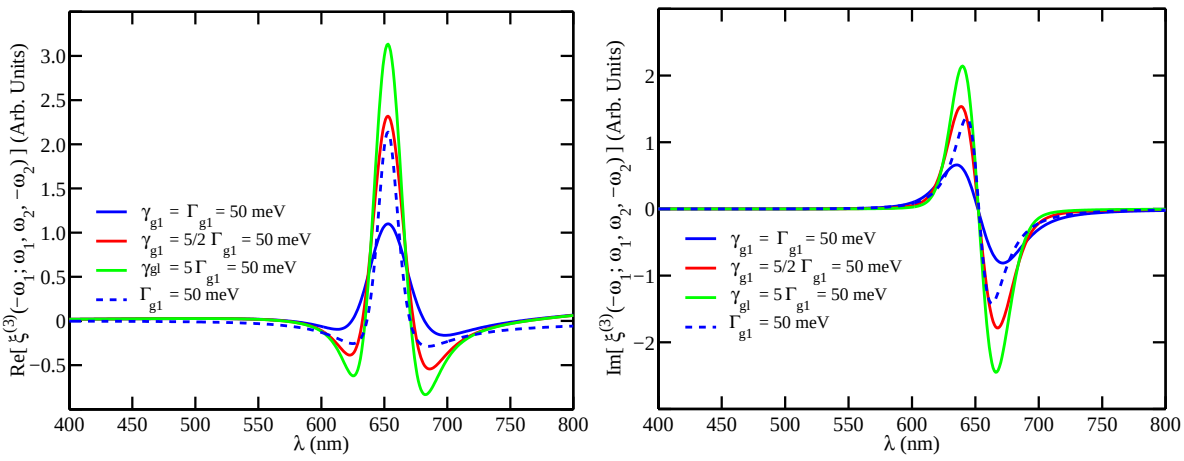

Fig. 2.27: Real and imaginary parts of $\xi^{(3)}(-\omega_1;\omega,\omega_2,-\omega_2)$ for a single excited state centered about 653 nm. The solid lines represent the inhomogeneously broadened electronic transitions for three different values of Γ_{g1} and the dashed line represents the homogeneously-broadened transitions when $n = l = 1$.

Figure 2.27 represents the real and imaginary parts of Equation (2.101) when the one-photon excited state is located at 653 nm, and the pump wavelength is 1064 nm. The pump wavelength will be fixed at 1064 nm for the remainder of this section, and we will continue to observe the third-order response due to a probe wavelength in the visible.

It should be noted that both the real and imaginary parts of the third-order pump-probe response are very similar to the third-order quadratic electrooptic response in the

two-level limit. There are slight differences in that the Lorentzian theory predicts the largest response for the quadratic electrooptic experiment (see Figure 2.11) but two of the three specifications of the inhomogeneous-broadening theory have a larger response for the pump-probe experiment. However, the general shapes are the same. This will not be the case when a two-photon state is modeled, but first we must derive the second one-photon energy denominator so that we can model any number of one-photon states.

Using the established procedure (see Section 2.4.2.2.1), the second one-photon contribution, Equation (2.97) when $n \neq l$, to the third-order molecular susceptibility can be transformed to the following inhomogeneous-broadening energy denominator:

$$
\begin{aligned}
D_{ln}^{IB}(-\omega_1;\omega_1,\omega_2,-\omega_2) = {} & \frac{-\pi}{\gamma_{gl}\gamma_{gn}}\times \\
& \left\{ \left[\frac{2(\Omega_{gl}-\omega_1)}{\gamma_{gl}^2} W\left(\frac{-(\Omega_{gl}-\omega_1)}{\gamma_{gl}}\right) + \frac{2i}{\sqrt{\pi}\gamma_{gl}} \right] \right. \\
& \qquad \left. \times \left[W\left(\frac{-(\Omega_{gn}-\omega_2)}{\gamma_{gn}}\right) + W\left(\frac{-(\Omega_{gn}+\omega_2)}{\gamma_{gn}}\right) \right] + \right. \\
& \left[\frac{2(\Omega_{gl}^*+\omega_1)}{\gamma_{gl}^2} W\left(\frac{-(\Omega_{gl}^*+\omega_1)}{\gamma_{gl}}\right) + \frac{2i}{\sqrt{\pi}\gamma_{gl}} \right] \\
& \qquad \times \left[W\left(\frac{-(\Omega_{gn}^*+\omega_2)}{\gamma_{gn}}\right) + W\left(\frac{-(\Omega_{gn}^*-\omega_2)}{\gamma_{gn}}\right) \right] + \\
& \frac{1}{\omega_1-\omega_2+2i\Gamma_{gn}} \left[W\left(\frac{-(\Omega_{gl}-\omega_2)}{\gamma_{gl}}\right) + W\left(\frac{-(\Omega_{gl}^*+\omega_2)}{\gamma_{gl}}\right) \right] \times \\
& \qquad \left[W\left(\frac{-(\Omega_{gn}-\omega_1)}{\gamma_{gn}}\right) + W\left(\frac{-(\Omega_{gn}+\omega_2)}{\gamma_{gn}}\right) \right. \\
& \qquad \left. -W\left(\frac{-(\Omega_{gn}^*-\omega_2)}{\gamma_{gn}}\right) - W\left(\frac{-(\Omega_{gn}^*+\omega_1)}{\gamma_{gn}}\right) \right] + \\
& \frac{1}{\omega_1+\omega_2+2i\Gamma_{gn}} \left[W\left(\frac{-(\Omega_{gl}+\omega_2)}{\gamma_{gl}}\right) + W\left(\frac{-(\Omega_{gl}^*-\omega_2)}{\gamma_{gl}}\right) \right] \times \\
& \qquad \left[W\left(\frac{-(\Omega_{gn}-\omega_2)}{\gamma_{gn}}\right) + W\left(\frac{-(\Omega_{gn}-\omega_1)}{\gamma_{gn}}\right) \right. \\
& \qquad \left. -W\left(\frac{-(\Omega_{gn}^*+\omega_2)}{\gamma_{gn}}\right) - W\left(\frac{-(\Omega_{gn}^*+\omega_1)}{\gamma_{gn}}\right) \right] + \\
& \frac{1}{2i\Gamma_{gn}} \left[W\left(\frac{-(\Omega_{gl}-\omega_1)}{\gamma_{gl}}\right) + W\left(\frac{-(\Omega_{gl}^*+\omega_1)}{\gamma_{gl}}\right) \right] \times \\
& \qquad \left[W\left(\frac{-(\Omega_{gn}+\omega_2)}{\gamma_{gn}}\right) + W\left(\frac{-(\Omega_{gn}-\omega_2)}{\gamma_{gn}}\right) \right.
\end{aligned}
$$

$$
\begin{aligned}
&-W\left(\frac{-(\Omega_{gn}^{*}-\omega_2)}{\gamma_{gn}}\right)-W\left(\frac{-(\Omega_{gn}^{*}+\omega_2)}{\gamma_{gn}}\right)\Bigg]+\\
&\frac{1}{\omega_1-\omega_2}\Bigg\{\Bigg[W\left(\frac{-(\Omega_{gl}-\omega_1)}{\gamma_{gl}}\right)-W\left(\frac{-(\Omega_{gl}-\omega_2)}{\gamma_{gl}}\right)\Bigg]\\
&\qquad\times\Bigg[W\left(\frac{-(\Omega_{gn}-\omega_1)}{\gamma_{gn}}\right)+W\left(\frac{-(\Omega_{gn}+\omega_2)}{\gamma_{gn}}\right)\Bigg]+\\
&\quad\Bigg[W\left(\frac{-(\Omega_{gl}^{*}+\omega_2)}{\gamma_{gl}}\right)-W\left(\frac{-(\Omega_{gl}^{*}+\omega_1)}{\gamma_{gl}}\right)\Bigg]\\
&\qquad\times\Bigg[W\left(\frac{-(\Omega_{gn}^{*}+\omega_1)}{\gamma_{gn}}\right)+W\left(\frac{-(\Omega_{gn}^{*}-\omega_2)}{\gamma_{gn}}\right)\Bigg]\Bigg\}+\\
&\frac{1}{\omega_1+\omega_2}\Bigg\{\Bigg[W\left(\frac{-(\Omega_{gl}-\omega_1)}{\gamma_{gl}}\right)-W\left(\frac{-(\Omega_{gl}+\omega_2)}{\gamma_{gl}}\right)\Bigg]\\
&\qquad\times\Bigg[W\left(\frac{-(\Omega_{gn}-\omega_1)}{\gamma_{gn}}\right)+W\left(\frac{-(\Omega_{gn}-\omega_2)}{\gamma_{gn}}\right)\Bigg]+\\
&\quad\Bigg[W\left(\frac{-(\Omega_{gl}^{*}-\omega_2)}{\gamma_{gl}}\right)-W\left(\frac{-(\Omega_{gl}^{*}+\omega_1)}{\gamma_{gl}}\right)\Bigg]\\
&\qquad\times\Bigg[W\left(\frac{-(\Omega_{gn}^{*}+\omega_1)}{\gamma_{gn}}\right)-W\left(\frac{-(\Omega_{gn}^{*}+\omega_2)}{\gamma_{gn}}\right)\Bigg]\Bigg\}\Bigg\}. \qquad (2.102)
\end{aligned}
$$

Equation (2.102) is a stark contrast to Equation (2.100), because we did not work through the algebra to reduce it to four terms. However, it allows us to construct a three-level inhomogeneous-broadening model for the third-order molecular susceptibility.

For the pump-probe experiment, $\xi^{(3)}(-\omega_1;\omega_1,\omega_2,-\omega_2)$, with two one-photon excited states, is generally written as,

$$
\begin{aligned}
\xi^{(3)}(-\omega_1;\omega_1,\omega_2,-\omega_2) = -\frac{1}{\epsilon_0 3!}\frac{1}{\hbar^3}\Big\{&|\mu_{g1}|^4 D_{11}(-\omega_1;\omega_1,\omega_2,-\omega_2)\\
&+|\mu_{g3}|^4 D_{33}(-\omega_1;\omega_1,\omega_2,-\omega_2)\\
&+|\mu_{g1}|^2|\mu_{g3}|^2\left[D_{13}(-\omega_1;\omega_1,\omega_2,-\omega_2)\right.\\
&\left.+D_{31}(-\omega_1;\omega_1,\omega_2,-\omega_2)\right]\Big\}, \qquad (2.103)
\end{aligned}
$$

where the energy denominators for the Lorentzian theory are calculated using Equation (2.97) and the energy denominators for the inhomogeneous-broadening theory are calculated using Equations (2.100) and (2.102).

Figure 2.28 shows the real and imaginary parts of Equation (2.103) for both the homogeneous-broadening model (dashed lines) and three specifications of the inhomogeneous-broadening model (solid lines) when the first one-photon state is located

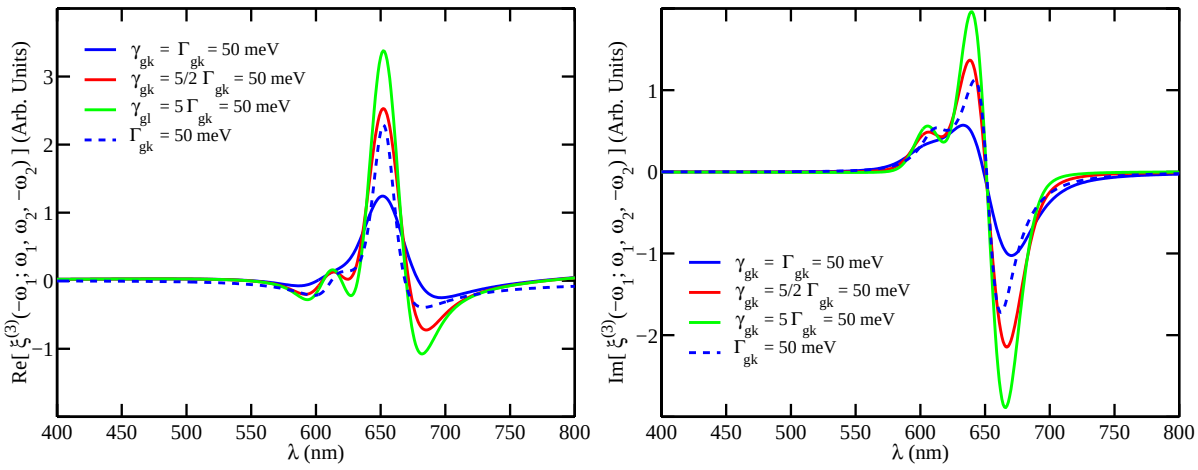

Fig. 2.28: Real and imaginary parts of $\xi^{(3)}(-\omega_1;\omega_1,\omega_2,-\omega_2)$ for two one-photon excited states centered about 653 nm and 614 nm. The solid lines represent the inhomogeneously broadened electronic transitions for three different values of Γ_{gk} where $k = \{1,3\}$ and the dashed line represents the homogeneously-broadened transitions.

at 653 nm, and the second one-photon state is located at 614 nm. Note that $|\mu_{g1}| = 2|\mu_{g3}|$. As in the quadratic electrooptic experiment, the addition of a one-photon state at 614 nm changes the third-order response in the entire region between the two one-photon states. This suggests that the mixing terms play a more significant role than in the intensity dependent refractive index experiment.

Two-photon contributions The two derivations for one-photon contributions to the third-order molecular susceptibility have been completed. They allow us to model third-order electronic responses for any number of one-photon excited states in the pump-probe experiment. However, we need to buckle down and complete the two derivations for the two-photon contributions to the third-order molecular susceptibility in order to model any number of arbitrary excited states. As in the derivations for the previous three experiments, we begin by transforming $D^{L}_{lml}(-\omega_1;\omega_1,\omega_2,-\omega_2)$ to $D^{IB}_{lml}(-\omega_1;\omega_1,\omega_2,-\omega_2)$. Once that transformation is complete we finish this section by deriving $D^{IB}_{lmn}(-\omega_1;\omega_1,\omega_2,-\omega_2)$.

Figure 2.29 shows the resonant enhancements for $D_{lml}(-\omega_1;\omega_1,\omega_2,-\omega_2)$, and $D_{lmn}(-\omega_1;\omega_1,\omega_2,-\omega_2)$. The solid horizontal lines represent real states and the dashed

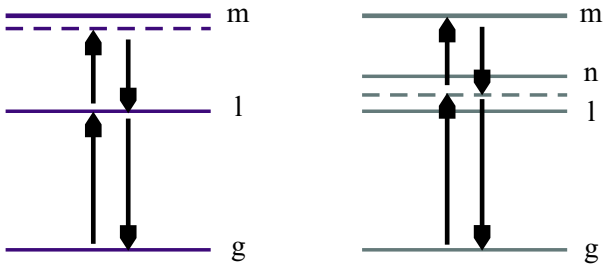

Fig. 2.29: Energy level diagrams for $D_{lml}(-\omega_1;\omega_1,\omega_2,-\omega_2)$ and $D_{lmn}(-\omega_1;\omega_1,\omega_2,-\omega_2)$, respectively. Each arrow represents a one-photon transition in the specified direction.

horizontal lines represent virtual states as discussed in Section 2.4.2.2.1. Because the two-photon state can only be reached through a two-photon process a large resonant enhancement occurs when the two-photon transition energy is the sum of the pump and probe photon energy $(\omega_1+\omega_2)$. An additional enhancement occurs when a there is second one-photon excited state if the pump or probe photon energy is similar to both the one-photon transition energies and the sum of the pump and probe photon energies is similar to the transition energy of the two-photon state.

As with the previous derivations, the Lorentzian energy denominator, Equation (2.98) when $n=l$, must be expanded using partial fractions. However, we do not believe this will add to the discussion so we refer the interested reader to Section 2.4.2.2.1 for more details on the procedure and to Appendix A for the result. Instead we quote the final result of the inhomogeneous-broadening transform on $D^L_{lml}(-\omega_1;\omega_1,\omega_2,-\omega_2)$ as:

$$
\begin{aligned}
D^{IB}_{lml}(-\omega_1;\omega_1,\omega_2,-\omega_2) = {} & \frac{-\pi}{\gamma_{gl}\gamma_{gm}}\times \\
& \left\{ \left[\frac{2(\Omega_{gl}-\omega_1)}{\gamma_{gl}^2} W\left(\frac{-(\Omega_{gl}-\omega_1)}{\gamma_{gl}}\right) + \frac{2i}{\sqrt{\pi}\gamma_{gl}} \right] \right. \\
& \qquad \left[W\left(\frac{-(\Omega_{gm}-\omega_1-\omega_2)}{\gamma_{gm}}\right) + W\left(\frac{-(\Omega_{gm}-\omega_1+\omega_2)}{\gamma_{gm}}\right) \right] \\
& + \left[\frac{2(\Omega^*_{gl}+\omega_1)}{\gamma_{gl}^2} W\left(\frac{-(\Omega^*_{gl}+\omega_1)}{\gamma_{gl}}\right) + \frac{2i}{\sqrt{\pi}\gamma_{gl}} \right] \\
& \qquad \left. \left[W\left(\frac{-(\Omega^*_{gm}+\omega_1+\omega_2)}{\gamma_{gm}}\right) + W\left(\frac{-(\Omega^*_{gm}+\omega_1-\omega_2)}{\gamma_{gm}}\right) \right] + \right. \\
& \frac{1}{\omega_1-\omega_2+2i\Gamma_{gl}} \left\{ \left[W\left(\frac{-\Omega^*_{gm}}{\gamma_{gm}}\right) + W\left(\frac{-(\Omega_{gm}-\omega_1-\omega_2)}{\gamma_{gm}}\right) \right] \right.
\end{aligned}
$$

$$
\begin{aligned}
&\times\left[W\left(\frac{-(\Omega_{gl}-\omega_1)}{\gamma_{gl}}\right)-W\left(\frac{-(\Omega^*_{gl}-\omega_2)}{\gamma_{gl}}\right)\right]\\
&+\left[W\left(\frac{-\Omega_{gm}}{\gamma_{gm}}\right)+W\left(\frac{-(\Omega^*_{gm}+\omega_1+\omega_2)}{\gamma_{gm}}\right)\right]\\
&\times\left[W\left(\frac{-(\Omega_{gl}+\omega_2)}{\gamma_{gl}}\right)-W\left(\frac{-(\Omega^*_{gl}+\omega_1)}{\gamma_{gl}}\right)\right]\Bigg\}+\\
&\frac{1}{\omega_1+\omega_2+2i\Gamma_{gl}}\Bigg\{\left[W\left(\frac{-\Omega^*_{gm}}{\gamma_{gm}}\right)+W\left(\frac{-(\Omega_{gm}-\omega_1+\omega_2)}{\gamma_{gm}}\right)\right]\\
&\times\left[W\left(\frac{-(\Omega_{gl}-\omega_1)}{\gamma_{gl}}\right)-W\left(\frac{-(\Omega^*_{gl}+\omega_2)}{\gamma_{gl}}\right)\right]\\
&+\left[W\left(\frac{-\Omega_{gm}}{\gamma_{gm}}\right)+W\left(\frac{-(\Omega^*_{gm}+\omega_1-\omega_2)}{\gamma_{gm}}\right)\right]\\
&\times\left[W\left(\frac{-(\Omega_{gl}-\omega_2)}{\gamma_{gl}}\right)-W\left(\frac{-(\Omega^*_{gl}+\omega_1)}{\gamma_{gl}}\right)\right]\Bigg\}+\\
&\frac{1}{\omega_1-\omega_2}\Bigg\{\left[W\left(\frac{-\Omega_{gm}}{\gamma_{gm}}\right)+W\left(\frac{-(\Omega_{gm}-\omega_1-\omega_2)}{\gamma_{gm}}\right)\right]\\
&\times\left[W\left(\frac{-(\Omega_{gl}-\omega_1)}{\gamma_{gl}}\right)-W\left(\frac{-(\Omega_{gl}-\omega_2)}{\gamma_{gl}}\right)\right]\\
&+\left[W\left(\frac{-\Omega^*_{gm}}{\gamma_{gm}}\right)+W\left(\frac{-(\Omega^*_{gm}+\omega_1+\omega_2)}{\gamma_{gm}}\right)\right]\\
&\times\left[W\left(\frac{-(\Omega^*_{gl}+\omega_2)}{\gamma_{gl}}\right)-W\left(\frac{-(\Omega^*_{gl}+\omega_1)}{\gamma_{gl}}\right)\right]\Bigg\}+\\
&\frac{1}{2i\Gamma_{gl}}\Bigg\{\left[W\left(\frac{-(\Omega^*_{gm}+\omega_1-\omega_2)}{\gamma_{gm}}\right)+W\left(\frac{-(\Omega_{gm}-\omega_1-\omega_2)}{\gamma_{gm}}\right)\right]\\
&\times\left[W\left(\frac{-(\Omega_{gl}-\omega_2)}{\gamma_{gl}}\right)-W\left(\frac{-(\Omega^*_{gl}-\omega_2)}{\gamma_{gl}}\right)\right]\\
&+\left[W\left(\frac{-(\Omega_{gm}-\omega_1+\omega_2)}{\gamma_{gm}}\right)+W\left(\frac{-(\Omega^*_{gm}+\omega_1+\omega_2)}{\gamma_{gm}}\right)\right]\\
&\times\left[W\left(\frac{-(\Omega_{gl}+\omega_2)}{\gamma_{gl}}\right)-W\left(\frac{-(\Omega^*_{gl}+\omega_2)}{\gamma_{gl}}\right)\right]\Bigg\}+\\
&\frac{1}{\omega_1+\omega_2}\Bigg\{\left[W\left(\frac{-\Omega_{gm}}{\gamma_{gm}}\right)+W\left(\frac{-(\Omega_{gm}-\omega_1+\omega_2)}{\gamma_{gm}}\right)\right]\\
&\times\left[W\left(\frac{-(\Omega_{gl}-\omega_1)}{\gamma_{gl}}\right)-W\left(\frac{-(\Omega_{gl}+\omega_2)}{\gamma_{gl}}\right)\right]+\\
&\left[W\left(\frac{-\Omega^*_{gm}}{\gamma_{gm}}\right)+W\left(\frac{-(\Omega^*_{gm}+\omega_1-\omega_2)}{\gamma_{gm}}\right)\right]\\
&\times\left[W\left(\frac{-(\Omega^*_{gl}-\omega_2)}{\gamma_{gl}}\right)-W\left(\frac{-(\Omega^*_{gl}+\omega_1)}{\gamma_{gl}}\right)\right]\Bigg\}\Bigg\}. \qquad (2.104)
\end{aligned}
$$

A third-order molecular response in the three-level limit, when there is one one-photon excited state and one two-photon excited state, can now be written for the inhomogeneous-broadening theory of the pump-probe experiment. Equation (2.96) can be reduced to the following, for the aforementioned model,

$$\xi^{(3)}(-\omega_1;\omega_1,\omega_2,-\omega_2) = \frac{1}{\epsilon_0 3!}\frac{1}{\hbar^3}\left\{|\mu_{g1}|^2|\mu_{12}|^2 D_{121}(-\omega_1;\omega_1,\omega_2,-\omega_2) - |\mu_{g1}|^4 D_{11}(-\omega_1;\omega_1,\omega_2,-\omega_2)\right\}. \quad (2.105)$$

The energy denominators are given by Equations (2.97) and (2.98) for the Lorentzian theory and by Equations (2.100) and (2.104) for the inhomogeneous-broadening theory.

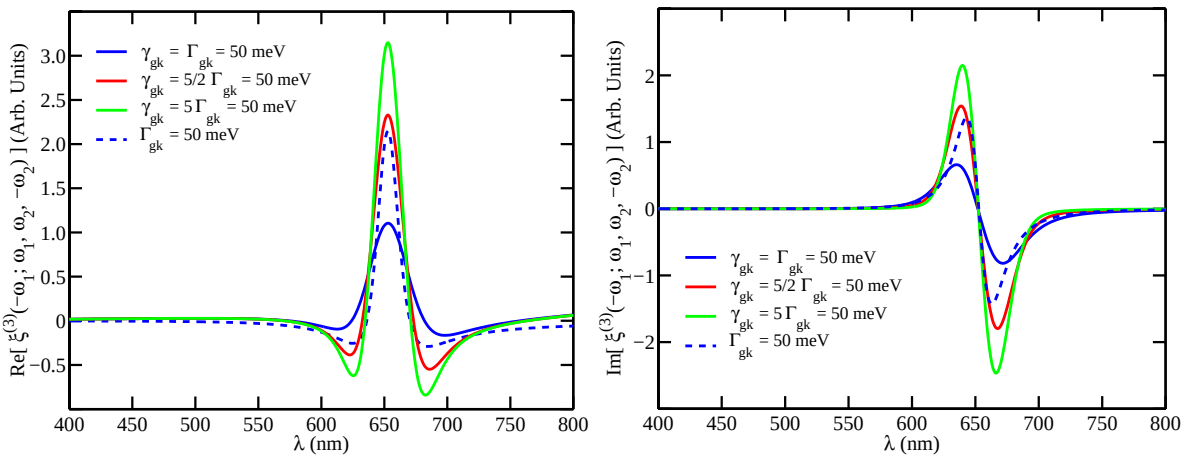

Fig. 2.30: Real and imaginary parts of $\xi^{(3)}(-\omega_1;\omega_1,\omega_2,-\omega_2)$ for one one-photon excited state and one two-photon state centered about 653 nm and 600 nm, respectively. The solid lines represent the inhomogeneously broadened electronic transitions for three different values of Γ_{gk} where $k \in \{1,2\}$ and the dashed line represents the homogeneously-broadened transitions.

Figure 2.30 represents the real and imaginary parts of Equation (2.105) for both the homogeneous-broadening model (dashed lines) and three specifications of the inhomogeneous-broadening model (solid lines) when the one-photon state is located at 653 nm, and the two-photon state is located at 600 nm. Note that $|\mu_{g1}| = 4|\mu_{g3}|$. However, the relative strengths are not very important in this case. Because the combination of excited states and photon energies do not match the resonant enhancement conditions there is no significant change to the electronic response from the two-level model (see

Figure 2.27). Therefore the pump-probe experiment, when the probe wavelength is 1064 nm and the probe wavelength is in the visible, is insensitive to two-photon states near the first excited state (653 nm). This is important because of some research groups in the nonlinear optics community postulate a two-photon state near the one-photon state.

To complete the this section, we must finish the final transformation of $D^{L}_{lmn}(-\omega_1;\omega_1,\omega_2,-\omega_2)$ to $D^{IB}_{lmn}(-\omega_1;\omega_1,\omega_2,-\omega_2)$. This will allow us to construct a general n-level inhomogeneous-broadening theory for the pump-probe experiment. We start with Equation (2.98) when $n \neq l$, which does not need to be expanded using partial fractions, and replace each Lorentzian term with the appropriate inhomogeneous-broadening term in Table 2.1 to get the following:

$$
\begin{aligned}
D^{IB}_{lmn}(-\omega_1;\omega_1,\omega_2,-\omega_2) = \frac{-i\pi^{3/2}}{\gamma_{gl}\gamma_{gm}\gamma_{gn}}\Bigg\{ & \\
W\left(\frac{-(\Omega_{gm}-\omega_1-\omega_2)}{\gamma_{gm}}\right)\left[W\left(\frac{-(\Omega_{gl}-\omega_1)}{\gamma_{gl}}\right)+W\left(\frac{-(\Omega^*_{gl}-\omega_2)}{\gamma_{gl}}\right)\right]\times & \\
\left[W\left(\frac{-(\Omega_{gn}-\omega_1)}{\gamma_{gn}}\right)+W\left(\frac{-(\Omega_{gn}-\omega_2)}{\gamma_{gn}}\right)\right] & \\
+W\left(\frac{-(\Omega_{gm}-\omega_1+\omega_2)}{\gamma_{gm}}\right)\left[W\left(\frac{-(\Omega_{gl}-\omega_1)}{\gamma_{gl}}\right)+W\left(\frac{-(\Omega^*_{gl}+\omega_2)}{\gamma_{gl}}\right)\right]\times & \\
\left[W\left(\frac{-(\Omega_{gn}-\omega_1)}{\gamma_{gn}}\right)+W\left(\frac{-(\Omega_{gn}+\omega_2)}{\gamma_{gn}}\right)\right] & \\
+W\left(\frac{-\Omega_{gm}}{\gamma_{gm}}\right)\left[W\left(\frac{-(\Omega_{gl}-\omega_1)}{\gamma_{gl}}\right)+W\left(\frac{-(\Omega^*_{gl}+\omega_1)}{\gamma_{gl}}\right)\right]\times & \\
\left[W\left(\frac{-(\Omega_{gn}-\omega_2)}{\gamma_{gn}}\right)+W\left(\frac{-(\Omega_{gn}+\omega_2)}{\gamma_{gn}}\right)\right] & \\
+W\left(\frac{-(\Omega^*_{gm}+\omega_1+\omega_2)}{\gamma_{gm}}\right)\left[W\left(\frac{-(\Omega^*_{gl}+\omega_1)}{\gamma_{gl}}\right)+W\left(\frac{-(\Omega^*_{gl}+\omega_2)}{\gamma_{gl}}\right)\right]\times & \\
\left[W\left(\frac{-(\Omega_{gn}+\omega_2)}{\gamma_{gn}}\right)+W\left(\frac{-(\Omega^*_{gn}+\omega_1)}{\gamma_{gn}}\right)\right] & \\
+W\left(\frac{-(\Omega^*_{gm}+\omega_1-\omega_2)}{\gamma_{gm}}\right)\left[W\left(\frac{-(\Omega^*_{gl}+\omega_1)}{\gamma_{gl}}\right)+W\left(\frac{-(\Omega^*_{gl}-\omega_2)}{\gamma_{gl}}\right)\right]\times & \\
\left[W\left(\frac{-(\Omega_{gn}-\omega_2)}{\gamma_{gn}}\right)+W\left(\frac{-(\Omega^*_{gn}+\omega_1)}{\gamma_{gn}}\right)\right] & \\
+W\left(\frac{-\Omega^*_{gm}}{\gamma_{gm}}\right)\left[W\left(\frac{-(\Omega^*_{gl}+\omega_2)}{\gamma_{gl}}\right)+W\left(\frac{-(\Omega^*_{gl}-\omega_2)}{\gamma_{gl}}\right)\right]\times & \\
\left[W\left(\frac{-(\Omega_{gn}-\omega_1)}{\gamma_{gn}}\right)+W\left(\frac{-(\Omega^*_{gn}+\omega_1)}{\gamma_{gn}}\right)\right]\Bigg\}. &
\end{aligned}
\tag{2.106}
$$

At last we have completed the four transformations which are necessary to construct a general n-level inhomogeneous-broadening model of the third-order susceptibility for the pump-probe experiment. Since the systems we are interested in may have a two-photon state near the first excited state, the four-level model will not tell us anything more than the three-level model with two one-photon excited states. Therefore we refer the reader back to Figure 2.28 for the three-level model with two one-photon states.

This completes the inhomogeneous-broadening derivations for the four third-order experiments. We have shown that there is a significant difference predicted in the third-order response (both real and imaginary) for all four experiments when inhomogeneous-broadening is modeled. Unfortunately, we do not know of a compact form for the energy denominators that account for inhomogeneous-broadening so the equations are much less succinct than the Lorentzian energy denominators. Hopefully, a simplified version of these results will be determined in the future.

In this thesis, the results of the derivations for the quadratic electrooptic experiment will be compared with QEA data for SiPc/PMMA and ISQ/PMMA thin films and the Lorentzian theory. These two systems should determine if the inhomogeneous-broadening (IB) theory is valid for third-order electronic responses.

2.5 Molecular Reorientation

In the previous section we discussed the electronic third-order responses for four experiments. However, the total third-order molecular susceptibility can have molecular reorienational effects as well as electronic effects. To account for molecular reorientation in the quadratic electroaborption measurement, we write the total third-order susceptibility as:

$$\xi_T^{(3)}(-\omega;\omega,0,0) = a_1\xi^{(3)}(-\omega;\omega,0,0) + \frac{a_2}{k_b T}\xi^{(1)}(-0;0)\xi^{(1)}(-\omega;\omega), \tag{2.107}$$

where the first- and third-order molecular susceptibilities are as previously defined, k_b is the Boltzmann constant, T is the temperature in Kelvin, a_1 and a_2 are Kirkwood factors [8]. For our case a_1 is unity and $0 \leq |a_2| \leq 1$, which will be determined by experiment.

2.6 Guest-Host systems

In this section, we define a couple of absorbing guest-host systems. The first guest-host system is a multimode dye-doped core fiber or core preform, and the second system is a dye-doped electrooptic thin film. In either system the general absorption coefficient, $\alpha(\lambda)$, is defined according to:

$$I(\lambda, z) \;=\; I_{inc}(\lambda)\exp(-\alpha(\lambda)\, z), \tag{2.108}$$

where $I_{inc}(\lambda)$ is the intensity at $z = 0$, and λ is the wavelength in free space. Since the absorption coefficient is dependent on the concentration, the absorption cross-section is often defined as,

$$\alpha(\lambda) = N\sigma(\lambda), \tag{2.109}$$

where N is the number density. $\sigma(\lambda)$ is the absorption cross-section and as defined is independent of concentration.

We are interested in relating the absorption coefficient, $\alpha(\lambda)$ to the linear and third-order susceptibilities, when applicable, for these dye-doped systems so that we can model

the absorption as a function of wavelength. The discussion will focus on core fibers and preforms, initially, because we will be working in the linear regime. After α is related to $\chi^{(1)}$ for the core fiber (preform) system, we will tighten up the boot straps and derive how $\chi^{(1)}$, and $\chi^{(3)}$ are related α for electrooptic thin films.

2.6.1 Core Fibers and Preforms

In the transmission spectroscopy experiment we can determine the linear absorption coefficient about resonance and in the SIF experiment we can determine the linear absorption coefficient off-resonance. If the transmission data is sufficiently resolved, we can determine the excited states that contribute contribute to the absorption in the guest-host polymer. If the fluorescence spectrum, in the SIF measurement, is broad enough, there will be sufficient information to generally characterize the excited states of the dye molecule in the guest-host polymer. To determine the excited state parameters like the transition moment (μ_{gn}), resonance frequency (ω_{gn}), and linewidths (γ_{gn} and/or Γ_{gn}), we need to relate the absorption coefficient, α, to $\chi^{(1)}$.

The wave equation, Equation (2.6), for the Fourier amplitudes from Section 2 can be reduced to the following,

$$-\frac{d^2E_\omega(z)}{dz^2} = \frac{\omega^2}{c^2}\,E_\omega(z) + \mu_0\omega^2 P_\omega(z), \tag{2.110}$$

where the polarization amplitude can be specified from Section 2.1, Equation 2.10, in MKS units, as:

$$P_\omega = P_\omega^{(1)} = \epsilon_o\chi^{(1)}(-\omega;\omega)E_\omega. \tag{2.111}$$

We have dropped all higher-order polarization amplitudes because we will be working in the linear regime. Thus we are only interested in one-photon absorption, which is related to the linear susceptibility, for the transmission spectroscopy and side-illumination fluorescence spectroscopy experiments. Information on two-photon absorption and the two-photon absorption coefficient can be found in D.1.

$\chi^{(1)}(-\omega;\omega)$ relates the polarization amplitude, P_ω, to the electric field amplitude, E_ω, where ϵ_o is the permittivity of free space. The specific forms of $\chi^{(1)}(-\omega;\omega)$ for the

Lorentzian theory, and the inhomogeneous-broadening (IB) theory, are defined in Section 2.4.

For the fiber and preform geometries we are studying, the polarization and electric field are oriented along the transverse direction, implying that $(P_\omega)_x = \epsilon_o \chi^{(1)}_{xx}(-\omega;\omega)(E_\omega)_x$. However, the subscripts have been dropped for the analysis, because only one tensor component of $\chi^{(1)}(-\omega;\omega)$ is being studied.

The solution to Equation (2.110) is the following,

$$k = \frac{n\omega}{c}, \tag{2.112}$$

, where k is the 1-D wavevector, and the index of refraction, $n = \sqrt{(1 + \chi^{(1)}(-\omega,\omega))}$.

Because we are studying dye-doped polymer systems, the linear optical susceptibility of the guest-host system for low dye concentration is the sum of the linear susceptibility of the dye and the polymer [8],

$$\chi^{(1)}_{\text{system}}(-\omega;\omega) = \chi^{(1)}_{\text{polymer}} + \chi^{(1)}_{\text{dye}}(-\omega;\omega). \tag{2.113}$$

The frequency dependence of $\chi^{(1)}_{\text{polymer}}$ has been dropped because the polymer can be approximated as dispersionless in the visible wavelength range as compared to the dye [18].

To relate the linear susceptibility, $\chi^{(1)}_{\text{system}}(-\omega;\omega)$, to the linear absorption coefficient, $\alpha(\lambda)$, we express the index of refraction, n, as:

$$n = n_R + i n_I = \sqrt{1 + \chi^{(1)}_{\text{system}}(-\omega;\omega)}, \tag{2.114}$$

where n_R and n_I are the real and imaginary parts of the index of refraction, respectively.

In the visible wavelength range, the absorption due to the polymer is negligible compared to that of the dye, so the imaginary part of $\chi^{(1)}_{\text{polymer}}$ is negligible. Also, the real part of $\chi^{(1)}_{\text{dye}}(-\omega;\omega)$ is negligible in comparison to that of the polymer because we are typically working with less than 0.1 wt.% dye in the guest-host systems. Taking these assumptions into account and expanding the square root for small n_I, the index of refraction becomes

$$n = n_R + i n_I = n_{\text{polymer}} + i\frac{\chi^{(1)}_{\text{dye}_I}(-\omega;\omega)}{2\, n_{\text{polymer}}}, \tag{2.115}$$

where $n_{\text{polymer}} = \sqrt{(1 + \chi^{(1)}_{\text{polymer}_R})}$.

With the imaginary part of the index of refraction defined, we can relate the linear absorption coefficient to $\chi^{(1)}_{\text{dye}_I}(-\omega;\omega)$ as follows:

$$\alpha(\lambda) = 2n_I\frac{\omega}{c} = \frac{\omega}{c}\frac{\chi^{(1)}_{\text{dye}_I}(-\omega;\omega)}{n_{\text{polymer}}}, \tag{2.116}$$

when $k = \beta + i\frac{\alpha}{2}$. The factor of on half is necessary because the absorption coefficient is related to the intensity and k is related to the electric field.

Therefore, $\alpha(\lambda)$ for propagation in a core polymer fiber or preform can be theoretically modeled using Equation (2.116), where $\chi^{(1)}_{\text{dye}_I}(-\omega;\omega)$ is modeled using either the Lorentzian theory or the inhomogeneous broadening theory.

2.6.2 Electrooptic Thin Films

In the previous section, we defined how the absorption was related to the linear optical susceptibility. For the quadratic electrooptic effect we are interested in an absorption that is proportional to the third-order susceptibility because of the pseudo-d.c. electric field which is applied across the sample. Therefore we need to define how this absorption is related to $\chi^{(3)}$, and the voltage across the sample.

For dye-doped thin films we approximate the system as 1-D and centrosymmetric because we will be performing the QEA experiment at normal incidence. Therefore Equation (2.6) for the Fourier amplitudes from Section 2 can be reduced to the following,

$$-\frac{d^2E_\omega(z)}{dz^2} = \frac{\omega^2}{c^2}\,E_\omega(z) + \mu_0\omega^2 P_\omega(z). \tag{2.117}$$

The polarization amplitude can be specified out to third-order from Equation (2.10),

$$\begin{aligned} P_\omega(z) &= P^{(1)}_\omega(z) + P^{(3)}_\omega(z) \\ &= \epsilon_o(\chi^{(1)}(-\omega;\omega)E_\omega(z) + K_3\chi^{(3)}(-\omega;\omega,0,0)E_\omega(z)E_0E_0), \end{aligned} \tag{2.118}$$

where $K_3 = K(-\omega;\omega,0,0) = 3$, and we have neglected the tensor nature of the first- and third-order susceptibilities since there is only one tensor component for normal incidence. Details about the quadratic electrooptic effect for oblique incidence can be found in the litertare [4, 19]

In the QEA experiment the pseudo-d.c voltage is related to the applied electric field as follows,

$$E_0 = \sqrt{2}\frac{V_{\text{rms}}}{d}, \tag{2.119}$$

where V_{rms} is the root-mean-square voltage and d is the thickness of the dye-doped thin film. Therefore Equation (2.117) can be simplified to the following,

$$-\frac{d^2E_\omega(z)}{dz^2} - \frac{\omega^2}{c^2}\left(1 + \chi^{(1)} + 3\chi^{(3)}E_0^2\right)E_\omega(z) = 0. \tag{2.120}$$

Equation (2.117) has been reduced to a linear equation in the optical electric field amplitude. Therefore the wavevector, k, is related to the first- and third-order susceptibilities as follows,

$$k = \frac{\omega}{c}(\epsilon_r + 3\chi^{(3)}E_0^2)^{\frac{1}{2}}, \tag{2.121}$$

where the relative permittivity is $\epsilon_r = 1 + \chi^{(1)}$.

Since $\chi^{(3)}$ is much smaller than the linear contribution to the right-hand-side of Equation 2.121, a Taylor series expansion to second order result in the following,

$$k = \frac{\omega n_o}{c} + \frac{\omega}{c}\frac{3\chi^{(3)}E_0^2}{2n_o}, \tag{2.122}$$

where the linear index of refraction is defined as $n_o = \sqrt{1 + \chi^{(1)}}$.

When the material being studied absorbs some of the incident light, the wavevector has both real and imaginary parts and is written as [7],

$$k = \beta + i\frac{\alpha}{2} \tag{2.123}$$

where the factor of $1/2$ is used so that α describes the absorption of the intensity. The right-hand-side of Equation (2.122) is more difficult to separate because, in general, both susceptibilities have real and imaginary parts,

$$\chi^{(1)} = \chi_R^{(1)} + i\chi_I^{(1)} \tag{2.124}$$

and

$$\chi^{(3)} = \chi_R^{(3)} + i\chi_I^{(3)}. \tag{2.125}$$

Since we are only interested in the imaginary part of the wavevector for the QEA experiment, the absorption coefficient can also be related to the imaginary part of Equation 2.122 as follows,

$$\alpha = \alpha_0 + \alpha_{\text{QEA}} E_0^2 = \frac{2\omega}{c} n_{o_I} + \frac{3\omega\chi_I^{(3)}}{c\, n_{o_R}} E_0^2, \tag{2.126}$$

where it has been assumed that $\chi_I^{(3)} n_{oR} \gg \chi_R^{(3)} n_{oI}$. (For the relation between the real part of the wave vector and $\chi^{(3)}$ please see Section D.1.) Therefore the zero voltage absorption coefficient is,

$$\alpha_0 = \frac{2\omega}{c} n_{o_I}, \tag{2.127}$$

and the QEA absorption coefficient is related to the imaginary part of $\chi^{(3)}$ as follows,

$$\alpha_{\text{QEA}} = \frac{3\omega\chi_I^{(3)}}{c\, n_{o_R}}. \tag{2.128}$$

From the results of Section 2.6.1, the imaginary parts of $\chi^{(1)}$ and $\chi^{(3)}$ are due to the dye even though we neglect the subscripts. Equations 2.127 and 2.128 will be calculated from the observables in the QEA experiment which is described in Section 4.4. The values of α_0 and α_{QEA} can then be related to the excited state parameters using the IB and Lorentzian theories for $\chi^{(1)}$ and $\chi^{(3)}$.

2.7 Fluorescence Generation

For the emission spectroscopy and side-illumination fluorescence experiments it is useful to model the fluorescence. A simple model of a fluorescence spectrum that is excited by a monochromatic light source which illuminates a planar surface is,

$$F(\lambda, \lambda_e) = Q_F(\lambda, \lambda_e) I_e(\lambda_e), \tag{2.129}$$

where $I_e(\lambda_e)$ is the excitation intensity at the excitation wavelength, λ_e, $Q_F(\lambda, \lambda_e)$ is the fluorescence quantum yield for all the wavelengths in the fluorescence band when generated by the excitation wavelength, and $F(\lambda, \lambda_e)$ is the transmitted fluorescence spectrum. Note that we have assumed that the fluorescence generation is isotropic about the excitation position since we are dealing with isotropic materials, and is generated in a

one-photon process. We have used the symbol F to avoid confusion with the transmitted intensity, I_t, at the laser wavelength.

This model for the fluorescence spectrum is only valid for the emission spectroscopy experiment (See Section 4.2) in the reflection geometry because the fluorescence is generated near the front surface of the material and propagates away from the material to be detected. If the fluorescence spectrum is observed in transmission our model must be modified to the following,

$$F(\lambda, \lambda_e, z) = Q_F(\lambda, \lambda_e) I_e(\lambda_e) \exp(-\alpha(\lambda)\, z), \tag{2.130}$$

where the exponential term accounts for the absorption of the fluorescence as it propagates as a plane wave through a sample of thickness, z. It should be noted that it is assumed that the fluorescence is generated in a small skin depth at the front of the material. Clearly, Equation (2.130) reduces to Equation (2.129) in the limit of small absorption or thickness.

2.7.1 Side-illumination

In the SIF measurement, the light source is the fluorescence light generated when a fiber is illuminated from the side. The geometry of fluorescence generation must be taken into account when modeling the wave propagation in the geometrical limit because the fluorescence is not being measured in the same direction as the incident excitation. Figure 2.31 shows a schematic diagram of the side-illumination experiment for an unclad, multimode fiber, which we call a core fiber [20]. Naively, the fluorescence can be assumed to be generated uniformly throughout the planar, circular cross-section of the fiber and thus produces plane waves traveling toward the front and back of the fiber. A slightly more sophisticated approach is to assume that the fluorescence is being generated by a point source at the fiber center. Assuming this point source radiates light radially with spherical symmetry, some of the light refracts out of the fiber and the rest guides in the fiber to the front and rear faces where it can be detected. Realistically, the generation pattern of the fluorescence is difficult to determine, but the general trend should become clear through these two limiting cases.

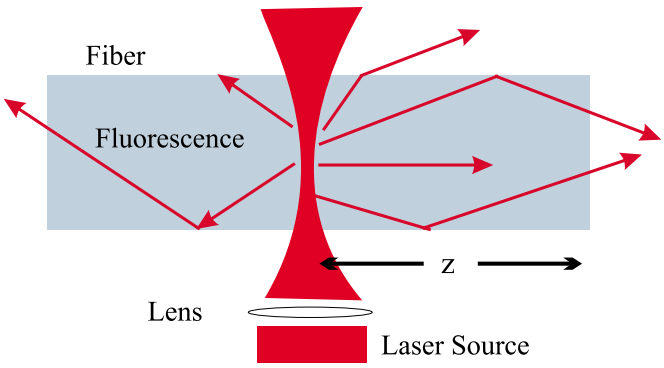

Fig. 2.31: Fluorescence generated in a core fiber with a monochromatic laser source.

2.7.1.1 Plane wave source

If we assume that the fiber diameter is small compared with the absorption length at the excitation source wavelength, λ_e, the illuminated portion of the fiber can be approximated as a homogeneous light source similar to Equation (2.130). However, the excitation is not incident on a planar surface so our model must be modified once more to take this into account. We use a general coefficient to model the coupling of the laser light into the fiber which gives us the following,

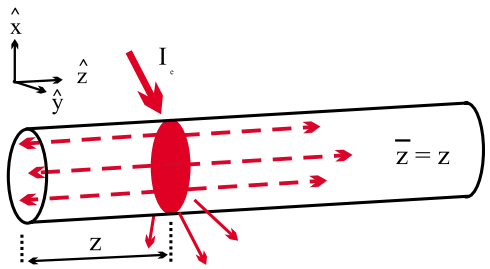

Fig. 2.32: Broadband fluorescence plane wave source model.

$$F(\lambda, \lambda_e, z) = C(d_f, d_e) Q_F(\lambda, \lambda_e) I_e(\lambda_e) \exp(-\alpha(\lambda)\, z), \tag{2.131}$$

where d_f is the diameter of the fiber, d_e is the diameter of the excitation laser beam, and $C(d_f, d_e)$ is the coupling coefficient. Since we are not interest particularly interested in determining $C(d_f, d_e)$ we define the to fluorescence at z=0 to be,

$$F_0(\lambda, \lambda_e, I_e) = C(d_f, d_e) Q_F(\lambda, \lambda_e) I_e(\lambda_e), \tag{2.132}$$

Note that, if the fiber is inhomogeneous along z, the initial fluorescence, $F_0(\lambda, \lambda_e, I_e)$, can also depend on z. We assume that the positional dependence in $F_0(\lambda, \lambda_e, I_e)$ is small.

For the remainder of the absorption analysis, we will regard the initial fluorescence as independent of position. Since a point source model for the fluorescence source distribution will be developed in the following section we define,

$$F_{PWM}(\lambda, z) \equiv F_0(\lambda) \exp(-\alpha(\lambda)\, z), \tag{2.133}$$

where PWM is short for plane wave model, and we have dropped the arguments, λ_e, and I_e, in the initial fluorescence to ease the notation.

2.7.1.2 Point source

In the point source model, we assume that all the fluorescence is produced at one point in the center of the fiber and the light is produced isotropically. This model is more complicated than the plane wave model because we have to trace all the rays that are beyond the critical angle of the fiber.

Assuming that the index of refraction is roughly constant in the fluorescence wavelength range – 1.49 for PMMA – the critical angle of the fiber is $\theta_c \simeq 48^o$. Those rays that are within the critical angle travel different distances to the end of the fiber, so each ray is absorbed differently. Since the integrated power of all rays beyond the critical angle after 1 cm of propagation contributes $< 0.01\%$ to the light intensity in the fiber, we ignore Fresnel reflections beyond θ_c and use the critical angle as the limits of integration. This yields the fluorescence intensity at z due to all the light rays inside $\theta = \theta_c$,

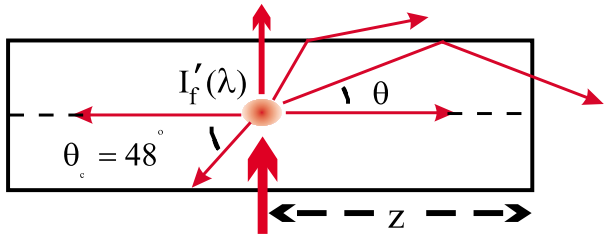

Fig. 2.33: Broadband fluorescence point source model where the distance traveled by a ray at angle θ is $z/\cos\theta$.

$$F_{PSM}(\lambda, z) = C(d_f, d_e) Q_f(\lambda, \lambda_e) I_e \frac{\int_0^{2\pi}\int_0^{\theta_c} \exp(-\alpha(\lambda)\, z/\cos\theta) \sin\theta d\theta d\phi}{\int_0^{2\pi}\int_0^{\pi/2} \sin\theta d\theta d\phi}, \tag{2.134}$$

where the denominator is the normalization factor. Integrating the denominator and with respect to ϕ in the numerator of Equation (2.134), we get the following,

$$F_{PSM}(\lambda, z) = F_0(\lambda) \int_0^{\theta_c} \exp(-\alpha(\lambda, \theta)\, z) \sin\theta d\theta. \tag{2.135}$$

For simplicity, we use Equation (2.132), $F_0(\lambda)$, as the initial fluorescence intensity at the point source, $\alpha(\lambda, \theta) = \alpha(\lambda)/\cos(\theta)$, and $C(d_f, d_e)$ and $Q_f(\lambda_m, \lambda)$ as previously described. The $z/\cos\theta$ term in Figure 2.33 expresses the distance traveled by a ray at an angle θ as a function of z.

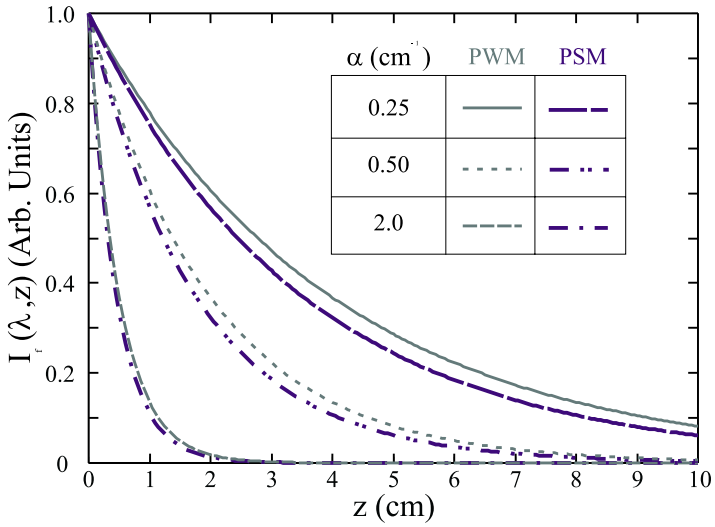

Fig. 2.34: Side-illumination fluorescence (SIF) for point source model (PSM) and plane wave model (PWM) for three values of α.

Figure 2.34 shows the transmitted fluorescence intensity, $F(\lambda, z)$, as a function of distance, z, for the plane wave and point source models. In all three cases, the point source fluorescence model appears to have higher loss because the rays, on average, travel further than in the plane wave case.

2.7.2 Correlation length

If the fiber is not perfectly homogeneous in diameter and/or dye concentration (Figure 2.35), the coefficient describing the fluorescence yield can depend on the fluorescence

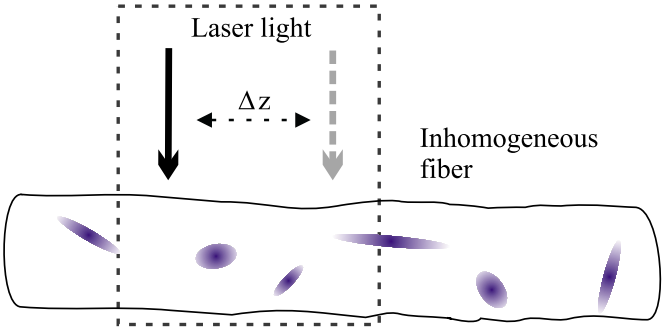

Fig. 2.35: Side-illumination of an inhomogeneous dye-doped fiber.

source coordinate, z, as follows,

$$F_0(\lambda, z) = F_0(\lambda)S(z), \tag{2.136}$$

where we have assumed that the excitation intensity is constant, and on average $\bar{S}(z)$=1. The deviation of $S(z)$ from unity gives a measure of the inhomogeneity in the fiber [21]. Because the light is detected at one end of the fiber, we define z relative to the front of the fiber. As defined, z is both the coordinate at which the light is produced, and the on-axis distance the light travels before exiting the fiber.

Applying the plane wave model of Equation (2.133) to an inhomogeneous fiber yields:

$$F^{'}(\lambda, z) = F_0(\lambda)S(z)\exp(-\alpha(\lambda)\, z). \tag{2.137}$$

Since $F^{'}(\lambda, z) = S(z)F(\lambda, z)$, the fluctuations of $F^{'}(\lambda, z)$ about the homogeneous fluorescence intensity, $F_(\lambda, z)$, at any given wavelength, are a measure of S(z).

We can quantify the inhomogeneities using the autocorrelation function which measures the similarities between the intensity generated at one position in the fiber, z, and the intensity generated at a neighboring point, $z + \zeta$, over a length, Z, of fiber, and is defined for a fixed wavelength, λ_o, as [22]

$$\langle I(0)I(\zeta)\rangle = \lim_{Z\to\infty}(\frac{1}{Z})\int_0^Z dz\; I(z)I(z+\zeta), \tag{2.138}$$

where we have generalized the fluorescence intensity, $I(z) \equiv F^{'}(\lambda_o, z)$, because this analysis is not restricted to fluorescence [21, 23]. For a discrete data set, Equation (2.138) is

approximated by

$$\langle I(0)I(\zeta)\rangle \cong \lim_{N\to\infty}(\frac{1}{N})\sum_{j=0}^{N} I_j I_{j+k}, \tag{2.139}$$

where N is the number of data points, $\zeta = k\Delta z$, and Δz is the interval between the data points as determined by the experiment.

Similarly, the autocorrelation function of the fluctuations of $I(z)$, $\delta I(z)$, is

$$\langle \delta I(0)\delta I(\zeta)\rangle \cong \lim_{N\to\infty}(\frac{1}{N})\sum_{j=0}^{N} \left(I_j - \bar{I}\,\right)\left(I_{j+k} - \bar{I}\,\right), \tag{2.140}$$

where $\bar{I}$ is the mean value of the intensities of the data set (i.e., over the measured length of fiber). However, Equation (2.140) assumes that the data fluctuates about a constant value (see for example the femtosecond hyper-Rayleigh scattering studies by Olbrechts and co-workers [23]).

When linear absorption is appreciable, the data fluctuates about a decaying exponential whose strength is defined by the linear absorption coefficient, $\alpha(\lambda_o)$. Taking into account the decay of the intensity with propagation distance, the autocorrelation function of $\delta I(z)$ is normalized and modified as follows:

$$\begin{aligned}\langle \delta I(z)\delta I(z+\zeta)\rangle_{Norm} &= \frac{\sum_{j=0}^{N}\left\{I_j - I_o\exp(-\alpha(\lambda_o)z_j)\right\}\left\{I_{j+k} - I_o\exp(-\alpha(\lambda_o)z_{j+k})\right\}}{\sum_{j=0}^{N}\left\{I_j - I_o\exp(-\alpha(\lambda_o)z_j)\right\}\left\{I_j - I_o\exp(-\alpha(\lambda_o)z_j)\right\}},\\ &= \frac{\sum_{j=0}^{N}\left\{I_j - I_j^{fit}\right\}\left\{I_{j+k} - I_{j+k}^{fit}\right\}}{\sum_{j=0}^{N}\left\{I_j - I_j^{fit}\right\}\left\{I_j - I_j^{fit}\right\}},\end{aligned} \tag{2.141}$$

where $I_o \equiv I_f(\lambda_o)$, and the fit intensity, I_j^{fit}, is calculated from the experimentally determined value of $\alpha(\lambda_o)$:

$$I_j^{fit} \equiv I_o\exp(-\alpha(\lambda_o)z_j). \tag{2.142}$$

Defining $\delta I_j = I_j - I_j^{fit}$ and $\delta I_{jk} = I_{j+k} - I_{j+k}^{fit}$, the form of the autocorrelation function is

$$\langle \delta I(z)\delta I(z+\zeta)\rangle_{Norm} = \frac{\sum_{j=0}^{N}\delta I_j \delta I_{jk}}{\sum_{j=0}^{N}{\delta I_j}^2}. \tag{2.143}$$

The autocorrelation function is often modeled as an exponential or Gaussian function of ζ. By fitting the autocorrelation function to one of these models, the length scale of the fluctuations is determined and called the correlation length. Mathematically, the

correlation length, ζ_c, is the value of ζ when the correlation function (Equation (2.143)) is at $1/e$ of its magnitude. The correlation length is thus related to the homogeneity of the fiber and can be used to characterize fiber quality.

2.8 Photosensitivity

Let us define the photon flux transmitted through an optically flat preform of dye-doped polymer as $\mathrm{n}(z,t)$. Normally, this photon flux is related to the incident photon flux as follows:

$$\mathrm{n}(z,t) = \mathrm{n}_o \exp(\sum_k -\sigma_k J_k(z,t)) \tag{2.144}$$

where n_o is the incident photon flux, σ_k is the absorption cross-section and $\mathrm{J}_k(z,t)$ is the number of molecules per area, respectively, for the k^{th} one photon excited state of the dye molecule. If we restrict the dye molecule to one excited state at the initial time, then as the dye molecules photobleach a new (second) excited state appears and gets stronger with time. We can then restrict the sum over k to two terms and replace $\mathrm{J}_2(z,t) = \mathrm{J_t}$ - $\mathrm{J}_1(z,t)$ in Equation (2.144) to get the following:

$$\mathrm{n}(z,t) = \mathrm{n}_o \exp(-(\sigma_1 - \sigma_2)J_1(z,t) - \sigma_2 J_\mathrm{t}) \tag{2.145}$$

Over time the number density of the dye molecule, N_1 will change due to photobleaching, where the total number of molecules is $N_t(z,t) = N_1(z,t) + N_2(z,t)$. Thus we write $J_1(z,t)$ as:

$$J_1(z,t) = \int_0^z N_1(z',t)dz'. \tag{2.146}$$

We determine the dependence of $\mathrm{J}_1(z,t)$ on time and position using two different techniques. The first method will assume that the bleaching occurs completely in a slice of some infinitesimal thickness δ before bleaching begins in the next slice.

Figure **??** shows the a sample of thickness, d. The first frame shows the completely unbleached sample or new sample, the second frame shows the sample with three slices of thickness δ bleached, and the final frame shows the sample with 20 slices of thickness δ bleached.

The assumption of uniform bleaching allows us to write the number density as:

$$N_1(z,t) = N_t\Theta(z-\beta' t), \tag{2.147}$$

where $\Theta(z-\beta' t)$ is the Heaviside-step function, which is defined as:

$$\Theta(z-\beta' t) = \begin{cases} 1 & z > \beta' t \\ 0 & z < \beta' t \end{cases} \tag{2.148}$$

Now we can explicitly determine $J_1(z,t)$ for all positions and time as follows:

$$\begin{aligned} J_1(z,t) &= \int_0^z N_t\Theta(z'-\beta' t)dz' \\ &= N_t\int_{\beta' t}^z dz' \\ &= N_t z - N_t\beta' t. \end{aligned} \tag{2.149}$$

Substituting Equation (2.149) into Equation (2.145) determines the transmitted photon flux for all times and positions. However, we are really interested in the photon flux at the end of the sample, so we let z = d, as follows

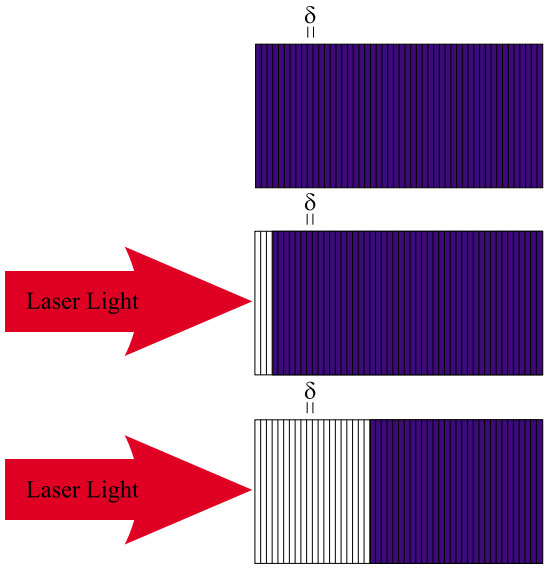

Fig. 2.36: Dye-doped polymer slab divided into 50 slices of thickness, δ. The first slab has a uniform number density, the second slab has 3 slices photobleached, and the third slab has 20 slices photobleached.

$$\mathrm{n}(d,t) = \mathrm{n}_o \exp(-N_t(\sigma_1-\sigma_2)(d-\beta' t) - \sigma_2 J_\mathrm{t}). \tag{2.150}$$

We recognize that β' has unit of velocity, so will be define it as the velocity of the bleaching front.

By defining the time derivative of $\mathrm{N}_1(z,t)$ as:

$$\frac{\partial N_1(z,t)}{\partial t} = -\beta N_1(z,t)n(z,t), \tag{2.151}$$

where β has units of cm^2 photons^{-1}, we can determine $J_1(z,t)$ in a more general way. As experimental results appear the functional dependence of β will be determined more rigorously.

Instead of integrating Equation (2.151) directly, we follow the work of Tomlinson [24, 25], and integrate both sides with respect to z, over the thickness of the sample, as follows,

$$\begin{aligned}
\frac{\partial J_1(d,t)}{\partial t} &= \int_0^d \frac{\partial N_1(z',t)}{\partial t}\, dz', \\
&= \int_0^d -\beta N_1(z,t) n(z,t)\, dz', \\
&= -\beta n_o \int_0^d N_1(z',t) \exp(-(\sigma_1-\sigma_2)\int_0^{z'} N_1(z'',t)\, dz'')\, dz', \quad (2.152)
\end{aligned}$$

We need to recognize that the integral with respect to z' can be completed because we have essentially the argument of the exponential multiplying the exponential. For example if we take the derivative of $\exp(-(\sigma_1-\sigma_2)\int_0^{z'} N_1(z'',t)\, dz'')$, with respect to z', we get $-(\sigma_1-\sigma_2)N_1(z',t)\exp(-(\sigma_1-\sigma_2)\int_0^{z'} N_1(z'',t)\, dz'')$. Therefore, the time derivative of $J_1(d,t)$ can be simplified as follows:

$$\begin{aligned}
\frac{\partial J_1(d,t)}{\partial t} &= \frac{\beta n_o}{(\sigma_1-\sigma_2)} \int_0^d -(\sigma_1-\sigma_2) N_1(z',t) \exp(-(\sigma_1-\sigma_2)\int_0^{z'} N_1(z'',t)\, dz'')\, dz', \\
&= \frac{\beta n_o}{(\sigma_1-\sigma_2)} \exp(-(\sigma_1-\sigma_2)\int_0^{z} N_1(z',t)\, dz')\Big|_{z=0}^{z=d}, \\
&= \frac{\beta n_o}{(\sigma_1-\sigma_2)} \left(\exp(-(\sigma_1-\sigma_2)J_1(d,t)) - 1\right). \quad (2.153)
\end{aligned}$$

Equation (2.153) is now in a form that can be integrated quite easily with respect to t. By moving all $J_1(d,t)$ dependence to the left-hand side, we can integrate both sides with respect to time.

$$\begin{aligned}
\int_{J_1(d,0)}^{J_1(d,t)} \frac{d' J_1(d,t)}{\exp(-(\sigma_1-\sigma_2)J_1'(d,t)) - 1} &= \int_0^t \frac{\beta n_o}{(\sigma_1-\sigma_2)}\, dt \\
&= \frac{\beta n_o t}{(\sigma_1-\sigma_2)} \quad (2.154)
\end{aligned}$$

The left-hand side of Equation (2.154) has the form

$$\int \frac{dx}{p + q\exp(ax)} = \frac{x}{p} - \frac{1}{ap}\ln(p + q\exp(ax)). \quad (2.155)$$

At time, t=0, we assume that we have a uniform distribution of dye molecules and no photobleached molecules ($N_2(t=0)=0$), so that $J_1(d,0)=N_t d$. Therefore the result of integrating the left-hand side is the following:

$$\frac{\beta n_o t}{\sigma_1-\sigma_2} = -J_1(d,t) + N_t\, d - \frac{1}{\sigma_1-\sigma_2}\ln\left(\frac{\exp(-(\sigma_1-\sigma_2)J_1(d,t))-1}{\exp(-(\sigma_1-\sigma_2)N_t\, d)-1}\right) \tag{2.156}$$

We begin simplifying Equation (2.156) by multiplying each side by $-(\sigma_1-\sigma_2)$, moving the first and second terms on the right-hand side to the left hand side, then take the anti-natural log of each side to get the following,

$$\exp(-\beta n_o t - (\sigma_1-\sigma_2)J_1(d,t) + (\sigma_1-\sigma_2)N_t\, d) = \frac{\exp(-(\sigma_1-\sigma_2)J_1(d,t))-1}{\exp(-(\sigma_1-\sigma_2)N_t\, d)-1}. \tag{2.157}$$

Only a couple more steps are necessary to isolate $J_1(d,t)$. If we multiply, each side by $\exp(-(\sigma_1-\sigma_2)N_t\, d)-1$, subtract $\exp(-(\sigma_1-\sigma_2)J_1(d,t))$ from each side, and finally multiply each side by -1, we get the following,

$$1 = \exp(-(\sigma_1-\sigma_2)J_1(d,t))(1-(\exp(-(\sigma_1-\sigma_2)N_t\, d)-1)\exp(-\beta n_o t)\exp((\sigma_1-\sigma_2)N_t\, d). \tag{2.158}$$

Finally, we isolate $J_1(d,t)$ by multiplying each side by $\exp((\sigma_1-\sigma_2)J_1(d,t))$, taking the natural log of each side and dividing each side by $(\sigma_1-\sigma_2)$,

$$J_1(d,t) = \frac{1}{\sigma_1-\sigma_2}\ln\left\{1+[\exp((\sigma_1-\sigma_2)N_t\, d)-1]\exp(-\beta n_o t)\right\}. \tag{2.159}$$

If $(\sigma_1-\sigma_2)N_t\, d$ is large, and t is small, then we can approximate the general description of $J_1(d,t)$ with the following,

$$J_1(d,t) = N_t\, d - \frac{\beta n_o t}{\sigma_1-\sigma_2}, \tag{2.160}$$

which is equivalent to Equation (2.146) when,

$$\frac{\beta n_o}{\sigma_1-\sigma_2} = N_t(\sigma_1-\sigma_2)\beta'. \tag{2.161}$$

Bibliography

[1] P. N. Butcher and D. Cotter, *The elements of nonlinear optics*, 1st ed. (Cambridge University Press, Cambridge, 1990).

[2] M.G. Kuzyk and C.W. Dirk, "Effects of centrosymmetry on the nonresonant electronic third-order nonlinear optical susceptibility," Phys. Rev. A **41**, 5098 (1990).

[3] J. H. Andrews, J. D. V. Khaydarov, and K. D. Singer, "Contribution of the 2^1Ag state to the third-order optical nonlinearity in a squaraine dye," Opt. Lett. **19**, 984–986 (1994).

[4] C. Poga, T. M. Brown, M. G. Kuyzk, and Carl W. Dirk, "Characterization of the excited states of a squaraine molecule with quadratic electrosorption spectroscopy," J. Opt. Soc. Am. B **12**, 531–43 (1995).

[5] K. S. Mathis, M. G. Kuzyk, C. W. Dirk, A. Tan, S. Martinez, and G. Gampos, "Mechanisms of the nonlinear optical properties of squarainne dyes in poly(methyl methacrylate) polymer," J. Opt. Soc. Am. B **15**, 871–883 (1998).

[6] M. G. Kuzyk, J. E. Sohn, and C. W. Dirk, "Mechanisms of quadratic electro-optic modulation of dye-doped polymer systems," J. Opt. Soc. Am. B **7**, 842–58 (1990).

[7] J. D. Jackson, *Classical Electrodynamics*, 2 ed. (Wiley, 1975).

[8] M. G. Kuzyk and C. W. Dirk, eds., *Characterization techniques and tabulations for organic nonlinear optical materials*, 1st ed. (Marcel Dekker, New York, 1998).

[9] B. J. Orr, "Perturbation theory of the non-linear optical polarization of an isolated system," Mol. Phys. **20**, 513–26 (1971).

[10] C. W. Dirk and M. G. Kuzyk, "Damping corrections and the calculation of optical nonlinearities in organic molecules," Phys. Rev. B **41**, 1636–39 (1990).

[11] R. A. Norwood, D. R. Holcomb, and F. F. So, "Polymers of nonlinear optics: absorption, two photon absorption, and photodegradation," Nonlinear Opt. **6**, 193–204 (1993).

[12] E. Toussaere, "Polymer electrooptiques pour l'optique non lineare characterisation optique et modeles statisques," Ph. D. dissertation (University of Paris, Paris, Paris, 1993).

[13] A. M. Stoneham, "Shapes of inhomogeneously broadened resonance lines in solids," Rev. Mod. Phys. **41**, 82–108 (1969).

[14] M. Abramowitz and I. E. Stegun, eds., *Handbook of Mathematical Functions* (U. S. Government Printing Office, Washington, D.C., 1972).

[15] A. Otomo, "Second order optical nonlinearties and wave mixing devices in poled polymer waveguides," Ph. D. dissertation (University of Central Florida, Orlando, 1995).

[16] R. J. Kruhlak and M. G. Kuzyk, "Side-illumination fluorescence spectroscopy. I. Principles," J. Opt. Soc. Am. B **16**, 1749–1755 (1999).

[17] J. H. Andrews, J. D. V. Karydarov, K. D. Singer, D. L. Hull, and K. C. Chuang, "Characterization of excited states of centrosymmetric and noncentrosymmetric squaraines by third-harmonic spectral dispersion," J. Opt. Soc. B **12**, 2360–2371 (1995).

[18] T. Kaino, "Absorption losses of low loss plastic optical fibers," Jpn. J. Appl. Phys. **24**, 1661–65 (1985).

[19] M. G. Kuzyk and C. Poga. "Quadratic electro-optics of guest-host polymers,". in J. Zyss, ed., *Molecular Nonlinear Optics: Materials, Physics, and Devices*, pages 299–336. Academic, San Diego, CA, (1993).

[20] D. W. Garvey, K. Zimmerman, P. Young, J. Tostenrude, J. S. Townsend, Z. Zhou, M. Lobel, M. Dayton, R. Wittorf, and M. G. Kuzyk, "Single-mode nonlinear-optical polymer fibers," J. Opt. Soc. Am. B **13**, 2017–23 (1996).

[21] R. J. Kruhlak, J. Young, and M. G. Kuzyk, "Loss and correlation measurements in squaraine-doped nonlinear polymer optical fibers," SPIE Proc. **3147**, 118–28 (1997).

[22] Bruce J. Berne and Robert Pecora, *Dynamic Light Scattering* (John Wiley & Sons, Inc., New York, 1976).

[23] G. Olbrechts, E. J. H. Put, D. Van Steenwinckel, K. Clays, A. Persoons, C. Samyn, and N. Matsuda, "Study of domain formation and relaxation in thin polymeric films by femtosecond hyper-Rayleigh scattering," J. Opt. Soc. Am. B **15**, 369–78 (1998).

[24] W. J. Tomlinson, "Phase holograms in photochromic materials," Appl. Opt. **11**, 823–831 (1972).

[25] I. P. Kaminow, L. W. Stulz, E. A. Chandross, and C. A. Pryde, "Photobleaching of Organic Laser Dyes in Solid Matrices," Appl. Opt. **11**, 1563–7 (1972).

Chapter 3

Sample Preparation

For the past 10 years the Nonlinear Optics Laboratory at Washington State University has been studying nonlinear dye-doped polymer optical fibers [1, 2, 3] and dye-doped polymer electrooptic thin films [4, 5]. The thin film and fiber fabrication methods have been slowly improved through trial and error. In this chapter we summarize electrooptic thin film and multimode core fiber fabrication processes.

3.1 Thin Film Fabrication

3.1.1 Electrooptic ITO slides

Standard 5 cm × 7.5 cm glass slides, where one surface is coated with Indium Tin Oxide (ITO), are used as substrates for the quadratic electrooptic thin film experiments to be described in Section 4.4. The ITO surface, which acts as an optically transparent electrode, is cleaned and etched before the thin-film solution is spin-coated on the ITO-electrode surface of the slide. The cleaning procedure has three steps [4]. Initially, the ITO side of the glass slide is wiped clean with acetone to remove trace organic substances. The slide is then submersed in a 10% (by volume) NaOH solution at 55 °C for three minutes. Finally, the excess base is removed with a one minute soak in deionized water.

Once the slides have been cleaned, the ITO surface is patterned into three strips as shown in Figure 3.1. These strips are created with 1.25 cm wide, acid resistant,

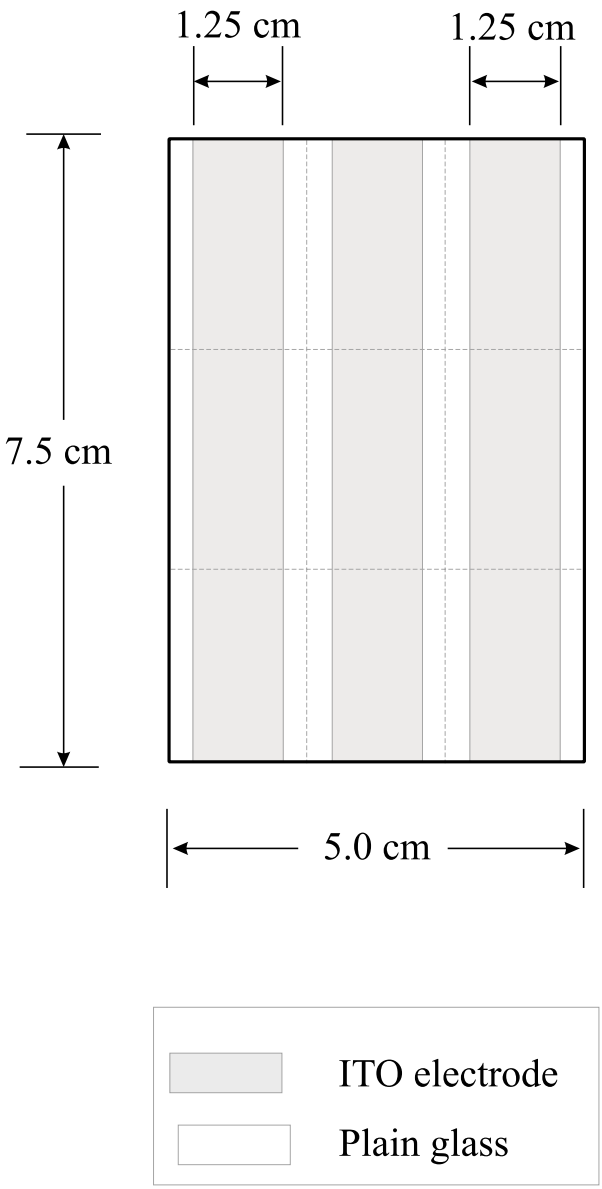

Fig. 3.1: ITO electrode pattern on glass slide.

laboratory marking tape, which is wrapped lengthwise around the slide (Two layers on the electrode side, and one layer on the opposite side.). Once taped the slide is submersed in a acidic solution (50 % concentrated HCl, 8 % concentrated HNO_3, and 46 % deionized H_20) for 5-6 minutes to etch away the exposed ITO. After etching the slide is soaked for one minute to remove excess acid and the taped is removed. Leftover glue is removed with Isopropyl Alcohol. The slides are checked with an Ohmmeter to assure that each electrode is continuous and the ITO has been completely removed between the electrodes.

3.1.2 Thin film solution

With the slides stored in a clean dry area, the dye-doped polymer thin film solution is prepared. The dyes are shown in Figures 3.5 and 3.6, and the polymer is medium molecular weight solid PMMA. Typically the thin film solution is prepared with 85 % solvents and 15 % solids (dye and polymer) to get a reasonable viscosity. Of the 85 % solvent, 67 % is propylene glycol methyl ether acetate which dissolves the dye, and 33 % γ-butyrolactone which dissolves the PMMA. For a 1 % by weight (wt.) solution of dye to polymer the following recipe is used:

85 % solvents:	67 % propylene glycol methyl ether acetate (PGMEA)
	33 % γ-butyrolactone
15 % solids:	1 % dye
	99 % poly(methyl methacrylate) (PMMA),

where the dye is added to the PGMEA and stirred for 5 minutes. Then the γ-butyrolactone is added, and finally the PMMA solid is stirred into solution. It should be noted that the mass of dye can be varied to any amount below the saturation concentration as long as the additional PMMA mass makes the total weight of the solids equal to 15 % of the total mass of the solution.

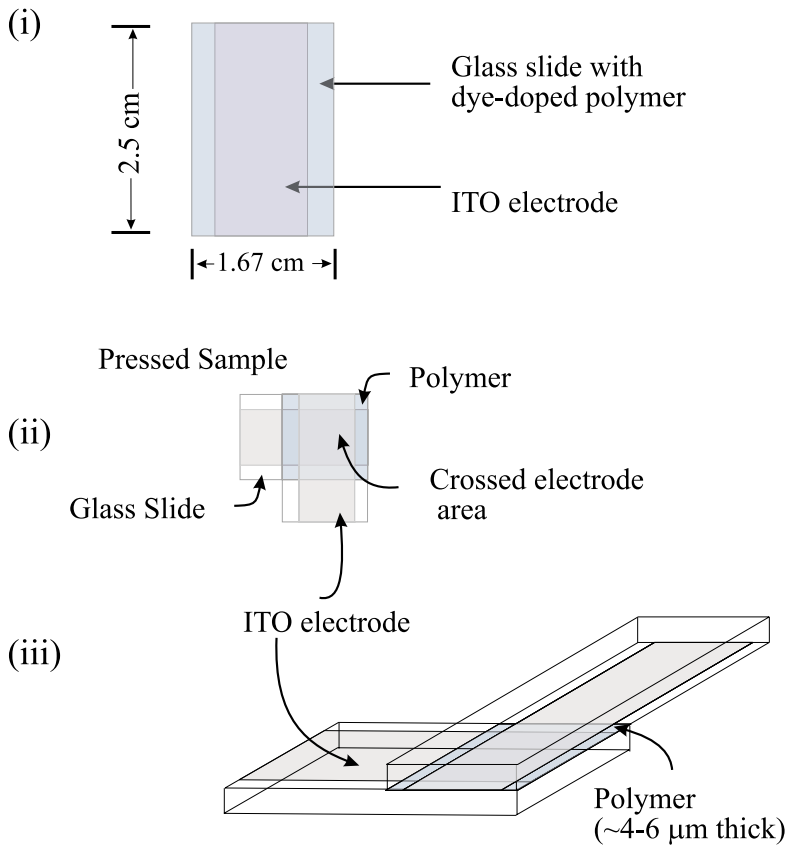

Fig. 3.2: Electrooptic thin film.

3.1.3 Electrooptic thin film

After the dye-doped polymer mixture is stirred at room temperature for a minimum of 8 hours to ensure that all solids go into solution, it is spin-coated onto the ITO surface of the substrate (Figure 3.1) at 990–1010 rpm for 30 seconds. This angular velocity creates film thicknesses of 2–3 μm [5]. Any excess solvent is evaporated by placing the slide in a 95 °C oven for approximately 20 minutes.

The full-size ITO slide is cut into 9 pieces (along the dashed lines in Figure 3.1), and half the thin film, on each piece, is removed to expose the ITO electrode. By pressing the thin film surfaces of two pieces together, at right angles to each other, we create a single electrooptic sample as shown in Figure 3.2. Thus one slide makes 4 electrooptic samples with one piece as a reserve. The perpendicular orientation of the two pieces allows the sample to be connected to the AC voltage source with standard alligator clips.

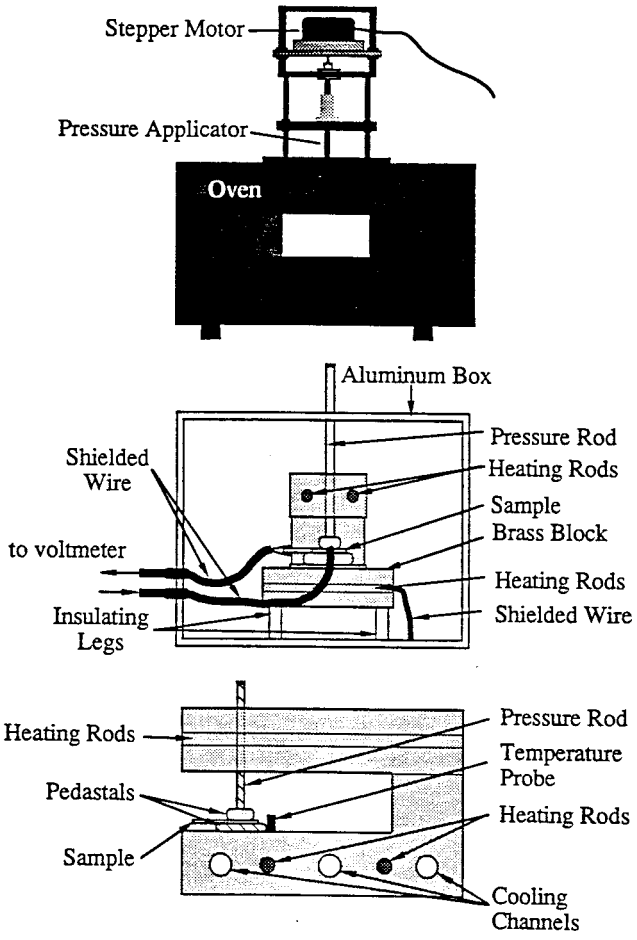

Fig. 3.3: Oven used to squeeze electrooptic sample.

Figure 3.3 shows the oven, built by Kurt Zimmerman, that is used to squeeze the electrooptic samples [4, 6]. A hand-screw is used to apply a pressure of about 50-60 lbs at room temperature. The temperature is ramped from room temperature to 110 °C over 15 minutes, where it is held for 1 hour. As the temperature increases, the pressure increases to about 120-140 lbs due to the expansion of the glass substrate causing the two layers of film to fuse. Subsequently, the temperature is decreased to room temperature over a 15 minute interval. The full temperature cycle is repeated at atmospheric pressure to relieve internal stresses which may make the film isotropic. A more detailed description of the squeezing procedure and the time dependence of the temperature, and pressure on the sample can be seen in the literature [7, 4].

3.2 Fiber Fabrication

In this section we describe the procedures used to fabricate dye-doped core fibers. We neglected core-cladding fibers because we measured only core fibers in this thesis. A complete description of the fiber fabrication process, which includes core-cladding fibers, can be found in the literature [3].

3.2.1 Preparation of monomer

The methyl(methacrylate) (MMA) and/or styrene monomers can contain up to 5-10% of their volume in impurities – typically toluene – when shipped from the supplier (Aldrich Chemical Co.). To make optical quality polymer (poly(methyl methacrylate) (PMMA) or poly(styrene) (PS)), we vacuum distill the monomer [8] before polymerization. The distillation is done using the apparatus shown in Figure 3.4.

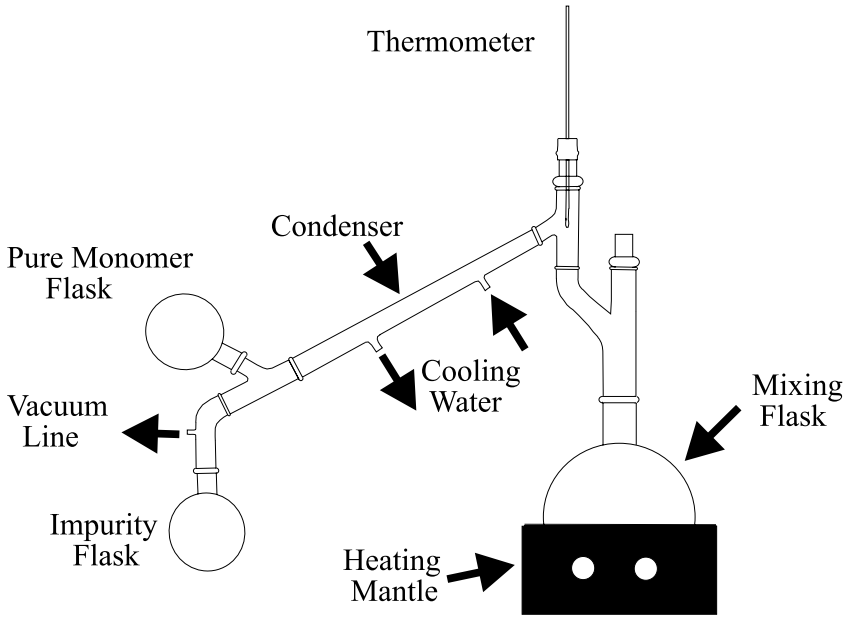

Fig. 3.4: Vacuum distillation apparatus for purifying liquid monomer.

Monomer is stirred over about 1% by weight of calcium hydride, CaH_2, in the mixing flask. The CaH_2 removes the polymerization inhibitor, which keeps the monomer from polymerizing during storage, and the absorbed water. By removing the water, we decrease the near IR attenuation in the polymers [9]. Above the mixing flask, a Claisen joint

prevents the undistilled monomer from bubbling into the condenser. The condenser allows cold water to flow through an outer region which is adjacent to the inner, distillation region. The flowing water cools the vapor more quickly than air which reduces the likely hood of an explosion. At the mouth of the condenser, the temperature of the vapor is monitored by a thermometer. The condensed vapor is then collected by one of two flasks at the tail of the condenser. Initially, the pure monomer flask is held upright so the low boiling point impurities collect in the impurity flask. The entire distillation region is under vacuum which includes both collection flasks, the inner region of the condenser, the Claisen joint and the mixing flask. This reduces the distillation time by reducing the boiling point of the monomer. Although the boiling point of the monomer is significantly reduced a heating mantle is still necessary to induce a constant boil – $\sim$ 27-32 ^{o}C. The joints below the mouth of the condenser are sealed using Teflon sleeves to prevent contamination of the pure monomer by vacuum grease, even though it reduces the vacuum slightly. All remaining joints are sealed using vacuum grease and every joint is solidified using elastic bands.

After the vacuum is applied with a mechanical roughing pump, 30 minutes is allowed for the CaH_2 to completely react with the water and polymerization inhibitor in the monomer. Raising the temperature of the heating mantle brings the contents of the mixing flask to a slow, steady boil – about one drop per second into the impurity flask. The boiling point depends on the degree of vacuum achieved but is typically about 27-32 ^{o}C at the mouth of the condenser. This initial boiling point is of the low boiling point impurities and is constant for about 5-10 % of the volume of the monomer.

Once these impurities have been distilled into the impurity flask, the distillation rate slows or stops. The temperature at the mouth of the condenser typically needs to be raised 4-6 °C to return to a one drop per second distillation rate. The elevation in temperature indicates that the monomer is distilling. About 10 minutes is allowed for the temperature to stabilize and the impurities to be flushed past the opening to the pure monomer flask. The pure monomer flask, which is wrapped in aluminum foil to prevent ultraviolet-induced polymerization, is then rotated below the tail of the condenser, while the impurity flask is held in place, to collect the pure monomer. The distillation is

continued until about 10% of the original amount of monomer remains in the mixing flask to prevent contamination from higher boiling point impurities and excess CaH_2. After the mantle has been turned off and the apparatus has to cooled to room temperature, the pure monomer flask is removed and sealed with a stopper and parafilm. The purified monomer should be used as soon as possible but when storage is necessary, the purified monomer is stored in a refrigerator wrapped in aluminum foil.

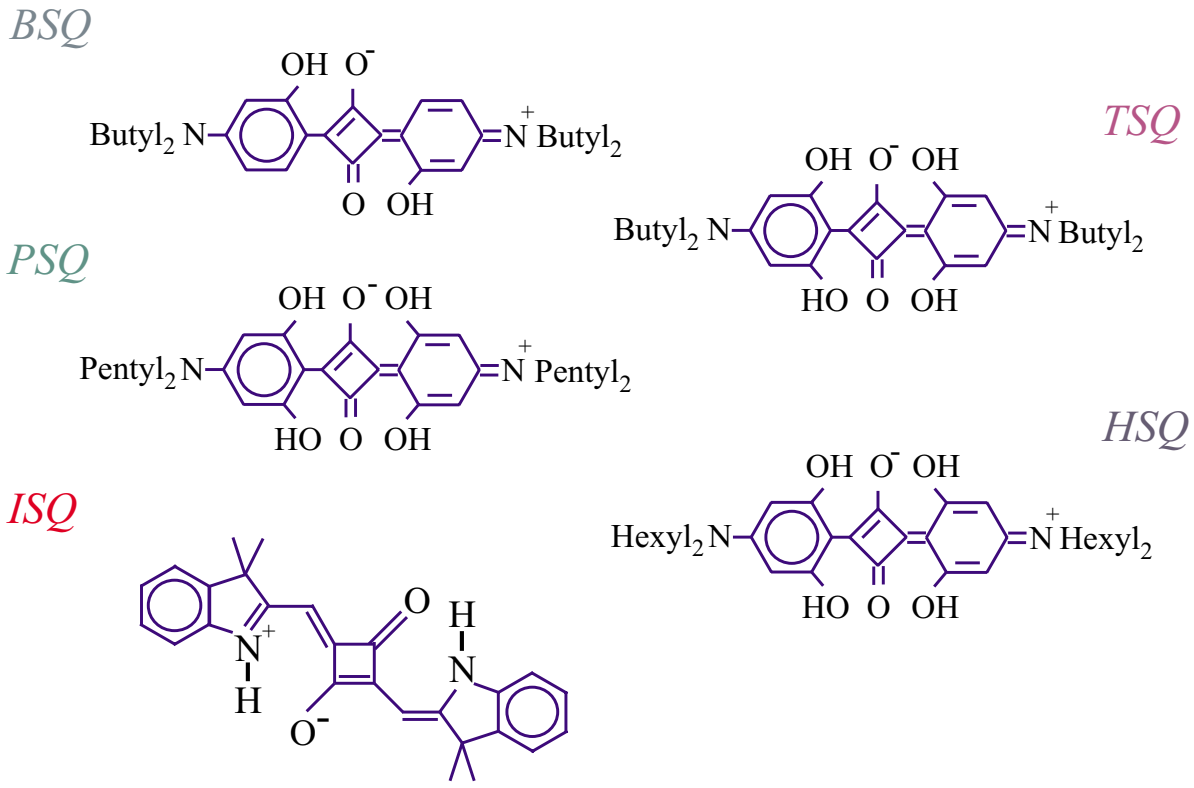

Fig. 3.5: Structures of squaraine dye molecules used as dopants in core material.

3.2.2 Dye-doped polymer fabrication

Once we have purified monomer, we are ready to make the solutions that become the dye-doped core preforms. The structures of the dye molecules are shown in Figures 3.5 and 3.6. Dye is massed on an electronic balance and then placed in a 20 ml scintillation vial with a small stir bar. The volume of monomer is measured with a graduated cylinder and added to the scintillation vial. Both the mass of the dye and the volume of monomer

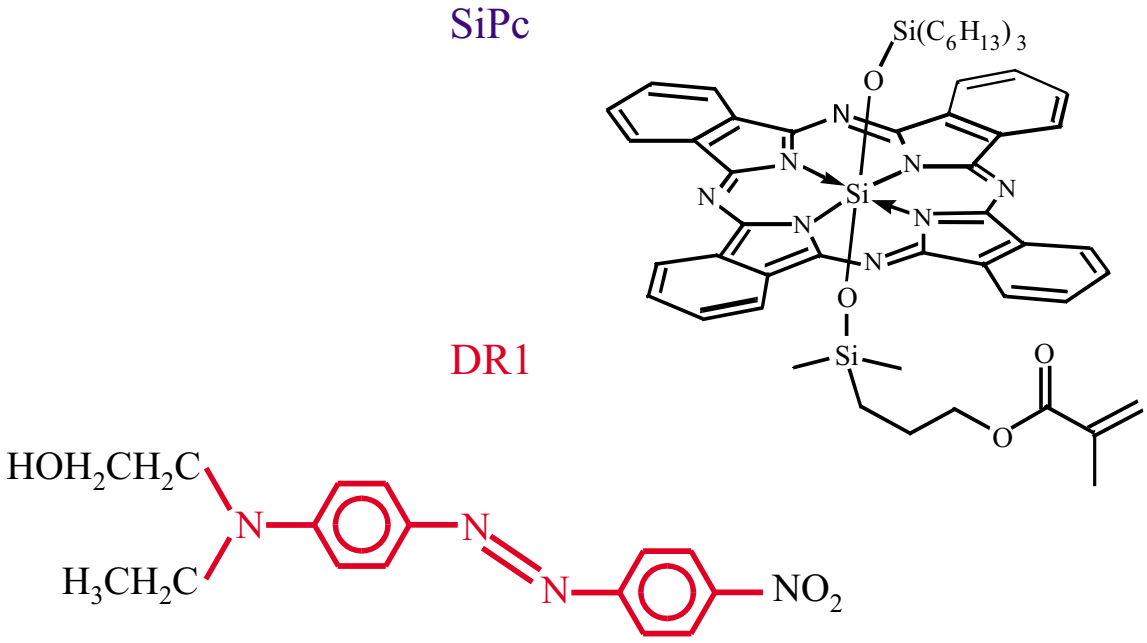

Fig. 3.6: Structures of other dye molecules used as dopants in core material.

are determined by the concentration needed; however, 15 cm^3 of monomer is typically used so the solution fits in a single test tube. Table 3.1 shows the maximum solubilities for several dyes at 25 °C and at 60 °C. The solution is either sonicated in a water bath for 30 minutes or stirred for 8 hours on a hot plate at the desired temperature to insure as homogeneous a mixture as possible. Typically, the concentration must be near 5×10^{18} cm^3 for step-index single mode polymer fibers that are compatible with glass fiber technology [3].

After mixing, polymerization initiator and chain transfer agent are added to the solution. Tert-butyl peroxide is used to initiate the polymerization reaction because it causes the least amount of bubbling during polymerization [3], and about 3.3 μl is added for every 1 ml of solution. To limit the polymerization reaction (and therefore the chain length) for the desired mechanical properties (flexibility, and low glass transition temperature) butanethiol is also added to the mixture at about 3.3 μl for every 1 ml of solution. This limits the average polymer molecular weight to about 70 000 g/mol [3]. If the molecular weight is much smaller, the preform will be very brittle and melt in the fiber drawing tower; and if the molecular weight is much larger, the glass transition

Table 3.1: Maximum dye solubilities in PMMA.

Maximum Solubility in PMMA						
Dye	M.W.	25 °C		60 °C		
	(g/mol)	% by weight	N (10^{18}cm^{-3})	% by weight	N (10^{18}cm^{-3})	Ref.
ISQ	372.5	0.26	4.0	0.52	7.9	†
BSQ	520.711	0.81	8.8	1.9	20.1	†
TSQ	552.709	0.09	0.9	0.32	3.3	†
PSQ	608.817	0.12	1.1	0.42	4.0	†
HSQ	664.924	0.15	1.3	0.52	5.7	†
DR1	314.343	1.17	26.4	2.91	66.0	[3]
SiPc	1041.53	>1	>6	–	–	†

† – this work

temperature will be too high for the dye molecules to survive the drawing process.

3.2.3 Core preform fabrication

Once the initiator and chain transfer agent have been added to the solution, it is filtered through a 0.2 micron syringe filter into a 125 x 16 mm test tube to remove any undissolved dye, reduce dye aggregation in the polymerization process, and remove potential large scattering centers in the solid polymer. After loosely capping the test tube to allow trapped gas to escape, it is placed in an aluminum block with several other test tubes, which is placed in a 95 °C oven for 24-36 hours. The aluminum block insures uniform heating and prevents the oven from being damaged in case of an explosion, which can occur if to cap is completely tightened.

Once the solution has fully polymerized the test tube is removed from the oven and cooled. The tubes are then broken and the dye-doped polymer cylinders, which we call core preforms, are placed on an aluminum rack in a 95 °C oven for five days to anneal and degas.

After the core preforms have been degassed they are placed into a rail squeezer (Figure 3.7). They are heated to 120 °C and compressed from the ends to force excess gas out of the preform, thus removing any small bubbles that formed during the polymerization process. Typically, three or four preforms are used to fill one squeezer, and the remaining longitudinal space can be filled with aluminum plugs of similar diameter. The preform is kept at 120 °C for approximately ten days. The longitudinal pressure is increased daily until there is no additional compression.

When the compression cycle is completed, the new core preform is removed from the squeezer. This preform is cut into the original core preforms and a fine outer layer is lathed off each preform. This layer is typically on the order of 100 μm but depends on the specific preform. It has been found that removing a thin outer layer from the preform improves the surface of the core fibers. There are a couple reasons for the improvement. The outer layer of a core preform occasionally contains small air bubbles that were not completely removed during the squeezing process and the surface can be slightly contaminated from the surface of the squeezer. A high quality surface on the core preform is important to reduce scattering losses in the step-index (core-cladding) fibers. These three or four core preforms are annealed at 95 °C to remove any stresses induced in the squeezing process. After annealing for several days, they are ready to be

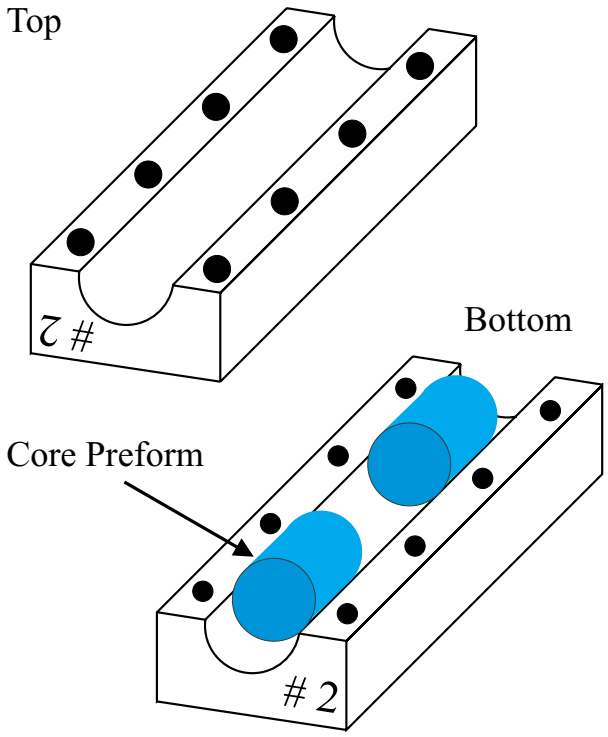

Fig. 3.7: Rail-squeezer used to compress preform.

drawn into core fibers.

(It should be noted that all core preforms did not have a thin outer layer removed after the compression cycle was completed. Only the most recent core fibers were made with this technique. The TSQ/PMMA, SiPc/PMMA, and the ISQ/PMMA fibers discussed in Sections 5.2.3.4 and 5.6.0.4 were made with core preforms that had the outer layer removed. We try to alert the reader in either case. If the method is not mentioned, the reader should assume that it is drawn from a core preform that doe not have an outer layer removed.)

3.2.4 Preform slice preparation

Occasionally, preforms or parts of preforms are chosen to be sliced into disks, using a lathe, for transmission and emission spectroscopy measurements (Section 4.1 and 4.2). This also allows us to determine if all the dye is dissolving in the monomer and helps to determine the maximum concentration of dye that can be dissolved at a specific temperature.

These slices are sequentially polished with 5 μm, and 3 μm lapping film in a figure 8 motion to insure a uniform surface. The slices are then polished with 1 μm, and 0.3 μm paste using a drum polisher until they are of high optical quality. It should be noted that the surfaces are free of scratches but are not always parallel because of inaccuracies introduced when using the lathe to make slices between 300 and 700 μm thick. Due to the wedge-shaped samples, a precise measurement of the average width is difficult and is the main inaccuracy in the transmission spectroscopy experiment.

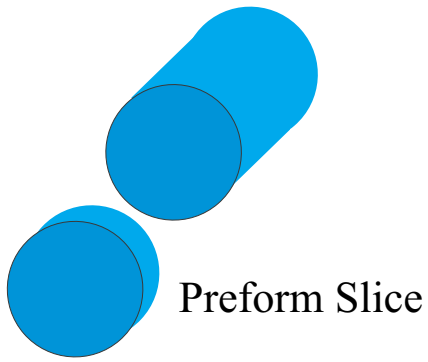

Fig. 3.8: Preform slice used for transmission spectroscopy experiments.

3.2.5 Core fiber fabrication

A schematic of the tower used to draw preforms into fiber is shown in Figure 3.9. At WSU, the fiber tower is in the common vertical configuration; however, horizontal towers are also in use [10]. The fundamental elements in the fiber tower are a stepper-motor-controlled linear translation stage, an oven for heating the polymer preform, and a stepper-motor-controlled rotation stage. In addition, a collet is mounted to an X-Y-Z micrometer stage which is attached to the linear translation stage at the top of the tower. The collet holds the polymer preform and the X-Y-Z micrometer stage is used to precisely position the preform in the glass oven. This is critical because the glass in fragile and the preform can not touch the walls of the oven at any time during the drawing process. A tension gauge is also placed between the oven and the take-up spool.

The stepper-motor-driven linear translation stage controls the rate at which the preform is fed into the oven, v_f, and the stepper-motor-driven rotation stage controls the rate at which the core fiber is removed from the oven, v_t. Using conservation of volume it is easy to show that the diameter of the fiber, d_f is related to the diameter of the preform, d_p as follows:

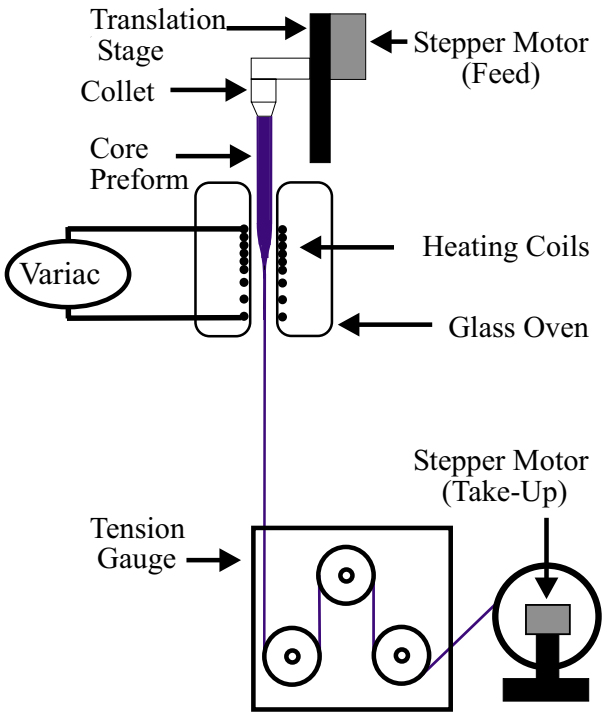

Fig. 3.9: Fiber drawing tower with a core fiber.

$$d_f = d_p \sqrt{\frac{v_f}{v_t}}, \tag{3.1}$$

because the polymer much leave the oven at the same rate that it enters. It should be noted that v_t is the velocity measured at a point on the circumference of the take up spool [3]. Garvey and co-workers showed that Equation (3.1) is valid once the drawing process reaches equilibrium [2].

Figure 3.10 shows the cross-section of the transparent glass oven. Inside the oven is an inner column which isolates the polymer from the heating element. This pillar has 14 coils of Nichrome heating wire (Watlow# CN-62P) wrapped about its exterior. The first seven coils are wrapped with no space between them and defines the heating zone of the oven (Note that there is an insulating coating on the exterior of the coils.).

Below the heating zone is the warm down zone which is defined by the second set of seven coils. These heating coils are wrapped so that the spacing between wires gradually increases from 1 cm at the top of the zone to 3 cm at the bottom of the zone. This creates a gradual decrease in the air temperature which has been found to eliminate induced stresses that would be caused by an abrupt temperature decrease [11].

The voltage across the entire heating element is controlled by a Variac and is proportional to the air temperature in the heating zone. Through trial and error, Garvey and co-workers determined that 57 V across the heating coils created the optimum air temperature for 5 cm diameter PMMA preforms [2] with a molecular weight of about 7×10^4 g/mol. The tension at this voltage is about 5×10^3 dynes which indicates that the fiber is not being pulled hard enough to align all the polymer chains [3].

Figure 3.10 shows the air (red) and polymer (blue) temperature profiles in the glass oven. The air temperature is roughly constant in the heating zone and gradually decreases from the top to bottom of the warm down zone. However, the temperature at the center of the polymer is not constant in the heating region.

The polymer temperature was determined by polymerizing a thermistor in the center of a 5 cm diameter preform, and then drawing the preform with the heating voltage set at 57 V, a feed speed of 160 μm/s, and a take up velocity of 4.0 cm/s until the fiber broke [2]. In the region where the preform diameter transitions to the fiber diameter, the temperature was measured to be 240 °C which is much higher than the air temperature in the heating region ($\sim$ 100 °C) and suggests that the polymer is heated through the

radiative process.

Typically, the core fiber is drawn to a 790 μm diameter for use in step-index (core-cladding) fibers which are described in the literature [2, 3]. However, we have developed a novel method for measuring the loss in core fibers called side-illumination fluorescence (SIF). In order to measure the loss as a function of the core fiber diameter, we have made core fibers which range from 150 μm to 790 μm by varying both v_f and v_t (see Equation (3.1)) during the drawing process.

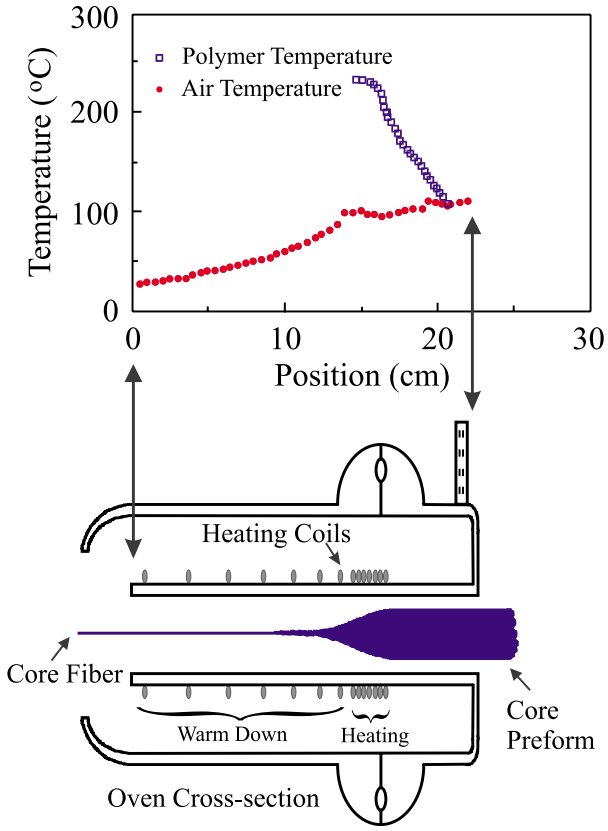

Fig. 3.10: Temperature profile and oven cross section.

Once the drawing process is complete the core fiber is removed from the spool and cut into 20 cm sections. These sections are bagged and stored in an evacuated bell jar covered with a dark cloth to prevent material degradation due to oxygen and ultraviolet light. The main reason for cutting the core fiber into sections is to keep it straight. When core fiber is stored as a coil, it relaxes into that shape by creep making it difficult to straighten for fabricating step-index fibers or the side-illumination experiment.

Bibliography

[1] D. W. Garvey, Q. Li, M. G. Kuzyk, C. W. Dirk, and S. Martinez, "Sagnac interferometric intensity-dependent refractive-index measurements of polymer optical fiber," Opt. Lett. **21**, 104–06 (1995).

[2] D. W. Garvey, K. Zimmerman, P. Young, J. Tostenrude, J. S. Townsend, Z. Zhou, M. Lobel, M. Dayton, R. Wittorf, and M. G. Kuzyk, "Single-mode nonlinear-optical polymer fibers," J. Opt. Soc. Am. B **13**, 2017–23 (1996).

[3] D. W. Garvey, "Nonlinear optics in polymer fibers," Ph. D. dissertation (Washington State University, Pullman, WA, 1999).

[4] C. Poga, "Characterization of the excited states of a squaraine molecule with quadratic electroabsorption spectroscopy," Ph. D. dissertation (Washington State University, Pullman, WA, 1994).

[5] K. S. Mathis, "Studies on the nature of excited states of squaraines using quadratic electroabsorption spectroscopy and essential state analysis," Master's Thesis (Washington State University, Pullman, WA, 1995).

[6] K. S. Mathis, M. G. Kuzyk, C. W. Dirk, A. Tan, S. Martinez, and G. Gampos, "Mechanisms of the nonlinear optical properties of squarainne dyes in poly(methyl methacrylate) polymer," J. Opt. Soc. Am. B **15**, 871–883 (1998).

[7] K. Zimmerman, F. Ghebremichael, M. G. Kuzyk, and C. W. Dirk, "Electric-field-induced polarization current studies in guest-host polymers," J. Appl. Phys. **75**, 1267–85 (1994).

[8] T. Kaino, M. Fujiki, S. Nara, and S. Oikawa Appl. Opt. **20**, 2886 (1981).

[9] P. Avakian, W. Y. Hsu, P. Meakin, and H.L. Snyder J. Polymer Sci. – Polymer Ed. **22**, 1607 (1984).

[10] G. D. Peng, P. L. Chu, Z. Xiong, T. W. Whitbread, and R. P. Chaplin, "Dye-doped step-index polymer optical fiber for broadband optical amplification," J. Lightwave Technol. **14**, 2215–23 (1996).

[11] D. Bosc and C. Toinen Polym. Compos. **14**, 410 (1993).

Chapter 4

Experiments

The experiments that were performed in this research project are described in this chapter. Since there are several experiments, the linear optical experiments will be described first. The linear experiments are conducted to develop a fundamental understanding of the linear optical properties of the polymer systems, which can be used to understand nonlinear phenomena. Transmission and emission spectroscopy are used to characterize the excited state behavior of bulk and thin film samples of dye-doped polymer, and side-illumination fluorescence (SIF) spectroscopy [1, 2] is used to determine excited state characteristics in dye-doped polymer fibers. Because the side-illumination fluorescence experiment is novel and produced the majority of the experimental data for this work, it will be explained in the most detail. Once the SIF experiment has been discussed, the quadratic electroabsorption (QEA) experiment [3, 4], which is used to determine imaginary part of the third-order susceptibility (see Section 2.6.2), will be discussed. The details of the transverse two-photon absorption experiment, discussed in the introduction, can be found in Appendix D. Finally, a brief description of the photosensitivity experiments will be presented.

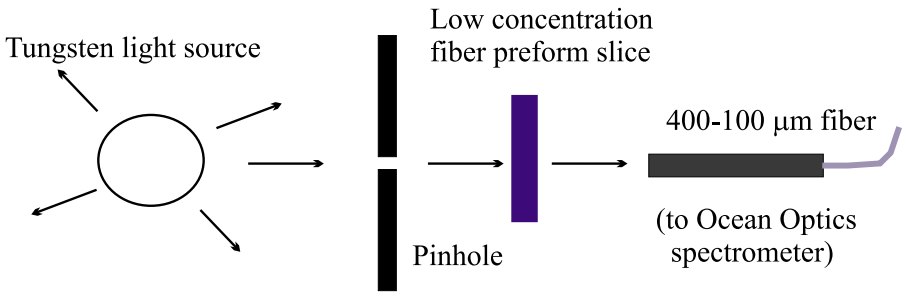

Fig. 4.1: Fiber preform slice and thin film transmission experiment.

4.1 Transmission Spectroscopy

Transmission spectroscopy is performed on low concentration, bulk samples of dye-doped polymer and high concentration dye-doped thin film samples to determine the linear resonance absorption of the molecules. This information is used to determine which wavelengths of incident light will generate a fluorescence spectrum in the dye-doped core fibers and characterize one-photon states which may contribute to the imaginary part of the third-order response, $\chi_I^{(3)}$, in the quadratic electroabsorption experiment (to be described in Section 4.4).

Transmission measurements on the preform slices are performed with a tungsten light source and the Ocean Optics 2000 spectrometer as the detector. A pinhole is placed before the sample, as shown in Figure 4.1, to reduce stray light from entering the spectrometer. To minimize the uncertainty due to the sample width, several locations in the preform are probed and an average transmission is determined. The transmission through the sample is referenced to the spectrum of the light source. The absorption coefficient, $\alpha(\lambda)$, is calculated from the ratio of the trans-

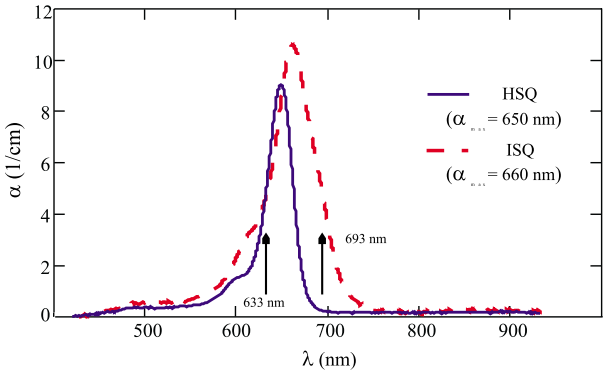

Fig. 4.2: Resonant linear absorption spectra of HSQ, and ISQ (wt.% $\approx 10^{-4}$ for both dyes)

mission through the sample, $I_t(\lambda)$, to the emission of the light source, $I_i(\lambda)$ as follows,

$$\alpha(\lambda) = -\frac{1}{d}\ln\left(\frac{I_t(\lambda)}{I_i(\lambda)}\right), \tag{4.1}$$

where d is the thickness of the sample.

Figure 4.2 shows typical absorption spectra of two squaraine-doped preform slices. The arrows indicate the wavelengths of the He/Ne laser and the 693 nm laser diode which are later used to excite a fluorescence spectrum in the dye-doped fibers for the majority of the side-illumination fluorescence experiments.

4.2 Emission Spectroscopy

As a compliment to the transmission spectroscopy experiment, an emission spectroscopy experiment can be performed. This experiment can be performed in the transmission geometry or the reflection geometry. Figure 4.1 which shows the transmission spectroscopy experiment for bulk or thin film samples can also be used for the emission spectroscopy experiment if the white light source is replaced by a laser light source. However, the sample must be very optically dense at the incident wavelength so that the laser line does not overwhelm the fluorescence signal.

It is more practical to measure the emission from a bulk sample in a reflection geometry as shown in Figure 4.3. In this experiment, a laser with a small beam diameter (see Appendix B) illuminates a bulk or thin film sample at an oblique angle. The detector is placed just far enough from the sample that it does not block the incident light or collect the reflected light. Typically, this distance was about half a cen-

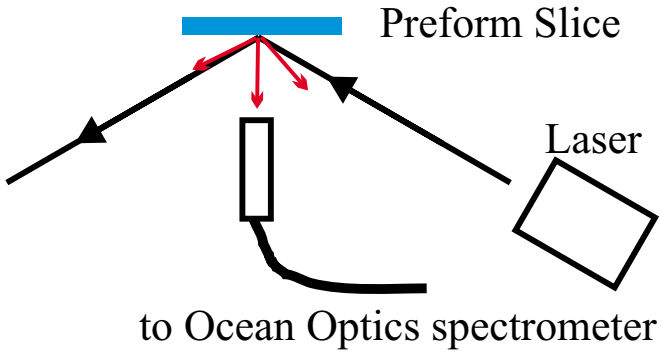

Fig. 4.3: Reflection geometry for measuring the fluorescence spectrum.

timeter but depends on the roughness of the surface. The face of the detector should also be normal to the sample so that the influence of scattered laser light is minimized. This only increases the sensitivity since the fluorescence should be emitted isotropically from the illumination position. Figure 4.4a shows the fluorescence generated by a 4 μm thin

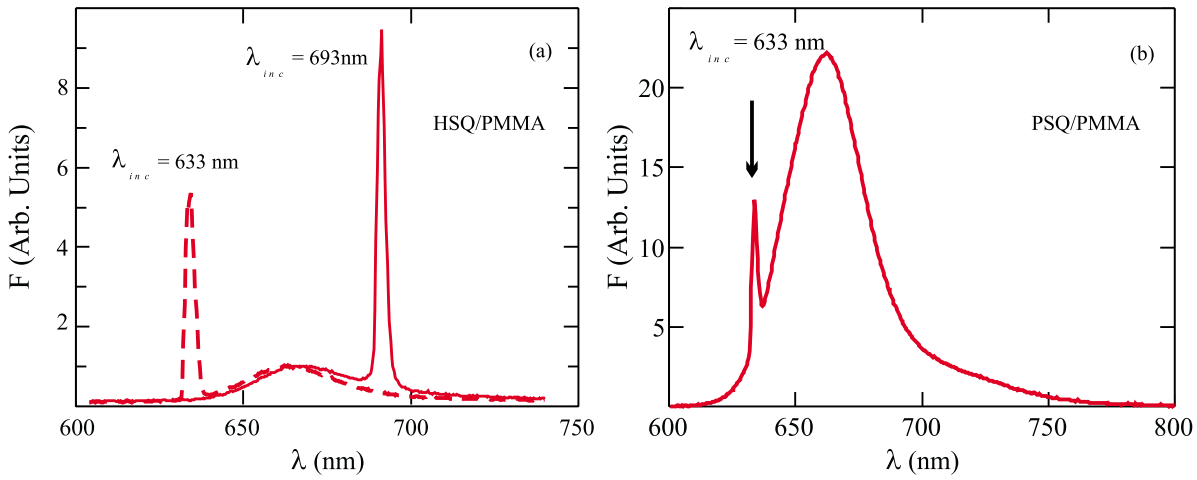

Fig. 4.4: (a)Reflected fluorescence from an HSQ/PMMA thin film for incident wavelengths of 633 nm and 693 nm, (b) Reflected fluorescence from a PSQ/PMMA preform slice for an incident wavelength of 633 nm

film of HSQ/PMMA in a reflection geometry. However, the laser lines at 633 nm and 693 nm overwhelm the fluorescence signal, making quantitative analysis difficult without precision filters. Note that because of thermal excitations at room temperature, the fluorescence spectrum peaks at about 665 nm for both incident wavelengths.

Improved results can be obtained for dye-doped preforms that are prepared using the technique described in Section 3.2.4. Figure 4.4b is an example of the emission spectrum from a PSQ-doped preform slice. Notice that the emission is much larger than the reflected laser wavelength. The improved result for dye-doped preforms is most likely due to the incident light encountering a smoother interface in comparison to the thin film sample. Thus there is minimal scattered laser light away from the reflected angle.

The larger fluorescence intensity is also caused by the thicker preform sample. If the fluorescence is generated in a "skin depth" which is deeper than the thickness of the thin film, then the fluorescence intensity from a thin film is smaller than from the thicker

preform slices.

Unfortunately, it was not known that the preform slices were a much better medium than thin films for characterizing the emission spectrum before the majority of the side-illumination fluorescence (Section 4.3) results were published [2]. However, the knowledge gained through emission spectroscopy experiments on dye-doped preforms in a reflection geometry will only help in the analysis of future side-illumination fluorescence results. Furthermore, SIF gives more information, particularly when controlled self-absorption of the emission is utilized.

4.3 Side-Illumination Fluorescence Spectroscopy

The previous two sections described the transmission and emission spectroscopy experiments which are typically performed on bulk or thin film sample of dye-doped polymers. However, we are mainly interested in the emission and transmission characteristics of dye-doped fibers. In order to characterize the emission and transmission characteristics of dye-doped fibers, a novel experiment was devised. This experiment is called side-illumination fluorescence (SIF) spectroscopy.

The side-illumination light source is a continuous wave (cw) laser diode at 643 nm, 667 nm, or 693 nm (Figure 4.5), a Helium/Neon (He/Ne) laser at 633 nm, or an Argon Ion pump variable wavelength (cw) Ti:Sapphire laser (Figure 4.6). These wavelengths cover both sides of the absorption maxima for the squaraine dyes (Figure 4.2) and were chosen to generate a large fluorescence spectrum from the dyes. The majority of wavelengths used to excite the fluorescence are also absorbed more strongly than the fluorescence wavelengths because they fall closer to resonance absorption of the dye. This essentially eliminates any transmission of the incident wavelength so very low level fluorescence intensities can be studied.

Figure 4.5 represents the SIF experiment with the laser diode source. The source is mounted on a translation and vertical axis rotation stage, and the incident light is focused through a 4× microscope objective onto the side of a multimode dye-doped polymer optical fiber without cladding. By translating the source along the fiber, we

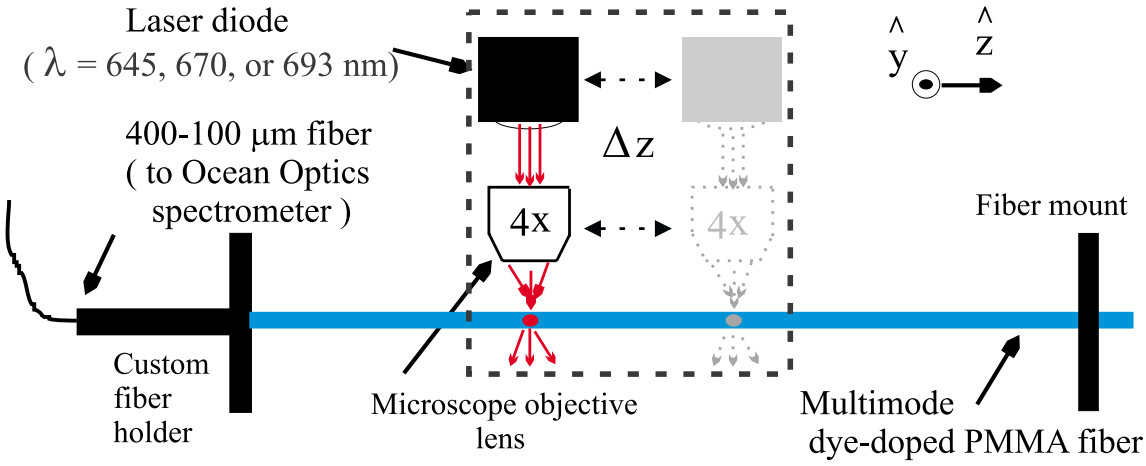

Fig. 4.5: Side-illumination fluorescence experiment with the light source on a translation stage.

measure the fluorescence signal at the end of the fiber with a spectrometer as a function of propagation distance. The laser source can be placed anywhere between grazing and normal incidence but is typically left at normal incidence when translating the source. By rotating the laser source about a fixed propagation distance, the angular dependence of the fluorescence generation can also be determined.

The angular dependent measurement is simple to perform but difficult to analyze because it is very difficult to determine the source distribution of the fluorescence inside the fiber due to an oblique excitation beam. For maximum room temperature concentration PSQ/PMMA core fibers, there is a small angular dependence to the side-illumination fluorescence intensity – about a 3 % increase in the maximum of the SIF spectrum between normal incidence and an incident angle of 20 °. Since the change was small it was determined that this measurement would not be pursued.

A lower concentration of dye dopant will cause the fluorescence to be generated in a larger portion of the cross-sectional area of the fiber. The angular dependence should increase in magnitude for lower concentration fibers because the cross-section for an oblique incident beam is larger than for a normally incident beam. Thus angular dependence measurements on low concentration fibers may reveal the nature of the fluorescence source distribution and should be considered in the future.

For a laser source that is fixed to the optical table like the He/Ne laser, the entire

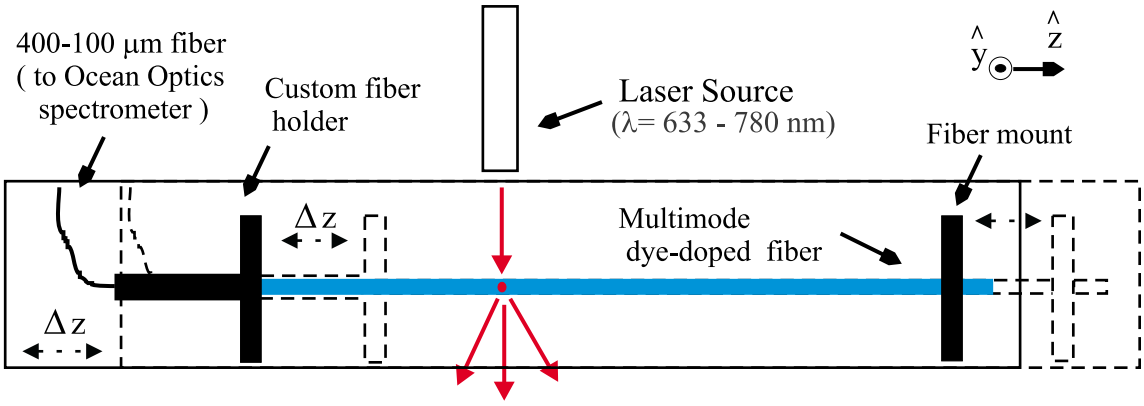

Fig. 4.6: Side-illumination fluorescence experiment with the fiber on a translation stage.

fiber system must be mounted on a translation stage. This configuration does not allow the angular dependence of the fluorescence to be measured, but is adaptable to high power pulsed laser sources that are capable of generating two-photon fluorescence. A microscope objective may or may not be necessary for this experiment because the fixed laser source may be sufficiently collimated to generate ample fluorescence.

A significant amount of the transverse illumination is diffracted about the fiber and can be used to level the fiber. For example, in the He/Ne SIF experiment, a long vertical card is placed opposite the laser. The diffraction pattern is monitored on the card as the propagation distance is varied across the range of interest. Fine adjustments are made to the height of the fiber with the rear vertical micrometer mount to keep the diffraction pattern constant. Starting will a completely level fiber is critical for the SIF experiment because it is assumed that the fluorescence generated at each illumination position is equivalent for the analysis in Section 5.6.

For high concentrations of dye there is little transmission through the fiber perpendicular to its axis so the remainder of light is either absorbed by the fiber or re-emitted as a red-shifted fluorescence spectrum. If the fluorescence signal is emitted within the critical angle of the fiber surface, it will travel down the core fiber and couple into a silica fiber which leads to an Ocean Optics 2000 spectrometer (see Figures 4.5 and 4.6.).

Before the quantitative experiments are performed with a new apparatus, the transmitted SIF spectrum should be measured as function of the incident intensity. This

measurement determines if the spectrometer is behaving linearly and if the core fiber is permanently modified by higher intensities. The addition of a glass slide between the laser source and the fiber can be used to reflect a small fraction of the laser light onto a photodiode or a power meter to monitor laser fluctuations. With the glass slide in place the SIF experiment shown in Figures 4.5 and 4.6 can be used to observe the fluorescence spectrum as a function of the incident intensity for any position in the fiber that generates sufficient transmitted fluorescence.

Figure 4.7 shows the transmitted SIF intensity for three wavelengths within the fluorescence band as a function of incident power (intensity) for an ISQ/P(MMA-d8) core fiber. The SIF intensity at each wavelength increases linearly as a function of the incident intensity. This is a general result for all the wavelengths in the fluorescence band that have an appreciable intensity even though only three are shown.

The slope is largest for 773 nm because it occurs at the maximum of the SIF spectrum shown in Figure 5.13, while 747 nm is to the left of the maximum where the absorption is larger and 805 nm is to the right of the maximum where the SIF quantum efficiency is lower. It should also be noted that the SIF intensity varies linearly over the same incident intensity range for all illumination positions not only 1.23 cm as shown in Figure 4.7.

When illuminated with 693 nm, the ISQ-doped fibers behave linearly as a function of incident intensity above 600 μW for short periods of time. Unfortunately, the nonlinearity is not due to a large third-order ($\chi^{(3)}$) response from a cw laser diode pump, but occurs because the dye is breaking down or changing confirmation, or the guest/host environment is changing due to diffusion. This will be explained in greater detail in Section 5.5. Figure 4.7 should be regarded as a lower limit on the linear behavior of the transmitted SIF intensity as a function of incident intensity because ISQ is the most sensitive squaraine dye in terms of optical breakdown.

Even though the other squaraines and SiPc are more stable than ISQ, highly concentrated fibers often require incident powers greater than 1 mW in order to generate a measurable SIF spectrum. Once an initial intensity dependence experiment has been performed to determine the linearity of the spectrometer it is no longer necessary to perform extensive intensity dependent experiments on each fiber to determine if the incident

intensity will modify the fiber. Instead, a position on the side of the fiber, outside of the region of interest, can be illuminated with the incident power of interest. Then the SIF spectrum can be observed for several minutes to several hours to determine if the incident intensity is causing the fiber to change. This is typically done for each new fiber at a position beyond the range of interest so that damage from an inappropriate choice of incident intensity does not affect future experiments on the fiber.

The method described above is valid for a stable laser sources like the cw He/Ne, Ti:Sapphire, or laser diodes where incident intensity is constant as a function of time so it is only necessary to record the incident intensity before and after the experiment. However, this method is not valid for short pulsed laser sources when there is a significant fluctuation in intensity from pulse to pulse. In this regime, the incident intensity should be monitored during all SIF experiments.

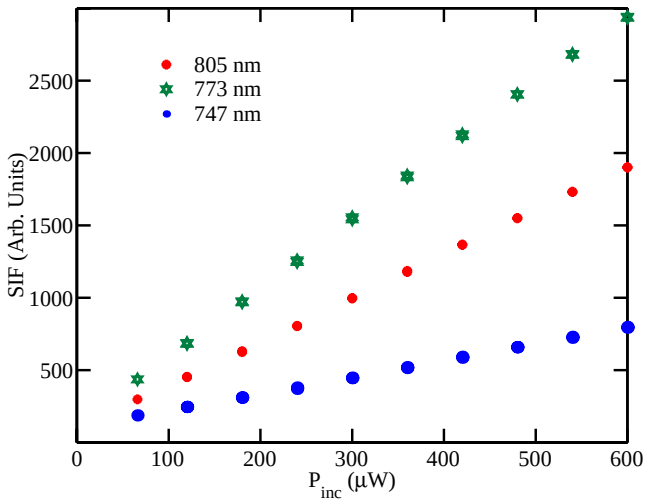

Fig. 4.7: SIF intensity from a multimode ISQ/P(MMA-d8) fiber for three wavelengths as a function of the incident power (λ_{inc} = 693 nm). The illumination position is 1.23 cm from the front face of the fiber.

As an added precaution we run a duplicate experiment whenever possible. For example, in a SIF experiment where the illumination position is varied, two experiments should be performed over the exact same section of fiber at the same incident intensity. If there is a significant deviation between the two data sets, then the incident intensity is most likely too high or the fiber was not securely positioned in the fiber chuck.

Figure 4.8 shows an example of how the demand for reproducibility prevents inaccurate results caused by an incident intensity that is too large. Initially, two low incident

intensity ($P_{inc} < 0.2$ mW) experiments were performed over the same section of TSQ-doped PMMA core fiber to show that the data is reproducible at this intensity. Then a high incident intensity experiment was conducted over the same region as shown in red ($P_{inc} > 8$ mW). Finally a third low intensity experiment, shown in green, was performed over the identical section of fiber ($P_{inc} < 0.2$ mW).

Obviously, there is very little difference between the first two low intensity experiments. However, the result of the high intensity experiment shows a large decrease in the SIF intensity in comparison to the low intensity experiments. If the high intensity experiment data set were used to calculate an absorption coefficient (see Section 2.7.1), the value would be incorrectly to high. Thus by confirming the results in a duplicate experiment, we eliminate several potential systematic errors in the data analysis.

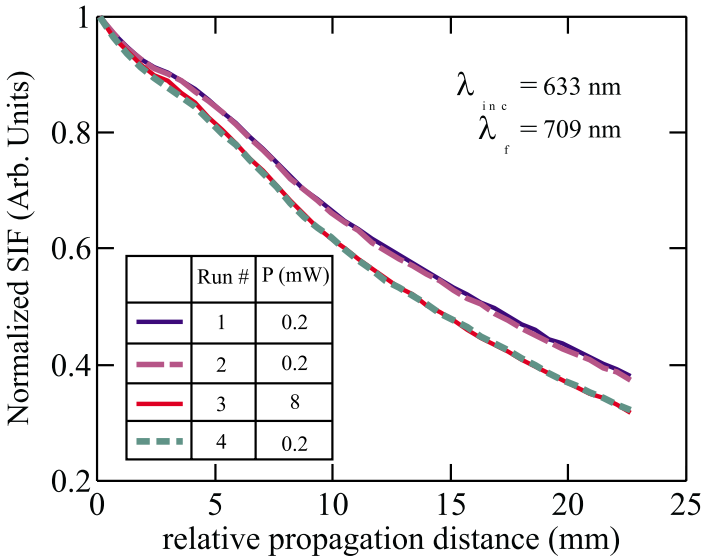

Fig. 4.8: Normalized SIF intensity at 706 nm from a TSQ-doped PMMA fiber. The blue and purple curves are due to an incident power of 0.2 mW at 633 nm. The red curve is due to an incident power of 8 mW, and the green curve is due to an incident power of 0.2 mW after the 8 mW experiment.

The final low intensity experimental data set shown in Figure 4.8 is almost identical to the high intensity experimental data set. This suggests that the high intensity permanently or semi-permanently changed the environment in the fiber and is not a $\chi^{(3)}$ process. It should be noted that an additional high intensity experiment caused an additional decrease in the normalized SIF intensity, which suggests that the guest/host environment can still be modified. The effects of high incident intensities and/or long

exposure times will be discussed in greater detail in Section 5.5.

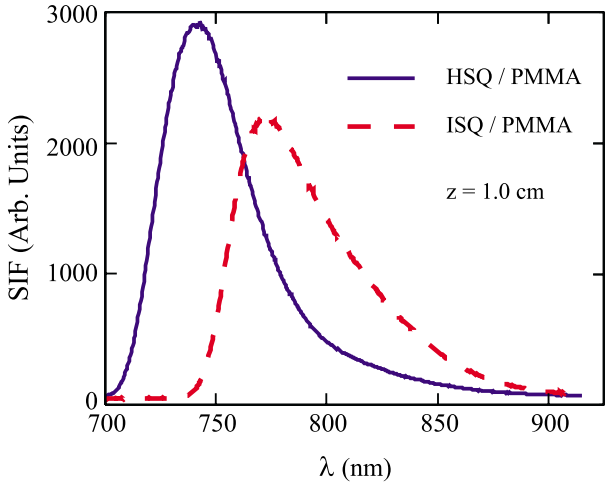

Fig. 4.9: SIF spectra for HSQ- and ISQ-doped PMMA fibers for an excitation position of $z = 1.0$ cm.

In Figure 4.4b, the peak of the emission spectrum is shifted 12 nm from the absorption peak of PSQ/PMMA. The SIF spectrum for an HSQ/PMMA fiber (see Figure 4.9) that propagates 1.0 cm to the front of the fiber has roughly a 100 nm spectral range and is red-shifted more than 75 nm from the fluorescence maximum in Figure 4.4b. This red-shift occurs because of self-absorption along the extended path length in the fiber geometry. The ISQ/PMMA SIF spectrum is slightly broader and red-shifted even further than the HSQ/PMMA SIF spectrum as a result of the red-shifted peak absorption of the ISQ molecule (see Figure 4.2).

By varying the illumination point in the fiber, the spectrometer at the front of the fiber measures the transmitted fluorescence as a function of propagation distance. Because the higher frequency light is more strongly absorbed, the SIF method is ideal for measuring the linear absorption coefficient at wavelengths in the tail of the absorption band of a dye molecule. This is extremely useful because standard methods for measuring $\alpha(\lambda)$ do an inadequate job in the tail region due to the large absorption at resonance (Figure 4.2) or the inaccuracies involved in cutting and measuring small increments of fiber.

The wavelength range of interest can also be varied by changing the dye concentration. Since the absorbance is proportional to the dye concentration, the larger the concentration of dye the larger the red-shift in the SIF spectrum for a fixed propagation distance. This implies that the SIF method is concentration tunable.

A similar experiment can be conducted with a cladded fiber but the incident light that scatters at the core-cladding and cladding-air interfaces couples into cladding modes,

and propagates with little absorption compared to the light in the core. These cladding modes lead to detector saturation at the incident wavelength. Thus an imaging system would be necessary to distinguish the light in the core from the light in the cladding. This type of experiment was not conducted, but is an interesting avenue to pursue in the future work.

4.4 Quadratic Electrooptic Absorption Spectroscopy

Figure 4.10 shows a diagram of the quadratic electroabsorption (QEA) experiment. A light beam (either from a xenon arc lamp or laser) passes through a dye-doped ITO thin-film sample (see Section 3.1) which has an oscillating voltage applied across it. The applied voltage is typically about 80 V at 1.433 kHz and is produced by the internal generator of a Stanford Research Systems (SRS) 850 lock-in amplifier. Since the lock-in amplifiers maximum output is 5 V, the voltage must be amplified with a Realistic MPA-30 Amplifier to reach 80 V.

When the Xenon Arc lamp is used as the light source, a stepper motor, which is interfaced with the computer, controls the wavelength exiting the monochromator. The incident wavelength can be varied throughout the visible region (typically 450 nm–750 nm). In this work the sample will be illuminated at normal incidence, but the angle the sample makes with the incident light can be varied if necessary [5].

In contrast to Mathis [4], the chopper is positioned immediately after the monochromator so that an incident intensity can also be determined during the same experiment. By measuring the incident intensity, we can determine the linear absorption coefficient as well as the imaginary part of the third-order susceptibility in the same experiment. However, it is necessary to have three lock-in amplifiers for the configuration shown in Figure 4.10. The incident intensity is monitored by reflecting a small portion of the beam with a glass slide onto a Thor Labs silicon wide-area silicon photodiode. The lock-in amplifier (SRS 530) that is connected to the incident detector is referenced to the chopper frequency.

After the sample the beam of light is split so that it illuminates two Thor Labs wide-

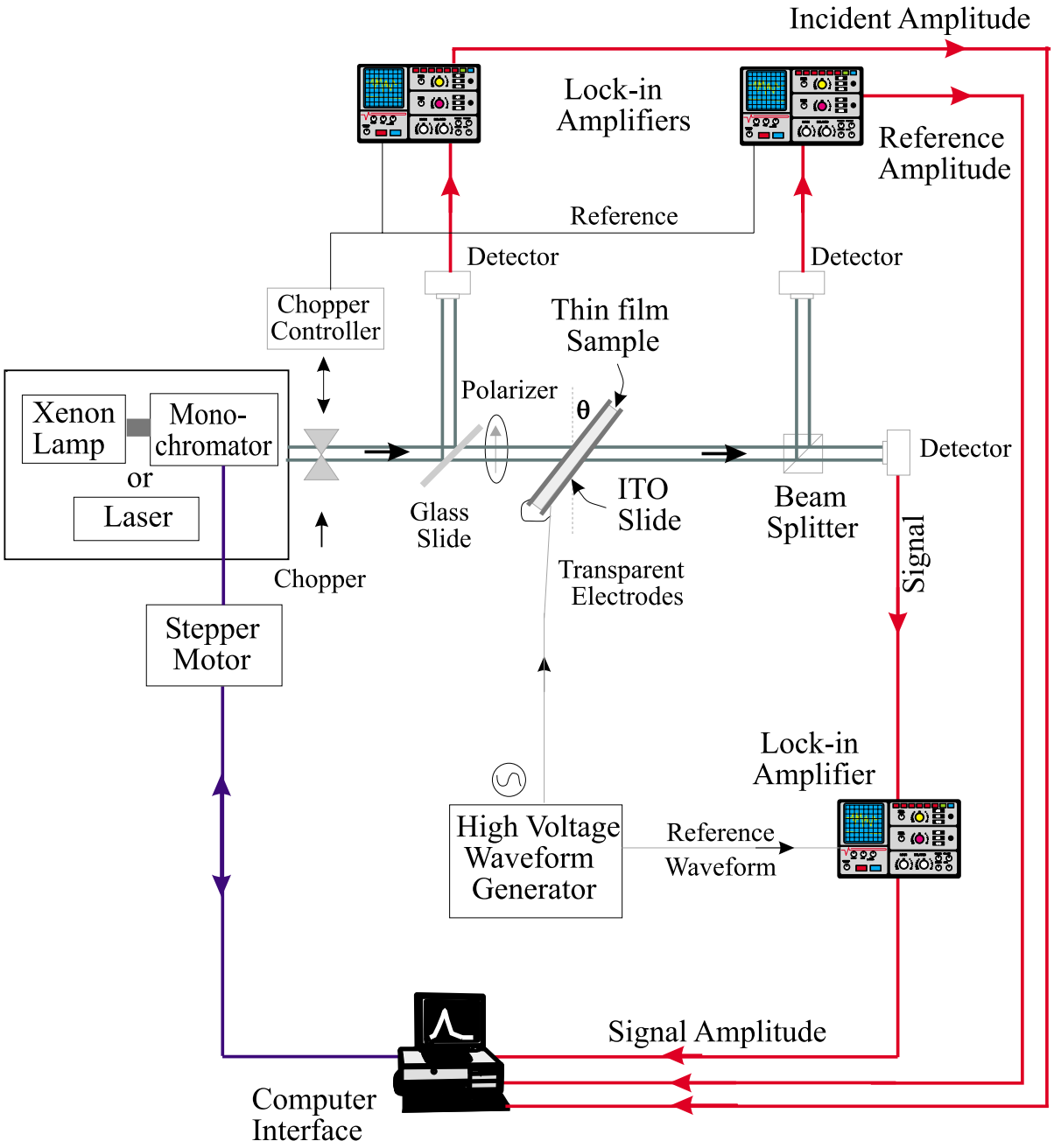

Fig. 4.10: The quadratic electroabsorption experiment.

area silicon photodiodes. The signal detector is connected to the high precision SRS 850 lock-in amplifier and referenced to twice the frequency of the applied voltage, 2Ω. The reference detector is connected to a second SRS 530 lock-in amplifier and referenced to the chopper frequency.

It should be noted that the chopper frequency is chosen so that it is lower than and not a rational subharmonic of the frequency of the applied voltage. Then it is tested to be certain that it does not effect the signal at twice the frequency of the applied voltage. Typically the chopper frequency is set to 461 Hz and does not adversely effect the signal measured at twice the frequency of the applied voltage (2.87 kHz).

The modulation of the applied voltage has been shown to increase the sensitivity of the experiment [6]. This increased sensitivity is necessary since the induced intensity changes are much smaller than the total intensity. Although the applied voltage is sinusoidal, it can be called a quasi-static field because the frequency is much smaller than the optical frequencies and smaller than the linewidth of the light sources.

If we write Equation (2.108) with Equation (2.126) substituted for $\alpha(\lambda)$, we get the transmitted intensity as,

$$\begin{aligned} I_t(\lambda, d) &= I_{inc}(\lambda) \exp(-\alpha_0(\lambda)\, d - \alpha_{\mathrm{QEA}}\, E_0^2\, d), & (4.2) \\ &= I_{t_0}(\lambda, d) \exp(-\alpha_{\mathrm{QEA}}(\lambda)\, E_0^2\, d), & (4.3) \end{aligned}$$

where the thickness of the dye-doped thin film is d, the zero-voltage transmitted intensity is

$$I_{t_0}(\lambda, d) = I_{inc}(\lambda) \exp(-\alpha_0(\lambda)\, d), \tag{4.4}$$

and $\alpha_0(\lambda)$, and $\alpha_{\mathrm{QEA}}(\lambda)$ are given in terms of the imaginary parts of the first- and third-order susceptibilities by Equations (2.127) and (2.128), respectively.

By assuming the QEA absorption is small in comparison the zero-field absorption, we can simplify Equation (4.3) to,

$$I_t(\lambda, d) = I_{t_0}(\lambda, d)\,(1 - \alpha_{\mathrm{QEA}}(\lambda)\, E_0^2\, d). \tag{4.5}$$

The applied electric field is related to the root-mean-square voltage as follows,

$$E_0 = \sqrt{2} \frac{V_{\mathrm{rms}}}{d} \cos(\Omega t), \tag{4.6}$$

where the "static field frequency", $\Omega \ll \omega$, the optical frequency. Therefore we can write the transmitted intensity in terms of Fourier components of Ω as follows,

$$I_t(\lambda, d) = I_t^0(\lambda, d) + I_t^{2\Omega}(\lambda, d) = I_{t_0}(\lambda, d) \left[1 - 2\frac{\alpha_{\mathrm{QEA}}(\lambda)\, V_{\mathrm{rms}}^2}{d} \cos^2(\Omega t)\right]. \tag{4.7}$$

With a simple trigonometry simplification, the transmitted intensity at twice the applied field frequency is,

$$I_t^{2\Omega}(\lambda, d) = -I_{t_0}(\lambda, d)\frac{\alpha_{\mathrm{QEA}}(\lambda)\, V_{\mathrm{rms}}^2}{d}. \tag{4.8}$$

Notice that Equation (4.8) is related to the square of the voltage and hence the name quadratic electroabsorption. Since the experimental set-up allows us to measure $I_t^{2\Omega}$, I_{t_0}, and I_{inc}, we can determine both the zero-voltage absorption, and the QEA absorption, as follows,

$$\alpha_0(\lambda) = -\frac{1}{d}\ln\left(\frac{\mathrm{I_{t_0}}}{\mathrm{I_{inc}}}\right), \tag{4.9}$$

and

$$\alpha_{\mathrm{QEA}}(\lambda) = -\frac{I_t^{2\Omega}}{I_{t_0} V_{\mathrm{rms}}^2} d, \tag{4.10}$$

respectively.

The reference detector measures the transmitted intensity at the chopper frequency which is proportional to the I_{t_0}, and the incident detector measures the fraction of the incident intensity which reflects of the glass slide, I_{inc}.

It should be noted that two calibration runs must be performed. The first calibration run is done without a sample in place to determine the correct ratio of intensities at the chopper frequency, and the second calibration run is done to determine how much sensitivity is lost when the detector measures a signal at 2Ω in comparison to the chopper frequency, 461 Hz. More details on the calibration experiments can be found in the literature [3, 7].

By measuring the linear absorption in the same experiment, we reduce the error associated with the analysis of the one-photon states. It is necessary to characterize the one-photon states in a linear measurement in case two-photon states contribute to the QEA response. If none of the excited states are characterized before analyzing the QEA data, there are too many floating parameters to make the analysis meaningful.

4.5 Photosensitivity

There is no particular experimental apparatus for conducting photosensitivity experiments. They can be conducted using transmission spectroscopy, emission spectroscopy, SIF spectroscopy, or QEA spectroscopy. Measuring the photosensitivity of a sample typically requires several experiments to be performed using one of the aforementioned experiments.

For example, if a preform slice is positioned in the transmission spectroscopy experiment, a photosensitivity experiment can be conducted by illuminating the sample with a high incident intensity and observing the transmission as a function of exposure time. If the transmitted intensity is too high, a low intensity experiment is conducted on an unexposed preform to determine the absorption. The sample is then exposed to high intensity light for a measured amount of time. Finally, the transmission is measured with a low intensity beam to determine the change in absorption due to the high intensity exposure.

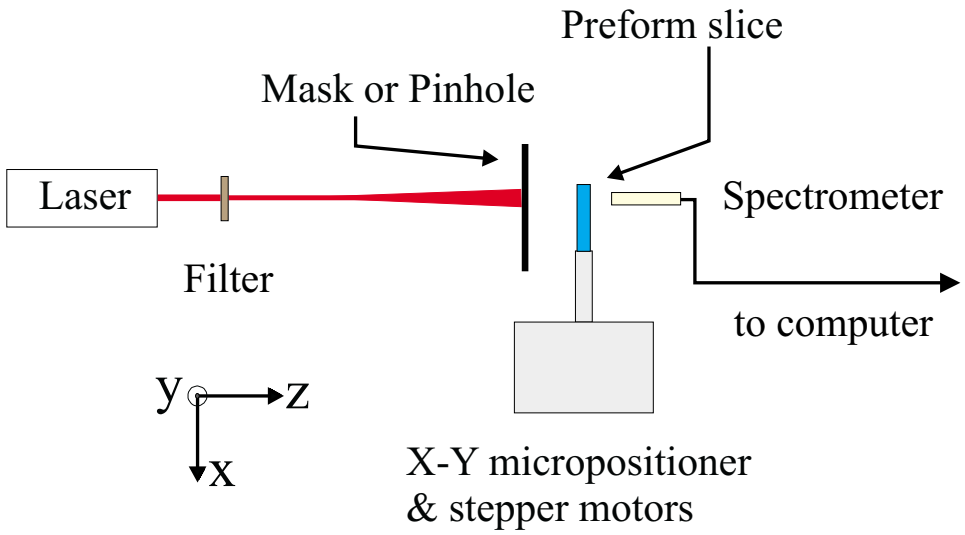

Fig. 4.11: Experimental apparatus for measuring the transmission through a preform slice as a function of position.

The photosensitivity experiment can be performed as a function of position in the preform. Figure 4.11 shows a schematic of a transmission spectroscopy experiment where

the preform sample can be moved in an X-Y raster pattern. This allows us to determine the localization of the exposure. Thus the sample can be measured over some cross-sectional area with a low intensity beam to determine the transmission properties of the unexposed sample. Then the sample is exposed to a high intensity pattern of light for a measured time interval. Finally, the same cross-sectional area is re-measured to determine the change in transmission from the original sample.

In the SIF experimental set-up, a photosensitivity measurement can be conducted by measuring the SIF intensity as a function of propagation distance at a low incident intensity. Then a fixed position can be exposed for a prolonged period of time while the SIF intensity is or is not monitored. Finally, the fiber can be measured using SIF as a function of propagation distance at the original low incident intensity.

These types of experiments help us develop an understanding of the stability of our dye-doped polymer systems. However, it is very difficult to determine a physical mechanism for the photosensitivity. Therefore we only discuss the results in terms of stability not in terms of what is changing in the particular dye-doped system.

Bibliography

[1] R. J. Kruhlak and M. G. Kuzyk, "Side-illumination fluorescence spectroscopy. I. Principles," J. Opt. Soc. Am. B **16**, 1749–1755 (1999).

[2] R. J. Kruhlak and M. G. Kuzyk, "Side-illumination fluorescence spectroscopy. II. Applications to squaraine dye-doped polymer optical fibers," J. Opt. Soc. Am. B **16**, 1756–1767 (1999).

[3] C. Poga, "Characterization of the excited states of a squaraine molecule with quadratic electroabsorption spectroscopy," Ph. D. dissertation (Washington State University, Pullman, WA, 1994).

[4] K. S. Mathis, M. G. Kuzyk, C. W. Dirk, A. Tan, S. Martinez, and G. Gampos, "Mechanisms of the nonlinear optical properties of squarainne dyes in poly(methyl methacrylate) polymer," J. Opt. Soc. Am. B **15**, 871–883 (1998).

[5] C. Poga, T. M. Brown, M. G. Kuyzk, and Carl W. Dirk, "Characterization of the excited states of a squaraine molecule with quadratic electrosorption spectroscopy," J. Opt. Soc. Am. B **12**, 531–43 (1995).

[6] M. G. Kuzyk and C. Poga. "Quadratic electro-optics of guest-host polymers,". in J. Zyss, ed., *Molecular Nonlinear Optics: Materials, Physics, and Devices*, pages 299–336. Academic, San Diego, CA, (1993).

[7] K. S. Mathis, "Studies on the nature of excited states of squaraines using quadratic electroabsorption spectroscopy and essential state analysis," Master's Thesis (Washington State University, Pullman, WA, 1995).

Chapter 5

Results and Discussion

5.1 Absorption Spectra

In this section we briefly discuss the absorption spectra for the squaraine and SiPc dyes when they are guests in preform slices or thin films. The absorption spectra for HSQ/PMMA, PSQ/PMMA, and TSQ/PMMA preform slices are so similar that we only show the results for PSQ/PMMA. ISQ/PMMA and SiPc/PMMA are discussed separately because they have some unique characteristics. The thin-film results shown for ISQ/PMMA and SiPc/PMMA in Section 5.1.2 are from the same films that will be characterized in Section 5.8.

5.1.1 Bulk Preform Slices

As previously mentioned the squaraines and SiPc are characteristically blue. The shade of blue depends on the concentration of dye in the polymer host. For high concentrations of dye (~ 0.1 wt%), preform slices on the order of 100 μm are, for all practical purposes, opaque at resonance . Therefore only low concentration or very thin samples can be characterized in the transmission spectroscopy experiment (see Section 4.1).

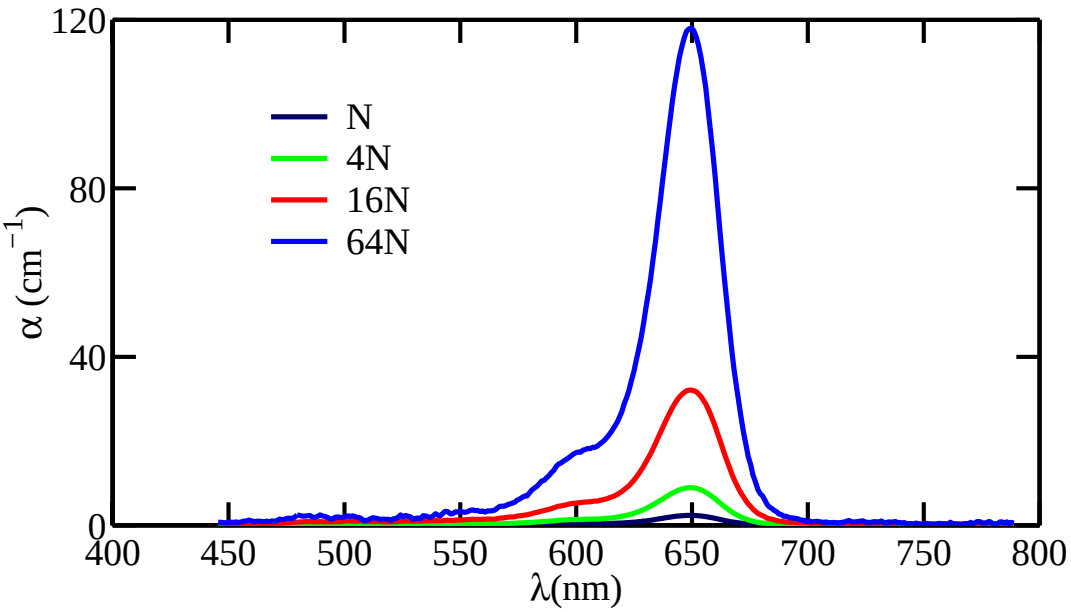

Fig. 5.1: Resonant linear absorption of PSQ/PMMA core preform slices for four concentrations (N= 1.5 × 10^{15} cm^{-3}).

5.1.1.1 HSQ, PSQ, TSQ

Figure 5.1 shows four different concentrations of PSQ/PMMA preform slices. They can be considered representative of HSQ/PMMA, and TSQ/PMMA at these low concentrations. These squaraines exhibit a large transition centered about 650 nm, which is responsible for the blue color. There is also a characteristic high-energy shoulder that is typically characterized as a vibronic of the state at 650 nm. Since the high-energy shoulder is not very well resolved it could be the sum of several different states. In Section 5.7, the excited state responsible for the large absorption about 650 nm from the HSQ, PSQ, and TSQ dyes will be discussed. The high-energy shoulder will be neglected since it does not affect the linear absorption at wavelengths longer than resonance, where the SIF fiber experiments are typically performed.

From Table 3.1 we know that the room temperature maximum number densities for squaraines are on the order of 10^{18} cm^{-3}. In contrast, the number density of the samples shown in Figure 5.1 are between 10^{15}-10^{17} cm^{-3}. The peak of the absorption spectra scales linearly with number density, within 10 % . However, it is a stretch to assume

that the trend will continue for another order of magnitude of increased number density. Therefore, a different method for measuring the loss in high concentration thick samples is necessary.

5.1.1.2 ISQ

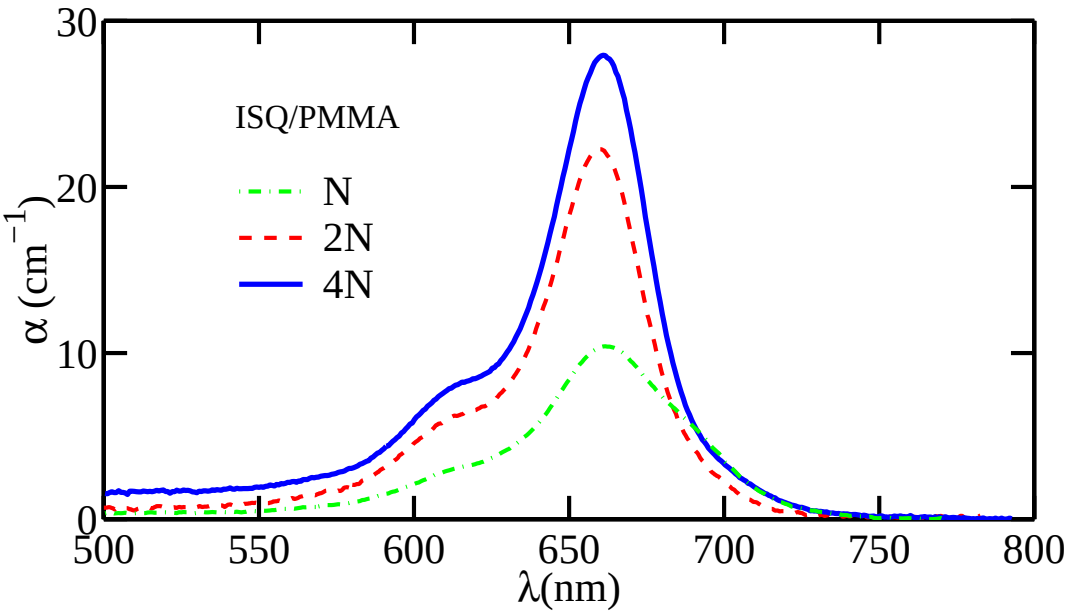

Fig. 5.2: Resonant linear absorption of ISQ/PMMA core preform slices for three concentrations (N= 3.1 × 10^{15} cm^{-3}).

The previous section showed that the absorption maxima are proportional to the number density for PSQ/PMMA, HSQ/PMMA, and TSQ/PMMA bulk preform slices. Unfortunately, this is not always the case for ISQ/PMMA samples, even at number densities that are low enough to be measured using the transmission spectroscopy experiment. We discuss a variety of ISQ/PMMA preform slices in this section – some of which are blue and some which are greenish because the dye has degraded. The degradation is most likely caused by oxidation.

Figure 5.2 represents the absorption spectra for three different preforms slices of ISQ/PMMA. The two lowest concentrations samples were made from the same initial ISQ/MMA solution. The highest concentration sample was made from the same ISQ-

dye approximately one year later. Notice that $\lambda_{max} \approx 660$ nm for all three samples. However, there is definitely not a linear increase in the absorption with number density. If there were a linear increase, the maximum absorption for the preform labeled 4N would have been ~ 45 cm^{-1}.

Even the shape of the spectrum is not consistent as a function of concentration. Each spectrum has the characteristic high-energy shoulder but the lowest concentration sample has an additional low-energy shoulder. We suggest that the low-energy shoulder is caused by degradation of the dye but the preform slice shows no visible signs of degradation.

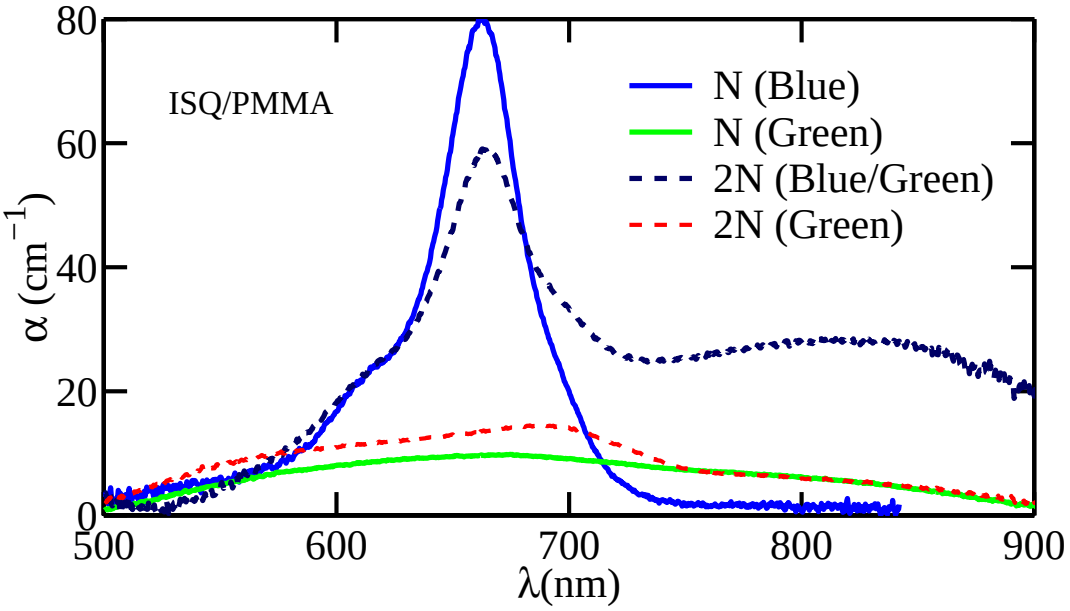

Fig. 5.3: Resonant linear absorption of ISQ/PMMA core preform slices at various stages of degradation (N= 2.4×10^{16} cm^{-3}).

To support the hypothesis that the low lying shoulder is caused by a slight degradation of the sample, four different samples were measured, three of which display visible signs of degradation. The samples that have degraded or are degrading are blue/green to green in color. Figure 5.3 shows the absorption spectra for these four preform slices.

For example, even though the blue sample was made with half the amount of dye, it has a larger absorption at 660 nm than the blue/green preform. The blue/green sample exhibits a similar low lying shoulder, in comparison to the lowest concentration

sample in Figure 5.2. However, the blue/green ISQ/PMMA sample has an additional large absorption in the near IR, which could possibly be caused by a degradation of the polymer. The two green samples have essentially no spectral characteristics similar to the blue ISQ/PMMA preform slice. There is a small peak in the absorption near the low lying shoulder region of the blue/green sample for the high concentration green sample. This suggests that almost all the dye has degraded and the majority of the absorption is now in the UV.

Thus it appears that the low lying shoulder is caused by the degradation of the ISQ dye. Unfortunately, the degradation may not be visible, as we saw in Figure 5.2, until the sample has been processed and measured in the transmission spectroscopy experiment.

Such properties of ISQ/PMMA and similar dye-doped polymers are beginning to be studied. Section 5.2 discusses how the SIF spectra change in the 700-900 nm as a function of incident wavelength and concentration, and Section 5.6 discusses the unique absorption features of ISQ/PMMA core fibers in the 700-900 nm range. These experiments complement the absorption measurements.

5.1.1.3 SiPc

Figure 5.4 shows the on resonance linear absorption spectrum for a SiPc/PMMA core preform slice that originated from the same core preform as the core fiber studied in Section 5.2.3.5. It is also the same preform slice that was measured in the emission spectroscopy experiment (see Section 5.4). Lower concentration samples of SiPc/MMA were not available because of a shortage of dye, so the absorption spectra shown in Figure 5.4 was the only preform measured.

The resonance occurs at 670 nm ($\langle 0|0\rangle$ vibronic) and the two high lying states are considered the $\langle 0|1\rangle$ and $\langle 0|2\rangle$ vibronics. The set of three peaks are called the Q or Soret band in the literature [1]. The parameters describing the resonance excited state will be determined in Section 5.7.1.3.

Notice that there are small noise fluctuations due to the small signal between 740 and 800 nm but are too small to quantify. This region will be discussed in greater detail when the SIF results for the SiPc/PMMA core fibers are analyzed in terms of the linear

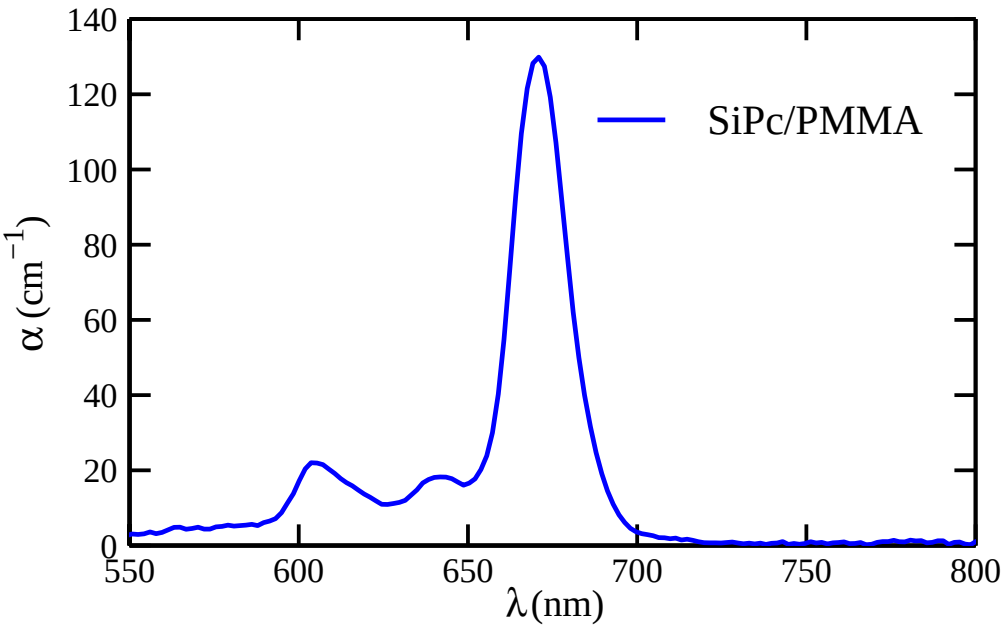

Fig. 5.4: Resonant linear absorption for a 225 μm thick SiPc/PMMA core preform slice (N= 1.28×10^{17} cm^{-3}).

absorption coefficient.

5.1.2 Thin films

The thin films discussed in this section were measured in the QEA experiment, specifically for determining the excited state parameters of the one-photons states. These excited state parameters are used to differentiate between one- and two-photon states as measured by the QEA experiment. A more complete set of linear absorption thin film measurements on the squaraine dyes can be found in the literature [2].

Because thin films are on the order of 4-6 μm, in comparison to 200 - 2000 μm for core preform slices, the absorption can be measured for much higher concentrations than for the preform slices. Both thin films are about three orders of magnitude higher in concentration than the preform samples measured in the previous section. However, they are made by dissolving the dye and PMMA in a solvent and evaporating the solvent very quickly. This process is very different from the polymerization process for the preforms

slices. Therefore the absorption spectra shown for high concentration thin films may not be equivalent to the spectra for high concentration core preform slices.

5.1.2.1 ISQ

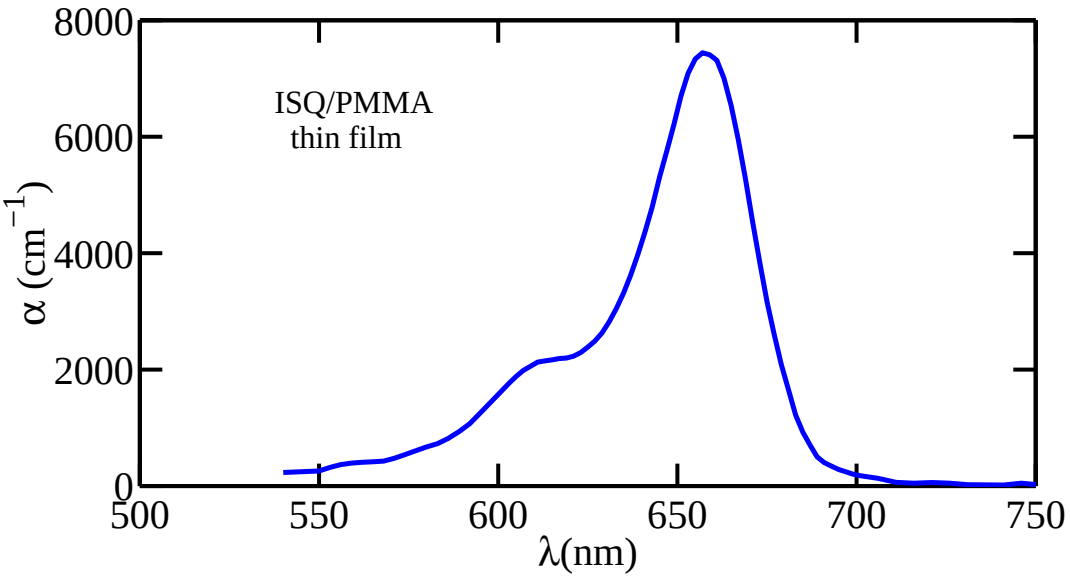

Fig. 5.5: Resonant linear absorption for an ISQ/PMMA thin film (N= 1.9 × 10^{19} cm^{-3}).

Figure 5.5 represents the absorption spectrum for a 1 wt.% ISQ/PMMA thin film. Similar to the spectra shown in Figure 5.2, the dominant excited state in centered near 660 nm and the characteristic high lying shoulder is present. There does not appear to be any sign of degradation. The resonant transition is also not as broad as the resonant transition for the ISQ/PMMA preform slices, which suggests that the thin film is more homogeneous.

This spectrum will be characterized in terms of the one-photon states which contribute to the absorption in Section 5.7.2.1. The excited state parameters will then be used to explain the QEA results in Section 5.8.

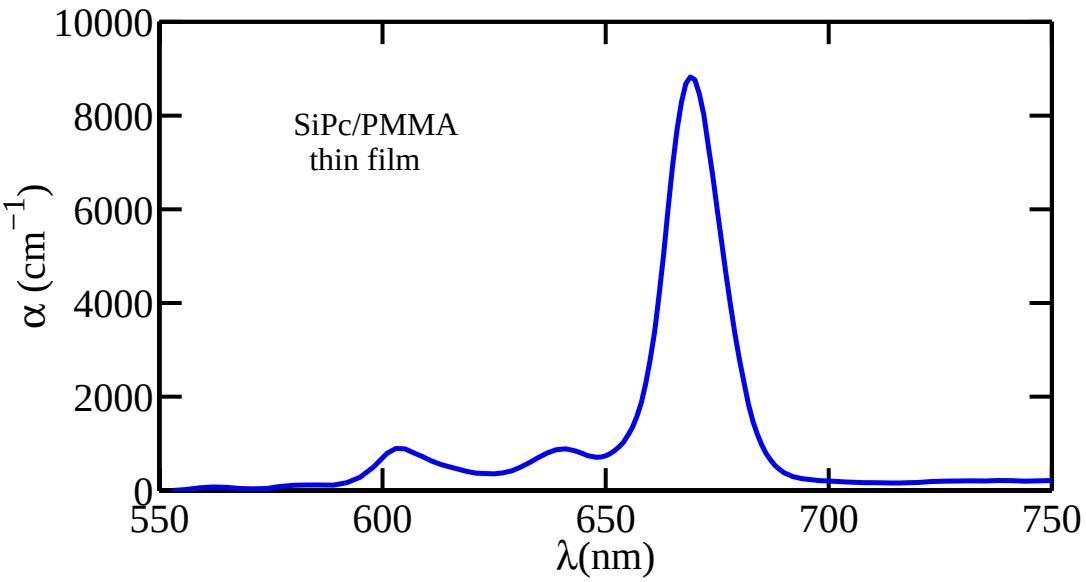

Fig. 5.6: Resonant linear absorption for a SiPc/PMMA thin film (N= 5.7 × 10^{18} cm^{-3}).

5.1.2.2 SiPc

Figure 5.6 represents the absorption spectra about resonance for a 1 wt. % SiPc/PMMA (guest/host) thin film. The absorption is much more localized than the ISQ/PMMA absorption. Clearly, the three significant absorption peaks are similar to the absorption peaks in Figure 5.4 for the preform slice.

It is interesting to note that there appear to be a couple of small higher energy vibronics that could not be resolved in the absorption spectra of the SiPc/PMMA (copolymer) preform slice. There also appears to be a contribution to the absorption spectrum in the 720 -750 nm range. This sample will be analyzed further in Sections 5.7.2.2 and 5.8.

5.2 SIF spectra

In this section, SIF spectra are discussed for PMMA and P(MMA-d8) fibers doped with one of the following dyes: BSQ, HSQ, ISQ, PSQ, TSQ, SiPc, DR1, or SP1822. As previously mentioned in Section 4.3, the SIF measurements are conducted at several incident wavelengths and propagation distances. (Note: For the data presented in this Section,

the beam from the laser diode (either 643 nm, 667 nm, 693 nm) is perpendicular to the fiber axis.) To become familiar with the possible observables that can be determined in the SIF experiment numerous SIF spectra are shown. The discussion of the SIF spectra will be organized into the following sections: SIF as a function of propagation distance, SIF as a function of fiber diameter, SIF as a function of concentration, SIF as a function of polymer host, SIF as a function of incident wavelength, and SIF as a function of exposure time. In each section the squaraine dyes will be discussed first since they have been studied in the most detail. When applicable the spectra for SiPc-, DR1-, and SP1822-doped fibers with also be discussed.

5.2.1 Propagation distance dependence

The SIF experiment can be conducted for any propagation distance given that the distance is short enough for a signal to register at the detector. Typically, we begin the SIF experiment about 1 cm from the beginning of the core fiber. The smallest fiber chuck we have made is 7 mm in length, so the additional 3 mm allows plenty of clearance to avoid stresses induced by the fiber holder.

As mentioned in Section 4.3, the maximum distance the fiber stage or laser diode can translate for a single experiment is 2.3 cm. If longer distances need to be studied, a second experiment is performed with the entire fiber stage or laser moved to a new (longer) incident illumination position. This restriction was rarely a problem because the SIF signal was usually depleted before 2.3 cm of propagation distance could be translated. For dye molecules that have an extremely large absorption a second experiment can, if necessary, be conducted at a new initial position with a longer integration time to cover the entire 2.3 cm of the translation stage. In either case the integration time for the second experiment on the same fiber needs to be increased to maximize the signal to noise ratio.

In the following sections BSQ, HSQ, and ISQ-doped multimode fibers results are shown for longer propagation distances than a single experiment can measure. Because these secondary experiments required longer integration times, the magnitudes of the

SIF spectra are arbitrary between the different figures of the same fiber. With this in mind we begin the discussion of the propagation dependence of the SIF spectra for squaraine-doped polymer core fibers.

5.2.1.1 BSQ

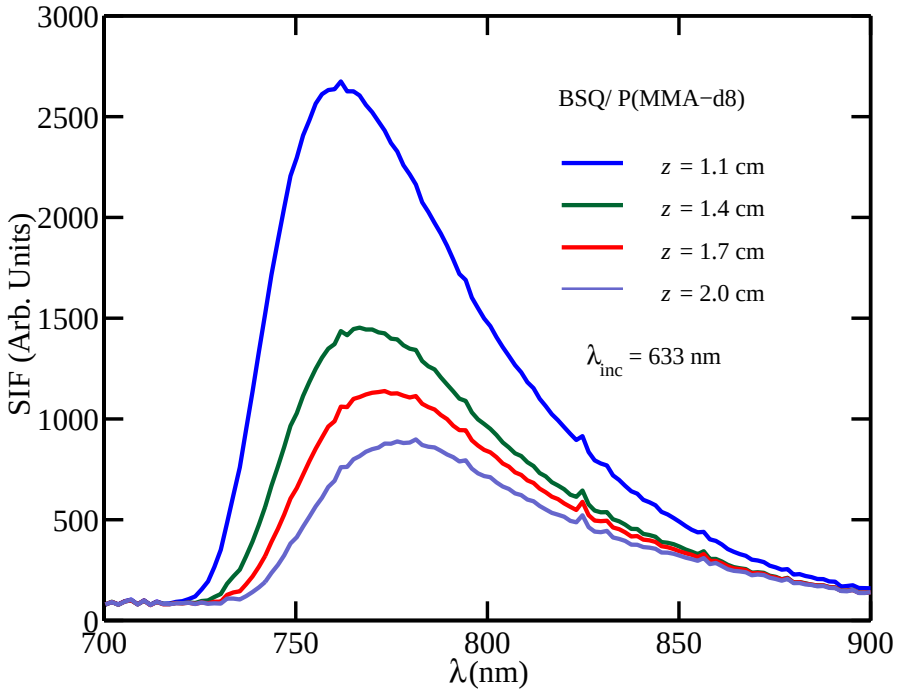

Fig. 5.7: SIF spectra for propagation distances, 1.1 cm $\leq z \leq$ 2.0 cm, in a multimode BSQ/P(MMA-d8) fiber ($\lambda_{inc} = 633$ nm). Each subsequent curve is measured for an excitation position 0.3 cm further into the fiber.

The SIF spectra for a core fiber of the maximum room temperature concentration of BSQ in P(MMA-d8) is shown in Figures 5.7 and 5.8 as a function of propagation distance (illumination position). Note that the data described here can also be thought of in terms of illumination position since the illumination position is the distance from the front of the fiber to the point where the laser illuminates the side of the fiber. P(MMA-d8) stands for poly(methylmethacrylate) which was polymerized from completed deuterated MMA monomer. In other words, all eight of the hydrogen ions on the monomer molecule were replaced with deuterium ions.

Replacing the hydrogen ions with deuterium ions is typically done to reduce the absorption due to the host since the majority of the loss from the polymer is due to overtones of the C-H stretch. By increasing the effective mass, the C-D vibrations are shifted to longer wavelengths, in comparison to the C-H vibrations – which reduces the loss in the near IR.

Figure 5.7 shows the SIF spectrum after propagating 1.1 cm, 1.4 cm, 1.7 cm, and 2.0 cm. As the propagation distance increases the magnitude of the spectrum decreases, as expected, because of loss mechanisms such as absorption and scattering. There is also a red-shift in maximum of the SIF spectrum as the illumination position is increased. This suggests that the loss is not constant as a function of wavelength but larger for the shorter wavelengths.

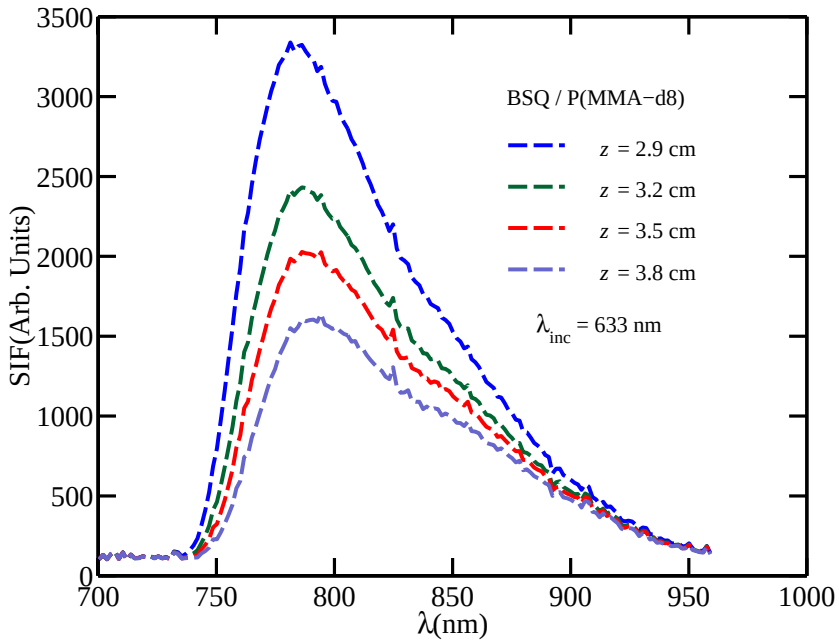

Fig. 5.8: SIF spectra for propagation distances, 2.9 cm $\leq z \leq$ 3.8 cm, in a multimode BSQ/P(MMA-d8) fiber ($\lambda_{inc} = 633$ nm). Each subsequent curve is measured for an excitation position 0.3 cm further into the fiber.

The SIF spectra, shown in Figure 5.8, also decrease in magnitude and red-shift as the propagation distance is increased. However, the decrease in magnitude and red-shift is much smaller over the full distance of the experiment, $\Delta z = 0.9$ cm, in comparison to

Figure 5.7. The maximum of the initial spectrum in Figure 5.8 (785 nm) is red-shifted 25 nm from maximum of the initial spectrum in Figure 5.7 (760 nm). This also indicates that the loss decreases at longer wavelengths. The functional dependence of the loss for BSQ-doped fibers will be studied in greater detail in Section 5.6.

If the little spike at about 825 nm is ignored, which is due to a hyperactive pixel in the CCD array, there appears to be a small valley in the SIF spectrum centered about 835 nm in Figure 5.8. It is not noticeable at shorter propagation distances (see Figure 5.7) because the magnitude of the SIF signal near 835 nm is a much smaller fraction of the maximum fluorescence. Thus, increasing the propagation distance that the fluorescence must travel to reach the detector can often reveal new features in the fluorescence band. Section 5.2.3 will look at this feature in more detail.

In this section we introduced the most basic results of the SIF experiment (see Section 4.3) for a BSQ-doped P(MMA-d8) core fiber. The SIF spectra all have magnitudes well above the noise level for a wavelength range greater than 100 nm and is generated from a single wavelength source. There is also very good resolution between the spectra for the various illumination positions, shown in Figures 5.7 and 5.8, suggesting that the loss is significant over 100 nm from the resonance absorption of the dye. This feature will be exploited in Sections 5.6 and 5.7 to determine the loss as a function of wavelength in the fluorescence band and the excited state parameters characterizing the resonant absorption of the dye molecule, respectively. Before proceeding, we need to introduce the basic SIF spectra as a function of propagation distance for the remainder of the dye molecules that we study.

5.2.1.2 HSQ

Figure 5.9 shows HSQ/P(MMA-d8) SIF spectra for propagation distances between z = 1.1 cm and z = 2.5 cm in 0.46 cm increments. These are typical spectra for HSQ core fibers, in the sense that the spectra decrease in intensity, red-shift, and show little difference in their shape as the propagation distance increases. The spectrum for a propagation distance of 1.1 cm is significantly red-shifted from that of the thin film fluorescence seen in Figure 4.4 because the fluorescence propagates much further through

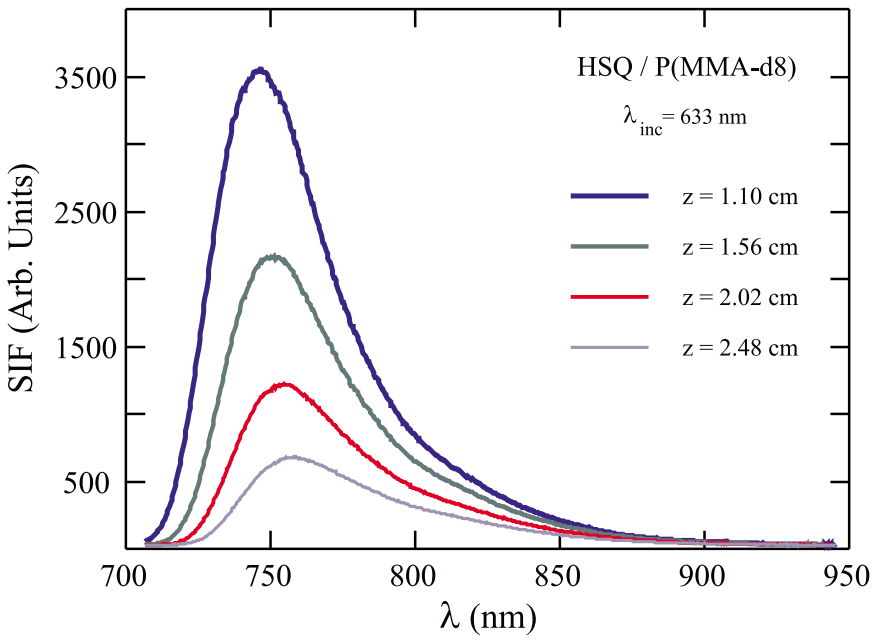

Fig. 5.9: SIF spectra for propagation distances, 1.1 cm $\leq z \leq$ 2.48 cm, in a multimode HSQ/P(MMA-d8) fiber (λ_{inc} = 633 nm). Each subsequent curve is measured for an excitation position 0.46 cm further into the fiber.

the dye-doped polymer to reach the detector. Because the SIF spectrum shows little change in shape with propagation distance we postulate that the loss is mainly a single exponential which may not be the case for the BSQ/P(MMA-d8) fiber shown in Figure 5.8. This postulate will be studied further in Section 4.3.

However, the shape of the spectrum, of the same section of fiber, evolves slightly for propagation distances between 4.2 cm and 5.7 cm. Figure 5.10 shows the appearance of a shoulder in and an eventual broadening of the SIF spectrum for these longer propagation distances. This broadening will be discussed in detail in Section 5.2.4.

5.2.1.3 PSQ

PSQ is very similar to HSQ in chemical structure and absorption spectrum. The only difference is the length on the four carbon chains attached to the nitrogen atoms (See Figure 3.5). Thus we expect that the SIF spectra for PSQ should be very similar to the SIF spectra for HSQ. Figure 5.11 shows the SIF spectra for an HSQ/PMMA and

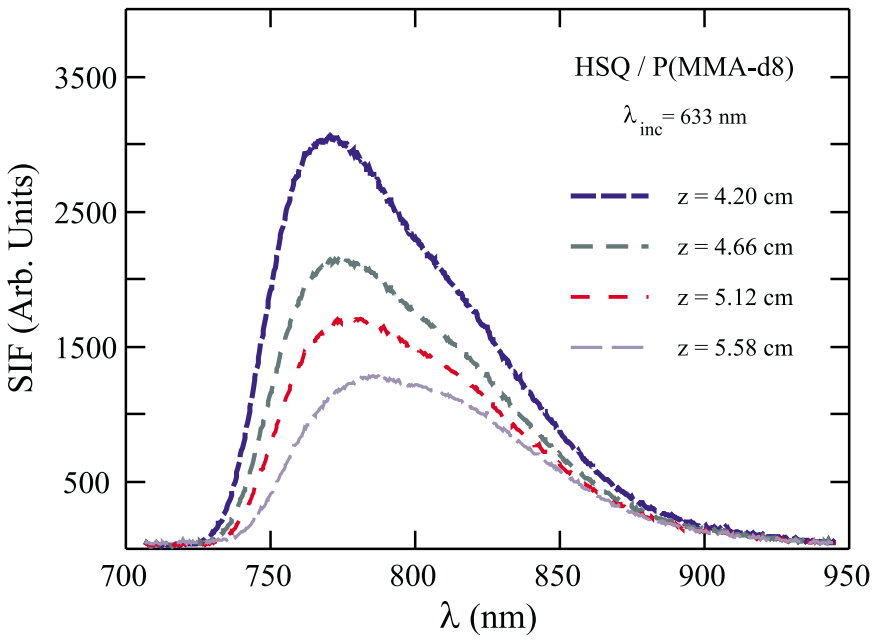

Fig. 5.10: SIF spectra for propagation distances, 4.2 cm $\leq z \leq$ 5.58 cm, in a multimode HSQ/P(MMA-d8) fiber (λ_{inc} = 633 nm). Each subsequent curve is measured for an excitation position 0.46 cm further into the fiber.

a PSQ/PMMA multimode core fiber illuminated with the 693 nm laser diode. The illumination position shown is 2.0 cm but the relative spectra between the dyes are similar at any value in the data set.

Clearly, the SIF spectra for similar concentration of HSQ- and PSQ-doped fibers are identical within the thickness of the line so we did not perform SIF measurements for longer propagation distances on PSQ-doped fibers. Instead we refer the reader back to Figures 5.9 and 5.10 for the HSQ-doped core fiber result.

5.2.1.4 TSQ

The SIF spectra from a TSQ/PMMA core fiber with a dye concentration of, N = 1.3 × 10^{17} cm^{-3}(below the saturation room temperature concentration), are shown in Figure 5.12. The lower concentration TSQ/PMMA fiber was measured to determine if the SIF experiment could be conducted at concentrations below the room temperature maximum. We were also able to fabricate a set of three low concentration TSQ/PMMA fibers,

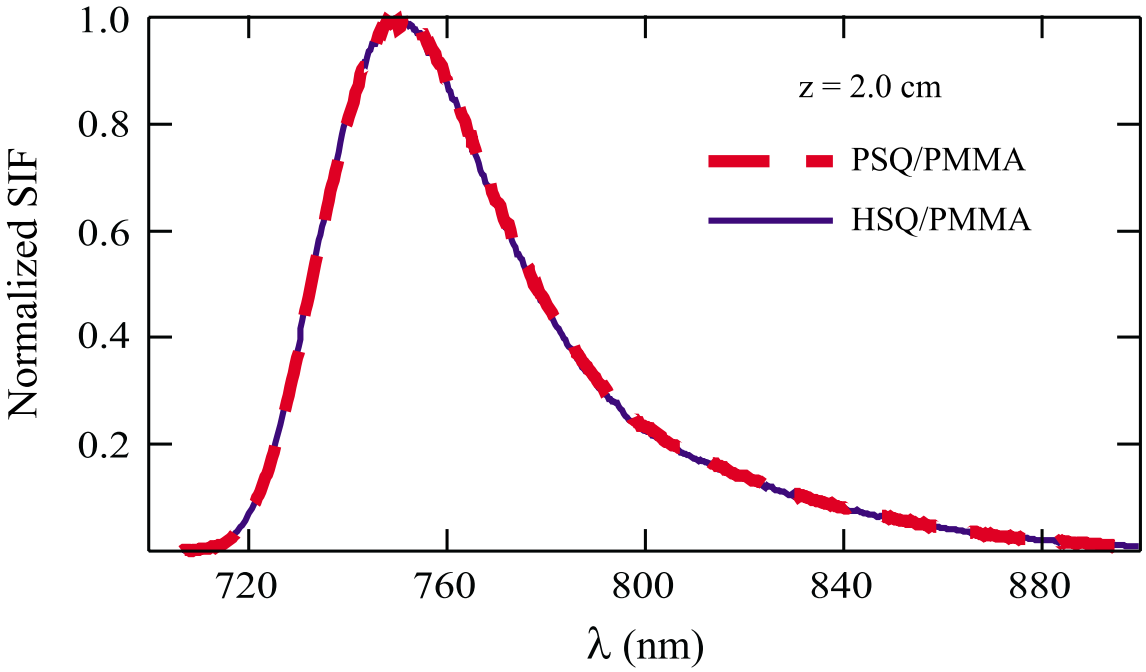

Fig. 5.11: SIF spectra for maximum room temperature concentration HSQ/PMMA and PSQ/PMMA multimode core fibers at $z = 2.0$ cm ($\lambda_{inc} = 693$ nm).

which is a rarity since the core fibers are usually made at maximum concentration to optimize nonlinear experiments. Since we did not have a room temperature maximum concentration of TSQ/PMMA we assume that it would be very similar to the PSQ and HSQ spectra which have already been discussed. The TSQ/PMMA core fiber is clearly of a lower concentration than the HSQ/PMMA core fiber, shown in Figure 5.9, because the peak wavelength of the SIF spectrum is shorter and there is a smaller change in magnitude as a function of increasing propagation distance. These are significant indicators because the absorbance scales with the number density when the dye molecules are in a low enough concentration to behave as individual molecules. In Figure 5.12, the maximum of the SIF spectrum for the lower concentration TSQ/PMMA fiber decreases in magnitude to about 1/2 of its initial value over a 2 cm change in propagation distance while the maximum of the SIF spectrum of the higher concentration HSQ/PMMA fiber decreases to about 1/6 of its initial value over about a 1.4 cm change in propagation distance. These types of features will be investigated in more detail in Section 5.2.3, when the

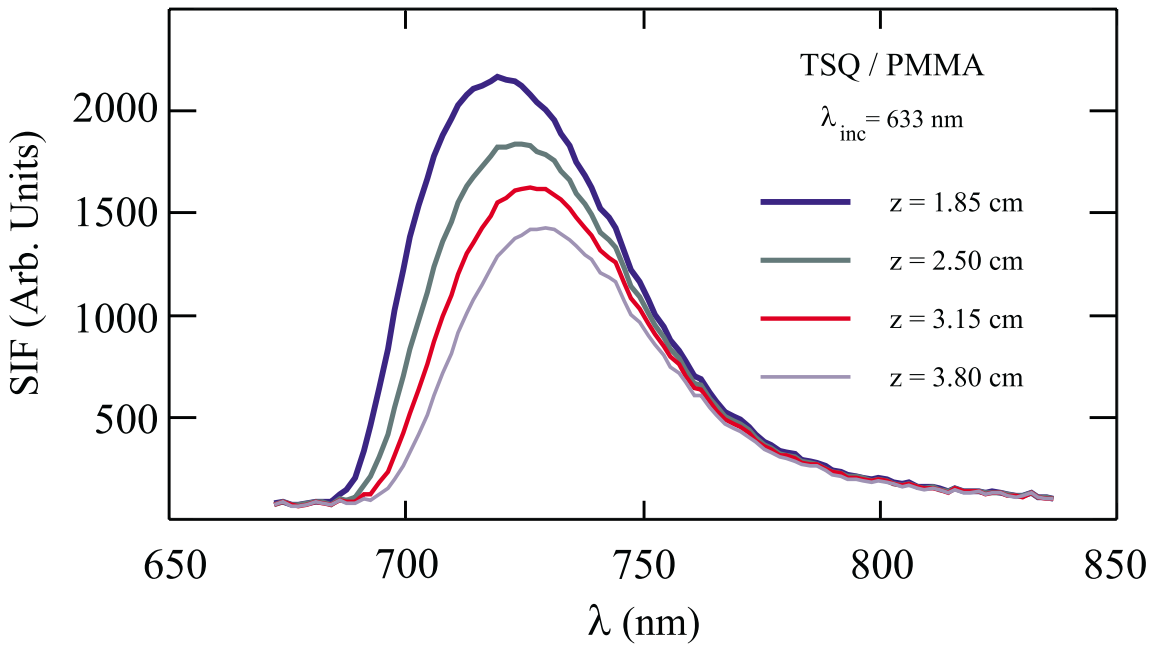

Fig. 5.12: SIF spectra for propagation distances, 1.85 cm $\leq z \leq$ 3.8 cm, in a multimode TSQ/PMMA fiber (λ_{inc} = 633 nm). Each subsequent curve is measured for an excitation position 0.65 cm further into the fiber.

concentration dependence of the SIF spectra are discussed.

5.2.1.5 ISQ

We have seen that the spectra for BSQ, HSQ, PSQ, and TSQ are quite similar due to the similarities in their molecular structures (see Figure 3.5). However, there are noticeable differences in the SIF spectra for ISQ. The first distinguishable feature, in Figure 5.13, is the red-shift in the peak of the SIF spectrum to about 765 nm which is greater than the red-shift in the peak of the HSQ/P(MMA-d8) SIF spectrum for a propagation distance of about 1 cm. The larger red-shift occurs because of the 10 nm red-shift in the resonant linear absorption spectrum of ISQ making it more optically dense at 750 nm than the other squaraine dyes.

There is also a clear change in the shape of the SIF spectrum as well as a decrease in intensity and red-shift in the peak fluorescence as the propagation distance increases. For propagation distances less than 3 cm, the data is too inhomogeneous to be quantitatively

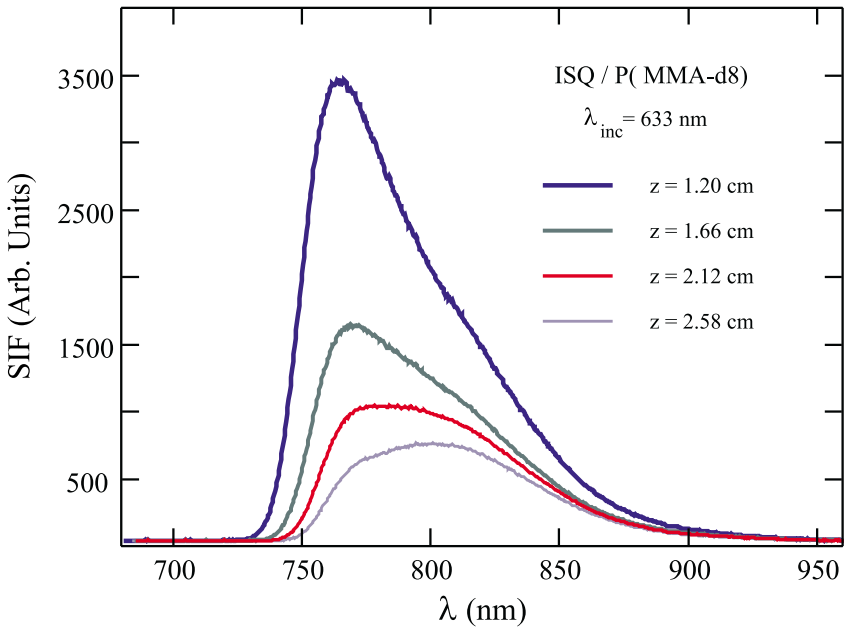

Fig. 5.13: SIF spectra for propagation distances, 1.2 cm $\leq z \leq$ 2.58 cm, in a multimode 30 % deuterated ISQ/P(MMA-d8) fiber (λ_{inc} = 633 nm). Each subsequent curve is measured for an excitation position 0.46 cm further from the front of the fiber.

analyzed (see Section 5.6) but the general change in shape of the SIF spectrum is clear. The broadening of the SIF peak with increasing z is reminiscent of that seen for the deuterated BSQ and deuterated HSQ fibers (see Figures 5.8 and 5.10). However, the broadening occurs at much shorter propagation distances.

As will be continuously shown over the course of this work, ISQ is quite inhomogeneous and rarely has a typical response from one fiber to the next. However, at propagation distances longer than 3.0 cm this section of fiber was particularly well-behaved and could be analyzed (see Section 5.6). Figure 5.14 shows the SIF spectra for propagation distances between 3.3 cm and 4.7 cm in 0.46 cm increments. Notice that there is a small remnant of a shoulder on the high energy side of the spectra, but other than that, the spectrum decreases in intensity and red-shifts similar to that of the other squaraines for the 1.4 cm change in propagation distance.

Specifically, for an excitation at z = 3.3 cm in Figure 5.14, the peak of the SIF spectrum is shifted to 815 nm compared to a peak at 760 nm for z = 1.2 cm (Figure

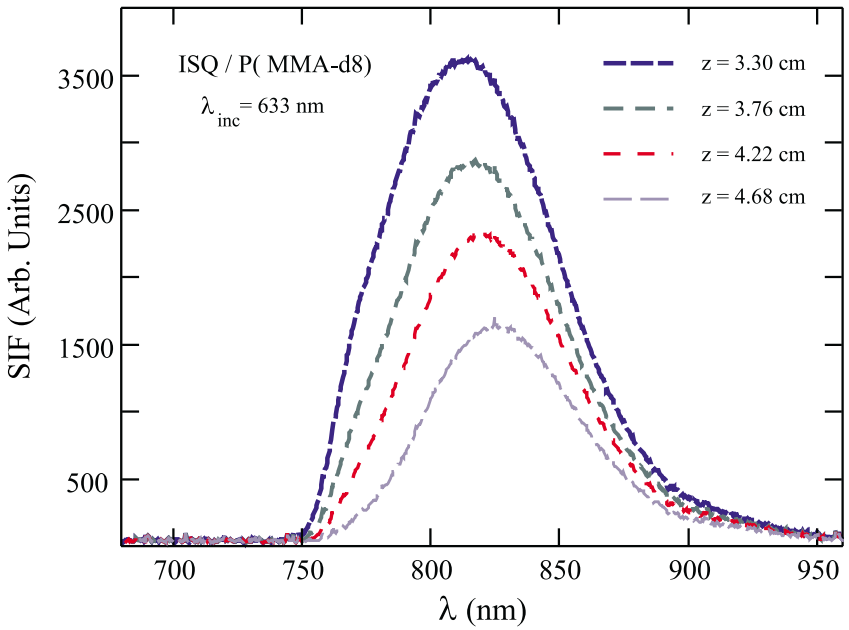

Fig. 5.14: SIF spectra for propagation distances, 3.3 cm $\leq z \leq$ 4.68 cm, in a multimode 30 % deuterated ISQ/P(MMA-d8) fiber (λ_{inc} = 633 nm). Each subsequent curve is measured for an excitation position 0.46 cm further from the front of the fiber.

5.13). This is almost three times the peak shift – 20 nm – seen in for the HSQ/P(MMA-d8) SIF spectrum between 1.1 and 4.2 cm (a larger δz). However, a comparison of the peak wavelength of SIF spectra of ISQ/P(MMA-d8) for excitation positions z = 3.3 cm and z = 5.1 cm, shows a 10 nm change which is similar to the 8 nm change in the HSQ/P(MMA-d8) SIF spectra peak wavelength for excitations at 1.0 cm and 2.4 cm. This suggests that the decrease in the fluorescence spectrum for propagation distances longer than 3.3 cm is mainly a single exponential, like that of HSQ and PSQ.

5.2.1.6 SiPc

At this point we have shown the SIF spectra for all the squaraine dyes that were available. The HSQ, PSQ, and TSQ fibers have very similar features. However, there are some interesting features unique to ISQ and BSQ which need to be discussed in greater detail. In this section, we continue the discussion of SIF spectra by showing the results for SiPc/PMMA which is a copolymer instead of a guest/host fiber. The SiPc molecule

is also 2-D. These differences lead us to expect that the SIF spectra for SiPc will be very different that the SIF spectra for the squaraines. The following section will discuss SIF spectra generated from fibers that are not blue in color (i.e. DR1/PMMA and SP1822/PMMA).

SIF spectra for a highly concentrated SiPc/PMMA copolymer fiber are shown in Figure 5.15. The number density of the SiPc/PMMA fiber is N = 1.22 $\times 10^{18}$ cm^{-3}. Since the absorption maximum for SiPc/PMMA occurs at about 670 nm, the SIF spectrum decreases in magnitude more rapidly than the SIF spectra for the squaraines as the propagation distance is increased. For example, the maximum of the SIF spectrum for SiPc/PMMA (Figure 5.15) decreases to less than 1/3 of its initial value between $z = 1.1$ cm and $z = 1.5$ cm, while the maximum of the SIF spectrum for HSQ/PMMA (Figure 5.9) decreases to about 1/2 of its initial value between $z = 1.1$ cm and $z = 1.56$ cm.

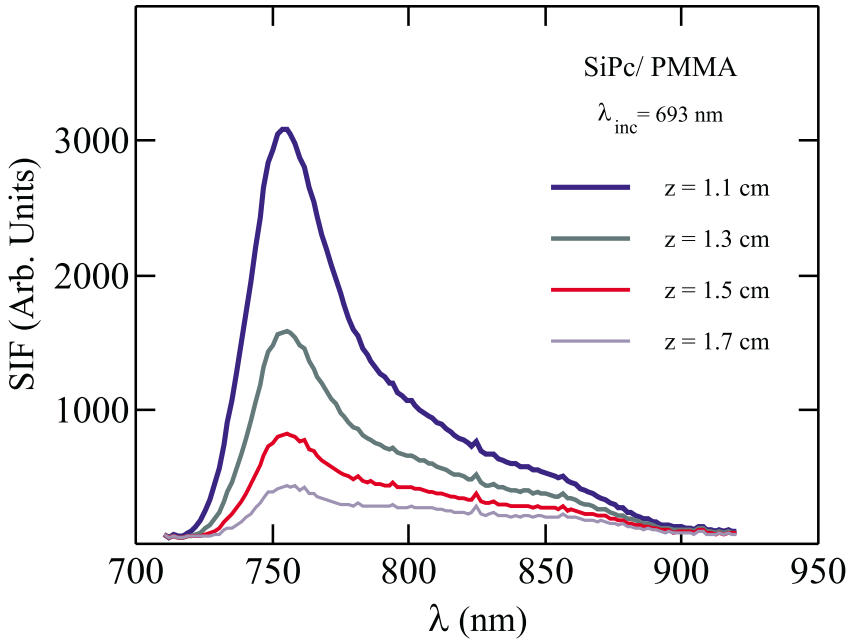

Fig. 5.15: SIF spectra for propagation distances, 1.1 cm $\leq z \leq$ 1.7 cm, in a multimode SiPc/PMMA fiber (λ_{inc} = 693 nm). Each subsequent curve is measured for an excitation position 0.2 cm further into the fiber.

The shape of the fluorescence spectra for SiPc/PMMA is also very different than the shape of the SIF spectra for the squaraine-doped fibers. There is a large narrow

contribution at about 750 nm and is most likely caused by a vibronic de-excitation near 750 nm. For more details the linear absorption spectrum for an SiPc/PMMA preform slice can be seen in Section 5.1.1.3 and the emission spectrum can be seen in Section 5.4.2.

All the SIF spectra which have been discussed are from blue dye-doped fibers. However, the SIF method is not limited to dyes that have a resonance absorption near the He/Ne laser line. To demonstrate that a blue dye is not a necessary condition for the SIF method, a red (DR1) and an orange (SP1822) fiber are characterized. Sections 5.2.1.7 and 5.2.1.8 discuss the SIF spectra as a function of propagation distance for DR1/PMMA and SP1822/PMMA core fibers, respectively.

5.2.1.7 DR1

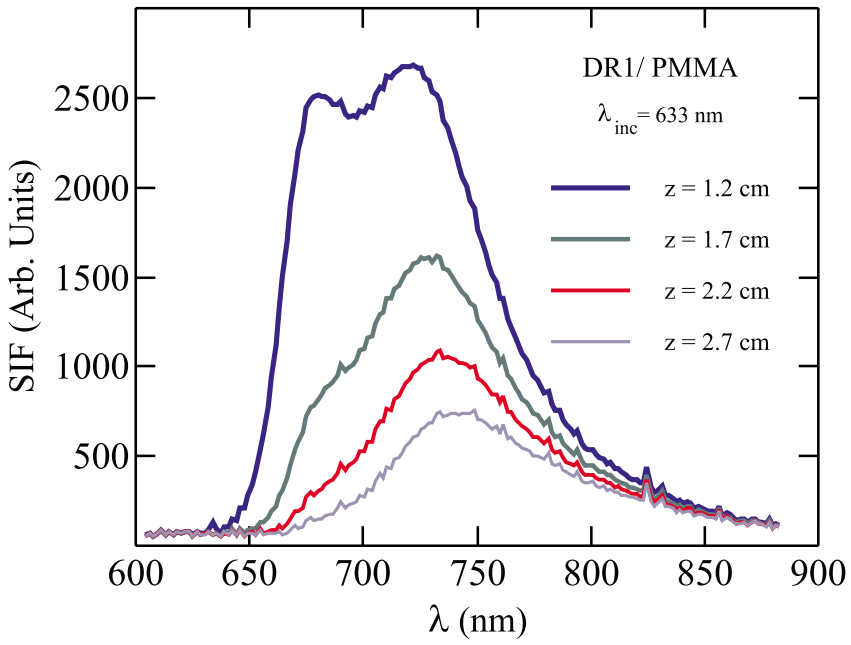

Fig. 5.16: SIF spectra for propagation distances, 1.1 cm $\leq z \leq$ 1.7 cm, in a multimode SiPc/PMMA fiber (λ_{inc} = 633 nm). Each subsequent curve is measured for an excitation position 0.2 cm further into the fiber.

DR1, which is a very well studied nonlinear molecule [3], has a very broad resonance absorption in comparison to the squaraines or SiPc near 490 nm. This absorption gives

the dye a deep red color when it is in powder form. When it is doped into a PMMA core fiber is becomes lighter red because of the reduction in concentration. Figure 5.16 shows the SIF spectra for a highly concentrated sample of DR1. The SIF spectrum for a propagation distance of 1.2 cm has two peaks which are most likely caused by the high concentration, because a cursory study of lower concentration DR1/PMMA fibers did not have the same feature. It could be a re-emission of absorbed fluorescence, an extra fluorescence due to vibronics, or a small excited state centered at 700 nm. Unfortunately, these features were not studied because the He/Ne is known to change the conformations of DR1 thus complicating the analysis. A more appropriate laser wavelength needs to be found before extensive quantitative work can be performed on DR1/PMMA core fibers.

Focusing on the longer wavelength peak in the SIF spectra (at 720 nm) in the initial spectrum, we see that this feature red-shifts and decreases in magnitude similar to the maximum in the SIF spectra for the squaraine dyes. This is not very interesting until we are reminded that the maximum of the DR1/PMMA SIF spectrum is about 200 nm from the absorption maximum for DR1. In comparison, the maximum of the HSQ/PMMA SIF spectrum is only shifted 100 nm from the HSQ absorption maximum. Since the magnitude of the fluorescence decreases rapidly 200 nm from resonance for the DR1/PMMA fiber, the linear loss may be too high for DR1/PMMA nonlinear optical devices to be practical in this wavelength range. The loss as a function of wavelength will be discussed for the DR1/PMMA core fiber in Section 5.6 in terms of the linear absorption coefficient, $\alpha(\lambda)$.

5.2.1.8 SP1822

The spiropyran (SP1822) dye is normally orange in color, $\lambda_{max} = 340$ nm, and exhibits interesting photo-reversible behavior in PMMA thin films [4]. Under UV illumination it undergoes a ring opening and the absorption maximum shifts to about 620 nm. Unfortunately, we were unable to study this type of behavior in spiropyran-doped PMMA fibers due to time constraints but this would be an interesting direction for future work. It is interesting that the SIF spectrum of the spiropyran dye was even measurable because the orange spiropyran absorbs very weakly at 633 nm. However, the fluorescence intensity

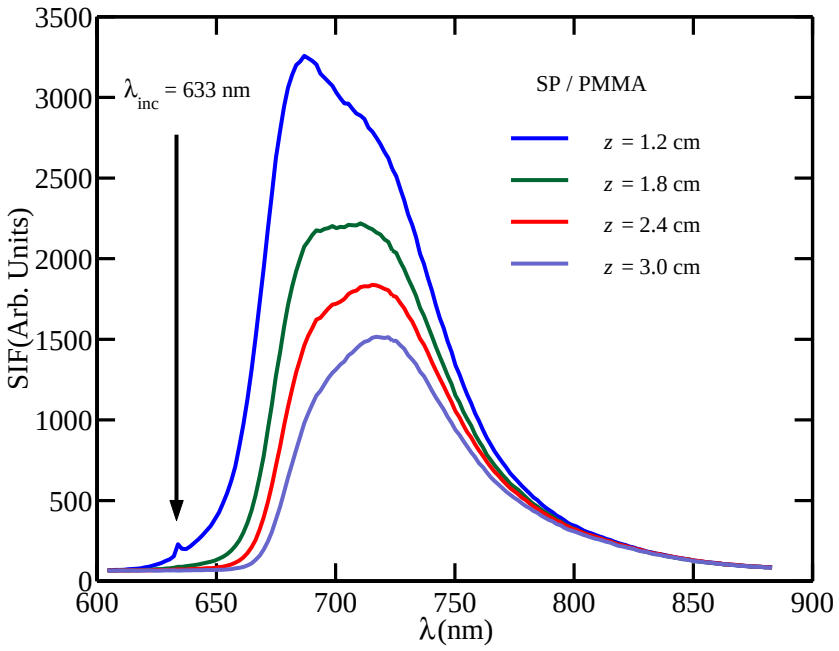

Fig. 5.17: SIF spectra for propagation distances, 1.2 cm $\leq z \leq$ 3.0 cm, in a multimode SP1822/PMMA fiber (λ_{inc} = 633 nm). Each subsequent curve is measured for an excitation position 0.6 cm further into the fiber.

was more than ample to do SIF experiments.

Figure 5.17 shows how the SIF spectrum of SP1822 changes as a function of illumination position. Because the SP1822 dye absorbs weakly in the visible, the spectrum is blue-shifted in comparison to the squaraine dyes. The SIF spectrum would most likely blue shift even more if a shorter wavelength source were used to illuminate the fiber because the He/Ne laser line can be seen in the SIF spectrum for the shortest propagation distance. The SIF spectra for SP1822 also has an interesting feature near 700 nm which is reminiscent of the feature seen in ISQ/PMMA SIF spectrum near 760 nm, and will be studied further in Section 5.6.0.7.

This concludes the introduction to the SIF experimental results. We have shown that in all cases the magnitude of the SIF spectrum decreases with increasing propagation distance. This feature will be exploited in Section 5.6 to calculate the linear absorption coefficient $\alpha(\lambda)$ for wavelengths in the fluorescence band. The results also show that there is a red-shift in the peak of the fluorescence for all dyes which suggests that the

absorption is higher at shorter wavelengths. Because the absorption is consistently larger at shorter wavelengths it is most likely caused by the tail of the resonant excited state. If this is the case, the SIF spectra at various propagation distances can be used to calculate transition moments and energy levels which characterize the resonant excited state (see Section 5.7).

5.2.2 Fiber diameter dependence

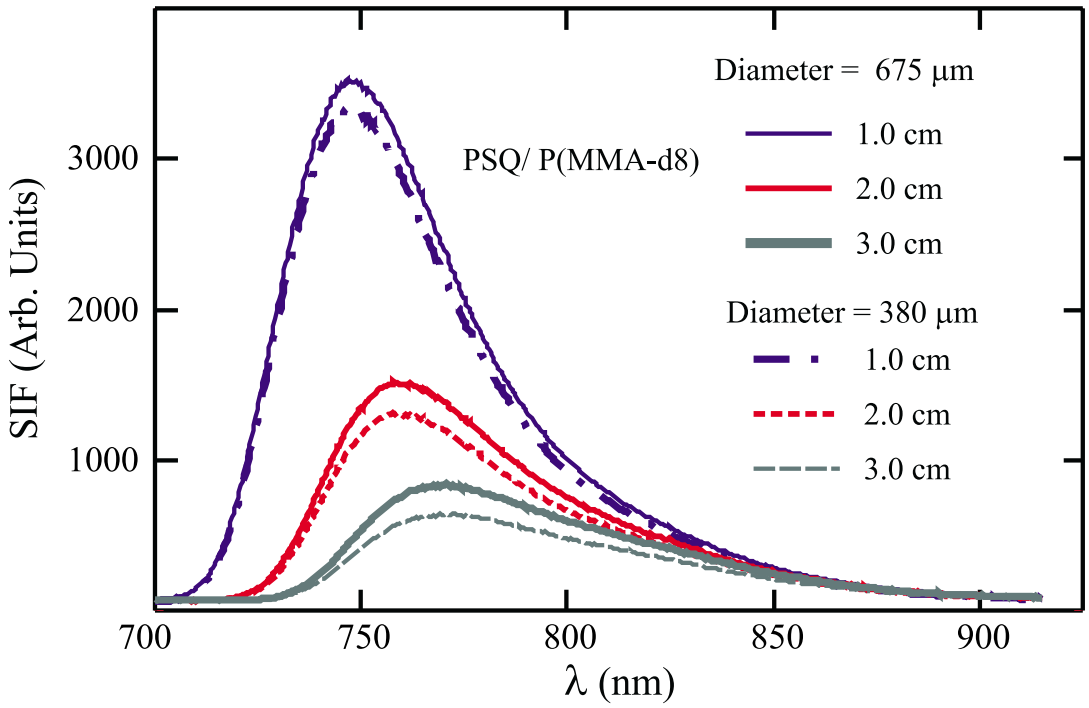

Fig. 5.18: SIF spectra for PSQ/P(MMA-d8) core fibers with diameters of 680 μm and 375 μm. Each subsequent curve is measured for an excitation position 1.0 cm further into the fiber.

Before discussing the concentration dependence of the SIF spectrum, it should be noted that we have determined that the fiber diameter has a negligible effect on the SIF spectrum and its dependence on propagation distance. Figure 5.18 represents the SIF spectra for a PSQ/P(MMA-d8) core fibers with diameters of 375 μm and 680 μm. The larger diameter fiber transmits slightly more fluorescence but there is little difference in the shape of SIF spectra for each illumination position.

This is a general phenomena for the dye-doped fibers we have studied and allows us to simplify the point source model so that it is independent of diameter (see Section 2.7.1). For the remainder of this chapter the diameter of the fiber will not be mentioned but it is always in between 175 μm and 800 μm making all the core fibers studied very multimode.

5.2.3 Concentration dependence

In this section, we show that an increase in concentration has the same effect on the SIF spectrum as an increase in propagation distance for the majority of dyes studied. The larger red-shift in the SIF spectra for higher concentration fibers should be helpful in determining $\alpha(\lambda)$ further from the absorption maximum. Initially we discuss the squaraine-doped core fibers. However, discussion of the most interesting effects that result from changing the dye concentration are left until the end because they occur in the SiPc/PMMA copolymer core fibers.

5.2.3.1 BSQ

SIF spectra are shown for two different concentrations of BSQ-doped core fibers in Figure 5.19. As the concentration (number density) increases the maximum of the SIF spectrum for BSQ-doped core fiber red-shifts for a fixed propagation distance ($z = 1.1$ cm). This red-shift occurs because the fluorescence must travel through more optically dense material on its way to the front of the fiber in the higher concentration fiber. Therefore the shorter wavelengths in the fluorescence band, which are closer to resonance, do not make it to the detector with a measurable intensity.

The dashed curves in Figure 5.19 show the SIF spectra for each fiber from $z = 2.0$ cm as a comparison to the spectra from $z = 1.0$ cm. Notice the maximum of the SIF spectrum for the higher concentration fiber decreases more rapidly over the same change in propagation distance suggesting that the high concentration loss at 765 nm for the BSQ/P(MMA-d8) fiber is larger than the low concentration loss at 745 nm for the lower concentration BSQ/PMMA fiber. This will be investigated further is Section 5.6.0.1.

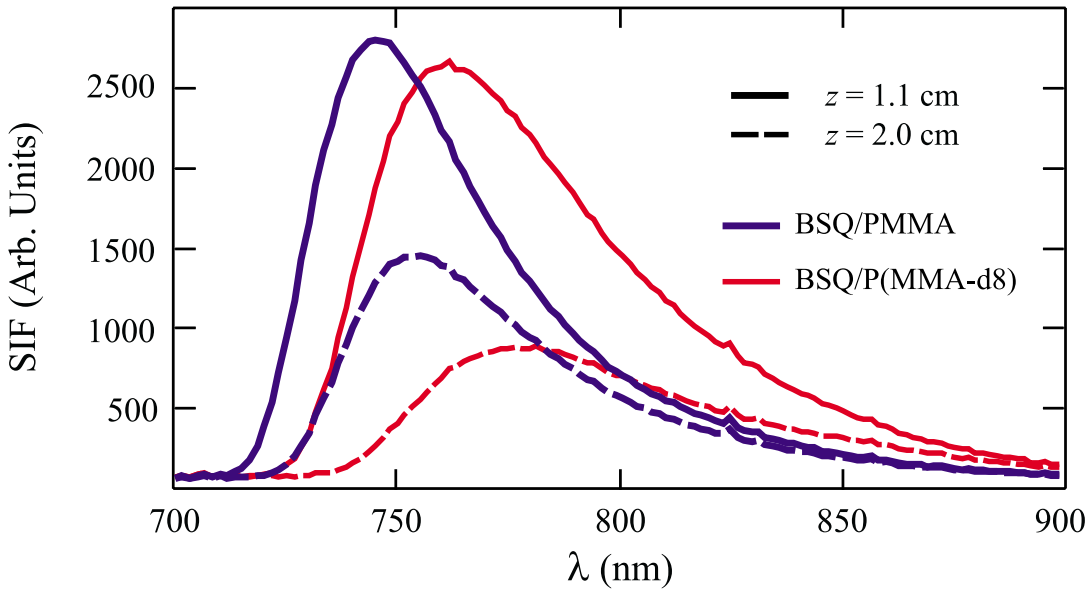

Fig. 5.19: SIF spectra for two excitation positions (i.e. propagation distances) for two different concentrations of BSQ-doped multimode core fibers (λ_{inc} = 633 nm). The BSQ/PMMA fiber has a number density, N = 4 $\times 10^{18}$ cm^{-3}, and the BSQ/P(MMA-d8) has a number density, N = 5.8 $\times 10^{18}$ cm^{-3}.

5.2.3.2 PSQ

Figure 5.20 shows results of SIF experiments on two different concentrations of PSQ-doped PMMA fibers at two different propagation distances. For each fiber, the peak of the fluorescence red-shifts due to self-absorption as the propagation distance increases. Similar to BSQ/PMMA fibers, the spectrum from the fiber with the higher concentration of dye is red-shifted relative to the spectrum from lower concentration fiber at the same propagation distance. Again, the absorption due to the resonant excited state extends further from resonance as the concentration increases causing the shorter wavelengths in the fluorescence band to be absorbed more quickly.

5.2.3.3 TSQ

Three low concentration TSQ/PMMA core fibers from the same original solution were measured using side-illumination fluorescence to show that the measurement can be per-

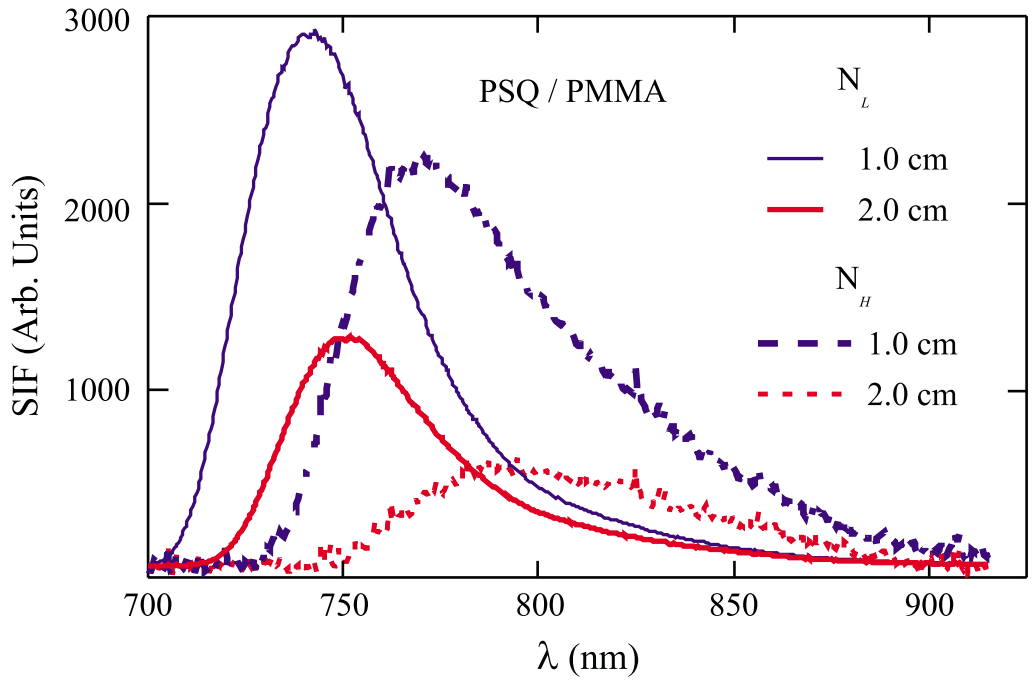

Fig. 5.20: SIF spectra for two excitation positions (i.e. propagation distances) and concentrations in multimode PSQ/PMMA fibers (λ_{inc} = 693 nm). $N_H = 4 \times 10^{18}$ cm^{-3} (saturation concentration for samples polymerized at 60 °C), and $N_L = 1.1 \times 10^{18}$ cm^{-3} (Saturation concentration for samples polymerized at 25 °C.).

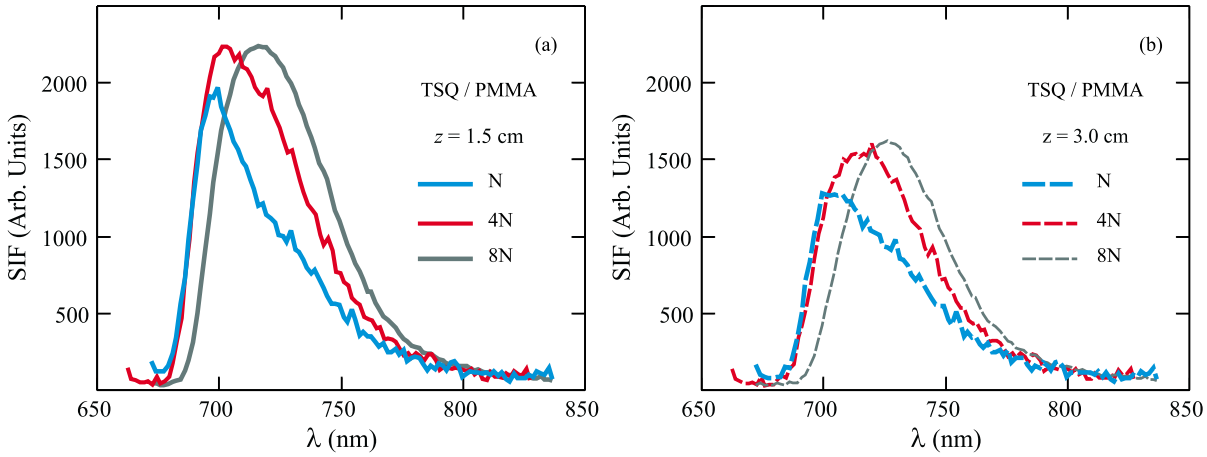

Fig. 5.21: SIF spectra from z=1.5 cm (a) and z=3.0 cm (b) for three low concentrations of multimode TSQ/PMMA fibers ($N_k \in \{N, 4N, 8N\}$ for $\lambda_{inc} = 633$ nm. The lowest concentration TSQ/PMMA fiber studied has a number density, $N = 1.6 \times 10^{16}$ cm^{-3}. Note the y-axis for (a) and (b) are measured in the same units which are arbitrary.

formed on low concentration fibers as well as high concentration fibers. The number densities of TSQ in PMMA, from high to low, are approximately 1.3 $\times 10^{17}$ cm^{-3}, 6.4 $\times 10^{16}$ cm^{-3}, and 1.6 $\times 10^{16}$ cm^{-3}, which are much lower than those for the PSQ-doped core fibers discussed in the previous section. We also measured a high concentration TSQ/PMMA fiber (200N) but have not shown the spectra because they are very similar to PSQ/PMMA or HSQ/PMMA spectra.

It should be noted that the lowest concentration TSQ/PMMA fiber is only slightly darker blue than a tinted contact lens. Thus the SIF signal is small because of the low density of molecules (i.e. few fluorescing dyes) not high absorption. Even though the units are arbitrary a smaller fluorescence intensity is noticeable because of the noise superimposed on the spectra. In the two lowest concentration TSQ/PMMA fibers there is noticeably more noise superimposed on the fluorescence spectra shown in Figure 5.21. As the TSQ concentration is increased, the SIF intensity becomes larger (smoother spectra) but also red-shifts in comparison to two lowest concentration fibers.

At $z = 1.5$ cm, there is about a 5 nm difference in the peak wavelength of SIF spectra for the two lowest concentration TSQ/PMMA fibers. This difference increases with increasing propagation distance. At $z = 3.0$ cm, the difference is to about 15 nm. This suggests that the absorption is significantly larger for the fiber labeled 4N in comparison to the fiber labeled N – which is expected from the measurement. However, we cannot determine if ratio of the absorption is identical to the ratio of the number densities until Section 5.6.0.3, where these three core fibers will be discussed in terms of the absorbance, $\alpha(\lambda)$, in the fluorescence band.

5.2.3.4 ISQ

Figures 5.22a and 5.22b show the SIF spectra for four concentrations of ISQ/PMMA core fibers. In Figure 5.22a the illumination position is $z = 1.3$ cm, and in Figure 5.22b, the illumination position is $z = 2.8$ cm (Note the y-axis units the same for Figure 5.22a and Figure 5.22b but are arbitrary for each fiber.).

As in the previous discussions of BSQ, PSQ, and TSQ, the peak of the SIF spectrum red-shifts with increasing concentration because of self-absorption. However, a unique

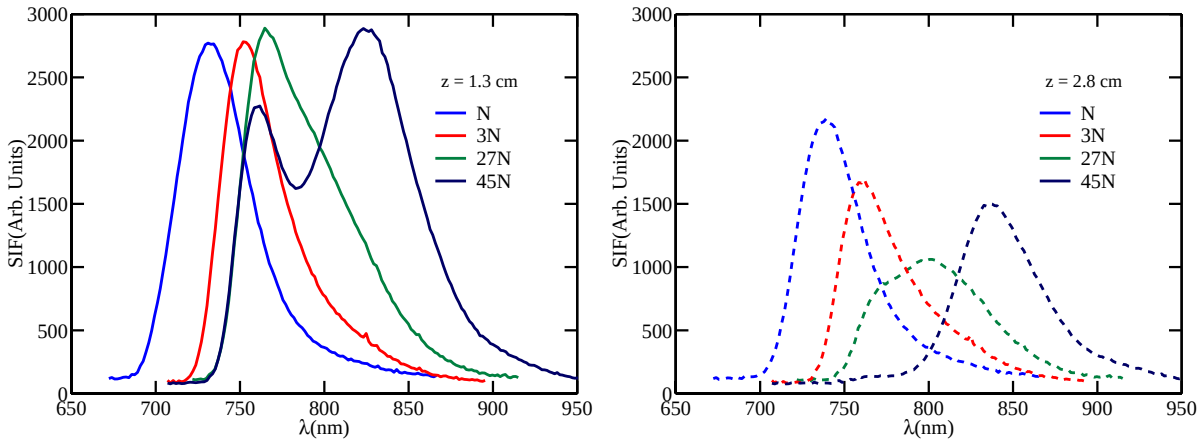

Fig. 5.22: SIF spectra from z=1.3 cm (a) and z=2.8 cm (b) for four concentrations of multimode ISQ/PMMA fibers ($N_k \in \{N, 3N, 27N, 45N\}$) for $\lambda_{inc} = 633$ nm ($N = 1.4 \times 10^{17}$ cm^{-3}). Note the y-axis for (a) and (b) are measured in the same units which are arbitrary.

effect occurs at higher concentrations of the ISQ dopant. At $z = 1.3$ cm, the spectrum labeled 27N has a dip at 770 nm and the spectrum labeled 45N has a double peak structure that is qualitatively different from the two lowest concentration fibers.

When the illumination position is increased to 2.8 cm, the spectrum labeled 27 N (green) shows a slightly larger depression near 770 nm and the peak of the spectrum has shifted beyond 770 nm. The red-shift in the peak fluorescence is larger than expected and is most likely caused by whatever creates the dip at 770nm.

The SIF spectrum labeled 45N has a completely different shape at $z = 2.8$ cm in comparison to $z = 1.3$ cm. There is no high energy peak and the shape of the spectra is similar to the two lowest concentration SIF spectra. If we observe the red-shift of the low energy peak from $z = 1.3$ cm to $z = 2.8$ cm, it is similar to the red-shift for the two lowest concentration fibers. This suggests that the loss beyond 820 nm is not influenced by whatever causes absorption near 775 nm.

Clearly, these unique features are worth investigating in terms of $\alpha(\lambda)$ and the excited state manifold. Because the large valley develops in the 45N spectrum for an illumination position of $z = 1.3$ cm, it seems reasonable that a previously unidentified excited state is the cause of the feature rather than an additional fluorescence. However, a rigorous

determination will have to wait until Section 5.6.0.4.

5.2.3.5 SiPc

Although change in the ISQ/PMMA SIF spectra with increasing concentration is very intriguing, the most interesting effect is for SiPc/PMMA. Figure 5.23 shows the SIF spectra for two concentrations of SiPc/PMMA copolymer when the fiber is illuminated at $z = 1.1$ cm and $z = 1.5$ cm. The short distance between the illumination positions is necessary because of the large loss and resulting decrease in the SIF spectrum for the high concentration core fiber. Note that SIF spectra for each fiber is normalized to approximately 3000 for $z = 1.1$ cm. This is done by varying the integration time on the spectrometer.

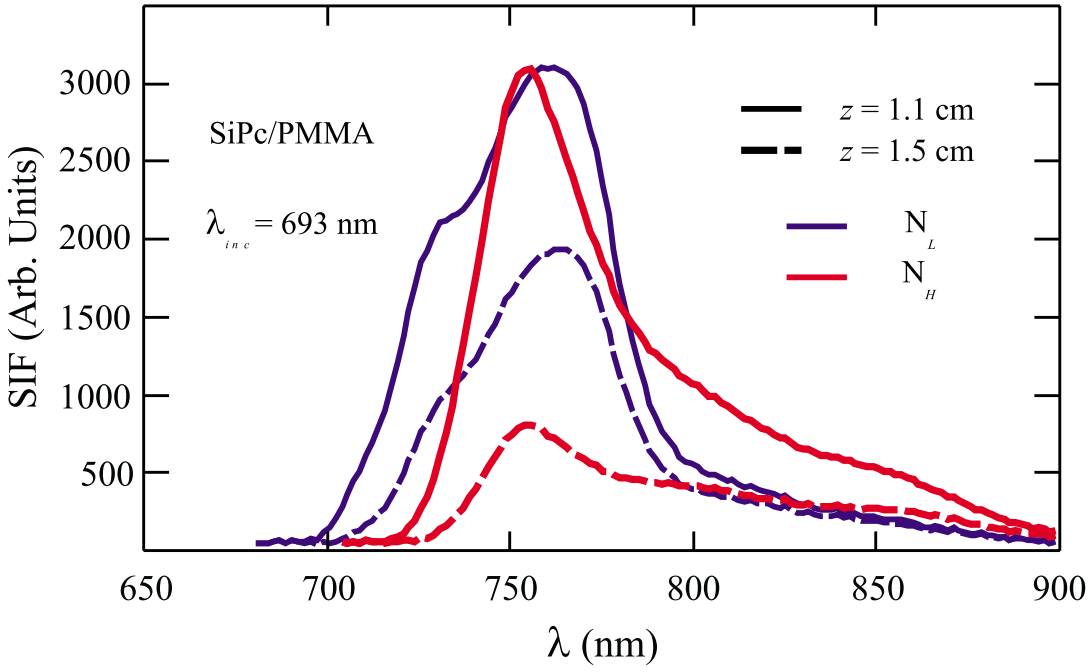

Fig. 5.23: SIF spectra for two illumination positions (1.1 cm and 1.5 cm) and two concentrations of multimode SiPc/PMMA fibers for $\lambda_{inc} = 693$ nm. $N_H = 1.2 \times 10^{18}$ cm^{-3} , and $N_L = 1.3 \times 10^{17}$ cm^{-3}.

In previous discussions, the SIF spectrum red-shifted as the concentration of dopant increased even if the shapes of the spectra were different. For SiPc there is a large change

in the shape of the spectrum from the low concentration fiber to the high concentration fiber, and a blue-shift in the maximum of the fluorescence.

For ISQ/PMMA the SIF spectrum became interesting at high concentrations but for the SiPc/PMMA copolymer core fiber the SIF spectrum is more intriguing at the lower concentration. We suggest that there are two distinct emissions that account for the shape of the lower concentration spectra, instead of an extra absorption.

For example, the emission which creates the short wavelength shoulder in the lower concentration SIF spectrum could correspond to the emission which creates the maximum of the SIF spectrum of the higher concentration fiber. The maximum of the higher concentration SIF spectrum is red-shift from the short wavelength shoulder in the lower concentration SIF spectrum because of higher self-absorption. As the illumination position is increased to $z = 1.5$ cm from $z = 1.1$ cm, the shapes of the SIF spectra decrease in magnitude but do not significantly change shape. This is in contrast to the evolution of the two high concentration SIF spectra for ISQ/PMMA (see Figure 5.22) which shows signs of aggregation. This type of analysis of the SiPc/PMMA spectra suggests that the maximum of the SIF spectrum for the low concentration SiPc/PMMA fiber is caused by an additional emission. To develop a better understanding of the features in the SIF spectra for SiPc/PMMA copolymer fibers, they will be studied in more detail in Section 5.2.5.5

5.2.4 Polymer dependence

At this stage, we have discussed how the SIF spectrum for various dye-doped core fibers varies as a function of illumination position and concentration. For the majority of fibers, increasing the illumination position is similar to increasing the concentration. In this section we explore how the polymer host affects the fluorescence generated by the dyes. There were only four dyes (BSQ, HSQ, PSQ, ISQ) that were polymerized in deuterated PMMA. Because there was very little MMA-d8, the entire amount was used to make four core preforms. 50 mg of PSQ, HSQ, and BSQ were dissolved in 10 ml of the deuterated monomer, and the final 3 ml of MMA-d8 with 7 ml of MMA was used to dissolve 50 mg

of ISQ. Even though the room temperature maximum concentrations for PSQ/PMMA, HSQ/PMMA, and ISQ/PMMA are much lower, the large amount of dye was used in case the deuterated monomer had a higher saturation concentration than MMA.

The BSQ/P(MMA-d8) core fiber is below the room temperature maximum concentration for BSQ/PMMA so there was no BSQ/PMMA core fiber at the same concentration for comparison in this section. However, there were HSQ/PMMA, PSQ/PMMA, and ISQ/PMMA core fibers at room temperature maximum concentrations to compare to the corresponding deuterated fibers. Since HSQ- and PSQ-doped fibers have very similar SIF spectra (see Figure 5.11) they will be discussed together and ISQ will be explored separately. In general, each fiber generates a different magnitude of fluorescence so the spectra may be normalized at the peak wavelength for ease of comparison.

5.2.4.1 HSQ and PSQ

In Section 5.2.1.3 it was shown that the normalized SIF spectra from HSQ/PMMA and PSQ/PMMA core fibers of similar concentration are identical within the thickness of the lines that represent them. This is also the case when HSQ/P(MMA-d8) and PSQ/P(MMA-d8) SIF spectra for fibers of similar concentrations are overlaid [5]. However, there is a slight difference when the SIF spectra are compared for the two different polymers.

Figure 5.24 summarizes the differences in the SIF spectra when HSQ is doped in a PMMA and a P(MMA-d8) environment. The normalized SIF spectrum of an HSQ/P(MMA-d8) fiber for a propagation distance of 1.8 cm is shown superimposed on the spectrum for an HSQ/PMMA fiber (2.0 cm). It should be noted that the two different propagation distances were chosen so that the high energy side of the SIF spectra would overlap. This is necessary because the fibers were made with slightly different concentrations of dye.

Clearly there is a small broadening of the SIF spectrum when the HSQ is a guest in the deuterated polymer. This small broadening can be emphasized by subtracting the HSQ/PMMA spectrum from the HSQ/P(MMA-d8). Figure 5.25 shows the change in the SIF spectrum due to the polymer host.

There is negligible difference on the short wavelength side of the fluorescence spec-

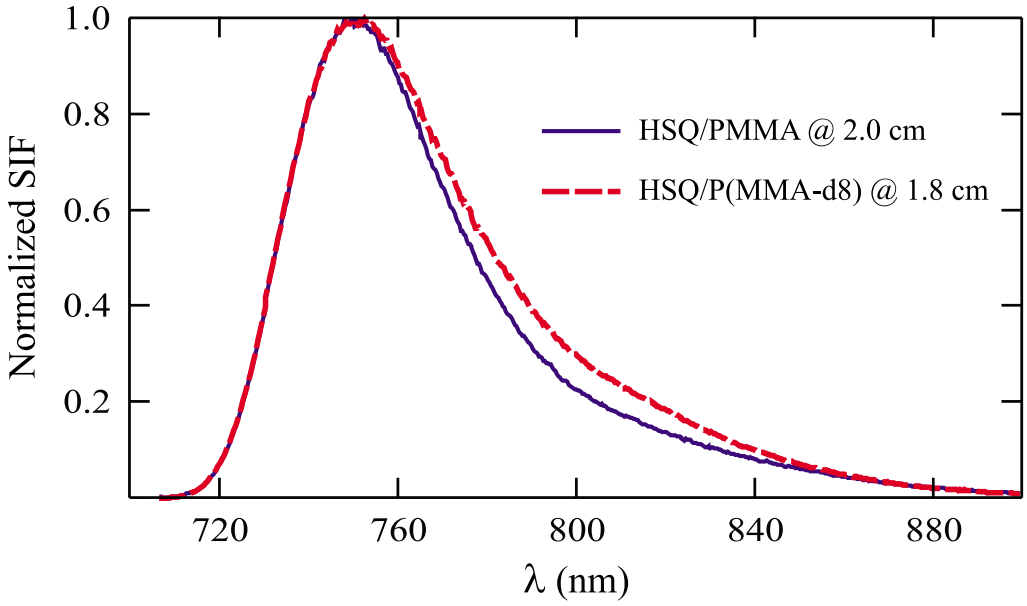

Fig. 5.24: SIF spectra for HSQ/PMMA (2.0 cm) and HSQ/P(MMA-d8) (1.8 cm) fibers.

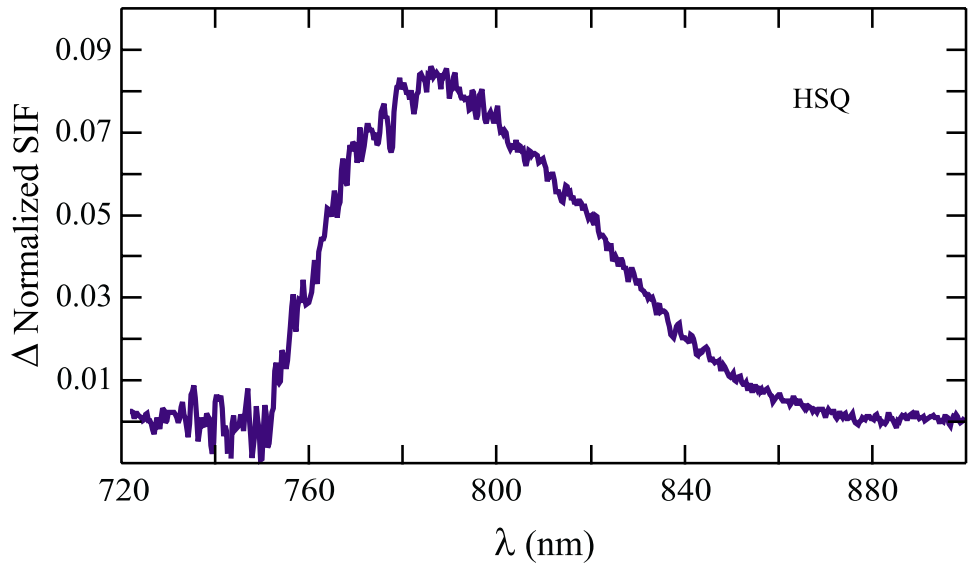

Fig. 5.25: Normalized SIF spectrum for a HSQ/PMMA (2.0 cm) fiber subtracted from the normalized SIF spectrum for a HSQ/P(MMA-d8) (1.8 cm) fiber.

trum. However, there is a clear feature centered at 785 nm. This could imply that there is an additional fluorescence due to HSQ's interaction with the deuterated PMMA, or that there is an additional small excited state peaked at 785 nm in the HSQ/PMMA environment which adds to the absorbance at that wavelength. In either case, this may be evidence for an unidentified state in HSQ and PSQ because analysis of PSQ shows similar results.

5.2.4.2 ISQ

The HSQ-doped and PSQ-doped core fibers exhibit the same change in the SIF spectrum when the host is changed from PMMA to P(MMA-d8). However, this is not the case for ISQ-doped fibers since it is difficult to find consistent behavior from one fiber to the next in the same polymer host. In this section we show some of the changes in the SIF spectrum when the polymer host is changed.

Figure 5.26 displays the SIF spectra for a partially deuterated and a non-deuterated ISQ-doped fiber at three propagation distances. The SIF spectrum for the ISQ/PMMA fiber decreases continuously as the propagation distance increases from 1.0 cm to 3.0 cm which is expected for absorption by a single excited state. However, the partially deuterated ISQ/P(MMA-d8) spectrum has a dramatically different shape at each propagation distance, z. This shape change is not consistent with an extra fluorescence because each color in the spectrum does not exponentially decrease with propagation distance according to a two-state model. The SIF spectrum for partially deuterated ISQ is qualitatively different at the three propagation distances: At $z = 1.0$ cm, the spectrum has a shoulder between 800 and 840 nm; at $z = 2.0$ cm, the spectrum has flattened and there is little difference in the intensity between 760 and 820 nm; and at $z = 3.0$ cm, the peak of the SIF spectrum has shifted to about 825 nm which corresponds to the shoulder for a propagation distance of $z = 1.0$ cm.

Ruling out an extra fluorescence for the interesting behavior of the ISQ/P(MMA-d8) SIF spectrum, the difference in the response is most likely caused a previously unidentified excited state. Figure 5.27 shows the ISQ/P(MMA-d8) spectrum subtracted from the 3.0 cm ISQ/PMMA spectrum and suggests where this excited state would be located. The

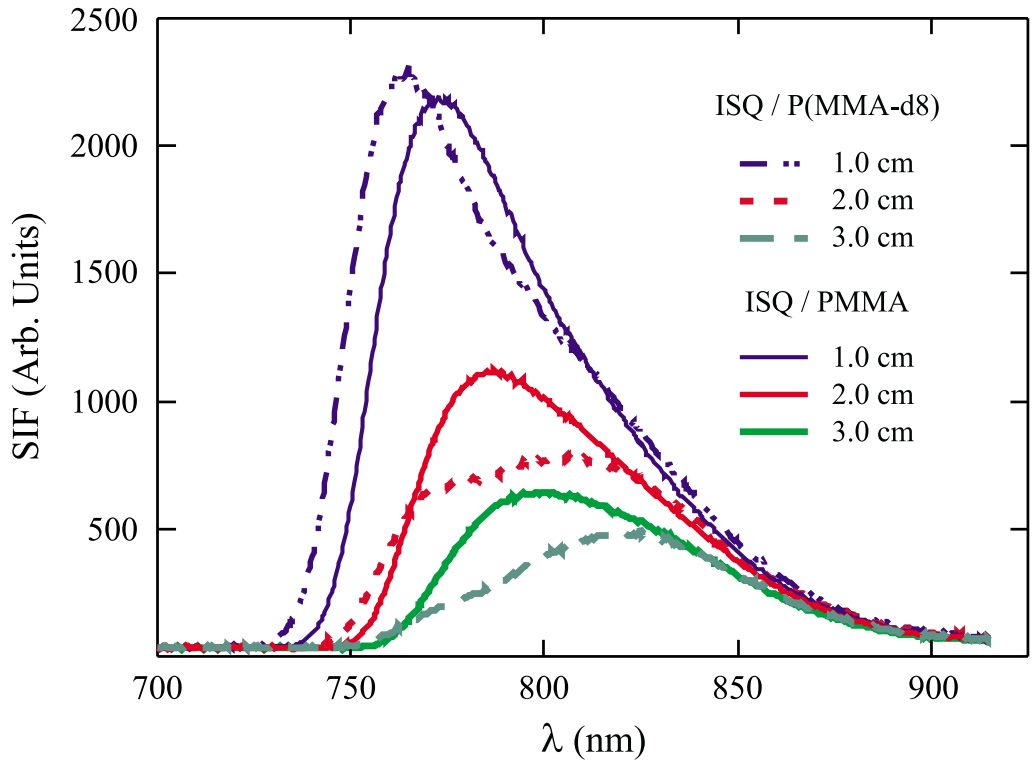

Fig. 5.26: SIF spectra for various propagation distances in multimode ISQ/PMMA and 30 % deuterated ISQ/P(MMA-d8) fibers (λ_{inc} = 693 nm). The inset shows the difference in fluorescence for the two spectra that propagated 3.0 cm.

maximum in the difference spectrum is at 790 nm and roughly half the magnitude of the peak ISQ/PMMA fluorescence intensity.

The change is the SIF spectrum for the ISQ/P(MMA-d8) core fiber is very similar to the evolution of the SIF spectrum for the ISQ/PMMA fiber labeled 27N in Figures 5.22a and 5.22b. Thus is seems like both ISQ/PMMA and ISQ/P(MMA-d8) core fibers exhibit unique behavior at high concentrations. These features will be further investigated in Section 5.6.0.4 to determine if the evolution of the SIF spectrum with propagation distance for high concentration fibers is indeed caused by a previously unidentified excited state.

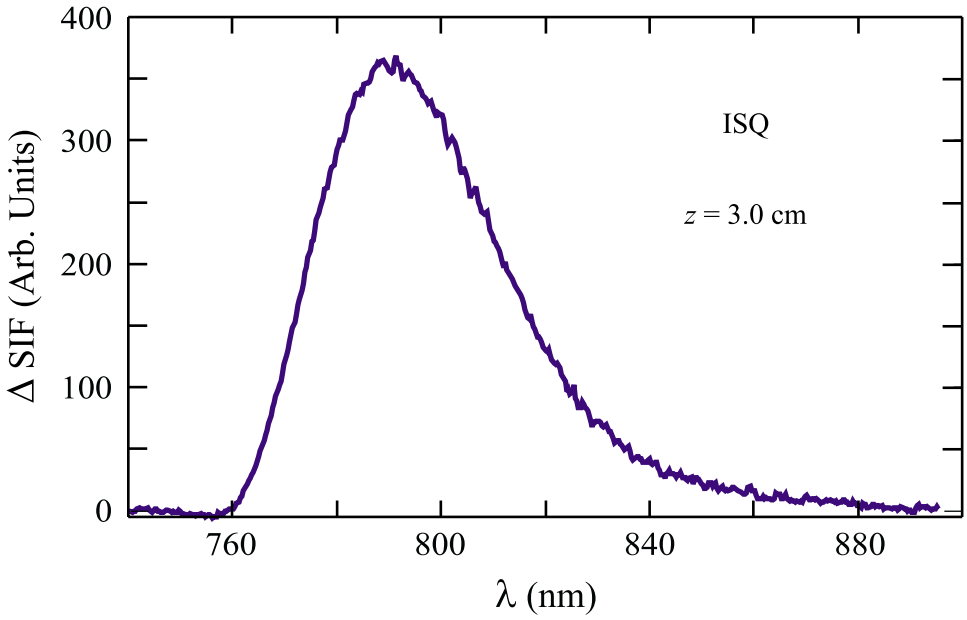

Fig. 5.27: SIF spectrum for a ISQ/P(MMA-d8) (3.0 cm) fiber subtracted from the SIF spectrum for a HSQ/PMMA (3.0 cm) fiber.

5.2.5 Incident wavelength dependence

As previously reported [6, 5], the SIF measurements were initially conducted at two incident wavelengths (633 nm and 693 nm). We have also used two more laser diodes (643 nm, and 667 nm), and a Argon Ion pumped Ti:Sapphire continuously tunable laser. In this section we discuss how the incident laser wavelength effects the fluorescence generation by studying the SIF spectrum for BSQ, HSQ, PSQ, ISQ, and SiPc core fibers. The laser diodes (643 nm, 667 nm, and 693 nm) are mounted to the optical table and illuminate the core fiber as shown in Figure 4.6 for all experiments discussed in this section.

In general, each incident wavelength has a different quantum efficiency for generating a fluorescence spectrum. To account for the variation in SIF intensity from one wavelength to the next, the SIF intensity may be normalized at the peak fluorescence for some of the comparisons. It should be noted that the squaraine-doped core fibers did not have a measurable SIF spectrum when illuminated with the Ti:Sapphire laser so only the SiPc/PMMA copolymer core fibers have been characterized beyond 693 nm.

5.2.5.1 BSQ

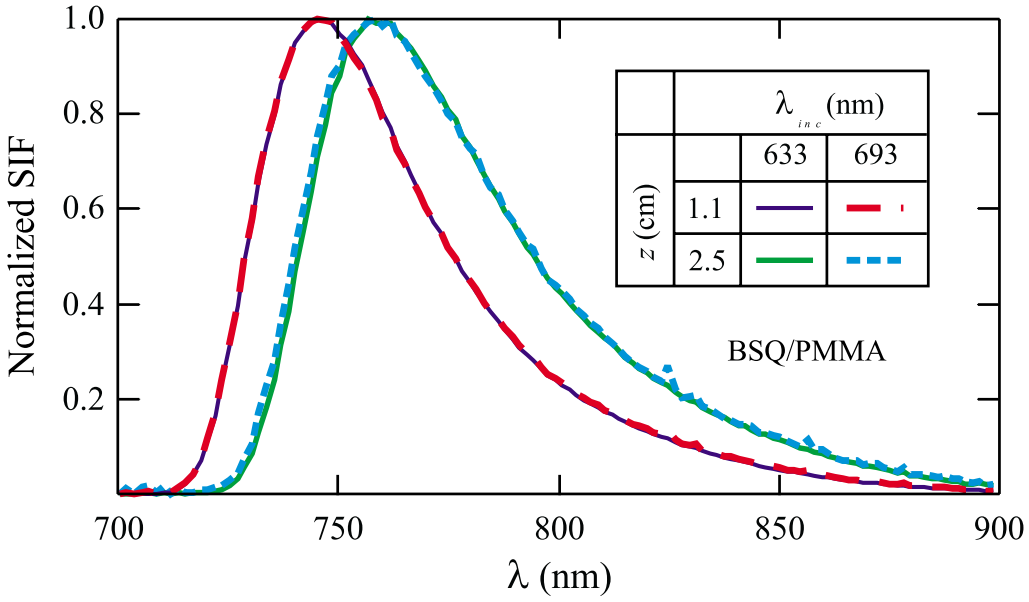

Fig. 5.28: Normalized SIF spectrum for a BSQ/PMMA core fiber for two illumination positions (1.1 cm and 2.5 cm) and two incident wavelengths (633 nm and 693 nm).

Figure 5.28 shows the normalized SIF spectrum for 633 nm and 693 nm incident light when generated at 1.1 cm and 2.5 cm from the beginning of the fiber. Clearly, the difference in the SIF spectrum when the incident wavelength is changed from 633 nm to 693 nm is negligible. This holds for all the illumination positions probed in the experiment and for the other two laser diodes. Consequently, further analysis of the SIF spectra from BSQ-doped core fibers will be discussed independently of the incident wavelength.

5.2.5.2 HSQ and PSQ

The fluorescence, shown in Figure 5.29, for the PSQ/PMMA fiber represents self-absorbed propagation of 1.0 cm, while the fluorescence for the HSQ/PMMA fiber is measured for a 2.0 cm propagation distance. These two propagation distances are intentionally chosen to avoid overlap between the PSQ/PMMA and HSQ/PMMA spectra, since there is little perceivable difference in the HSQ and PSQ spectra when the fluorescence propagates the

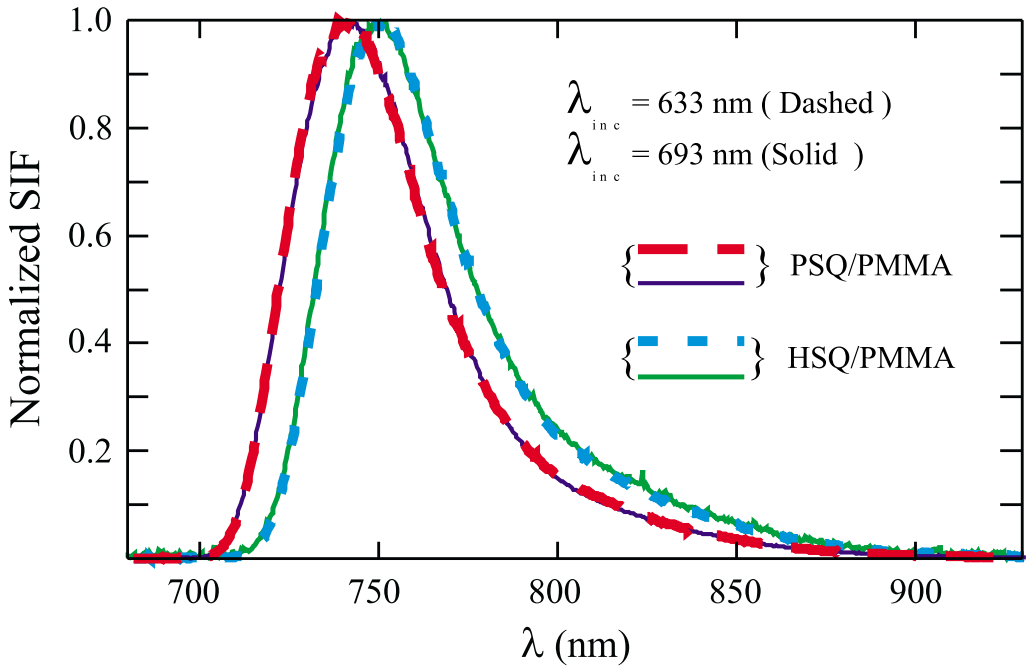

Fig. 5.29: Side-illumination fluorescence (SIF) spectra for incident wavelengths of 633 nm and 693 nm in multimode HSQ/PMMA and PSQ/PMMA fibers. The spectra for PSQ is recorded for illumination 1.0 cm into the fiber and the spectrum for HSQ is from illumination 2.0 cm into the fiber.

same distance as was previously discussed in Section 5.2.4.

Clearly, the HSQ/PMMA and PSQ/PMMA spectra show no dependence on the incident laser wavelength. Deuterated fibers doped with HSQ and PSQ also have SIF spectra that are independent of incident wavelength so, for clarity of presentation, they are not displayed in Figure 5.29. Results for HSQ and PSQ-doped PMMA and P(MMA-d8) fibers will therefore be shown independent of the incident wavelength in subsequent analyses.

5.2.5.3 TSQ

The dependence of the SIF spectrum on incident wavelength for PSQ, HSQ, was measured from high concentration fibers at or near room temperature maximum concentration. Unfortunately, this will also be the case for TSQ/PMMA because the three low concen-

tration fibers, discussed in Section 5.21, did not generate a large enough fluorescence signal when illuminated with 693 nm. Clearly, the low concentration of dye molecules accounts for the lack of measurable SIF spectra for the 693 nm excitation wavelength.

Therefore we introduce results from a TSQ/PMMA fiber with a number density of N=3.3 $\times$ 10^{18} cm^{-3}. This high concentration fiber was polymerized from a TSQ/MMA solution that was held at 60 °C (see Section 3.2.2) until it was placed in the 95 °C oven to polymerize, and corresponds to the maximum amount of dye that dissolves in MMA at 60 °C.

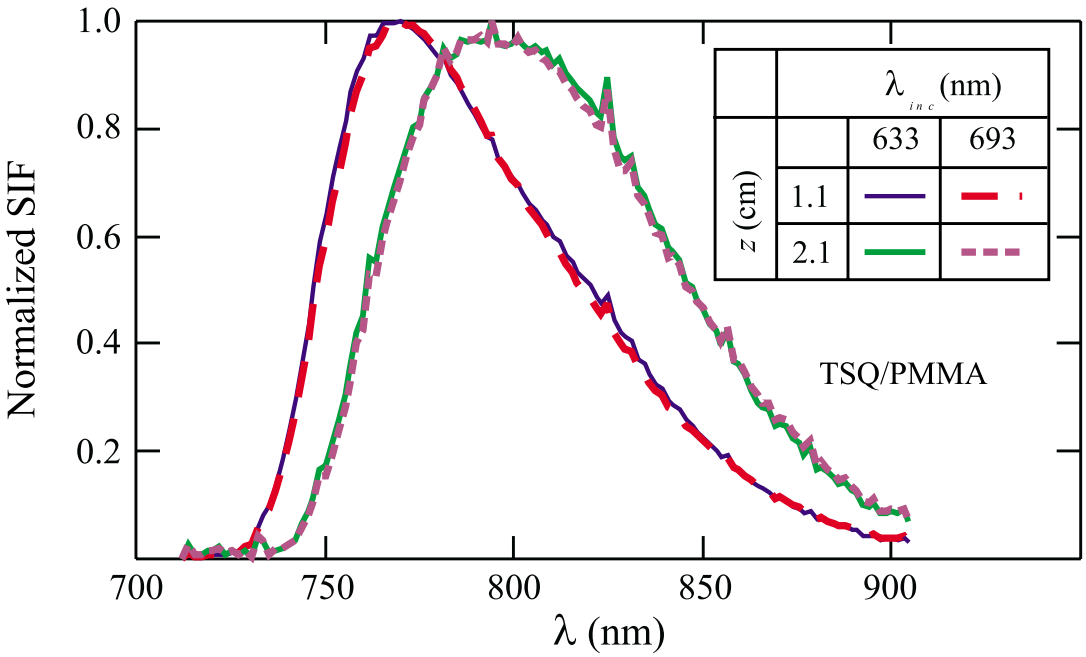

Fig. 5.30: Normalized SIF spectrum for a high concentration TSQ/PMMA core fiber for two illumination positions (1.1 cm and 2.1 cm) and two incident wavelengths (633 nm and 693 nm).

The high concentration TSQ/PMMA fiber was polymerized from a TSQ/PMMA solution that was above the room temperature maximum concentration even though it was made at room temperature. Thus we assume that the number density is approximately the room temperature maximum value shown in Table 3.1. Section 5.6.0.3 will discuss $\alpha(\lambda)$ to determine if this assumption is correct.

Figure 5.30 shows the superposition of the SIF spectra for the high concentration TSQ/PMMA core fiber when it is excited with 633 nm or 693 nm light. As with all

the squaraine-doped fibers except for ISQ, the SIF spectra are independent of incident wavelength in the 633 nm to 693 nm range. There could possibly be a difference if a shorter wavelength source were used but for this research the SIF spectra for BSQ, HSQ, PSQ, and TSQ can be regarded as independent of the incident wavelength.

5.2.5.4 ISQ

Figure 5.31 shows that ISQ/PMMA is noticeably broadened on the longer wavelength side of the fluorescence when it is pumped with 633 nm light (ISQ_3) than when it is pumped with 693 nm light (ISQ_9). This seems to imply that the 633 nm light is better at generating fluorescence in this region. The dependence of SIF on wavelength in ISQ-doped fibers is more complicated when partially deuterated ISQ fibers (ISQ/P(MMA-d8)) are compared to the ISQ/PMMA fibers.

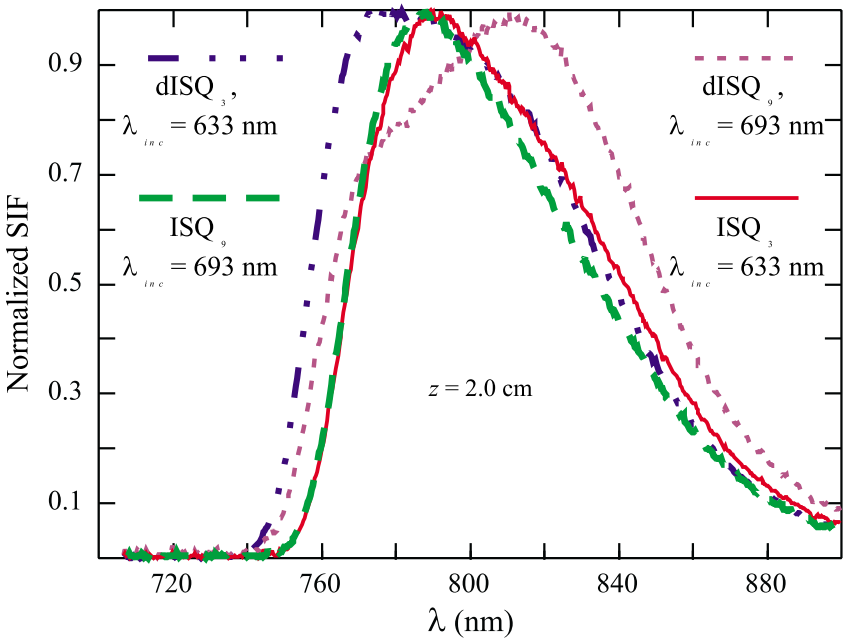

Fig. 5.31: SIF spectra (at $z = 2.0$ cm) for incident wavelengths of 633 nm and 693 nm in ISQ-doped PMMA and partially deuterated PMMA fibers. The spectra for the partially deuterated fibers are denoted $dISQ_3$ and $dISQ_9$, and the spectra for the PMMA fibers are denoted ISQ_3 and ISQ_9, where 3 and 9 refer to 633 nm and 693 nm incident illumination respectively.

The broadening of the SIF spectrum is enhanced when 633 nm light illuminates a

partially deuterated ISQ fiber, $dISQ_3$, in comparison to the ISQ_3 and ISQ_9 spectra. The peak of the $dISQ_3$ spectrum is also wider than the spectra for both non-deuterated results, which may be due to absorption by an unidentified excited state in the partially deuterated fiber. However, the SIF spectrum of the $dISQ_9$ fiber is significantly different than the $dISQ_3$ spectrum. The anomalous feature in the $dISQ_9$ spectrum at 770-820 nm and the large shift in its peak wavelength suggests there is an additional absorption due to a previously unidentified excited state with a larger oscillator strength than the $dISQ_3$ fiber. The possibility of an unidentified excited state will be discussed in more detail in Section 5.2.4.

The complexity in Figure 5.31 is not totally unexpected because the ISQ dye has two possible configurations – cis- and trans-isomers – while the HSQ and PSQ molecules do not because they are symmetric about their long axis. According to Mathis [7], the trans configuration is the preferred lower energy state but both configurations are present at room temperature in ISQ/PMMA thin films. Thus it is possible that one incident wavelength may excite one isomer better than the other due to the slight difference in transition energies, causing the fluorescence spectrum to have a different shape.

If the two isomers have closely spaced transition energies, the host could also affect the ratio of cis- and trans-isomers by virtue of how it interacts with the different isomers. Because there is a combination of PMMA and P(MMA-d8) in the partially deuterated ISQ fibers, there could also be high concentration domains of PMMA and P(MMA-d8) in various sections of fiber.

Since the four spectra in Figure 5.31 were generated from different sections of core fiber the differences in the spectra cannot be conclusively associated with the incident wavelength. Instead the differences in the spectra can arise from a number of different conditions from cis-trans isomerization, to high concentration domains, to the incident wavelength. Taking all these possibilities into account makes the data too complicated to fully analyze. However, future study is clearly warranted when more deuterated monomer becomes available.

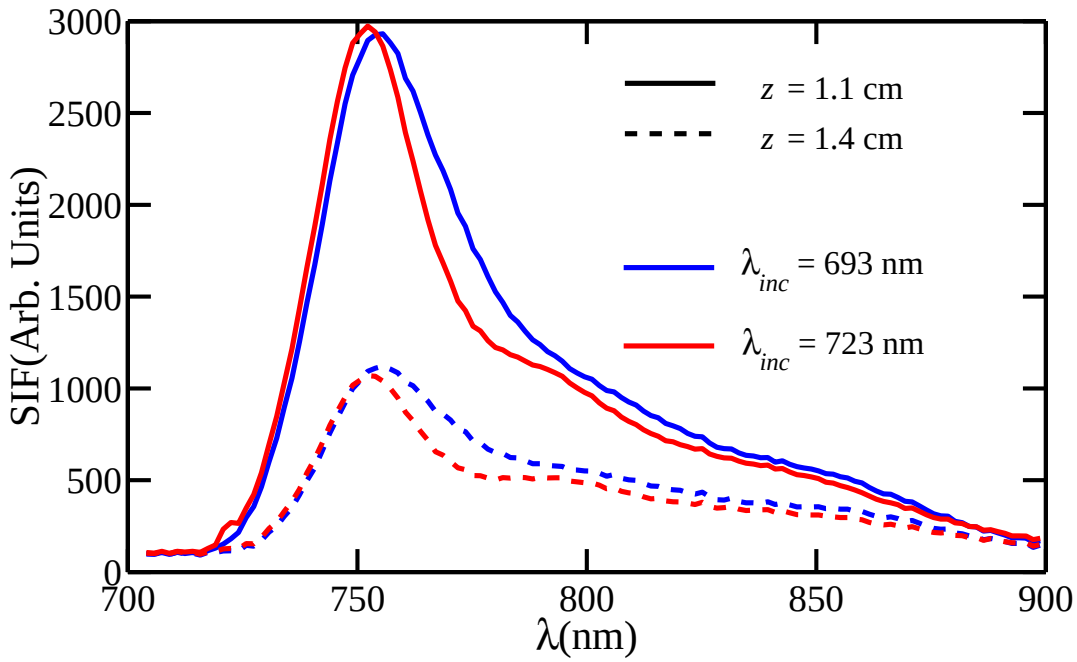

Fig. 5.32: SIF spectra for incident wavelengths of 693 nm and 723 nm in high concentration SiPc/PMMA copolymer fiber ($N_H = 1.2 \times 10^{18}$ cm^{-3}) . The solid lines represent $z = 1.1$ cm, and the dashed lines represent $z = 1.4$ cm.

5.2.5.5 SiPc

In contrast to the ISQ-doped fibers, SiPc/PMMA copolymer core fibers show a very interesting and quantitative dependence on the incident wavelength. The results shown in Figure 5.32 represent data from the same section of the high concentration SiPc/PMMA copolymer core fiber (see Section 5.40). In the SIF experiments, the 693 nm laser diode is fixed to the optical table (see Figure 4.6) and illuminates the fiber from one side. The Ti:Sapphire laser tuned to 723 nm illuminates the fiber from the opposite side. The beams are overlapped so that they have approximately the same initial illumination position.

Figure 5.32 shows that there is a small change in the shape of the fluorescence spectrum due to the different incident wavelengths. The Ti:Sapphire laser was also tuned to 728 nm, 733 nm, and 738 nm, and 743 nm to generate a fluorescence spectrum. The shape of SIF spectra tended toward the shape of the SIF spectra for 693 nm as the incident wavelength was lengthened. It also became much more difficult to collect data at

the longer wavelengths because the fluorescence intensity was much smaller.

The difference in the shape of the spectra is hugely magnified when similar experiments are performed on the same section of low concentration SiPc/PMMA core fiber. In these experiments, the 633 nm He/Ne or the Ti:Sapphire laser illuminates the fiber from one side and the 693 nm, 667 nm, or 643 nm laser diode, which is fixed to the optical table, illuminates the fiber from the opposite side. The laser beams from each side of the fiber are overlapped so that the incident illumination positions are equivalent within experimental uncertainty.

Figure 5.33 shows the drastic differences in the SIF spectra from the low concentration SiPc/PMMA copolymer core fiber for four different the incident wavelengths (633 nm, 693 nm, 703 nm, and 713 nm). It should be noted that each spectrum has been normalized to a unit excitation intensity so that it is apparent which wavelength creates the largest fluorescence magnitude.

When the He/Ne laser excites the low concentration SiPc/PMMA core fiber there is plenty of fluorescence intensity in comparison to the high concentration SiPc/PMMA core fiber. For an illumination position of 1.0 cm, the peak of the SIF spectrum generated with 633 nm light occurs about 750 nm and the spectrum appears "triangular". When the incident wavelength is changed to 693 nm, the peak of the fluorescence, for an illumination position of 1.0 cm, shifts to about 765 nm and is no longer triangular. There appears to be a secondary peak near 730 nm.

Since the SIF spectrum has propagated the same distance and is from the same fiber we expect the absorption to be approximately equal for both illumination wavelengths. The linear absorption coefficient for both spectra will be discussed in Section 5.6.0.5. The assumption that the absorption is equivalent implies that the change in shape of the SIF spectrum is caused by the increase in the incident wavelength. If this is the case, the 693 nm laser must generate a larger fluorescence in the 750-800 nm range in order to account for the maximum in the spectrum at about 760 nm.

The incident wavelength dependence is even more interesting when the SIF spectrum generated by 703 nm laser light is compared to the spectra from 633 nm and 693 nm laser light. The green curves in Figure 5.33 represent the SIF spectra generated by the

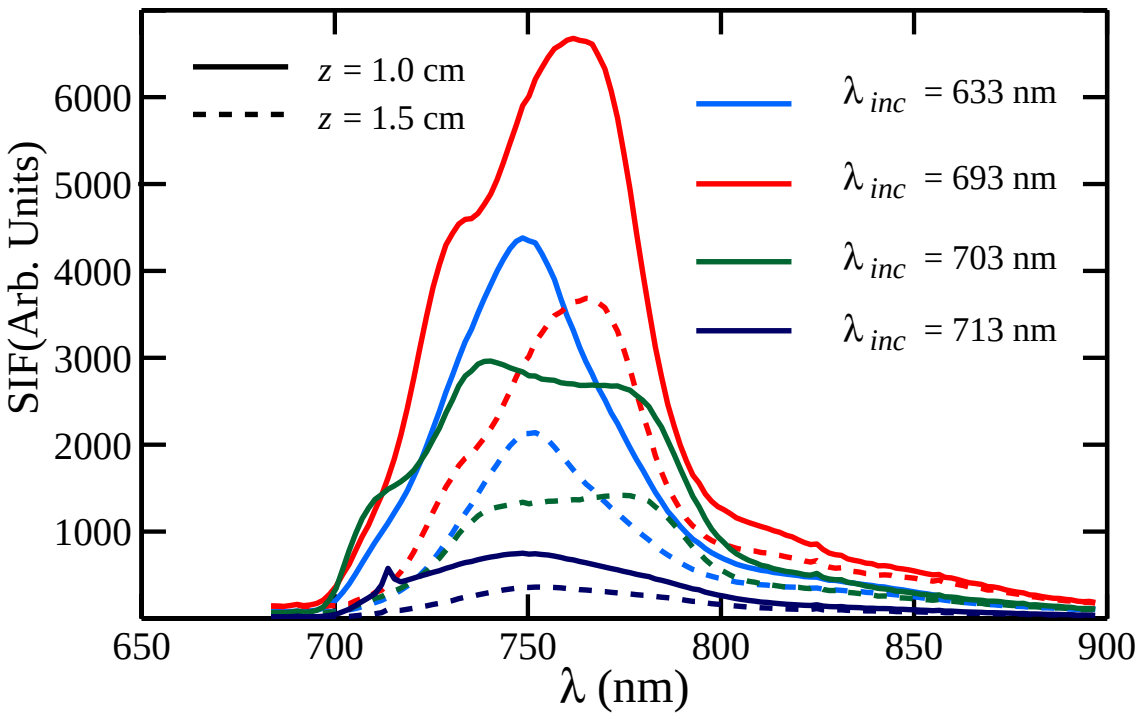

Fig. 5.33: SIF spectra from $z = 1.0$ cm and $z = 1.5$ cm for incident wavelengths of 633 nm, 693 nm, 703 nm, and 713 nm of low concentration SiPc/PMMA copolymer fiber ($N_L = 1.3 \times 10^{17}$ cm^{-3}).

Ti:Sapphire laser tuned to 703 nm. The maximum of the spectrum, for an illumination position of 1.0 cm, has shift back to about 745 nm and a secondary peak occurs about 780 nm. The shape of the SIF spectrum generated with 703 nm, in the 770-800 nm range, shows that there is a smaller fluorescence efficiency in comparison to the 693 nm excitation but a larger fluorescence efficiency than the 633 nm excitation.

These three results suggest that there is an additional excited state that is being excited more strongly by 693 nm and 703 nm light than 633 nm light and de-excites in the 750-800 nm range. Since the 693 nm laser diode generates the largest additional fluorescence for a unit intensity, the excited state is most likely located closer to 693 nm than 703 nm. Unfortunately, we were unable to tune the Ti:Sapphire laser below 703 nm. Thus we could not determine a precise location of the excited state which is responsible for the additional fluorescence.

A fourth set of SIF spectra are shown in Figure 5.33 for an incident wavelength of 713 nm. There are several notable features in the SIF spectra generated by the Ti:Sapphire laser tuned to 713 nm. Obviously the magnitude is much smaller than the SIF spectra generated by the other three wavelengths. The low efficiency is due to the incident wavelength being over 40 nm from $\lambda_{max} = 670$ nm.

It is more interesting to consider that the shape of the SIF spectra generated by 713 nm light is very similar in shape to the SIF spectra generated by 633 nm light. The shape of the 713 nm generated spectrum reinforces the idea that there is an additional excited state located below 700 nm that contributes to the fluorescence spectrum for 693 nm and 703 nm excitations.

We were able to generate a measurable SIF spectrum out to 719 nm. The SIF spectrum is very similar to 713 nm generated spectrum in shape but smaller in magnitude so it was not included in Figure 5.33. The 643 nm and 667 nm laser diodes also generate ample fluorescence intensity and the spectra they excite are very similar in shape to the 633 nm generated spectrum but larger in magnitude. Therefore they were not included in Figure 5.33. The spectra for all the incident wavelengths studied will be discussed in more detail in more detail in Section 5.4.

Two illumination positions are included in Figure 5.33 to emphasize that the shape of the SIF spectrum is not due to the illumination position. For each incident wavelength there is decrease in the magnitude of the spectrum with an increase in propagation distance and the change in the shape of each spectrum is consistent with an absorption coefficient that is larger at shorter wavelengths in the fluorescence band. The linear absorption coefficient, for each excitation wavelength, at each wavelength in the SIF spectrum will be discussed in greater detail in Section 5.6.0.5.

5.3 Fluorescence Quantum Yield

In this section, we discuss how the relative quantum fluorescence yield can be determined from emission spectroscopy or SIF spectroscopy data. We choose to determine the relative quantum yield because the coupling coefficient for the SIF measurement has not been

determined, and, at this time, the absolute quantum efficiency of the spectrometer is not known as a function of wavelength. By determining the relative quantum fluorescence yield we eliminate both of these unknowns.

The relative quantum fluorescence yield can be used to determine which pump wavelength is most effective. This knowledge can be used to optimize the excitation wavelength for fiber lasers. The relative quantum fluorescence yield can also be used to determine the location of molecular excited states.

5.3.1 Core fibers

For the SIF spectroscopy experiment or the transmission geometry emission spectroscopy experiment the fluorescence is self-absorbed as it travels through the dye-doped sample. The absorption of the fluorescence intensity is taken into account by assuming that the fluorescence travels as a plane wave and decays exponentially with α and z. A point source model for the self-absorption could replace the plane wave model for the absorption in the analysis of the SIF data. However, we show that, as long as the fluorescence is generated at the same location, the self-absorption of the fluorescence does not effect the relative quantum fluorescence yield.

By taking the ratio of transmitted fluorescence for two incident wavelengths we get the following,

$$\frac{F(\lambda,\lambda_{e_2})}{F(\lambda,\lambda_{e_1})} = \frac{C_2}{C_1}\frac{Q_F(\lambda,\lambda_{e_2})}{Q_F(\lambda,\lambda_{e_1})}\frac{I_{e_2}(\lambda_{e_2})}{I_{e_1}(\lambda_{e_1})}\frac{\exp(-\alpha(\lambda)z_2)}{\exp(-\alpha(\lambda)z_1)}, \tag{5.1}$$

where $Q_F(\lambda,\lambda_{e_i})$ is the quantum fluorescence yield, C_i is the coupling constant for the particular experiment, and $\mathrm{I}_{e_i}(\lambda_{e_i})$ is the excitation intensity at the excitation wavelength, λ_{e_i}. These quantities were described in more detail in Section 2.130. In a reflection geometry emission spectroscopy experiment C_i=1, but for the SIF spectroscopy experiment $\mathrm{C}_i < 1$ because we are coupling into the side of the fiber.

When it is assumed the coupling coefficient for the SIF experiment is approximately equal for all excitation wavelengths, and the illumination positions are equal ($z_1 = z_2$), the result can be rearranged to give the relative quantum yield as a function of fluorescence

wavelength,

$$Q_{F_{21}}(\lambda) = \frac{Q_F(\lambda, \lambda_{e_2})}{Q_F(\lambda, \lambda_{e_1})} = \frac{F(\lambda, \lambda_{e_2})}{F(\lambda, \lambda_{e_1})} \frac{I_{e_1}(\lambda_{e_1})}{I_{e_2}(\lambda_{e_2})}. \tag{5.2}$$

We have chosen the low concentration SiPc/PMMA copolymer fiber to demonstrate the relative quantum fluorescence yield as a function of fluorescence wavelength because the data was taken for the largest range of incident wavelengths and it has the most interesting spectrum. Figure 5.34 shows the result of applying Equation (5.2) to the SIF spectrum for excitation wavelengths of 643 nm, 693 nm, 703 nm, 705 nm, 708 nm, 713 nm, and 719 nm relative to the SIF spectrum generated by 633 nm light. We did not include the relative quantum fluorescence yield for an excitation wavelength of 667 nm because it was so large that all the other curves look like horizontal lines near the origin, and for an excitation wavelength of 633 nm because it is unity for all wavelengths shown.

The spectrum for 643 nm is relatively unstructured in comparison to the spectra for excitation wavelengths of 693 nm, 703 nm, and 705 nm. This suggests that the 643 nm spectrum is mainly generated by the same excited state as the 633 nm spectrum. However, there is very interesting structure in the 693 nm, 703 nm, and 705 nm spectra relative to the 633 nm spectrum. This suggests that an additional excited state(s) contribute to the fluorescence quantum yield for these three excitation wavelengths. Unfortunately, we were not able to measure the SIF spectrum in between 693 nm and 703 nm to determine a precise location for the excited state(s) responsible for this intriguing structure of the quantum fluorescence yield because we do not have a laser source in that regime. Future work should focus on exciting the SIF spectrum using incident wavelengths between 670 nm and 705 nm in 1-2 nm increments to determine where this excited state is located.

Before the advent of quick spectrometers, the integrated fluorescence quantum yield was typically measured using a photodiode or a photomulitplier tube. For this type of experiment we need to integrate Equation (2.131) as follows,

$$F_{int} = \int_{\lambda_o}^{\lambda_f} F(\lambda, \lambda_e) \exp(\alpha(\lambda) z) d\lambda = C I_e(\lambda_e) \int_{\lambda_o}^{\lambda_f} Q_F(\lambda, \lambda_e) d\lambda, \tag{5.3}$$

where λ_o is the shortest wavelength in the fluorescence band, and λ_f is the longest wavelength in the fluorescence band. If $z \to 0$ then the integral of the quantum fluorescence

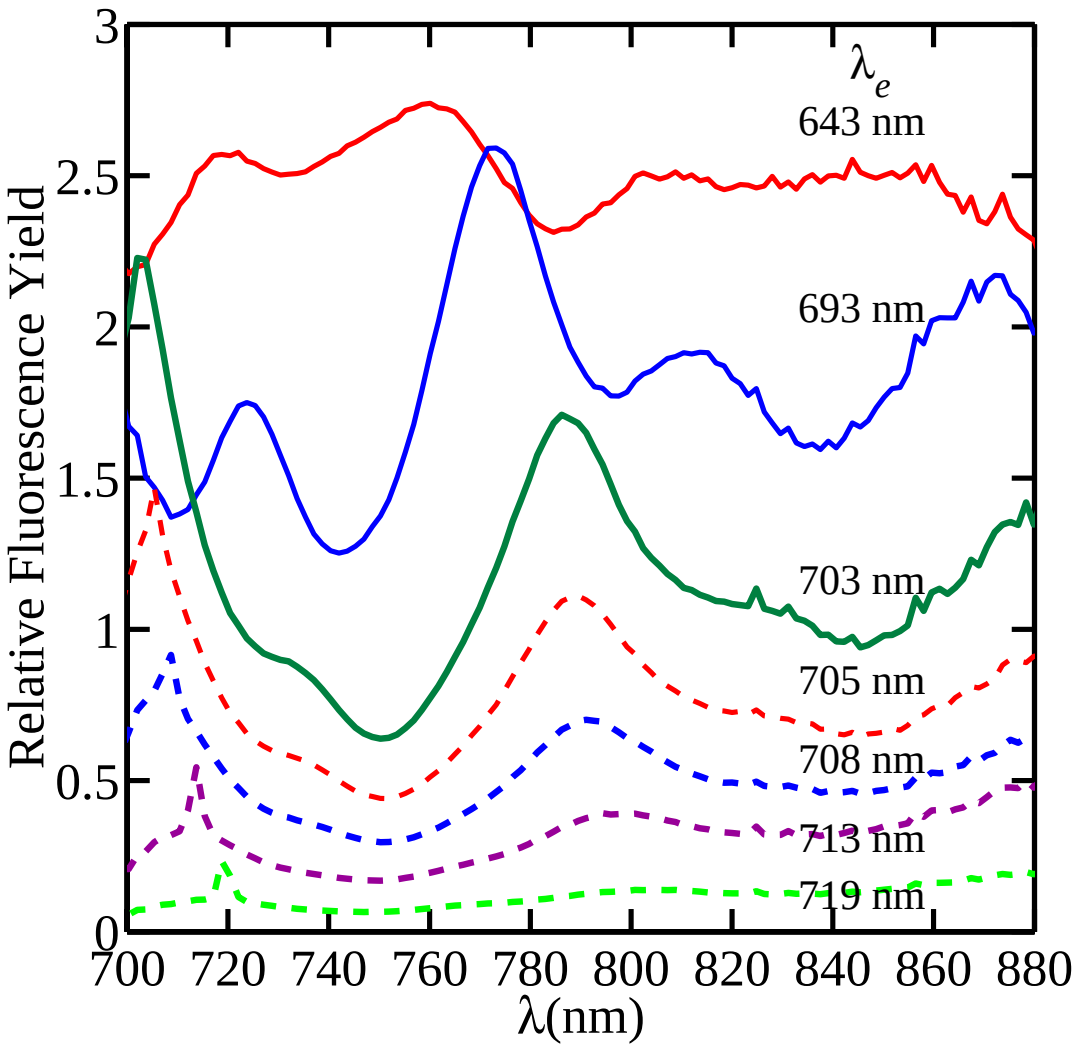

Fig. 5.34: Relative fluorescence yield for the low concentration SiPc/PMMA copolymer core fiber. Each spectrum is relative to the fluorescence generated by 633 nm (N= 1.3 $\times 10^{17}$ cm^{-3}).

yield is,

$$Q_F(\lambda_{inc}) = \int_{\lambda_o}^{\lambda_f} Q_F(\lambda_{inc}, \lambda) d\lambda, \tag{5.4}$$

equivalent to integrating the transmitted fluorescence. The relative quantum yield as a function of fluorescence wavelength can also be integrated from λ_o to λ_f as follows,

$$Q_{F_{21}} = \int_{\lambda_o}^{\lambda_f} Q_{F_{21}}(\lambda) d\lambda. \tag{5.5}$$

Figure 5.35 shows the integrated relative quantum fluorescence yield for all incident wavelengths shown in Figure 5.34 and for 667 nm and 633 nm. Clearly, the yield for

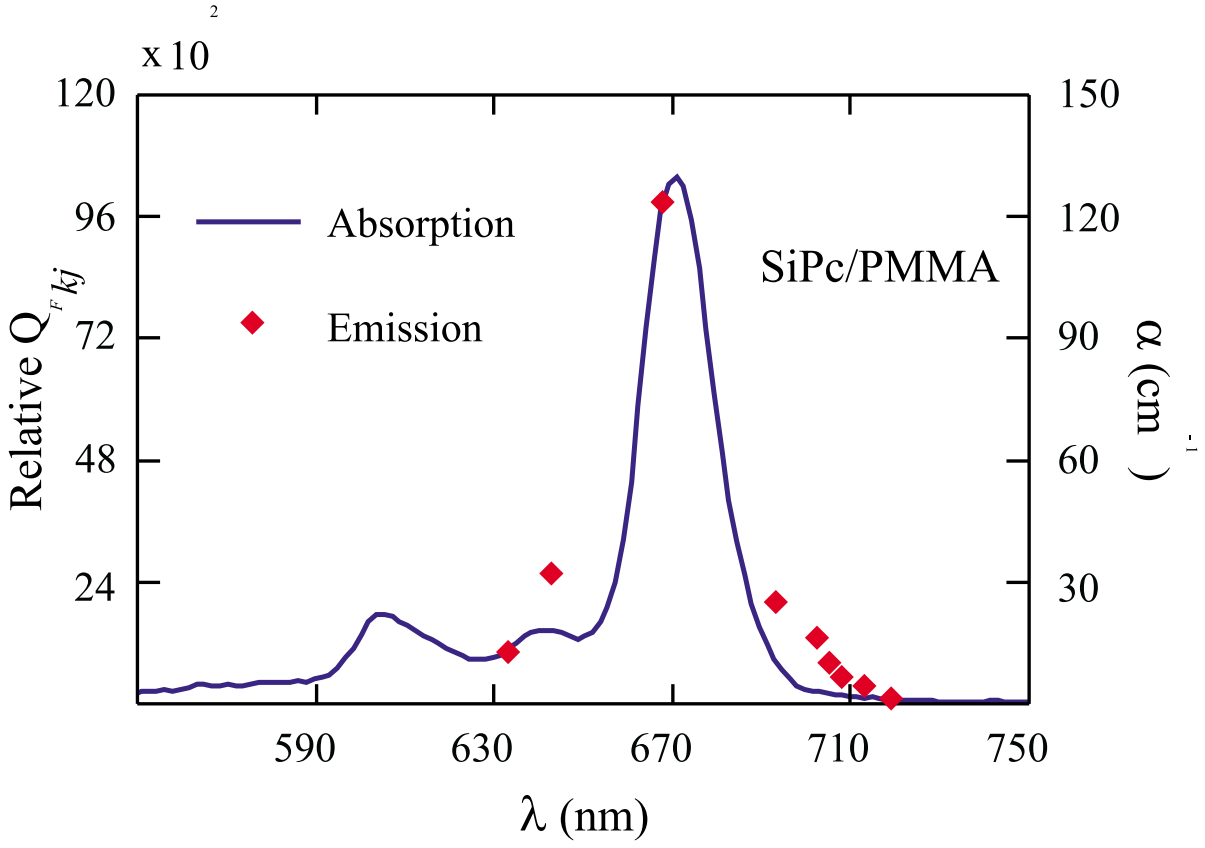

Fig. 5.35: Relative fluorescence yield for the low concentration SiPc/PMMA copolymer core fiber. Each point is relative to the fluorescence generated by 633 nm (N= 1.3 $\times 10^{17}$ cm^{-3}).

an excitation by 667 nm light is the largest and the general shape of the integrated relative fluorescence yield is similar to the shape of the resonant absorption peak for SiPc/PMMA. This confirms that the fluorescence is mainly generated by the de-excitation of the resonant excited state at 670 nm. It is also interesting to note that the yield for the 703 nm excitation seems to be a little higher relative to its neighbors but more incident wavelength data is necessary to confirm this hypothesis. Therefore we conclude that molecular excited states can be characterized by analyzing the SIF data in terms of the relative quantum fluorescence yield and/or the integrated relative fluorescence yield.

5.4 Bulk Emission Spectra

Several squaraine-doped PMMA and SiPc/PMMA copolymer preform slices were measured in the emission spectroscopy experiment (see Section 4.2). The majority of the results were collected using the reflection geometry but there are a few collected in the transmission geometry. Since the reflection measurements were conducted after the SIF measurements were complete they were performed to confirm some of the more interesting SIF results and not as a complete set of measurements. As stated in Section 4.2, a smooth surface is critical for this experiment but is not difficult to obtain for the dye-doped preform slices. Therefore this measurement should be easily extended to pulsed laser systems in the future.

5.4.1 Squaraines

This section discusses the results of the emission spectroscopy experiments for squaraine-doped preform slices. The measurements were not conducted on every dye but the results may be considered as general when more than one dye exhibits the same behaviour. PSQ/PMMA and TSQ/PMMA preform slices were characterized as a function of concentration and ISQ/PMMA preform slices were characterized as a function of degradation – which is expressed as a color change.

Figures 5.36a and 5.36b shown the emission spectra for two different concentrations of PSQ/PMMA and TSQ/PMMA respectively. The PSQ/PMMA preforms are doped with $N_H = 3.8 \times 10^{17}$ cm^{-3} and $N_L = 9.6 \times 10^{16}$ cm^{-3} dye molecules, and the TSQ/PMMA preforms are doped with $N_H = 4.4 \times 10^{17}$ cm^{-3} and $N_L = 6.8 \times 10^{15}$ cm^{-3} dye molecules. It should be noted that the low concentration PSQ/PMMA preform slice was polymerized from a 1/4 dilution of the solution which polymerized into the high concentration PSQ/PMMA preform, and the low concentration TSQ/PMMA preform slice was polymerized from a 1/64 dilution of the solution which polymerized into the high concentration TSQ/PMMA preform.

Clearly, there is a red-shift in the maximum of the emission spectrum as the concentration of dye molecules is increased for both squaraines and should be considered a

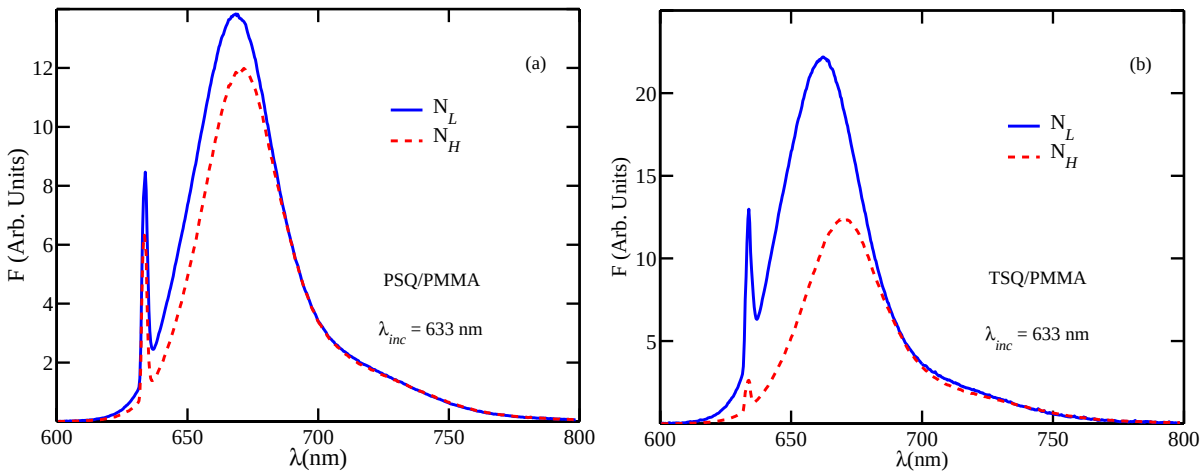

Fig. 5.36: Reflection geometry emission spectra from PSQ/PMMA (N_H =3.8×10^{17} cm^{-3} and $N_L = 9.6 \times 10^{16}$ cm^{-3}) and TSQ/PMMA ($N_H = 4.4 \times 10^{17}$ cm^{-3} and $N_L = 6.8 \times 10^{15}$ cm^{-3}) preform slices. The spectra are normalized to unity at 750 nm.

general effect for most squaraines. The red-shift in the maximum of the spectra is also much larger in Figure 5.36b which is consistent with the larger difference in TSQ/PMMA concentrations. The red-shift which scales with concentration suggests that the fluorescence is not a surface effect but occurs within some finite skin depth.

The spectra, in both Figures 5.36a and 5.36b, are normalized to unity at 740 nm to emphasize that there is no perceivable difference in the shape of the emission spectra in the SIF regime (730 - 900 nm). Thus if the dye molecules do not interact or aggregate as the concentration is increased there should be no perceivable difference in the shape of the SIF spectrum.

When we were interested in bleaching squaraine-doped preform slices, we measured the emission spectrum for HSQ/PMMA and ISQ/PMMA in the transmission geometry. Figure 5.37 shows the results of these experiments. The spectrum for HSQ/PMMA is a testament to the difficultly in finding an appropriate thickness/concentration combination in which the incident intensity does not overwhelm the fluorescence. For the same HSQ/PMMA sample the He/Ne light is completely absorbed but the 693 nm light passes through the sample with only modest attenuation.

Notice the large red-shift in the emission spectra of ISQ/PMMA in comparison to

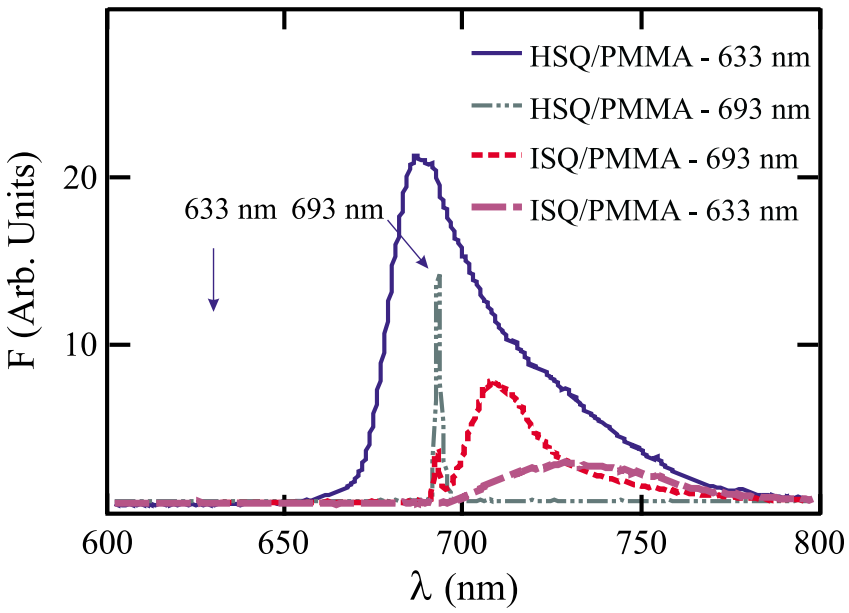

Fig. 5.37: Emission spectra from HSQ/MMA and ISQ/PMMA preform slices in the transmission geometry.

Figures 5.36a and 5.36b. The large red-shift in the maximum of the fluorescence is due to the fluorescence being generated near the front of the preform and then being self-absorbed as it travels through the sample to reach the detector. This is very similar to the SIF experiment but the propagation distance through the sample is much smaller and cannot be modified. Thus the side-illumination method is better suited to study fluorescence spectra as a function of propagation distance through the sample.

Since ISQ/PMMA has very different absorption spectra as the dye changes color, the emission spectra were measured from the N (Blue) ISQ/PMMA preform and the 2N (Green) ISQ/PMMA preform – previously discussed in Section 5.1.1.2. ISQ/PMMA is typically blue, like the other squaraines, because its absorption maximum is about 660 nm. When the dye breaks down because of exposure to light, oxygen, or heat the ISQ/PMMA sample turns green. The green color is assumed to be a combination of UV absorbing byproducts and the remaining dye. The absorption spectrum of two different green ISQ/PMMA preform slices are discussed in Section 5.1.1.2.

Figure 5.38 shows the emission spectrum excited by the He/Ne laser for the N(Blue)

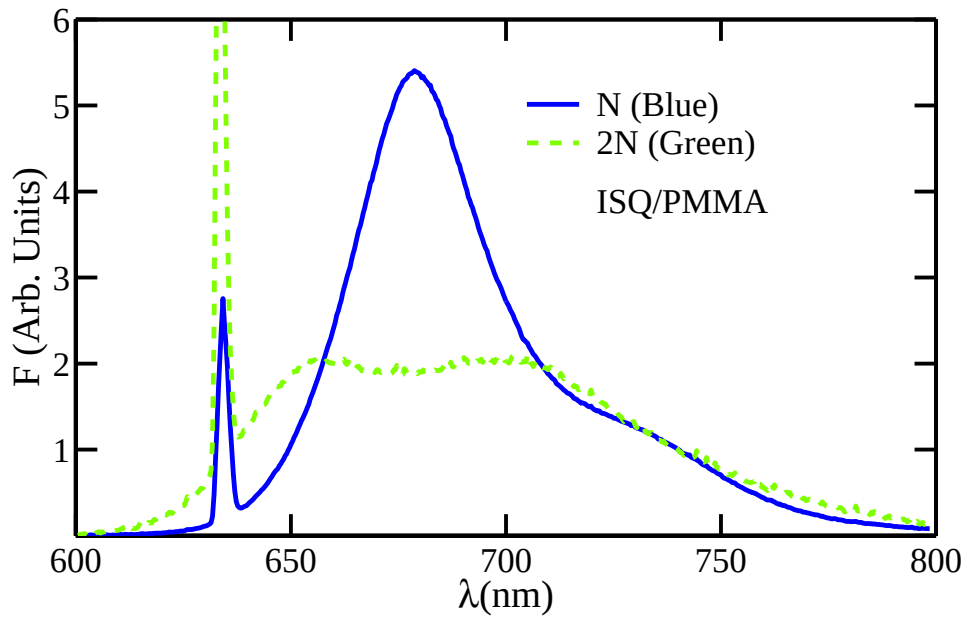

Fig. 5.38: Reflection geometry emission spectra from a Blue ISQ/PMMA preform slice and a Green ISQ/PMMA preform slice. The spectra are normalized to unity at 740 nm.

and 2N (Green) ISQ/PMMA preform slices. The emission spectrum from the N (Blue) sample is very similar to the emission spectra for PSQ/PMMA and TSQ/PMMA shown in Figures 5.36a and 5.36b but is red-shifted because the absorption maximum for ISQ is red-shifted from that of PSQ and TSQ. However, the emission spectrum for the 2N (Green) sample is very different.

At this time it is difficult to describe the features in the emission spectrum of the Green sample because we don't know which species are involved in the absorption. However, the 2N (Green) sample is not very efficient at generating fluorescence so it should not be considered for a broadband light source. Before moving on to the SiPc results we should mention that there is relatively broader fluorescence beyond 750 nm from the Green sample, compared to the Blue sample, which is in the regime of the SIF measurement.

5.4.2 SiPc

The emission spectra from several SiPc/PMMA copolymer preform slices were measured using the emission spectroscopy experiment in the reflection geometry. Figure 5.39 shows

the emission spectra for three different SiPc/PMMA copolymer preform slices. The theoretical number densities are $N_H = 2.4 \times 10^{18}$ cm^{-3}, $N_M = 1.2 \times 10^{18}$ cm^{-3}, and $N_L = 1.3 \times 10^{17}$ cm^{-3}. We qualify number density with "theoretical" because the samples were made using slightly different procedures.

Section 3.2 discussed the complete procedure used to fabricate core preforms. Typically, the dye/MMA solution is filtered with a 0.22 μm Teflon syringe filter to remove large aggregates of dye or impurity. However, when making the SiPc/PMMA sample labeled N_H it was found to be extremely difficult to filter the solution of SiPc/MMA.

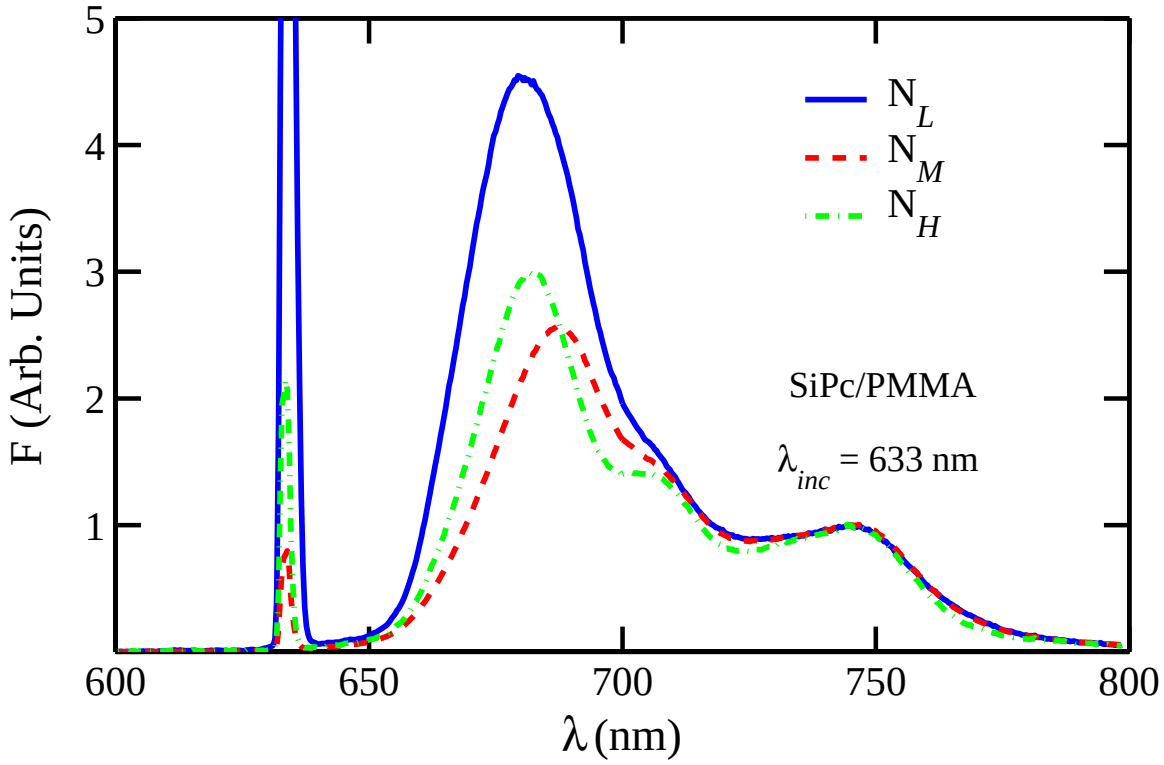

Fig. 5.39: Reflection geometry emission spectra from three concentrations of SiPc/PMMA copolymer preform slices when excited with 633 nm light ($N_H = 2.4 \times 10^{18}$ cm^{-3}, $N_M = 1.2 \times 10^{18}$ cm^{-3}, and $N_L = 1.3 \times 10^{17}$ cm^{-3}). The spectra are normalized to unity at 747 nm.

The difficulty is believed to arise because the solution was stirred for about 8 hours, to make sure all the dye dissolved, before adding the initiator and chain transfer agent. For guest/host solutions, the addition of the initiator starts the polymerization, but in

a co-monomer solution, the initiator may not be necessary to begin the polymerization reaction. Therefore the filter is most likely removing dye which has already begun to polymerize during the stirring step and reduces the actual number density of the polymerized core preform. To test this hypothesis the samples denoted by N_M and N_L were polymerized without filtering.

There is another relation between samples N_M and N_L. The solution that polymerized to the core preform denoted by N_L is a 1/9 dilution of the solution which polymerized to the core preform denoted by N_M. N_L is also from the same preform that was drawn into the low concentration SiPc/PMMA core fiber discussed in Section 5.2.1.6.

The solution which polymerized into the preform, which was drawn into high concentration SiPc/PMMA fiber discussed in Section 5.2.1.6, is a 1/2 dilution of the solution which polymerized into the preform denoted by N_H in this section. However, both samples were filtered through the 0.22 μm Teflon syringe filter so the actual ratio of the concentrations may not be 1/2.

Figure 5.39 reveals a significant red-shift in the maximum of the emission spectrum as the concentration is increased for the non-filtered samples. This is similar to the red-shift observed for the PSQ/PMMA and TSQ/PMMA preforms shown in Figures 5.36a and 5.36b. However, there is little red-shift in the maximum of the emission spectrum for the filtered sample, N_H, in comparison to the non-filtered sample, N_L, even though there is almost an order of magnitude change in the theoretical number densities. This suggests that the actual number density of the filtered sample is smaller than the theoretical number density. The linear absorption coefficient calculated in Section 5.6.0.5 also suggests a similar conclusion.

It is interesting to note that the shape of the emission spectra of the two non-filtered samples in the SIF regime are identical, within the thickness of the line. However, there is a slight relative decrease in the emission in the SIF regime for the filtered sample. More notably, the emission from the filtered sample is much more resolved which suggests that it is more homogeneous than the non-filtered samples.

There is a distinct difference in the shape of the emission in the SIF regime between the N_M and N_L samples when the fluorescence is excited using the 693 nm laser diode.

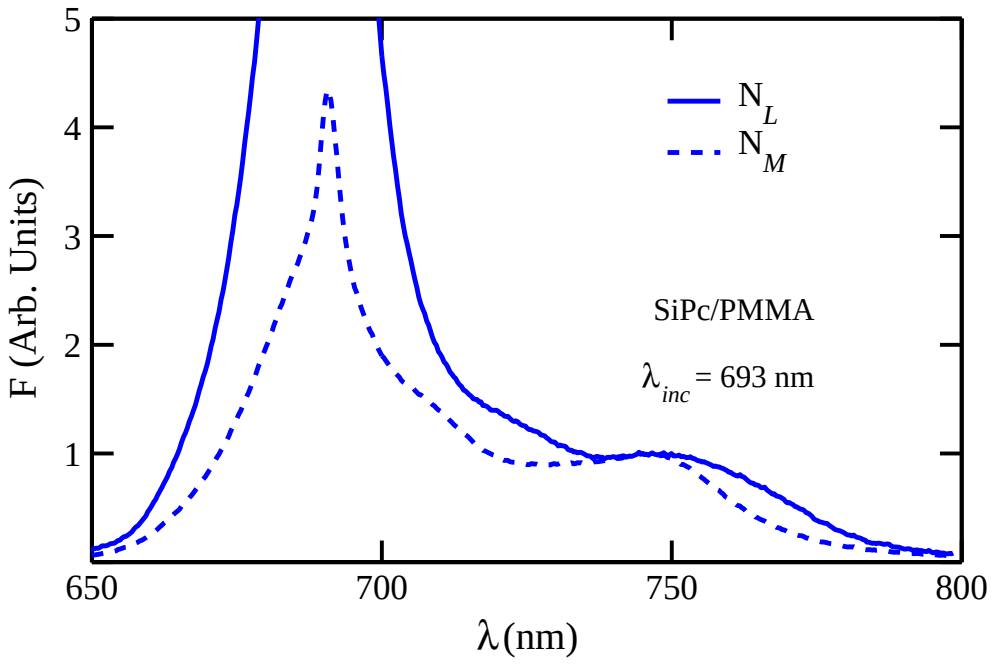

Fig. 5.40: Reflection geometry emission spectra from two concentrations of SiPc/PMMA copolymer preform slices when excited with 693 nm light (N_M = 1.2 $\times 10^{18}$ cm^{-3}, and N_L = 1.3 $\times 10^{17}$ cm^{-3}). The spectra are normalized to unity at 747 nm.

Figure 5.40 shows the emission spectra from the N_M and N_L preform slices which have been normalized to unity at 747 nm. The normalization was performed at 747 nm to emphasize the difference in the shape of the spectra in the SIF regime. Clearly, the lower concentration sample generates a broader signal in the SIF regime which confirms the results from the SIF measurements in Section 5.2.3.5.

5.4.2.1 Incident Wavelength Dependence

We can also analyze the emission spectra from the reflection emission spectroscopy experiment as a function of the incident wavelength. Figure 5.41 shows the emission spectra from the N_M preform slice when excited by 633 nm or 693 nm light. Obviously, there is a large difference near 693 nm because a significant amount of scattered laser light reaches the detector; however, there is negligible difference in the emission in the SIF regime.

This is quite different in comparison to the emission from the SiPc/PMMA preform

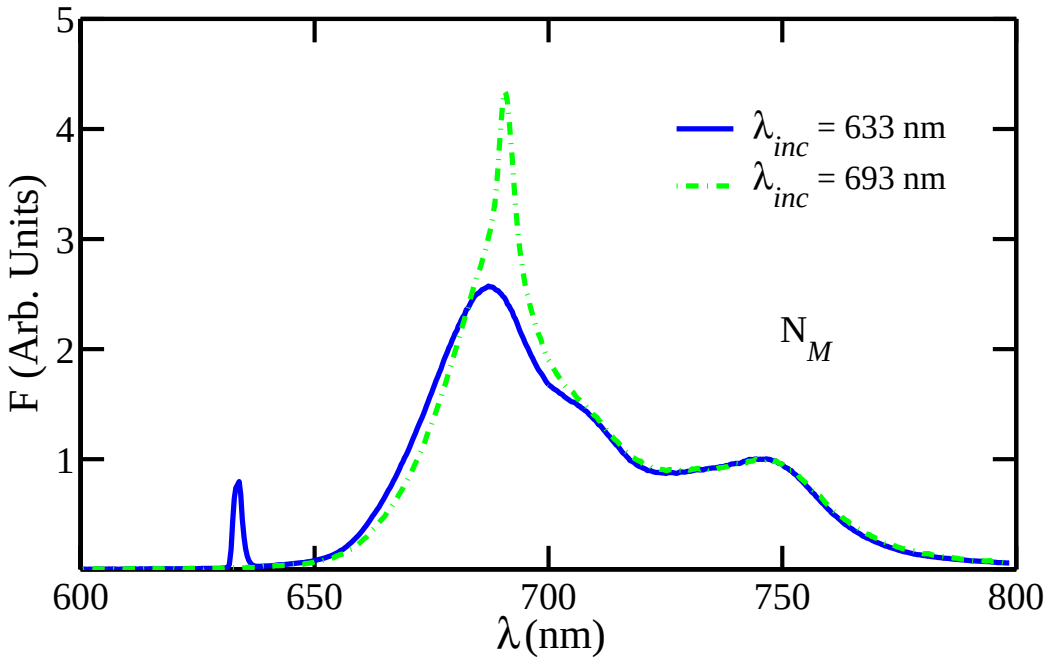

Fig. 5.41: Reflection geometry emission spectra from the N_M SiPc/PMMA copolymer preform slice when it is excited with 633 nm or 693 nm light ($N_M = 1.2 \times 10^{18}$ cm^{-3}). The spectra are normalized to unity at 747 nm.

slice labeled N_L. Figure 5.42 shows that there is a significant change in the shape of the emission in the SIF regime. We also found, during the SIF experiments in Section 5.2.5.5, that the fluorescence spectrum in the SIF regime was different for the low concentration fiber when the incident wavelength was changed from 633 nm to 693 nm.

The emission spectroscopy results confirmed several a SIF results. When the concentration is increased the emission peak red-shifts for the both all the dyes studied. The squaraines show no change in the emission in the SIF regime unless there is a degradation of the dye as the concentration of dye is changed. However, there is a clear difference in the emission in the SIF regime from the SiPc/PMMA for both preforms and fibers as the concentration is varied. The emission from the low concentration SiPc/PMMA, N_L, also changes, in the SIF regime, when the excitation wavelength is varied from 633 nm to 693 nm.

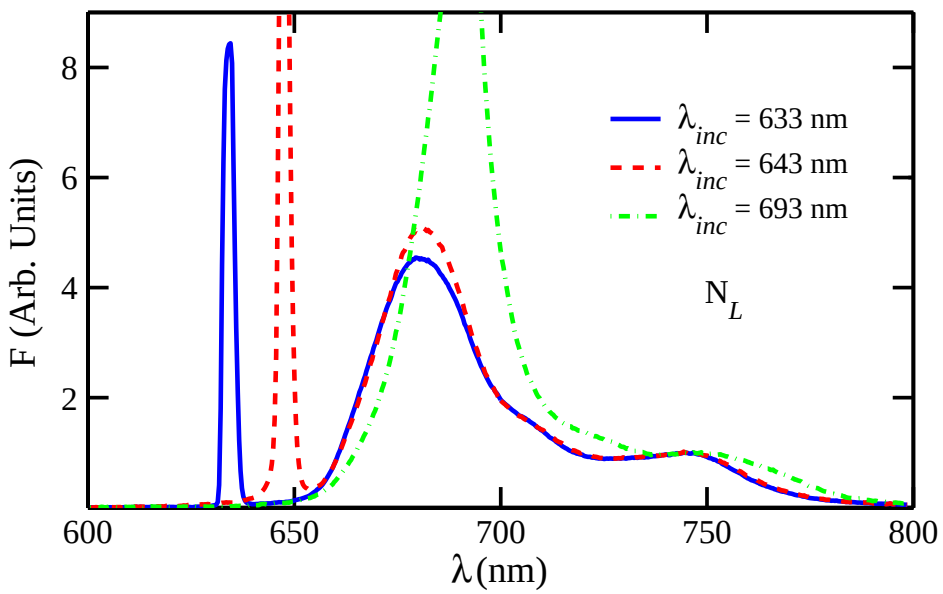

Fig. 5.42: Reflection geometry emission spectra from the N_L SiPc/PMMA copolymer preform slice when it is excited with 633 nm, 643 nm, or 693 nm light (N_L = 1.3 $\times 10^{17}$ cm^{-3}). The spectra are normalized to unity at 747 nm.

5.5 Photosensitivity

5.5.1 Preform Slices

In this section, we study photosensitivity by exposing a sample to a high intensity light pattern We image the color change using linear absorption and/or fluorescence. The experimental details can be seen in Section 4.5, Figure 4.11. The majority of the investigation focuses on ISQ-doped preform slices because it is the most unstable molecule. Thus the effects caused by exposure to light are larger than in other dyes. If properties such as a refractive index profile could be patterned into at dye-doped polymer, many applications for the resulting 2-D and 3-D structures would be made possible.

The ISQ/PMMA preform slice, characterized in the transmission geometry emission spectroscopy experiment (see Section 5.4.1, Figure 5.37), was initially exposed to 355 nm light – at 7 mJ/pulse before the grating – for 26 minutes using a double-slit mask with a 1.4 mm slit separation. Immediately after the exposure, the sample was slightly

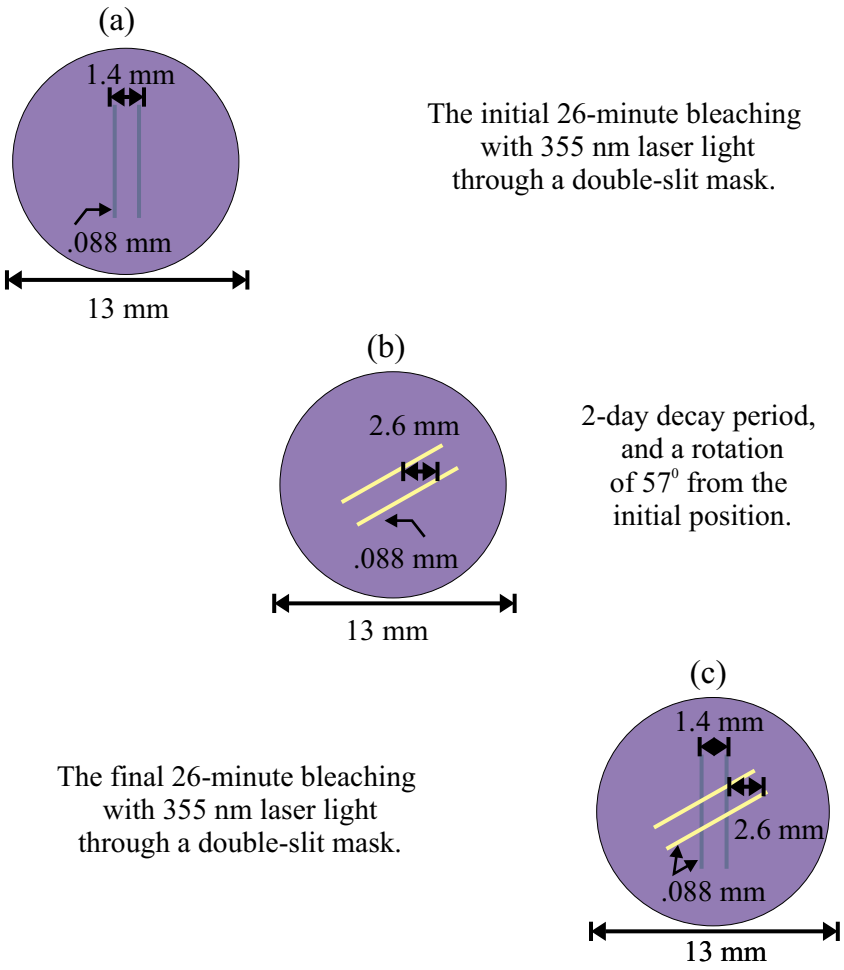

Fig. 5.43: Progress of UV exposure in a ISQ/PMMA preform slice: (a) Initial exposure at 355 nm, (b) 2 days time delay and rotation of 57°, (c) Final exposure at 355 nm.

darker blue in the exposed area. Unfortunately, the original sample holder did not allow the spectrometer to get close enough to the sample for precise measurements. Thus the sample was removed and placed in a better holder. In the process the sample was rotated 57° from its original position leaving the bleached lines at a 33° angle from horizontal. Because of the problem with the sample holder, the first valid data was not collected until 2 days after the initial bleaching, and the bleached area had already changed from the darker blue to faint yellow.

After scanning the sample over the cross-sectional area to measure the effects of the 355 nm exposure, the sample was exposed again under the same conditions but in the

vertical direction. The double slit mask was oriented in the vertical direction so that the absorption could be characterized while the exposed area was in the darker blue state and the pattern would not overlap the original exposure. The darker blue vertical pattern shown in Figure 5.43c was observed with the naked eye after the second exposure to 355 nm pulse laser light.

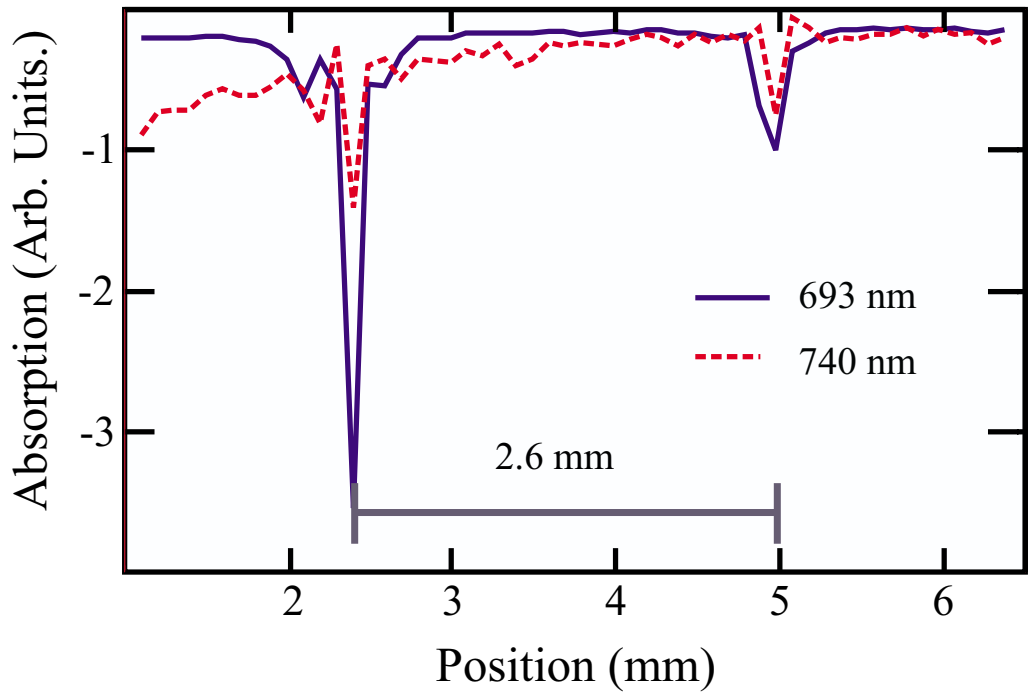

Fig. 5.44: Change in absorption of the ISQ sample 2 days after initial 26 minute exposure to 355 nm laser light. Probed at 693 nm.

Using 693 nm low intensity light, the first measurement on the ISQ/PMMA sample was done 2 days after the initial exposure. The sample was translated horizontally through the laser beam from one edge, through the exposed areas, to the other edge. The result of the 1-D measurement shows that there was a decrease in absorption at two locations in the sample. We also observed a decrease in the absorption of the fluorescence at the same locations. The distance between the decreases in absorption is 2.60 mm, as shown in Figure 5.44, which is consistent with the 1.4 mm slit separation tilted at 33° from horizontal. This suggests that the decrease in absorption is caused by the exposure to 355 nm light.

It is interesting that both wavelengths shown in Figure 5.44 show a decrease in the amount of absorption in the bleached area. Because fluorescence intensity was found to increase in the exposed regions, it can be argued that the fluorescence is generated in some thin layer at the front face of the sample when it has not been exposed to the 355 nm light. After exposure, the dye molecules near the front of the sample have degraded and the fluorescence is generated closer to the back of the preform slice. Thus the fluorescence is generated with approximately the same intensity but suffers less self-absorption as it propagates to the spectrometer.

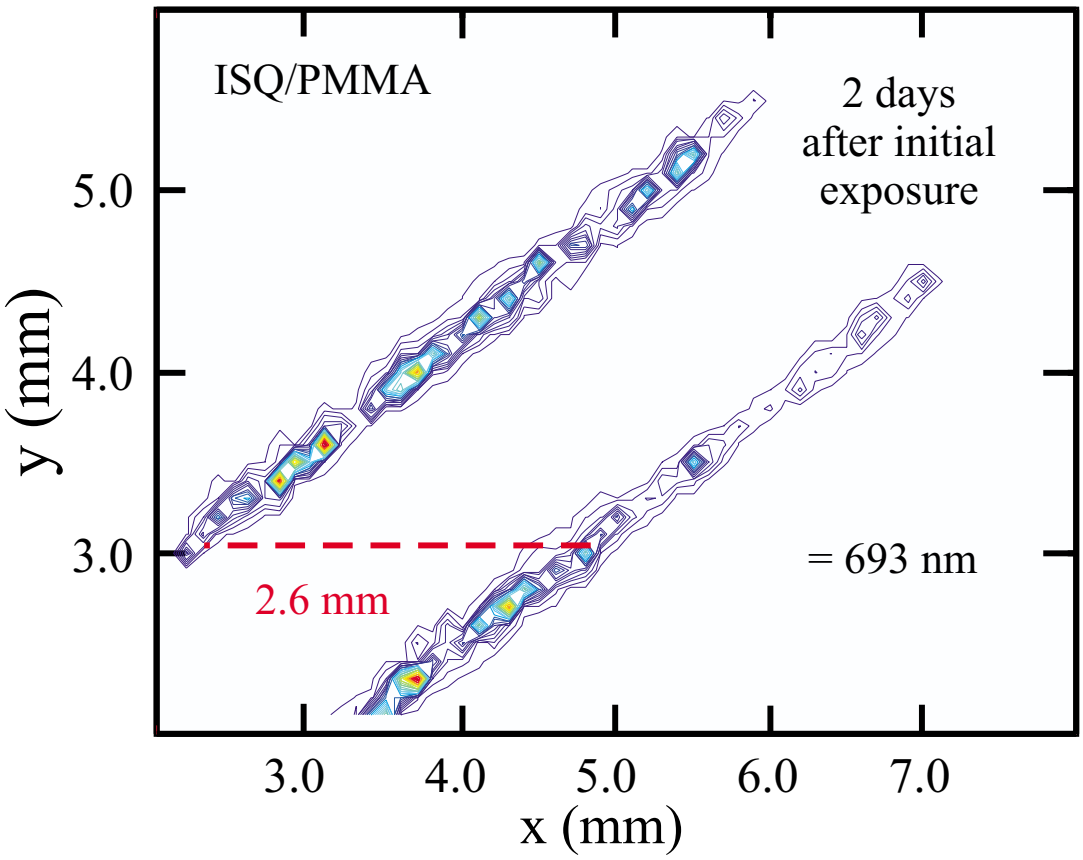

Fig. 5.45: Change in transmission contours for the ISQ sample 2 days after the initial bleaching with 355 nm laser light. Viewed at the incident wavelength, 693 nm.

To determine if the decrease in absorption is localized to the exposed areas, we probed a cross-sectional area of the sample with 693 nm light. This 2-D scan of the ISQ/PMMA sample (Figure 5.45) shows the relative change in transmission contours for λ=693 nm.

The distance between the contours denotes the slope, red is the largest change in transmission, and dark blue is smallest change in transmission. Clearly, there is a one to one correspondence between the observed color change and the measured change in absorption due to the initial exposure to 355 nm pulsed laser light. There is also a similar, but smaller, increase in transmission for the fluorescence wavelengths in the exposed regions. They are not shown because they do not add anything new to the discussion.

Because the area where the sample was bleached with 355 nm laser light decayed from slightly darker blue, seen immediately after exposing the sample, to faint yellow, after about 2 days, we suggest that the molecules are excited to an unstable state, that decays to smaller component molecules. These smaller molecules should absorb in the ultraviolet range and thus have a yellow to white color. However, ISQ molecules remain in the exposed regions because a fluorescence spectrum is still generated.

To probe the ISQ molecules in the darker blue state, the ISQ/PMMA sample was exposed a second time to 355 nm light (see Figure 5.43). Figure 5.46 shows the change in transmission contours, immediately after the final exposure to 355 nm light, for $\lambda = 633$ nm. We see that the final exposure did not create as large of a change in transmission because there are fewer contour lines for the vertical slits than the two slits at 33° to horizontal. These results are consistent with the color changes observed with the naked eye (see Figure 5.43). The final exposed region was still bluish – absorbing red – when the final measurements were taken, thus there is a much smaller change in the absorption in comparison to an un-exposed region.

We notice an even more interesting change in the sample if we study the change in transmission at a fluorescence wavelength. Figure 5.47 shows additional decreases in absorption (increases in fluorescence transmission) that run along the x-axis at various heights in the sample. These contours were not noticeable in the 633 nm results because the decrease in absorption at that wavelength was significantly larger. Because the change in fluorescence and subsequent re-absorption is much smaller than the change in absorption at the laser wavelength, these horizontal strips become visible and possibly obscure the vertical strips caused by the second 355 nm exposure.

The changes in fluorescence that run parallel to the x-axis are easily explained after

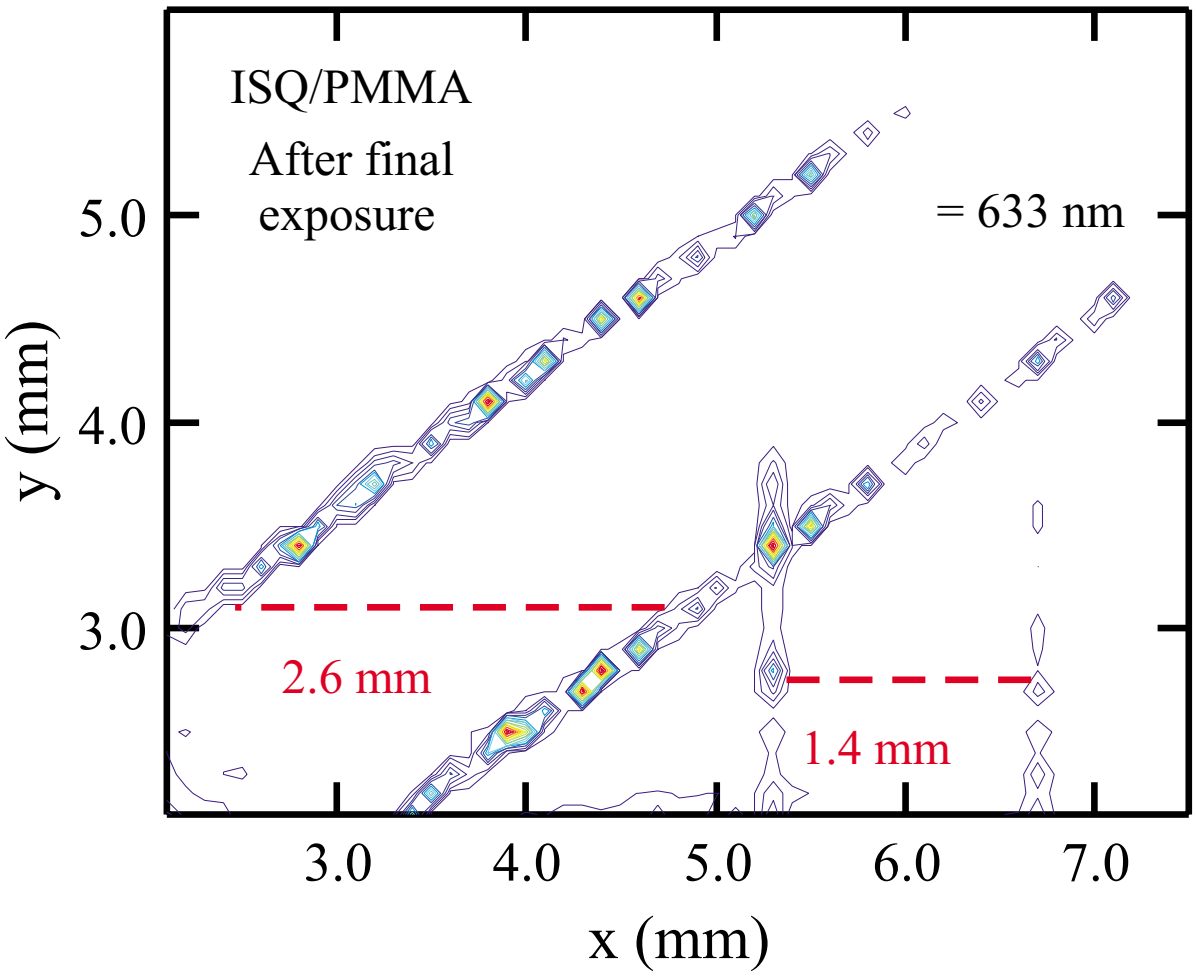

Fig. 5.46: Change in transmission contours for the ISQ sample immediately after the final bleaching with 355 nm laser light. Viewed at the incident wavelength, 633 nm.

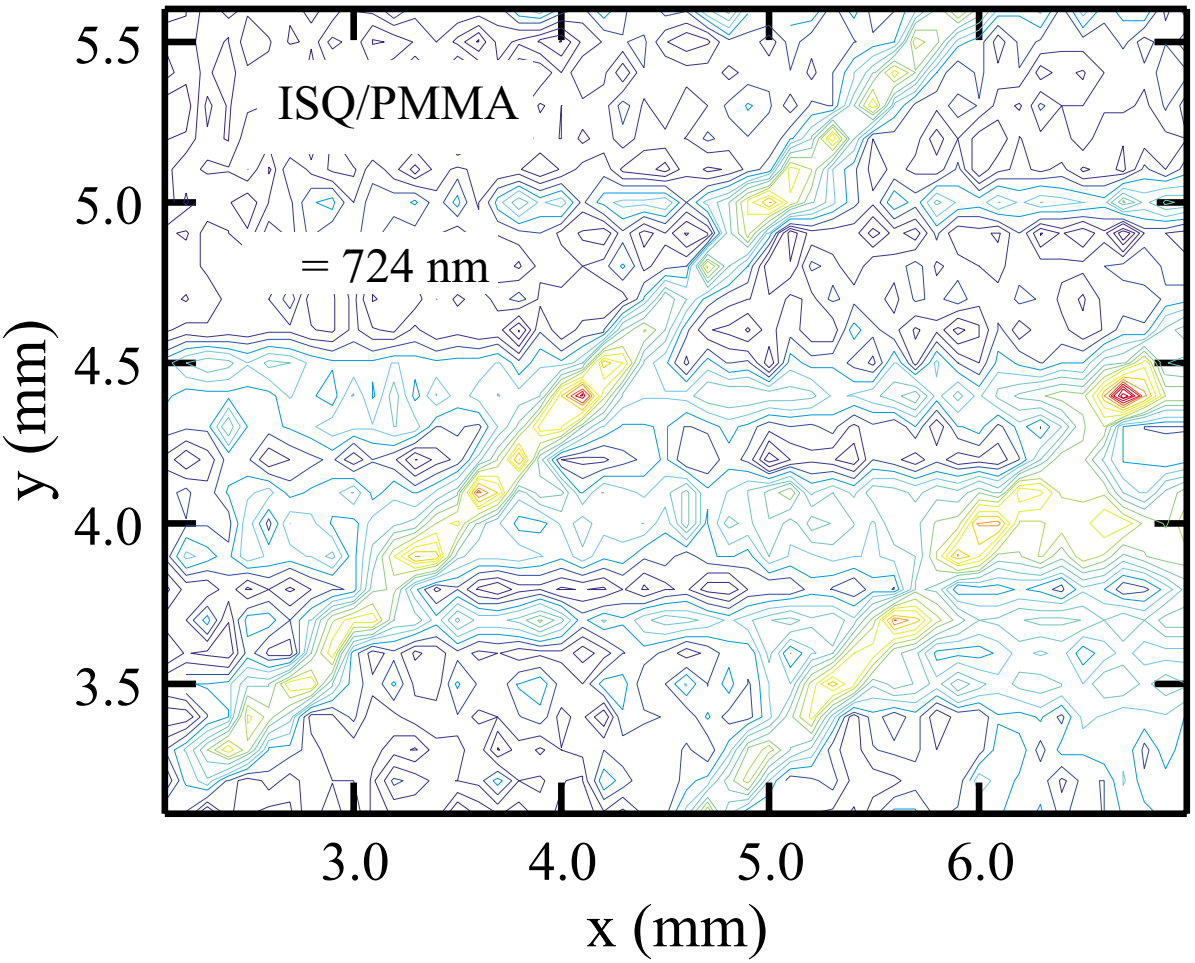

Fig. 5.47: Change in transmission contours for the ISQ sample immediately after the final bleaching with 355 nm laser light. Viewed at a fluorescence wavelength, 724 nm (λ_{inc} = 633 nm).

realizing that the sample was probed in an x-axis raster pattern. Therefore we were inducing color changes in the ISQ/PMMA preform slice with our probe light. This was a rather unexpected and disappointing result because the probe lasers were below 2 mW and the exposure time was less than 1 minute at each position.

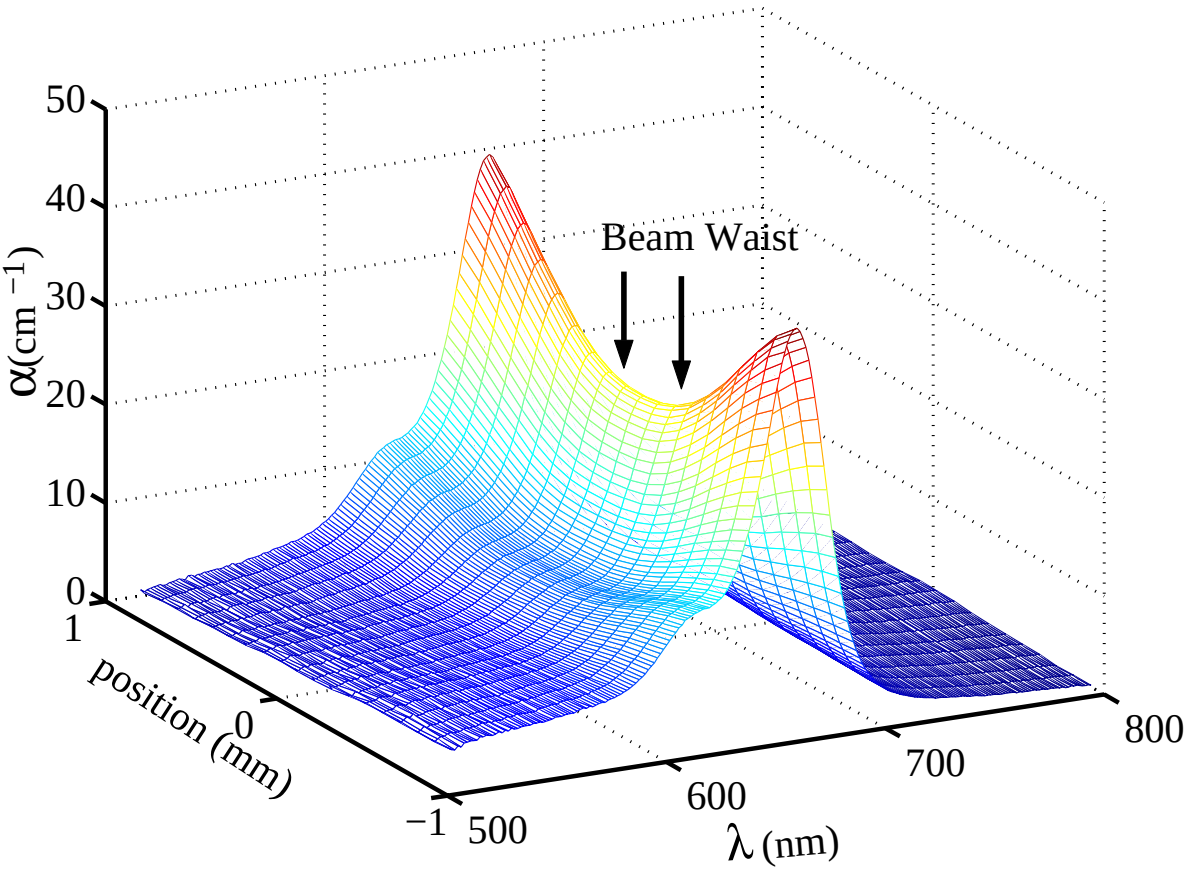

Fig. 5.48: Resonant absorption of a line through an ISQ/PMMA preform slice that was previously exposed to 633 nm light for 3 hours at 0.5 mW. The beam was centered at zero mm, and the diameter was 400 μm.

To confirm that the probe light is causing the ISQ/PMMA preform to change color, we exposed a low concentration ISQ/PMMA preform slice to 633 nm light for an extended period of time. A low concentration was chosen so we could measure the absorption coefficient, $\alpha(\lambda)$, about resonance with a white light source in the exposed and unexposed regions. Two exposures were conducted at different locations in the sample with the He/Ne laser collimated to a 400 μm beam waist. The first exposure was for 3 hours

0.5 mW and the second exposure was for 5 minutes at 5 mW. Two intensities were chosen to determine if there was any additional effects caused by a higher input power.

Figure 5.48 represents $\alpha(\lambda)$ for a line through the region exposed by 0.5 mW He/Ne light. Clearly, there is a decrease in the linear absorption that increases in magnitude at the center of the bleached region. It is interesting to note that there is no significant change in the shape of the linear absorption spectrum in the exposed region, which suggests that the molecules are degrading in to smaller molecules which absorb in the UV or diffusing out of the exposed region, instead of aggregating into larger molecules which absorb closer to the IR.

There is a similar decrease in the absorption spectrum for a 1-D slice through the region exposed by 5 mW He/Ne light which does not warrant special consideration. However, there is an overall increase in the background absorption (i.e. the absorption is increased for all wavelengths in a relatively constant amount) which could possibly be caused by increased scattering in the polymer. This result suggests that there is a secondary degradation of the polymer.

To test this hypothesis we measured the transmitted power as a function of time for both the incident wavelength and fluorescence wavelengths. To do this properly, a high concentration sample – similar to the one discussed at the beginning of this section – was necessary to absorb enough of the power at the incident wavelength as to not saturate the spectrometer. The incident power was monitored during the experiment and did not fluctuation more than 3% from 1 mW.

Figure 5.5.1 shows the result of the time dependence experiment at the 633 nm with a fit to the following:

$$\ln[\mathrm{n}(t)] = \ln[\mathrm{n}_0] - \ln[1 + (\exp(\alpha_1 d) - 1)\exp(-\alpha_1 \beta_1' t)] - \alpha_2 d + \alpha_2 \beta_2' t, \qquad (5.6)$$

where $\mathrm{n}(t)$ is the transmitted photon flux in (counts/s), n_0 is the incident photon flux, α_i is an absorption coefficient cm^{-1}, β_i' is a speed (cm/hours), d is the thickness of the sample, and t is the exposure time in hours. The details for the derivation of Equation (5.6) can be found in Section 2.8.

Clearly, there are two different processes that occur in the sample as the exposure time

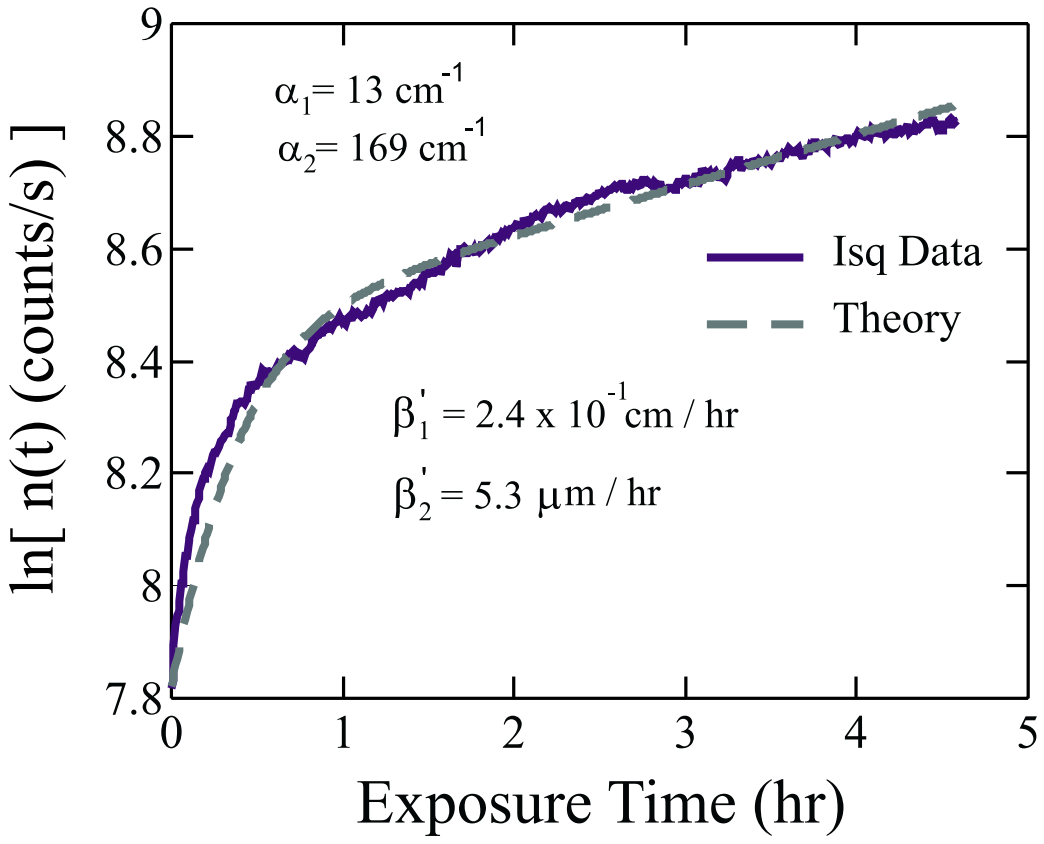

Fig. 5.49: Natural log of the photon flux as a function of exposure time for an ISQ/PMMA preform slice. The solid line represents a least-squares for to the data for two decay speeds ($\beta_1' = 2.4 \times 10^1$ cm/hour, and $\beta_2' = 2.4 \times 10^1 \mu$m/hour.

increases. Initially, the fast change in the transmitted photon flux, which is most likely a surface effect, makes up about 13% of the total absorption. Since the slope decreases significantly after about one hour, a different process must be dominating the change in transmission through the preform. This change in transmission could be caused by the dye molecules diffusing out of the illuminated region, cis-trans isomerization, different species of dye molecules breaking down, etc. It is beyond the scope of this work to determine the specific mechanisms for the change in transmission. However, it should be noted that the fluorescence intensity increases in time, and also red-shifts.

From results obtained for TSQ/PMMA, and SiPc/PMMA preform samples, which we do not show, it is clear that the fast change in transmission is dye and position

specific and does not necessarily scale with intensity, which was the assumption for the derivation for Equation 5.6. The fast process was not observed for dye-doped thin films which are not directly exposed to the air. This suggests that there is a surface layer of dye molecules in the core preform slices which are more vulnerable to light than the remainder of the sample. Since PMMA absorbs oxygen, and oxygen is known to mediate dye decomposition, a surface layer in an oxygen atmosphere may breakdown more easily than the bulk when illuminated.

However, the slow process, which also causes an increase in transmission as a function of exposure time, is more similar from dye to dye and position to position than the fast process. This suggests that it is related to the distribution of sites in a polymer.

5.5.2 Core Fibers

Similar photosensitivity experiments can be conducted on dye-doped core fibers. In this section we briefly describe two photosensitivity results. The first is for an ISQ/PMMA core fiber and the second is for a BSQ/PMMA core fiber.

We saw in photosensitivity experiments on ISQ/PMMA preform slices that the preform initially became darker when exposed to UV light then decayed to a yellowish color. A photosensitivity experiment on an ISQ/PMMA core fiber shows similar results but it was exposed to 633 nm light.

Initially, the fiber is characterized in a propagation distance SIF experiment which is called "New Fiber" in Figure 5.5.2. The fluorescence wavelength is 758 nm and occurs near the peak of the SIF spectrum. The fiber was then exposed to 633 nm light for 40 minutes at 4.2 mm ($P_{inc} = 0.4$ mW). After the prolonged exposure, the fiber was measured twice more in the propagation distance SIF experiment – 1 hour after exposure and 14 hours after exposure. The decrease in the SIF spectrum immediately after the prolonged exposure at 4.2 mm suggests that there is a reduction in the number of ISQ molecules. However, the SIF spectrum decreases even more at 1, and 14 hours after the prolonged exposure. This suggests that dye molecules in the 4.2 mm region are breaking down over extended period of time even when they are not being exposed to laser light. We saw

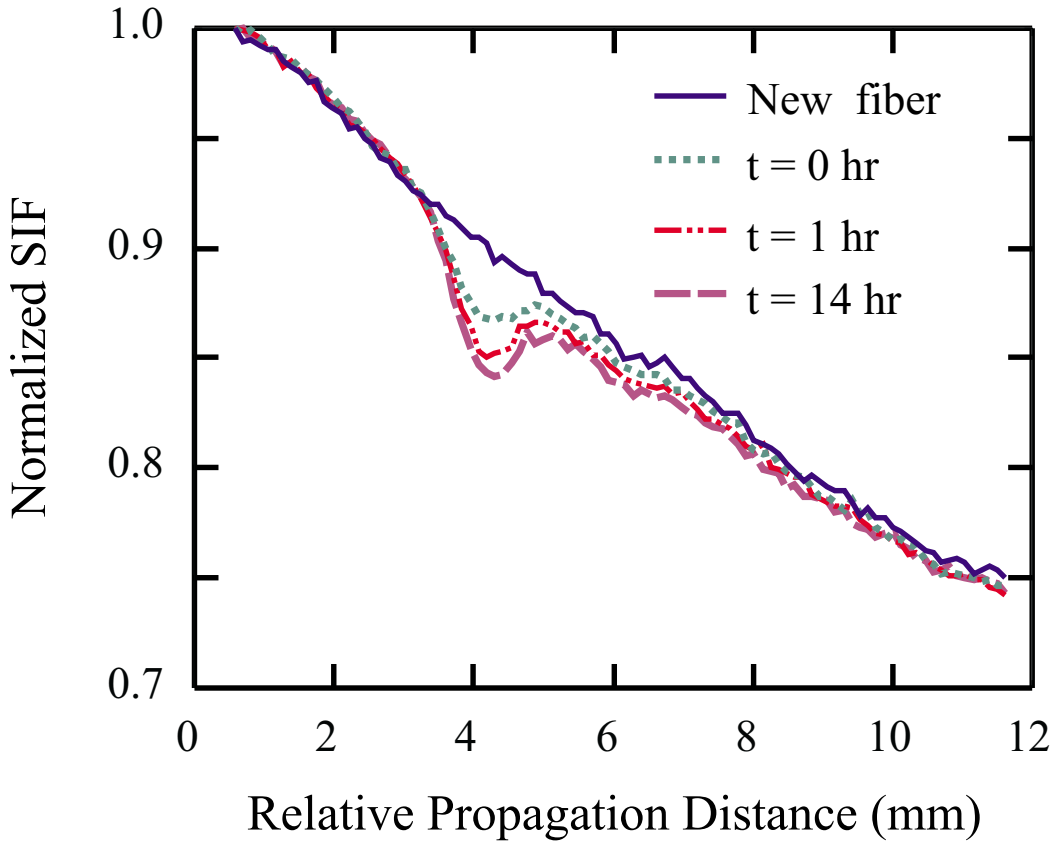

Fig. 5.50: SIF intensity for a BSQ/PMMA core fiber: before, immediately after, 1 hour after, and 14 hours after a 40 minute exposure at 3.0 mm with 633 nm light (P_{inc} =0.4 mW, λ_f = 758 nm).

a similar decay mechanism in the ISQ/PMMA core preform slices that were exposed to UV light. Since the incident power was only 0.4 mW for the prolonged exposure the ISQ molecule can be considered very unstable and not practical for optical devices.

A more promising result was found for BSQ/PMMA. In a similar procedure to the ISQ/PMMA photosensitivity experiment, a BSQ/PMMA core fiber was exposed to 633 nm light for 40 minutes at 3 mm (P_{inc} = 1mW). Figure 5.5.2 summarizes the photosensitivity experiment on the BSQ/PMMA core fiber. Immediately after the extended exposure at 3 mm, the SIF intensity at 721 nm (near the peak of the SIF spectrum) shows a large decrease near 3 mm. This change is quite different from the change in the exposed region for the ISQ/PMMA core fiber. Because exposed region is not a valley

but a change in slope we suggest that the exposed region is actually optically denser at 721 nm. In addition the dye molecules in this new state may not fluorescence with the same intensity as the unexposed BSQ molecules.

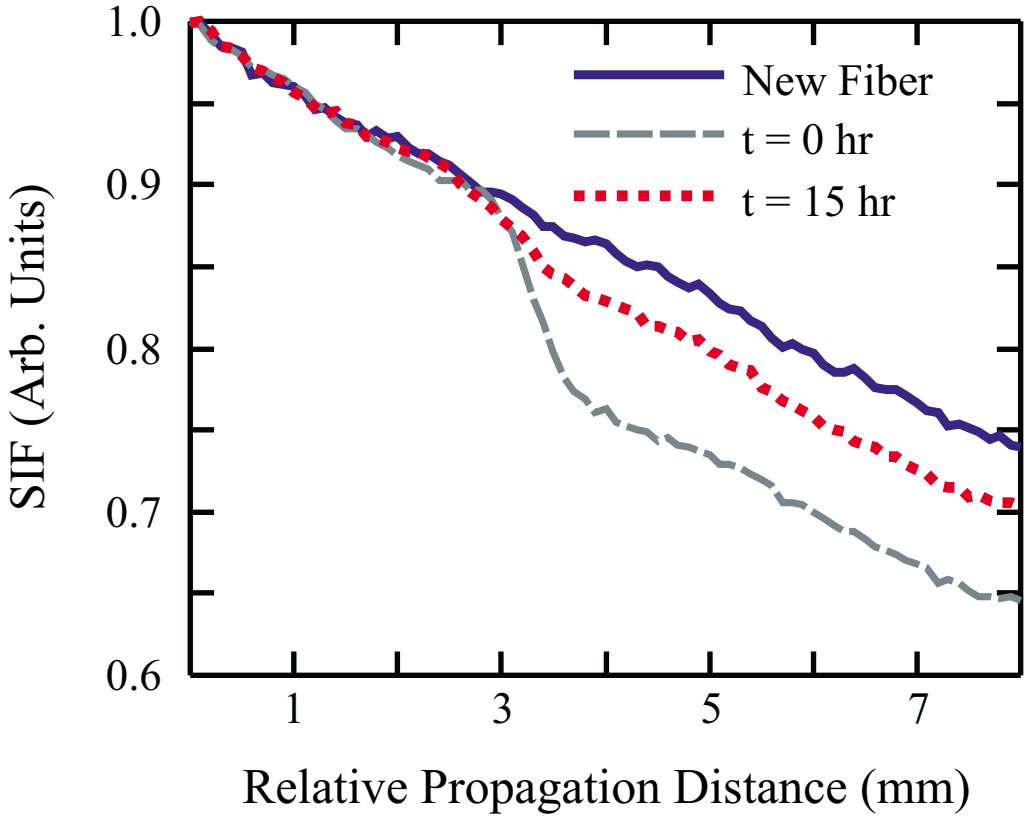

Fig. 5.51: SIF intensity for a BSQ/PMMA core fiber: before, immediately after, and 15 hours after a 40 minute exposure at 3.0 mm with 633 nm light (P_{inc} =1 mW, λ_f = 721 nm).

The results are even more interesting when the exposed region is probed 15 hours after the extended exposure at 3 mm. Clearly, the measured SIF intensity at and beyond 3 mm has increased toward the original SIF intensity. This suggests that the dye molecules are deexciting back to there original state. However, all the molecules have not returned by 15 hours and we see results similar to ISQ/PMMA when the power of the light is increased beyond 5 mW. If a faster mechanism could be found to return the BSQ molecules to there original state BSQ/PMMA fibers at low intensities could be used in optical logic devices.

The results of these experiments show that the dye-doped polymer systems are less

stable than anticipated when exposed to visible light. We can induce color changes in dye-doped samples with either UV or visible laser light. This feature could be exploited to manufacture 2-D and 3-D structured optical devices. However, prolonged exposure to relatively low intensity visible light would eventually "erase" the structures "written" into the samples.

ISQ is clearly the least stable dye studied and hence was shown in greatest detail. The other squaraines are at least an order of magnitude more stable than ISQ, and SiPc is about another order of magnitude more stable than the other squaraines. Unfortunately, there is also a slow process which occurs in dye-doped preforms, and core fibers where by the transmission increases as a function of exposure time. The slow process has a similar slope (speed) for all the preforms that we studied, which suggests that the polymer environment is also affected by the light exposure.

5.6 Linear absorption in core fibers

In this section we use SIF data to determine the off-resonant linear absorption spectrum of several dye-doped polymer fibers. The absorption maximum for these fibers range from 340 nm to 670 nm. Depending on the concentration of dye in the fiber, we can calculate the absorption coefficient as close as 30 nm from resonance and as far as 230 nm from resonance. This is a spectral range that is not easily measured by direct transmission or destructive fiber measurements such as the cut-back method [8]. We calculate $\alpha(\lambda)$ using a least-squares fitting routine that compares the SIF data to the theoretical SIF intensity for the plane wave,

$$F_{PWM}(\lambda, z) = F(\lambda) \exp(-\alpha(\lambda)\, z), \tag{5.7}$$

and point source models,

$$F_{PSM}(\lambda, z) = F(\lambda) \int_0^{\theta_c} \exp(-\alpha(\lambda, \theta)\, z) \sin\theta \, d\theta, \tag{5.8}$$

respectively, where $F(\lambda)$ is the fluorescence at $z = 0$ or the initial excitation position. We have used $F(\lambda, z)$ to denote the transmitted fluorescence. These models were derived in Section 2.7.1.

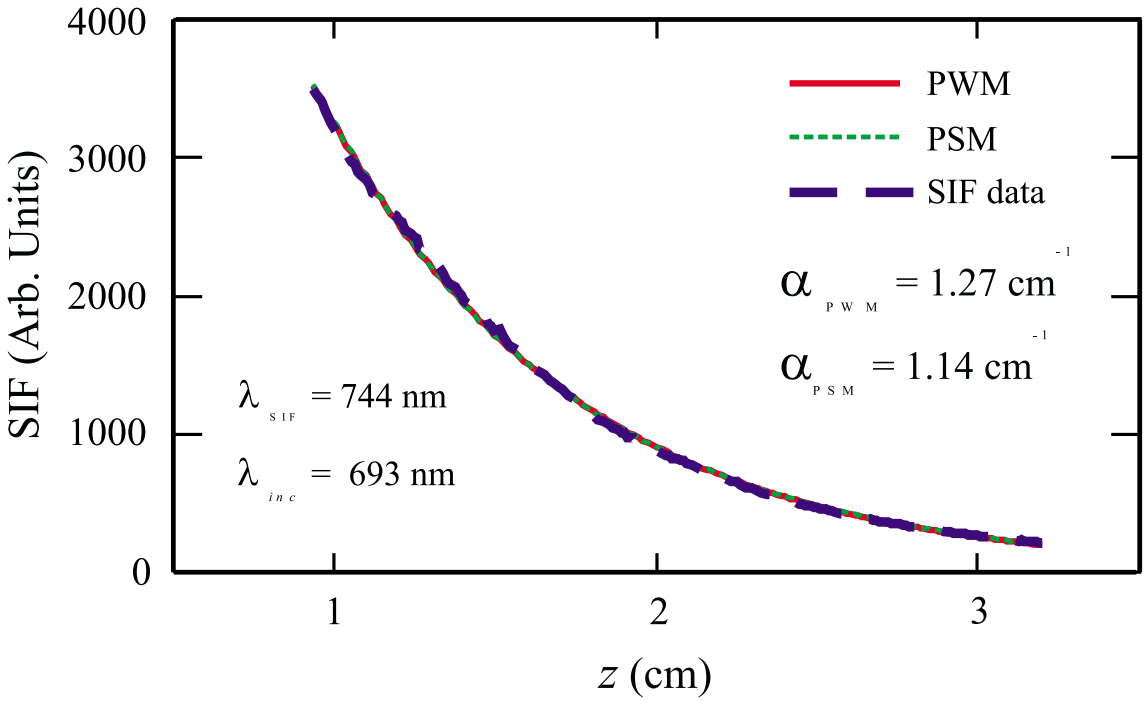

Fig. 5.52: SIF as a function of z for PSQ/P(d-PMMA) at 744 nm , and the two theories for the absorption: plane wave model (PWM) and point source model (PSM). The plane wave and point source curves are coincident on this scale.

The value of $\alpha(\lambda)$ was found to be about 10 % smaller for the point source model (Figure 5.52) for the PSQ/P(MMA-d8) core fiber because the distribution of path lengths (due to the integral in Equation (5.8)). The relative difference between the theories is not fixed and varies between 10 % and 20 % for the concentrations and propagation distances we have measured. It should be noted that both of these models are approximations of how the light propagates in the multimode core fibers, and represent upper and lower limits on $\alpha(\lambda)$.

Figure 5.53 shows the linear absorption spectrum, $\alpha(\lambda)$, of a deuterated PSQ-doped fiber for a plane wave source and a point source as generators of the fluorescence. Note that each point in Figure 5.53 is derived from a fit similar to Figure 5.52. Since the SIF spectrum is fairly broad (over 100 nm) the analysis can be quite time consuming. Therefore it is important to perform a duplicate SIF experiment to confirm an initial result before beginning this analysis.

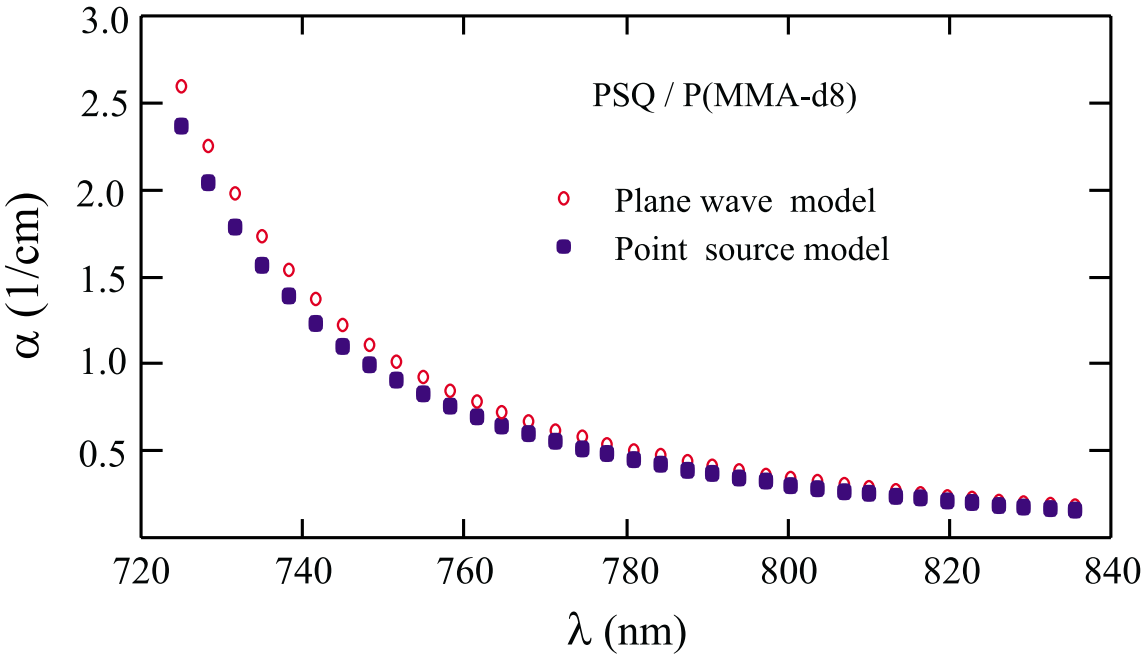

Fig. 5.53: Linear absorption spectrum, $\alpha(\lambda)$, of PSQ/P(MMA-d8) determined from SIF data using plane wave (PWM) and point source (PSM) models in the range, 720 nm $< \lambda <$ 840 nm.

The remainder of the linear absorption results will be shown in terms of the point source model, because the point source model approximates a lower limit for the value of $\alpha(\lambda)$ and we are interested in determining if the dye is causing the absorption. As in previous sections, the results will be grouped according to dopant with an emphasis on the squaraine and phthalocyanine dyes.

5.6.0.1 BSQ

In Section 5.2, we discussed the SIF spectra as a function of propagation distance for BSQ/PMMA and BSQ/P(MMA-d8) multimode core fibers. We use those spectra and the point source model to calculate $\alpha(\lambda)$. Figure 5.54 represents the results of those computations.

The points represent the average $\alpha(\lambda_i)$ from several propagation distance experiments, where each $\alpha(\lambda_i)$ must be calculated for each wavelength, λ_i, within the fluorescence band as shown in Figure 5.52. Because the fibers were of poor quality, the uncertainty

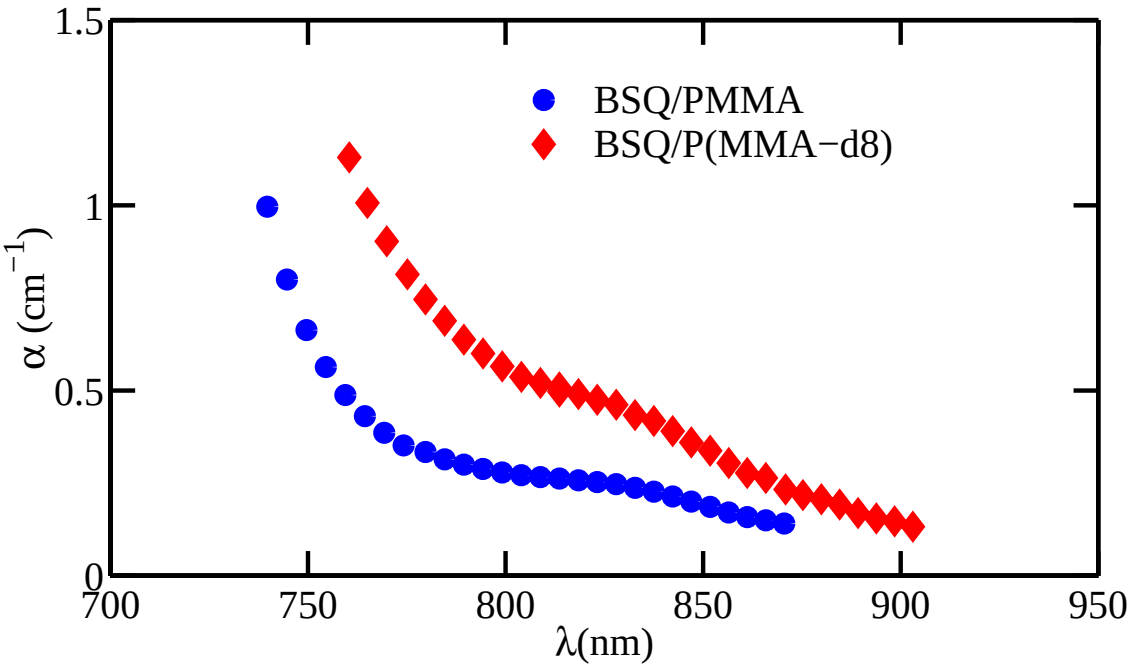

Fig. 5.54: Linear absorption coefficient measured using the point source model for BSQ/PMMA (N= 4.1 $\times 10^{18}$ cm^{-3}) and BSQ/P(MMA-d8) (N= 5.8 $\times 10^{18}$ cm^{-3})core fibers.

associated with each point is quite large, $\pm$ 13 %. The fibers were made using the old fiber fabrication procedure [9] and thus did not have the surface layer of the preform removed before they were drawn into core fibers. The core fibers were also stored in small tightly wound bundles which created a semi-permanent curve in the core fiber. In several sections small lumps could be felt when sliding a finger tip along the fiber. Unfortunately, this procedure could not be done before the experiments were performed because it would have contaminated the fiber even further.

Even though there was a relatively large change in the magnitudes of α from one section of fiber to the next, the shape of the absorption as a function of wavelength was consistent. Thus the small hump in absorption near 830 nm should be considered a real effect. Notice that it occurs for both BSQ/PMMA and BSQ/P(MMA-d8) which suggests that it is caused be the dye and not the polymer host.

The BSQ/P(MMA-d8) spectrum, in Figure 5.8, developed a slight valley in the 830 nm range, but we could not determine if the valley was caused by absorption in the

830 nm range or an additional emission beyond 830 nm. Figure 5.54 strongly suggests that the valley in the SIF spectrum is caused by an excited state located near 830 nm. The nature of this previously unidentified state deserves future consideration, if better BSQ/PMMA core fibers become available.

5.6.0.2 HSQ and PSQ

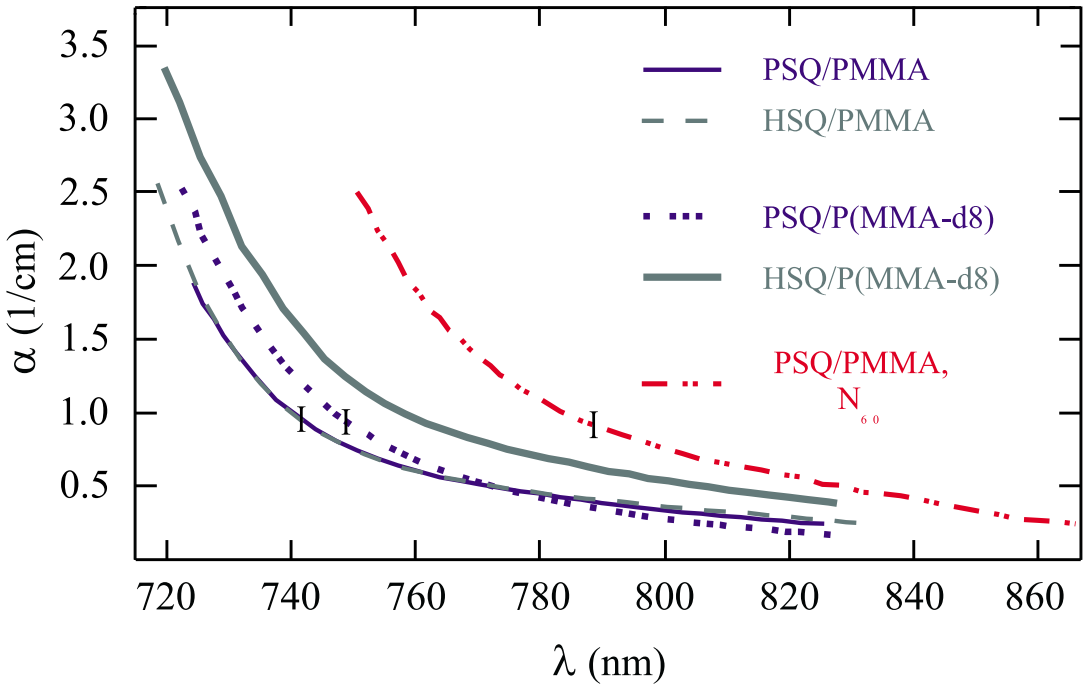

Fig. 5.55: Linear absorption coefficient calculated using the point source model for the HSQ-doped and PSQ-doped core fibers studied discussed in Section 5.2. The error associated with each curve is denoted by the error bar except for the HSQ/P(MMA-d8) curve since there was only one fiber measured. All fibers are room temperature maximum concentration except the fiber denoted $N_{60} = 4.0 \times 10^{18}$ cm $^{-3}$.

$\alpha(\lambda)$, assuming a point source generated the fluorescence, is shown in Figure 5.55 for HSQ- and PSQ-doped fibers. Each curve is determined by averaging the absorption spectra of several fibers of the same composition while the uncertainty is determined from the standard deviation divided by the square root of the number of fibers used in the composite results. Solid lines were used so the result for each fiber is discernible.

While the fluctuations in the SIF data, for multiple experiments on a single section of fiber, are in the range of 2 %, variation in loss between different sections of fiber is ± 10 %. The error bars on the curves show an estimate of the magnitude of the uncertainty that is representative of each type of fiber. (The HSQ/P(MMA-d8) result was determined from a single section of fiber, so no error bar is shown.)

Since the point source model results in a lower bound for $\alpha(\lambda)$, the results from Figure 5.55 show that the absorption in the 700 nm – 840 nm range is significantly larger than undoped polymer fibers; for example, at 832 nm – which is close to the lowest absorption coefficient measured – the deuterated PSQ fiber has a coefficient $\alpha_{PSQ/P(MMA-d8)}(832\,\text{nm}) \approx 0.15\,\text{cm}^{-1}$ while the non-deuterated PSQ fiber has a coefficient $\alpha_{PSQ/PMMA}(832\,\text{nm}) \approx 0.2\,\text{cm}^{-1}$. In comparison neat PMMA and P(MMA-d8) were measured by Kaino [10] at 832 nm as $\alpha_{PMMA}(832\,\text{nm}) \approx 4.5 \times 10^{-3}\,\text{cm}^{-1}$ and $\alpha_{P(MMA-d8)}(832\,\text{nm}) \approx 4.5 \times 10^{-4}\,\text{cm}^{-1}$. Clearly, the dye is the source of the loss in this wavelength range, which implies that to take advantage of a low loss polymer, like P(MMA-d8), the working wavelength for a device needs to be greater than 200 nm from resonance.

Several months after the data in Figure 5.55 was analyzed, we measured a PSQ/PMMA fiber that was made with the new core preform procedure (see Section 3.2.3). Thus we became interested in determining if there is a reduction in the linear absorption coefficient because of the new process. In order to compare the results for PSQ/PMMA fibers of various concentrations, we calculated the absorption cross-section as a function of wavelength for each core fiber.

The absorption cross-section was defined in Section 2.6, which we rearrange to get,

$$\sigma = \frac{\alpha}{N}. \tag{5.9}$$

Since $\sigma(\lambda)$ is independent of concentration, we expect that $\sigma(\lambda)$ should be approximately equal for all the PSQ/PMMA core fibers. Figure 5.56 represents the absorption cross-section of the two PSQ/PMMA core fibers shown in Figure 5.55 (N, 3.6N), which were made using the old fiber fabrication process, and a PSQ/PMMA (2.7N) core fiber, that was made using the new fiber fabrication process.

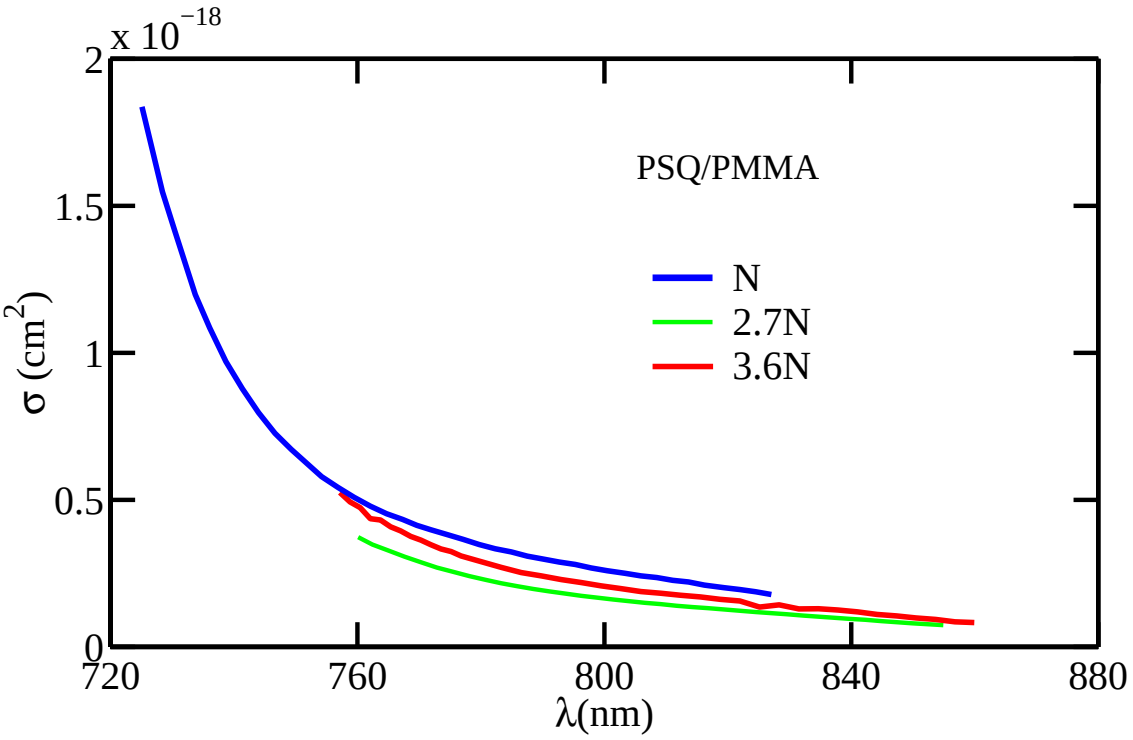

Fig. 5.56: Absorption cross-section for 3 concentrations of PSQ/PMMA core fiber. ($N_k \in$ { N , 2.7N, 3.6N}).

Since there is about $\pm$ 10 % uncertainty for each curve, the highest concentration fiber and the lowest concentration fiber are equivalent within experimental error. However, the lowest concentration fiber and the middle concentration fiber are not. The lower absorption cross-section for the middle concentration fiber suggests that removing a surface layer from the core preform before drawing the core fiber, and storing the core fiber in straight strands reduces the absorption coefficient calculated from SIF experimental data. However, more experimental results are necessary to confirm that the reduction in the loss is actually caused by the new fabrication process.

5.6.0.3 TSQ

TSQ/PMMA was one of the last dyes to be studied. Thus we used the experience gained in the study of HSQ/PMMA and PSQ/PMMA to systematically make four different concentrations of core fiber. At this point in the SIF experiment we had only measured fibers

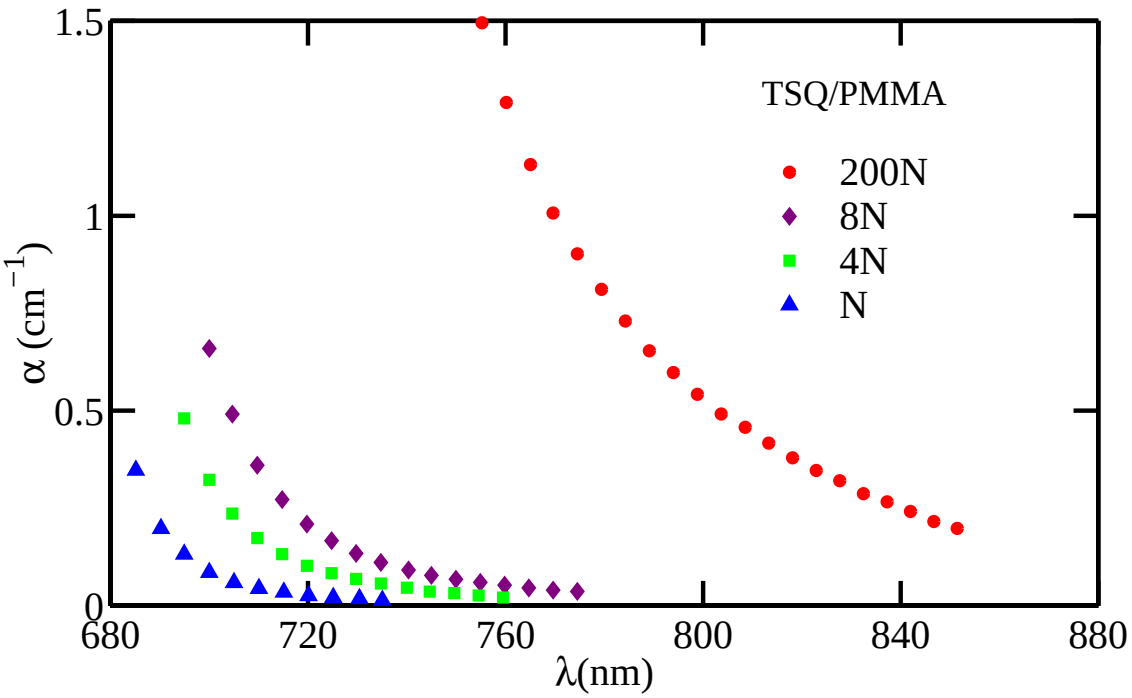

Fig. 5.57: Linear absorption coefficient measured using the point source model for 4 concentrations of TSQ/PMMA core fiber. ($N_k \in$ { N , 4N 8N, 200N}, where N= 0.16 $\times 10^{17}$).

that were too optically dense to measure with the transmission spectroscopy experiment 4.1. So we decided to test the following hypothesis: Can the SIF experiment determine the linear absorption coefficient for low concentration multimode core fibers as well as high concentration fibers?

In order to measure low concentration fibers they had to be made using the procedure in Section 3.2 since none existed when the question was posed. The three fibers labeled N, 4N, and 8N were made from the same initial solution of TSQ/PMMA at room temperature. In other words, the solution that polymerized into the fiber marked N is a 1/8 dilution of the solution that polymerized into the fiber marked 8N, etc. The fiber labeled 200N was polymerized from a different TSQ/MMA solution at 60 °C which was our high concentration control fiber. It should be noted that all four core preforms had a thin outer layer lathed off before they were drawn into core fiber. They were also immediately removed from the fiber spool, and cut into 20 cm segments so they could be stored without being bent.

By performing propagation dependence experiments on all the TSQ/PMMA core fibers (see Section 5.2.3.3), we collected data that enabled us to calculate the linear absorption coefficient as a function of wavelength in the fluorescence band. As the concentration increased, we observed that the SIF spectra red-shifted which allowed us to determine $\alpha(\lambda)$ for various wavelength ranges.

Figure 5.57 represents the linear absorption for the four TSQ/PMMA fibers. $\alpha(\lambda)$ was calculated using the point source model described in Section 2.7.1.2 and the error associated with each point is approximately $\pm 3\%$. As we expected, there was an increase in the linear absorption and a red-shift in the measurable wavelength range as the concentration of TSQ/PMMA was increased. However, the results shown in Figure 5.57 do not tell us if the absorption is proportional to the number density.

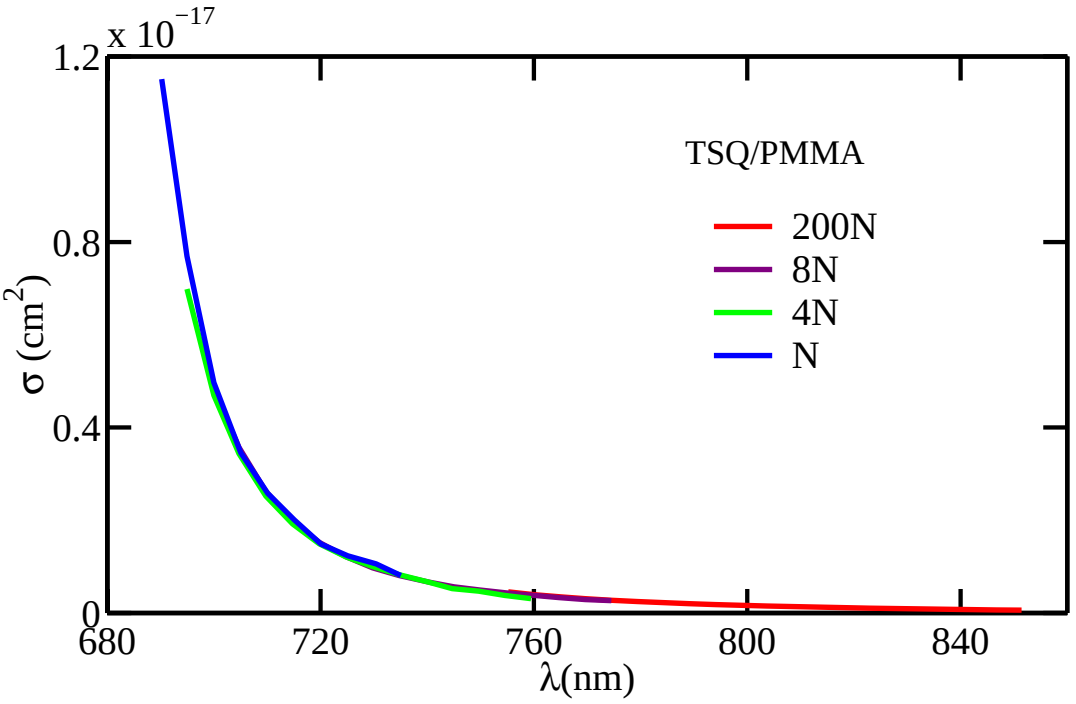

Fig. 5.58: Absorption cross-section for 4 concentrations of TSQ/PMMA core fiber. ($N_k \in$ { N, 4N, 8N, 200N}).

To determine if $\alpha(\lambda)$ is proportional to the number density, we calculated the absorption cross-section, $\sigma(\lambda)$, which is measured in cm^2. As defined, the absorption cross-section is independent of number density so we expect, if the SIF experiment is valid for

low concentration fibers, that $\sigma(\lambda)$ would be identical for each fiber when the wavelength regions overlap.

Figure 5.58 shows the absorption cross-section for all four TSQ/PMMA fibers. We have represented the data with solid lines so that it is easier to identify each curve. Clearly, $\sigma(\lambda)$ is identical, within experimental uncertainty, for each fiber in the overlap regions. Thus we have shown that the SIF experiment can be used to determine the linear absorption coefficient for any concentration of dopant as long as there is enough dye to generate a sufficient large SIF spectrum, and that TSQ/PMMA absorption, $\alpha(\lambda)$, is proportional to concentration is the tail of the absorption band.

We should note that the TSQ results are much cleaner than the HSQ, PSQ, and BSQ results because of the new preform fabrication method (see Section 3.2.3). We had much straighter, smoother surfaces for coupling the incident light into the fiber and better propagation of the fluorescence inside the fiber. This suggests that the systematic error from one section of fiber to the next has been reduced. We did not, however, measure more than one section of fiber at each concentration to determine reproducibility.

5.6.0.4 ISQ

As usual, we have left the ISQ-doped fibers to the end of the squaraine discussion because they exhibit the most intriguing behavior. In the previous section, it was confirmed that the point source model could be used to calculate the absorption coefficient for low concentration fibers measured in the SIF experiment. With this knowledge, we analyzed the SIF spectra from the four ISQ/PMMA fibers discussed in section 5.2.3.4 using the point source model.

Figure 5.59 shows the results of the absorption coefficient measurements. Notice that $\alpha(\lambda)$ increases with increasing concentration and red-shifts as it did for the TSQ/PMMA fibers in the previous section. However, the shape of $\alpha(\lambda)$ evolves with increasing concentration for the ISQ/PMMA fibers. For the highest concentration fiber, which exhibited a large valley in its SIF spectrum (see Figure 5.22), there is a large hump in the absorption spectrum in the 775 nm range. The ISQ/P(MMA-d8) absorption spectrum is very similar to $\alpha(\lambda)$ for the fiber labeled 27N so it was not included in Figure 5.59 [5].

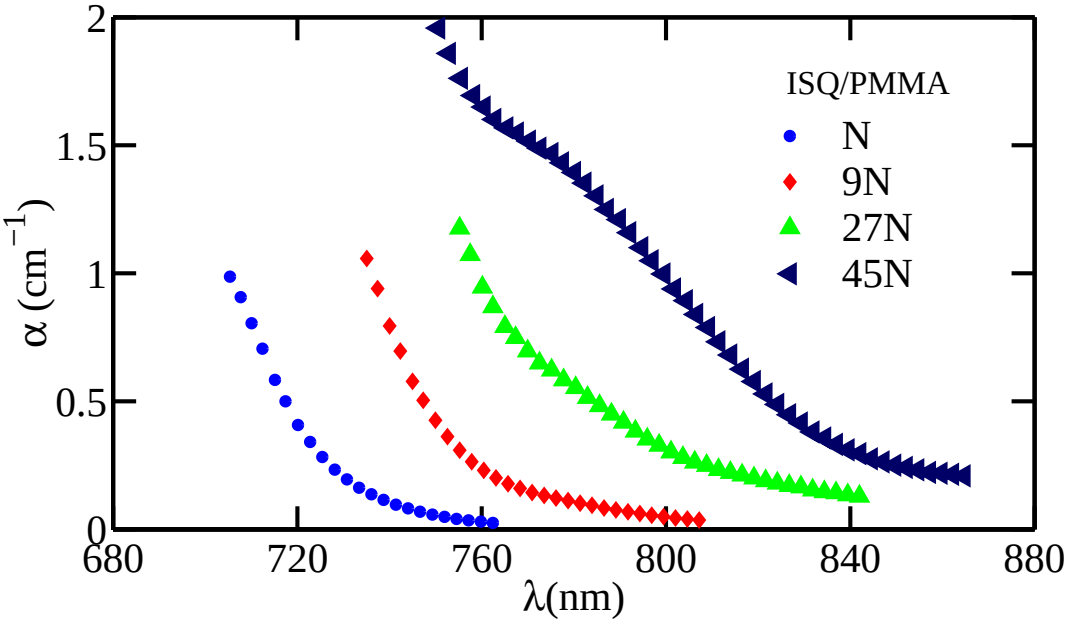

Fig. 5.59: Linear absorption coefficient measured using the point source model for 4 concentrations of ISQ/PMMA core fiber. ($N_k \in$ { N , 9N, 27N, 45N}, where N= 1.4 $\times 10^{17}$).

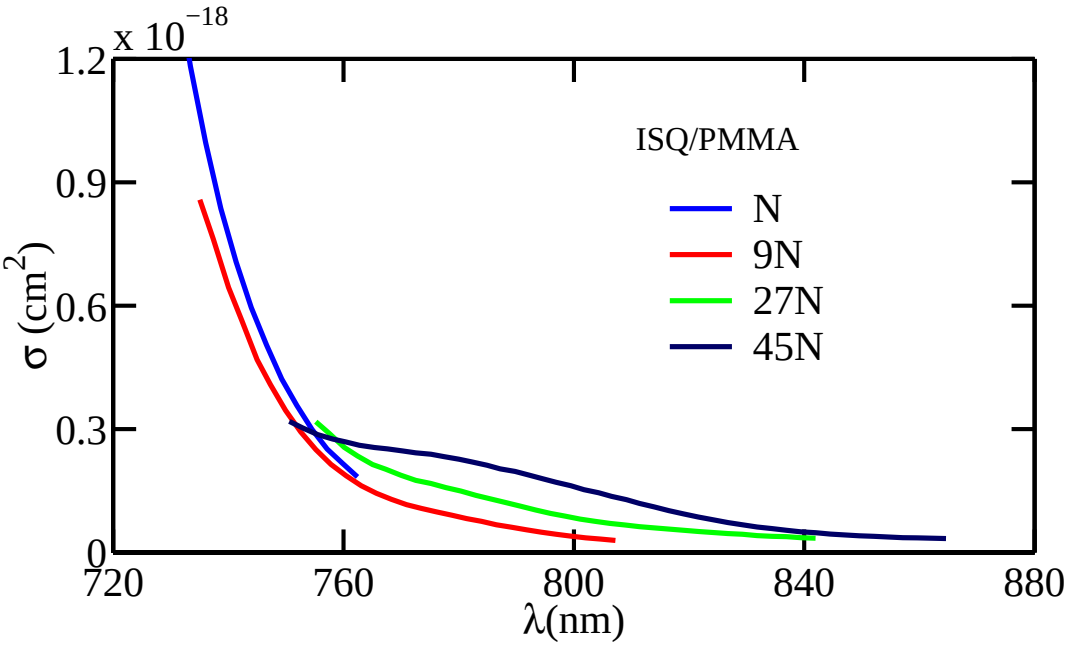

Fig. 5.60: Absorption cross-section for 4 concentrations of ISQ/PMMA core fiber. ($N_k \in$ { N, 9N, 27N, 45N}, where N= 1.4 $\times 10^{17}$).

To confirm that the ISQ/PMMA absorption is not behaving linearly with number density, we determined $\sigma(\lambda)$ for the four fibers in Figure 5.59. Figure 5.60 represents the absorption cross-section as a function of wavelength, $\sigma(\lambda)$, for these four fibers. In comparison to the absorption cross-section for TSQ/PMMA core fibers, the absorption cross-section for ISQ/PMMA fibers is not constant as a function of concentration. In other words the linear absorption coefficient for ISQ/PMMA is not scaling linearly with number density.

The significant shoulder in $\sigma(\lambda)$ between 770-820 nm for the highest concentration ISQ/PMMA fiber is most likely caused by dye-aggregation. This shoulder also corresponds to the spectral region of the unidentified absorption in Figure 5.27, which confirms the hypothesis of a weak excited state.

Several groups have reported, in their studies of Langmuir-Blodgett thin films, optical transitions in squaraine dye J-aggregates between 750-800 nm [11, 12, 13, 14], where a J-aggregate is a face-to-face dimer arrangement of dye molecules when a donor region of one molecule overlaps the acceptor region of the other molecule. Unfortunately, dye aggregation is not uniform over the length of a fiber so some sections of the same fiber do not exhibit the same amount of aggregation as others. Therefore ISQ at these concentrations is of limited use for potential optical applications.

It is interesting to compare the results from Figure 5.58 and Figure 5.60, of TSQ/PMMA core fibers and ISQ/PMMA core fibers, respectively. $\sigma(\lambda)$ is greater than an order of magnitude larger for the non-aggregating ISQ/PMMA fibers. Thus, shifting the absorption maximum further to the UV may have many benefits for nonlinear optical devices in the 750 -900 nm range.

5.6.0.5 SiPc

We continue the discussion of the off-resonant absorption coefficient in this section. However, we have classified the results in terms of excitation wavelength instead of concentration. There are two reasons for the change. For the squaraines, the SIF spectra are independent of the excitation wavelength with the possible exception of ISQ, so it did not make sense to explore the loss as a function of the excitation wavelength, and all

the squaraine core fibers were fabricated by filtering the dye-doped solution with 0.22 μm Teflon filters. Both concentrations of SiPc/PMMA were not filtered, so it does not

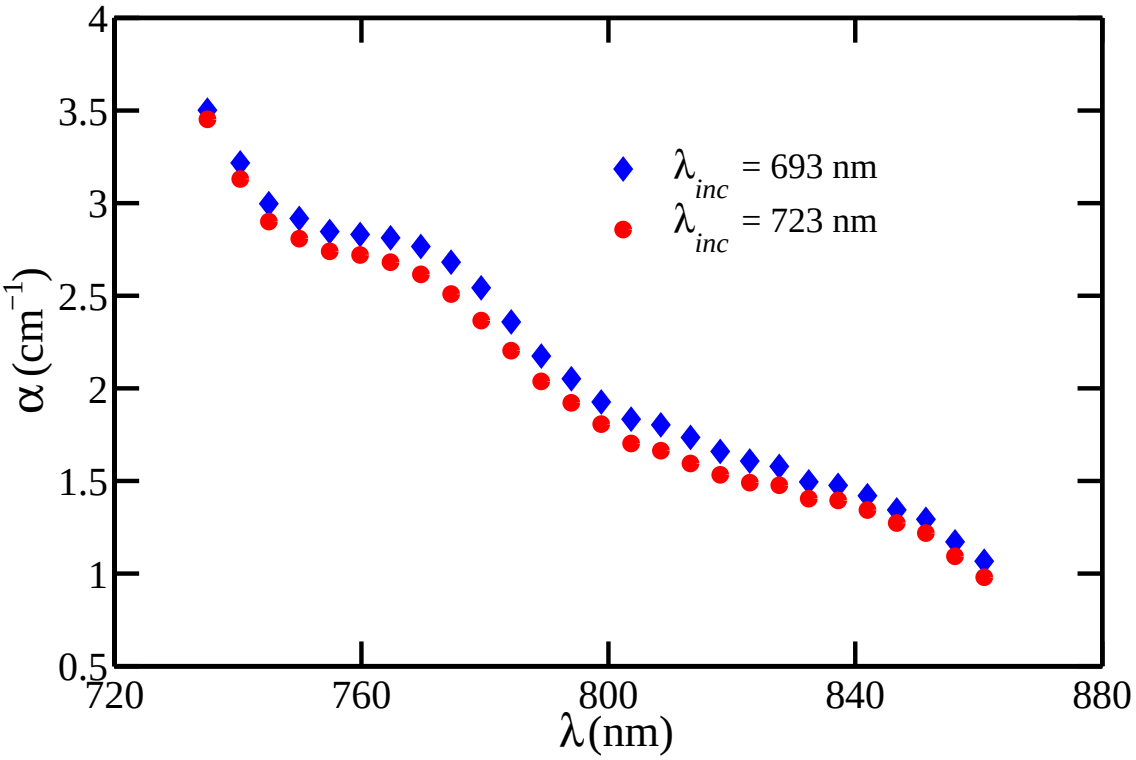

Fig. 5.61: Linear absorption coefficient determined from the SIF spectra shown in Figure 5.32 using the point source model for the high concentration, $N_H = 1.2 \times 10^{18}$ cm^{-3}, SiPc/PMMA core fiber. ($\lambda_{inc} \in \{693$ nm, 723 nm $\}$).

make sense to rigorously explore the concentration dependence. However, the SIF spectra for SiPc/PMMA are dependent on the excitation wavelength so it is more interesting to determine if the absorption of the SIF intensity is also dependent on the excitation wavelength. Therefore we discuss the absorption in the SIF regime for high concentration, N_H, SiPc/PMMA and low concentration, N_L, SiPc/PMMA core fiber at the same incident wavelengths that were shown in Figures 5.32 and 5.33.

Figure 5.61 represents $\alpha(\lambda)$ for the high concentration SiPc/PMMA copolymer core fiber. As we previously discussed, the 693 nm laser diode illuminates the fiber from one side, and the Ti:Sapphire laser tuned to 723 nm illuminates the fiber from the opposite side. Thus the small difference in the absorption maybe caused by the different

illumination positions. However, the difference is $< 10\%$, so the absorption in the SIF region, as expected, can be considered independent of the excitation wavelength for the high concentration SiPc/PMMA core fiber.

Of more interest is the shape of the absorption spectrum. There are at least two, possibly three, humps in $\alpha(\lambda)$. The humps in the absorption coefficient are most likely caused by low lying vibronic states of the SiPc/PMMA molecule, as opposed to aggregation which was the case for ISQ/PMMA.

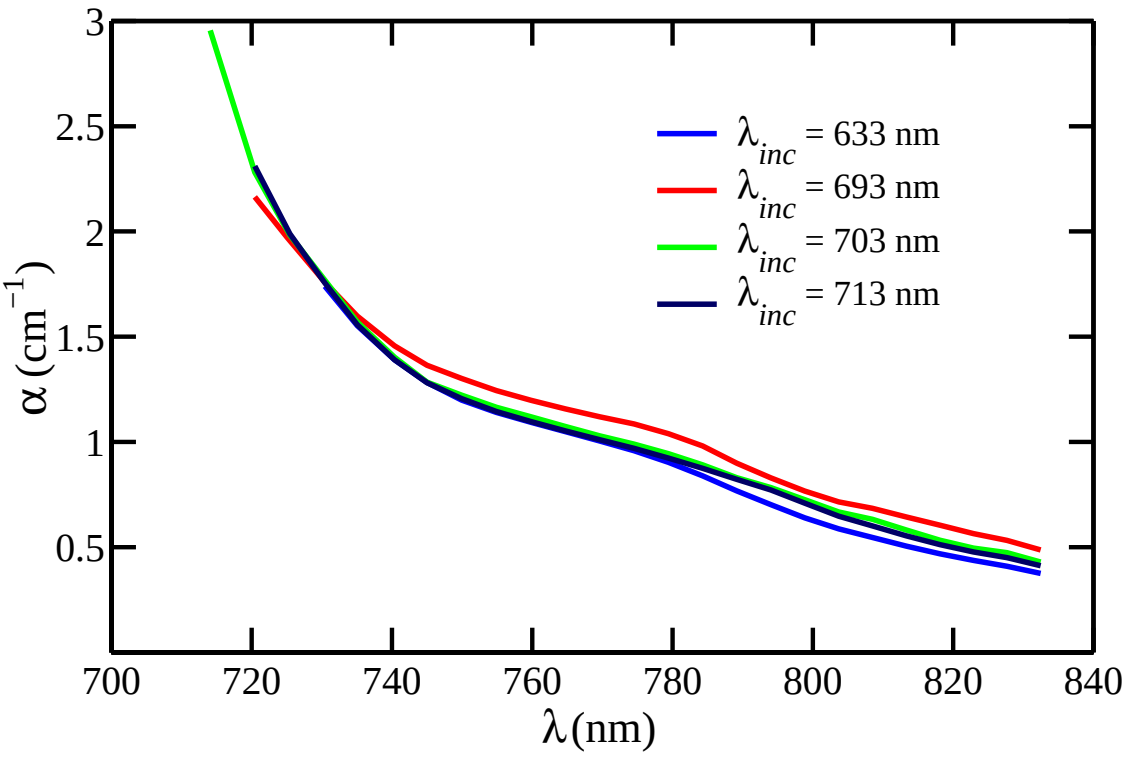

Fig. 5.62: Linear absorption coefficient calculated using the point source model for the low concentration, $N_L = 1.3 \times 10^{17}$ cm^{-3}, SiPc core fiber. ($\lambda_{inc} \in$ { 633 nm, 693 nm, 703 nm, 713 nm }).

Figure 5.62 shows the linear absorption coefficient as a function of wavelength. Each curve was calculated using the point source model in Section 2.7.1.2. Notice that there is negligible difference in the absorption when the fluorescence for the incident wavelengths, 633 nm, 703 nm, and, 713 nm. The slight increase in absorption for the 693 nm incident wavelength is most likely because the 693 nm experiment was conducted on the opposite

side of the fiber from the other three experiments. These results strongly suggest that linear absorption can be measured with any incident wavelength that generates a strong enough SIF spectrum for any concentration of SiPc/PMMA copolymer fiber, even though the spectra generated may be completely different.

We should note that the loss, $\alpha(\lambda)$, in the SIF regime is only 2-3 times greater for the higher concentration SiPc/PMMA fiber, N_H, even though the nominal number density is about 10 times larger than the lower concentration fiber, N_L. This difference is most likely caused by the filtration process since it was only performed on the solution which polymerized into the higher concentration SiPc/PMMA fiber. The humps in the absorption occur at the same wavelengths at both excitation wavelengths, which could indicate vibronic states or aggregation at both concentrations.

Because linear absorption is constant as a function of incident wavelength and the SIF spectra are so different (see Figure 5.33) as a function of incident wavelength, it is clear that there is more than one excited state contributing to the fluorescence emission in the low concentration SiPc/PMMA core fiber. To get a better idea of the differences in fluorescence generation for the specific incident wavelengths we can calculate the relative quantum yield as a function of excitation wavelength in the SIF regime. This calculation will be discussed in Section 5.4 for the low concentration SiPc/PMMA copolymer fiber.

5.6.0.6 DR1

Figure 5.63 shows the linear absorption coefficient for a Disperse Red 1 (DR1) doped PMMA core fiber as function of wavelength in the fluorescence band. The larger markers indicate that there is more uncertainty in the DR1 measurement in comparison to the SP1822 measurement. The uncertainty is larger for DR1 because the fluorescence signal was much smaller and there was a noticeable difference in the duplicate experiment. The difference in fluorescence signal between experiments indicates that the incident intensity is too high. The high intensity causes the molecules or their environment in the fiber to change, such as the dye breaking down or diffusing away from the illumination position. Future experiments on DR1 would definitely benefit from a shorter wavelength source to excite the fluorescence – Krypton lines should work well.

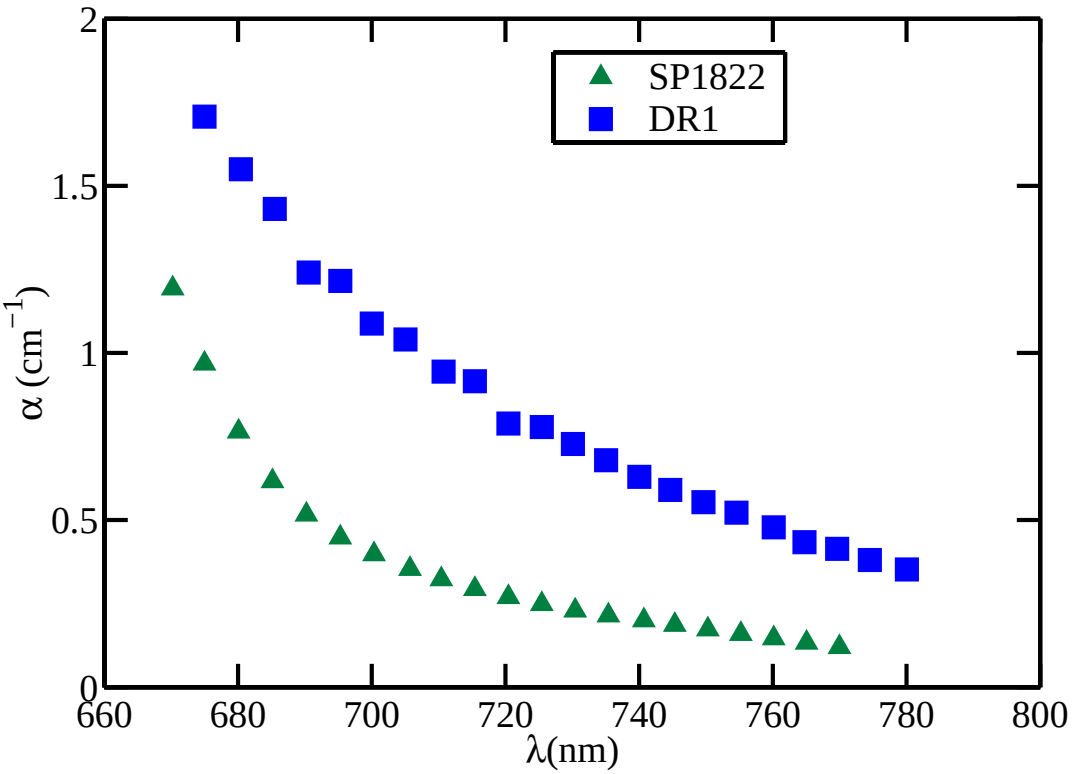

Fig. 5.63: Linear absorption coefficient using the point source model for DR1- (blue) and SP1822-doped (green) core fibers. (λ_{inc} = 633 nm).

As previously, discussed DR1/PMMA has a resonance absorption about 490 nm. Figure 5.63 indicates that there is significant absorption 200-300 nm from resonance when the DR1 number density is N= 1.5 $\times 10^{19}$ cm^{-3} and is much larger than the linear absorption seen in squaraine doped fibers for a similar distance from resonance. Because the linear absorption is so significant in the 680-780 nm range for a highly concentrated DR1 core fiber, nonlinear devices incorporating DR1 should be optimized for wavelengths longer than 800 nm.

5.6.0.7 SP1822

The green triangles in Figure 5.63 represent the linear absorption coefficient between 670-770 nm for a spiropyran-doped core fiber. The point source model was used to calculate $\alpha(\lambda)$ from the SIF data shown in Figure 5.17. Unfortunately, there was a limited amount

of the SP1822 dye so we were unable to measure the linear absorption near resonance from a bulk sample. However, Tamaoki and coworkers [4] showed that there is a resonance at about 340 nm when it is in the orange form and about 610 nm for its blue isomer. The linear absorbance in the 670 to 770 nm range as measured using SIF is most likely due to a small percentage of the dye being in the blue form because it so far from 340 nm. It should be noted that the SIF intensity was much larger for the SP1822 core fiber than the DR1 core fiber when illuminated with equal incident intensity at 633 nm. Therefore it would be an interesting future project to measure the fluorescence spectra and the linear absorption of both forms of SP1822 using the SIF method.

5.7 Linear Spectroscopy

This section is dedicated to the general problem of characterizing the response of one-photon excited states in guest-host systems. Since all the SIF data is collected at a longer wavelength than the resonant excited state, information about the transition frequency of the resonance state is needed before the SIF data can be analyzed. We therefore characterize the resonant excited state using the transmission from dye-doped preform slices. The higher lying states which make up the shoulder region could easily be modeled but they have no effect on the absorption in the SIF regime and thus are disregarded for this analysis. However, the response from the thin films discussed in Section 5.1.2, will be characterized for all distinguishable one-photon states. We extend the analysis beyond a two-level model for the thin films because the nonlinear response, from the QEA experiment, is affected by the higher lying states.

Three methods for determining the transition moment (μ_{gn}), transition frequency (ω_{gn}), homogeneous linewidth (Γ_{gn}), and inhomogeneous linewidth (γ_{gn}) will be used to characterize the dominant excited state for the dye doped preform slices. Two of which were developed in Section 5.6, and the third will be introduced shortly. The third method, where the absorbance is integrated, is not easily applied to molecules with more than one-excited state so we restrict our discussion of multiple excited states, in the dye-doped thin films, to the Lorentzian and inhomogeneous-broadening (IB) theories.

5.7.1 Preform Slices

Initially, we characterize the dominant excited state in PSQ and HSQ, TSQ, ISQ, and SiPc from bulk preform slice transmission spectroscopy data. From these results we will determine which model(s) can be applied to the characterization of SIF data. The results for dye-doped preform slices will be tabulated with Mathis' [7] results for PSQ/PMMA, HSQ/PMMA, TSQ/PMMA, and ISQ/PMMA thin films, and discussed in detail.

The assumption of two states (ground and dominant excited state) reduces the sum in the Lorentzian model (L) and the inhomogeneous broadening model (IB) of $\chi^{(1)}(-\omega;\omega)$ to one term (n=1) (see Section 5.6):

$$\chi_L^{(1)}(-\omega;\omega) = \frac{\mathrm{N\ f}(\omega)\phi}{\epsilon_o\hbar}|\mu_{1g}|^2\left[\frac{1}{\omega_{1g}-i\Gamma_{1g}-\omega}+\frac{1}{\omega_{1g}+i\Gamma_{1g}+\omega}\right], \tag{5.10}$$

and,

$$\chi_{IB}^{(1)}(-\omega;\omega) = \frac{i\sqrt{\pi}}{\gamma_{1g}}\frac{\mathrm{N\ f}(\omega)\phi}{\epsilon_o\hbar}|\mu_{1g}|^2\left[W\left(\frac{-\omega_{1g}+\omega+i\Gamma_{1g}}{\gamma_{1g}}\right)+W\left(\frac{-\omega_{1g}-\omega-i\Gamma_{1g}}{\gamma_{1g}}\right)\right], \tag{5.11}$$

respectively, where $W(z)$ is the complex error function [15]. The Lorentz form for the local field factor, $\mathrm{f}(\omega) = (n^2(\omega)+2)/3$, will be used, where $\mathrm{n}(\omega) \approx 1.49$. We also assume that the dye is randomly distributed in the polymer host so that the orientational average for 1-D molecules yields $\phi = 1/3$ [16] and for 2-D molecules yields $\phi = 2/3$ [17]. Note that the squaraines are approximated as 1-D molecules and SiPc is approximated as a 2-D molecule.

Using the Equation (2.116) in Section 2.6.1, we can write two relations for $\alpha(\lambda)$ in terms of $\chi^{(1)}$:

$$\alpha_L(\lambda) = \frac{\epsilon_o\,\omega}{c}\frac{\chi_{L_I}^{(1)}(-\omega;\omega)}{n_{\mathrm{polymer}}}, \tag{5.12}$$

and,

$$\alpha_{IB}(\lambda) = \frac{\epsilon_o\,\omega}{c}\frac{\chi_{IB_I}^{(1)}(-\omega;\omega)}{n_{\mathrm{polymer}}}, \tag{5.13}$$

where it is understood that the imaginary part of $\chi^{(1)}(-\omega;\omega)$ is due to the dye (The polymer is transparent throughout the visible and near IR).

5.7.1.1 HSQ, PSQ, TSQ

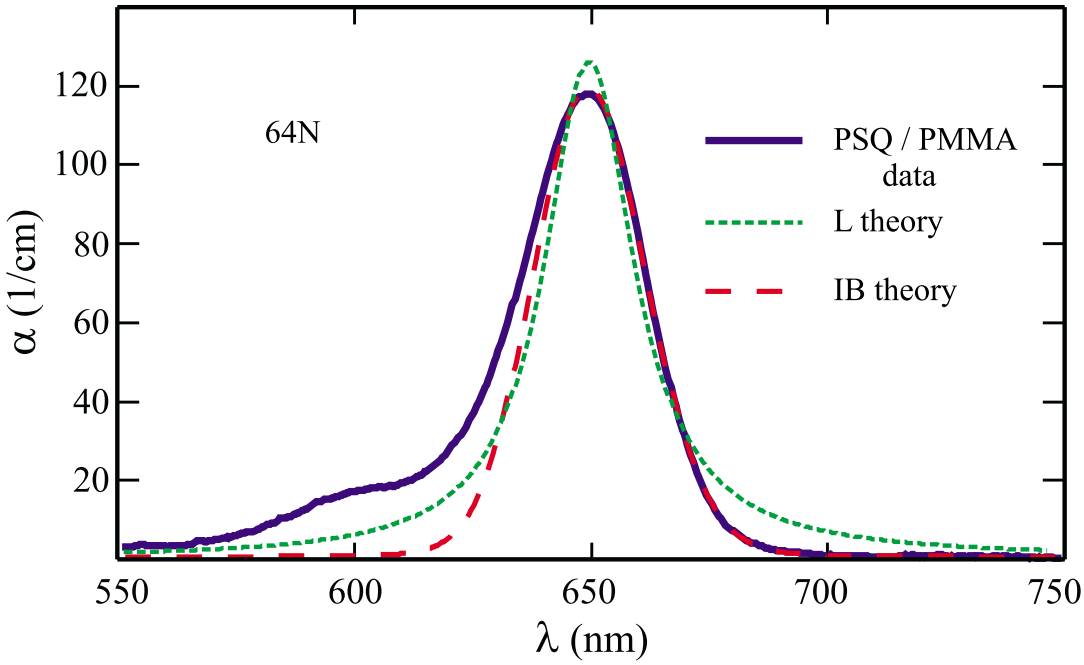

Fig. 5.64: Bulk PSQ/PMMA resonant absorption modeled as a Lorentzian (L) transition and an inhomogeneously-broadened (IB) transition (N = 1.5×10^{15} cm^{-3}).

Since $\alpha(\lambda)$ has been measured in transmission spectroscopy experiments, we can compare the data for various dye-doped preform slices to the predicted response from the inhomogeneous broadening (IB) and Lorentzian (L) models of $\chi^{(1)}(-\omega;\omega)$ by minimizing the least-squares difference. An example of this comparison is shown in Figure 5.64 for the 64N PSQ/PMMA preform slice, where N = 1.5×10^{15} cm^{-3}. The green short-dashed curve is a least-squares fit of $\alpha_L(\lambda)$ (Equation (5.12)) to the PSQ/PMMA data and the red long-dashed curve is the same fit using $\alpha_{IB}(\lambda)$ (Equation (5.13)) when $\phi = 1/3$. These fits are performed on the low energy side of the spectra to avoid the influence of the higher energy shoulder which is due to the vibronic structure of the dye molecule. Clearly, the theory that takes into account inhomogeneous broadening is much more effective at describing the dominant electronic transition in the PSQ/PMMA preform, even though the magnitudes of the transition moment are similar for both models (Table 5.1).

Results for the remainder of the PSQ preforms (see Figure 5.1), HSQ and TSQ bulk preform slices are similar to that of the PSQ/PMMA preform shown in Figure 5.64 and do not merit further discussion. However, the results for the ISQ/PMMA and SiPc/PMMA preforms merit additional consideration and will be discussed shortly.

Transition frequencies, ω_{1g}, in Table 5.1 correspond to the frequency at which $\alpha(\lambda)$ is a maximum for the bulk samples and the error is half the optical resolution of the Ocean Optics 2000 spectrometer. The transition moment (μ_{1g}), homogeneous linewidth (Γ_{1g}), and inhomogeneous linewidth (γ_{1g}) for the IB fit to the bulk sample data of PSQ, HSQ, and TSQ are averages over several different concentrations, all of which had number densities $< 0.1 \times 10^{18}$ cm^{-3}. Variation in the thickness of the bulk slices is the main contribution to the error for the bulk measurements. The Lorentzian (homogeneous) fit was only done for one PSQ sample because it does not accurately model the system in the long wavelength tail of the absorption band. A very accurate agreement in this region is necessary to predict the loss for core fibers. Approximate values for the Lorentzian theory are thus listed for comparison only.

According to Herzberg [18] or Dirk [19], the transition moments can also be calculated from the integral of the absorbance,

$$|\mu_{1g}| = \left[\frac{3hc}{8\pi^3 N}\left(\frac{\int \alpha(\nu)d\nu}{\nu_{1g}}\right)\right]^{1/2}, \tag{5.14}$$

where N is the number density in cm^{-3}, ν is the wave number in cm^{-1}, $\alpha(\nu)$ is the linear absorption coefficient in cm^{-1}, and ν_{1g} is the wave number corresponding to the maximum absorption for the ground to first excited state electronic transition. The speed of light, c, and Plank's constant, h, are in cgs units.

If the transition has a Gaussian-shaped peak instead of Lorentzian-shaped (due to Doppler broadening, for example [19]), the integrated absorption can also be used to find the width of the transition,

$$\Gamma_G = \frac{\int \alpha(\nu)d\nu}{\pi^{1/2}\alpha_{max}}, \tag{5.15}$$

where α_{max} is the maximum value of $\alpha(\nu)$. The value of Γ_G obtained from Equation (5.15) is tabulated here as γ_{1g} because it can be described as inhomogeneous broadening when the homogeneous broadening factor Γ_{1g} is negligible. To avoid influence from the

Table 5.1: Excited state fit parameters for HSQ/PMMA, PSQ/PMMA, and TSQ/PMMA preform slices with comparison to thin film measurements. IB – inhomogeneous broadening, L – Lorentzian, G – Gaussian, and M – Mathis.

Expt.	Anal. *	Dye	$\hbar\omega_{1g}(\lambda)$ eV (nm)	$\hbar\Gamma_{1g}$ meV	$\hbar\gamma_{1g}$ meV	μ_{1g} D	N 10^{18} cm^{-3}
BULK	IB	PSQ	1.909(649.5±1.1)	1±1	51±4	12.9±1.2	< 0.1
BULK	L	PSQ	1.909(649.5±1.1)	∼34	–	∼14	< 0.1
BULK	G	PSQ	1.909(649.5±1.1)	–	51±4	12.9±1.6	<0.1
SF	IB	PSQ	1.909(649.5±1.1)	1±1	54±1	11.9±0.7	1.09±0.2
TF	M	PSQ	1.909(649.5±1.5)	47.2±4.0	–	11.58	11.9
BULK	IB	HSQ	1.908(650±1.1)	1±1	48±2	11.6±0.7	<0.1
BULK	G	HSQ	1.908(650±1.1)	–	50±3	11.8±0.6	<0.1
TF	M	HSQ	1.907(650.1±1.5)	50.0± 4.0	–	11.58	13.9
BULK	IB	TSQ	1.91(649±1.1)	1±1	49±3	13.1±1	≤0.1
BULK	G	TSQ	1.91(649±1.1)	–	50±3	13.4±0.9	<0.1
TF	M	TSQ	1.921(645.1±1.5)	53.0± 4.0	–	11.52	6.5

* - The Thin Film (TF) measurements were conducted by Mathis [7].

high energy shoulder in the data, the integration was performed over the low energy half of the spectrum and doubled as described by Dirk [19].

The results from Equations (5.14) and (5.15), tabulated as analysis G, agree with the results from the IB model, and it is clear that the inhomogeneous broadening in PSQ-doped polymers can be described accurately by either method. The values for the transition moments, obtained using the IB theory, also compare favorably with the values found by Mathis [7] for PSQ/PMMA, HSQ/PMMA, and TSQ/PMMA thin films, which were characterized using Equation (5.14) and a physical measurement of the width of the absorption peak at half the maximum (Tabulated as M for Mathis).

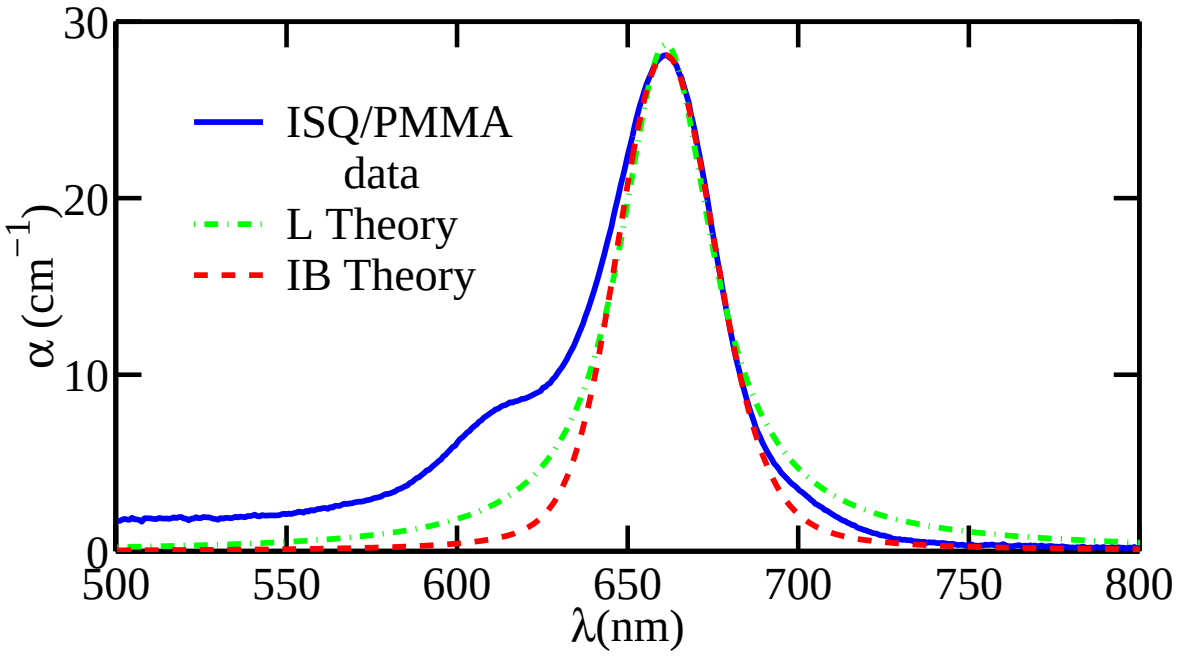

Fig. 5.65: Bulk ISQ/PMMA resonant absorption modeled as a Lorentzian (L) transition and an inhomogeneously-broadened (IB) transition (N= 1.4 $\times 10^{17}$ cm^{-3}).

5.7.1.2 ISQ

Unlike the three aforementioned squaraine-doped preforms, ISQ/PMMA bulk preform samples do not fit either theory very well in the two-level limit. Figure 5.65 shows the absorption spectrum for the dye-doped preform slice, labeled 4N in Figure 5.2, compared to the Lorentzian (L) and inhomogeneous-broadening (IB) theories, in the two-level limit, after the least-squares difference between the data and theory has been minimized.

The Lorentzian model is too broad in the tail of the absorption and the IB model is too slight in the tail of the absorption. This suggests that there is a small contribution from a low lying excited state which may be caused by degradation of the sample. The transition moment, μ_{g1}, is significantly smaller than measurements in thin films and liquid which also suggests that the dye has degraded over time. It should be noted that this dye was approximately 5 years old when the preform sample was polymerized. Based on Mathis' value of μ_{g1} =11.5 D, the measured transition moment of 5.5 D suggests that approximately 3/4 of the dye molecules have decomposed.

Other samples were calculated to have larger transition moments but not equivalent to the thin film or liquid results. We have tabulated this result because the preform is related to the ISQ/PMMA core fibers studied in Sections 5.2.3.4 and 5.6.0.4.

Table 5.2: Excited state fit parameters for ISQ/PMMA preform slices with comparison to thin film (TF) and liquid ($CHCl_3$) measurements. IB – inhomogeneous broadening, L – Lorentzian, G – Gaussian, and M – Mathis.

Expt.	Anal.	Dye	$\hbar\omega_{1g}(\lambda)$ eV (nm)	$\hbar\Gamma_{1g}$ meV	$\hbar\gamma_{1g}$ meV	μ_{1g} D	N 10^{18} cm^{-3}	Ref.
BULK	IB	ISQ	1.875(661±1)	~ 15	~ 45	~ 5.5	0.14	*
BULK	L	ISQ	1.875(661±1)	~ 43	–	~ 6.3	0.14	*
TF	M	ISQ	1.880(657±1)	45.0±5.0	–	11.50	19.4	[7]
$CHCl_3$	G	ISQ	1.896±0.004	45±3	–	10.3±1.4		[20]

* - present work

As we saw in Section 5.1.1.2, the absorption spectra is very sensitive to the dye age and processing conditions. Thus the values listed in Table 5.2 will be labeled as approximations and are only valid for the sample measured and possibly relatives of the sample (i.e. preforms made from the same solution). In Section 5.7.3.2, we will determine the contribution from the dominant excited state to the linear absorption spectrum in the 720-860 nm range for ISQ/PMMA core fibers. This will be very difficult because neither the Lorentzian theory nor the IB theory model the absorption very accurately on the long wavelength side of the dominant excited state. However, it is necessary to determine the strength of the J-aggregate state for the highest concentration ISQ/PMMA fibers.

5.7.1.3 SiPc

Squaraine-doped PMMA is well studied so we could compare our results with the literature values of the excited state parameters. Unfortunately, there is no such body of literature on SiPc/PMMA copolymer. There are a wealth of absorption spectra available for phthalocyanines but nobody, to our knowledge, has analyzed the data in terms of

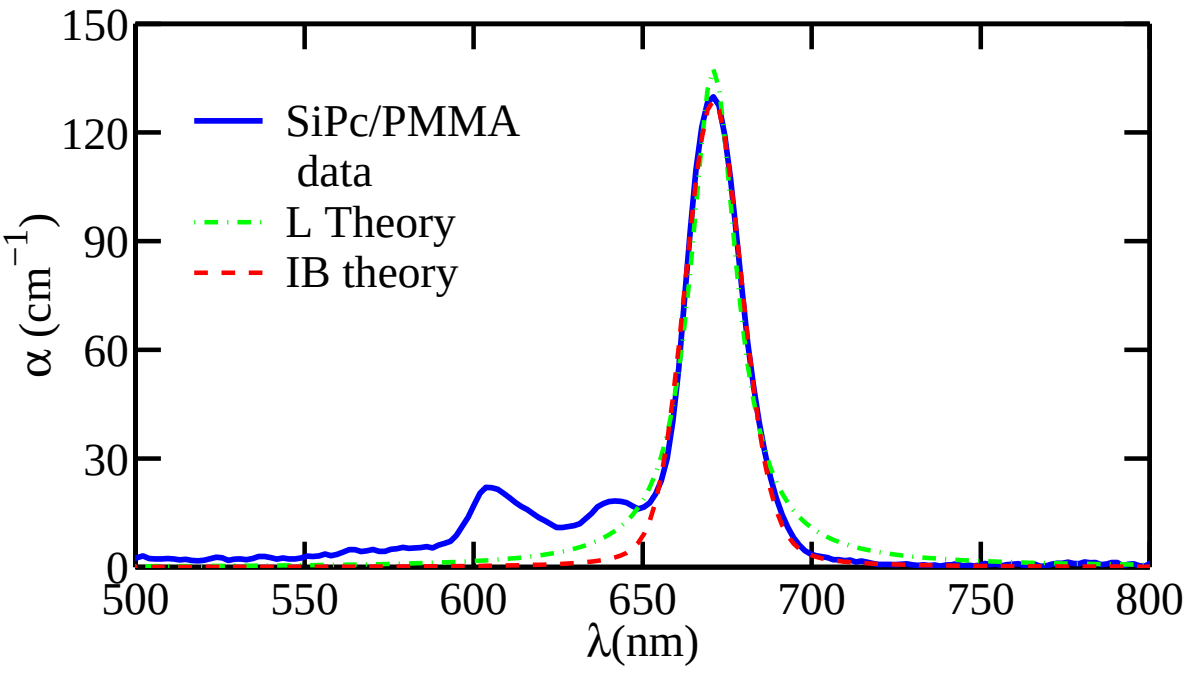

Fig. 5.66: Bulk SiPc/PMMA resonant absorption modeled as a Lorentzian (L) transition and an inhomogeneously-broadened (IB) transition (N= 1.3 $\times 10^{17}$ cm^{-3}).

Lorentzian or inhomogeneously-broadened (IB) transitions. We use the Lorentzian local field factor model and the isotropic orientational average of a 2-D molecule, which yields $\phi = 2/3$ in Equations (5.12) and (5.13).

Figure 5.66 shows the absorption spectra for the SiPc/PMMA copolymer preform (see Section 5.1.1.3), with a least-squares comparison to the Lorentzian and inhomogeneous-broadening models of the dominant excited state. The values for the excited state parameters will be tabulated in Section 5.7.2.2 along with the results for SiPc/PMMA (guest/host) thin films.

As in the discussion of the dominant excited state of the squaraine molecules in PMMA preforms, the IB model characterizes the dominant electronic transition in SiPc/PMMA much better than the Lorentzian model. These results suggest that it should be necessary to model the third-order susceptibilities using a third-order version of the IB theory, which motivated the lengthy derivations in Section 2.4.

5.7.2 Thin Films

In this section, we extend the Lorentzian and inhomogeneous broadening models to four levels to characterize the manifold of one-photon excited state in the visible region for ISQ/PMMA and SiPc/PMMA thin films. The results will be used to explain the quadratic electroabsorption (QEA) response in Section 5.8

The Lorentzian and IB theories for the linear optical susceptibility in the four-level limit are (see Section 5.6):

$$\chi^{(1)}_{L_4}(-\omega;\omega) = \frac{\mathrm{N\ f}(\omega)\phi}{\epsilon_o\hbar}\sum_{n=1,3,5}|\mu_{gn}|^2\left[\frac{1}{\omega_{gn}-i\Gamma_{gn}-\omega}+\frac{1}{\omega_{gn}+i\Gamma_{gn}+\omega}\right], \tag{5.16}$$

and,

$$\begin{aligned}\chi^{(1)}_{IB_4}(-\omega;\omega) &= i\sqrt{\pi}\frac{\mathrm{N\ f}(\omega)\phi}{\epsilon_o\hbar}\sum_{n=1,3,5}\frac{|\mu_{gn}|^2}{\gamma_{gn}}\times \\ &\left[W\left(\frac{-\omega_{gn}+\omega+i\Gamma_{gn}}{\gamma_{gn}}\right)]+W\left(\frac{-\omega_{gn}-\omega-i\Gamma_{gn}}{\gamma_{gn}}\right)\right],\end{aligned} \tag{5.17}$$

respectively. We have used odd indices to remind us that the one-photon states must have opposite parity to the ground state for a centrosymmetric system, and to avoid confusion between two-photon states that may contribute to the QEA response – we label two-photon states with even indices in future discussions.

5.7.2.1 ISQ

Because the high lying shoulder in the ISQ/PMMA absorption spectrum is not isolated from the resonant absorption, it takes more than one excited state to describe its features. Thus we have broken the discussion into two parts. The first part will describe how to build a 4-level model to characterize the manifold of one-photon states responsible for the linear absorption using the Lorentzian theory and the second part will do the same for the IB theory. At the end of the discussion we tabulate the parameters that describe the three one-photon states for each theory.

Figure 5.67 shows the contributions to a four-level Lorentzian model of the ISQ/PMMA absorption spectrum. The dotted curves represent the individual excited states as they

would appear in a two-level model, and the dashed curves represent the three-level models for the three linear combinations of two excited states. The sum of all three excited states (4-level model) is shown as a solid blue curve, and the ISQ/PMMA data is shown as a solid red curve.

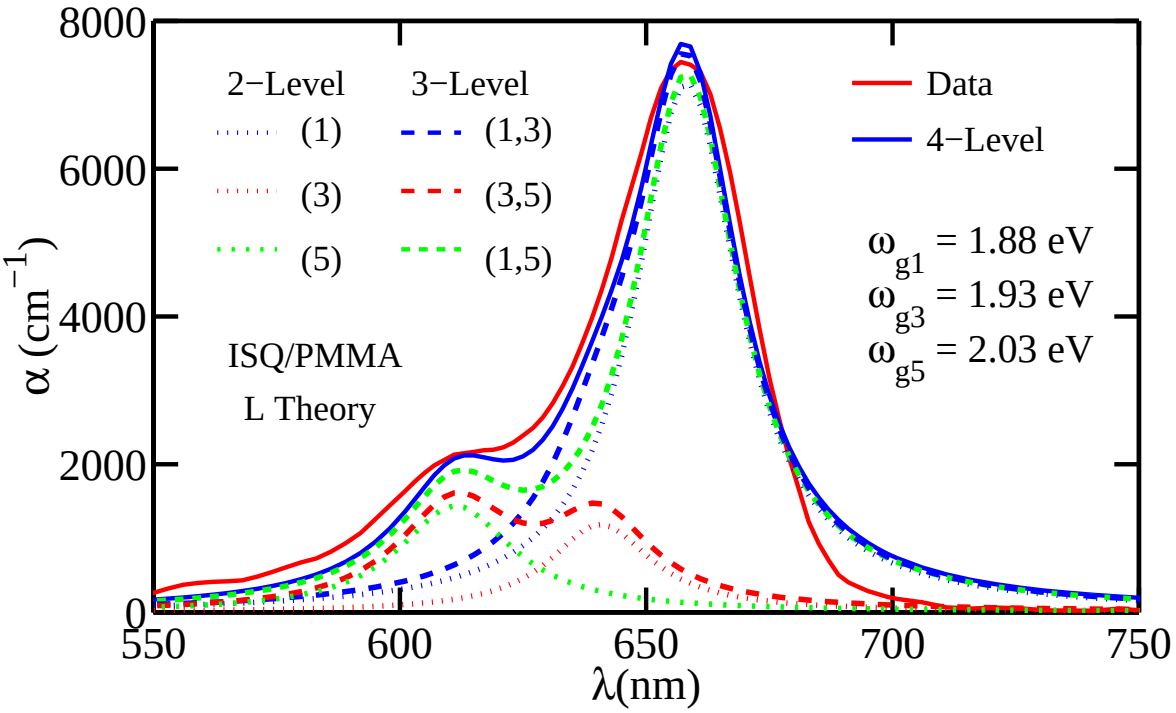

Fig. 5.67: Thin film ISQ/PMMA resonant absorption compared with Lorentzian (L) transitions up to a 4-Level model (N = 19.4 $\times 10^{18}$ cm^{-3}).

Similar to the bulk preform analysis, the least-squares fit is initially performed in the two-level limit for the resonant excited state. Once the resonant state has been satisfactorily characterized, a third-level is added. We added the state located at 2.04 eV before the state at 1.96 eV because we could match the high energy side of the 2.04 eV state with the high energy side of absorption shoulder. Once we are satisfied with the fit on both extremes of the absorption spectrum, we added the third excited state to fill the gap in the middle. For our purposes we fixed the state halfway between 1.88 eV and 2.04 eV, but it could be located anywhere in between the first two excited states. The final step in the fitting procedure minimizes the difference between the data and the

4-level Lorentzian theory by allowing all three transition moments.

From Figure 5.67 it is clear that the Lorentzian theory does not predict the long wavelength tail of the absorption. In the shoulder region the two additional states appear to be too "pointy" in comparison to the data. Thus there may be more than two excited states that contribute to the shoulder region. Before adding another level to our model we investigate how well the IB theory characterizes the ISQ/PMMA absorption spectrum.

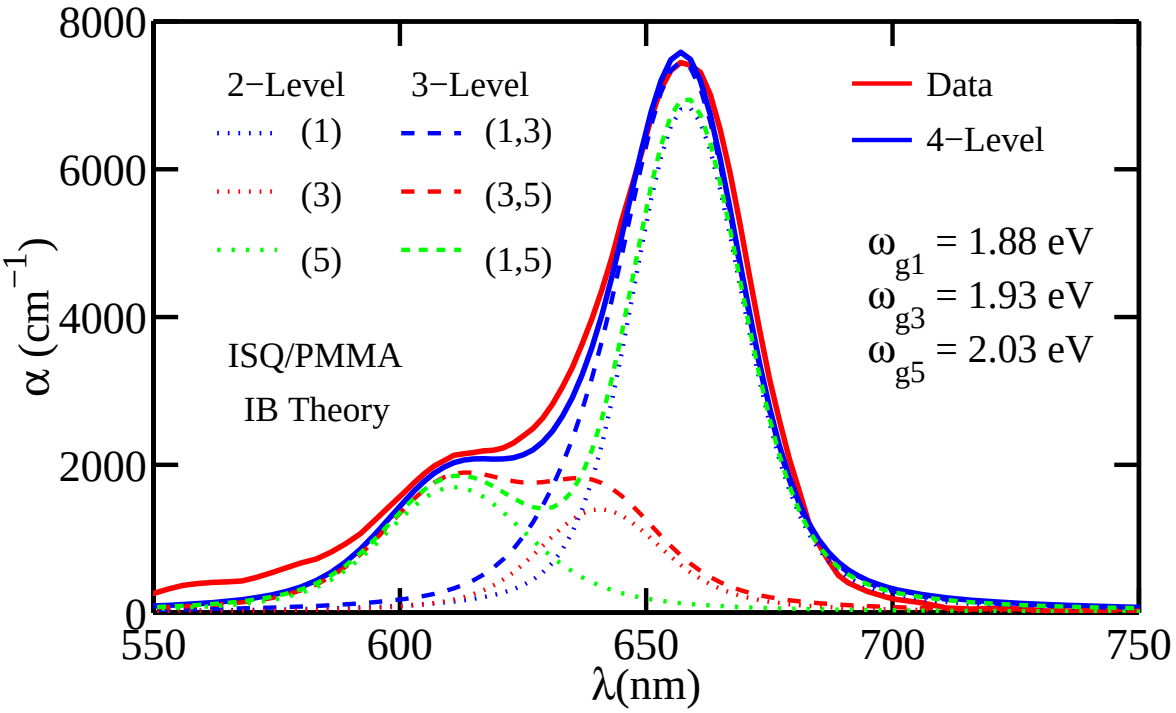

Fig. 5.68: Thin film ISQ/PMMA resonant absorption compared with inhomogeneously-broadened (IB) transitions up to a 4-Level model (N = 19.4 $\times 10^{18}$ cm^{-3}).

Figure 5.68 shows all the contributions to a four-level IB model of the ISQ/PMMA absorption spectrum. Three two-level models – the individual excited states – are represented by the dotted curves, and three three-level models are represented by the dashed curves – the three linear combinations of two excited states. The ISQ/PMMA linear absorption data is shown as a solid red curve, and the sum of all three excited states (4-level model) is shown as a solid blue curve.

The routine for determining the best fit 4-level IB theory is the same as was described

for the 4-level Lorentzian theory. Therefore we refer the reader back to the beginning of this section.

As in the core preform results, the IB theory characterizes the long wavelength tail of the absorption better than the Lorentzian theory. The IB theory also does a better job of characterizing the majority of the high lying shoulder. However, at wavelengths shorter than 600 nm the Lorentzian theory is better because of the long tail.

Because the IB theory does not characterize the ISQ/PMMA absorption well for wavelengths shorter than 590 nm, there is most likely an additional one or two small higher lying excited states in the manifold. However, we neglect them in future analysis because of their small oscillator strengths.

Table 5.3: Excited state fit parameters for ISQ/PMMA thin films (TF) with comparison to ISQ/PMMA preform slice measurements (BULK). IB – inhomogeneous broadening, L – Lorentzian, and M – Mathis.

Expt.	Anal.	Dye	$\hbar\omega_{1g}(\lambda)$ eV (nm)	$\hbar\Gamma_{1g}$ meV	$\hbar\gamma_{1g}$ meV	μ_{1g} D	N 10^{18} cm^{-3}	Ref.
BULK	IB	ISQ	1.875(661±1)	$\sim$ 15	$\sim$ 45	$\sim$ 5.5	0.14	*
BULK	L	ISQ	1.875(661±1)	$\sim$ 43	–	$\sim$ 6.3	0.14	*
TF	IB	ISQ	1.885(657±2)	12.0±5.0	38± 4	6.7±1.4	19.4	*
TF	IB	ISQ	1.935(641±6)	20.0±7.0	40± 4	3.3±0.7	19.4	*
TF	IB	ISQ	2.03(608±3)	28.0±8.0	50± 4	4.0±0.7	19.4	*
TF	L	ISQ	1.885(657±2)	37.0±5.0	–	7.75±1.4	19.4	*
TF	L	ISQ	1.935(641±6)	38.0±6.0	–	3.1±0.7	19.4	*
TF	L	ISQ	2.03(610±3)	47.0±6.0	–	3.7±0.7	19.4	*
TF	M	ISQ	1.880(657±1)	45.0±5.0	–	11.50	19.4	[7]

* - present work

Table 5.3 shows all the parameters which characterize the three one-photon states used to model the ISQ/PMMA linear absorption. It is interesting to note that the homogeneous linewidth is smaller for the thin film samples in comparison to the bulk sample.

This suggests that the polymerization process creates a slightly more inhomogeneous material than the spin coating technique. The homogeneous linewidths for ISQ/PMMA are also broader than the homogeneous linewidths for HSQ/PMMA, PSQ/PMMA, and TSQ/PMMA, which could be caused by the cis-trans isomers of ISQ. It is also interesting to note that the inhomogeneous linewidth for the resonant state for the IB theory and the Lorentzian linewidth for the Lorentzian theory are smaller than those found by Mathis for similar ISQ/PMMA thin films.

5.7.2.2 SiPc

To characterize the linear absorption spectrum for SiPc/PMMA thin films, we follow the procedure outlined for ISQ/PMMA thin films with a slight modification. Because the excited states in the SiPc/PMMA system are more well defined than in the ISQ/PMMA system, the data is much easier to fit. The three transition frequencies can be determined from the three local maxima, then each state is fit in a two-level model. Once there is satisfactory agreement for each state individually, the three excites states are added together to build a 4-level model. A final minimization is done by varying all three transition moments until the least-squares difference between the data and theory is minimized.

Because the excited states for SiPc/PMMA are well defined, we do not describe them individually as we did with ISQ/PMMA. This allows us to discuss the Lorentzian and IB theories in the same figure. Figure 5.69 compares the absorption spectra for a SiPc/PMMA (guest/host) thin film to Lorentzian (L) and a inhomogeneous-broadening (IB) four-level models for the manifold of one-photon excited states. Again it is clear, that the IB model characterizes the dominant excited state much better than the Lorentzian theory. However, it is a toss up when it comes to the high lying states.

Since the IB model describes the excited state manifold very well except in the 610-630 nm, it could be argued that there is a 4^{th} excited state located near 613 nm. However, the difference is quite small so it will be disregarded for the remainder of the analysis.

Table 5.4 combines the SiPc/PMMA preform and thin film results. The results from the IB theory for the dominant excited state tell us the high concentration thin film

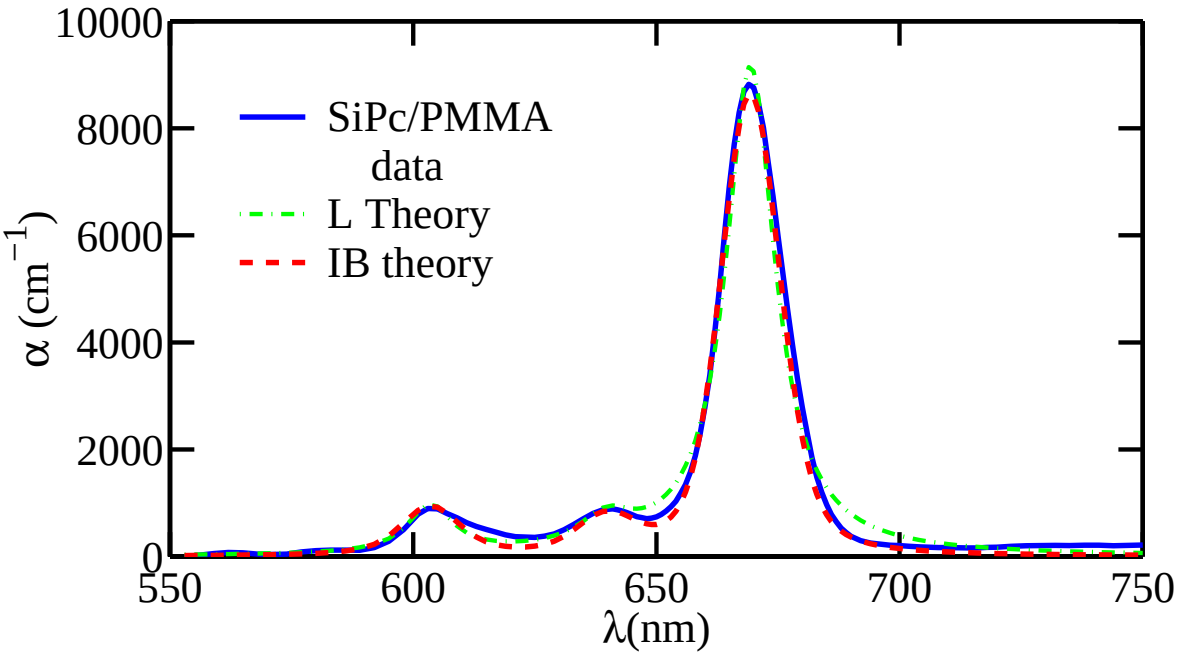

Fig. 5.69: Thin film SiPc/PMMA resonant absorption modeled as Lorentzian (L) transitions and inhomogeneously-broadened (IB) transitions (N = 5.7 $\times 10^{18}$ cm^{-3}).

and low concentration perform slice have to the same transition moment and homogeneous linewidth, within experimental uncertainty. As we saw in the ISQ/PMMA results, the resonant excited state for the preform is characterized to have a larger inhomogeneous linewidth, γ_{g1} than the resonant excited state of the thin film. This suggests that the polymerization process creates a more inhomogeneous material than the thin film preparation.

The Lorentzian theory predicts the same, within experimental uncertainty, transition moment for the preform slice and the thin film, but it predicts a slightly smaller homogeneous linewidth for the thin film. Unfortunately, there is not a clear interpretation of this result because the homogeneous linewidth should be characteristic of the dye not the system.

In Section 5.8, the parameters listed in Tables 5.3 and 5.4 for ISQ/PMMA and SiPc/PMMA thin films, respectively, will be used to help quantify their QEA response. Before moving on to the nonlinear response, we finish the discussion of the linear re-

Table 5.4: Excited state fit parameters for a 1 wt. % SiPc/PMMA thin film (TF) with comparison to SiPc/PMMA copolymer preform (BULK). IB – inhomogeneous broadening, and L – Lorentzian.

Expt.	Anal.	Dye	$\hbar\omega_{1g}(\lambda)$ eV (nm)	$\hbar\Gamma_{1g}$ meV	$\hbar\gamma_{1g}$ meV	μ_{1g} D	N 10^{18} cm^{-3}	Ref.
BULK	IB	SiPc	1.85(670±1)	7 ± 3	28 ± 3	6.8 ± 0.7	0.13	*
BULK	L	SiPc	1.85(670±1)	23 ± 3	–	7.3 ± 0.8	0.13	*
TF	IB	SiPc	1.85(670±1)	8 ± 2	19 ± 3	7.2 ± 1.5	5.7	*
TF	IB	SiPc	1.94(640±2)	10 ± 4	20 ± 3	2.1 ± 1	–	*
TF	IB	SiPc	2.05(605±2)	12 ± 4	20 ± 3	2.4 ± 1	–	*
TF	L	SiPc	1.85(670±1)	17 ± 2	–	7.7 ± 1.5	5.7	*
TF	L	SiPc	1.94(640±2)	20 ± 3	–	2.0± 1	–	*
TF	L	SiPc	2.05(605±2)	19 ± 3	–	2.4± 1	–	*

* - present work

sponse. At this point we have characterized the absorption spectra for bulk perform slices and thin films by minimizing the least-squares difference between the theoretical and experimental absorption coefficient. In the next section we characterize the absorption for core fibers in terms of the dominant excited state and possibly additional low lying states.

5.7.3 Core Fibers

As previously mentioned, the preform slices measured are 1 to 2 orders of magnitude less concentrated than the majority of the dye-doped fibers. At the higher concentrations, the preform slice is too optically dense for a simple transmission spectrum to be obtained. Without this type of measurement, the integral in Equation (5.14) cannot be evaluated, and the IB theory and Lorentzian theories are the most straight forward methods for determining the parameters, which characterize the dominant excited state in dye-doped core fibers. However, the Lorentzian theory did not characterize the longer wavelength tail of the dominant excited state very well, so the analysis of the core fibers will be

restricted to the IB theory for the linear susceptibility (see Equation (5.17)).

To determine the excited state parameters for our dye-doped fibers, a least-squares fit to the SIF data (using the IB model) is performed on the spectrum at one position in the fiber based on the measured spectrum at another position. The SIF spectrum generated at the position nearest the front end of the fiber is designated, $F_o(\lambda)$, and the remaining fluorescence at the second position in the fiber is designated $F_1(\lambda)$. Using the plane wave model, the function that relates $F_1(\lambda)$ to $F_o(\lambda)$ is,

$$F_1(\lambda) = F_o(\lambda)e^{-\alpha_{IB}(\lambda)\Delta z} \tag{5.18}$$

where $\Delta z = z_1 - z_o$ is the distance between the two positions in the fiber, and $\alpha_{IB}(\lambda)$ is given by Equation (5.13) for a two-level model. In the least-squares fit, the mean transition frequency, which was determined in the analysis of the bulk samples, is kept constant, Γ_{1g} is held fixed, and γ_{1g} and μ_{1g} are the floating parameters. The uncertainty in Γ_{1g}, γ_{1g}, and μ_{1g} are determined by the range of Γ_{1g} that converges to a good fit.

The excited state parameters are determined for HSQ/PMMA, PSQ/PMMA, and TSQ/PMMA core fibers using a 2-level model for the linear susceptibility (see Equation (5.11)). The ISQ/PMMA and SiPc/PMMA results are more complicated so we use up to a 4-level model, Equation (5.17), for the linear susceptibility to characterize the linear absorption.

5.7.3.1 HSQ, PSQ, and TSQ

Figure 5.70 compares the SIF data to the IB theory at various propagation distances for a PSQ/PMMA fiber. The least-squares fit of Equation (5.18) for this specific fiber was performed using the first frame as $F_o(\lambda)$, the last frame as $F_1(\lambda)$, and $\Delta z \approx 1.8$ cm. Clearly the experiment and theory agree well at each propagation distance even though the excited state parameters are determined using only the first and last frame – making a more sophisticated fitting procedure unnecessary.

Figure 5.71 highlights the final frame of Figure 5.70 and reveals that the SIF spectrum calculated using IB theory for PSQ/PMMA is slightly larger than the data in the 780-820 nm range. Remembering that (see Section 5.2.1) we saw an extra absorbance for

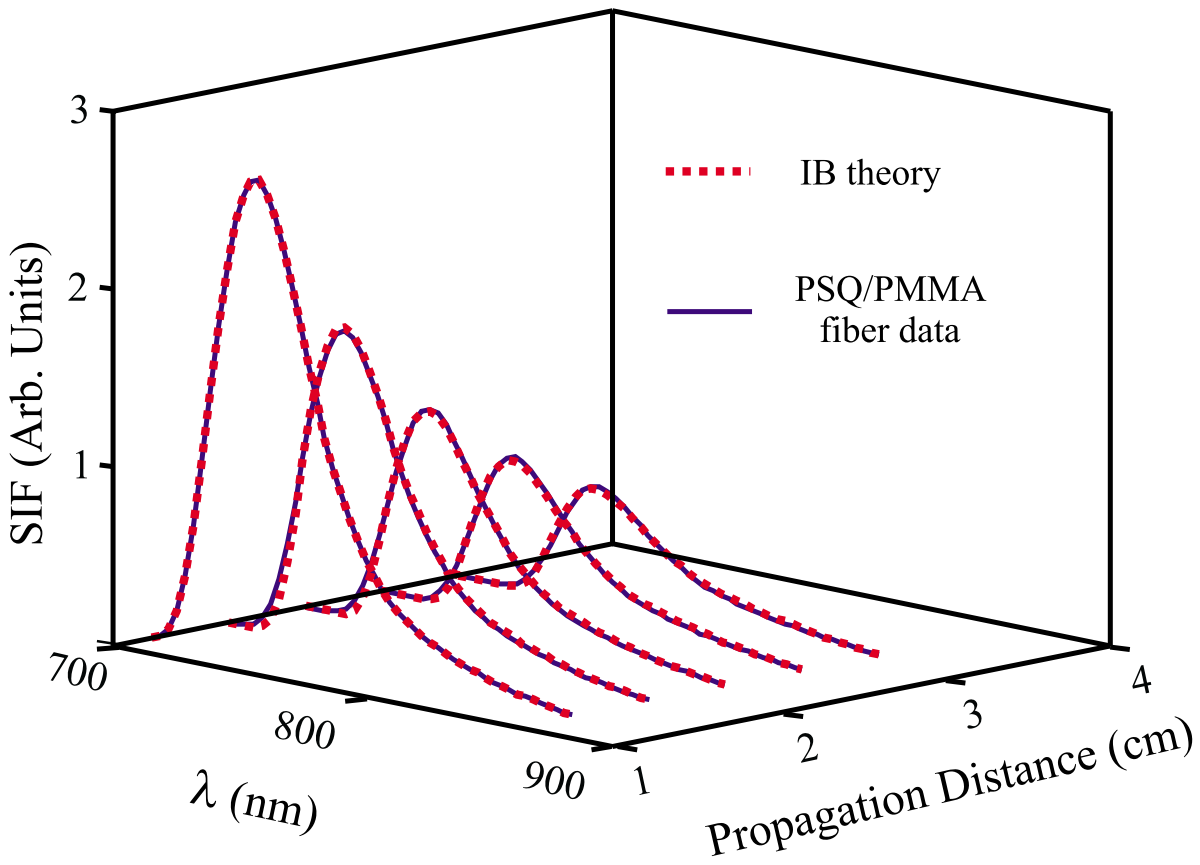

Fig. 5.70: SIF measurement as a function of propagation distance (—) and theory for inhomogeneous broadening (- -).

PSQ and HSQ in the same wavelength range, the slight difference in absorption confirms that the two-state model cannot fully describe the HSQ and PSQ molecules. This extra absorption is reminiscent of the J-aggregate absorption found in studies of squaraine Langmuir-Blodgett thin films [11, 12, 13, 14]. The absorption peak for the face-to-face squaraine J-aggregates are between 750-800 nm.

Similar calculations were performed for all the PSQ, HSQ, and TSQ fibers. The average results for each concentration are recorded in Table 5.5. It should be noted that the analysis for the deuterated HSQ fibers is less accurate than the non-deuterated fibers because a smaller portion of the data set was used to fit the data. This was done to avoid the 780-820 nm range, which happened to fall in the middle of the longer wavelength side of the fluorescence band at longer propagation distances.

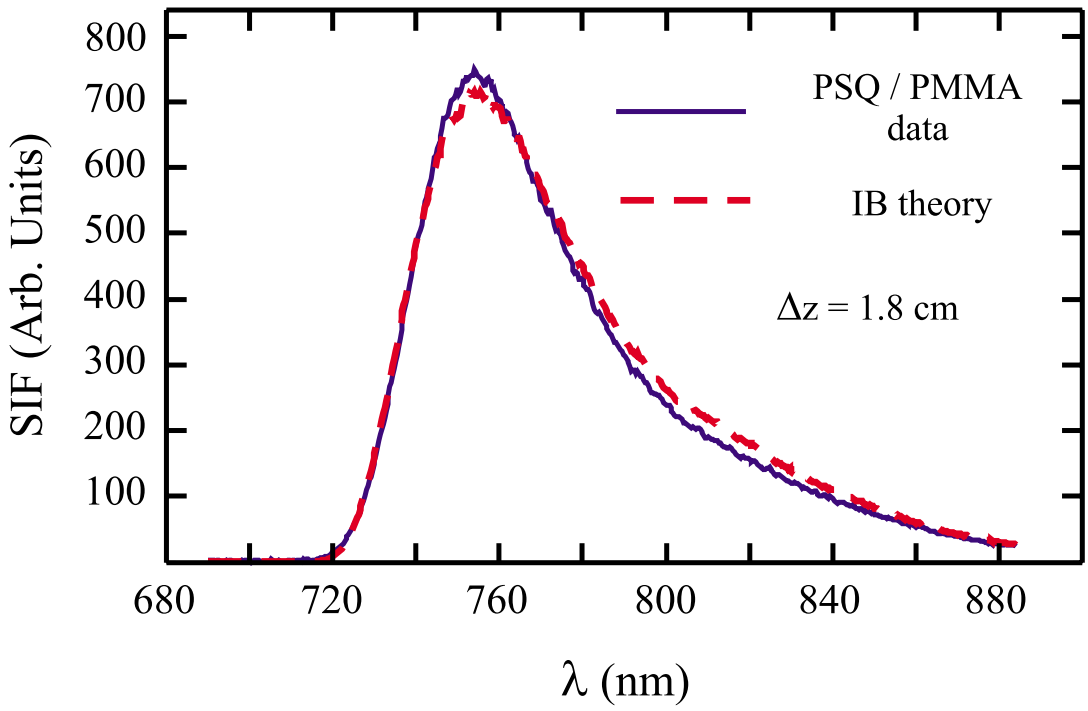

Fig. 5.71: SIF spectra for a PSQ/PMMA core fiber (—) and theory for inhomogeneous broadening (- -).

The transition moments for the all three squaraine-doped fibers are equivalent within experimental uncertainty to the dye-doped preform slices and thin films. However, the inhomogeneous broadening linewidths, γ_{1g}, for the high concentration ($N \geq 1 \times 10^{18}$ cm^{-3}) dye-doped fibers are all larger than those for the dye-doped preforms. This suggests that there is more inhomogeneous-broadening at the higher concentration. Unfortunately, the approximation that the fluorescence propagates as a plane wave also leads to systematically larger values of γ_{1g}. Therefore a better description of the fluorescence source is necessary to determine the precise amount of inhomogeneous-broadening cause by the increased concentration.

From the linear absorption results for bulk preform slices, thin films, and core fibers, it is apparent that the HSQ-, PSQ-, and TSQ-doped systems behave linearly as the concentration is increased to its respective saturation value. We have shown that two methods can be used to determine the characterize the linear absorption properties in highly concentrated core fibers. The method where $\alpha(\lambda)$ is calculated at each wavelength

Table 5.5: Excited state fit parameters for HSQ-, PSQ-, and TSQ-doped core fibers measured in the SIF experiment and analyzed using the inhomogeneous-broadening (IB) model.

Dye	Polymer	$\hbar\omega_{1g}(\lambda)$ eV (nm)	$\hbar\Gamma_{1g}$ meV	$\hbar\gamma_{1g}$ meV	μ_{1g} D	N 10^{18} cm^{-3}
PSQ	PMMA	1.909(649.5±1.1)	1.7±0.5	75±4	11.2±2.1	1.09±0.2
PSQ	PMMA	1.909(649.5±1.1)	1.4±0.4	94±2	10.1±2.1	3.96±0.3
PSQ	P(MMA-d8)	1.909(649.5±1.1)	1.9±0.5	78±2	12.1±2.0	∼1.09
HSQ	PMMA	1.908(650±1.1)	1.7±0.5	70±4	10.7±2.0	1.27±0.18
HSQ	P(MMA-d8)	1.908(650±1.1)	1.7±0.5	66±3	12.8±2.4	∼1.27
TSQ	PMMA	1.91(649±1.1)	2.3±0.5	47±5	14.8±2.4	0.016±0.002
TSQ	PMMA	1.91(649±1.1)	2.2±0.5	53±3	11.8±1.9	0.064±0.008
TSQ	PMMA	1.91(649±1.1)	2.0±0.5	59±3	11.3±1.7	0.13±0.01
TSQ	PMMA	1.91(649±1.1)	1.5±0.4	95±2	9.8±2.1	3.27±0.3

is much more time consuming than the excited state analysis but should be used if a precise measurement of the linear absorption coefficient is needed. If a general description of the linear absorption spectrum is desired, the excited state analysis can quickly be performed if the resonant transition frequency is known ahead of time.

There does appear to be a small aggregate state in the 780 nm - 820 nm range in the high concentration fibers but the oscillator strength is so small that it can be disregarded for all practical purposes. This is not the case for ISQ/PMMA fibers. The following section will use the aforementioned excited state analysis to determine the strength of the aggregate state in comparison to the resonant excited state.

5.7.3.2 ISQ

ISQ/PMMA results from Section 5.1.1.2 showed that there was an increase in the absorption cross-section as the ISQ concentration was increased. To characterize this increase in terms of a excited state parameters, we need to extend the IB theory to three levels

for the higher concentration fibers as follows,

$$\chi^{(1)}_{IB_3}(-\omega;\omega) = i\sqrt{\pi}\frac{\mathrm{N\ f}(\omega)\phi}{\epsilon_o\hbar}\sum_{n=1,3'}\frac{|\mu_{gn}|^2}{\gamma_{gn}}\times \left[W\left(\frac{-\omega_{gn}+\omega+i\Gamma_{gn}}{\gamma_{gn}}\right)+W\left(\frac{-\omega_{gn}-\omega-i\Gamma_{gn}}{\gamma_{gn}}\right)\right]. \quad (5.19)$$

Thus the linear absorption coefficient is related to the three-level IB model of the linear susceptibility as,

$$\alpha_{IB_3}(\lambda) = \frac{\epsilon_o\,\omega}{c}\frac{\chi^{(1)}_{IB_{3I}}(-\omega;\omega)}{n_{\mathrm{polymer}}}. \quad (5.20)$$

Since we do not know how many molecules are acting as the aggregates, we define the quantity $\mathrm{S}_{gn} = \mathrm{N}|\mu_{gn}|^2$ (DeBye/m^3) to help us describe the amount of aggregation. We can think of S_{gn} as the strength of the excited state.

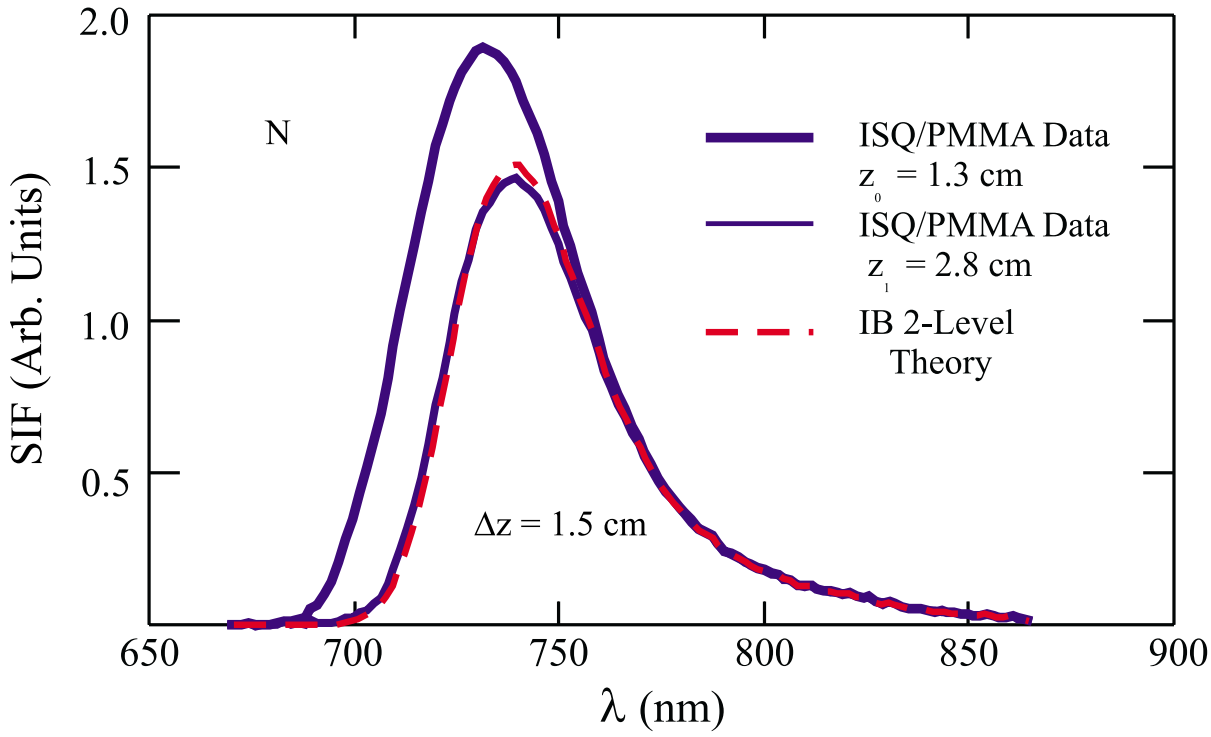

Fig. 5.72: Side-illumination fluorescence for an ISQ/PMMA fiber (N = 1.4 $\times 10^{17}$ cm^{-3}) for z_0 = 1.3 cm and z_1 = 2.8 cm and a comparison with the two-level IB model for the self-absorption where the z_0 = 1.3 cm SIF data is used as the initial condition.

5.7.3.2.1 Two-Level Model When there is no apparent aggregation as determined from the SIF spectra (see Figure 5.72), we use Equation (5.11) to model the linear absorption of the SIF spectrum. In other words, we model the dominant excited state of ISQ ($\lambda_{max} = 660$ nm) as the main cause for the self-absorption of the fluorescence intensity as it propagates in the fiber. Figure 5.72 shows the SIF spectrum for a propagation distance of 3.2 cm ($F_1(z_1 = 3.2 \text{ cm}, \lambda)$), and the a least-squares fit to difference between the right and left hand sides of Equation (5.18), where $F_o(z_o = 2.2 \text{ cm}, \lambda)$ is the SIF spectrum for a propagation distance of 2.2 cm and $\Delta z = 1.0$ cm. In the fit, the transition frequency, ω_{g1}, is fixed at the bulk value, the homogeneous linewidth is fixed, and the transition moment and the inhomogeneous linewidth are allowed to vary. The result shown in Figure 5.72 is typical and can be performed for any $\Delta z \leq 2.25$ cm – the maximum range of the translation stage. The results are summarized in Table 5.6.

Notice that the inhomogeneous linewidth, γ_{g1}, is almost twice as wide as the value found for a bulk sample of ISQ/PMMA. The transition moment is also lower than that found for the bulk sample. There are a couple of possible explanations for this discrepancy. The plane wave model is only an approximation to the actual propagation in the fiber, and we could not fit the linear absorption spectra in the long wavelength tail of the absorption with the IB model because of small low lying excited states. Therefore these quantities are quoted as approximate.

5.7.3.2.2 Three-Level Model At higher concentrations we observed an increase in the absorption cross-section in the 780-820 nm range. To characterize this novel feature in the SIF spectra we use Equation (5.19) to model the imaginary part of the linear susceptibility. Note that we call the second one-photon state "3" since "2" is typically used for the dominant two-photon state. Therefore we model the resonant state and one low lying excited state as the cause for the self-absorption of the fluorescence intensity, in the higher concentration ISQ/PMMA fibers (see Figure 5.73). In the three-level fit, the transition frequency of the dominant excited state is held fixed at the bulk value, the transition frequency of the aggregate state is initially chosen as the minimum of the valley in the SIF spectrum at $z = 2.4$ cm (see Figure 5.73), the homogeneous linewidths

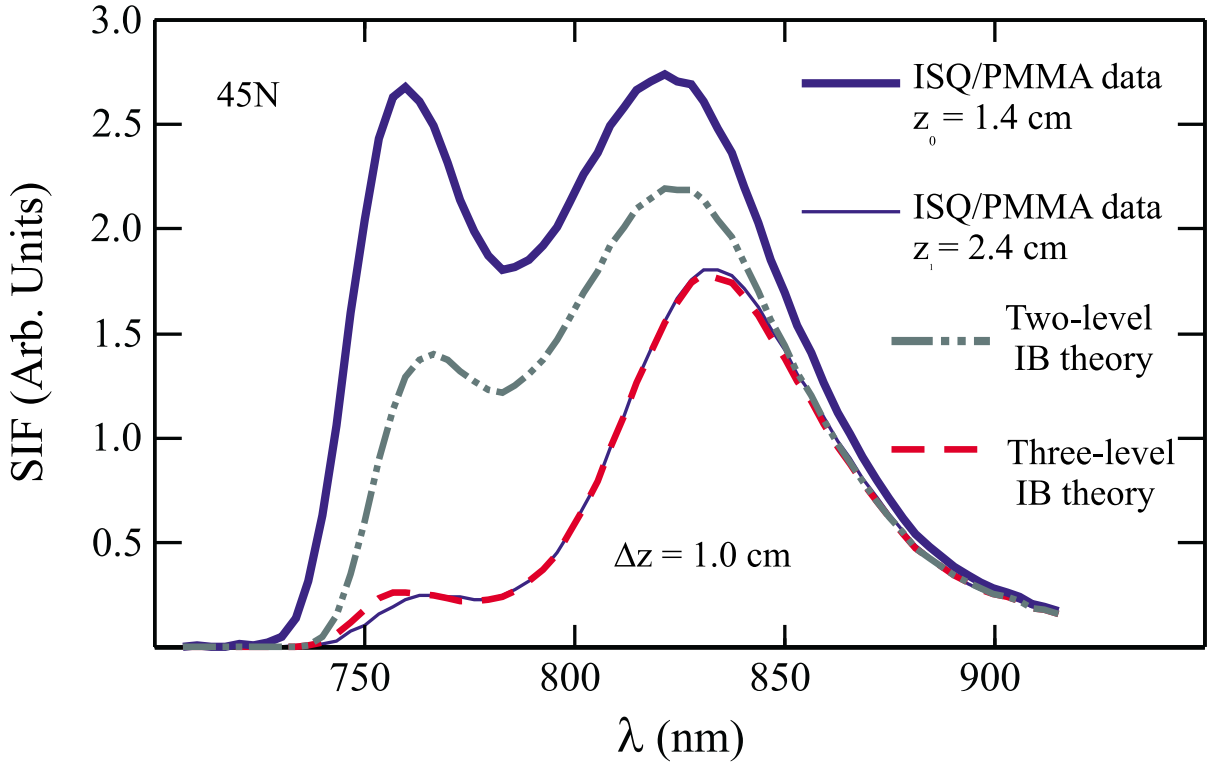

Fig. 5.73: Side-illumination fluorescence at two propagation distances ($z_o = 1.4$ cm and $z_1 = 2.4$ cm) for ISQ/PMMA (N = 6.3 $\times 10^{18}$ cm^{-3}) and two- and three- level models for self-absorption of the SIF intensity, which use the z_o SIF data as the initial condition.

are initially chosen to coincide with the homogeneous linewidth which was determined in the two-level fit of the lower concentration ISQ-doped fiber, and the remaining four variables ($\gamma_{g1}, \gamma_{g3}, \mu_{g1}, \mu_{g3}$) are allowed to vary to minimize the difference between the right and left hand sides of Equation (5.18) with $z_1 = 2.4$ cm, z_o =1.4 cm, and $\Delta z =$ 1.0 cm. Then the aggregate transition frequency and homogeneous linewidths are varied until the least-squares error is minimized. The results are tabulated in Table 5.6.

From these results, we see that the inhomogeneous linewidth for the dominant excited state is approximately the same in the ISQ/PMMA core fibers but much larger than the inhomogeneous linewidth for the bulk preform slice. The transition of moment for the resonant state decreases with increasing concentration which supports the notion that dye aggregation occurs at higher concentrations. By taking the ratio, $S_{g1}/S_{g3'} \sim 130$ for the highest concentration ISQ/PMMA fiber, we see that the dominant excited state is

Table 5.6: Excited state fit parameters for ISQ/PMMA fibers with comparison to bulk ISQ/PMMA sample. S^b_{gn}= strength of the resonant state for the bulk preform slice, and N_b is the number density of the bulk preform slice.

Expt.	n	$\hbar\omega_{gn}(\lambda)$ eV (nm)	$\hbar\Gamma_{gn}$ meV	$\hbar\gamma_{gn}$ meV	μ_{gn} DeBye	S_{gn}/S^b_{gn}	N 10^{18} cm^{-3}	N/N_b
Bulk	1	1.88 (660±1.1)	∼15	∼45	∼5.5	1	0.14	1
SIF	1	1.88(660±1.1)	∼2	∼ 92	∼ 4.4	0.6	0.14	1
SIF	1	1.88(660±1.1)	∼2	∼92	∼4.7	7	1.2	9
SIF	1	1.88(660±1.1)	∼2	∼92	3.8	13	3.6	27
	3'	1.635(758 ±4)	2±1	79±8	–	0.024	–	–
SIF	1	1.88(660±1.1)	∼5	∼100	2.5	9	6	45
	3'	1.595(777 ± 3)	2.5±1	65±5	–	0.072	–	–

still at least two orders of magnitude stronger than the aggregate state.

Figure 5.74 shows S_{gn} as a function of the relative number density for the four ISQ/PMMA core fibers characterized in the Table 5.6. The red line represents the expected value if $\alpha(\lambda)$ is linearly proportional to the number density. However, there is a large deviation from the expected value for the resonant state as the concentration of ISQ increases. The reduction in strength of the resonant state appears to be directly responsible for the increase in the aggregate state strength or vice versa.

Obviously, ISQ/PMMA has many intriguing properties. We have observed that it changes color over time and due to light exposure. At high concentrations it aggregates during the polymerization process. Unfortunately, these features are not beneficial when the goal is to make stable nonlinear optical devices. Therefore, while ISQ is scientifically interesting, it is not suitable as a device material.

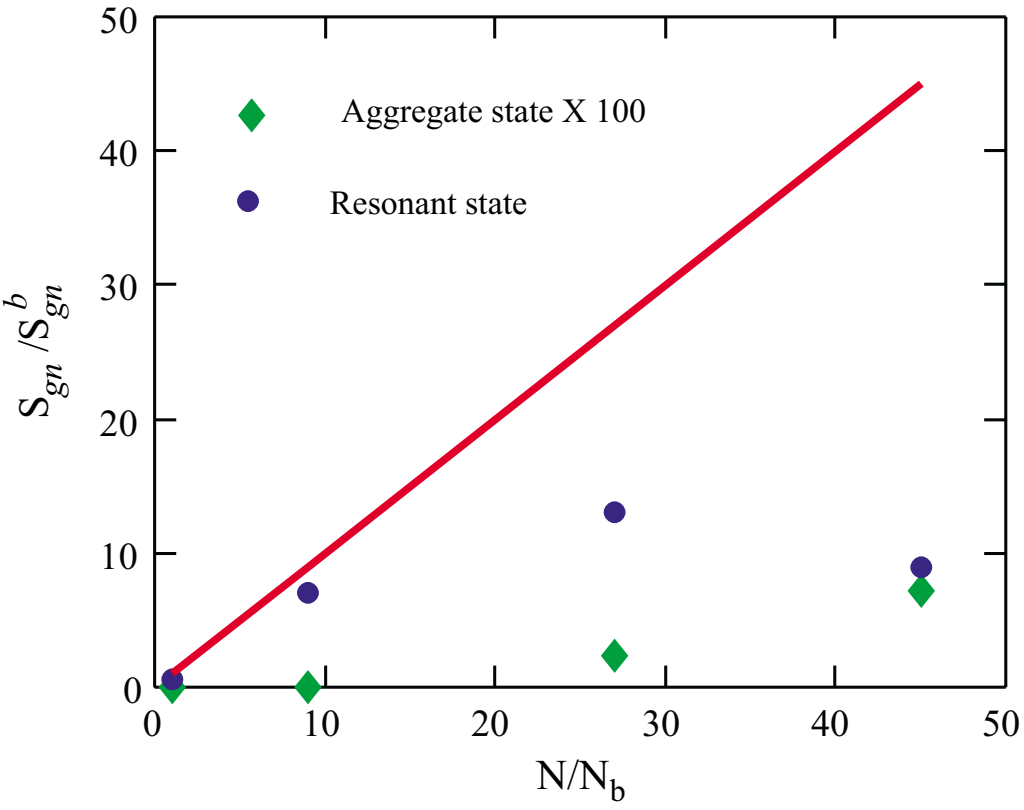

Fig. 5.74: Strength of the resonant excited and aggregate states as a function of the relative number density (N_b is the number density of the bulk sample). The red line denotes the theoretical value for no aggregation.

5.7.3.3 SiPc

For the SiPc/PMMA core fibers we knew that a two-level model would not be sufficient to model the absorption in the long-wavelength tail of the resonant state because of the results from Section 5.6.0.5. However, we began with a 2-level model for the linear susceptibility (Equation (5.10)) and worked our way to a satisfactory fit by adding low lying states.

Figure 5.75 shows the SIF spectrum generated with 703 nm light for the low concentration SiPc/PMMA fiber at z=1.2 cm and z=2.0 cm. Included in the figure are predictions for the decrease in SIF intensity for two two-level IB models, a three-level IB model and a four-level IB model for the absorption. The two-level IB model labeled (a) uses the mean values for the excited state parameters from Table 5.4 and the two-level

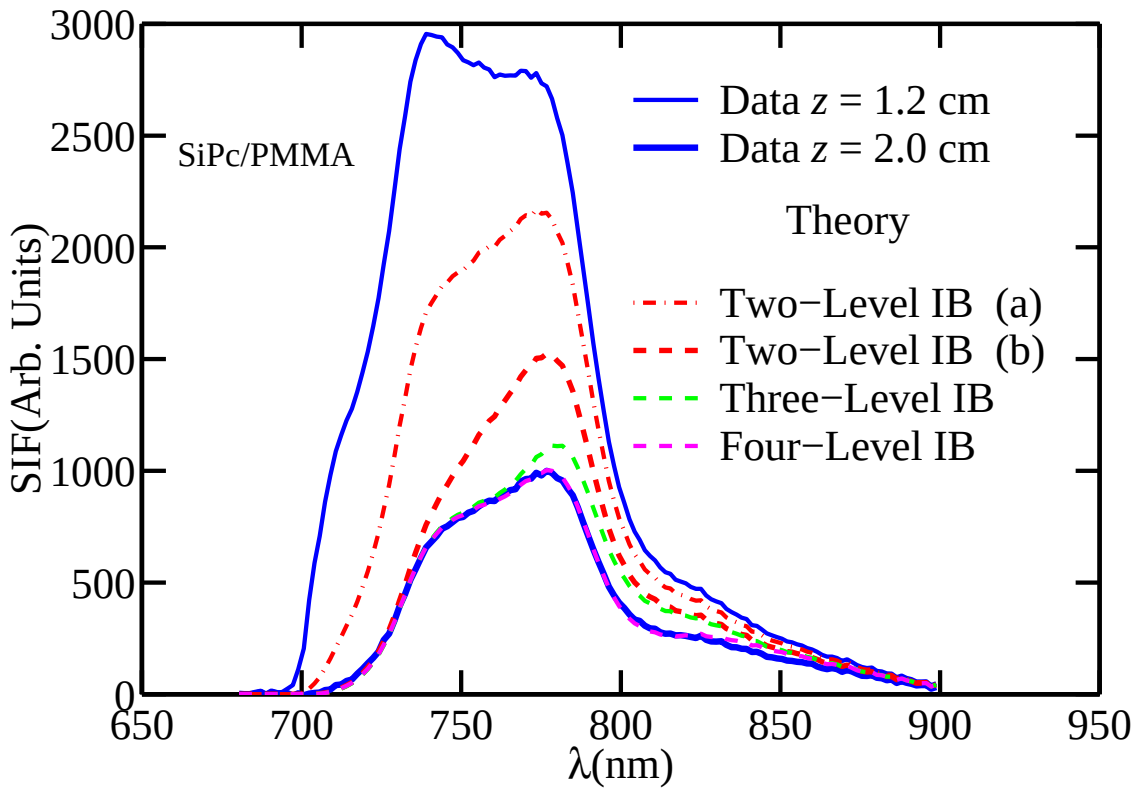

Fig. 5.75: Side-illumination fluorescence at two propagation distances (z_o = 1.2 cm and z_1 = 2.0 cm) for SiPc/PMMA (N = 0.13 $\times 10^{18}$ cm^{-3}) and two-, three-, and four-level models for self-absorption of the SIF intensity, which use the z_o SIF data as the initial condition.

IB model labeled (b) was calculated by increasing μ_{g1} until the leading edge of the theoretical spectrum and the SIF spectrum for z=2.0 cm coincided. We found that if we tried to minimize the difference between the data at z=2.0 cm and a two-level IB model for $\alpha(\lambda)$ we ended up with a theoretical spectrum that was similar at 760 nm but too small for wavelengths shorter than 760 nm and too large beyond 760 nm.

Obviously, the two-level IB model (a) does not predict the absorption of the SIF spectrum; however, the two-level IB model (b) is closer to predicting the absorption. The two-level model (b) does not predict absorption beyond 750 nm as strongly enough as seen in the data but there is good agreement with the leading edge. Therefore we added a third-level to the IB theory for $\alpha(\lambda)$. This level is located at about 768 nm where the hump in the linear absorption spectrum occurs in Figure 5.62. The green

dashed curve in Figure 5.75 represents the three-level model where μ_{g1} is kept at the value used for the two-level IB theory (b) prediction.

Clearly, the three-level IB model is closer to the actual absorption of the SIF spectrum in the low concentration SiPc/PMMA copolymer fiber. However, the theoretical prediction does not absorb enough of the fluorescence beyond 780 nm. Therefore we added a fourth-level to the IB model of $\alpha(\lambda)$. The additional level is centered near the same wavelength (818 nm) as the second small hump in the linear absorption spectrum shown in Figure 5.62. Obviously, there is very good agreement with the data for the

Table 5.7: Excited state fit parameters for SiPc/PMMA copolymer core fibers from the inhomogeneous-broadening (IB) model.

Expt.	n	$\hbar\omega_{gn}(\lambda)$	$\hbar\Gamma_{gn}$	$\hbar\gamma_{gn}$	μ_{gn}	N	Ref.
		eV (nm)	meV	meV	DeBye	10^{18} cm^{-3}	
SIF	1(a)	1.85 (671±1.1)	7	28	6.8	0.13	*
SIF	1(b)	1.85(671±1.1)	7	27	10.8	0.13	*
SIF	3'	1.62(770±4)	∼10	∼70	∼0.6	0.13	*
SIF	5'	1.52(816 ± 6)	∼ 10	∼ 50	∼0.5	0.13	*
SIF	1(b)	1.85(671±1.1)	7	27	6.6	1.2	*
SIF	3'	1.61(768±3)	∼10	∼60	∼0.3	1.2	*
SIF	5'	1.5(825 ± 3)	∼10	∼ 80	∼0.4	1.2	*

* - present work

four-level IB theory. Table 5.7 shows the excited state parameters for all the models shown in Figure 5.75. The four-level model is the average of the results for the four excitation wavelengths discussed in Section 5.1.1.3. Notice that μ_{g1} for the two-level IB theory (a) is approximately 2/3's of μ_{g1} for the two-level IB theory (b) and remainder of the parameters are equal. If we remember that the orientational average for a 2-D disk is 2/3 when the disks are isotropically oriented in the material. However, if the cross-sections of the disks are preferentially aligned with the cross-section of the fiber, the orientational average becomes unity. This suggests that the drawing process for the

SiPc/PMMA copolymer fiber oriented the SiPc molecules which causes the light that propagates in the fiber to experience a larger absorption than expected.

It was also necessary to use a 4-level model to characterize the absorption in the high concentration SiPc/PMMA copolymer fiber. The results are also shown in Table 5.7. The most interesting feature is the transition moment for the resonant state is equal to the SiPc/PMMA preform transition moment. There are a couple possible explanations for this result. First, the SiPc/PMMA molecules may have aligned as the low concentration results suggest but the filtering procedure reduced the actual number density to about 1/2 the nominal value. Second, if there were more cross-linking in the polymerization process at the higher concentration, the value of transition moment would be lower than the high concentration fiber, because the molecules would not align as easily in the drawing process. This phenomena should be investigated systematically in future works.

5.8 QEA Spectroscopy

From Sections 2.6.2 and 4.4 we can relate the imaginary part of the third-order susceptibility to the QEA response as follows:

$$\chi_I^{(3)}(-\omega;\omega,0,0) = -\frac{\lambda n_{0_R} d}{6\pi V_{\text{rms}}^2}\frac{I_t^{2\Omega}}{I_{t_0}}, \tag{5.21}$$

where λ is the free space wavelength, n_{0_R} is the real part of the linear index of refraction, d is the thickness of the sample, and V_{rms} is the root-mean-square voltage applied to the thin film. The derivations in Section 2.4.2.2.2 allow us to calculate $\chi_I^{(3)}(-\omega;\omega,0,0)$ using the Lorentzian and/or the IB theory so we can predict the QEA third-order response. We will use both models to characterize the third-order response from ISQ/PMMA and SiPc/PMMA electrooptic thin films. The linear absorption spectra for these two systems where previously discussed in Section 5.7.2, where the excited state parameters for the one-photon excited state manifolds were determined. These values will be used to predict the QEA response, which will be compared to the experimental results.

5.8.1 ISQ

Figure 5.76 is a comparison of the negative of the imaginary part of $\chi_I^{(3)}(-\omega;\omega,0,0)$ for an ISQ/PMMA thin film measured in the QEA experiment and two-level models for the Lorentzian and IB theories. We chose the negative of $\chi^{(3)}$ because it has, unfortunately, become the standard way to plot QEA spectra due to a sign error in early analyses of QEA responses. The two theoretical responses use the calculated values for $\omega_{g1}, \Gamma_{g1}, \gamma_{g1}$, and μ_{g1} from Table 5.3. Thus there are no floating parameters for the theoretical curves shown in Figure 5.76. Although the IB theory predicts the third-order response beyond 670 nm fairly well, neither two-level theory accounts for the actual response in the 600-650 nm range.

Because the two-level models do not compare very well to the ISQ/PMMA data,

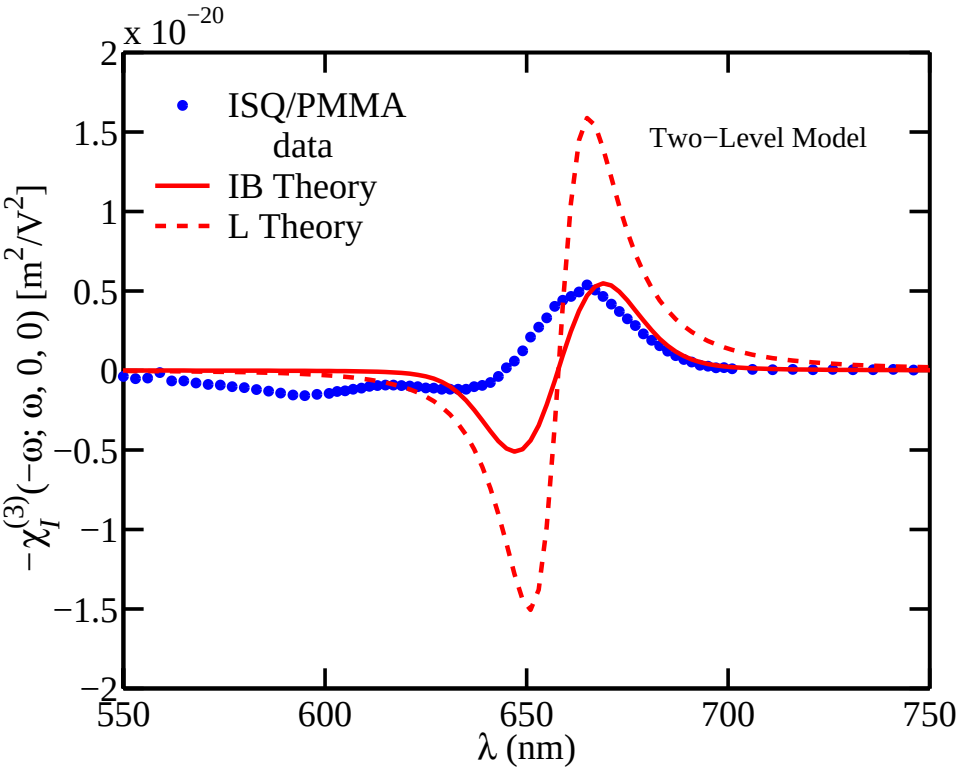

Fig. 5.76: $\chi_I^{(3)}(-\omega;\omega,0,0)$ for an ISQ/PMMA thin film in comparison to Lorentzian (L) (dashed-red) and inhomogeneously-broadened (IB) (solid-red) two-level models (N = 19.4 $\times 10^{18}$ cm^{-3}).

we increase the number of levels to 4. The two one-photon states that were used to characterize the high-lying shoulder in the linear absorption spectrum make up the 3^{rd} and 4^{th} levels. Figure 5.77 compares the ISQ/PMMA data with the Lorentzian and IB theories. Clearly, both theories predict a more realistic response but the magnitude of the Lorentzian response is much too large. Note that there were no floating parameters involved in the calculation of either theory since the excited state parameters for the three one-photon states were taken from Table 5.3.

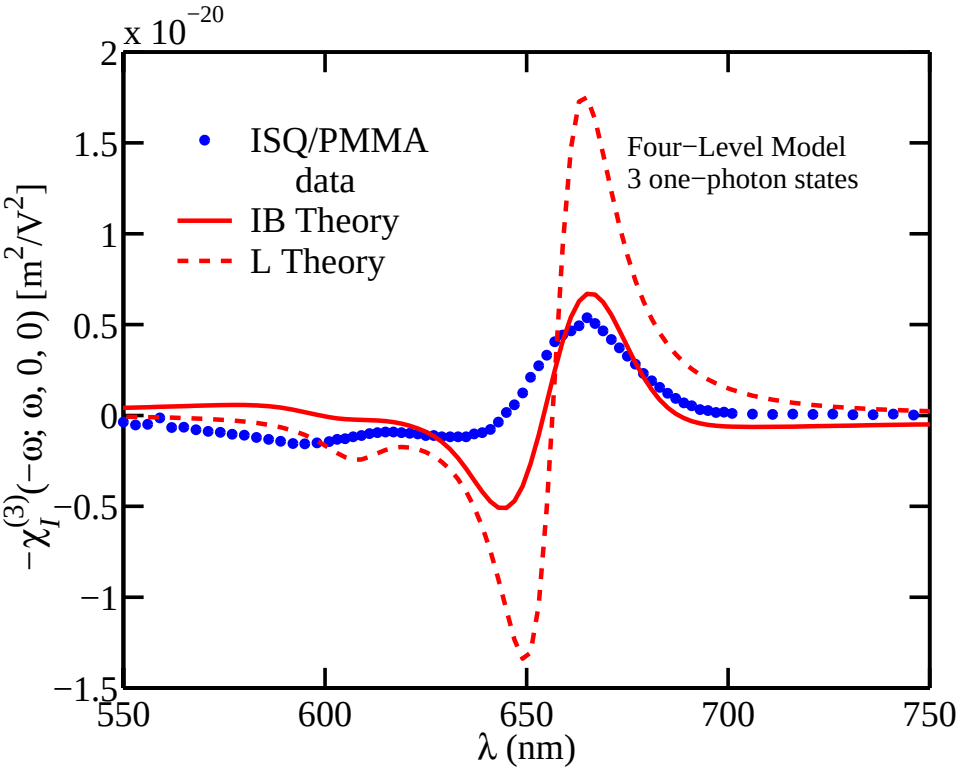

Fig. 5.77: $\chi_I^{(3)}(-\omega;\omega,0,0)$ for an ISQ/PMMA thin film in comparison to Lorentzian (L) (dashed-red) and inhomogeneously-broadened (IB) (solid-red) four-level models (N = 19.4 $\times 10^{18}$ cm^{-3}).

Mathis [7] and Poga [21] proposed a two-photon state near 2.09 eV to account for the third-order response in the 600-650 nm range. To account for the two-photon state we need to expand our theories to a 5-level model. Since there are many ways to construct a 5-level model we separate the analysis in terms of the Lorentzian 5-level models and the

IB 5-level models. Table 5.8 summarizes the excited state parameters of the two-photon state in ISQ/PMMA thin films for the Lorentzian theory (The excited state parameters for the IB theory will be discussed shortly.).

Table 5.8: Excited state fit parameters for the two-photon state in ISQ/PMMA thin films from QEA spectroscopy (TF) using the Lorentzian (L) model.

Expt.	Anal.	m	n	$\hbar\omega_{gn}(\lambda)$	$\hbar\Gamma_{gn}$	μ_{mn}	N
				eV (nm)	meV	D	10^{18} cm^{-3}
QEA	L(a,b,c)	1	2	2.09(593±20)	75.0	3±1	19.4
QEA	L(a)	3	2	2.09(593±20)	75.0	1.2±1	19.4
QEA	L(a)	5	2	2.09(593±20)	75.0	1.4±1	19.4

(c) - states 3 and 5 are conformational isomers of state 1.

The values for the Lorentzian modeled two-photon state, in Table 5.8, are similar to the ones used by Mathis [7], except we that have lowered the transition moment because the transition moment for the resonant one-photon state in our sample, as determined from the linear absorption, was lower than her value. μ_{12} was reduced in size proportional to the reduction in size of the transition moment for the resonant state.

Three variations of a 5-level Lorentzian model along with the ISQ/PMMA data are shown in Figure 5.78. The Lorentzian 5-level (a) model allows all three one-photon states to couple to the additional two-photon state, 5-level (b) only allows transitions to the two-photon state through the resonant one-photon state at 657 nm, and 5-level (c) only allows transitions to the two-photon state through the resonant one-photon state at 657 nm and assumes that the two nonresonant one-photon states are cis-isomers of the resonant state. This final restriction does not allow a third-order transition caused by a coupling of one high-lying vibronic to the resonant state.

Figure 5.78 shows that the Lorentzian 5-level (c) model is most representative of the ISQ/PMMA data, but there is not very good agreement on resonance. Therefore we attempt to model the ISQ/PMMA data using IB 5-level models to gain a better understanding of the electronic response.

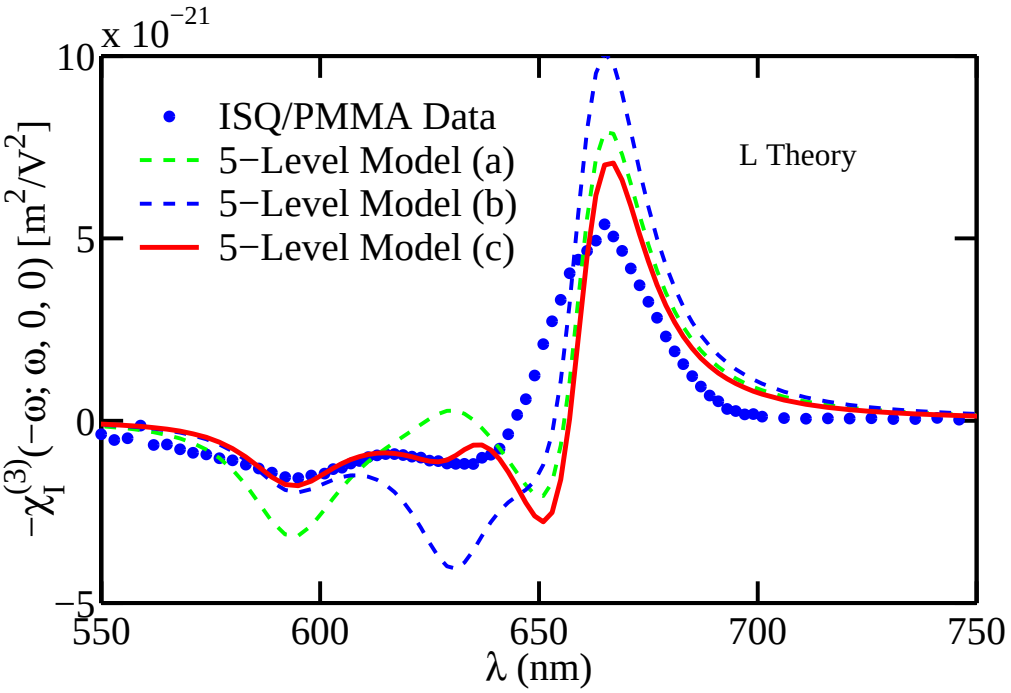

Fig. 5.78: $\chi_I^{(3)}(-\omega;\omega,0,0)$ for an ISQ/PMMA thin film in comparison to three variations on a 5-Level Lorentzian (L) model (N = 19.4 $\times 10^{18}$ cm^{-3}). 5-level (a) model allows all three one-photon states to couple to the additional two-photon state, 5-level (b) only allows transitions to the two-photon state through the resonant one-photon state at 657 nm, and 5-level (c) only allows transitions to the two-photon state through the resonant one-photon state at 657 nm and considers the two high-lying states to be conformational isomers of the resonant excited state.

Table 5.9 summarizes the excited state parameters for the two-photon state when the inhomogeneous-broadening theory is used in least-squares fits to the ISQ/PMMA QEA data. We have examined the same three variations on the IB 5-level model (a,b,c) that were used with the Lorentzian model plus an additional case. The additional case, (d), models a 0.1 % reorientation effect along with the electronic effect from the IB 5-level (b) model (Note: The 0.1 % reorientational response is relative to the electronic response.).

Figure 5.79 shows the results of the four IB 5-level least-squares fits to the ISQ/PMMA data. It is interesting to note that there is very little differenence between the (a), (b), and (c) variations of the 5-level model for the IB theory. Obviously, the 5-level model

Table 5.9: Excited state fit parameters for the two-photon state in ISQ/PMMA thin films from QEA spectroscopy (TF) using the inhomogeneous-broadening (IB) model.

Expt.	Anal.	m	n	$\hbar\omega_{gn}(\lambda)$ eV (nm)	$\hbar\Gamma_{gn}$ meV	$\hbar\gamma_{gn}$ meV	μ_{mn} D	N (10^{18}) cm^{-3}
QEA	IB(a,b,c)	1	2	2.09(593±20)	20.0	50	2.4±1	19.4
QEA	IB(a)	3	2	2.09(593±20)	20.0	50	1.2±1	19.4
QEA	IB(a)	5	2	2.09(593±20)	20.0	50	1.4±1	19.4

(c) – states 3 and 5 are conformational isomers of state 1.

(d) – 0.1% reorientational effect.

that allows the two high-lying one-photon states to couple to the two-photon state is the most dissimilar prediction.

Clearly, neither theory models the entire ISQ/PMMA QEA spectrum properly. The Lorentzian theory is better at predicting the off-resonant structure, and the IB theory is better at predicting the resonant structure. Because the resonance structure is much larger in magnitude the error associated with the least-squares fit for the IB theory is an order of magnitude smaller than the error associated with the least-squares fit for the Lorentzian theory.

Before attempting to model more complicated scenarios, we decided to test an assumption that there are fewer ISQ-dye molecules in the thin film than theoretically predicted. We believe this is a reasonable assumption because ISQ is a very unstable molecule, the ISQ used to make the samples was about 5 years old, and the average transition moment for the first excited state of the ISQ/PMMA thin films, which was determined in linear absorption measurements, is lower than the value found by Mathis [7].

To correct the number density for the ISQ/PMMA thin films, we use the theoretical number density, N_t, the mean value of the calculated transition moment for the first excited state, μ_c, and the transition moment for the first excited state as determined by Mathis [7], μ_M (Note: the Lorentzian value of the calculated transition moment was used

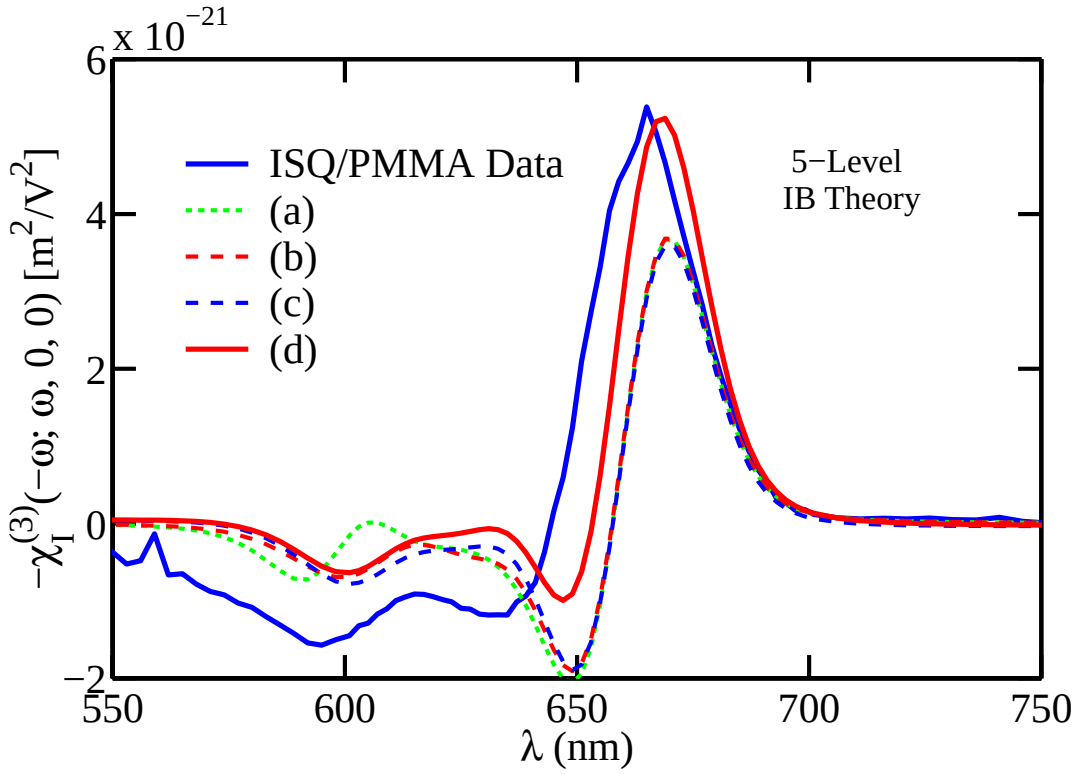

Fig. 5.79: $\chi_I^{(3)}(-\omega;\omega,0,0)$ for an ISQ/PMMA thin film in comparison to various inhomogeneously broadened (IB) models (N = 19.4 $\times 10^{18}$ cm^{-3}). 5-level (a) model allows all three one-photon states to couple to the additional two-photon state, 5-level (b) only allows transitions to the two-photon state through the resonant one-photon state at 657 nm, and 5-level (c) only allows transitions to the two-photon state through the resonant one-photon state at 657 nm and considers the two high-lying states to be conformational isomers of the resonant excited state, and 5-level (d) is 5-level (b) plus 0.1% reorientational effect.

because it is most similar to Mathis' calculation). The following equation allows us to determine the actual number density in our sample:

$$N_{actual} = N_t \frac{|\mu_c|^2}{|\mu_M|^2} \tag{5.22}$$

The renormalization of the number density does not affect the least-squares fit to the linear absorption data because $N_1|\mu_1|^2 = N_2|\mu_2|^2$ for the one-photon states; however, it does change the least-squares fit to the QEA data because, for example, $N_1|\mu_1|^4 =$

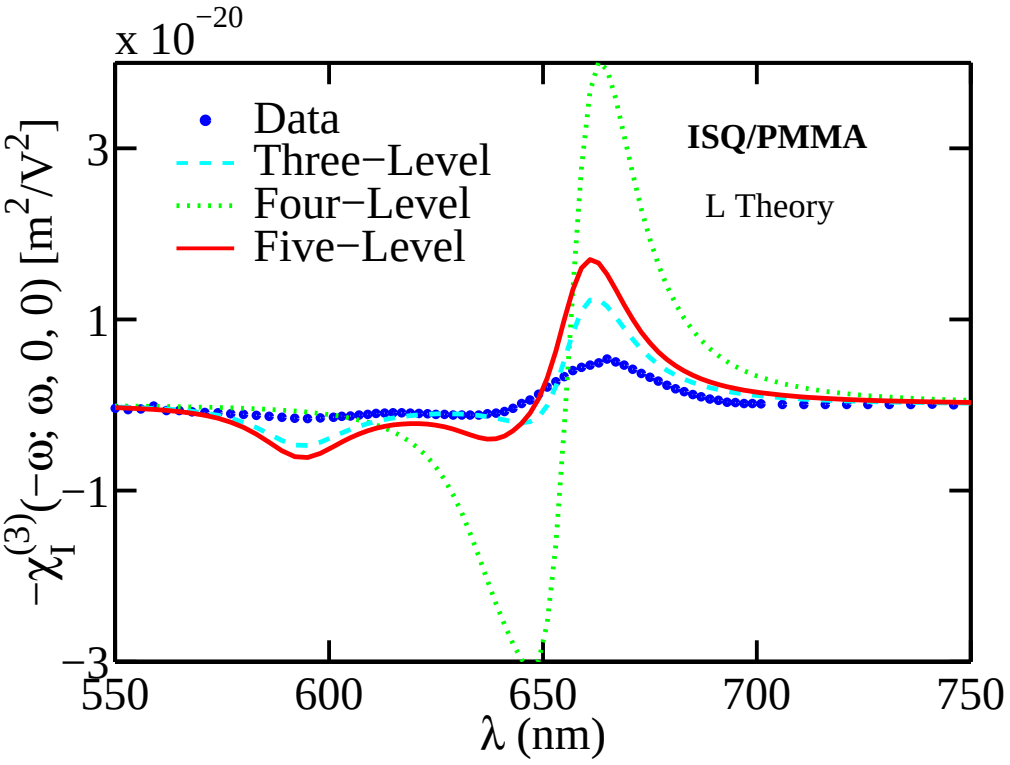

Fig. 5.80: $\chi_I^{(3)}(-\omega;\omega,0,0)$ for an ISQ/PMMA thin film in comparison to 3-level (blue-dashed), 4-level (green-dotted), and 5-level (solid-red) Lorentzian (L) models (N = 8.8 $\times 10^{18}$ cm^{-3}).

$N_2|\mu_2|^4$ (Note: we have used 1 to denote the original number density and transition moment, and 2 to denote the renormalized number density and transition moment.). After renormalizing the number density, we get $\mathrm{N}_{actual} = 8.8 \times 10^{18}$ cm^{-3}.

When we use N_{actual} instead of N_t in the least-squares fit with the Lorentzian model we do not improve the prediction of the theoretical response in comparison to the data (see Figure 5.80). However, we tabulate the results of the Lorentzian least-squares fit to show that the ratio of the resonant one-photon state transition moment, μ_{g1} to the two-photon state transition moment is similar to the uncorrected prediction and the ratio found by Mathis [7]. It should be noted that it is no longer necessary to eliminate transitions from the high-lying one-photon states to the two-photon state to get the best fit. This suggests that the high-lying one-photon states are vibronics rather than excited states due to conformational isomers.

Table 5.10: Excited state fit parameters for ISQ/PMMA thin films from QEA and transmission spectroscopy (TF) after the number density has been corrected (L – Lorentzian).

Expt.	Anal.	m	n	$\hbar\omega_{gn}(\lambda)$ eV (nm)	$\hbar\Gamma_{gn}$ meV	$\hbar\gamma_{gn}$ meV	μ_{mn} D	N (10^{18}) cm^{-3}
TF	L	g	1	1.885(657±2)	37.0±5.0	–	11.5±0.8	8.8
TF	L	g	3	1.935(641±6)	38.0±5.0	–	4.6±0.5	8.8
TF	L	g	5	2.03(608±3)	40.0±5.0	–	5.6±0.5	8.8
QEA	L	1	2	2.09(593±20)	45	–	4.75±0.5	8.8
QEA	L	3	2	2.09(593±20)	45	–	1.0	8.8
QEA	L	5	2	2.09(593±20)	45	–	1.2	8.8

Three-Level – state 1 and state 2.

Clearly, the results from Lorentzian models are not great, but they are more realistic than previous attempts because the only floating parameters are the two-photon excited state parameters. This is an improvement because the previous analysis normalized the Lorentzian theory to the peak of the QEA response [2] and did not account for the high-lying vibronic shoulder. Without the magnitude of the theory as a constraint, it is much simpler to determine the ratio of transitions moments that fit the data very well.

Luckily, there is a drastic improvement in the IB model's prediction of the ISQ/PMMA QEA data when the actual number density is used in the least-squares fit instead of the theoretical number density. Figure 5.81 shows the theoretical predictions for three-level (blue-dashed), four-level (green-dotted), and five-level (red-solid) IB models in comparison to the ISQ/PMMA QEA data. As before, the three-level model accounts for the resonant one-photon state at 657 nm and the two-photon state at 593 nm; the four-level model accounts for the three one-photon state predicted from the IB linear absorption analysis; and the five-level model accounts for the three one-photon states and the two-photon state.

Table 5.11 summarizes the excited states used to predict the ISQ/PMMA QEA data shown in Figure 5.81. As in the previous Lorentzian analysis, electronic transitions

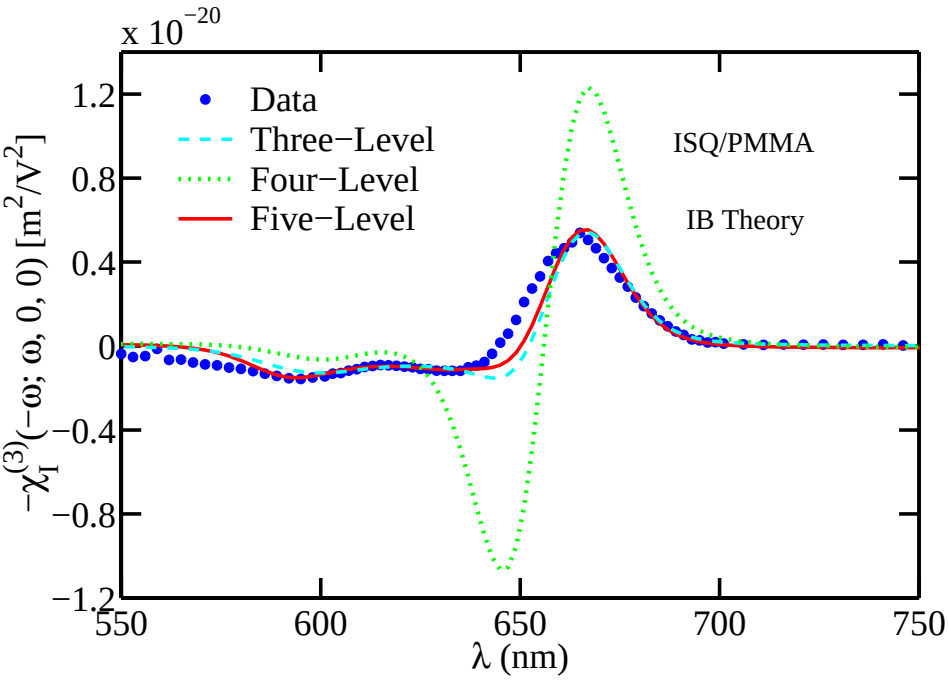

Fig. 5.81: $\chi_I^{(3)}(-\omega;\omega,0,0)$ for an ISQ/PMMA thin film in comparison to 3-level (blue-dashed), 4-level (green-dotted), and 5-level (solid-red) inhomogeneously-broadened (IB) models (N = 8.8 $\times 10^{18}$ cm^{-3}).

between the high-lying vibronics states and the two-photon state are not eliminated. Clearly, the four-level model which only accounts for one-photon states does not predict the ISQ/PMMA QEA response very accurately. However, there is little difference between the predicted responses for the three- and five-level models, which tells us that the high-lying vibronic states only play a minor role in the third-order response of the ISQ/PMMA system.

We also tried a number of variations on higher-level IB models with no apparent improvement in the characterization the ISQ/PMMA data. Using the Lorentzian model, Andrews and co-workers [20] proposed a large two-photon state in the UV (365 nm, 9.8 D) to model their third-harmonic data of ISQ in $CHCl_3$. In pump-probe optical Kerr effect measurements, Vigil also determined, using a Lorentzian analysis, that a similar two-photon state (370 nm, 7 D) is necessary to model the spectroscopic third-order response of ISQ in CCl_4 [22]. The inclusion of a two-photon state in the 365-370 nm

Table 5.11: Excited state fit parameters for ISQ/PMMA thin films from QEA and transmission spectroscopy (TF) after the number density has been corrected (IB – inhomogeneous broadening).

Expt.	Anal.	m	n	$\hbar\omega_{gn}(\lambda)$ eV (nm)	$\hbar\Gamma_{gn}$ meV	$\hbar\gamma_{gn}$ meV	μ_{mn} D	N (10^{18}) cm^{-3}
TF	IB	g	1	1.885(657±2)	12.0±5.0	38± 4	10.1±0.8	8.8
TF	IB	g	3	1.935(641±6)	20.0±7.0	40± 4	4.7±0.5	8.8
TF	IB	g	5	2.03(608±3)	28.0±8.0	50± 4	6.0±0.5	8.8
QEA	IB	1	2	2.09(593±20)	40	50	3.9±0.5	8.8
QEA	IB	3	2	2.09(593±20)	40	50	< 0.3	8.8
QEA	IB	5	2	2.09(593±20)	40	50	1.3±0.3	8.8

Three-Level – state 1 and state 2.

range QEA IB model of ISQ/PMMA is reasonable when the transition moment is less than 5.0 D. However, the contribution is not very well resolved since the linewidths (both homogeneous and inhomogeneous) of the UV two-photon state can be between 20 and 100 meV with out significantly effecting the third-order response. The reduction in the transition moment of the UV two-photon state could be caused by the solvent effect, the inclusion of the high-lying one-photon states, or the fact that we use an IB model as opposed to the Lorentzian model used by Andrews [20] or Vigil [22].

In terms of the ISQ/PMMA QEA data, the two-photon state at 593 nm plays a more important role in the QEA response than the two-photon state in the UV. Thus the QEA measurement is not the best measurement for determining the characteristics of two-photon states in the UV.

For a very complex ISQ system, we must conclude that the IB theory is a more accurate model for predicting QEA electronic response than the standard Lorentzian theory. The next section discusses the SiPc/PMMA QEA response in terms of the Lorentzian and IB theories.

5.8.2 SiPc

Because of the very distinct linear absorption spectrum for SiPc/PMMA, we thought it would be much simpler to characterize the QEA response than the ISQ/PMMA case. However, that did not turn out to be the case. As we will soon show, the SiPc/PMMA QEA spectrum is upside down in comparison to the ISQ/PMMA QEA spectrum and 4-level predictions by the Lorentzian and IB theories. This section discusses the attempts to reconcile the "upside down" behavior with the IB and Lorentzian theories.

Figure 5.82 shows the $\chi_I^{(3)}(-\omega;\omega,0,0)$ for the SiPc/PMMA thin film discussed in Section 5.7.2.2, and the predictions for a 4-level model using both the Lorentzian and IB theories. The excited state parameters for the three-one photon states are taken from Table 5.4 and used as input parameters for the theoretical responses. Clearly, neither theory describes the actual QEA response. The IB theory predicts a magnitude for the electronic response that is smaller than the Lorentzian theory but is still much larger than the data. Even more disconcerting is the fact that the actual resonant response (near 670 nm) is upside down in comparison to both theoretical predictions. For example, in between 660-670 nm the QEA response is positive and the theoretical responses are negative. Because of this discrepancy, we were motivated to determine what other excited states or effects could cause the theoretical responses to change sign.

We added 4^{th} and 5^{th} one-photon states in the IR predicted by the SIF measurement and found no change in the resonant response. This was not surprising because the low lying states have transition moments which are over an order of magnitude smaller than the transition moment of the resonant state, and the third-order response is proportional to the 4^{th} power of the transition moment.

We then investigated if a reorientation of the molecules under the influence of the applied field would cause the actual response shown in Figure 5.82. This reorientational effect is proportional to $\xi^{(1)}(0;0)\xi^{(1)}(-\omega;\omega)$ [16]. The result of adding a 0.1% reorientational effect to the third-order electronic response is shown as the blue curves in Figure 5.82. Clearly, the addition of the reorientational effects only make the predictions worse.

Because the shape of the resonant response is similar to the upside down shape the

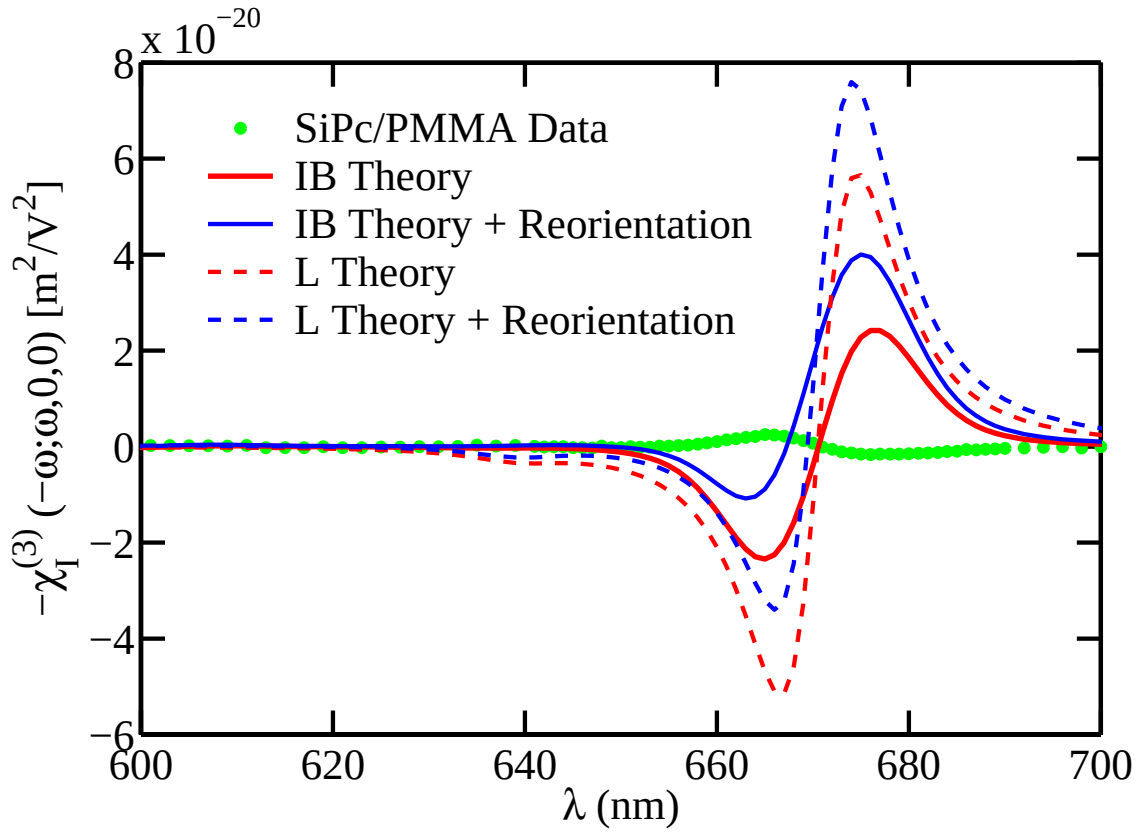

Fig. 5.82: $\chi_I^{(3)}(-\omega;\omega,0,0)$ for an SiPc/PMMA thin film in comparison Lorentzian (L) (dashed-red) and inhomogeneously-broadened (IB) (solid-red) models (N = 5.7 $\times 10^{18}$ cm^{-3}). The blue theory curves are the red electronic effects plus a 0.1% reorientational effect.

two theories predict, we are confident there is no two-photon state in the 550-570 nm range that would cause the upside down response. Therefore we experimented with allowing vibronics of the ground state, which are located in the IR, to influence the theoretical electronic response. This did not influence the magnitude or shape of the resonant response either.

The final option we was to try a two-photon state in the UV. We initially tried a two-photon state a 3.4 eV (365 nm) with a transition moment of 10 DeBye. Similar to the one predicted for the ISQ dye by Andrews and co-workers [20] from third-harmonic generation experiments. The influence of this two-photon state changed the parity of the resonant response for the IB theory, but not the L theory. At this point, we discontinued

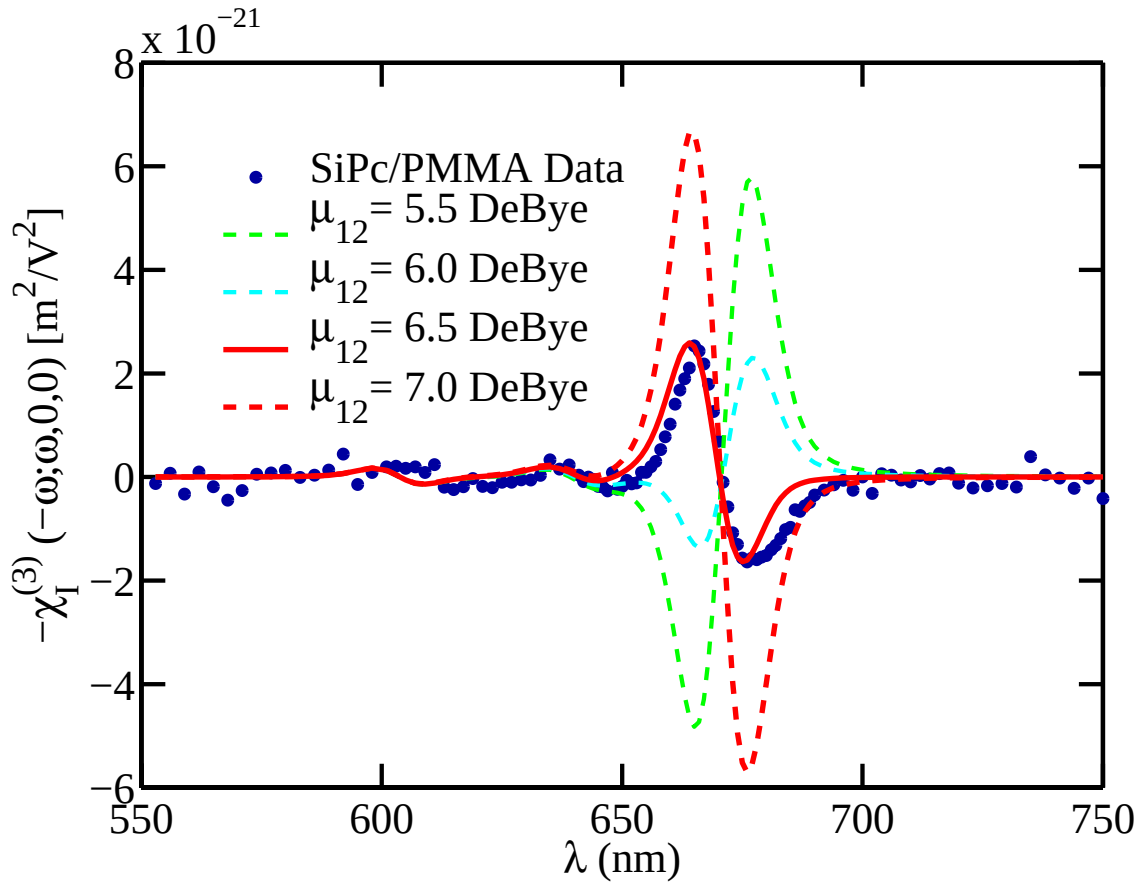

Fig. 5.83: $\chi_I^{(3)}(-\omega;\omega,0,0)$ for an SiPc/PMMA thin film in comparison to a 5-level inhomogeneously broadened (IB) model (N = 5.7 $\times 10^{18}$ cm^{-3}). The four theoretical curves correspond to $\mu_{12} = \{5.5, 6.0, 6.5, 7.0\}$ D.

attempts to characterize the SiPc/PMMA QEA response using the L theory, because it could not predict the change of sign in the electronic response unless the two high-lying vibronics were removed from the excited state manifold.

Although the IB theory predicted the change in sign of the resonant response, the magnitude of the response was much larger than the actual response. Therefore we lowered the transition moment until the magnitude of the 5-level IB theory (three one-photon states, and one two-photon state) and the data were comparable. Unfortunately, this did not solve all our problems. The theoretical response for the resonant state was much more symmetric about zero than the actual response.

Instead of attempting to add in reorientational effects, we moved the transition frequency of the two-photon state towards the visible. When the transition frequency of the two-photon state was between 2.55 eV and 2.7 eV (460 nm and 485 nm), we found that the IB theory predicts an asymmetric resonant response. Figure 5.83 shows the actual QEA response for the SiPc/PMMA thin film, and the 5-level IB model for the electronic response. The two-photon state is centered at 485 nm, and the transition moment is varied between 5.5 D and 7.0 D to show the influence of the two-photon state on the structure of the resonant response.

Table 5.12: Excited state fit parameters for a 1 wt. % SiPc/PMMA thin film for QEA and transmission spectroscopy (TF). IB – inhomogeneous broadening, L – Lorentzian.

Expt.	Anal.	Dye	n	$\hbar\omega_{1g}(\lambda)$	$\hbar\Gamma_{1g}$	$\hbar\gamma_{1g}$	μ_{1g}	N
				eV (nm)	meV	meV	D	10^{18} cm^{-3}
TF	IB	SiPc	1	1.85(670±1)	8 ± 2	19 ± 3	7.2 ± 1.5	5.7
TF	IB	SiPc	3	1.94(640±2)	10 ± 4	20 ± 3	2.1 ± 1	–
TF	IB	SiPc	5	2.05(605±2)	12 ± 4	20 ± 3	2.4 ± 1	–
QEA	IB	SiPc	2	2.63(472±12)	∼10	∼20	6.85 ± 0.35	–

The average values for the excited state parameters used in the fit of the SiPc/PMMA QEA data are shown in Table 5.12. We chose to leave the homogeneous and inhomogeneous linewidths similar to the corresponding one-photon linewidths because we cannot directly probe this state with the current QEA experiment. It should be noted that the two-photon state can not be located at wavelengths longer than 485 nm because the asymmetry of the response becomes too large, and the resonant effects of the two-photon state would begin to show in the 550 nm range. However, the transition energy could be located at a higher energies than stated in Table 5.12, if reorientation effects contribute to the total third-order response (see Figure 5.82). The transition moment, μ_{12}, would have to be increased to compensate for shifting the transition frequency toward the UV and a small reorientational effect ($\sim$ 0.1%) would be necessary to compensate for the asymmetry in the QEA data. However, we choose the simplest explanation until future

experiments, which probe the two-photon state directly, can be conducted.

We conclude the discussion of the SiPc/PMMA dye-doped systems with a short recap of the excited state which effect linear and nonlinear absorption. From transmission spectroscopy, we determined that a large excited state centered at 670 nm was the resonant one-photon state in the visible for both SiPc/PMMA thin films, and SiPc/PMMA copolymer preform slices. There are also at least two high-lying vibronics states that absorb in the visible (640 nm and 608 nm). The SIF spectroscopy measurements confirmed that the resonant excited state is the main cause of the absorption in the SIF regime. However, there are at least two additional weak one-photon states located beyond 750 nm. Their transition moments are over an order of magnitude smaller than the transition moment of the resonant excited state. These low lying states are most likely caused by low lying vibronics of the resonant state but could be small aggregate states.

The QEA experimental results show that the three one-photon states measured in the transmission spectroscopy experiment contribute to the third-order response but the low lying states measured in the SIF experiment are two small to have an appreciable effect. We also determined that a two-photon state at a wavelength equal to or shorter than 485 nm has a significant influence on the nonlinear response in the visible region. Even though all three one-photon states characterized in the linear absorption spectrum have roles in the nonlinear response, the third-order response is dominated by the contributions from the resonant one-photon state and the two-photon state.

Bibliography

[1] J. R. Sounik, "Side-chain copolymers for third-order nonlinear optical applications," Polym. Prepr. Am. Chem. Soc. **32**, 158–159 (1991).

[2] K. S. Mathis, "Studies on the nature of excited states of squaraines using quadratic electroabsorption spectroscopy and essential state analysis," Master's Thesis (Washington State University, Pullman, WA, 1995).

[3] M. G. Kuzyk ed., "Nonlinear optical properties of organic materials X," SPIE Proc. **3147** (1997).

[4] N. Tamaoki, E. Van Keuren, H. Matsuda, K. Hasegawa, and T. Yamaoka, "Photoreversible optical nonlinearities of polymeric films containing spiropyran with long alkyl chains," Appl. Phys. Lett. **69**, 1188–1190 (1996).

[5] R. J. Kruhlak and M. G. Kuzyk, "Side-illumination fluorescence spectroscopy. II. Applications to squaraine dye-doped polymer optical fibers," J. Opt. Soc. Am. B **16**, 1756–1767 (1999).

[6] R. J. Kruhlak and M. G. Kuzyk, "Side-illumination fluorescence spectroscopy. I. Principles," J. Opt. Soc. Am. B **16**, 1749–1755 (1999).

[7] K. S. Mathis, M. G. Kuzyk, C. W. Dirk, A. Tan, S. Martinez, and G. Gampos, "Mechanisms of the nonlinear optical properties of squarainne dyes in poly(methyl methacrylate) polymer," J. Opt. Soc. Am. B **15**, 871–883 (1998).

[8] D. W. Garvey, K. Zimmerman, P. Young, J. Tostenrude, J. S. Townsend, Z. Zhou, M. Lobel, M. Dayton, R. Wittorf, and M. G. Kuzyk, "Single-mode nonlinear-optical polymer fibers," J. Opt. Soc. Am. B **13**, 2017–23 (1996).

[9] D. W. Garvey, "Nonlinear optics in polymer fibers," Ph. D. dissertation (Washington State University, Pullman, WA, 1999).

[10] T. Kaino, "Absorption losses of low loss plastic optical fibers," Jpn. J. Appl. Phys. **24**, 1661–65 (1985).

[11] S. Kim, M. Furuki, L.S. Pu, H. Nakahara, and K. Fukuda, "Unique monolayer assembly of squarylium dye with short alkyl chains," J. Chem. Soc., Chem. Commun. pages 1201–03 (1987).

[12] M. Iwamoto, Y. Majima, F. Hirayama, M. Furuki, and L. S. Pu, "Generation of the displacement current by the transformation of J-aggregates in spreading monolayers of squarylium dye," Chem. Phys. Lett. **195**, 45–9 (1992).

[13] G. J. Ashwell, P. C. Williamson, A. Green, G. S. Bahra, and C. R. Brown, "Aggregation-induced linear and non-linear optical properties of four hydroxy-substituted analogues of 2,4-Bis[4-(dibutylamino)phenyl]squaraine," Aust. J. Chem. **51**, 599–604 (1998).

[14] G. J. Ashwell, P. Leeson, G. S. Bahra, and C. R. Brown, "Aggregation-induced second-harmonic generation," J. Opt. Soc. Am. B **15**, 484–8 (1998).

[15] M. Abramowitz and I. E. Stegun, eds., *Handbook of Mathematical Functions* (U. S. Government Printing Office, Washington, D.C., 1972).

[16] M. G. Kuzyk and C. W. Dirk, eds., *Characterization techniques and tabulations for organic nonlinear optical materials*, 1st ed. (Marcel Dekker, New York, 1998).

[17] Robert W. Boyd, *Nonlinear Optics* (Academic Press, San Deigo, 1992).

[18] G. Herzberg, *Spectra of Diatomic Molecules*, Vol. 1, 2nd ed. (D. Van Nostrand Co., New York, 1950).

[19] C. W. Dirk, H. E. Katz, M. L. Schilling, and L. A. King, "Use of thiazole rings to enhance molecular second-order nonlinear optical susceptibilities," Chem. Mater. **2**, 700–5 (1990).

[20] J. H. Andrews, J. D. V. Karydarov, K. D. Singer, D. L. Hull, and K. C. Chuang, "Characterization of excited states of centrosymmetric and noncentrosymmetric squaraines by third-harmonic spectral dispersion," J. Opt. Soc. B **12**, 2360–2371 (1995).

[21] C. Poga, T. M. Brown, M. G. Kuyzk, and Carl W. Dirk, "Characterization of the excited states of a squaraine molecule with quadratic electrosorption spectroscopy," J. Opt. Soc. Am. B **12**, 531–43 (1995).

[22] S. R. Vigil, "Nonlinear optical studies of organic liquids and polymer optical fibers," Ph. D. dissertation (Washington State University, Pullman, WA, 2000).

Chapter 6

Conclusions

We have developed a novel method for measuring the linear absorption in the long wavelength tail of the dominant excited state for multimode dye-doped polymer optical fibers called side-illumination fluorescence (SIF) spectroscopy. We used two methods to characterize the linear absorption measured in the SIF experiment as a function of the wavelengths in the fluorescence band. When the point source model was used to characterize the absorption in multimode dye-doped PMMA fibers, we determined that the absorption was caused by the dye, instead of the host, further than 180 nm from the resonant absorption wavelength. From the SIF experiments, we determined that the linear absorption coefficient is an order of magnitude larger for saturation concentration squaraine-doped PMMA than neat PMMA and two orders of magnitude larger than deuterated PMMA at 830 nm. This result suggests that optical devices need to be optimized for wavelengths greater than 200 nm from resonance to take advantage of a low loss polymer host.

From the SIF experiment we also characterized the resonant excited state and some low lying states in several dye-doped fibers. The inhomogeneous-broadening model for electronic transitions was used in this characterization. From this analysis we learned that the propagation of light in the low concentration fibers is very similar to a plane wave. The fluorescence in high concentration fibers does not propagate like a plane wave; however, we can still estimate the absorption due to the resonant excited state. In addition, we determined that the dye molecules are not aggregating up to and including the saturation concentration for HSQ, PSQ, and TSQ dye-doped polymer optical fibers.

However, in ISQ-doped fibers we determined that at higher concentrations an aggregate state develops in the 770 -790 nm range. This state is located in the same spectral region as the J-aggregate state for squaraine doped Langmuir-Blodgett thin films. The ISQ/PMMA fibers are very inhomogeneous, in terms of concentration. Different sections of the same fiber have very different fluorescence intensity and absorption profiles. Therefore ISQ is not a good candidate for optical devices.

The SiPc/PMMA copolymer fibers exhibit some of the most interesting behavior. We determined that different incident wavelength sources excited different SIF spectra. The absorption of the different spectra are equivalent, within experimental uncertainty, which tells us that the difference in the fluorescence intensity at a specific position is caused by the excitation of different excited states. We determined the relative quantum yield of the fluorescence for each excitation wavelength for all the wavelengths in the SIF spectrum and the integrated relative quantum yield as a function of incident wavelength. The integrated relative quantum yield shows that there is an additional excited state near 695 nm which contributes to the fluorescence when the SiPc/PMMA copolymer fiber is excited between 693 and 713 nm. In the future, the relative quantum yield analysis of SIF data can be used to determine the most efficient excitation wavelength for fiber lasers.

We determined, from the linear absorption results, that the IB model for electronic transitions characterizes the excited state manifold much better than the Lorentzian model. Because of this result, we extended the IB model to third-order responses. We developed a third-order IB model for three $\chi^{(3)}$ processes: third harmonic generation, the quadratic electrooptic effect, and the optical Kerr effect. The IB model for the quadratic electrooptic effect was compared to QEA data from ISQ/PMMA and SiPc/PMMA, and the standard Lorentzian model.

From these comparisons, we determined that the IB model characterizes the QEA resonance response better than the Lorentzian model for both ISQ/PMMA and SiPc/PMMA thin films. The IB analysis of the ISQ/PMMA data shows that there is a two-photon state at approximately 593 nm in addition to the one-photon states characterized in the linear absorption analysis, and possibly of a second two-photon state near 370 nm. The data is characterized slightly more accurately when the two-photon state near 370 nm is

neglected but its inclusion is reasonable when the transition moment of the two-photon state at 370 nm is less than 5.0 D. This high-lying state has been found to be crucial in a Lorentzian analysis of THG experiments on ISQ in $CHCl_3$, but its location and strength, to date, has not been determined with a high degree of accuracy [1]. In pump-probe optical Kerr effect measurements, Vigil also determined using a Lorentzian analysis that a similar two-photon state (370 nm, 7 D) is necessary to model the spectroscopic third-order response of ISQ in CCl_4 [2]. In terms of the ISQ/PMMA QEA data, the two-photon state at 593 nm plays a more important role in the nonlinear response than the high-lying (UV) two-photon state.

Figure 6.1 represents the energy levels of ISQ/PMMA systems studied in this dissertation. All the energy levels were determined using the IB model for electronic excitations. The two two-photon states (red) were determined using QEA spectroscopy on ISQ/PMMA thin-films, the lowest energy one-photon state (dashed-green) was determined using SIF spectroscopy, and the remaining three one-photon states (blue) were determined using linear absorption spectroscopy.

The SiPc/PMMA QEA results were also compared to the IB and Lorentzian theories. We determined that the manifold of one-photon states, determined from transmission spectroscopy, can not account for the QEA response when modeled with either theory. However, the addition of a two-photon state near 480 nm with a transition moment of about 6.8 D to the manifold of one-photon states can account for the QEA response of SiPc/PMMA when modeled with the IB theory. The Lorentzian model can not account for the QEA response even with the addition of the two-photon state. It should be noted that 480 nm was not probed directly in the QEA experiment, so the two-photon state could be located at a shorter wavelength than 480 nm. If this is the case, reorientational effects need to be modeled to predict the QEA response. Because there has been no previous nonlinear spectroscopic studies of SiPc, to our knowledge, we settle on 480 nm as the location of the two-photon state until future experiments can probe this region directly.

Figure 6.2 represents the energy levels of SiPc/PMMA systems studied in this dissertation. As with ISQ/PMMA, the energy levels were determined using the IB model

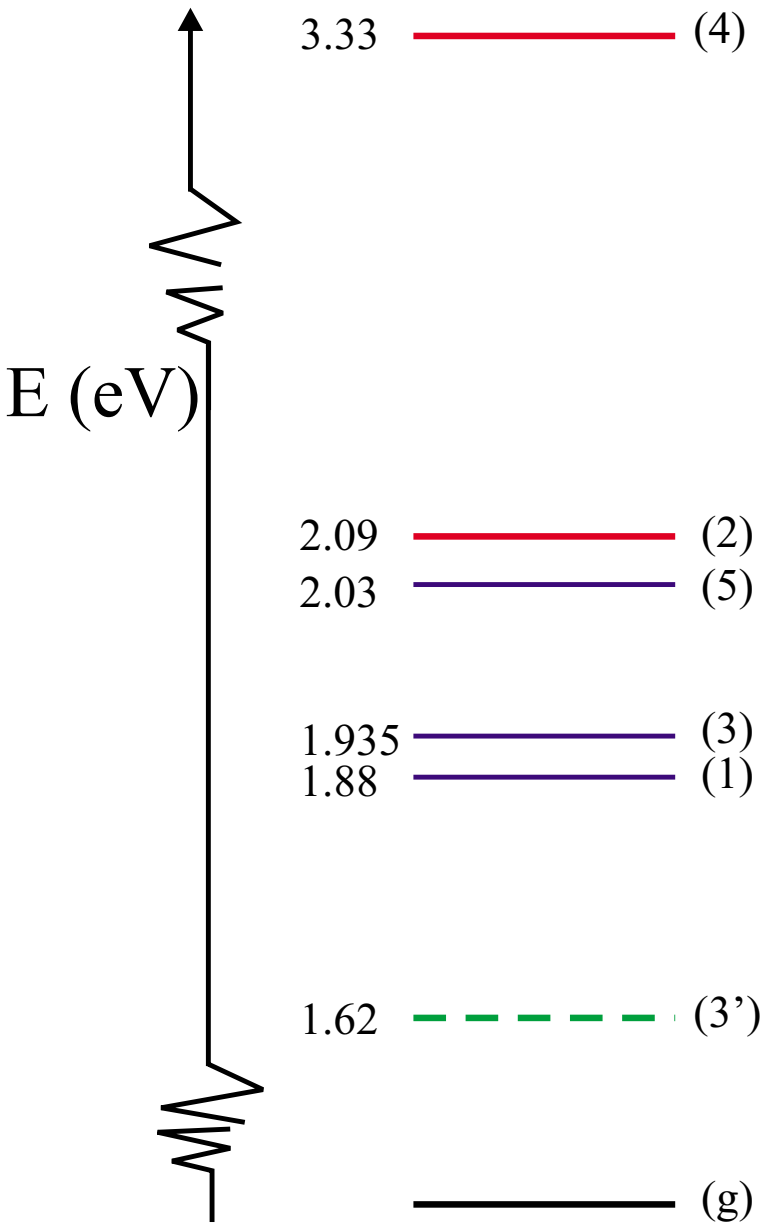

Fig. 6.1: Energy level diagram for ISQ/PMMA. The dashed-green states were determined using SIF spectroscopy, the blue states were determined using linear absorption spectroscopy, and the red states were determined using QEA spectroscopy. Each number on the right-hand-side of the energy level diagram corresponds to the state as tabulated in Chapter 5, and g refers to the ground state.

for electronic excitations. The two-photon state (red) was determined using QEA spectroscopy on SiPc/PMMA thin-films, the two lowest energy one-photon states (dashed-

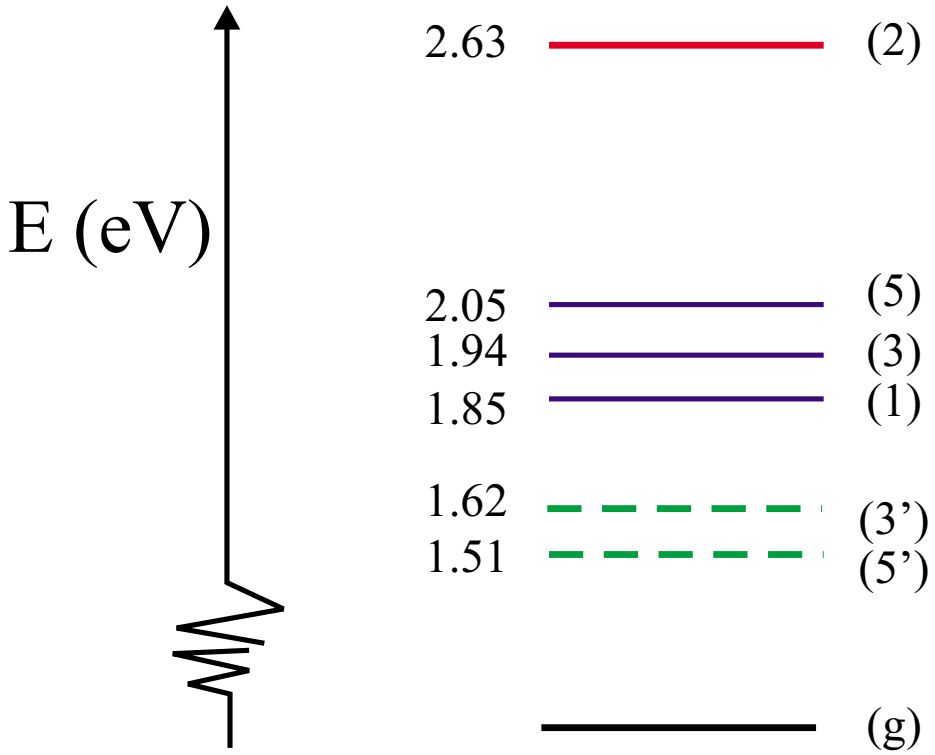

Fig. 6.2: Energy level diagram for SiPc/PMMA. The dashed-green states were determined using SIF spectroscopy, the blue states were determined using linear absorption spectroscopy, and the red states were determined using QEA spectroscopy. Each number on the right-hand-side of the energy level diagram corresponds to the state as tabulated in Chapter 5, and g refers to the ground state.

green) were determined using SIF spectroscopy on SiPc/PMMA copolymer fiber, and the remaining three one-photon states (blue) were determined using linear absorption spectroscopy on bulk preform slices.

We have shown that in combination linear absorption, SIF, and QEA spectroscopy can be used to measure the manifold of one- and two-photon states of dye-doped polymer systems. In addition, we developed a third-order inhomogeneous-broadening (IB) model which can be used to predict the QEA response of dye-doped thin films more accurately than the standard Lorentzian theory.

Bibliography

[1] J. H. Andrews, J. D. V. Karydarov, K. D. Singer, D. L. Hull, and K. C. Chuang, "Characterization of excited states of centrosymmetric and noncentrosymmetric squaraines by third-harmonic spectral dispersion," J. Opt. Soc. B **12**, 2360–2371 (1995).

[2] S. R. Vigil, "Nonlinear optical studies of organic liquids and polymer optical fibers," Ph. D. dissertation (Washington State University, Pullman, WA, 2000).

Appendix A

Third-Order Inhomogeneous-Broadening Energy Denominators

In this appendix we show a couple examples of expanded Lorentzian energy denominators for the optical Kerr effect. This should help the reader follow the transformations from the Lorentzian to IB model which were discussed in Chapter 2. The two Kerr experiments we discuss are the intensity dependent refractive index – where there is one incident wavelength on the sample, and the pump-probe experiment – where there are two specific incident wavelengths on the sample.

A.1 Intensity Dependent Refractive Index

The long version of $D_{ll}^{L}(-\omega;\omega,-\omega,\omega)$, which is an intermediary step in the transformation from the Lorentzian model to the IB model for third-order electronic transitions, is:

$$
\begin{aligned}
&D_{ll}^{L}(-\omega;\omega,\omega,-\omega) = \\
&\quad\left\{\frac{1}{(\omega_{gl}-i\Gamma_{gl}-\omega)^3}+\frac{1}{(\omega_{gl}+i\Gamma_{gl}+\omega)^3}\right. \\
&\quad\left.+\left[\frac{2\Gamma_{gl}^2-\omega^2+2i\Gamma_{gl}\omega}{4\Gamma_{gl}^2\omega^2}\right]\left[\frac{1}{\omega_{gl}-i\Gamma_{gl}+\omega}+\frac{1}{\omega_{gl}+i\Gamma_{gl}-\omega}\right.\right.
\end{aligned}
$$

$$-\frac{1}{\omega_{gl}-i\Gamma_{gl}-\omega}-\frac{1}{\omega_{gl}+i\Gamma_{gl}+\omega}\Bigg]$$
$$+\left[\frac{2i\Gamma_{gl}+\omega}{2i\Gamma_{gl}\omega}\right]\left[\frac{1}{(\omega_{gl}-i\Gamma_{gl}-\omega)^2}-\frac{1}{(\omega_{gl}+i\Gamma_{gl}+\omega)^2}\right]\Bigg\}. \tag{A.1}$$

The Lorentzian energy denominator for the intensity dependent refractive index experiment which involves two one-photon states has the following expanded form:

$$\begin{aligned}
&D^L_{ln}(-\omega;\omega,\omega,-\omega)= \\
&\quad\frac{1}{(\omega_{gl}-i\Gamma_{gl}-\omega)^2}\left[\frac{1}{(\omega_{gn}-i\Gamma_{gn}-\omega)}+\frac{1}{(\omega_{gn}-i\Gamma_{gn}+\omega)}\right] \\
&\quad+\frac{1}{(\omega_{gl}+i\Gamma_{gl}+\omega)^2}\left[\frac{1}{(\omega_{gn}+i\Gamma_{gn}+\omega)}+\frac{1}{(\omega_{gn}+i\Gamma_{gn}-\omega)}\right] \\
&\quad+\frac{1}{2i\Gamma_{gn}}\left[\frac{1}{\omega_{gn}-i\Gamma_{gn}-\omega}+\frac{1}{\omega_{gn}-i\Gamma_{gn}+\omega}-\frac{1}{\omega_{gn}+i\Gamma_{gn}-\omega}-\frac{1}{\omega_{gn}+i\Gamma_{gn}+\omega}\right]\times \\
&\qquad\left[\frac{1}{\omega_{gl}-i\Gamma_{gl}-\omega}+\frac{1}{\omega_{gl}+i\Gamma_{gl}+\omega}\right] \\
&\quad+\frac{1}{2(\omega+i\Gamma_{gn})}\left[\frac{1}{\omega_{gn}-i\Gamma_{gn}-\omega}-\frac{1}{\omega_{gn}+i\Gamma_{gn}+\omega}\right]\times \\
&\qquad\left[\frac{1}{\omega_{gl}-i\Gamma_{gl}+\omega}+\frac{1}{\omega_{gl}+i\Gamma_{gl}-\omega}\right] \\
&\quad+\frac{1}{2\omega}\left\{\frac{1}{(\omega_{gn}-i\Gamma_{gn}-\omega)}\left[\frac{1}{(\omega_{gl}-i\Gamma_{gl}-\omega)}-\frac{1}{(\omega_{gl}-i\Gamma_{gl}+\omega)}\right]+\right. \\
&\qquad\left.\frac{1}{(\omega_{gn}+i\Gamma_{gn}+\omega)}\left[\frac{1}{(\omega_{gl}+i\Gamma_{gl}-\omega)}-\frac{1}{(\omega_{gl}+i\Gamma_{gl}+\omega)}\right]\right\}.
\end{aligned} \tag{A.2}$$

A.2 Pump-Probe

In this section we show three Lorentzian energy denominators in expanded form. The first two involve only one-photon states, and the third involves a one-photon state and a two-photon state. The expanded Lorentzian energy denominator that accounts for one one-photon state has the following form for the pump-probe experiment:

$$\begin{aligned}
&D^L_{ll}(-\omega_1;\omega_1,\omega_2,-\omega_2)=2\times \\
&\quad\left\{\frac{2\,\omega_1}{(\omega_1+\omega_2)(\omega_1-\omega_2)}\left[\frac{1}{(\Omega_{gl}-\omega_1)^2}-\frac{1}{(\Omega^*_{gl}+\omega_1)^2}\right]+\right. \\
&\quad\left.\frac{2(\omega_1^4-2\,\omega_1^2\,\omega_2^2+\omega_2^4+2i\Gamma^2_{gl}\omega_1^2+6\Gamma^2_{gl}\omega_2^2-8i\Gamma_{gl}\omega_1\omega_2^2)}{(\omega_1+\omega_2)^2(\omega_1-\omega_2)^2(\omega_1+\omega_2+2i\Gamma_{gl})(\omega_1-\omega_2+2i\Gamma_{gl})}\left[\frac{1}{\Omega_{gl}-\omega_1}+\frac{1}{\Omega^*_{gl}+\omega_1}\right]+\right.
\end{aligned}$$

$$\frac{(\omega_2^3-\omega_1\omega_2^2+3i\Gamma_{gl}\omega_2^2-i\Gamma_{gl}\omega_1\omega_2-3\Gamma_{gl}^2\omega_2+\Gamma_{gl}^2\omega_1)}{i\Gamma_{gl}\omega_2(\omega_1-\omega_2)^2(\omega_1+\omega_2+2i\Gamma_{gl})}\left[\frac{1}{\Omega_{gl}-\omega_2}+\frac{1}{\Omega_{gl}^*+\omega_2}\right]+$$
$$\frac{(\omega_2^3+\omega_1\omega_2^2-3i\Gamma_{gl}\omega_2^2-i\Gamma_{gl}\omega_1\omega_2-3\Gamma_{gl}^2\omega_2-\Gamma_{gl}^2\omega_1)}{i\Gamma_{gl}\omega_2(\omega_1+\omega_2)^2(\omega_1-\omega_2+2i\Gamma_{gl})}\left[\frac{1}{\Omega_{gl}+\omega_2}+\frac{1}{\Omega_{gl}^*-\omega_2}\right]\Bigg\}, \quad \text{(A.3)}$$

and the expanded Lorentzian energy denominator that accounts for two one-photon states is:

$$\begin{aligned}
&D_{ln}^L(-\omega_1;\omega_1,\omega_2,-\omega_2)= \\
&\quad\frac{1}{(\Omega_{gl}-\omega_1)^2}\left[\frac{1}{\Omega_{gn}-\omega_2}+\frac{1}{\Omega_{gn}+\omega_2}\right]+\frac{1}{(\Omega_{gl}^*+\omega_1)^2}\left[\frac{1}{\Omega_{gn}^*+\omega_2}+\frac{1}{\Omega_{gn}^*-\omega_2}\right]+ \\
&\quad\frac{1}{\omega_1-\omega_2+2i\Gamma_{gn}}\left[\frac{1}{\Omega_{gl}-\omega_2}+\frac{1}{\Omega_{gl}^*+\omega_2}\right]\times \\
&\qquad\left[\frac{1}{\Omega_{gn}-\omega_1}+\frac{1}{\Omega_{gn}+\omega_2}-\frac{1}{\Omega_{gn}^*-\omega_2}-\frac{1}{\Omega_{gn}^*+\omega_1}\right]+ \\
&\quad\frac{1}{\omega_1+\omega_2+2i\Gamma_{gn}}\left[\frac{1}{\Omega_{gl}+\omega_2}+\frac{1}{\Omega_{gl}^*-\omega_2}\right]\times \\
&\qquad\left[\frac{1}{\Omega_{gn}-\omega_2}+\frac{1}{\Omega_{gn}-\omega_1}-\frac{1}{\Omega_{gn}^*+\omega_2}-\frac{1}{\Omega_{gn}^*+\omega_1}\right]+ \\
&\quad\frac{1}{2i\Gamma_{gn}}\left[\frac{1}{\Omega_{gl}-\omega_1}+\frac{1}{\Omega_{gl}^*+\omega_1}\right]\times\left[\frac{1}{\Omega_{gn}+\omega_2}+\frac{1}{\Omega_{gn}-\omega_2}-\frac{1}{\Omega_{gn}^*-\omega_2}-\frac{1}{\Omega_{gn}^*+\omega_2}\right]+ \\
&\quad\frac{1}{\omega_1-\omega_2}\left\{\left[\frac{1}{\Omega_{gl}-\omega_1}-\frac{1}{\Omega_{gl}-\omega_2}\right]\times\left[\frac{1}{\Omega_{gn}-\omega_1}+\frac{1}{\Omega_{gn}+\omega_2}\right]+\right. \\
&\qquad\left.\left[\frac{1}{\Omega_{gl}^*+\omega_2}-\frac{1}{\Omega_{gl}^*+\omega_1}\right]\times\left[\frac{1}{\Omega_{gn}^*+\omega_1}+\frac{1}{\Omega_{gn}^*-\omega_2}\right]\right\}+ \\
&\quad\frac{1}{\omega_1+\omega_2}\left\{\left[\frac{1}{\Omega_{gl}-\omega_1}-\frac{1}{\Omega_{gl}+\omega_2}\right]\times\left[\frac{1}{\Omega_{gn}-\omega_1}+\frac{1}{\Omega_{gn}-\omega_2}\right]+\right. \\
&\qquad\left.\left[\frac{1}{\Omega_{gl}^*-\omega_2}-\frac{1}{\Omega_{gl}^*+\omega_1}\right]\times\left[\frac{1}{\Omega_{gn}^*+\omega_1}-\frac{1}{\Omega_{gn}^*+\omega_2}\right]\right\}. \qquad \text{(A.4)}
\end{aligned}$$

Finally, we state the expanded form of the Lorentzian energy denominator for the pump-probe experiment which accounts for the electronic response caused by one one-photon state and one two-photon state as follows:

$$\begin{aligned}
&D_{lml}^L(-\omega_1;\omega_1,\omega_2,-\omega_2)= \\
&\quad\left\{\frac{1}{(\Omega_{gl}-\omega_1)^2}\left[\frac{1}{\Omega_{gm}-\omega_1-\omega_2}+\frac{1}{\Omega_{gm}-\omega_1+\omega_2}\right]\right.
\end{aligned}$$

$$
\begin{aligned}
&+\frac{1}{(\Omega_{gl}^{*}+\omega_1)^2}\left[\frac{1}{\Omega_{gm}^{*}+\omega_1+\omega_2}+\frac{1}{\Omega_{gm}^{*}+\omega_1-\omega_2}\right]+\\
&\frac{1}{\omega_1-\omega_2+2i\Gamma_{gl}}\left\{\left[\frac{1}{\Omega_{gm}^{*}}+\frac{1}{\Omega_{gm}-\omega_1-\omega_2}\right]\left[\frac{1}{\Omega_{gl}-\omega_1}-\frac{1}{\Omega_{gl}^{*}-\omega_2}\right]\right.\\
&\qquad\left.+\left[\frac{1}{\Omega_{gm}}+\frac{1}{\Omega_{gm}^{*}+\omega_1+\omega_2}\right]\left[\frac{1}{\Omega_{gl}+\omega_2}-\frac{1}{\Omega_{gl}^{*}+\omega_1}\right]\right\}+\\
&\frac{1}{\omega_1+\omega_2+2i\Gamma_{gl}}\left\{\left[\frac{1}{\Omega_{gm}^{*}}+\frac{1}{\Omega_{gm}-\omega_1+\omega_2}\right]\left[\frac{1}{\Omega_{gl}-\omega_1}-\frac{1}{\Omega_{gl}^{*}+\omega_2}\right]\right.\\
&\qquad\left.+\left[\frac{1}{\Omega_{gm}}+\frac{1}{\Omega_{gm}^{*}+\omega_1-\omega_2}\right]\left[\frac{1}{\Omega_{gl}-\omega_2}-\frac{1}{\Omega_{gl}^{*}+\omega_1}\right]\right\}+\\
&\frac{1}{\omega_1-\omega_2}\left\{\left[\frac{1}{\Omega_{gm}}+\frac{1}{\Omega_{gm}-\omega_1-\omega_2}\right]\left[\frac{1}{\Omega_{gl}-\omega_1}-\frac{1}{\Omega_{gl}-\omega_2}\right]\right.\\
&\qquad\left.+\left[\frac{1}{\Omega_{gm}^{*}}+\frac{1}{\Omega_{gm}^{*}+\omega_1+\omega_2}\right]\left[\frac{1}{\Omega_{gl}^{*}+\omega_2}-\frac{1}{\Omega_{gl}^{*}+\omega_1}\right]\right\}+\\
&\frac{1}{2i\Gamma_{gl}}\left\{\left[\frac{1}{\Omega_{gm}^{*}+\omega_1-\omega_2}+\frac{1}{\Omega_{gm}-\omega_1-\omega_2}\right]\left[\frac{1}{\Omega_{gl}-\omega_2}-\frac{1}{\Omega_{gl}^{*}-\omega_2}\right]\right.\\
&\qquad\left.+\left[\frac{1}{\Omega_{gm}-\omega_1+\omega_2}+\frac{1}{\Omega_{gm}^{*}+\omega_1+\omega_2}\right]\left[\frac{1}{\Omega_{gl}+\omega_2}-\frac{1}{\Omega_{gl}^{*}+\omega_2}\right]\right\}+\\
&\frac{1}{\omega_1+\omega_2}\left\{\left[\frac{1}{\Omega_{gm}}+\frac{1}{\Omega_{gm}-\omega_1+\omega_2}\right]\left[\frac{1}{\Omega_{gl}-\omega_1}-\frac{1}{\Omega_{gl}+\omega_2}\right]+\right.\\
&\qquad\left.\left.\left[\frac{1}{\Omega_{gm}^{*}}+\frac{1}{\Omega_{gm}^{*}+\omega_1-\omega_2}\right]\left[\frac{1}{\Omega_{gl}^{*}-\omega_2}-\frac{1}{\Omega_{gl}^{*}+\omega_1}\right]\right\}\right\}. \qquad \text{(A.5)}
\end{aligned}
$$

Appendix B

Beam Diameter

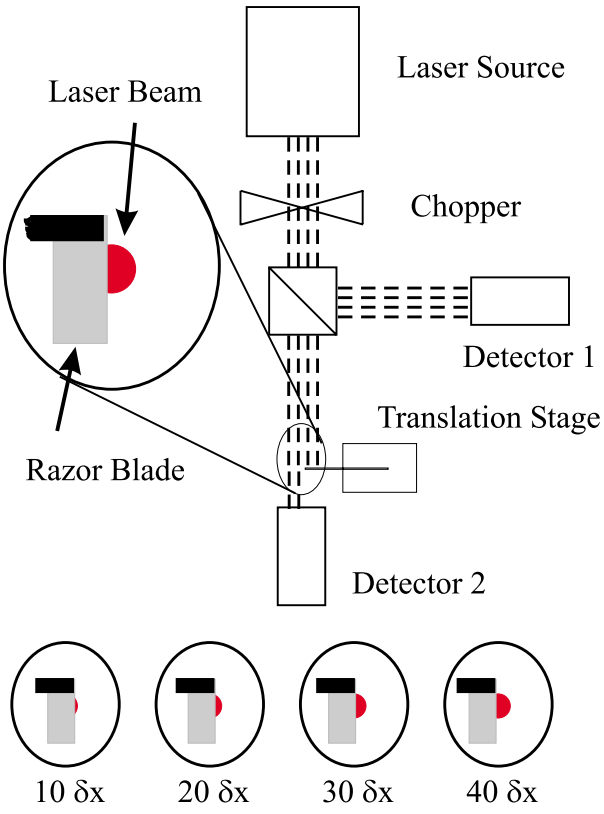

Fig. B.1: Knife-edge experiment to determine the beam diameter of a laser.

Let us define the photon flux transmitted through air as n. Normally, this photon flux is related to the absolute power, P, as follows:

$$\mathrm{n} = \frac{P}{\pi \frac{d^2}{4}}, \tag{B.1}$$

where d is the $1/e$ beam diameter (beam waist). We typically measure the power with a Coherent power meter and the beam diameter is measured in a knife-edge experiment (Figure B.1).

In the knife-edge experiment, the laser beam propagates through a chopper, to modulate the intensity, and is split with a 50/50 beam-splitter. This allows us to measure a reference intensity (detector 1) to account for power fluctuations, and a transmitted intensity with two lock-in amplifiers. Directly after the beam-splitter, a razor blade is mounted, vertically and perpendicular to the propagation direction of the laser beam, to an optical post. This post is mounted on a translation stage, which is controlled by a personal computer and translates the razor blade perpendicular to the propagation direction. At the beginning of the experiment the razor blade completely blocks the beam from reaching detector 2. The razor beam translates in increments across the beam until the entire beam illuminates detector 2. At each increment the computer records the intensity detected by the Thor Labs Si:1 detector. Thus we measure an intensity profile as a function of position.

The intensity profile can be fit to an error function to determine the $1/e$ beam diameter, where the error function is denoted by:

$$\mathrm{erf}(\frac{x - x_o}{x_w}) = \int_{-\infty}^{\frac{x-x_o}{x_w}} \exp(-t^2)dt. \tag{B.2}$$

The upper limit of integration is $(x - x_o)/x_w$, where x_o is the horizontal off-set in the data, x_w represents the $1/e$ beam diameter (width), and x is the measured position of the front edge of the razor blade. Since the error function goes has a range from -1 to 1, we calculate $2{\times}T(x)/T_{\max}(x) - 1$, where $\mathrm{T}(x) = I(x)/I_{\max}(x)$. This allows us to determine the beam diameter using a least-squares fitting routine, with x_w as the only parameter that is minimized in the fit.

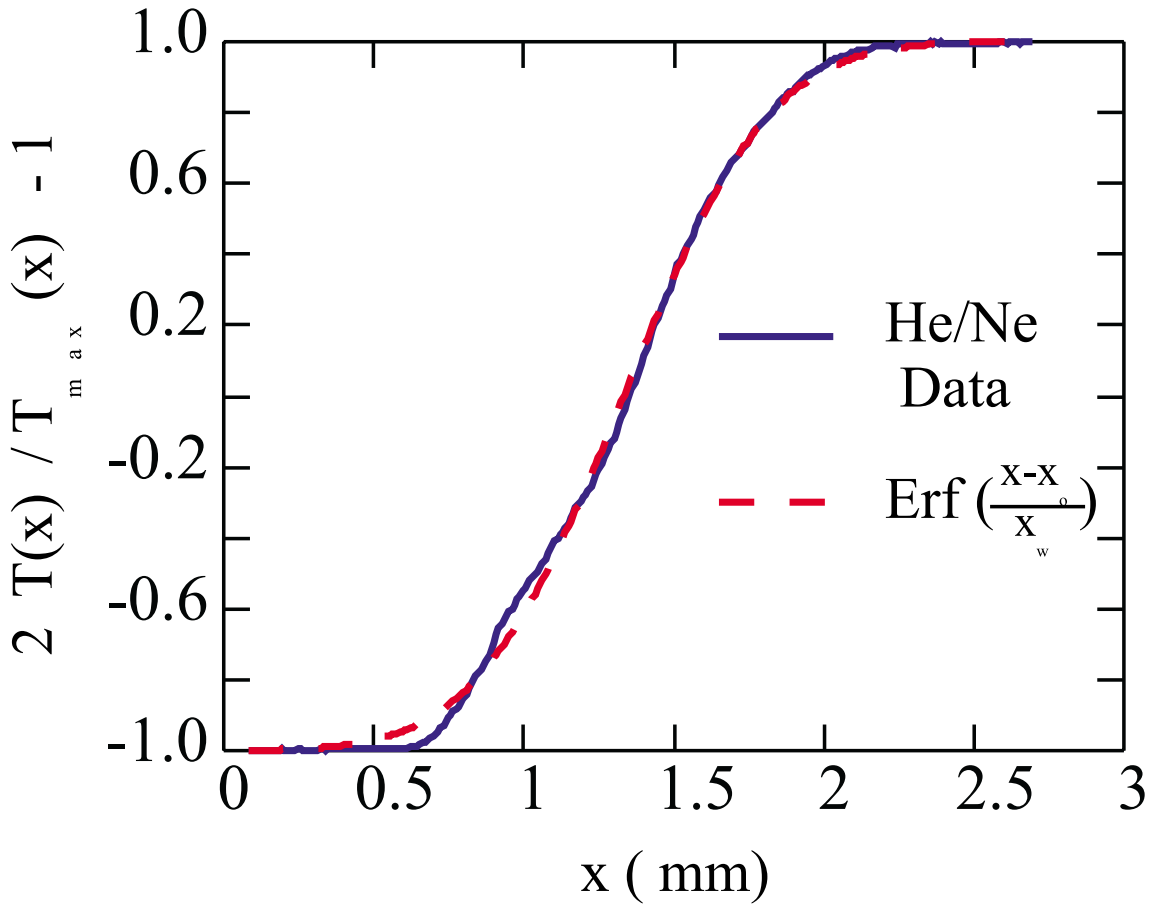

Fig. B.2: Knife-edge experimental data fit to an error function to determine the beam diameter of a laser.

Appendix C

Matlab Code

C.1 Quadratic Electrooptic Effect

This appendix shows the Matlab code for the four inhomogeneous-broadening energy denominator contributions to the microscopic third-order optical susceptibility. All four denominators must be used to construct a general n-level model of the third-order electronic response. (Note: The energy denominators for the other three third-order processes can be found in the $\chi^{(3)}$ directory of the Matlab code.)

C.1.1 $\mathbf{D}_{ll}(-\omega;\omega,0,0)$

```
function  value=Dll_woo(x,param1)
%%%%%%%%%%%%%%%%%%%%%%%%%%%%%%%%%%%%%%%%%%%%%%
%function  value=Dll_woo(x,param1)
% Written by Rob Kruhlak at Washington State
% University.
% Optimized this subroutine by creating variables
% so the ww_rjk function is only called as many
% times as necessary. This gives almost a factor
% of two increase in speed over D11_woo_old.m
%  modified 2-28-99
%
% Removed the third argument param2, since it is
% unnecessary and shoul not be need for compatibility any more.
% Last modified 1-10-00
% Removed the extra terms because they are zero.1/10/00
%%%%%%%%%%%%%%%%%%%%%%%%%%%%%%%%%%%%%%%%%%%%%%
```

```
omega_ev=x;
omega_ev_1g=param1(1);
gamn_ev_1g=param1(2);
gamo_ev_1g=param1(3);

aa=(1+2*(gamn_ev_1g./omega_ev).^2)./((omega_ev +2*i*gamn_ev_1g).^2);
bb=(omega_ev_1g - i*gamn_ev_1g -omega_ev)./gamo_ev_1g;
cc=(omega_ev_1g + i*gamn_ev_1g +omega_ev)./gamo_ev_1g;
dd=(omega_ev_1g + i*gamn_ev_1g)./gamo_ev_1g;
ee=(omega_ev_1g - i*gamn_ev_1g)./gamo_ev_1g;

bb_ex=0;
cc_ex=0;
dd_ex=0;
ee_ex=0;
% these terms are all zero as of 1/10/00
% see derivation for D11 qea page 4 second part.
W1pp1=WW_rjk(-bb);
W1mm1=WW_rjk(-cc);
W1m=WW_rjk(-dd);
W1p=WW_rjk(-ee);

value= 2*i*sqrt(pi)./(gamo_ev_1g).*...
     ( aa.*( W1pp1 + W1mm1) ... %term 1
     +2./(omega_ev.*gamo_ev_1g).*(bb.*W1pp1+bb_ex-cc.*W1mm1-cc_ex)...
         %term 2
     +2*i.*(gamn_ev_1g./omega_ev)./...
       ((omega_ev +2*i*gamn_ev_1g).*gamo_ev_1g).*...
           (dd.*W1m + dd_ex - ee.*W1p -ee_ex)... %term3
     -aa.*( W1m + W1p)...%term 4
    );
 % 12/23/99 removed the 1/3 from the expression for D11
 % since butcher and cotter define
 % the intrinsic permutation operator as the sum
 % of the distinct permutations not the
 % average. This differs from Mathis by who defines
 % it as the average of the distinct
 % permutations, but she does not use the 1/n!
 % which is common in physics.
```

C.1.2 $\mathbf{D}_{ln}(-\omega;\omega,0,0)$

```
function  value=Dln_woo(x,param1,param1p)
%%%%%%%%%%%%%%%%%%%%%%%%%%%%%%%%%%%%%%%%%%%%%%%%
% value=Dln_woo(x,param1,param1p)
% the p -> prime ( a second one-photon excited state)
% Written by Rob Kruhlak at Washington State
% University.
% Last modified 1/10/00
% set bbex to zero due to correction in the quadratic
% transform. See qea calc D11 page 4 second half.
% Note that this term did not effect the function anyway. 1/10/00
%%%%%%%%%%%%%%%%%%%%%%%%%%%%%%%%%%%%%%%%%%%%%%%%

omega_ev=x;

omega_ev_1g=param1(1);
gamn_ev_1g=param1(2);
gamo_ev_1g=param1(3);


omega_ev_1pg=param1p(1);
gamn_ev_1pg=param1p(2);
gamo_ev_1pg=param1p(3);

aa=(-pi)./(gamo_ev_1g.*gamo_ev_1pg);

bb=2*i./(sqrt(pi).*gamo_ev_1g);

bbex=0; % no correction due to the
        % lower limit of integration being finite 1/10/00
cc=(omega_ev_1g - i*gamn_ev_1g -omega_ev)./gamo_ev_1g;
dd=(omega_ev_1g + i*gamn_ev_1g +omega_ev)./gamo_ev_1g;
ee=(omega_ev_1g + i*gamn_ev_1g)./gamo_ev_1g;
ff=(omega_ev_1g - i*gamn_ev_1g)./gamo_ev_1g;
gg=(omega_ev_1pg + i*gamn_ev_1pg)./gamo_ev_1pg;
hh=(omega_ev_1pg - i*gamn_ev_1pg)./gamo_ev_1pg;

ii=(omega_ev_1pg - i*gamn_ev_1pg -omega_ev)./gamo_ev_1pg;
jj=(omega_ev_1pg + i*gamn_ev_1pg +omega_ev)./gamo_ev_1pg;

W1pp1=WW_rjk(-cc);
W1mm1=WW_rjk(-dd);
W1m=WW_rjk(-ee);
W1p=WW_rjk(-ff);
```

```
Wp1m=WW_rjk(-gg);
Wp1p=WW_rjk(-hh);
Wp1pp1=WW_rjk(-ii);
Wp1mm1=WW_rjk(-jj);

value=aa.*...
      ( Wp1p*((2*cc./gamo_ev_1g).*W1pp1 + bb +bbex) + ... %term 1
       Wp1m*((2*dd./gamo_ev_1g).*W1mm1 + bb -bbex) + ... %term 2
      (1./omega_ev).*( (W1m - W1mm1 ).*(Wp1mm1 + Wp1m) +... %term 3
                      (W1pp1 - W1p ).*(Wp1pp1 + Wp1p) ) + ...
      (1./(2*i*gamo_ev_1pg)).*( (W1pp1 + W1mm1 ).*(Wp1p + Wp1m) )+ ...
       %term 4
      (1./(omega_ev + 2*i*gamo_ev_1pg)).*...
           ( (Wp1p - Wp1m + Wp1pp1 - Wp1mm1).*(W1p + W1m ) ) ...
          );
```

C.1.3 $\mathbf{D}_{lml}(-\omega;\omega,0,0)$

```
function  value=Dlml_woo(omega_ev,param1, param2)
%%%%%%%%%%%%%%%%%%%%%%%%%%%%%%%%%%%%%%%%%%%%%%%
% value=Dlml_woo(omega_ev,param1, param2)
%
% Written by Rob Kruhlak at Washington State
% University.
% Optimized this subroutine by creating variables
% so the ww_rjk function is only called as many
% times as necessary. This gives almost a factor
% of 3.5 increase in speed over D121_woo_old.m
%
% Last modified 1/10/00
% set the extra terms to zero. See Dln_woo for explanation.1/10/00
%%%%%%%%%%%%%%%%%%%%%%%%%%%%%%%%%%%%%%%%%%%%%%%

omega_ev_1g=param1(1);
gamn_ev_1g=param1(2);
gamo_ev_1g=param1(3);

omega_ev_2g=param2(1);
gamn_ev_2g=param2(2);
gamo_ev_2g=param2(3);

aa=(-pi)./(gamo_ev_1g.*gamo_ev_2g);
% 12/23/99 --removed the factor of 1/3 so that
% the intrinic permuation operation is the sum
```

```
% of all distinct permutations (b&c)
% instead of the average( mathis)

bb=2*i./(sqrt(pi).*gamo_ev_1g);
cc=(omega_ev_1g - i*gamn_ev_1g -omega_ev)./gamo_ev_1g;
dd=(omega_ev_1g + i*gamn_ev_1g +omega_ev)./gamo_ev_1g;
ee=(omega_ev +2*i*gamn_ev_1g);

%cc_ex=-i./(pi).*(1./(cc - omega_ev_1g./gamo_ev_1g.^2));
%dd_ex=-i./(pi).*(1./(dd - omega_ev_1g./gamo_ev_1g.^2));
cc_ex=0;
dd_ex=0;
% this is due to a correction to the quadratic transform.
% see D11pwoo for explanation. 1/10/00
W1pp1=WW_rjk(-cc);
W1mm1=WW_rjk(-dd);
W2pp1=WW_rjk((-omega_ev_2g +i*gamn_ev_2g + omega_ev)./gamo_ev_2g);
W2mm1=WW_rjk((-omega_ev_2g -i*gamn_ev_2g - omega_ev)./gamo_ev_2g);
W1m=WW_rjk((-omega_ev_1g -i*gamn_ev_1g)./gamo_ev_1g);
W1p=WW_rjk((-omega_ev_1g +i*gamn_ev_1g)./gamo_ev_1g);
W2m=WW_rjk((-omega_ev_2g -i*gamn_ev_2g)./gamo_ev_2g);
W2p=WW_rjk((-omega_ev_2g +i*gamn_ev_2g)./gamo_ev_2g);

value= aa.*...
     ( W2pp1.*( 2.*cc./(gamo_ev_1g).*W1pp1 + bb + cc_ex)... %term 1
      + W2mm1.*(2.*dd./(gamo_ev_1g).*W1mm1 + bb + dd_ex)... %term 2
     + 2.*(1+i*gamn_ev_1g./omega_ev)./ee.* ...
         (W2pp1.*W1pp1 -W2mm1.*W1mm1)...   %term 3
     +(1+i*omega_ev./(2.*gamn_ev_1g))./omega_ev.* ...
         (W2mm1.*W1m - W2pp1.*W1p )... %term 4
     + 2*(1-i*omega_ev./(4.*gamn_ev_1g))./ee.* ...
         (W2mm1.*W1p - W2pp1.*W1m )... %term 5
     + 2*i.*(gamn_ev_1g./omega_ev)./ee.*...
         (W2m.*W1m - W2p.*W1p )... % term 6
     +(1./omega_ev).*...
         ( W2p.*W1pp1 - W2m.*W1mm1 )... %term 7
     + 1./ee.*...
        ( W2m.*W1pp1 - W2p.*W1mm1 ) ... %term 8
      );
```

C.1.4 $\mathbf{D}_{lmn}(-\omega;\omega,0,0)$

```
function  value=Dlmn_woo(omega_ev,param1, param2, param1p)
%%%%%%%%%%%%%%%%%%%%%%%%%%%%%%%%%%%%%%%%%%%%%%%%
% value=Dlmn_woo(omega_ev,param1, param2, param1p)
%
% Written by Rob Kruhlak at Washington State
% University. Created 3-1-99
%
% Last modified 12-23-99
%%%%%%%%%%%%%%%%%%%%%%%%%%%%%%%%%%%%%%%%%%%%%%%%

omega_ev_1g=param1(1);
gamn_ev_1g=param1(2);
gamo_ev_1g=param1(3);

omega_ev_2g=param2(1);
gamn_ev_2g=param2(2);
gamo_ev_2g=param2(3);

omega_ev_1pg=param1p(1);
gamn_ev_1pg=param1p(2);
gamo_ev_1pg=param1p(3);

aa=-(pi).^(3/2)./(gamo_ev_1g.*gamo_ev_2g.*gamo_ev_1pg);
% 12/23/99 --removed the factor of 1/3 so that
% the intrinic permuation operation is the sum
% of all distinct permutations (b&c)
% instead of the average( mathis)


bb=(omega_ev_1g - i*gamn_ev_1g - omega_ev)./gamo_ev_1g;
cc=(omega_ev_1g + i*gamn_ev_1g + omega_ev)./gamo_ev_1g;
dd=(omega_ev_1g + i*gamn_ev_1g)./gamo_ev_1g;

ee=(omega_ev_2g - i*gamn_ev_2g - omega_ev)./gamo_ev_2g;
ff=(omega_ev_2g + i*gamn_ev_2g + omega_ev)./gamo_ev_2g;
gg=(omega_ev_2g - i*gamn_ev_2g)./gamo_ev_2g;
hh=(omega_ev_2g + i*gamn_ev_2g)./gamo_ev_2g;

ii=(omega_ev_1pg - i*gamn_ev_1pg - omega_ev)./gamo_ev_1pg;
jj=(omega_ev_1pg + i*gamn_ev_1pg + omega_ev)./gamo_ev_1pg;
kk=(omega_ev_1pg - i*gamn_ev_1pg)./gamo_ev_1pg;

W1pp1=WW_rjk(-bb);
```

```
W1mm1=WW_rjk(-cc);
W1m=WW_rjk(-dd);

W2pp1=WW_rjk(-ee);
W2mm1=WW_rjk(-ff);
W2p=WW_rjk(-gg);
W2m=WW_rjk(-hh);

Wp1pp1=WW_rjk(-ii);
Wp1mm1=WW_rjk(-jj);
Wp1p=WW_rjk(-kk);

value= aa.*...
     ( W1pp1.*( W2pp1.*(Wp1pp1 + Wp1p) +... %term 1
                W2p.*Wp1p) +...
       W1m.*(W2pp1.*( Wp1pp1 + Wp1p ) +... %term 2
             W2mm1.*( Wp1p + Wp1mm1 ) +...
             W2m.*(Wp1pp1 + Wp1mm1 ) ) +...
       W1mm1.*( W2mm1.*( Wp1p + Wp1mm1 ) + ... %term 3
                W2p.*Wp1p) );
```

Appendix D

Two-photon Absorption

D.1 Theory

When the incident intensity is large nonlinear absorption can occur. For third-order materials the absorption coefficient can be expanded to first-order in the intensity to account for the nonlinear absorption. From the introduction we restate Equation (1.4),

$$\alpha = \alpha_o + \alpha_2 I, \tag{D.1}$$

where α_0 is the linear absorption coefficient, and α_2 is the two photon absorption (TPA) coefficient. The differential equation which describes α is typically written in terms of the intensity as follows,

$$\frac{dI(z)}{dz} = -\alpha I(z) \tag{D.2}$$

Substituting Equation (D.1) into Equation (D.2) we get the standard differential equation that describes both linear and two-photon absorption,

$$\frac{dI(z)}{dz} = -\alpha_0\, I(z) - \alpha_2\, I^2(z). \tag{D.3}$$

If we have a fiber of length L and we can couple a fraction of the incident intensity C_1 into the core fiber and a capture a fraction C_2 of the output light at the output detector the solution to Equation (D.3) is:

$$I(L) = C_1\, C_2\, I_0\, \frac{\exp(-\alpha_0\, L)}{1 + C_1\, I_0\, \alpha_2 L_{eff}}, \tag{D.4}$$

where I_0 is the intensity at $z = 0$, and the effective length is,

$$L_{eff} = \frac{1 - \exp(-\alpha_0 L)}{\alpha_0}. \tag{D.5}$$

Equation (D.4) tells us that as the incident intensity becomes large the transmitted intensity will no longer be proportional to the incident intensity. Since the $\alpha_2 I$ is typically smaller than unity, the denominator can be expanded in a power series as follows,

$$I(L) = C_1 C_2 I_0 \exp(-\alpha_0 L) - C_1 I_0^2 \alpha_2 L_{eff} \exp(-\alpha_0 L). \tag{D.6}$$

Equation (D.6) tells us that there will be both a linear and quadratic dependence on the incident intensity where there is the intensity is large enough.

Section D.2 describes the transverse two-photon absorption measurement for core fibers. To understand the results of this experiment, Section D.2, we need to relate the two-photon absorption coefficient, α_2, to the third-order susceptibility, and linear absorption coefficient to the linear susceptibility. In the process we will also so define the relation between the intensity dependent refractive index and the third order susceptibility.

For dye-doped core fibers we approximate the system as 1-D and centrosymmetric because there are too many modes to do a modal analysis. Therefore Equation (2.6) for the Fourier amplitudes from Section 2 can be reduced to the following,

$$-\frac{d^2 E_\omega(z)}{dz^2} = \frac{\omega^2}{c^2} E_\omega(z) + \mu_0 \omega^2 P_\omega(z). \tag{D.7}$$

The polarization amplitude can be specified out to third-order from Equation (2.10),

$$\begin{aligned} P_\omega(z) &= P_\omega^{(1)}(z) + P_\omega^{(3)}(z) \\ &= \epsilon_o(\chi^{(1)}(-\omega;\omega)E_\omega(z) + K_3\chi^{(3)}(-\omega;\omega,\omega,-\omega)E_\omega(z)E_\omega(z)E_{-\omega}(z)), \end{aligned} \tag{D.8}$$

where $K_3 = K(-\omega;\omega,\omega,-\omega)$, and we have neglected the tensor nature of the first- and third-order susceptibilities since there is only one tensor component for the 1-D system.

The transverse two-photon absorption experiment will only be performed at 1064 nm, so the frequency arguments of the first- and third-order susceptibilities, and the Fourier amplitudes will be dropped for the remainder of the derivation. (Note that $E_{-\omega} = E_\omega^*$

was substituted before dropping the frequency subscripts). Therefore Equation (D.7) can be simplified to the following,

$$-\frac{d^2E(z)}{dz^2} - \frac{\omega^2}{c^2}\left(1 + \chi^{(1)} + K_3\chi^{(3)}|E|^2\right)E(z) = 0. \tag{D.9}$$

Equation (D.9) has been reduced to a linear equation in the electric field amplitude which we are familiar with from linear optics. Therefore the wavevector, k, is related to the first- and third-order susceptibilities as follows,

$$k = \frac{\omega}{c}(\epsilon_r + K_3\chi^{(3)}|E|^2)^{\frac{1}{2}}, \tag{D.10}$$

where the relative permittivity is $\epsilon_r = 1 + \chi^{(1)}$.

Since $\chi^{(3)}$ is much smaller than the linear contribution to the right-hand-side of Equation D.10, a Taylor series expansion to second order result in the following,

$$k = \frac{\omega n_o}{c} + \frac{\omega}{\epsilon_o c^2}\frac{K_3\chi^{(3)}I}{n_o n_{o_R}}, \tag{D.11}$$

where the linear index of refraction is defined as $n_o = \sqrt{1 + \chi^{(1)}}$, n_{o_R} is the real part of the linear index of refraction, and the intensity is defined as $I = 1/2\epsilon_o c n_{o_R}|E|^2$.

When the material being studied absorbs some of the incident light, the wavevector has both real and imaginary parts and is written as [1],

$$k = \beta + i\frac{\alpha}{2} \tag{D.12}$$

where the factor of $1/2$ is used so that α describes the absorption of the intensity. The right-hand-side of Equation (D.11) is more difficult to separate because, in general, both susceptibilities have real and imaginary parts,

$$\chi^{(1)} = \chi_R^{(1)} + i\chi_I^{(1)} \tag{D.13}$$

and

$$\chi^{(3)} = \chi_R^{(3)} + i\chi_I^{(3)}. \tag{D.14}$$

Assuming $\chi_R^{(3)} \gg \chi_I^{(3)}$, the real part of the wavevector becomes,

$$\beta = \frac{\omega}{c}n_{o_R} + \frac{\omega K_3\chi_R^{(3)}}{\epsilon_o c n_{o_R}^2}I. \tag{D.15}$$

When $\beta = \beta_0 + \beta_2 I$ the linear and nonlinear contributions can be separated as follows,

$$\beta_0 = \frac{\omega}{c} n_{o_R}, \tag{D.16}$$

and

$$\beta_2 = \frac{\omega K_3 \chi_R^{(3)}}{\epsilon_o c n_{o_R}^2} = \frac{\omega}{c} n_{2_R}, \tag{D.17}$$

where the intensity dependent refractive index is defined as,

$$n_2 = \frac{3\chi^{(3)}}{4\epsilon_o c\, n_{o_R}^2}, \tag{D.18}$$

because $K_3 = 3/4$.

The absorption coefficient can also be related to the imaginary part of Equation D.11 as follows,

$$\alpha = \alpha_0 + \alpha_2 I = \frac{2\omega}{c} n_{o_R} + \frac{2\omega K_3 \chi_I^{(3)}}{\epsilon_o c^2\, n_{o_R}^2} I, \tag{D.19}$$

where it has been assumed that $\chi_I^{(3)} n_{oR} \gg \chi_R^{(3)} n_{oI}$ Therefore the linear absorption coefficient is,

$$\alpha_0 = \frac{2\omega}{c} n_{o_I}, \tag{D.20}$$

and the two-photon absorption coefficient is related to the imaginary part of $\chi^{(3)}$ as follows,

$$\alpha_2 = \frac{3\omega \chi_I^{(3)}}{2\epsilon_o c^2\, n_{o_R}^2}. \tag{D.21}$$

D.2 Transverse two-photon absorption

In the previous section, a laser source illuminated a dye-doped core fiber from the side to generate a fluorescence spectrum that propagated inside the fiber to either end where it could be detected using a spectrometer. For the transverse two-photon absorption experiment we become a little more traditional. The core fiber is illuminated, as it should be, along its fiber axis as shown in Figure D.2. However, the detector is not positioned at the end of the fiber. Instead it is positioned transverse to the fiber axis to monitor the light which is scattered out of the fiber transverse to the fiber axis. This is the same configuration used for the transverse loss experiment [2]. In both experiments it is

assumed that the scattered intensity, measured by the transverse detector, is proportional to the intensity inside the fiber at that position.

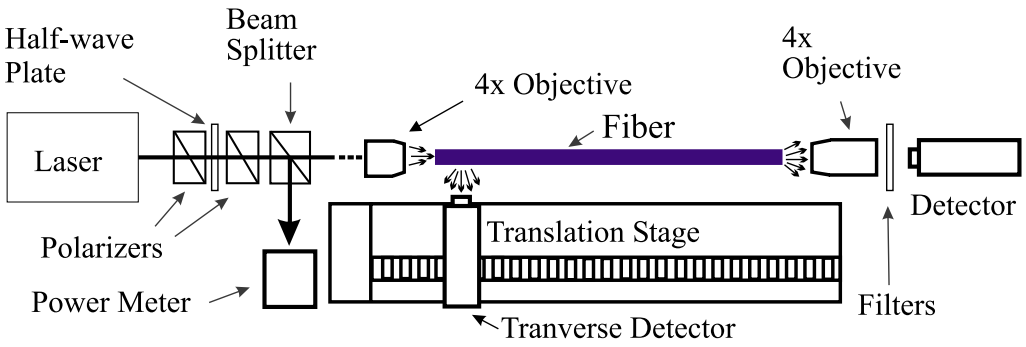

Fig. D.1: The transverse two-photon absorption experiment.

Unlike the transverse loss experiment, this experiment requires a high powered pulsed laser system so that the photon flux is large enough for two-photon absorption to be observed. A Continuum 40 picosecond pulse width, 20 Hz repetition rate, Nd:YAG laser at 1.064 μm is used for this purpose but any high powered pulsed laser system can potentially be used.

To determine the TPA coefficient of core fibers the transverse detector is positioned at a location where TPA will be the largest. This position is the 1/e length of the fiber or where the incident intensity has fallen to 1/e of its magnitude. Figure D.2a shows a plot of the transmitted intensity as a function of propagation distance for a system where only linear absorption occurs and one where both linear and TPA absorption occurs. The largest difference between the two curves occurs at the 1/e length of the fiber.

With the detector in position, the incident intensity is increased to about 30 % below the damage threshold of the polymer then it is decreased to it initial value. During this cycle both the incident intensity and the scattered intensity are averaged over 100 pulses and recorded for each incident intensity. The incident intensity is controlled by rotating a $\lambda/2$ plate in between two crossed-polarizers to minimize beam walk. Note that the core fibers are have a very large diameter ≈ 800 μm making them extremely multimode. Therefore it is not difficult to couple the laser beam into the fiber unlike single-mode fibers [3]. The TPA coefficient can then be determined if scattered intensity has a the

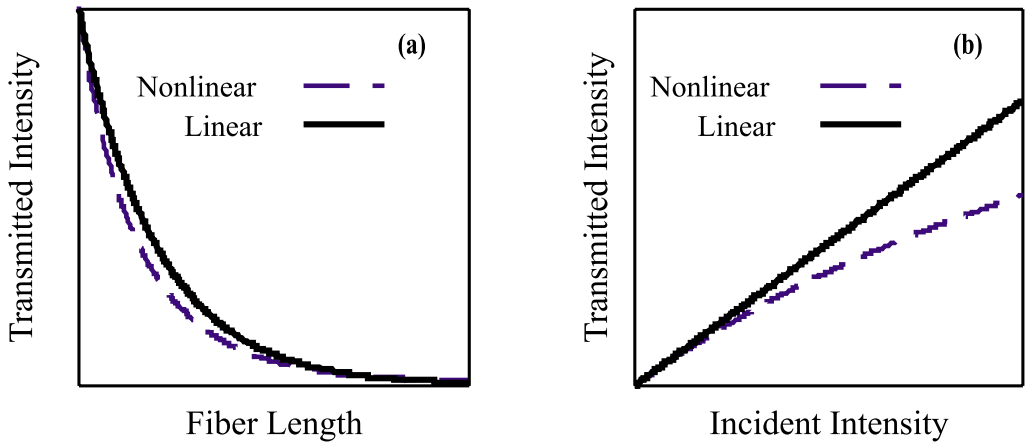

Fig. D.2: Transmitted intensity as a function of fiber length and incident intensity. The solid lines indicate the linear regime and the dashed lines indicate the nonlinear regime.

quadratic dependence of the incident intensity (see Section D.1).

Arguably the most important benefit of positioning the detector transverse to the fiber axis is that the need for complicated filtering schemes is eliminated. When the detector is placed at the end of the fiber the transmitted signal overloads the detector unless filters are used to decrease its magnitude. Once filters are introduced into the experiment they must also be characterized in terms of their two-photon absorption coefficients as well. However, the intensity scattered transverse to the fiber axis is much smaller and allows at least a couple orders of magnitude variation in the incident intensity to be measured will out filters. This range of incident intensities is sufficient to determine if the TPA coefficient is measureable or not.

Bibliography

[1] J. D. Jackson, *Classical Electrodynamics*, 2 ed. (Wiley, 1975).

[2] R. J. Kruhlak, J. Young, and M. G. Kuzyk, "Loss and correlation measurements in squaraine-doped nonlinear polymer optical fibers," SPIE Proc. **3147**, 118–28 (1997).

[3] D. W. Garvey, "Nonlinear optics in polymer fibers," Ph. D. dissertation (Washington State University, Pullman, WA, 1999).